INSTITUTO SUPERIOR DE ENGENHARIA DE LISBOA

Department of Mechanical Engineering

ISEL



Mechanical Behaviour of Adaptive Structures

DIOGO MIGUEL SILVA COSTA
(B.Sc. in Mechanical Engineering)

Master's Thesis submitted for the degree of
M.Sc. in Mechanical Engineering

Supervisor:
Maria Amélia Ramos Loja, Ph.D.

Jury:

President:	João Manuel Ferreira Calado, Ph.D.
Vogues:	Aurélio Lima Araújo, Ph.D.
	Maria Amélia Ramos Loja, Ph.D.

December 2016

COPYRIGHT © 2016
DIOGO MIGUEL SILVA COSTA
ALL RIGHTS RESERVED

To my dear parents and girlfriend...

Acknowledgements

For the past four or five years I have been a committed and hard working student. I am happy for being able to accomplish the majority of my academic/professional goals during B.Sc. and M.Sc. However, that was only possible because I have the best parents in the world, that support me everyday, no matter what. Their love, kindness and, of course, financial investment, helped me a lot in this journey. During certain times it was hard, but still it was possible to overcome the problems. I wish to thank to my parents, for everything, as well as my girlfriend, for the love, patience, motivation and comprehension. A special thank to my aunt Júlia, for loving me as a second mother.

I specially thank to my supervisor, professor Maria Amélia Ramos Loja, for all the constant motivation, support, availability and work opportunities. I had the privilege of working with her, almost in a daily basis, since the beginning of the M.Sc. and it was an experience, which I consider to be extremely relevant in my professional career! I will never forget the excellent person and teacher that she is. Thank you for everything!

I thank to professor Joaquim Infante Barbosa, also for all the support and advice along my journey in ISEL. Thank you very much!

I thank to professor João Manuel Ferreira Calado, and the previous people too, for giving me a chance in the research project I was member of, in their team. I learned a lot and it was an amazing opportunity to grow up as a person and researcher.

Thank you professor Mário Mendes for all the help and suggestions about sensors and actuators! and professor Afonso Leite for the Linux help, as well as teaching me a lot of MAPDL! and professor Tiago Silva for the LaTeX influence and template, as well as 3D printing!

I thank to all those professors of this institute, which helped me in a constructive way and taught me a big portion of what I know today.

Thank you ISEL Formula Student, as a project, all the people I met in the team that I was member of (and previous ones), as well as my Lab Monitor colleagues. Big friends and comrades for life!

Thank to all my true friends, for all the support and interest shown in my work. As well as, for sharing with me all those moments of fun, relaxation and friendship.

Agradecimentos

Durante os últimos quatro ou cinco anos tenho vindo a ser um estudante determinado e empenhado. Sinto-me feliz por ter conseguido atingir a maioria dos meus objectivos académicos/profissionais durante a Licenciatura e Mestrado. No entanto, isso apenas foi possível porque tenho os melhores pais do mundo, que me apoiam todos os dias, aconteça o que acontecer. O seu amor, bondade e, claro, investimento financeiro, ajudaram-me imenso neste percurso. Durante alguns momentos foi difícil, mas mesmo assim foi possível ultrapassar os problemas. Eu quero agradecer aos meus pais, por tudo, tal como à minha namorada, pelo amor, paciência, motivação e compreensão. Um agradecimento especial à minha tia Júlia, por me amar como uma segunda mãe.

Agradeço especialmente à minha orientadora, professora Maria Amélia Ramos Loja, por toda a constante motivação, apoio, disponibilidade e oportunidades de trabalho. Tive o privilégio de trabalhar com ela, quase todos os dias, desde o início do Mestrado e foi uma experiência que considero extremamente relevante na minha carreira profissional! Nunca esquecerei a excelente pessoa e professora que ela é. Obrigado por tudo!

Agradeço ao professor Joaquim Infante Barbosa, também por todo o apoio e aconselhamento durante a minha caminhada no ISEL. Muito obrigado!

Agradeço ao professor João Manuel Ferreira Calado, e também às pessoas anteriores, por me terem concedido a oportunidade de fazer parte da sua equipa, no projecto de investigação no qual participei. Aprendi bastante e foi uma óptima oportunidade para crescer como pessoa e investigador.

Obrigado professor Mário Mendes por toda a ajuda e sugestões sobre sensores e actuadores! tal como o professor Afonso Leite pelas dicas sobre Linux e por me ter ensinado tanto sobre MAPDL! também ao professor Tiago Silva pela influência e template LaTeX, assim como impressão 3D!

Agradeço a todos aqueles professores deste instituto, que me ajudaram construtivamente e me ensinaram uma grande parte daquilo que sei hoje.

Obrigado ISEL Formula Student, como projecto, a todas as pessoas que conheci na equipa da qual fiz parte (e anteriores) e aos meus colegas Monitores. Grandes amigos e camaradas para a vida!

Obrigado a todos os meus verdadeiros amigos, por todo o apoio e interesse demonstrado no meu trabalho. Assim como, por terem partilhado comigo todos aqueles momentos de diversão, descontracção e amizade.

Abstract

Adaptive structures constituted by composites and smart materials are a remarkable engineering combination that join together the already known composites' advantages, associated with ratios between (mechanical strength and stiffness)/weight and the possibility of actively controlling the mechanical response of a structure (e.g. by means of electronics, with sensors/actuators). These versatile structures are able to react and interact with their surrounding environments, continuously, to accomplish specific objectives. In this work, the main objective is to study, model and predict the mechanical behaviour of adaptive structures by programming the Finite Element Method and optimization algorithms based on micro-bats' echolocation capacity. An integrated symbolic-numerical-graphical package devoted to the analysis of plate/beam-type structures and its meta-heuristic optimization is implemented, with capabilities of simulating active multilayered structures, constituted by a variable number of different material models, ranging from hybrid functionally graded materials constituted by carbon nano-tubes to graded mixtures of piezoelectric particles and non-active materials. Several validation, parametric and optimization case studies are computed, for different types of structures and materials. The results obtained are compared, discussed and conclusions are drawn.

Keywords: adaptive structures; bat-inspired optimization; carbon nano-tubes; composite materials; finite element modelling; functionally graded materials; piezoelectricity.

Resumo

Estruturas adaptativas constituídas por materiais compósitos e materiais inteligentes é uma excelente combinação de engenharia, que junta as vantagens tão bem conhecidas dos compósitos, associadas a rácios entre (resistência mecânica e rigidez)/peso e a possibilidade de controlar activamente a resposta mecânica de uma estrutura (ex. através de electrónica, com sensores e actuadores). Estas estruturas versáteis são capazes de reagir e interagir com o seu meio envolvente, continuamente, para cumprirem determinados objectivos. Neste trabalho, o objectivo principal é estudar, modelar e prever o comportamento mecânico de estruturas adaptativas através da programação de algoritmos com Método dos Elementos Finitos e optimização baseada na capacidade de eco-localização dos micro-morcegos. Foi implementada uma plataforma simbólica-numérica-gráfica dedicada à análise de estruturas do tipo viga/placa, assim como a sua optimização meta-heurística, com capacidade de simular estruturas activas multi-camada, constituídas por um número variável de modelos de materiais, desde funcionais gradativos híbridos constituídos por nano-tubos de carbono até misturas gradativas de partículas piezoeléctricas e materiais passivos. Diversos casos de estudo de validação, paramétricos e optimização são desenvolvidos, para diferentes tipos de estruturas e materiais. Os resultados são obtidos, comparados, discutidos e as conclusões extraídas.

Palavras-chave: estruturas adaptativas; optimização inspirada em morcegos; nano-tubos carbono; materiais compósitos; modelação elementos finitos; materiais funcionais gradativos; piezoelectricidade.

List of Figures

1.1 Example of bio-inspired variable camber wing. From Nguyen (2014). 4
1.2 Example of adaptive structure, with sensor/actuator control. From Carrera et al. (2011). . 5
1.3 Example of shape morphing in adaptive airfoil. From Carrera et al. (2011). 5
1.4 Example of shape morphing in adaptive structure (airfoil-shaped wing). From Ermanni (2009). 5
1.5 Examples of smart materials and stimulus-response relation. From Soh, C.-K. et al. (2012). 7
1.6 Piezoelectric crystal lattice before (left) and after (right) polarization. From Carrera et al. (2011). 8
1.7 Electric dipoles when unpolarized (ferroelectric ceramic) (1), during (2) and after poling (piezoelectric ceramic) (3). From PI-Ceramic® (2016b). 9
1.8 Example of piezoelectric patches, DuraAct Patch Transducers. From PI-Ceramic® (2016a). 9
1.9 Scheme of composites classification. Adapted from Vepa (2010). 10
1.10 Example of composite resin (left) and long fibres (right). From Brigante (2014). 11
1.11 Airbus A350 materials overview. From Airbus (2013). 12
1.12 Examples of FGM variations in different structures' directions, for beams and plates. . . 13
1.13 Graded bimorph actuator with linear composition profile. From Takagi et al. (2002). . . . 14
1.14 Scanning Electron Microscopy (SEM) micrographs of each layer of the actuator in Figure 1.13, where (a) PZT/0 % Pt, (b) PZT/10 % Pt, (c) PZT/20 % Pt and (d) PZT/30 % Pt. From Takagi et al. (2002). 14
1.15 Classification of multi-materials according to the types, sizes and organizations of constituents. From Ferreira et al. (2016). 15
1.16 Carbon atom and its allotropes, including CNTs. From Rahmandoust and Ayatollahi (2016). 17
1.17 Bundles of CNTs. From Janocha (2007). 17
1.18 Process flowchart in engineering product design. From Liu and Quek (2014). 18
1.19 Comparison between experimental and simulation results, of a thin-walled, axially loaded, crash-absorbing section. From Wehrle (2015). 19
1.20 Example of car frame mesh created for FEM model. From Wehrle (2015). 20
1.21 Example of connecting rod's mesh used in FEM analysis, obtained with 3D Laser Scanning. From Costa et al. (2015c). 20
1.22 Example of frontal car crash simulation (explicit dynamics) results, before and after impact (mesh from Figure 1.20). Adapted from Wehrle (2015). 21
1.23 Several meshes using both beam and shell elements, inside the same FEM model (aerodynamic hybrid trailer) (AMAPDL). From Costa (2014); Costa and Barbosa (2015). 22
1.24 CFD velocity field results from the aerodynamic hybrid trailer in Figure 1.23 (SOLIDWORKS Flow Simulation®). From Costa (2014); Costa and Barbosa (2015). 22

1.25 Von Mises stress field around elliptical crack tips (AMAPDL). From Costa and Venâncio (2015). 23
1.26 Classification of some meta-heuristic algorithms. Adapted from Kaveh (2014). 26
1.27 Time-line of bio-inspired algorithms' development. Adapted from Kar (2016). 27
1.28 Paradigm of evolution of algorithms with increase of complexity of problems. Adapted from Kar (2016). 27
1.29 BA's convergence on *eggcrate* function (40 bats in the last 10 iterations). From Yang, X.-S. (2014). 28

2.1 Bending achieved in a prototype aircraft wing by heating of SMA strips. (a) Un-morphed and (b) morphed. From Ferreira et al. (2016). 35
2.2 Full-scale flight tests of SMA-actuated variable-geometry chevrons on a Boeing 777-300ER with GE-115B engines. Adapted from Sun et al. (2016). 36
2.3 BK117 S7045 flight test with active rotor trailing-edge flaps actuated by piezoelectric actuators. From Sun et al. (2016). 37
2.4 "*At last, a shape-morphing aircraft wing is here – no flaps*". From `https://www.youtube.com/watch?v=9ZpAHxMj5lU`. Please click 2 times on the button above this caption to start the video. After clicking the video use Spacebar (play/pause), Home / End (go to start/end), ← / → (seek backwards/forwards) and m (mute/unmute). . 38
2.5 "*Morphing automotive wing*". Please notice the red arrows region in the video wing. From `https://www.youtube.com/watch?v=RhuB1TDp67A`. Please click 2 times on the button above this caption to start the video. After clicking the video use Spacebar (play/pause), Home / End (go to start/end), ← / → (seek backwards/forwards) and m (mute/unmute). 39
2.6 Scopus search results of bio-inspired optimization algorithms, in percentages. Adapted from Kar (2016). 39
2.7 Scopus search results of bio-inspired optimization algorithms, in discrete numbers. Adapted from Kar (2016). 40
2.8 26-Story, 942-bar space truss tower. From Hasançebi et al. (2013). 42

3.1 Geometrical notations of a multilayered plate. From Carrera et al. (2011). 46
3.2 Undeformed and deformed geometries of a plate according to the Reissner-Mindlin hypotheses. Adapted from Carrera et al. (2011). 48
3.3 Displacement components through the thickness direction. Adapted from Carrera et al. (2011). 48
3.4 In-plane displacement components and transverse shear stresses through the thickness direction. Adapted from Carrera et al. (2011). 49
3.5 Reference system for polarization of a piezoelectric material in transverse direction. From Carrera et al. (2011). 59
3.6 Piezoelectric coefficients. Coupling between mechanical and electrical fields. From Carrera et al. (2011). 60

3.7 Interaction between variables: A) The Heckmann triangle (left) shows the complete set of thermodynamical variables; the variables chosen for constitutive equations are in white circles and the constant variables (entropy and temperature) in circles with grey shading. B) The interaction square (right) with strain, stress, electric displacement and electric field variables at constant entropy and temperature. The piezoelectric tensors $\mathbf{a}$, $\mathbf{d}$, $\mathbf{b}$ and $\mathbf{e}$ in the direct effect are marked with arrows towards bottom and in the converse effect towards to top. Adapted from Mainprice et al. (2014). 60
3.8 A lamina with problem and material coordinate systems. Adapted from Reddy (2004). . 65
3.9 Meaning and effects of some piezoelectric coefficients. From Carrera et al. (2011). . . . 66
3.10 FGMs possibilities in terms of both volume fraction distribution directions and approximation approaches, as well as homogenization methods. 70
3.11 Plot of the volume fraction power law along transversal direction, with continuous approximation, considering several p exponents and thickness from -50 to $50\,\mathrm{mm}$. 71
3.12 Plot of the volume fraction power law along longitudinal direction, with continuous approximation, considering several p exponents and length from 0 to $100\,\mathrm{mm}$. 74
3.13 Mesh for a generic plate by means of several master elements. From Carrera et al. (2011). 79
3.14 The quadrilateral master elements' enumeration with natural coordinate system. 79
3.15 Mesh numbering order, considering ten Q4 elements in each xy-direction (10×10). . . 81
3.16 The first four two-dimensional Gauss product rules $p = 1, 2, 3, 4$ depicted over a straight-sided quadrilateral region. Sample points are marked with black circles. The areas of these circles are proportional to the integration weights. From Felippa (2016a). 84
3.17 Software main sequence scheme, inside the chosen cloud. 92
3.18 Global computational scheme for both FEM and bat algorithms. 94
3.19 FEM algorithm architecture scheme. 95
3.20 Original BA pseudo-code. From Fister Jr. et al. (2013). 98
3.21 HBA pseudo-code. From Fister Jr. et al. (2013). 98
3.22 MHBA architecture scheme. 99

4.1 SHELL181 stress output. From ANSYS®, Inc. (2016). 105
4.2 Validation case study scheme of bimorph beam (actuation (CFFF)). 109
4.3 Deflections obtained in the validation case study of bimorph beam (actuation (CFFF)). . 109
4.4 Evolution of elastic moduli E versus CNT weight fractions w_{CNT}, for nano-composites. 118

A.1 Plot of the volume fraction power law along transversal direction, with discrete approximation ($N_{sl} = 5$ sub-layers), considering several p exponents and thickness from -50 to $50\,\mathrm{mm}$. A-1
A.2 Plot of the volume fraction power law along transversal direction, with discrete approximation ($N_{sl} = 10$ sub-layers), considering several p exponents and thickness from -50 to $50\,\mathrm{mm}$. A-2
A.3 Plot of the volume fraction power law along transversal direction, with discrete approximation ($N_{sl} = 50$ sub-layers), considering several p exponents and thickness from -50 to $50\,\mathrm{mm}$. A-2
A.4 Plot of the volume fraction power law along longitudinal direction, with discrete approximation ($N_{ex} = 6$ elements), considering several p exponents and length from 0 to $100\,\mathrm{mm}$. A-3

A.5 Plot of the volume fraction power law along longitudinal direction, with discrete approximation ($N_{ex} = 10$ elements), considering several p exponents and length from 0 to 100 mm. A-3
A.6 Plot of the volume fraction power law along longitudinal direction, with discrete approximation ($N_{ex} = 16$ elements), considering several p exponents and length from 0 to 100 mm. A-4

C.1 3D shape function plots of 4BlinLag element, including nodes and Gauss points spatial locations, on the local element natural coordinate system. Please click on the buttons above this caption to run the animation and toggle between plotted results. C-2
C.2 2D shape function plots of 4BlinLag element, including nodes and Gauss points spatial locations, on the local element natural coordinate system. Please click on the buttons above this caption to run the animation and toggle between plotted results. C-2
C.3 3D shape function plots of 9BquadLag element, including nodes and Gauss points spatial locations, on the local element natural coordinate system. Please click on the buttons above this caption to run the animation and toggle between plotted results. C-3
C.4 2D shape function plots of 9BquadLag element, including nodes and Gauss points spatial locations, on the local element natural coordinate system. Please click on the buttons above this caption to run the animation and toggle between plotted results. C-3
C.5 3D shape function plots of 16BcubLag element, including nodes and Gauss points spatial locations, on the local element natural coordinate system. Please click on the buttons above this caption to run the animation and toggle between plotted results. C-4
C.6 2D shape function plots of 16BcubLag element, including nodes and Gauss points spatial locations, on the local element natural coordinate system. Please click on the buttons above this caption to run the animation and toggle between plotted results. C-4
C.7 3D shape function plots of 4BlinKrig element, including nodes and Gauss points spatial locations, on the local element natural coordinate system. Please click on the buttons above this caption to run the animation and toggle between plotted results. C-5
C.8 2D shape function plots of 4BlinKrig element, including nodes and Gauss points spatial locations, on the local element natural coordinate system. Please click on the buttons above this caption to run the animation and toggle between plotted results. C-5
C.9 3D shape function plots of 9BlinKrig element, including nodes and Gauss points spatial locations, on the local element natural coordinate system. Please click on the buttons above this caption to run the animation and toggle between plotted results. C-6
C.10 2D shape function plots of 9BlinKrig element, including nodes and Gauss points spatial locations, on the local element natural coordinate system. Please click on the buttons above this caption to run the animation and toggle between plotted results. C-6
C.11 3D shape function plots of 9BquadKrig element, including nodes and Gauss points spatial locations, on the local element natural coordinate system. Please click on the buttons above this caption to run the animation and toggle between plotted results. C-7
C.12 2D shape function plots of 9BquadKrig element, including nodes and Gauss points spatial locations, on the local element natural coordinate system. Please click on the buttons above this caption to run the animation and toggle between plotted results. C-7
C.13 3D shape function plots of 16BlinKrig element, including nodes and Gauss points spatial locations, on the local element natural coordinate system. Please click on the buttons above this caption to run the animation and toggle between plotted results. C-8

C.14 2D shape function plots of 16BlinKrig element, including nodes and Gauss points spatial locations, on the local element natural coordinate system. Please click on the buttons above this caption to run the animation and toggle between plotted results. C-8
C.15 3D shape function plots of 16BquadKrig element, including nodes and Gauss points spatial locations, on the local element natural coordinate system. Please click on the buttons above this caption to run the animation and toggle between plotted results. C-9
C.16 2D shape function plots of 16BquadKrig element, including nodes and Gauss points spatial locations, on the local element natural coordinate system. Please click on the buttons above this caption to run the animation and toggle between plotted results. C-9
C.17 3D shape function plots of 16BcubKrig element, including nodes and Gauss points spatial locations, on the local element natural coordinate system. Please click on the buttons above this caption to run the animation and toggle between plotted results. C-10
C.18 2D shape function plots of 16BcubKrig element, including nodes and Gauss points spatial locations, on the local element natural coordinate system. Please click on the buttons above this caption to run the animation and toggle between plotted results. C-10

F.1 Statics and dynamics (free vibrations) results obtained from the isotropic simply-supported plate validation model using AMAPDL, considering a (30×30) mesh. Please click on the buttons above this caption to run the animation and toggle between plotted results. . . F-3
F.2 Statics and dynamics (free vibrations) results obtained from the isotropic simply-supported plate validation model using the present FEM platform. 4BlinLag elements with a (30×30) mesh. Please click on the buttons above this caption to run the animation and toggle between plotted results. F-4
F.3 Validation case study scheme of bimorph beam (sensing (CFFF)). F-9
F.4 Voltages obtained in the validation case study of bimorph beam (sensing (CFFF)). F-9
F.5 Validation case study scheme of bimorph beam (sensing (CCFF)). F-11
F.6 Voltages obtained in the validation case study of bimorph beam (sensing (CCFF)). F-11
F.7 Validation case study scheme of bimorph plate (dynamics (SSFF)) (Wang, 2004). F-12
F.8 Validation case study scheme of cantilever beam (dyn.) (Saravanos and Heyliger, 1995). F-12
F.9 Validation case study scheme of hybrid rectang. plate (dynamics) (Farsangi et al., 2013). F-13
F.10 Validation case study scheme of a 5-ply laminated plate (dyn.) (Saravanos et al., 1997). . F-14
F.11 Validation case study scheme of skew plate (optimization) (Correia et al., 2016). F-18
F.12 Optimization results from 79 case studies of maximization of plates' natural frequency, considering different BA inputs; optimization validation (Correia et al., 2001). DVs are each ply angle θ [°]. Please click on the buttons above this caption to toggle between plotted results. F-20
F.13 3D and 2D amplitude plots of the fundamental free vibrational mode along all successive best iterations found in the overall best case study, out of all 79, associated with Table F.11 (cs_no. 79). Please click on the buttons above this caption to run the animation and toggle between plotted results. F-20

G.1 Convergence results plot of DOF $\max |w|$ [m], for all elements. Please click on the buttons above this caption to run the animation and toggle between plotted results. G-7
G.2 Convergence results plot of DOF $\max |\theta_x|$ [rad], for all elements. Please click on the buttons above this caption to run the animation and toggle between plotted results. G-7
G.3 Convergence results plot of strain $\max |\epsilon_{xx}|$, for all elements. Please click on the buttons above this caption to run the animation and toggle between plotted results. G-8

G.4 Convergence results plot of strain $\max|\gamma_{xy}|$, for all elements. Please click on the buttons above this caption to run the animation and toggle between plotted results. G-8
G.5 Convergence results plot of strain $\max|\gamma_{xz}|$, for all elements. Please click on the buttons above this caption to run the animation and toggle between plotted results. G-9
G.6 Convergence results plot of stress $\max|\sigma_{xx}|$ [Pa], for all elements. Please click on the buttons above this caption to run the animation and toggle between plotted results. G-9
G.7 Convergence results plot of stress $\max|\tau_{xy}|$ [Pa], for all elements. Please click on the buttons above this caption to run the animation and toggle between plotted results. G-10
G.8 Convergence results plot of stress $\max|\tau_{xz}|$ [Pa], for all elements. Please click on the buttons above this caption to run the animation and toggle between plotted results. G-10
G.9 Convergence results plot of stress $\max|\sigma_{VM}|$ [Pa], for all elements. Please click on the buttons above this caption to run the animation and toggle between plotted results. G-11
G.10 Convergence results plot of natural frequency ω_1 [Hz], for all elements. Please click on the buttons above this caption to run the animation and toggle between plotted results. G-11
G.11 Convergence results plot of natural frequency ω_2 [Hz], for all elements. Please click on the buttons above this caption to run the animation and toggle between plotted results. G-12
G.12 Convergence results plot of natural frequency ω_3 [Hz], for all elements. Please click on the buttons above this caption to run the animation and toggle between plotted results. G-12
G.13 Convergence results plot of natural frequency ω_4 [Hz], for all elements. Please click on the buttons above this caption to run the animation and toggle between plotted results. G-13
G.14 Convergence results plot of natural frequency ω_5 [Hz], for all elements. Please click on the buttons above this caption to run the animation and toggle between plotted results. G-13
G.15 Convergence results plot of computation time [s], for all elements. Please click on the buttons above this caption to run the animation and toggle between plotted results. G-14
G.16 Statics and dynamics (free vibrations) results obtained from the convergence model using the present FEM platform. 9BquadLag elements with a (10×10) mesh. Please click on the buttons above this caption to run the animation and toggle between plotted results. . . G-15
G.17 Statics and dynamics (free vibrations) results obtained from the convergence model using the present FEM platform. 16BcubLag elements with a (10×10) mesh. Please click on the buttons above this caption to run the animation and toggle between plotted results. . . G-16
G.18 Statics and dynamics (free vibrations) results obtained from the convergence model using the present FEM platform. 4BlinKrig elements with a (30×30) mesh. Please click on the buttons above this caption to run the animation and toggle between plotted results. G-17
G.19 Statics and dynamics (free vibrations) results obtained from the convergence model using the present FEM platform. 9BlinKrig elements with a (10×10) mesh. Please click on the buttons above this caption to run the animation and toggle between plotted results. G-18
G.20 Statics and dynamics (free vibrations) results obtained from the convergence model using the present FEM platform. 9BquadKrig elements with a (10×10) mesh. Please click on the buttons above this caption to run the animation and toggle between plotted results. . . G-19
G.21 Statics and dynamics (free vibrations) results obtained from the convergence model using the present FEM platform. 16BlinKrig elements with a (10×10) mesh. Please click on the buttons above this caption to run the animation and toggle between plotted results. . . G-20
G.22 Statics and dynamics (free vibrations) results obtained from the convergence model using the present FEM platform. 16BquadKrig elements with a (10×10) mesh. Please click on the buttons above this caption to run the animation and toggle between plotted results. . . G-21

G.23 Statics and dynamics (free vibrations) results obtained from the convergence model using the present FEM platform. 16BcubKrig elements with a (10×10) mesh. Please click on the buttons above this caption to run the animation and toggle between plotted results. . . G-22
G.24 Von Mises stress results obtained from the convergence model using the present FEM platform, only for visualization. 4BlinLag elements; meshes from (2×2) by (2×2) to (30×30). Please click on the buttons above this caption to run the animation and toggle between plotted results. G-23
G.25 Non-dimensional max. deflection $\overline{w}$ versus CNT weight fractions w_{CNT} (MWCNTs). . . G-24
G.26 Non-dimensional max. deflection $\overline{w}$ versus exponents p. G-24
G.27 Non-dimensional max. deflection $\overline{w}$ versus CNT weight fractions w_{CNT}. G-25
G.28 In-plane non-dimensional normal stress $\overline{\sigma}_{xx}$ $(w_{CNT} = 0)$ (3D). G-26
G.29 In-plane non-dimensional normal stress $\overline{\sigma}_{xx}$ $(w_{CNT} = 0)$ (2D). G-27
G.30 In-plane shear stress $\overline{\tau}_{xy}$ $(w_{CNT} = 0)$ (3D). G-28
G.31 In-plane shear stress $\overline{\tau}_{xy}$ $(w_{CNT} = 0)$ (2D). G-29
G.32 Interlaminar shear stress $\overline{\tau}_{xz}$ $(w_{CNT} = 0)$ (3D). G-30
G.33 Interlaminar shear stress $\overline{\tau}_{xz}$ $(w_{CNT} = 0)$ (2D). G-31
G.34 Interlaminar shear stress $\overline{\tau}_{xz}$ $(w_{CNT} = 0, a/h = 10)$ (3D). G-32
G.35 Interlaminar shear stress $\overline{\tau}_{xz}$ $(w_{CNT} = 0, a/h = 20)$ (3D). G-33
G.36 Fundamental natural frequency ω_1 versus CNT weight fractions w_{CNT} (MWCNTs). . . G-34
G.37 Fundamental natural frequency ω_1 versus exponents p (SWCNTs). G-34
G.38 Fundamental natural frequency ω_1 versus exponents p (FGM1). G-35
G.39 Fundamental nat. freq. ω_1 versus CNT weight fractions w_{CNT} (FGM2 with SWCNTs). . G-35
G.40 Fundamental nat. freq. ω_1 versus CNT weight fractions w_{CNT} (FGM2 with MWCNTs). G-36
G.41 Fundamental free vibrational mode considering $p = 0$ (3D). G-37
G.42 Fundamental free vibrational mode considering $p = 0$ (2D). G-38
G.43 Fundamental free vibrational mode considering (CFFF) MBCs (3D). G-39
G.44 Fundamental free vibrational mode considering (CFFF) MBCs (2D). G-40
G.45 Fundamental free vibrational mode considering (CCSF) MBCs (3D). G-41
G.46 Fundamental free vibrational mode considering (CCSF) MBCs (2D). G-42
G.47 Second free vibrational mode considering (SSSS) MBCs, FGM1 and $p = 0$ (3D). G-43
G.48 Second free vibrational mode considering (SSSS) MBCs, FGM1 and $p = 0$ (2D). G-44
G.49 Parametric CS scheme of longitudinal FGM bimorph beam (statics actuation (CFFF)). . G-45
G.50 Parametric CS scheme of longitudinal FGM bimorph beam (statics actuation (CCFF)). . G-45
G.51 Parametric CS scheme of longitudinal FGM bimorph beam (statics sensing (CFFF)). . . G-46
G.52 Parametric CS scheme of longitudinal FGM bimorph beam (statics sensing (CCFF)). . . G-46
G.53 Deflection results from the parametric case study of longitudinal FGM bimorph beam (statics actuation (CFFF)), mixing up LaRC-Si and PVDF, considering several meshes and p-exponents (0, 0.1, 0.5 and 1). Please click on the buttons above this caption to toggle between plotted results. G-47
G.54 Deflection results from the parametric case study of longitudinal FGM bimorph beam (statics actuation (CCFF)), mixing up LaRC-Si and PVDF, considering several meshes and p-exponents (0, 0.1, 0.5 and 1). Please click on the buttons above this caption to toggle between plotted results. G-47
G.55 Deflection results from the parametric case study of longitudinal FGM bimorph beam (statics actuation (CFFF)), mixing up LaRC-Si and PZT-7A, with several meshes and p-exponents (0, 0.1, 0.5 and 1). Please click on the buttons above this caption to toggle between plotted results. G-48

G.56 Deflection results from the parametric case study of longitudinal FGM bimorph beam (statics actuation (CCFF)), mixing up LaRC-Si and PZT-7A, with several meshes and p-exponents (0, 0.1, 0.5 and 1). Please click on the buttons above this caption to toggle between plotted results. G-48

G.57 Deflection results from the parametric case study of longitudinal FGM bimorph beam (statics actuation (CFFF)), mixing up LaRC-Si and PVDF, considering several meshes and p-exponents (0, 1, 2 and 5). Please click on the buttons above this caption to toggle between plotted results. G-49

G.58 Deflection results from the parametric case study of longitudinal FGM bimorph beam (statics actuation (CCFF)), mixing up LaRC-Si and PVDF, considering several meshes and p-exponents (0, 1, 2 and 5). Please click on the buttons above this caption to toggle between plotted results. G-49

G.59 Deflection results from the parametric case study of longitudinal FGM bimorph beam (statics actuation (CFFF)), mixing up LaRC-Si and PZT-7A, with several meshes and p-exponents (0, 1, 2 and 5). Please click on the buttons above this caption to toggle between plotted results. G-50

G.60 Deflection results from the parametric case study of longitudinal FGM bimorph beam (statics actuation (CCFF)), mixing up LaRC-Si and PZT-7A, with several meshes and p-exponents (0, 1, 2 and 5). Please click on the buttons above this caption to toggle between plotted results. G-50

G.61 Deflection results from the parametric CS of longitudinal FGM bimorph beam (statics actuation (CFFF)), mixing up LaRC-Si and PVDF, with several p-exponents (0, 0.1, 0.5, 1, 2 and 5). G-51

G.62 Deflection results from the parametric CS of longitudinal FGM bimorph beam (statics actuation (CCFF)), mixing up LaRC-Si and PVDF, with several p-exponents (0, 0.1, 0.5, 1, 2 and 5). G-51

G.63 Deflection results from the parametric CS of longitudinal FGM bimorph beam (statics actuation (CFFF)), mixing up LaRC-Si and PZT-7A, with several p-exponents (0, 0.1, 0.5, 1, 2 and 5). G-52

G.64 Deflection results from the parametric CS of longitudinal FGM bimorph beam (statics actuation (CCFF)), mixing up LaRC-Si and PZT-7A, with several p-exponents (0, 0.1, 0.5, 1, 2 and 5). G-52

G.65 Deflection results from the parametric case study of longitudinal FGM bimorph beam (statics actuation (CFFF)), mixing up LaRC-Si and PVDF, considering 251 p-exponents (from 0 by 0.02 to 5). Note that the bold numbers above the x-axis correspond to the percentage $[\%]$ of piezoelectric material, $V_{f,r}^{ex}$, mixed up in each element along the beam's length, at each frame. Please click on the buttons above this caption to run the animation and toggle between plotted results. G-55

G.66 Deflection results from the parametric case study of longitudinal FGM bimorph beam (statics actuation (CCFF)), mixing up LaRC-Si and PVDF, considering 251 p-exponents (from 0 by 0.02 to 5). Note that the bold numbers above the x-axis correspond to the percentage $[\%]$ of piezoelectric material, $V_{f,r}^{ex}$, mixed up in each element along the beam's length, at each frame. Please click on the buttons above this caption to run the animation and toggle between plotted results. G-55

G.67 Deflection results from the parametric case study of longitudinal FGM bimorph beam (statics actuation (CFFF)), mixing up LaRC-Si and PZT-7A, considering 251 p-exponents (from 0 by 0.02 to 5). Note that the bold numbers above the x-axis correspond to the percentage $[\%]$ of piezoelectric material, $V_{f,r}^{ex}$, mixed up in each element along the beam's length, at each frame. Please click on the buttons above this caption to run the animation and toggle between plotted results. G-56
G.68 Deflection results from the parametric case study of longitudinal FGM bimorph beam (statics actuation (CCFF)), mixing up LaRC-Si and PZT-7A, considering 251 p-exponents (from 0 by 0.02 to 5). Note that the bold numbers above the x-axis correspond to the percentage $[\%]$ of piezoelectric material, $V_{f,r}^{ex}$, mixed up in each element along the beam's length, at each frame. Please click on the buttons above this caption to run the animation and toggle between plotted results. G-56
G.69 Voltage results from the parametric case study of longitudinal FGM bimorph beam (statics sensing (CFFF)), mixing up LaRC-Si and PVDF, considering several meshes and p-exponents (0, 0.1, 0.5 and 1). Please click on the buttons above this caption to toggle between plotted results. G-57
G.70 Voltage results from the parametric case study of longitudinal FGM bimorph beam (statics sensing (CCFF)), mixing up LaRC-Si and PVDF, considering several meshes and p-exponents (0, 0.1, 0.5 and 1). Please click on the buttons above this caption to toggle between plotted results. G-57
G.71 Voltage results from the parametric case study of longitudinal FGM bimorph beam (statics sensing (CFFF)), mixing up LaRC-Si and PZT-7A, considering several meshes and p-exponents (0, 0.1, 0.5 and 1). Please click on the buttons above this caption to toggle between plotted results. G-58
G.72 Voltage results from the parametric case study of longitudinal FGM bimorph beam (statics sensing (CCFF)), mixing up LaRC-Si and PZT-7A, considering several meshes and p-exponents (0, 0.1, 0.5 and 1). Please click on the buttons above this caption to toggle between plotted results. G-58
G.73 Voltage results from the parametric case study of longitudinal FGM bimorph beam (statics sensing (CFFF)), mixing up LaRC-Si and PVDF, considering several meshes and p-exponents (0, 1, 2 and 5). Please click on the buttons above this caption to toggle between plotted results. G-59
G.74 Voltage results from the parametric case study of longitudinal FGM bimorph beam (statics sensing (CCFF)), mixing up LaRC-Si and PVDF, considering several meshes and p-exponents (0, 1, 2 and 5). Please click on the buttons above this caption to toggle between plotted results. G-59
G.75 Voltage results from the parametric case study of longitudinal FGM bimorph beam (statics sensing (CFFF)), mixing up LaRC-Si and PZT-7A, considering several meshes and p-exponents (0, 1, 2 and 5). Please click on the buttons above this caption to toggle between plotted results. G-60
G.76 Voltage results from the parametric case study of longitudinal FGM bimorph beam (statics sensing (CCFF)), mixing up LaRC-Si and PZT-7A, considering several meshes and p-exponents (0, 1, 2 and 5). Please click on the buttons above this caption to toggle between plotted results. G-60
G.77 Voltage results from the parametric CS of longitudinal FGM bimorph beam (statics sensing (CFFF)), mixing up LaRC-Si and PVDF, with several p-exponents (0, 0.1, 0.5, 1, 2 and 5). G-61

G.78 Voltage results from the parametric CS of longitudinal FGM bimorph beam (statics sensing (CCFF)), mixing up LaRC-Si and PVDF, with several p-exponents (0, 0.1, 0.5, 1, 2 and 5). G-61

G.79 Voltage results from the parametric CS of longitudinal FGM bimorph beam (statics sensing (CFFF)), mixing up LaRC-Si and PZT-7A, with several p-exponents (0, 0.1, 0.5, 1, 2 and 5).G-62

G.80 Voltage results from the parametric CS of longitudinal FGM bimorph beam (statics sensing (CCFF)), mixing up LaRC-Si and PZT-7A, with several p-exponents (0, 0.1, 0.5, 1, 2 and 5).G-62

G.81 Voltage results from the parametric case study of longitudinal FGM bimorph beam (statics sensing (CFFF)), mixing up LaRC-Si and PVDF, considering 251 p-exponents (from 0 by 0.02 to 5). Note that the bold numbers above the x-axis correspond to the percentage [%] of piezoelectric material, $V_{f,r}^{ex}$, mixed up in each element along the beam's length, at each frame. Please click on the buttons above this caption to run the animation and toggle between plotted results. G-65

G.82 Voltage results from the parametric case study of longitudinal FGM bimorph beam (statics sensing (CCFF)), mixing up LaRC-Si and PVDF, considering 251 p-exponents (from 0 by 0.02 to 5). Note that the bold numbers above the x-axis correspond to the percentage [%] of piezoelectric material, $V_{f,r}^{ex}$, mixed up in each element along the beam's length, at each frame. Please click on the buttons above this caption to run the animation and toggle between plotted results. G-65

G.83 Voltage results from the parametric case study of longitudinal FGM bimorph beam (statics sensing (CFFF)), mixing up LaRC-Si and PZT-7A, considering 251 p-exponents (from 0 by 0.02 to 5). Note that the bold numbers above the x-axis correspond to the percentage [%] of piezoelectric material, $V_{f,r}^{ex}$, mixed up in each element along the beam's length, at each frame. Please click on the buttons above this caption to run the animation and toggle between plotted results. G-66

G.84 Voltage results from the parametric case study of longitudinal FGM bimorph beam (statics sensing (CCFF)), mixing up LaRC-Si and PZT-7A, considering 251 p-exponents (from 0 by 0.02 to 5). Note that the bold numbers above the x-axis correspond to the percentage [%] of piezoelectric material, $V_{f,r}^{ex}$, mixed up in each element along the beam's length, at each frame. Please click on the buttons above this caption to run the animation and toggle between plotted results. G-66

G.85 Parametric case study scheme of longitudinal FGM bimorph beam (dynamics (CFFF)). . G-67

G.86 Parametric case study scheme of longitudinal FGM bimorph beam (dynamics (CCFF)). . G-67

G.87 Natural frequencies results of the first five free vibrational modes from the parametric case study of longitudinal FGM bimorph beam (dynamics (CFFF)), mixing up LaRC-Si and PVDF, considering several EBCs and p-exponents (0, 0.1, 0.5 and 1). Please click on the buttons above this caption to toggle between plotted results. G-68

G.88 Natural frequencies results of the first five free vibrational modes from the parametric case study of longitudinal FGM bimorph beam (dynamics (CCFF)), mixing up LaRC-Si and PVDF, considering several EBCs and p-exponents (0, 0.1, 0.5 and 1). Please click on the buttons above this caption to toggle between plotted results. G-68

G.89 Natural frequencies results of the first five free vibrational modes from the parametric case study of longitudinal FGM bimorph beam (dynamics (CFFF)), mixing up LaRC-Si and PZT-7A, considering several EBCs and p-exponents (0, 0.1, 0.5 and 1). Please click on the buttons above this caption to toggle between plotted results. G-69

G.90 Natural frequencies results of the first five free vibrational modes from the parametric case study of longitudinal FGM bimorph beam (dynamics (CCFF)), mixing up LaRC-Si and PZT-7A, considering several EBCs and p-exponents (0, 0.1, 0.5 and 1). Please click on the buttons above this caption to toggle between plotted results. G-69

G.91 Natural frequencies results of the first five free vibrational modes from the parametric case study of longitudinal FGM bimorph beam (dynamics (CFFF)), mixing up LaRC-Si and PVDF, considering several EBCs and p-exponents (0, 1, 2 and 5). Please click on the buttons above this caption to toggle between plotted results. G-70

G.92 Natural frequencies results of the first five free vibrational modes from the parametric case study of longitudinal FGM bimorph beam (dynamics (CCFF)), mixing up LaRC-Si and PVDF, considering several EBCs and p-exponents (0, 1, 2 and 5). Please click on the buttons above this caption to toggle between plotted results. G-70

G.93 Natural frequencies results of the first five free vibrational modes from the parametric case study of longitudinal FGM bimorph beam (dynamics (CFFF)), mixing up LaRC-Si and PZT-7A, considering several EBCs and p-exponents (0, 1, 2 and 5). Please click on the buttons above this caption to toggle between plotted results. G-71

G.94 Natural frequencies results of the first five free vibrational modes from the parametric case study of longitudinal FGM bimorph beam (dynamics (CCFF)), mixing up LaRC-Si and PZT-7A, considering several EBCs and p-exponents (0, 1, 2 and 5). Please click on the buttons above this caption to toggle between plotted results. G-71

G.95 Fundamental natural frequencies results from the parametric case study of longitudinal FGM bimorph beam (dynamics (CFFF)), considering several EBCs and p-exponents (0, 0.1, 0.5 and 1), to compare both LaRC-Si + (PVDF or PZT-7A) mixtures. Please click on the buttons above this caption to toggle between plotted results. G-72

G.96 Fundamental natural frequencies results from the parametric case study of longitudinal FGM bimorph beam (dynamics (CCFF)), considering several EBCs and p-exponents (0, 0.1, 0.5 and 1), to compare both LaRC-Si + (PVDF or PZT-7A) mixtures. Please click on the buttons above this caption to toggle between plotted results. G-72

G.97 Fundamental natural frequencies results from the parametric case study of longitudinal FGM bimorph beam (dynamics (CFFF)), considering several EBCs and p-exponents (0, 1, 2 and 5), to compare both LaRC-Si + (PVDF or PZT-7A) mixtures. Please click on the buttons above this caption to toggle between plotted results. G-73

G.98 Fundamental natural frequencies results from the parametric case study of longitudinal FGM bimorph beam (dynamics (CCFF)), considering several EBCs and p-exponents (0, 1, 2 and 5), to compare both LaRC-Si + (PVDF or PZT-7A) mixtures. Please click on the buttons above this caption to toggle between plotted results. G-73

G.99 The first five free vibrational modes (3D and 2D views) from the parametric case study of longitudinal FGM bimorph beam (dynamics (CFFF)), mixing up LaRC-Si and PVDF, considering closed-circuit and several p-exponents (0, 0.1, 0.5, 1, 2 and 5). Please click on the buttons above this caption to run the animation and toggle between plotted results. . . G-80

G.100 The first five free vibrational modes (3D and 2D views) from the parametric case study of longitudinal FGM bimorph beam (dynamics (CCFF)), mixing up LaRC-Si and PVDF, considering closed-circuit and several p-exponents (0, 0.1, 0.5, 1, 2 and 5). Please click on the buttons above this caption to run the animation and toggle between plotted results. . . G-81

G.101 The first five free vibrational modes (3D and 2D views) from the parametric case study of longitudinal FGM bimorph beam (dynamics (CFFF)), mixing up LaRC-Si and PZT-7A, considering closed-circuit and several p-exponents (0, 0.1, 0.5, 1, 2 and 5). Please click on the buttons above this caption to run the animation and toggle between plotted results. . . . G-82

G.102 The first five free vibrational modes (3D and 2D views) from the parametric case study of longitudinal FGM bimorph beam (dynamics (CCFF)), mixing up LaRC-Si and PZT-7A, considering closed-circuit and several p-exponents (0, 0.1, 0.5, 1, 2 and 5). Please click on the buttons above this caption to run the animation and toggle between plotted results. . . . G-83

H.1 Optimization case study scheme for minimization of beams' deflections. H-2

H.2 Optimization results from 25 case studies ($N_{gen} = 50$ gens and $n = 50$ bats each) of min. of beams' deflections, mixing up LaRC-Si and PVDF, considering $p = 1$ and different random combinations of DE perturbation factors $Fper_i$ and $Fper_f$. DVs are the electric potentials ϕ [V] applied to each patch. Please click on the buttons above this caption to toggle between plotted results. H-4

H.3 Optimization results, for all generations, from the best case study found in Figure H.2. Please click on the buttons above this caption to toggle between plotted results. H-4

H.4 Deflection plots of all successive best iterations found in the case study associated with Figure H.3. Note that the bold numbers above the x-axis (first row) correspond to the percentage [%] of piezoelectric material, $V_{f,r}^{ex}$, mixed up in each element along the beam's length, at each frame. Note that the bold numbers above the x-axis (second row) correspond to the voltage [V] in each element along the beam's length, at each frame. Please click on the buttons above this caption to run the animation and toggle between plotted results. . . H-5

H.5 3D and 2D deflection plots of all successive best iterations found in the case study associated with Figure H.3. Please click on the buttons above this caption to run the animation and toggle between plotted results. H-5

H.6 Electric potentials plots of all successive best iterations found in the case study associated with Figure H.3. Note that the bold numbers above the x-axis (first row) correspond to the percentage [%] of piezoelectric material, $V_{f,r}^{ex}$, mixed up in each element along the beam's length, at each frame. Note that the bold numbers above the x-axis (second row) correspond to the voltage [V] in each element along the beam's length, at each frame. Please click on the buttons above this caption to run the animation and toggle between plotted results. H-6

H.7 Voltage plots of all successive best iterations found in the case study associated with Figure H.3. Note that the bold numbers above the x-axis (first row) correspond to the percentage [%] of piezoelectric material, $V_{f,r}^{ex}$, mixed up in each element along the beam's length, at each frame. Note that the bold numbers above the x-axis (second row) correspond to the voltage [V] in each element along the beam's length, at each frame. Please click on the buttons above this caption to run the animation and toggle between plotted results. . . H-6

H.8 Optimization results, for all generations, for the best case study found in Figure H.2, i.e. $Fper_i = 1.5$ and $Fper_f = 0$, but computed with $N_{gen} = 100$. Please click on the buttons above this caption to toggle between plotted results. H-7

H.9 Deflection plots of all successive best iterations found in the case study associated with Figure H.8. Note that the bold numbers above the x-axis (first row) correspond to the percentage $[\%]$ of piezoelectric material, $V_{f,r}^{ex}$, mixed up in each element along the beam's length, at each frame. Note that the bold numbers above the x-axis (second row) correspond to the voltage $[\mathrm{V}]$ in each element along the beam's length, at each frame. Please click on the buttons above this caption to run the animation and toggle between plotted results. . . . H-8
H.10 3D and 2D deflection plots of all successive best iterations found in the case study associated with Figure H.8. Please click on the buttons above this caption to run the animation and toggle between plotted results. H-8
H.11 Electric potentials plots of all successive best iterations found in the case study associated with Figure H.8. Note that the bold numbers above the x-axis (first row) correspond to the percentage $[\%]$ of piezoelectric material, $V_{f,r}^{ex}$, mixed up in each element along the beam's length, at each frame. Note that the bold numbers above the x-axis (second row) correspond to the voltage $[\mathrm{V}]$ in each element along the beam's length, at each frame. Please click on the buttons above this caption to run the animation and toggle between plotted results. H-9
H.12 Voltage plots of all successive best iterations found in the case study associated with Figure H.8. Note that the bold numbers above the x-axis (first row) correspond to the percentage $[\%]$ of piezoelectric material, $V_{f,r}^{ex}$, mixed up in each element along the beam's length, at each frame. Note that the bold numbers above the x-axis (second row) correspond to the voltage $[\mathrm{V}]$ in each element along the beam's length, at each frame. Please click on the buttons above this caption to run the animation and toggle between plotted results. . . . H-9
H.13 Optimization results, for all generations, for the same case study in Figure H.8, i.e. $Fper_i = 1.5$ and $Fper_f = 0$, $N_{gen} = 100$, but computed with $p = 5$ instead of $p = 1$. Please click on the buttons above this caption to toggle between plotted results. H-10
H.14 Deflection plots of all successive best iterations found in the case study associated with Figure H.13. Note that the bold numbers above the x-axis (first row) correspond to the percentage $[\%]$ of piezoelectric material, $V_{f,r}^{ex}$, mixed up in each element along the beam's length, at each frame. Note that the bold numbers above the x-axis (second row) correspond to the voltage $[\mathrm{V}]$ in each element along the beam's length, at each frame. Please click on the buttons above this caption to run the animation and toggle between plotted results. . . . H-11
H.15 3D and 2D deflection plots of all successive best iterations found in the case study associated with Figure H.13. Please click on the buttons above this caption to run the animation and toggle between plotted results. H-11
H.16 Electric potentials plots of all successive best iterations found in the case study associated with Figure H.13. Note that the bold numbers above the x-axis (first row) correspond to the percentage $[\%]$ of piezoelectric material, $V_{f,r}^{ex}$, mixed up in each element along the beam's length, at each frame. Note that the bold numbers above the x-axis (second row) correspond to the voltage $[\mathrm{V}]$ in each element along the beam's length, at each frame. Please click on the buttons above this caption to run the animation and toggle between plotted results. H-12
H.17 Voltage plots of all successive best iterations found in the case study associated with Figure H.13. Note that the bold numbers above the x-axis (first row) correspond to the percentage $[\%]$ of piezoelectric material, $V_{f,r}^{ex}$, mixed up in each element along the beam's length, at each frame. Note that the bold numbers above the x-axis (second row) correspond to the voltage $[\mathrm{V}]$ in each element along the beam's length, at each frame. Please click on the buttons above this caption to run the animation and toggle between plotted results. . . . H-12

H.18 Optimization case study scheme for minimization of plates' deflections. H-13

H.19 Optimization results from 50 case studies ($N_{gen} = 50$ gens and $n = 10$ bats each) of min. of plates' deflections, bottom passive layer (LaRC-Si) with 1 patch on top (PZT-7A), considering different random combinations of DE perturbation factors $Fper_i$ and $Fper_f$. DVs are the electric potential ϕ [V] applied to the patch and its location, i.e. minimum coordinates x_{min} [m] and y_{min} [m]. Population's locations reinitialized randomly before each generation. Please click on the buttons above this caption to toggle between plotted results. H-16

H.20 3D and 2D deflection plots of all successive best iterations found in the overall best case study, out of all 50, associated with Figure H.19. Please click on the buttons above this caption to run the animation and toggle between plotted results. H-16

H.21 Optimization results from 25 case studies ($N_{gen} = 50$ gens and $n = 10$ bats each) of min. of plates' deflections, bottom passive layer (LaRC-Si) with 2 independent patches on top (PZT-7A), considering the combinations of DE perturbation factors $Fper_i$ and $Fper_f$ matching the 25 best CSs in Table H.4. DVs are the electric potentials ϕ [V] applied to each patch and their locations, i.e. minimum coordinates x_{min} [m] and y_{min} [m]. Population's locations reinitialized randomly before each gen. Please click on the buttons above this caption to toggle between plotted results. H-17

H.22 3D and 2D deflection plots of all successive best iterations found in the overall best case study, out of all 25, associated with Figure H.21. Please click on the buttons above this caption to run the animation and toggle between plotted results. H-17

H.23 Optimization results from 25 case studies ($N_{gen} = 50$ gens and $n = 10$ bats each) of min. of plates' deflections, bottom passive layer (LaRC-Si) with 3 independent patches on top (PZT-7A), considering the combinations of DE perturbation factors $Fper_i$ and $Fper_f$ matching the 25 best CSs in Table H.4. DVs are the electric potentials ϕ [V] applied to each patch and their locations, i.e. minimum coordinates x_{min} [m] and y_{min} [m]. Population's locations reinitialized randomly before each gen. Please click on the buttons above this caption to toggle between plotted results. H-18

H.24 3D and 2D deflection plots of all successive best iterations found in the overall best case study, out of all 25, associated with Figure H.23. Please click on the buttons above this caption to run the animation and toggle between plotted results. H-18

H.25 Optimization results from 25 case studies ($N_{gen} = 50$ gens and $n = 10$ bats each) of min. of plates' deflections, bottom passive layer (LaRC-Si) with 4 independent patches on top (PZT-7A), considering the combinations of DE perturbation factors $Fper_i$ and $Fper_f$ matching the 25 best CSs in Table H.4. DVs are the electric potentials ϕ [V] applied to each patch and their locations, i.e. minimum coordinates x_{min} [m] and y_{min} [m]. Population's locations reinitialized randomly before each gen. Please click on the buttons above this caption to toggle between plotted results. H-19

H.26 3D and 2D deflection plots of all successive best iterations found in the overall best case study, out of all 25, associated with Figure H.25. Please click on the buttons above this caption to run the animation and toggle between plotted results. H-19

H.27 Optimization results from 25 case studies ($N_{gen} = 50$ gens and $n = 10$ bats each) of min. of plates' deflections, bottom passive layer (LaRC-Si) with 1 patch on top (PZT-7A), considering the combinations of DE perturbation factors $Fper_i$ and $Fper_f$ matching the 25 best case studies in Table H.4. DVs are the electric potential ϕ [V] applied to the patch and its location indirectly, i.e. the element no. (discrete integer) selection from the (10×10) mesh. Reinits Step 5 Gens. Please click on the buttons above this caption to toggle between plotted results. H-20
H.28 3D and 2D deflection plots of all successive best iterations found in the overall best case study, out of all 25, associated with Figure H.27. Please click on the buttons above this caption to run the animation and toggle between plotted results. H-20
H.29 Optimization results from 25 case studies ($N_{gen} = 50$ gens and $n = 10$ bats each) of min. of plates' deflections, bottom passive layer (LaRC-Si) with 2 independent patches on top (PZT-7A), considering the combinations of DE perturbation factors $Fper_i$ and $Fper_f$ matching the 25 best case studies in Table H.4. DVs are the electric potentials ϕ [V] applied to each patch and their locations indirectly, i.e. the element no. (discrete integers) selection from the (10×10) mesh. Reinits Step 5 Gens. Please click on the buttons above this caption to toggle between plotted results. H-21
H.30 3D and 2D deflection plots of all successive best iterations found in the overall best case study, out of all 25, associated with Figure H.29. Please click on the buttons above this caption to run the animation and toggle between plotted results. H-21
H.31 Optimization results from 25 case studies ($N_{gen} = 50$ gens and $n = 10$ bats each) of min. of plates' deflections, bottom passive layer (LaRC-Si) with 3 independent patches on top (PZT-7A), considering the combinations of DE perturbation factors $Fper_i$ and $Fper_f$ matching the 25 best case studies in Table H.4. DVs are the electric potentials ϕ [V] applied to each patch and their locations indirectly, i.e. the element no. (discrete integers) selection from the (10×10) mesh. Reinits Step 5 Gens. Please click on the buttons above this caption to toggle between plotted results. H-22
H.32 3D and 2D deflection plots of all successive best iterations found in the overall best case study, out of all 25, associated with Figure H.31. Please click on the buttons above this caption to run the animation and toggle between plotted results. H-22
H.33 Optimization results from 25 case studies ($N_{gen} = 50$ gens and $n = 10$ bats each) of min. of plates' deflections, bottom passive layer (LaRC-Si) with 4 independent patches on top (PZT-7A), considering the combinations of DE perturbation factors $Fper_i$ and $Fper_f$ matching the 25 best case studies in Table H.4. DVs are the electric potentials ϕ [V] applied to each patch and their locations indirectly, i.e. the element no. (discrete integers) selection from the (10×10) mesh. Reinits Step 5 Gens. Please click on the buttons above this caption to toggle between plotted results. H-23
H.34 3D and 2D deflection plots of all successive best iterations found in the overall best case study, out of all 25, associated with Figure H.33. Please click on the buttons above this caption to run the animation and toggle between plotted results. H-23
H.35 Optimization results from 25 case studies ($N_{gen} = 50$ gens and $n = 10$ bats each) of min. of plates' deflections, bottom passive layer (LaRC-Si) with 1 patch on top (PZT-7A), considering the combinations of DE perturbation factors $Fper_i$ and $Fper_f$ matching the 25 best case studies in Table H.4. DVs are the electric potential ϕ [V] applied to the patch and its location indirectly, i.e. the element no. (discrete integer) selection from the (10×10) mesh. Reinits Step 10 Gens. Please click on the buttons above this caption to toggle between plotted results. H-24

H.36 3D and 2D deflection plots of all successive best iterations found in the overall best case study, out of all 25, associated with Figure H.35. Please click on the buttons above this caption to run the animation and toggle between plotted results. H-24
H.37 Optimization results from 25 case studies ($N_{gen} = 50$ gens and $n = 10$ bats each) of min. of plates' deflections, bottom passive layer (LaRC-Si) with 2 independent patches on top (PZT-7A), considering the combinations of DE perturbation factors $Fper_i$ and $Fper_f$ matching the 25 best case studies in Table H.4. DVs are the electric potentials ϕ [V] applied to each patch and their locations indirectly, i.e. the element no. (discrete integers) selection from the (10×10) mesh. Reinits Step 10 Gens. Please click on the buttons above this caption to toggle between plotted results. H-25
H.38 3D and 2D deflection plots of all successive best iterations found in the overall best case study, out of all 25, associated with Figure H.37. Please click on the buttons above this caption to run the animation and toggle between plotted results. H-25
H.39 Optimization results from 25 case studies ($N_{gen} = 50$ gens and $n = 10$ bats each) of min. of plates' deflections, bottom passive layer (LaRC-Si) with 3 independent patches on top (PZT-7A), considering the combinations of DE perturbation factors $Fper_i$ and $Fper_f$ matching the 25 best case studies in Table H.4. DVs are the electric potentials ϕ [V] applied to each patch and their locations indirectly, i.e. the element no. (discrete integers) selection from the (10×10) mesh. Reinits Step 10 Gens. Please click on the buttons above this caption to toggle between plotted results. H-26
H.40 3D and 2D deflection plots of all successive best iterations found in the overall best case study, out of all 25, associated with Figure H.39. Please click on the buttons above this caption to run the animation and toggle between plotted results. H-26
H.41 Optimization results from 25 case studies ($N_{gen} = 50$ gens and $n = 10$ bats each) of min. of plates' deflections, bottom passive layer (LaRC-Si) with 4 independent patches on top (PZT-7A), considering the combinations of DE perturbation factors $Fper_i$ and $Fper_f$ matching the 25 best case studies in Table H.4. DVs are the electric potentials ϕ [V] applied to each patch and their locations indirectly, i.e. the element no. (discrete integers) selection from the (10×10) mesh. Reinits Step 10 Gens. Please click on the buttons above this caption to toggle between plotted results. H-27
H.42 3D and 2D deflection plots of all successive best iterations found in the overall best case study, out of all 25, associated with Figure H.41. Please click on the buttons above this caption to run the animation and toggle between plotted results. H-27
H.43 Summary of the optimization results (OF best and PR) from the case studies associated with Figures H.19, H.21, H.23 and H.25. Population's locations reinitialized randomly before each generation. Please click on the buttons above this caption to toggle between plotted results. H-28
H.44 Summary of the optimization results (OF best and PR) from the case studies associated with Figures H.27, H.29, H.31 and H.33. Reinits Step 5 Gens. Please click on the buttons above this caption to toggle between plotted results. H-28
H.45 Summary of the optimization results (OF best and PR) from the case studies associated with Figures H.35, H.37, H.39 and H.41. Reinits Step 10 Gens. Please click on the buttons above this caption to toggle between plotted results. H-29
H.46 Summary of the optimization results (OF best) from all case studies (Figures H.43 to H.45), comparing the three types of population's locations reinitializations, for 1, 2, 3 and 4 patches, individually. Please click on the buttons above this caption to toggle between plotted results. H-30

H.47 Summary of the optimization results (PR) from all case studies (Figures H.43 to H.45), comparing the three types of population's locations reinitializations, for 1, 2, 3 and 4 patches, individually. Please click on the buttons above this caption to toggle between plotted results. H-30

H.48 Optimization case study scheme for approx. of beams' deflections to 2 control points. . . H-32

H.49 Optimization results, for all generations, from the case study of approximation of beams' deflections to 2 control points, mixing up LaRC-Si and PVDF, considering $p = 1$ and the same BA parameters from Figure H.8. DVs are the electric potentials ϕ [V] applied to each patch. Please click on the buttons above this caption to toggle between plotted results. . . H-33

H.50 Deflection plots of all successive best iterations found in the case study associated with Figure H.49. Note that the bold numbers above the x-axis (first row) correspond to the percentage [%] of piezoelectric material, $V_{f,r}^{ex}$, mixed up in each element along the beam's length, at each frame. Note that the bold numbers above the x-axis (second row) correspond to the voltage [V] in each element along the beam's length, at each frame. Note that the bold percentages above each control point correspond to the deviation [%] between w_{CP} and $\overline{w}_{CP}$, at each frame. Please click on the buttons above this caption to run the animation and toggle between plotted results. H-34

H.51 3D and 2D deflection plots of all successive best iterations found in the case study associated with Figure H.49. Please click on the buttons above this caption to run the animation and toggle between plotted results. H-34

H.52 Electric potentials plots of all successive best iterations found in the case study associated with Figure H.49. Note that the bold numbers above the x-axis (first row) correspond to the percentage [%] of piezoelectric material, $V_{f,r}^{ex}$, mixed up in each element along the beam's length, at each frame. Note that the bold numbers above the x-axis (second row) correspond to the voltage [V] in each element along the beam's length, at each frame. Please click on the buttons above this caption to run the animation and toggle between plotted results. H-35

H.53 Voltage plots of all successive best iterations found in the case study associated with Figure H.49. Note that the bold numbers above the x-axis (first row) correspond to the percentage [%] of piezoelectric material, $V_{f,r}^{ex}$, mixed up in each element along the beam's length, at each frame. Note that the bold numbers above the x-axis (second row) correspond to the voltage [V] in each element along the beam's length, at each frame. Please click on the buttons above this caption to run the animation and toggle between plotted results. . . H-35

H.54 Optimization results, for all generations, from the case study of approximation of beams' deflections to 2 control points, mixing up LaRC-Si and PVDF, considering $p = 5$ and the same BA parameters from Figure H.8. DVs are the electric potentials ϕ [V] applied to each patch. Please click on the buttons above this caption to toggle between plotted results. . . H-36

H.55 Deflection plots of all successive best iterations found in the case study associated with Figure H.54. Note that the bold numbers above the x-axis (first row) correspond to the percentage [%] of piezoelectric material, $V_{f,r}^{ex}$, mixed up in each element along the beam's length, at each frame. Note that the bold numbers above the x-axis (second row) correspond to the voltage [V] in each element along the beam's length, at each frame. Note that the bold percentages above each control point correspond to the deviation [%] between w_{CP} and $\overline{w}_{CP}$, at each frame. Please click on the buttons above this caption to run the animation and toggle between plotted results. H-37

H.56 3D and 2D deflection plots of all successive best iterations found in the case study associated with Figure H.54. Please click on the buttons above this caption to run the animation and toggle between plotted results. H-37
H.57 Electric potentials plots of all successive best iterations found in the case study associated with Figure H.54. Note that the bold numbers above the x-axis (first row) correspond to the percentage $[\%]$ of piezoelectric material, $V_{f,r}^{ex}$, mixed up in each element along the beam's length, at each frame. Note that the bold numbers above the x-axis (second row) correspond to the voltage $[\mathrm{V}]$ in each element along the beam's length, at each frame. Please click on the buttons above this caption to run the animation and toggle between plotted results. H-38
H.58 Voltage plots of all successive best iterations found in the case study associated with Figure H.54. Note that the bold numbers above the x-axis (first row) correspond to the percentage $[\%]$ of piezoelectric material, $V_{f,r}^{ex}$, mixed up in each element along the beam's length, at each frame. Note that the bold numbers above the x-axis (second row) correspond to the voltage $[\mathrm{V}]$ in each element along the beam's length, at each frame. Please click on the buttons above this caption to run the animation and toggle between plotted results. . . H-38
H.59 Optimization results, for all generations, from the case study of approximation of beams' deflections to 2 control points, mixing up LaRC-Si and PVDF, considering $p = 5$ and the same BA parameters from Figure H.8. DVs are the electric potentials ϕ $[\mathrm{V}]$ applied to each patch, one different p-exponent for both patches no.1 and 7, one different p-exponent for both patches no.2 and 8. Please click on the buttons above this caption to toggle between plotted results. H-39
H.60 Deflection plots of all successive best iterations found in the case study associated with Figure H.59. Note that the bold numbers above the x-axis (first row) correspond to the percentage $[\%]$ of piezoelectric material, $V_{f,r}^{ex}$, mixed up in each element along the beam's length, at each frame. Note that the bold numbers above the x-axis (second row) correspond to the voltage $[\mathrm{V}]$ in each element along the beam's length, at each frame. Note that the bold percentages above each control point correspond to the deviation $[\%]$ between w_{CP} and $\overline{w}_{CP}$, at each frame. Please click on the buttons above this caption to run the animation and toggle between plotted results. H-40
H.61 3D and 2D deflection plots of all successive best iterations found in the case study associated with Figure H.59. Please click on the buttons above this caption to run the animation and toggle between plotted results. H-40
H.62 Electric potentials plots of all successive best iterations found in the case study associated with Figure H.59. Note that the bold numbers above the x-axis (first row) correspond to the percentage $[\%]$ of piezoelectric material, $V_{f,r}^{ex}$, mixed up in each element along the beam's length, at each frame. Note that the bold numbers above the x-axis (second row) correspond to the voltage $[\mathrm{V}]$ in each element along the beam's length, at each frame. Please click on the buttons above this caption to run the animation and toggle between plotted results. H-41
H.63 Voltage plots of all successive best iterations found in the case study associated with Figure H.59. Note that the bold numbers above the x-axis (first row) correspond to the percentage $[\%]$ of piezoelectric material, $V_{f,r}^{ex}$, mixed up in each element along the beam's length, at each frame. Note that the bold numbers above the x-axis (second row) correspond to the voltage $[\mathrm{V}]$ in each element along the beam's length, at each frame. Please click on the buttons above this caption to run the animation and toggle between plotted results. . . H-41
H.64 Optimization case study scheme for approx. of beams' deflections to 3 control points. . . H-42

H.65 Optimization results, for all generations, from the case study of approximation of beams' deflections to 3 control points, mixing up LaRC-Si and PVDF, considering $p = 1$ and the same BA parameters from Figure H.8. DVs are the electric potentials ϕ [V] applied to each patch. Please click on the buttons above this caption to toggle between plotted results. . . . H-43

H.66 Deflection plots of all successive best iterations found in the case study associated with Figure H.65. Note that the bold numbers above the x-axis (first row) correspond to the percentage [%] of piezoelectric material, $V_{f,r}^{ex}$, mixed up in each element along the beam's length, at each frame. Note that the bold numbers above the x-axis (second row) correspond to the voltage [V] in each element along the beam's length, at each frame. Note that the bold percentages above each control point correspond to the deviation [%] between w_{CP} and $\overline{w}_{CP}$, at each frame. Please click on the buttons above this caption to run the animation and toggle between plotted results. H-44

H.67 3D and 2D deflection plots of all successive best iterations found in the case study associated with Figure H.65. Please click on the buttons above this caption to run the animation and toggle between plotted results. H-44

H.68 Electric potentials plots of all successive best iterations found in the case study associated with Figure H.65. Note that the bold numbers above the x-axis (first row) correspond to the percentage [%] of piezoelectric material, $V_{f,r}^{ex}$, mixed up in each element along the beam's length, at each frame. Note that the bold numbers above the x-axis (second row) correspond to the voltage [V] in each element along the beam's length, at each frame. Please click on the buttons above this caption to run the animation and toggle between plotted results. H-45

H.69 Voltage plots of all successive best iterations found in the case study associated with Figure H.65. Note that the bold numbers above the x-axis (first row) correspond to the percentage [%] of piezoelectric material, $V_{f,r}^{ex}$, mixed up in each element along the beam's length, at each frame. Note that the bold numbers above the x-axis (second row) correspond to the voltage [V] in each element along the beam's length, at each frame. Please click on the buttons above this caption to run the animation and toggle between plotted results. . . . H-45

H.70 Optimization results, for all generations, from the case study of approximation of beams' deflections to 3 control points, mixing up LaRC-Si and PVDF, considering $p = 5$ and the same BA parameters from Figure H.8. DVs are the electric potentials ϕ [V] applied to each patch. Please click on the buttons above this caption to toggle between plotted results. . . . H-46

H.71 Deflection plots of all successive best iterations found in the case study associated with Figure H.70. Note that the bold numbers above the x-axis (first row) correspond to the percentage [%] of piezoelectric material, $V_{f,r}^{ex}$, mixed up in each element along the beam's length, at each frame. Note that the bold numbers above the x-axis (second row) correspond to the voltage [V] in each element along the beam's length, at each frame. Note that the bold percentages above each control point correspond to the deviation [%] between w_{CP} and $\overline{w}_{CP}$, at each frame. Please click on the buttons above this caption to run the animation and toggle between plotted results. H-47

H.72 3D and 2D deflection plots of all successive best iterations found in the case study associated with Figure H.70. Please click on the buttons above this caption to run the animation and toggle between plotted results. H-47

H.73 Electric potentials plots of all successive best iterations found in the case study associated with Figure H.70. Note that the bold numbers above the x-axis (first row) correspond to the percentage $[\%]$ of piezoelectric material, $V_{f,r}^{ex}$, mixed up in each element along the beam's length, at each frame. Note that the bold numbers above the x-axis (second row) correspond to the voltage $[\mathrm{V}]$ in each element along the beam's length, at each frame. Please click on the buttons above this caption to run the animation and toggle between plotted results. H-48

H.74 Voltage plots of all successive best iterations found in the case study associated with Figure H.70. Note that the bold numbers above the x-axis (first row) correspond to the percentage $[\%]$ of piezoelectric material, $V_{f,r}^{ex}$, mixed up in each element along the beam's length, at each frame. Note that the bold numbers above the x-axis (second row) correspond to the voltage $[\mathrm{V}]$ in each element along the beam's length, at each frame. Please click on the buttons above this caption to run the animation and toggle between plotted results. . . . H-48

H.75 Optimization results, for all generations, from the case study of approximation of beams' deflections to 3 control points, mixing up LaRC-Si and PVDF, considering $p = 5$ and the same BA parameters from Figure H.8. DVs are the electric potentials ϕ $[\mathrm{V}]$ applied to each patch, one different p-exponent for both patches no.1 and 7, one different p-exponent for both patches no.2 and 8. Please click on the buttons above this caption to toggle between plotted results. H-49

H.76 Deflection plots of all successive best iterations found in the case study associated with Figure H.75. Note that the bold numbers above the x-axis (first row) correspond to the percentage $[\%]$ of piezoelectric material, $V_{f,r}^{ex}$, mixed up in each element along the beam's length, at each frame. Note that the bold numbers above the x-axis (second row) correspond to the voltage $[\mathrm{V}]$ in each element along the beam's length, at each frame. Note that the bold percentages above each control point correspond to the deviation $[\%]$ between w_{CP} and $\overline{w}_{CP}$, at each frame. Please click on the buttons above this caption to run the animation and toggle between plotted results. H-50

H.77 3D and 2D deflection plots of all successive best iterations found in the case study associated with Figure H.75. Please click on the buttons above this caption to run the animation and toggle between plotted results. H-50

H.78 Electric potentials plots of all successive best iterations found in the case study associated with Figure H.75. Note that the bold numbers above the x-axis (first row) correspond to the percentage $[\%]$ of piezoelectric material, $V_{f,r}^{ex}$, mixed up in each element along the beam's length, at each frame. Note that the bold numbers above the x-axis (second row) correspond to the voltage $[\mathrm{V}]$ in each element along the beam's length, at each frame. Please click on the buttons above this caption to run the animation and toggle between plotted results. H-51

H.79 Voltage plots of all successive best iterations found in the case study associated with Figure H.75. Note that the bold numbers above the x-axis (first row) correspond to the percentage $[\%]$ of piezoelectric material, $V_{f,r}^{ex}$, mixed up in each element along the beam's length, at each frame. Note that the bold numbers above the x-axis (second row) correspond to the voltage $[\mathrm{V}]$ in each element along the beam's length, at each frame. Please click on the buttons above this caption to run the animation and toggle between plotted results. . . . H-51

H.80 Optimization case study scheme for max. ω_1 of non-skewed beams. H-52

H.81 Parametric 2D plots of all successive best iterations found in the case study associated with Figure H.80, concerning DVs' fibre orientations in [°], as well as OF best ω_1 and PI, at each frame. Please click on the buttons above this caption to run the animation and toggle between plotted results. H-53
H.82 3D and 2D fundamental free vibrational mode amplitude's distributions of all successive best iterations found in the case study associated with Figure H.80. Please click on the buttons above this caption to run the animation and toggle between plotted results. H-54
H.83 Optimization case study scheme for max. ω_1 of skewed beams. H-55
H.84 Parametric 2D plots of all successive best iterations found in the case study associated with Figure H.83, concerning DVs' fibre orientations in [°], as well as OF best ω_1 and PI, at each frame. Please click on the buttons above this caption to run the animation and toggle between plotted results. H-57
H.85 3D and 2D fundamental free vibrational mode amplitude's distributions of all successive best iterations found in the case study associated with Figure H.83. Please click on the buttons above this caption to run the animation and toggle between plotted results. H-57
H.86 Optimization case study scheme for max. ω_1 of skewed plates. H-58
H.87 Parametric 2D plots of all successive best iterations found in the case study associated with Figure H.86, concerning DVs' fibre orientations in [°], as well as OF best ω_1 and PI, at each frame. Please click on the buttons above this caption to run the animation and toggle between plotted results. H-60
H.88 3D and 2D fundamental free vibrational mode amplitude's distributions of all successive best iterations found in the case study associated with Figure H.86. Please click on the buttons above this caption to run the animation and toggle between plotted results. H-61

I.1 Main simulator panel. I-2
I.2 Definition of the load imposed to the plate. I-2
I.3 Characterization of the different type materials' properties. I-3
I.4 Characterization of the plate's transverse deflection. I-3
I.5 Micro-controller Arduino® UNO. From Arduino® (2016). I-4
I.6 Micro-computer Raspberry Pi® 2 Model B V1.1. From Raspberry Pi® (2016). I-4
I.7 Piezoelectric patches, DuraAct Patch Transducers. From PI-Ceramic® (2016a). I-5
I.8 DRV8662 Piezo Haptic Driver with Integrated Boost Converter (functional block diagram). From Texas Instruments® (2016). I-5
I.9 PI-Ceramic® piezoelectric patches' quotation. I-8

List of Tables

3.1 Passive and active materials' properties used in case studies, from several references (continues in Table 3.2). . . . 68
3.2 Passive and active materials' properties used in case studies, from several references (continued from Table 3.1). . . . 69
3.3 Material properties of metal-ceramic FGMs. . . . 75
3.4 Material and geometrical properties of CNTs (Kim et al., 2009; Rafiee et al., 2014a). . . . 77
3.5 Nodes coordinates on local element natural coordinate system. . . . 80
3.6 Different integration schemes for Lagrangian elements and respective quadrature rules. Adapted from Bocskai and Nagy (2013). . . . 84

4.1 Non-dimensional maximum deflection $\overline{w}$. 4BlinLag elements. . . . 106
4.2 Non-dimensional maximum deflection $\overline{w}$. 9BquadLag elements. . . . 106
4.3 Non-dimensional stress $\overline{\sigma}_{xx}$ at plate outer surfaces' centroids. 4BlinLag elements. . . . 107
4.4 Non-dimensional stress $\overline{\sigma}_{xx}$ at plate outer surfaces' centroids. 9BquadLag elements. . . . 107
4.5 Non-dimensional natural frequencies $\overline{\omega}$. 4BlinLag / 9BquadLag elements (same results). 108
4.6 Comparison of deflections' deviations obtained in the validation case study of bimorph beam (actuation (CFFF)), with Loja et al. (2001). . . . 110
4.7 Comparison of closed and open-circuit natural frequencies' deviations, for several meshes (10×1), (20×1) and (30×1), obtained in the validation case study of three-layer active/sensory cantilever composite beam, with Saravanos and Heyliger (1995). . . . 111
4.8 Comparison of closed and open-circuit non-dimensional natural frequencies' deviations, for several aspect ratios, obtained in the validation case study of a 5-ply $[p/0°/90°/0°/p]$ laminated simply-supported square plate, with Saravanos et al. (1997). . . . 112
4.9 Validation of both first and second modes' natural frequencies, considering ply angles of $[0°/0°/0°/0°]$ and $[70°/70°/70°/70°]$ (substrate). Comparison between the present FEM 4BlinLag elements and the ones from Correia et al. (2001) (Q9-HSDT 11P, Q9-HSDT 9P and Q9-FSDT 5P). . . . 113
4.10 Optimal ply angles for maximum natural frequency of first vibration mode. Comparison between results obtained using the simulated annealing method and gradient-based optimization method from Correia et al. (2001), and the present MHBA, considering an initial design of $[0°/0°/0°/0°]$. . . . 114
4.11 Non-dimensional maximum deflections, $\overline{w}$ (MWCNTs). . . . 117
4.12 Properties of MWCNTs (U.S. Research Nanomaterials, Inc., 2016). . . . 117
4.13 Non-dimensional maximum deflections, $\overline{w} \times 10^{-4}$ (MWCNTs). . . . 119
4.14 Non-dimensional stress $\overline{\sigma}_{xx}$ at plate outer surfaces' centroids ($w_{CNT} = 0$). . . . 119
4.15 Non-dimensional stress $\overline{\sigma}_{xx}$ at plate outer surfaces' centroids ($w_{CNT} = 0.05$, SWCNTs). 119

4.16 Non-dimensional stress $\overline{\sigma}_{xx}$ at plate outer surfaces' centroids (SWCNTs). 120
4.17 Non-dimensional stress $\overline{\sigma}_{xx}$ at plate outer surfaces' centroids (MWCNTs). 120
4.18 Non-dimensional maximum shear stresses, $\overline{\tau}_{xy}$ and $\overline{\tau}_{xz}$. 121
4.19 Non-dimensional maximum shear stresses, $\overline{\tau}_{xy}$ and $\overline{\tau}_{xz}$ (MWCNTs). 121
4.20 Non-dimensional maximum shear stresses, $\overline{\tau}_{xy}$ and $\overline{\tau}_{xz}$ (SWCNTs). 121
4.21 Non-dimensional maximum deflections, $\overline{w}$ (SWCNTs). 122
4.22 Non-dimensional maximum in-plane stresses, $\overline{\sigma}_{xx}$ (SWCNTs). 122
4.23 Non-dimensional maximum shear stresses, $\overline{\tau}_{xy}$ and $\overline{\tau}_{xz}$ ($w_{CNT} = 0$, SWCNTs). 122
4.24 Non-dimensional maximum shear stresses, $\overline{\tau}_{xy}$ and $\overline{\tau}_{xz}$ (SWCNTs). 122
4.25 Non-dimensional maximum deflections, $\overline{w}$ (SWCNTs). 123
4.26 Non-dimensional maximum in-plane stresses, $\overline{\sigma}_{xx}$ (SWCNTs). 123
4.27 Non-dimensional maximum shear stresses, $\overline{\tau}_{xy}$ (SWCNTs). 124
4.28 Non-dimensional maximum shear stresses, $\overline{\tau}_{xz}$ (SWCNTs). 124
4.29 Natural frequencies ω in [Hz] (Hertz) (MWCNTs, $w_{CNT} = 5\,\%$). 125
4.30 Deviations in [%], from continuous approach, of nat. freqs. ω (MWCNTs, $w_{CNT} = 5\,\%$). 126
4.31 Fundamental natural frequency ω_1 in [Hz] (Hertz) (MWCNTs). 126
4.32 Natural frequencies ω in [Hz] (Hertz) (SWCNTs, $w_{CNT} = 4\,\%$, $p = 5$). 127
4.33 Fundamental natural frequency ω_1 in [Hz] (Hertz) (SWCNTs). 127
4.34 Natural frequencies ω in [Hz] (Hertz) (SWCNTs, $p = 5$). 127
4.35 Natural frequencies ω in [Hz] (Hertz) (FGM1 with SWCNTs). 128
4.36 Natural frequencies ω in [Hz] (Hertz) (MWCNTs). 129

D.1 Gauss points natural coordinates associated with (1×1) two-dimensional product rule ($p = 1$). D-1
D.2 Gauss points integration weights associated with (1×1) two-dimensional product rule ($p = 1$). D-1
D.3 Gauss points natural coordinates associated with (2×2) two-dimensional product rule ($p = 2$). D-1
D.4 Gauss points integration weights associated with (2×2) two-dimensional product rule ($p = 2$). D-2
D.5 Gauss points natural coordinates associated with (3×3) two-dimensional product rule ($p = 3$). D-2
D.6 Gauss points integration weights associated with (3×3) two-dimensional product rule ($p = 3$). D-2
D.7 Gauss points natural coordinates associated with (4×4) two-dimensional product rule ($p = 4$). D-3
D.8 Gauss points integration weights associated with (4×4) two-dimensional product rule ($p = 4$). D-4

F.1 The effect of reduced integration, thickness, and mesh refinement on the centre deflections and stresses of a simply-supported, isotropic, square plate under an uniform transverse load. Comparison between the results from Reddy (2006) and the present FEM algorithm. F-2
F.2 Comparison of DOFs obtained from the isotropic simply-supported plate validation model using AMAPDL and the present FEM platform, considering 15 different meshes. F-5
F.3 Comparison of strains obtained from the isotropic simply-supported plate validation model using AMAPDL and the present FEM platform, considering 15 different meshes. F-6

F.4 Comparison of stresses obtained from the isotropic simply-supported plate validation model using AMAPDL and the present FEM platform, considering 15 different meshes. F-7
F.5 Comparison of natural freqs. obtained from the isotropic simply-supported plate validation model using AMAPDL and the present FEM platform, considering 15 different meshes. F-8
F.6 Comparison of voltages' deviations, along x-coordinates, obtained in the validation case study of bimorph beam (sensing (CFFF)), with other references. F-10
F.7 Comparison of voltages' deviations, for each element number, obtained in the validation case study of bimorph beam (sensing (CFFF)), with other references. F-10
F.8 Comparison of closed-circuit natural frequencies' deviations, for several approaches, obtained in the validation case study of bimorph plate, $L/h = 10$, (SSFF), with Wang (2004). F-15
F.9 Comparison of open-circuit natural frequencies' deviations, for several approaches, obtained in the validation case study of bimorph plate, $L/h = 10$, (SSFF), with Wang (2004). F-16
F.10 Comparison of natural frequencies' deviations, for several geometry variables, MBCs, EBCs, mesh (15×15), $a = 1$ m, obtained in the validation case study of hybrid rectangular plate, with Farsangi et al. (2013). a is the length and b the width of the plate, $2h$ the core thickness and h_p the thickness of each piezoelectric layer. F-17
F.11 Optimization results for 79 CSs, about the validation case study (Correia et al., 2001). . . F-19

G.1 Convergence results of DOF $\max |w|$ [m], for all elements. G-2
G.2 Convergence results of DOF $\max |\theta_x|$ [rad], for all elements. G-2
G.3 Convergence results of strain $\max |\epsilon_{xx}|$, for all elements. G-2
G.4 Convergence results of strain $\max |\gamma_{xy}|$, for all elements. G-3
G.5 Convergence results of strain $\max |\gamma_{xz}|$, for all elements. G-3
G.6 Convergence results of stress $\max |\sigma_{xx}|$ [Pa], for all elements. G-3
G.7 Convergence results of stress $\max |\tau_{xy}|$ [Pa], for all elements. G-4
G.8 Convergence results of stress $\max |\tau_{xz}|$ [Pa], for all elements. G-4
G.9 Convergence results of stress $\max |\sigma_{VM}|$ [Pa], for all elements. G-4
G.10 Convergence results of natural frequency ω_1 [Hz], for all elements. G-5
G.11 Convergence results of natural frequency ω_2 [Hz], for all elements. G-5
G.12 Convergence results of natural frequency ω_3 [Hz], for all elements. G-5
G.13 Convergence results of natural frequency ω_4 [Hz], for all elements. G-6
G.14 Convergence results of natural frequency ω_5 [Hz], for all elements. G-6
G.15 Convergence results of computation time [s], for all elements. G-6
G.16 Deflections [m] associated with plotted results in Figure G.61. . . . . G-53
G.17 Deflections [m] associated with plotted results in Figure G.62. . . . . G-53
G.18 Deflections [m] associated with plotted results in Figure G.63. . . . . G-54
G.19 Deflections [m] associated with plotted results in Figure G.64. . . . . G-54
G.20 Voltages [V] associated with plotted results in Figure G.77. . . . . G-63
G.21 Voltages [V] associated with plotted results in Figure G.78. . . . . G-63
G.22 Voltages [V] associated with plotted results in Figure G.79. . . . . G-64
G.23 Voltages [V] associated with plotted results in Figure G.80. . . . . G-64
G.24 Natural frequencies [Hz] associated with plotted results in Figures G.87 and G.91. . . . . G-74
G.25 Natural frequencies [Hz] associated with plotted results in Figures G.88 and G.92. . . . . G-75
G.26 Natural frequencies [Hz] associated with plotted results in Figures G.89 and G.93. . . . . G-76
G.27 Natural frequencies [Hz] associated with plotted results in Figures G.90 and G.94. . . . . G-77
G.28 Differences between closed and open-circuit natural frequencies [Hz] from Table G.24. . G-78

G.29 Differences between closed and open-circuit natural frequencies [Hz] from Table G.25. . G-78
G.30 Differences between closed and open-circuit natural frequencies [Hz] from Table G.26. . G-79
G.31 Differences between closed and open-circuit natural frequencies [Hz] from Table G.27. . G-79

H.1 HBA parameters used to compute all case studies presented in Figure H.2. . . . . H-2
H.2 Random combinations of DE perturbation factors $Fper_i$ and $Fper_f$, sorted from the minimum (best) to the maximum (worst) deflection obtained from the CSs presented in Figure H.2. . . . . H-3
H.3 MHBA parameters used to compute all case studies presented in Figures H.46 and H.47. H-14
H.4 Random combinations of DE perturbation factors $Fper_i$ and $Fper_f$, sorted from the minimum (best) to the maximum (worst) deflection obtained from the CSs presented in Figure H.19. . . . . H-15
H.5 Deflections $(\times 10^{-5}\,[\mathrm{m}])$ / PR $[\%]$ associated with plotted results in Figures H.46 and H.47. H-31
H.6 MHBA parameters used to compute the case study presented in Figure H.80. . . . . H-53
H.7 Optimization results for 8 CSs, about the optimization case study in Figure H.83. . . . . H-56
H.8 Optimization results for 8 CSs, about the optimization case study in Figure H.86. . . . . H-59

Nomenclature

Acronyms

16BcubKrig	**16**-Node **Bi**c**ub**ic **Krig**ing Quadrilateral
16BcubLag	**16**-Node **Bi**c**ub**ic **Lag**range Quadrilateral
16BlinKrig	**16**-Node **Bi**l**in**ear **Krig**ing Quadrilateral
16BquadKrig	**16**-Node **Bi**q**uad**ratic **Krig**ing Quadrilateral
4BlinKrig	**4**-Node **Bi**l**in**ear **Krig**ing Quadrilateral
4BlinLag	**4**-Node **Bi**l**in**ear **Lag**range Quadrilateral
9BlinKrig	**9**-Node **Bi**l**in**ear **Krig**ing Quadrilateral
9BquadKrig	**9**-Node **Bi**q**uad**ratic **Krig**ing Quadrilateral
9BquadLag	**9**-Node **Bi**q**uad**ratic **Lag**range Quadrilateral
AFC	**A**ctive **F**ibre **C**omposite
AMAPDL	**A**NSYS **M**echanical **APDL**®
BA	**B**at-**A**lgorithm
BBA	**B**inary **B**at **A**lgorithm
BC	**B**oundary **C**ondition
CBA	**C**haotic **B**at **A**lgorithm
CFD	**C**omputational **F**luid **D**ynamics
CNT	**C**arbon **N**ano-**T**ube
CP	**C**ontrol **P**oint
CS	**C**ase **S**tudy
DE	**D**ifferential **E**volution
DEBA	**D**oppler **E**ffect **B**at **A**lgorithm
DOF	**D**egree **O**f **F**reedom

DV	**D**esign **V**ariable
EBC	**E**lectric **B**oundary **C**ondition
ESL	**E**quivalent **S**ingle **L**ayer
FCC	**F**ace **C**entred **C**ubic
FEM	**F**inite **E**lement **M**ethod
FEUP	University of Porto / ***F**aculdade de **E**ngenharia da **U**niversidade do **P**orto*
FGM	**F**unctionally **G**raded **M**aterial
FLBA	**F**uzzy **L**ogic **B**at **A**lgorithm
FNN	**F**eedforward **N**eural **N**etwork
FSDT	**F**irst-Order **S**hear **D**eformation **T**heory
GA	**G**enetic **A**lgorithm
GUI	**G**raphical **U**ser **I**nterface
HBA	**H**ybrid-**B**at-**A**lgorithm
IBA	**I**mproved **B**at **A**lgorithm
ISEL	Lisbon Superior Engineering Institute / ***I**nstituto **S**uperior de **E**ngenharia de **L**isboa*
KMBA	**K** **M**eans **B**at **A**lgorithm
LSAT	**L**ove **S**econd **A**pproximation **T**heory
MAPDL	**M**echanical **APDL**
MBA	**M**odified **B**at **A**lgorithm
MBC	**M**echanical **B**oundary **C**ondition
MECHCOMP2	**2**nd International Conference on **Mech**anics of **Comp**osites
MFC	**M**acro **F**ibre **C**omposite
MHBA	**M**icro-**H**ybrid-**B**at-**A**lgorithm
MOBA	**M**ulti **O**bjective **B**at **A**lgorithm
MWCNT	**M**ulti **W**alled **C**arbon **N**ano-**T**ube
OF	**O**bjective **F**unction
OPF	**O**ptimum **P**ath **F**orest

PCA	**P**rincipal **C**omponent **A**nalysis
PD	**P**ercent **D**eviation
PI	**P**ercentage **I**ncrease
PR	**P**ercentage **R**eduction
PSO	**P**article **S**warm **O**ptimization
PVD	**P**rinciple of **V**irtual **D**isplacements
RESM	**R**esearch on **E**ngineering **S**tructures and **M**aterials
SEM	**S**canning **E**lectron **M**icroscopy
SI	The International System of Units
SMA	**S**hape **M**emory **A**lloy
SWCNT	**S**ingle **W**alled **C**arbon **N**ano-**T**ube
WEMEM	4th Workshop on Mechanical Engineering and Maintenance Engineering / *4º **W**orkshop em **E**ngenharia **M**ecânica e em **E**ngenharia da **M**anutenção*

Subscripts

1	3D Cartesian coord. system component (x_1-axis) (principal material coordinate system)
2	3D Cartesian coord. system component (y_2-axis) (principal material coordinate system)
3	3D Cartesian coord. system component (z_3-axis) (principal material coordinate system)
cn	identifies centre coordinates
eff	identifies the resulting material effective property
ex	finite element number along x-direction
MC	denotes multiscale composite
NC	denotes nano-composite
nsk	denotes non-skewed
pl	denotes piezoelectric layer
sk	denotes skewed
sk	sub-layer number

VM	denotes Von Mises
ϕ or $\phi\phi$	identifies quantities associated with pure electrical contributions
b	identifies *body* loads
b	identifies components associated with *bending* contributions
c	identifies *concentrated* loads
e	finite element number
k	layer number
m	matrix phase
r	reinforcement phase
s	identifies *surface* loads
s	identifies components associated with *shear* contributions
u or uu	identifies quantities associated with pure mechanical contributions
$u\phi$ or ϕu	identifies quantities associated with coupling between mechanical/electrical contributions
x	3D Cartesian coord. system component (x-axis) (problem reference coordinate system)
y	3D Cartesian coord. system component (y-axis) (problem reference coordinate system)
z	3D Cartesian coord. system component (z-axis) (problem reference coordinate system)

Superscripts

0	identifies quantities associated with the structure's (beam/plate) reference mid-surface Ω, at plane $z_\Omega = 0$
$*$	asterisk (temporary), identifies plane stress-reduced material coefficients
(0)	identifies membrane strains
(1)	identifies flexural (bending) strains (curvatures)
ex	finite element number along x-direction
e	finite element number
k	layer number

Chemical Symbols / Formulas

Acronym	Chemical Element or Compound Name	Symbol / Formula
–	Aluminium	Al
–	Barium	Ba
–	Beryllium	Be
–	Carbon	C
–	Fluorine	F
–	Hydrogen	H
–	Lead	Pb
–	Nickel	Ni
–	Oxygen	O
–	Platinum	Pt
–	Silicon	Si
–	Titanium	Ti
–	Zirconium	Zr
AO	**A**luminium **O**xide	Al_2O_3
BT	**B**arium **T**itanate	$BaTiO_3$
Gr	**Gr**aphite	C
LaRC-Si	**La**ngley **R**esearch **C**enter-**S**oluble **I**mide	LaRC-Si
LiTa	**Li**thium **Ta**ntalate	$LiTaO_3$
LN	**L**ithium **N**iobate	$LiNbO_3$
LT	**L**ead **T**itanate	$PbTiO_3$
NiTiNOL	**Ni**ckel **Ti**tanium **N**aval **O**rdnance **L**aboratory	NiTiNOL
PVDF	Polyvinylidene Fluoride	$(C_2H_2F_2)_n$
PZT	Lead Zirconate Titanate	$Pb[Zr_xTi_{1-x}]O_3$ $(0 \leq x \leq 1)$
SC	**S**ilicon **C**arbide	SiC
SD	**S**ilicon **D**ioxide	SiO_2
TA	**T**itanium **A**luminide	TiAl
ZD	**Z**irconium **D**ioxide (Zirconia)	ZrO_2

Base and Derived SI Units

Unit Name	Base or Derived Quantity Name	SI Unit
Ampere	electric current	$[\mathrm{A}]$
Coulomb	electric charge, amount of electricity	$[\mathrm{C}] = [\mathrm{s} \cdot \mathrm{A}]$
Farad	capacitance	$[\mathrm{F}] = \left[\mathrm{m}^{-2} \cdot \mathrm{kg}^{-1} \cdot \mathrm{s}^{4} \cdot \mathrm{A}^{2}\right]$
Hertz	frequency	$[\mathrm{Hz}] = \left[\mathrm{s}^{-1}\right]$
Joule	energy, work	$[\mathrm{J}] = \left[\mathrm{m}^{2} \cdot \mathrm{kg} \cdot \mathrm{s}^{-2}\right]$
kilogram	mass	$[\mathrm{kg}]$
metre	length, width, height, depth, etc.	$[\mathrm{m}]$
Newton	force	$[\mathrm{N}] = \left[\mathrm{m} \cdot \mathrm{kg} \cdot \mathrm{s}^{-2}\right]$
Pascal	pressure, stress	$[\mathrm{Pa}] = \left[\mathrm{m}^{-1} \cdot \mathrm{kg} \cdot \mathrm{s}^{-2}\right]$
radian	plane angle	$[\mathrm{rad}] = \left[\mathrm{m} \cdot \mathrm{m}^{-1}\right]$
second	time, duration	$[\mathrm{s}]$
Volt	electric potential, elect. potent. difference (voltage)	$[\mathrm{V}] = \left[\mathrm{m}^{2} \cdot \mathrm{kg} \cdot \mathrm{s}^{-3} \cdot \mathrm{A}^{-1}\right]$

Dimensions Symbols

Symbol	Base Quantity Name	SI Unit
I	electric current	$[\mathrm{A}]$
L	length, width, height, depth, etc.	$[\mathrm{m}]$
M	mass	$[\mathrm{kg}]$
T	time, duration	$[\mathrm{s}]$

Greek Symbols

Symbol	Description	Dimensions	SI Unit
α	constant that enables a progressive variation of loudness in BA	–	–
α	skew angle	dimensionless	$[\mathrm{rad}]$
β_{dd}	auxiliary variable associated with relations between the elastic moduli of the CNTs E_{CNT} and metallic matrix E_m, outer diameter d_{CNT} and thickness t_{CNT} of the CNTs	dimensionless	$\left[\mathrm{m} \cdot \mathrm{m}^{-1}\right]$

β_{dl}	auxiliary variable associated with relations between the elastic moduli of the CNTs E_{CNT} and metallic matrix E_m, outer diameter d_{CNT}, length l_{CNT} and thickness t_{CNT} of the CNTs	dimensionless	$\left[\mathrm{m} \cdot \mathrm{m}^{-1}\right]$
$\boldsymbol{\mathcal{J}}$	Jacobian matrix	–	–
χ	shear correction factor	–	–
δ	variational operator	–	–
$\delta\epsilon_{ij}$	virtual strain ij-component	dimensionless	$\left[\mathrm{m} \cdot \mathrm{m}^{-1}\right]$
$\delta\mathbf{a}$	virtual variation of a generic variable in xy-plane	–	–
$\Delta\phi$	electric potential difference (voltage)	$\mathrm{L}^2\mathrm{M}\mathrm{T}^{-3}\mathrm{I}^{-1}$	$[\mathrm{V}]$
δE_c	virtual kinetic energy	$\mathrm{L}^2\mathrm{M}\mathrm{T}^{-2}$	$[\mathrm{J}]$
δU	internal virtual work	$\mathrm{L}^2\mathrm{M}\mathrm{T}^{-2}$	$[\mathrm{J}]$
δu	virtual displacement	L	$[\mathrm{m}]$
δU_e	virtual electrical internal work	$\mathrm{L}^2\mathrm{M}\mathrm{T}^{-2}$	$[\mathrm{J}]$
δU_m	virtual strain energy	$\mathrm{L}^2\mathrm{M}\mathrm{T}^{-2}$	$[\mathrm{J}]$
δV	external virtual work	$\mathrm{L}^2\mathrm{M}\mathrm{T}^{-2}$	$[\mathrm{J}]$
δW	virtual work done by the applied (actual) forces	$\mathrm{L}^2\mathrm{M}\mathrm{T}^{-2}$	$[\mathrm{J}]$
δW_ϕ	virtual work done by the applied surface electrical charge	$\mathrm{L}^2\mathrm{M}\mathrm{T}^{-2}$	$[\mathrm{J}]$
δW_b	virtual work done by the applied mechanical body forces	$\mathrm{L}^2\mathrm{M}\mathrm{T}^{-2}$	$[\mathrm{J}]$
δW_c	virtual work done by the applied mechanical concentrated forces	$\mathrm{L}^2\mathrm{M}\mathrm{T}^{-2}$	$[\mathrm{J}]$
δW_s	virtual work done by the applied mechanical surface forces (pressures)	$\mathrm{L}^2\mathrm{M}\mathrm{T}^{-2}$	$[\mathrm{J}]$
ϵ	scaling factor in BA	–	–
ϵ_{ij}	(normal) strain ij-component, $ij = \{xx, yy, zz\}$	dimensionless	$\left[\mathrm{m} \cdot \mathrm{m}^{-1}\right]$
η	2D Cartesian coord. system component (η-axis) (natural coordinate system)	–	–
Γ	area or boundary	L^2	$\left[\mathrm{m}^2\right]$
γ	constant that enables a progressive variation of pulse rate in BA	–	–

Γ_ϕ	external electrical loading surface	L^2	$\left[\mathrm{m}^2\right]$
Γ_σ	external mechanical loading surface	L^2	$\left[\mathrm{m}^2\right]$
γ_{ij}	shear strain ij-component, $ij = \{xy, yz, xz\}$	dimensionless	$\left[\mathrm{m} \cdot \mathrm{m}^{-1}\right]$
$\hat{\Omega}$	surface associated with master finite element	L^2	$\left[\mathrm{m}^2\right]$
$\{\phi\}$	generalized electrical response vector	$\mathrm{L}^2\mathrm{MT}^{-3}\mathrm{I}^{-1}$	$[\mathrm{V}]$
$\mathcal{D}$	electric displacement	$\mathrm{L}^{-2}\mathrm{TI}$	$\left[\mathrm{C} \cdot \mathrm{m}^{-2}\right]$
$\mathcal{D}_i$	i-direction electric displacement, $i = \{x, y, z\}$	$\mathrm{L}^{-2}\mathrm{TI}$	$\left[\mathrm{C} \cdot \mathrm{m}^{-2}\right]$
$\mathcal{E}$	electric field	$\mathrm{LMT}^{-3}\mathrm{I}^{-1}$	$\left[\mathrm{V} \cdot \mathrm{m}^{-1}\right]$
$\mathcal{E}_i$	i-direction electric field, $i = \{x, y, z\}$	$\mathrm{LMT}^{-3}\mathrm{I}^{-1}$	$\left[\mathrm{V} \cdot \mathrm{m}^{-1}\right]$
$\mathcal{G}^i_{\xi\eta}$	Gauss point natural coordinates	–	–
$\mathcal{G}^i_w$	Gauss point weight	–	–
$\mathcal{G}^i_{xy}$	Gauss point global coordinates	L	$[\mathrm{m}]$
ν_{NC}	Poisson's ratio of nano-composite	dimensionless	$\left[\mathrm{m} \cdot \mathrm{m}^{-1}\right]$
ν_{ij}	Poisson's ratio ij-component, $ij = \{12, 21, 13, 31, 23, 32\}$	dimensionless	$\left[\mathrm{m} \cdot \mathrm{m}^{-1}\right]$
Ω	structure's (beam/plate) reference mid-surface, at plane $z_\Omega = 0$	L^2	$\left[\mathrm{m}^2\right]$
Ω	surface associated with generic finite element	L^2	$\left[\mathrm{m}^2\right]$
Ω_k	layer k mid-surface, at plane $z_{\Omega_k} = z_k + (z_{k+1} - z_k)/2$	L^2	$\left[\mathrm{m}^2\right]$
Ω_{sk}	sub-layer sk mid-surface, at plane $z_{\Omega_{sk}} = z_k + (z_{k+1} - z_k)/(2N_{sl})(2sk - 1)$	L^2	$\left[\mathrm{m}^2\right]$
ω_n	natural frequency associated with mode n	T^{-1}	$[\mathrm{Hz}]$
$\overline{\varepsilon}_{ij}$	transformed plane stress-reduced permittivity ij-component, $ij = \{11, 22, 33, 12\}$	$\mathrm{L}^{-3}\mathrm{M}^{-1}\mathrm{T}^4\mathrm{I}^2$	$\left[\mathrm{F} \cdot \mathrm{m}^{-1}\right]$
ϕ	electric potential	$\mathrm{L}^2\mathrm{MT}^{-3}\mathrm{I}^{-1}$	$[\mathrm{V}]$
ρ	(mass) density	$\mathrm{L}^{-3}\mathrm{M}$	$\left[\mathrm{kg} \cdot \mathrm{m}^{-3}\right]$

ρ_{CNT}	(mass) density of CNT	$\mathrm{L}^{-3}\mathrm{M}$	$\left[\mathrm{kg}\cdot\mathrm{m}^{-3}\right]$
ρ_{NC}	(mass) density of nano-composite	$\mathrm{L}^{-3}\mathrm{M}$	$\left[\mathrm{kg}\cdot\mathrm{m}^{-3}\right]$
ρ_m	(mass) density of matrix	$\mathrm{L}^{-3}\mathrm{M}$	$\left[\mathrm{kg}\cdot\mathrm{m}^{-3}\right]$
σ_{ij}	(normal) stress ij-component, $ij = \{xx, yy, zz\}$	$\mathrm{L}^{-1}\mathrm{MT}^{-2}$	[Pa]
τ_{ij}	shear stress ij-component, $ij = \{xy, yz, xz\}$	$\mathrm{L}^{-1}\mathrm{MT}^{-2}$	[Pa]
θ	material angular orientation in the xy-plane	dimensionless	[rad]
θ_x	rotation of a transverse normal around the y-axis	dimensionless	[rad]
θ_y	rotation of a transverse normal around the x-axis	dimensionless	[rad]
ε_{ij}	permittivity ij-component, $ij = \{11, 22, 33, 12\}$	$\mathrm{L}^{-3}\mathrm{M}^{-1}\mathrm{T}^{4}\mathrm{I}^{2}$	$\left[\mathrm{F}\cdot\mathrm{m}^{-1}\right]$
ξ	2D Cartesian coord. system component (ξ-axis) (natural coordinate system)	–	–

Roman Symbols

Symbol	Description	Dimensions	SI Unit
1	3D Cartesian coord. system component (x_1-axis) (principal material coordinate system)	L	[m]
2	3D Cartesian coord. system component (y_2-axis) (principal material coordinate system)	L	[m]
3	3D Cartesian coord. system component (z_3-axis) (principal material coordinate system)	L	[m]
$\ddot{\mathbf{u}}$	acceleration field vector	LT^{-2}	$\left[\mathrm{m}\cdot\mathrm{s}^{-2}\right]$
det	determinant operator (linear algebra)	–	–
$\dot{\mathbf{u}}$	velocity field vector	LT^{-1}	$\left[\mathrm{m}\cdot\mathrm{s}^{-1}\right]$
$[B_\phi]$	electric potential matrix	–	–
$[B_b]$	strain-displacement coupling matrix of bending contribution	–	–
$[B_m]$	strain-displacement coupling matrix of membrane contribution	–	–
$[B_s]$	strain-displacement coupling matrix of shear contribution	–	–
$[B_u]$	strain-displacement coupling matrix of mechanical contribution (bending plus membrane)	–	–

$[K_{\phi\phi}]$	stiffness matrix of pure electrical contribution	$\mathrm{L}^{-2}\mathrm{M}^{-1}\mathrm{T}^{4}\mathrm{I}^{2}$	$[\mathrm{F}]$
$[K_{u\phi}]$, $[K_{\phi u}]$	stiffness matrix of coupling between mechanical/-electrical contribution	$\mathrm{L}^{-1}\mathrm{TI}$	$\left[\mathrm{C}\cdot\mathrm{m}^{-1}\right]$
$[K_{uu}]$	stiffness matrix of pure mechanical contribution	MT^{-2}	$\left[\mathrm{N}\cdot\mathrm{m}^{-1}\right]$
$[M_{uu}]$	mass matrix	M	[kg]
$[R]$	correlation matrix (Kriging)	–	–
$\{F_{\phi}(t)\}$	generalized time-dependent electrical load vector	TI	[C]
$\{F_{u}(t)\}$	generalized time-dependent mechanical load vector	LMT^{-2}	[N]
$\{u\}$	generalized mechanical response vector	L, dimensionless	[m], [rad]
$\mathbf{q}$	nodal values	–	–
$\mathbf{u}$	displacement field vector	L, dimensionless	[m], [rad]
$\mathrm{d}\eta$	infinitesimal dimension along natural direction η, in the natural coordinate system of the master element	–	–
$\mathrm{d}\xi$	infinitesimal dimension along natural direction ξ, in the natural coordinate system of the master element	–	–
$\mathrm{d}S$	area or surface element	L^2	$\left[\mathrm{m}^2\right]$
$\mathrm{d}t$	infinitesimal time instant	T	[s]
$\mathrm{d}V$	volume element	L^3	$\left[\mathrm{m}^3\right]$
$\mathrm{d}x_1$	element dimension in the x_1-direction, in the principal material coordinate system	L	[m]
$\mathrm{d}y_2$	element dimension in the y_2-direction, in the principal material coordinate system	L	[m]
$\mathrm{d}z_3$	element dimension in the z_3-direction, in the principal material coordinate system	L	[m]
T	transpose operator (linear algebra)	–	–
$Fper$	perturbation factor in DE (HBA)	–	–
sc	denotes shear components	–	–
sp	auxiliary variable to control which FGM's phase is on the bottom or top surfaces (along thickness); $sp = \{-1, 1\}$	–	–
$\overline{e}_{ij}$	transformed plane stress-reduced stress-charge piezoelectric coefficient ij-component, $ij = \{31, 32, 36, 14, 15, 24, 25\}$	$\mathrm{L}^{-2}\mathrm{TI}$	$\left[\mathrm{C}\cdot\mathrm{m}^{-2}\right]$

$\overline{Q}_{ij}$	transformed plane stress-reduced elastic coefficient ij-component, $ij = \{11, 12, 16, 22, 26, 66, 44, 45, 55\}$	$\mathrm{L^{-1}MT^{-2}}$	$[\mathrm{Pa}]$
a	length (x-direction)	L	$[\mathrm{m}]$
A_i^t	loudness of the i-th bat at the instant t	–	–
A_{ij}	extensional stiffness ij-component, $ij = \{11, 12, 16, 22, 26, 66, 44, 45, 55\}$	$\mathrm{MT^{-2}}$	$\left[\mathrm{N \cdot m^{-1}}\right]$
b	width (y-direction)	L	$[\mathrm{m}]$
B_{ij}	bending-extensional coupling stiffness ij-component, $ij = \{11, 12, 16, 22, 26, 66\}$	$\mathrm{LMT^{-2}}$	$[\mathrm{N}]$
d	total number of DVs used in an optimization case study	–	–
D_{ij}	bending stiffness ij-component, $ij = \{11, 12, 16, 22, 26, 66\}$	$\mathrm{L^2MT^{-2}}$	$[\mathrm{N \cdot m}]$
d_{ij}	strain-charge piezoelectric coefficient ij-component, $ij = \{31, 32, 33, 14, 15, 24, 25, 36\}$	$\mathrm{L^{-1}M^{-1}T^3I}$	$\left[\mathrm{C \cdot N^{-1}}\right]$
E_c	kinetic energy	$\mathrm{L^2MT^{-2}}$	$[\mathrm{J}]$
E_p	potential energy	$\mathrm{L^2MT^{-2}}$	$[\mathrm{J}]$
e_{ij}	stress-charge piezoelectric coefficient ij-component, $ij = \{31, 32, 33, 14, 15, 24, 25, 36\}$	$\mathrm{L^{-2}TI}$	$\left[\mathrm{C \cdot m^{-2}}\right]$
E_i	i-direction elastic modulus, $i = \{1, 2, 3\}$	$\mathrm{L^{-1}MT^{-2}}$	$[\mathrm{Pa}]$
F	force	$\mathrm{LMT^{-2}}$	$[\mathrm{N}]$
f_i^t	pulse frequency of the i-th bat at an instant t	–	–
f_m	auxiliary variable associated with matrix's m bulk and shear moduli relations	dimensionless	$\left[\mathrm{m \cdot m^{-1}}\right]$
f_{max}	pulse frequency maximum lateral bound	–	–
f_{min}	pulse frequency minimum lateral bound	–	–
G_{NC}	shear modulus of nano-composite	$\mathrm{L^{-1}MT^{-2}}$	$[\mathrm{Pa}]$
G_{ij}	shear modulus ij-component, $ij = \{23, 13, 12\}$	$\mathrm{L^{-1}MT^{-2}}$	$[\mathrm{Pa}]$
h	thickness (z-direction)	L	$[\mathrm{m}]$
I_0	translational inertia	$\mathrm{L^{-2}M}$	$\left[\mathrm{kg \cdot m^{-2}}\right]$
I_2	rotational inertia	M	$[\mathrm{kg}]$

K_i	bulk modulus, with $i = \{r, m, \mathit{eff}\}$ (reinforcement, matrix, effective)	$\mathrm{L}^{-1}\mathrm{MT}^{-2}$	[Pa]
L	length quantity (along x-direction)	L	[m]
M	order of the polynomial basis considered (Kriging)	–	–
m	mass	M	[kg]
M_{ij}	moment resultant ij-component per unit length, $ij = \{xx, yy, xy\}$	LMT^{-2}	[N]
n	number of bat individuals (population size), in each generation N_{gen}	–	–
N_l	total number of layers	–	–
N_{ex}	total number of finite elements in the x-direction	–	–
N_{ey}	total number of finite elements in the y-direction	–	–
N_{gen}	number of optimization generations in BA	–	–
N_{pl}	total number of piezoelectric layers	–	–
N_{sl}	total number of sub-layers	–	–
N_{ij}	in-plane force resultant ij-component per unit length, $ij = \{xx, yy, xy\}$	MT^{-2}	$\left[\mathrm{N \cdot m^{-1}}\right]$
$N_i\,(\xi, \eta)$	shape function associated with node number i	–	–
N_n	total number of nodes per element	–	–
P	pressure	$\mathrm{L}^{-1}\mathrm{MT}^{-2}$	[Pa]
p	exponent of the volume fraction power law	–	–
Pt	point	–	–
q_0	surface charge density	$\mathrm{L}^{-2}\mathrm{TI}$	$\left[\mathrm{C \cdot m^{-2}}\right]$
Q_i	i-direction transverse force resultant per unit length, $i = \{x, y\}$	MT^{-2}	$\left[\mathrm{N \cdot m^{-1}}\right]$
Q_{ij}	elastic coefficient ij-component, $ij = \{11, 12, 13, 16, 22, 23, 26, 33, 36, 44, 45, 55, 66\}$	$\mathrm{L}^{-1}\mathrm{MT}^{-2}$	[Pa]
r	Euclidean distance between two given points	–	–
r_i^t	pulse rate of the i-th bat at the instant t	–	–
R_i	denotes reference number i, to shorten reference designation	–	–

t	time, duration	T	[s]
t_f	final time instant	T	[s]
t_i	initial time instant	T	[s]
u	resultant membrane displacement (x-direction)	L	[m]
V	volume or solid body	L^3	$[m^3]$
v	resultant membrane displacement (y-direction)	L	[m]
v_i^t	velocity of the i-th bat at the instant t	–	–
$V_{f,CNT}$	volume fraction distribution of dispersed CNTs	dimensionless	$[m \cdot m^{-1}]$
$V_{f,NC}$	volume fraction distribution of nano-composite	dimensionless	$[m \cdot m^{-1}]$
$V_{f,c}$	volume fraction distribution of ceramic particles	dimensionless	$[m \cdot m^{-1}]$
$V_{f,m}$	volume fraction distribution of a matrix m	dimensionless	$[m \cdot m^{-1}]$
$V_{f,r}$	volume fraction distribution of a reinforcement r	dimensionless	$[m \cdot m^{-1}]$
V_f	volume fraction power law	dimensionless	$[m \cdot m^{-1}]$
w	resultant transverse displacement (z-direction)	L	[m]
w_{CNT}	CNT weight fraction	dimensionless	$[m \cdot m^{-1}]$
x	3D Cartesian coord. system component (x-axis) (problem reference coordinate system)	L	[m]
x_i^t	position of the i-th bat at the instant t	–	–
y	3D Cartesian coord. system component (y-axis) (problem reference coordinate system)	L	[m]
z	3D Cartesian coord. system component (z-axis) (problem reference coordinate system)	L	[m]
z_k	z-coordinate associated with the bottom surface of layer k	L	[m]
z_{k+1}	z-coordinate associated with the top surface of layer k	L	[m]
C	means “clamped”, to specify MBCs	–	–
F	means “free”, to specify MBCs	–	–
S	means “simply-supported”, to specify MBCs	–	–

Other Symbols

Symbol	Description	Dimensions	SI Unit
$\int$	integral operator	–	–
$\int_\Gamma$	boundary integral	–	–
$\int_V$	volume integral	–	–
$[...]$	square brackets, identify matrices (or **bold**)	–	–
$\{...\}$	curly brackets, identify vectors (or **bold**)	–	–
$\overline{...}$	overline, identifies non-dimensionalized quantities (computed deflections, stresses, natural frequencies, etc.)	–	–
$\overline{...}$	overline, identifies transformed material coeffs.	–	–
$\sum$	summation operator	–	–
$...^{-1}$	inverse operator (linear algebra)	–	–
.eps	Encapsulated PostScript format	–	–
.m	MATLAB® Code format	–	–
.mpl	Maple® Input format	–	–
.pdf	Portable Document format	–	–
.xlsm	Excel® Macro-Enabled Workbook format	–	–
.xlsx	Excel® Workbook format	–	–

Contents

Acknowledgements . . . . . **i**

Agradecimentos . . . . . **iii**

Abstract . . . . . **v**

Resumo . . . . . **vii**

List of Figures . . . . . **ix**

List of Tables . . . . . **xxxi**

Nomenclature . . . . . **xxxv**

Contents . . . . . **xlix**

1 Introduction **1**
- 1.1 Objectives 1
- 1.2 Motivation 2
- 1.3 Research topics 2
  - 1.3.1 Smart structures and materials 2
    - 1.3.1.1 Piezoelectricity 7
    - 1.3.1.2 Composite materials 10
    - 1.3.1.3 Functionally Graded Materials (FGMs) 12
    - 1.3.1.4 Carbon Nano-Tubes (CNTs) 16
  - 1.3.2 Finite Element Method (FEM) 16
  - 1.3.3 Optimization 23
    - 1.3.3.1 Bat-inspired optimization 25
- 1.4 Thesis structure 29
- 1.5 Remarks to the reader 30

2 Literature Review **31**
- 2.1 Advanced structures 31
- 2.2 Bat-inspired optimization 37

3 Methodology **45**
- 3.1 Plate theories 45
  - 3.1.1 First-Order Shear Deformation Theory (FSDT) 46

3.1.1.1 Displacement and strain fields . . . 47
3.1.1.2 Constitutive equations . . . 50
3.1.1.3 Governing equations of motion . . . 54
3.2 Material models . . . 59
3.2.1 Piezoelectrics and monoclinics . . . 59
3.2.2 Functionally Graded Materials (FGMs) . . . 68
3.2.2.1 Along thickness (z-direction) . . . 70
3.2.2.2 Along length (x-direction) . . . 73
3.2.3 Carbon Nano-Tubes (CNTs) . . . 75
3.2.3.1 1st hybridization stage: nano-composite . . . 75
3.2.3.2 2nd hybridization stage: multiscale composite . . . 77
3.3 Finite element modelling . . . 78
3.3.1 Finite element discretization . . . 78
3.3.2 Lagrange formulation . . . 79
3.3.3 Kriging formulation . . . 85
3.3.4 Elementary governing equations of motion . . . 86
3.3.5 Strains and stresses computation . . . 91
3.3.6 Finite element implementation . . . 91
3.4 Micro-Hybrid-Bat-Algorithm (MHBA) . . . 93
3.4.1 Optimization implementation . . . 97

4 Case Studies . . . 101
4.1 Validation studies . . . 102
4.1.1 Standard, benchmarking study: Reddy, J.N. . . . 102
4.1.2 Standard, benchmarking study: AMAPDL . . . 103
4.1.3 Functionally graded plates . . . 105
4.1.3.1 Statics . . . 106
4.1.3.2 Dynamics (free vibrations) . . . 107
4.1.4 Multilayered smart structures . . . 108
4.1.4.1 Statics . . . 108
4.1.4.2 Dynamics (free vibrations) . . . 110
4.1.4.3 Optimization . . . 112
4.2 Parametric studies . . . 115
4.2.1 Finite element convergence . . . 115
4.2.2 Functionally graded, multiscale & hybrid composite structures . . . 116
4.2.2.1 Statics . . . 116
4.2.2.2 Dynamics (free vibrations) . . . 123
4.2.3 Multilayered smart structures . . . 128
4.2.3.1 Statics . . . 129
4.2.3.2 Dynamics (free vibrations) . . . 133
4.3 Optimization studies . . . 134
4.3.1 Multilayered smart structures . . . 134
4.3.1.1 Minimization of beams' deflections . . . 134
4.3.1.2 Minimization of plates' deflections . . . 136
4.3.1.3 Approximation of beams' deflections to 2 control points . . . 139
4.3.1.4 Approximation of beams' deflections to 3 control points . . . 140
4.3.1.5 Maximization of fundamental natural frequencies (non-skewed beams) 141

4.3.1.6 Maximization of fundamental natural frequencies (skewed beams) 141
4.3.1.7 Maximization of fundamental natural frequencies (skewed plates) . 142

5 Conclusions . . . 143
5.1 General overview . . . 143
5.2 Most relevant conclusions by main topic . . . 144
5.3 Future work . . . 146

Bibliography . . . 149

APPENDICES . . . 163

A FGMs Discrete Distributions . . . A-1
A.1 Along thickness (z-direction) . . . A-1
A.2 Along length (x-direction) . . . A-3

B Shape Functions . . . B-1
B.1 Lagrange elements . . . B-1
B.1.1 4-Node Bilinear Quadrilateral (4BlinLag) . . . B-1
B.1.2 9-Node Biquadratic Quadrilateral (9BquadLag) . . . B-1
B.1.3 16-Node Bicubic Quadrilateral (16BcubLag) . . . B-2
B.2 Kriging elements . . . B-3
B.2.1 4-Node Bilinear Quadrilateral (4BlinKrig) . . . B-3
B.2.2 9-Node Bilinear Quadrilateral (9BlinKrig) . . . B-4
B.2.3 9-Node Biquadratic Quadrilateral (9BquadKrig) . . . B-5
B.2.4 16-Node Bilinear Quadrilateral (16BlinKrig) . . . B-7
B.2.5 16-Node Biquadratic Quadrilateral (16BquadKrig) . . . B-11
B.2.6 16-Node Bicubic Quadrilateral (16BcubKrig) . . . B-17

C Shape Functions (Plots) . . . C-1
C.1 Lagrange elements . . . C-2
C.1.1 4-Node Bilinear Quadrilateral (4BlinLag) . . . C-2
C.1.2 9-Node Biquadratic Quadrilateral (9BquadLag) . . . C-3
C.1.3 16-Node Bicubic Quadrilateral (16BcubLag) . . . C-4
C.2 Kriging elements . . . C-5
C.2.1 4-Node Bilinear Quadrilateral (4BlinKrig) . . . C-5
C.2.2 9-Node Bilinear Quadrilateral (9BlinKrig) . . . C-6
C.2.3 9-Node Biquadratic Quadrilateral (9BquadKrig) . . . C-7
C.2.4 16-Node Bilinear Quadrilateral (16BlinKrig) . . . C-8
C.2.5 16-Node Biquadratic Quadrilateral (16BquadKrig) . . . C-9
C.2.6 16-Node Bicubic Quadrilateral (16BcubKrig) . . . C-10

D Gauss Quadrature Rules . . . D-1

E Algorithms' Directory Trees . . . E-1

F Validation Studies: Schemes & Results . . . F-1
F.1 Standard, benchmarking study: Reddy, J.N. . . . F-2

F.2 Standard, benchmarking study: AMAPDL F-3
F.3 Multilayered smart structures F-9
F.3.1 Statics F-9
F.3.2 Dynamics (free vibrations) F-12
F.3.3 Optimization F-18

G Parametric Studies: Schemes & Results G-1
G.1 Finite element convergence G-2
G.2 Function. graded, multiscale & hybrid comp. structs. G-24
G.2.1 Statics G-24
G.2.2 Dynamics (free vibrations) G-34
G.3 Multilayered smart structures G-45
G.3.1 Statics G-45
G.3.2 Dynamics (free vibrations) G-67

H Optimization Studies: Schemes & Results H-1
H.1 Multilayered smart structures H-2
H.1.1 Minimization of beams' deflections H-2
H.1.2 Minimization of plates' deflections H-13
H.1.3 Approximation of beams' deflections to 2 control points H-32
H.1.4 Approximation of beams' deflections to 3 control points H-42
H.1.5 Maximization of fundamental natural frequencies (non-skew. beams) H-52
H.1.6 Maximization of fundamental natural frequencies (skewed beams) H-55
H.1.7 Maximization of fundamental natural frequencies (skewed plates) H-58

I Future Work I-1
I.1 Maplet® GUI platform I-2
I.2 Experimental set-up: smart testing workbench I-4
I.2.1 Equipment and materials I-4
I.2.2 Companies' emails I-6
I.2.2.1 Example of email sent to companies I-6
I.2.2.2 Example of email received from companies no.1 . . . . . I-6
I.2.2.3 Example of email received from companies no.2 . . . . . I-7
I.2.2.4 Example of email received from companies no.3 . . . . . I-7
I.2.2.5 Piezoelectric patches' quotation I-8

Chapter 1

Introduction

In the present chapter, a general overview of this work is carried out, summarizing its main objectives, motivation, research topics, overall structure and remarks to the reader.
NOTE: This chapter contains pages 1 to 30, which is 30 in total.

1.1 Objectives

The combination of different types of materials has been used in a wide range of engineering applications, where composite materials play a crucial role in terms of structural design, since their intrinsic characteristics provide several advantages. In comparison with conventional isotropic steel structures, with composites it is possible to tailor the material's constituents in order to optimize different parameters, such as stiffness/weight ratios, etc. On top of that, by incorporating smart or active materials on this type of structures, they become controllable when required (actively and continuously), to accomplish a set of objectives. These combinations are being widely studied by the scientific and industrial communities, presenting promising and innovative features in the future, throughout numerous engineering fields, e.g. aerospace, automotive, biomedical, etc.

The main objective, as partially explained by the thesis title, is to study, model and predict the mechanical behaviour of adaptive structures, by programming the **F**inite **E**lement **M**ethod (FEM) and optimization algorithms. In addition, a specific path must be completed before reaching the smart structures, considering several intermediate validations with consistent proof that both FEM and optimization algorithms give reliable and efficient outputs. Only after successfully predicting the mechanical behaviour of passive structures is possible to solve more complex problems, considering multiple **D**esign **V**ariables (DVs) and other characteristics. To accomplish these requirements and restrictions, several types of case studies (validation, parametric and optimization) are specified and developed, starting with smaller and less complex problems, evolving to the main ones.

Both static and dynamic (free vibrations) behaviours of beams and plates are modelled, considering a wide range of up-to-date innovative materials, e.g. functionally graded, orthotropic composite laminates, hybrid and multiscale **F**unctionally **G**raded **M**aterials (FGMs) incorporating **C**arbon **N**ano-**T**ubes (CNTs), graded mixtures of piezoelectric and non-active materials, etc. Different finite elements are programmed, i.e. Lagrangian and Kriging based, for evaluating their convergence rates and other

aspects, different integration schemes, number of nodes per element (4, 9 and 16) and others. Also, in terms of optimization, several aspects are tested and compared, with the objective of evaluating the capabilities and interaction between the programmed algorithms, e.g. mixing **G**enetic **A**lgorithms (GAs) with **D**ifferential **E**volution (DE) characteristics and micro approaches, etc.

In non-scientific terms, other crucial objective is to gather, in one single document (the present pdf file), an interactive virtual experience to maximize the number of analyses' perspectives of each case study, using LaTeX packages. A considerable number of tables and interactive plot animations are created to try to achieve that purpose, presenting the results in an innovative way to avoid exhausting numerical tabular formats.

In sum, an integrated symbolic-numerical-graphical package devoted to the finite element analysis of beam/plate-type structures and its non-linear meta-heuristic optimization is implemented, with capabilities of simulating generic active multilayered structures, constituted by a variable number of distinct material models, DVs and optimization objectives.

1.2 Motivation

Nowadays, considering the fast technology evolution, computers have high performance capabilities and are widely used throughout all scientific fields. Mechanical engineering is no exception and simulations, mostly based on FEM, are relevant tools to perform structural design, due to time constraints and economic issues. Adaptive structures, as explained further in detail, have several types of interesting applications in the aerospace/aeronautical and automotive industries, being a hi-tech subject with huge potential in the future.

Adding to the previous aspects, and since a master's thesis should gather the objectives, personal tastes of each author and adequate difficulty level, this theme was chosen. It provides the opportunity of going *one or more steps further* in the final phase of this masters' degree, enabling a deeper study concerning FEM in structural analysis, since commercial software is here used only for comparison/-validation purposes. For a mechanical engineer that seeks more and more everyday, putting together the passion for research and the objective of one day be able to design and optimize aircraft/automotive structures, this probably is a proper starting point.

Dealing with everyday issues and new problems to solve, inside innovative ways of thinking, can result in important scientific contributions and personal challenge: this is the main goal.

1.3 Research topics

This thesis is supported upon several different types of research topics, which are briefly described in this section. It starts with smart structures and materials, which is subdivided into piezoelectricity, composite materials, FGMs and CNTs, evolving towards FEM and optimization.

1.3.1 Smart structures and materials

The present subsection is intended to address smart structures, in terms of definition, features, characteristics, historical developments and applications. In addition, it makes sense to introduce at the same time the smart materials that these kind of structures can incorporate. Following this, other types of materials that are relevant to this work are also introduced.

As explained in Carrera et al. (2011), several international declarations state that the development of advanced structures in different fields, such as automotive, shipbuilding and aeronautical/space, depends on the development of these smart structures, themselves. This proves the importance of the addressed topic.

At this point, the most pertinent question to ask, is the following: *yes, a smart structure is awesome, but what is that?* A definition for a system like this is not so straightforward as it seems and was a subject of controversy from the late 1970s to the late 1980s (Carrera et al., 2011; Soh, C.-K. et al., 2012). However, in 1988 a proper definition resulted from a special workshop organized by the U.S. Army Research Office (Ahmad, 1988):

Definition 1.3.1. **Smart Structure** *"A system or material which has built-in or intrinsic sensor(s), actuator(s) and control mechanism(s) whereby it is capable of sensing a stimulus, responding to it in a predeterminated manner and extent, in a short/appropriate time, and reverting to its original state as soon as the stimulus is removed."*

Here, Rogers et al. (1988) recognized the words *sensors*, *actuators*, *control mechanism* and *timely response* as the four main characteristics of an adaptive structure. In addition, two years after this workshop, Rogers (1990) divided smart structures into five categories, in order to classify them in terms of complexity (Soh, C.-K. et al., 2012):

1. **Sensory structures:** These structures possess sensors that enable the determination or monitoring of system states/characteristics;
2. **Adaptive structures:** These structures possess actuators that enable the alteration of system states/characteristics in a controlled manner;
3. **Controlled structures:** These result from the intersection of the sensory and the adaptive structures. They possess both sensors and actuators integrated in feedback architecture for the purpose of controlling the system states/characteristics;
4. **Active structures:** These structures possess both sensors and actuators that are highly integrated into the structure and exhibit structural functionality in addition to control functionality;
5. **Intelligent structures:** These structures are basically active structures possessing highly integrated control logic and electronics that provide the cognitive element of distributed or hierarchic control architecture.

In terms of nomenclature, as stated by Chopra and Sirohi (2013), smart structures are also commonly "*referred to as intelligent, adaptive, active, sensory, and metamorphic structures (...) and/or systems*" or even *adaptronics*, in German-speaking areas (Janocha, 2007); in this work, *smart* and *adaptive* are the most used terms.

The development of these structures was only possible due to the continuous development of new and high-performance materials, more specifically smart ones. Once again, and similarly to all engineering technologies, this kind of research was mostly boosted by civil and military demands.

Since the Big Bang, different Eras and Ages were marked and characterized by specific types of materials, e.g. Stone Age, Bronze Age, Iron Age and Synthetic Material Age (Chopra and Sirohi, 2013). The former one goes back to one million years BC and the latter to the early twentieth century, marking the exponential evolution of synthetic materials and, in consequence, the development of high-performance goods associated with aerospace, computers, medical, automotive, telecommunication systems, etc. At this point, composites started to show off their evident structural advantages and literally helped man reaching the moon, having a huge impact on structural capabilities, manufacturing

and maintenance costs (Costa, 2016a); these increased performance, payload, speed and range, reducing life-cycle cost.

The twenty-first century, visualized as the Multifunctional Materials Age by Chopra and Sirohi (2013), is being the stage for innovations inspired by nature, including smart structures, multifunctional, nano-structured and smart materials. For this reason, these are sometimes referred to as bio-inspired materials (see Figure 1.1). Smart structures, by themselves, are designed with several purposes, such as the minimization of life-cycle cost and maximization of performance envelope. As stated in this reference, the "*ultimate goal is to develop biologically inspired multifunctional materials with the capability to adapt their structural characteristics (stiffness, damping, viscosity, etc.) as required, monitor their health condition, perform self-diagnosis and self-repair, morph their shape, and undergo significant controlled motion over a wide range of operating conditions*".

Adaptive structures feature sensing and actuation capabilities because are normally constituted by materials that benefit from natural smart effects (e.g. piezoelectric materials). Figure 1.2 represents an example of an adaptive plate, with both sensing and actuation configurations, clearly illustrating the possibility of controlling a structure using an electronic control loop/cycle. When this generic structure is performing its job, e.g. dealing with aerodynamic solicitations, actuators can stiffer the structure up in strategic locations, based upon the data received from the sensors, in real time, to accomplish determined objectives. This way, in comparison with passive structures, active ones allow precise shape variation, enabling the possibility of vibration attenuation in specific situations (Carrera et al., 2011). Adaptive structures are able to react and interact with their surrounding environments, continuously, having specific predefined objectives (e.g. to maximize natural frequencies, minimize deflections, etc.). Shape morphing is particularly an interesting application, which is addressed in this work by means of parametric and optimization case studies, modelled using a FEM approach – Figures 1.3 and 1.4 illustrate examples of shape control for adaptive aircraft wings (small models), incorporating smart patches in specific regions.

Figure 1.1: Example of bio-inspired variable camber wing. From Nguyen (2014).

Smart structures are considered, by several authors, as the major innovation in the structural mechanics field, since composite structures in 1970s (Gaudenzi, 2009). The growth of smart structures' applications mostly increased since 1990s, in terms of constituent parts and fields range. Apart from the ones already mentioned, other applications include self-diagnostic features (used for e.g. in structural health/integrity monitoring), active optics, micro-electromechanical systems, noise suppression, stability, damping augmentation, condition-based maintenance, etc. (Carrera et al., 2011; Chopra and

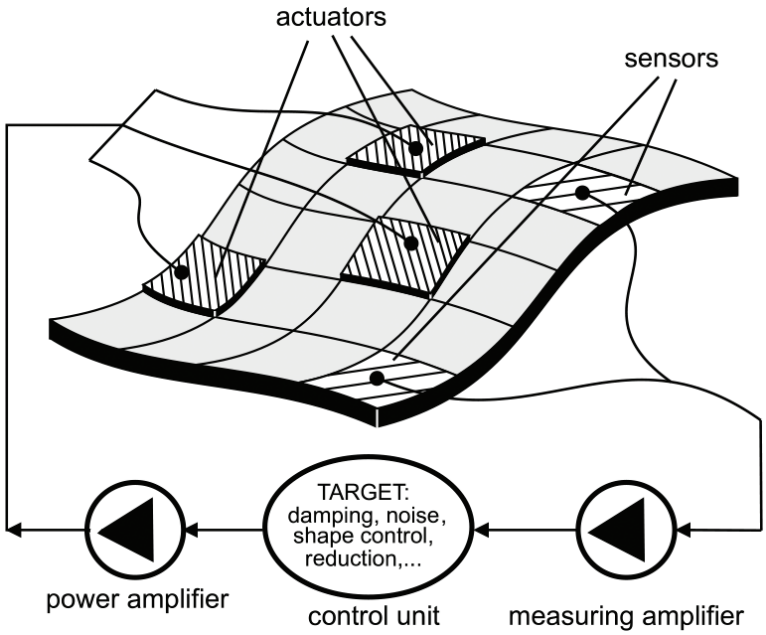

Figure 1.2: Example of adaptive structure, with sensor/actuator control. From Carrera et al. (2011).

Figure 1.3: Example of shape morphing in adaptive airfoil. From Carrera et al. (2011).

Figure 1.4: Example of shape morphing in adaptive structure (airfoil-shaped wing). From Ermanni (2009).

Sirohi, 2013). The following potential smart systems, presented in Srinivasan and McFarland (2001), are excellent examples of the application range of this topic:

- **Aircraft:** Monitoring at key locations on the aircraft the state of strains to warn the pilot of any impending development and propagations of cracks; wings that alter shape with respect to air speed and pressure to increase performance and fuel efficiency;
- **Bridges:** Remote monitoring of strains, deflections, and vibration characteristics in order to warn of impending failures;
- **Buildings:** Buildings designed to resist earthquake damage; smart windows: electrochromic windows that sense weather changes and human activity and automatically adjust light and heat;
- **Jet engines:** Fan, compressor, and turbine blades that exploit asymmetry arising out of non-uniformities in structural and/or aerodynamic properties;
- **Machinery:** Tool chatter suppression; rotor critical speed control;
- **Medical devices:** Blood sugar sensors, insulin delivery pumps, micromotor capsules that unclog arteries. Filters that expand after insertion into a vessel to trap blood clots;
- **Pipelines:** Monitoring of leakage and damage to underground pipes for water, oil, and gas;
- **Ships:** Hulls and propulsion systems that detect noise, remove turbulence and prevent detection;
- **Spacecraft:** Pointing accuracy of large antennas maintained through an elaborate network of sensors and actuators.

Based on all these applications, it is possible to say that adaptive structures are widely used in sensing, actuating and diagnosing. Carrera et al. (2011) also state that some structures can save and analyse information, to use in a learning process. After this overview of smart structures, the following paragraphs focus on smart materials themselves.

Smart materials are peculiar, nature masterpieces. Since Harry Potter movies, people dream about having an invisible cloak. If that were ever possible, it would be due to smart materials and science effort. Military organizations crave for ways to create stealth assets and enhance their camouflage capabilities, making smart materials a valuable research target.

These materials have adaptive features that interact with their surroundings. Rogers et al. (1988) defined smart materials as the following:

Definition 1.3.2. **Smart Materials** *"Materials which possess the ability to change their physical properties in a specific manner in response to specific stimulus inputs."*

According to Soh, C.-K. et al. (2012), stimuli can be, for e.g., pressure, temperature, electric and magnetic fields, chemical or nuclear radiation. In consequence, the change of physical properties can be shape, stiffness, viscosity or damping. Piezoelectric, piezomagnetic, electrostrictive, magnetostrictive, **S**hape **M**emory **A**lloys (SMAs), electrorheological fluids and fibre optics are examples of smart materials (Carrera et al., 2011). Figure 1.5 presents an interesting scheme that relates stimulus to several smart materials response.

Soh, C.-K. et al. (2012) state that these materials can be classified in either *passive* or *active*, where the latter have the possibility of changing their geometry or properties under the application of electric, thermal or magnetic fields, acquiring the capacity to transduce energy. Examples of active smart materials are the piezoelectric, SMAs and electrorheological fluids, whereas fibre optics are considered passive. Active ones can be used as actuators/sensors/transducers, whereas passive ones can only act as sensors.

For instance, SMAs have the ability to return to a predetermined shape when heated, having a critical transformation temperature. They can be deformed to new shapes, but when their temperature

Figure 1.5: Examples of smart materials and stimulus-response relation. From Soh, C.-K. et al. (2012).

exceeds the critical one, a crystal structure change occurs, returning to the initial shape. **Ni**ckel **Ti**tanium **N**aval **O**rdnance **L**aboratory NiTiNOL (NiTiNOL) (Srinivasan and McFarland, 2001) is a common example of these smart materials, being integrated in shape memory actuators for vibration control, actuating plate structures, hydrofoils and adaptive wing structures, i.e. applications where large control forces are required (Vepa, 2010).

Since the smart material modelled in this work is the piezoelectric and it is crucial to describe its structural behaviour, the fundamentals of piezoelectricity are introduced in the following subsection.

1.3.1.1 Piezoelectricity

Until this point, it was said that piezoelectrics are active smart materials, which are widely used in several adaptive structures, as sensors and actuators. However, it is necessary to dig a little bit more and understand in what consists the piezoelectric effect, who discovered it, and how. The word *piezoelectricity* means "*electricity by pressure*", derived from the Greek word *piezein*, which means *to squeeze* or *press* (Zieliński, 2016).

Piezoelectricity was discovered by Jacques and Pierre Currie in 1880. Their research showed that certain crystals, when subjected to a mechanical force or pressure, generated a proportional electric charge, in response to that stimuli, and vice-versa (Curie and Curie, 1880). So, the concepts of piezoelectric *actuation* and *sensing* started here.

The former is related to the *inverse effect* (actuator configuration), stating that a geometry made of piezoelectric material varies its shape when subjected to an electric charge. In contrast, the latter effect states exactly the opposite (the *direct effect*, sensor configuration), meaning that a piezoelectric structure, when subjected to a mechanical force field, creates and returns an electric charge (positive or negative, depending on the strain field), due to molecular electrical dipoles (Carrera et al., 2011); in sum, there is a linear conversion between both mechanical and electrical fields. Crystals with these properties can be found in nature, such as quartz and tourmaline. Since these materials are naturally

characterized by the coupling between both mechanical and electrical fields, they can be used in structural design in order to work as actuators, sensors or both, for example by means of electronic control systems.

In addition, there are also man-made synthetic crystals with these properties, e.g. lithium sulfate, polymers and polarized ceramics. According to Carrera et al. (2011), commonly used piezoelectric materials are ***B**arium **T**itanate* $BaTiO_3$ (BT) and *piezo Lead Zirconate Titanate* $Pb[Zr_xTi_{1-x}]O_3$ $(0 \leq x \leq 1)$ (PZT).

Chemical phenomena is involved and the piezoelectric effect has its origin at atomic and molecular scales. The crystal lattice of piezoelectric materials is ***F**ace **C**entred **C**ubic* (FCC), as explained in Carrera et al. (2011). At the cube's vertex are located metallic atoms and oxygen ones at the centre of cube's faces. When an electric field is applied to the crystal (polarization), the heavier atom located at the cube's centre of gravity can *exceed the potential energy threshold and move to a lower energy configuration*. Following this, the cube becomes asymmetric and an electric dipole is created, as presented in Figure 1.6. This phenomena results in the deformation of the crystal lattice, but only below the *Curie temperature*, because the piezoelectric effect is cancelled above this temperature (high thermal agitation).

Figure 1.6: Piezoelectric crystal lattice before (left) and after (right) polarization. From Carrera et al. (2011).

It is also important to refer that in order to obtain efficient piezoelectric materials, or patches, artificial polarization must be carried out. The first step to start this process is to heat the piezoelectric material above the *Curie temperature*. Afterwards, during cooling, it must be subjected to an intense electrical field. This will result in dipoles oriented in the same direction, as presented in Figure 1.7, ensuring a workable polarization when incorporated in structures. In Figure 1.8 are presented several real piezoelectric ceramic patches, with different geometry configurations.

Although the intensive research has only started in the 1990s, the first applications of piezoelectrics were recorded in submarine detection, during World War I (1914–1918) (Carrera et al., 2011). Afterwards, with PZT piezoceramics, the interest became to grow at the end of the first half of the twentieth century. However, these materials were limited to sound and ultrasound fields. Then, in the 1970s *Polyvinylidene Fluoride* $(C_2H_2F_2)_n$ (PVDF) was discovered, having high sensor features. Both PZT and PVDF are modelled in this work, when incorporated in smart structures, revealing distinct behaviours. As reported in Carrera et al. (2011), different types of applications demand particular objectives and the selection of the ideal piezoelectric material can have huge influence on its performance.

It is important to be able to tailor the material properties to each equipment or device, and in order to achieve this, hybrid composites incorporating innovative materials must be modelled and studied. In

the present work, an approach based on material diversity is carried out, in order to create a virtual simulation tool with wide range capabilities, incorporating structural heuristic optimization.

Nowadays, with the available technology in expansion, active materials can be integrated/embedded into composite materials (e.g. laminates), as already mentioned in Section 1.1. This is why the following subsection briefly introduces composite materials.

Figure 1.7: Electric dipoles when unpolarized (ferroelectric ceramic) (1), during (2) and after poling (piezoelectric ceramic) (3). From PI-Ceramic® (2016b).

Figure 1.8: Example of piezoelectric patches, DuraAct Patch Transducers. From PI-Ceramic® (2016a).

The piezoelectric materials will be addressed once more in Chapter 3 (as well as composites, functionally graded and CNTs), but with a mathematical approach to support the structural models here created (materials modelling).

Since the algorithms of the present work predict, not only the behaviour of active materials, but also composites, functionally graded and CNTs (alone and mixed together), it is important to briefly introduce their concepts and purposes. The following three material subsections are very brief and have the objective of only explaining the materials basics.

1.3.1.2 Composite materials

Composite materials have been used intensively for the past decades and in terms of engineering, are a major technology and great discovery of science. On the other hand, they were used in nature since before human civilization. Wood, cellulose and bones are only a few examples of natural composite materials, in their natural concept (Brigante, 2014).

The conceptual idea of a composite material, is to put together *the best of several worlds*; i.e. several materials that have average properties, individually, can be used together (literally) to create new ones, having improved outstanding properties. Of course that this involves hi-tech and costs, but the income result and advantages are huge.

In terms of history, there are records showing that even in Ancient Egypt natural fibres were used for masonry strengthening. Later, in the nineteenth-century, reinforced concrete using steel iron bars was a major contribute to civil engineering in building construction (Brigante, 2014; Reddy, 2004). With the passing years, structures have evolved very fast in terms of material innovation and since engineering demand do not stop growing, e.g. boats, cars, airplanes, spacecrafts, buildings, sports equipment, biomedical products... nowadays composites are everywhere. A considerable number of categories for composites exist (see Figure 1.9), due to the immense variety of possible material combinations.

Normally, composite materials result in structures with properties that are distinct depending on different directions, i.e. anisotropy. This can be a problem for simulations and material modelling, to predict the real structural behaviour, introducing more variables to the problems and a lot of unknowns. Sometimes it is possible to simplify composites problems, by assuming an orthotropic behaviour, e.g. in laminates. In any case, the algorithms created during this thesis are prepared to receive orthotropic inputs for a specified number of structures' layers.

Figure 1.9: Scheme of composites classification. Adapted from Vepa (2010).

Composites are normally constituted by two or more phases, with different properties. Usually, there is a continuous phase, the *matrix* and a discontinuous one, the *strengthening/reinforcement*. The former one is normally resins and the latter is fibres (see Figure 1.10) or even particles. The matrices are commonly less stiff or weaker in comparison with the reinforcements. In terms of manufacturing concepts, matrices give the structure structural homogenization, creating an environment to "bind/carry"

the fibres, whose main objective is to support tensile stresses. Without the matrix, fibres would not provide any efficient structural solutions. Mazumdar (2001) defined very well the differences between each phase contributions. The following list summarizes the fibres' functions:

- To carry the load. In a structural composite, 70 to 90 % of the load is carried by fibres;
- To provide electrical conductivity or insulation, depending on the type of fibre used;
- To provide stiffness, strength, thermal stability, and other structural properties.

Figure 1.10: Example of composite resin (left) and long fibres (right). From Brigante (2014).

In contrast, matrices contribute with the following:

- Binds the fibres together and transfers the load to the fibres. It provides rigidity and shape to the structure;
- Depending on the matrix material selected, performance characteristics such as ductility, impact strength, etc. are also influenced. A ductile matrix will increase the toughness of the structure. For higher toughness requirements, thermoplastic-based composites are selected;
- Isolates the fibres so that individual fibres can act separately. This stops or slows the propagation of a crack;
- Provides a good surface finish quality and aids in the production of net-shape or near-net-shape parts;
- Provides protection to reinforcing fibres against chemical attack and mechanical damage (wear);
- The failure mode is strongly affected by the type of matrix material used in the composite as well as its compatibility with the fibre.

The following list, from Brigante (2014), enumerates several composites advantages:

- *Ad hoc* design can be performed according to different directions of stresses;
- Increase of structural ductility;
- No additional loads are put on the structure;
- No change to the original geometry;
- Non-invasive aesthetic application;
- Reversibility of reinforcement application;

- Speedy and easy application.

On the other hand, similarly to all engineering technologies, composites have drawbacks too. In general, composite materials are more expensive than steel and aluminium, have temperature restrictions that depend on the matrix (since most of them are polymer-based), their properties can change in the presence of moisture absorption and their behaviour is more difficult to predict, due to interactions between phases, material variability, etc. (Mazumdar, 2001).

Composite materials can be hard to predict. However, the world has been witnessing to composites developments. Not too many years ago, commercial original equipment manufacturers were receptive in using composites in the main structural components of aircrafts, to ensure airworthiness requirements (Costa, 2015). In the year of 2014, the new Airbus A350 was released and its first commercial flight took place in 2015. This airplane proves that composites are making vehicles more efficient due to significant weight reductions and that companies are investing in this kind of structural solutions. As shown in Figure 1.11, 53 % of composites in structural parts is a lot, comparing to previous aircrafts.

Figure 1.11: Airbus A350 materials overview. From Airbus (2013).

1.3.1.3 Functionally Graded Materials (FGMs)

Until here, smart and composite materials were introduced. However, what if, instead of only embedding piezoelectric patches in laminates or sandwich structures, it was possible to incorporate all these together, tailoring the different materials constituents, by means of gradative mixtures in several structure's directions? It is perfectly possible to conceptualize a structure, that due to design constraints, would require a bigger or smaller percentage of smart material in a specific region. Also thinking about economic issues, these concepts can be useful. Why spending more smart material, which is expensive, at unnecessary regions of a structure? Or, why gluing a piezoelectric patch to a carbon lightweight structure, increasing its weight? If the materials' technology could create piezoelectric particles to be

mixed up with other materials and still have efficient piezoelectric properties (polarization, etc.), the active composites concept could become easier in terms of manufacturing, structures would be less complex and more efficient.

FGMs are created by mixing different materials, resulting in structures with varying properties along specific directions. Normally, one defines a specific volume fraction distribution of the mixed phases along a determined structure's direction, i.e. depth, width or thickness. In this work, beams and plates are modelled considering different types of FGMs, passive and active, in two distinct directions, i.e. transversal (e.g. along plates' thickness) and longitudinal (e.g. along beams' length). This volume fraction distribution can be thought as effectively having a continuous variation of their constituent phases and consequently their properties, or by resulting from the stacking of a specified number of layers, each having constant properties. Figure 1.12 shows four examples of beams and plates with FGM variation along length and thickness, respectively, assuming continuous or discrete material gradients, modelled by the present algorithm.

Figure 1.12: Examples of FGM variations in different structures' directions, for beams and plates.

Since FGMs are common particulate composites with varying spatial distributions of the inclusion particles (ceramics or even piezoelectric materials, in theory) in matrices, these are materials that can be tailor-made to fulfill specific design requirements. For instance, a great advantage of the inclusion of ceramic particles within a metallic matrix, is that it puts together the high temperature resistance of ceramics and mechanical strength of metals, in a single structure (used for e.g. in nuclear plants,

fusion reactors, aerospace structural applications, where both high temperature and stress fields must be supported).

Already in 2002, Takagi et al. (2002) designed and fabricated a functionally graded PZT/Platinum Pt piezoelectric bimorph actuator, by powder stacking and sintering – this FGM can be seen in Figures 1.13 and 1.14. After applying a voltage of $100\,\mathrm{V}\cdot\mathrm{m}^{-1}$, the actuator exhibited acceptable deflection curvature and low stress fields, which is better than bonded actuators. FGMs are well known by having the capacity of minimizing abrupt stresses transitions, being useful in several applications comparing to conventional composites, e.g. fibre reinforced laminates. Since both thermal and mechanical stress concentrations can result in laminates delamination, which contributes to the consequent degradation and structure failure, FGMs are of great interest (Ferreira et al., 2016). This mechanical behaviour can be achieved due to the continuous mixture variation of the constituents.

Figure 1.13: Graded bimorph actuator with linear composition profile. From Takagi et al. (2002).

Figure 1.14: **S**canning **E**lectron **M**icroscopy (SEM) micrographs of each layer of the actuator in Figure 1.13, where (a) PZT/0 % Pt, (b) PZT/10 % Pt, (c) PZT/20 % Pt and (d) PZT/30 % Pt. From Takagi et al. (2002).

In terms of common FGMs applications, Ferreira et al. (2016) enumerate the following:

- **Aerospace:** *rocket components such as rocket nozzles (*Titanium Aluminide-Silicon Carbide TiAl-SiC (TA-SC) *fibres), thermal protection systems for atmosphere re-entry vehicles*;
- **Medical:** *artificial bones, skins, dentistry*;
- **Energy:** *solar cells, sensors, thermoelectric generators, heat exchanger panels (*Beryllium-Aluminium Be-Al*)*;
- **Communication:** *optical fibres, lenses, semiconductors*;
- **Miscellaneous:**
    - o *Engine cylinder liners (*Al-SiC*)*;
    - o *Brake rotors and leaf springs (e-glass-epoxy)*;
    - o *Drive-shafts (*Aluminium-Carbon Al-C*)*;
    - o *Cylindrical pressure hull (graphite-epoxy)*;
    - o *Sonar domes (glass-epoxy)*.

Since this thesis deals with several types of materials, at different scale levels, it is important to clarify some aspects in terms of nomenclature. Throughout this work, concepts such as composites, FGMs, multiscale, hierarchical and hybrid composites are mentioned; for that reason, they must be defined at this point, to avoid misinterpretations. Figure 1.15 shows a classification of multi-materials, in terms of types, sizes and constituents organization.

Figure 1.15: Classification of multi-materials according to the types, sizes and organizations of constituents. From Ferreira et al. (2016).

In fact, Ferreira et al. (2016) carried out a very interesting and useful state-of-the-art review about multifunctional material systems. They addressed this innovative and vast topic, reviewing and analyzing the associated nomenclature for each type of material classification, pointing out several state-of-the-art applications.

According to this reference, nano-composites and composites are materials with one or more fillers, in which the reinforcement happens on nano-scale level (e.g. CNT-reinforced matrix) or micro

to meso-scale, respectively (e.g. carbon fibre reinforced matrix). This means that CNTs are nano-materials and carbon or fibreglass are micro-materials. Then, they specify that a multiscale composite is the same as the previous composites, but with an additional differentiation, i.e. different filler sizes. They give the e.g. of carbon fibre (micro-material) plus CNT (nano-material), reinforcing an epoxy matrix. Afterwards, hierarchical composites take into account the structural organization of fillers, in a hierarchical way, e.g. when filler A is inside filler B, which is inside C, and so on. Finally, hybrid materials integrate different constituents at a molecular level.

The FEM algorithm here developed, is able to simulate beams and plates, with several different layers, each one constituted by all the previous material classifications. For instance: the first layer is carbon fibre with epoxy (with user-defined fibre orientations), the second layer isotropic, the third layer FGM between a metal and ceramic, the fourth layer FGM considering CNTs mixed with a matrix inside other FGM with ceramic inclusions, the fifth layer FGM considering metallic matrix with piezoelectric particles, and so on. The algorithm also supports FGM variation along x- or y-direction (length/width), as well as z-direction (thickness). In addition, one can use two different FGM homogenization schemes, Voigt's Rule of Mixtures or Mori-Tanaka. On top of that, one can choose between discrete or continuous variation, specifying the discrete number of layers or a user-defined volume fraction distribution (functions, exponents, etc.), respectively.

1.3.1.4 Carbon Nano-Tubes (CNTs)

CNTs were first discovered in 1991 and as shown further in Chapter 2, are being widely studied throughout several engineering areas. This is happening because they are *unique valuable nano-structures, with many outstanding properties*, resulting in many applications with CNT-reinforced structures (Rahmandoust and Ayatollahi, 2016). The incredible mechanical strength of CNTs has to do with their perfect hexagonal structure and high length to diameter or aspect ratio. Since engineering products are evolving towards smaller and smaller dimensions, nanotechnology and these kind of materials are more promising every day.

Carbon has been known by the fact that, depending on several atomic structures with this element, different allotropes are formed, which are characterized by having very distinct properties. Figure 1.16 intends to illustrate these allotropes and their differences, e.g. graphite, diamond, fullerene and CNTs.

According to Janocha (2007), CNTs are *a recent addition to the class of electroactive organic materials* and can be described as *a graphite mono-atomic sheet rolled to form a tube*. As their name reflects, CNTs are nano-materials, having typical lengths and diameters of $1\,\mu\text{m}$ and $1\,\text{nm}$, respectively. As shown in Figure 1.17, CNTs are normally grouped in bundles, creating structures with diameters of $10\,\text{nm}$.

In terms of classification, CNTs can be either **S**ingle **W**alled **C**arbon **N**ano-**T**ubes (SWCNTs) or **M**ulti **W**alled **C**arbon **N**ano-**T**ubes (MWCNTs), and both classes are modelled in the present work. The former class consists of a single film rolled to create a tube, whereas the latter consists of several films (Janocha, 2007). As concluded in this work further ahead, MWCNTs may have lower mechanical performance in comparison with SWCNTs, if its geometrical parameters are not adequately chosen.

1.3.2 Finite Element Method (FEM)

As already stated before, the FEM nowadays is an essential technology used for modelling and simulation of advanced engineering systems, throughout an immense quantity of engineering fields. Engineers and designers must follow a specific path in the process of product development, to ensure

Figure 1.16: Carbon atom and its allotropes, including CNTs. From Rahmandoust and Ayatollahi (2016).

Figure 1.17: Bundles of CNTs. From Janocha (2007).

its safety, functionality, workability and efficiency. This path, according to Liu and Quek (2014) is based in eight main phases, as presented in Figure 1.18.

Figure 1.18: Process flowchart in engineering product design. From Liu and Quek (2014).

Companies struggle every day with innovation and economics, in an environment full of competitiveness. Design, manufacturing and maintenance costs play an important role in these engineering processes and engineers must take into account a huge variety of different factors. Along with technology developments, mechanical structures (and not only) impose several design requirements and restrictions, where equipments are becoming more and more complex and, in a way, difficult to predict. That is why, FEM, as a mathematical method helps a lot.

According to Liu and Quek (2014), FEM *is a numerical method that seeks an approximated solution of the distribution of field variables in the problem domain that is often difficult to obtain analytically*, which is *done by first dividing the problem domain into a number of small pieces called elements, often of simple geometry*. So, the idea is to have a "continuous" real body and discretize it with smaller elements, creating a mesh and solving the mathematical problem. However, it is important to say that the method only works because these elements are well known and for that reason, physical principles and laws that are applied to them are also known. Normally elements are triangles, squares, and so on; there are also meshless methods, but that is not a subject to approach here.

In sum, several elements, constituted by nodes, are connected to each other in order to approximate a generic geometry, generating a mesh. The objective is to find a discrete solution, at each element node, corresponding to the field variables that the user seeks, e.g. structures' deflections, active elements' voltages, temperatures, etc. For each element, physical/mathematical principles are used to establish governing equations. Then, with all elements connected, it is possible to describe the field distribution

of the geometry. Finally, linear algebraic equations are solved to obtain all desired field variables (Liu and Quek, 2014).

Since the main objective of a simulation inside a real design process should be predicting the real behaviour of the product in question, theoretical and experimental results are often compared. Of course that deviations occur, as in everything around engineering, due to uncertainties, methods' handicaps, etc., but that is the beauty of this subject. Engineers must be creative and overcome those problems, with experience, safety factors, statistics, new methods, experimental tests and find reasonable equilibrium between simulations and the real world. In any case, Figure 1.19 shows a comparison between experimental and simulation results, of a thin-walled, axially loaded, crash-absorbing section. It is interesting to see the general accuracy, at naked eye level, between these results.

Figure 1.19: Comparison between experimental and simulation results, of a thin-walled, axially loaded, crash-absorbing section. From Wehrle (2015).

Figure 1.20 presents a FEM model of a lightweight car frame from Wehrle (2015). This FEM model was used in design optimization of lightweight space frame structures considering crashworthiness and parameter uncertainty. Instead of a mesh generated inside a FEM software, Figure 1.21 shows a connecting rod's mesh, obtained using a 3D Laser Scan of a real automotive engine part.

This particular model from Figure 1.20 was crashed into a wall and had to be simulated using explicit dynamics, which is adequate for computationally costly transient non-linear FEM, with explicit time integration. The comparison of this FEM model before and after the impact is presented in Figure 1.22. The creation of this simulation must have been difficult and very time consuming. Now, how much would cost to design, manufacture and test, let's say, five different models for optimization purposes? Probably too much. It is easier and cheaper to change a geometry of a CAD model and run the simulation again. This is why FEM is such an useful tool, when used carefully of course.

In the FEM procedures programmed in this work, only quadrilateral elements were modelled, because since only square/rectangular beams/plates were programmed, these are enough. However, FEM models can be solved using several types of elements, e.g. beam and shell elements, as presented in Figure 1.23 (**A**NSYS **M**echanical **APDL**® (AMAPDL)). This approach was adequate in this model

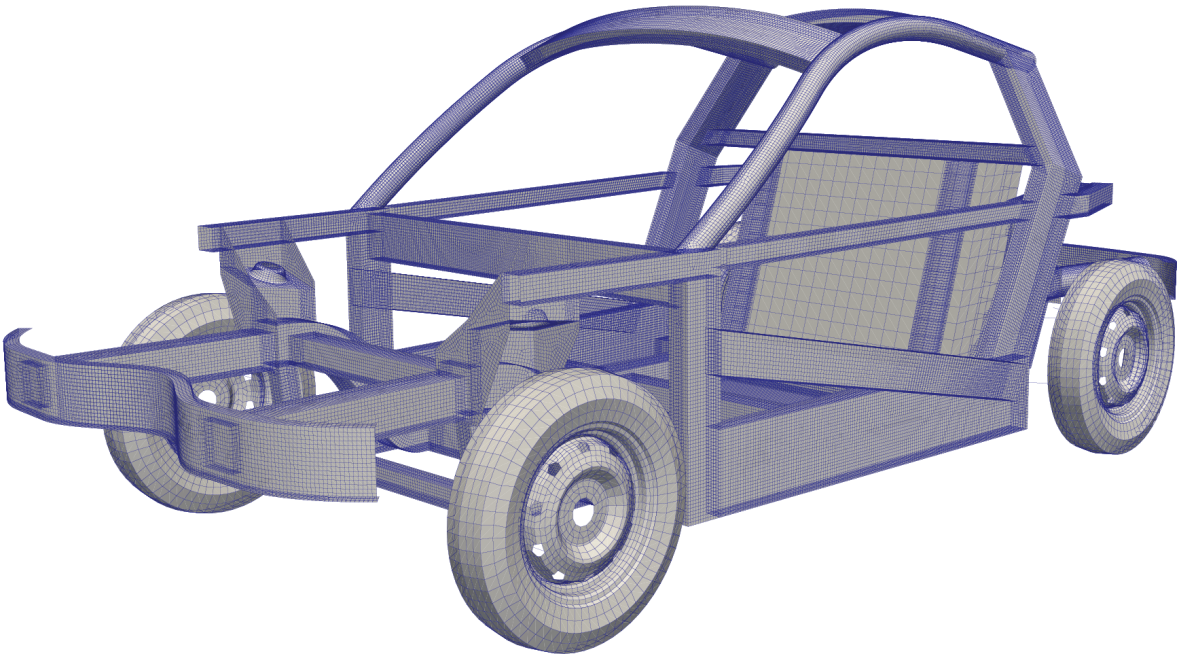

Figure 1.20: Example of car frame mesh created for FEM model. From Wehrle (2015).

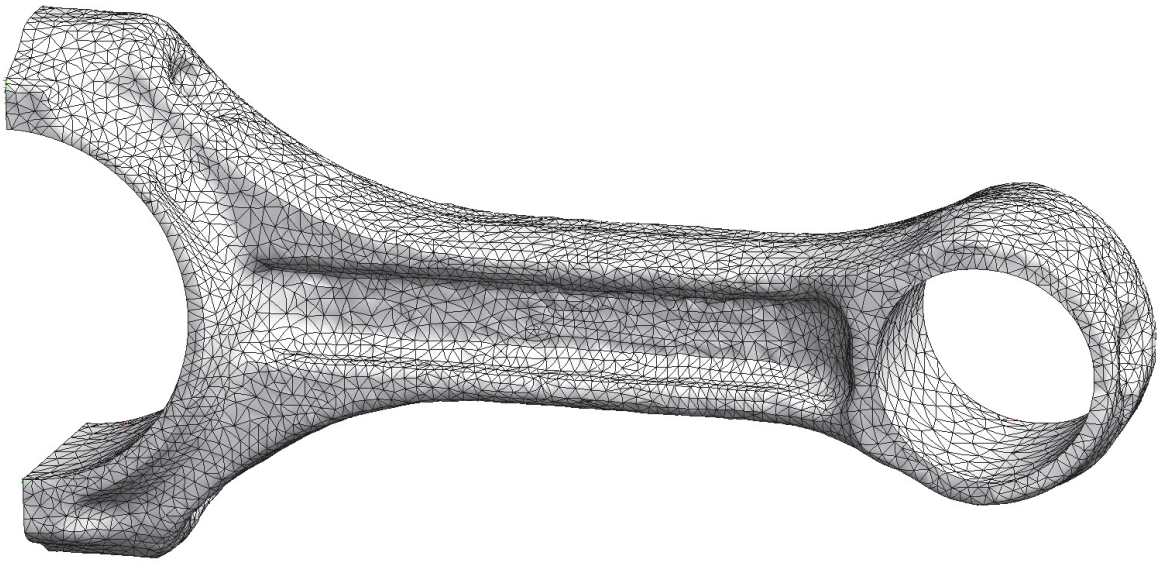

Figure 1.21: Example of connecting rod's mesh used in FEM analysis, obtained with 3D Laser Scanning. From Costa et al. (2015c).

Figure 1.22: Example of frontal car crash simulation (explicit dynamics) results, before and after impact (mesh from Figure 1.20). Adapted from Wehrle (2015).

because the trailer frame is constituted by aluminium welded elements, which can be modelled by beam elements. On the other hand, shell elements were necessary to model the mechanical behaviour of the aerodynamic external shell, which is a monocoque composite laminate (fibreglass with epoxy).

FEM is not only used to solve structural problems, in fact this method is so versatile that is used to solve many problems, such as, thermal, fluid flow, acoustics, heat transfer, piezoelectric, etc. It is also possible to solve multiphysics problems, mixing different physical fields.

For instance, the same trailer model from Figure 1.23 was subjected to **C**omputational **F**luid **D**ynamics (CFD) analysis in order to identify geometry regions vulnerable to turbulence spots, which can increase drag and make the trailer less efficient. Figure 1.24 shows an example of FEM outputs for this model (velocity field of the air around the external geometry).

Another example is fracture mechanics, shown in Figure 1.25, where is possible to analyse the Von Mises stress field results around an elliptical corner crack's tips at the edge of a hole in a finite three-dimensional plate.

The FEM computational modelling is almost like a standard recipe, with a defined order of processes, which is common to every commercial software and other ones (generically). Several aspects from the real world must be modelled to fully define a problem, i.e. *geometry/domain*, *material*, *boundary conditions* and *loads*. Liu and Quek (2014) state that computational implementation of FEM consists of four main steps, which are: modelling of geometry, meshing (discretization), definition of material properties and specification of boundary, initial and loading conditions. Each of these steps have particular details to take into account when programming the method, which are not fully explained in this work. In any case, the whole process was programmed and validated, i.e. *pre-processing*, *solution/processing* and *post-processing*.

There are several commercial FEM software that already have design optimization tools. However, in this work those types of software are only used for validation purposes. Then, as explained in the following subsection, a meta-heuristic optimization algorithm was also implemented. Since one of the

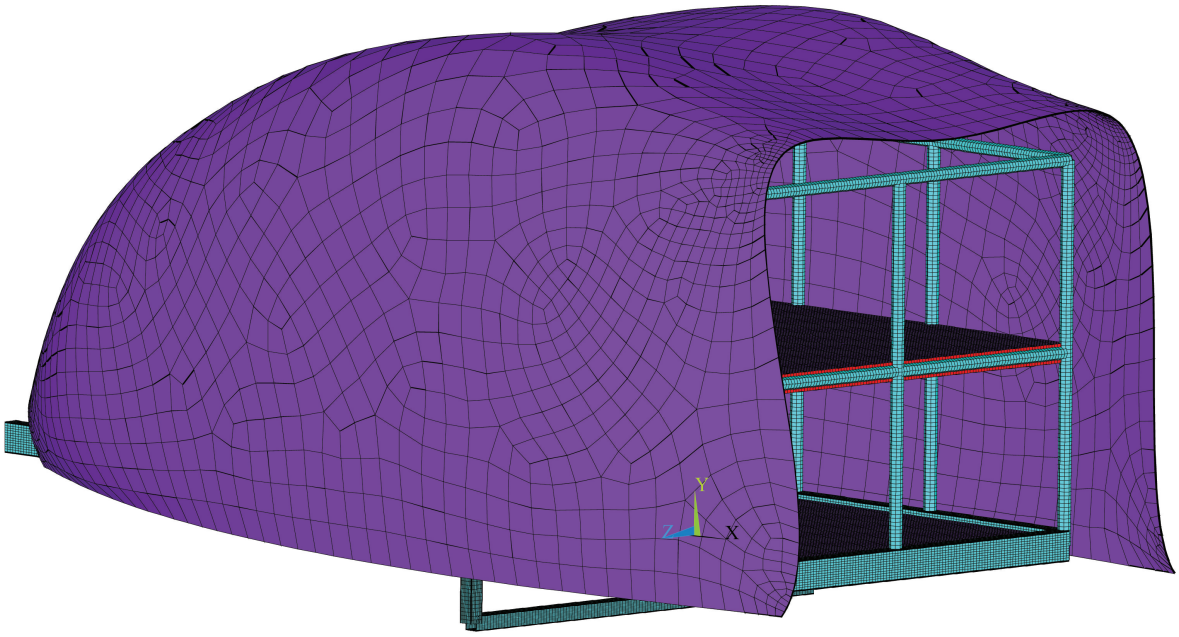

Figure 1.23: Several meshes using both beam and shell elements, inside the same FEM model (aerodynamic hybrid trailer) (AMAPDL). From Costa (2014); Costa and Barbosa (2015).

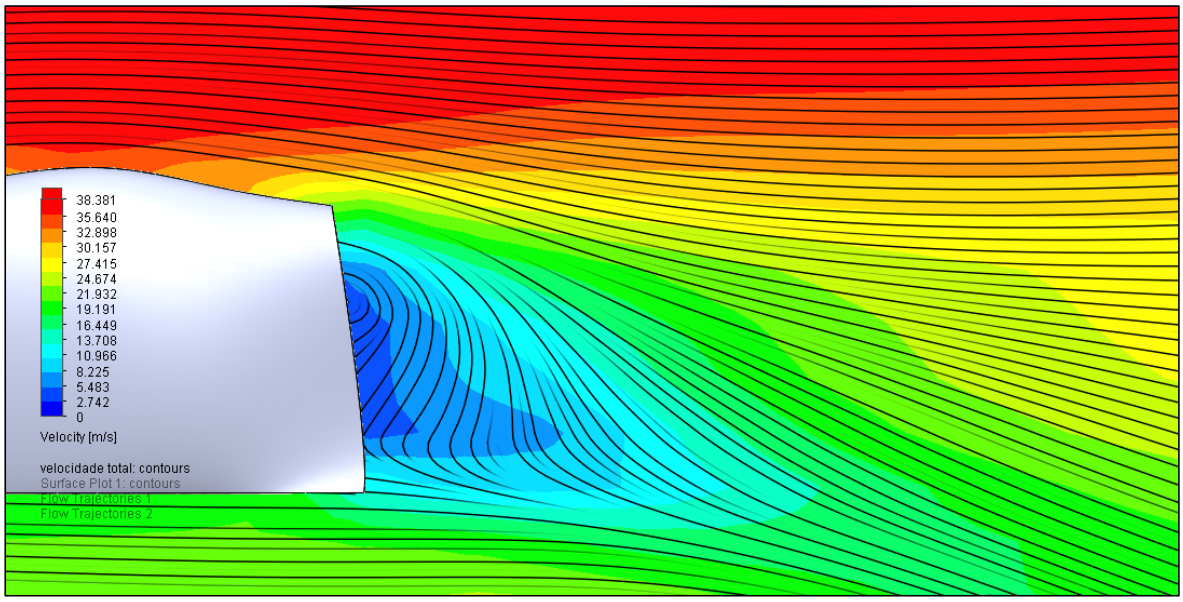

Figure 1.24: CFD velocity field results from the aerodynamic hybrid trailer in Figure 1.23 (SOLIDWORKS Flow Simulation®). From Costa (2014); Costa and Barbosa (2015).

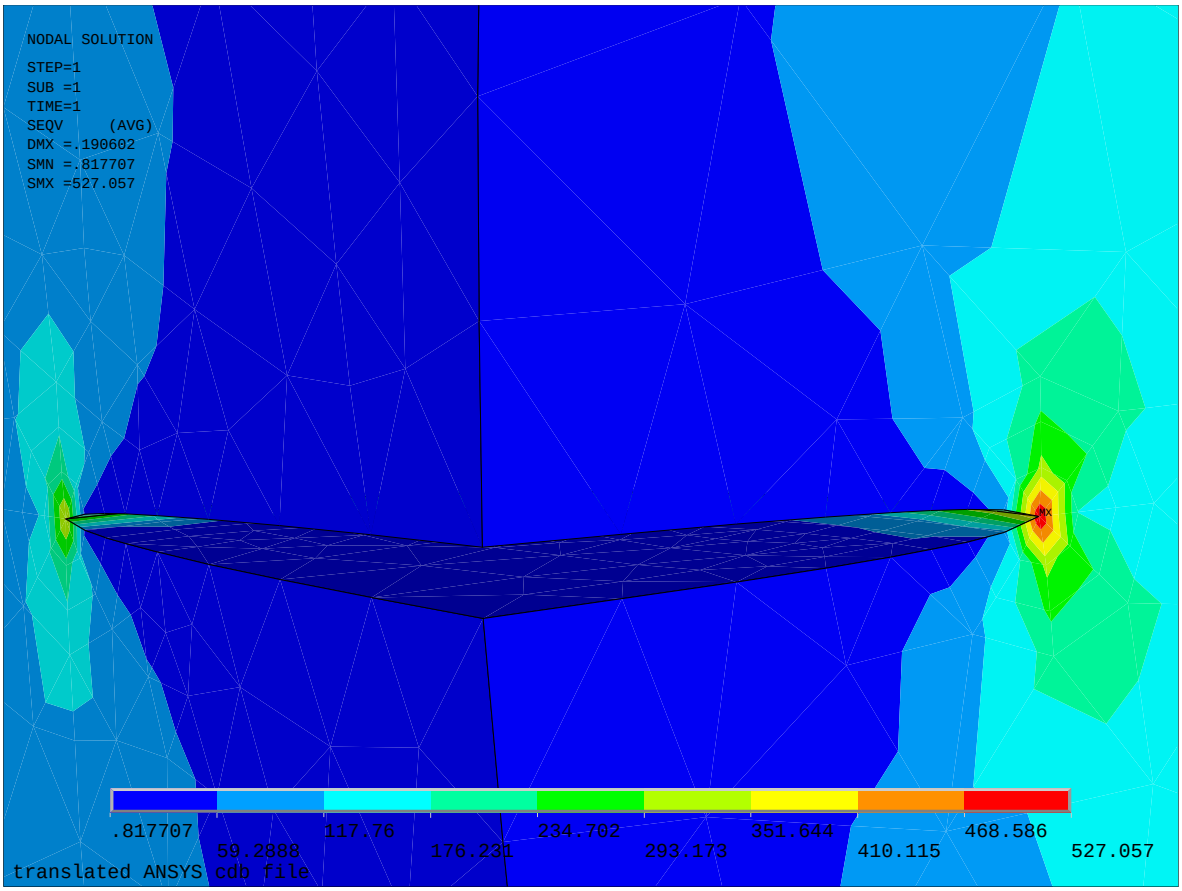

Figure 1.25: Von Mises stress field around elliptical crack tips (AMAPDL). From Costa and Venâncio (2015).

objectives of this work is to develop and evaluate different types of case studies, incorporating all the previous types of structures and materials, a FEM program was also designed and programmed from scratch, to interact directly and automatically with the optimization one. Considering the characteristics of the beams/plates structures of the numerical studies to carry out, the chosen FEM approach is based on the **F**irst-Order **S**hear **D**eformation **T**heory (FSDT) (Reddy, 2004), which is adequate for the analysis of moderately thick to thin plates. In addition, this decision was also made due to the considerable amount of other works already published, which provide numerous sources for results' validation and comparison purposes, as well as the fact of this being a theory relatively easy to implement. In Chapter 3, the algorithms' procedures are addressed.

1.3.3 Optimization

Optimization algorithms are widely used nowadays to solve and improve solutions to the engineering problems. There is no such thing as a perfect system and engineers struggle to make them more cost-effective, maximizing performance.

In the early ages of engineering, structural design *simply meant a selection of the dimensions of load-bearing components of a structure* (Srinivasan and McFarland, 2001). According to this reference, two disciplines, mainly, were used together to design structures: *mathematics*, ensuring equilibrium of

structures and *materials science*, specifying material properties to work with. Finally, the design was completed after defining a suitable safety factor, with a final test to ensure structural stability. Nowadays, with complex systems, innovative geometries and different materials mixed together, such approach is not enough. In structural design, a large non-linear domain of solutions exist, considering global and local optima. It is only possible to test and explore those domains, via powerful computational resources, with intelligent and innovative optimization algorithms. The present subsection intends to introduce the types of algorithms that exist, focusing on the type used in the present work.

In the previous section FEM was introduced. This method, when interacting with optimization algorithms is a powerful design tool. With a computer, depending on the complexity and problem dimension, it is possible to draw several conclusions about a specific case study. In more complex problems, more expensive computational resources are needed, such as servers, etc.

What is the purpose of optimizing something? An objective. The first thing to establish, is an objective, or several, when the problem is multi-objective. Without a well defined objective, optimization would be pointless. This objective can be either *minimization* or *maximization* of something, a quantity, a solution of an **O**bjective **F**unction (OF). Then, it is necessary to think about which parameters can influence that objective, known as DVs. Finally, restrictions are specified. For instance, in this work an example of an objective is the minimization of the overall deflection of a beam, while DVs can be the electric potentials applied to the active material of that beam; it is possible to formulate questions during structural design, for e.g. if one has a beam constituted by smart materials, piezoelectric patches, which are the voltages that need to be applied to that material in order to minimize the deflection of the beam? To answer this question, even before the optimization approach, a validated physical model of that beam is necessary. In this case, using FEM, that model is obtained. Finally, with an iterative optimization algorithm, the FEM model is solved several times until converging to an acceptable solution, or when exceeding a specified maximum number of iterations. Several types of optimization exist, such as:

- Linear;
- Non-linear;
- Discrete;
- Combinatorial;
- Stochastic.

In terms of history, Arora (2015) states that mathematical analysis of optimization problems was carried out during the twentieth century. However, even in 300 BC a Greek mathematician called Euclid evaluated the minimum distance between a point and a line. The optimization concept started to be more addressed by Leonid Kantorovich (1939) and George Dantzig (1947), presenting the linear programming model and a simplex model, respectively. Once more, the World War was a great boost in these concepts. In the 1980s, with computers, optimization algorithms started to grow. Gradient-based optimization was very popular until the 1990s. Nowadays, a large number of complex problems are approached with guided random search methods (e.g. GAs, simulated annealing, **P**article **S**warm **O**ptimization (PSO), etc.). There are also hybrid algorithms, e.g. combination of gradient-based and stochastic methods.

According to Arora (2015), to use gradient information to locate the optimum, it is necessary to have a continuous and differentiable OF. In addition, the solution depends on the chosen initial conditions. For this reason, *these methods are not efficient in handling discrete variables and are more likely to stay at a local optimum for a multimodal* OF (Arora, 2015). To overcome these problems, meta-heuristic search algorithms are a viable solution and Hasançebi et al. (2013) state the following three reasons:

- *The lack of dependency on gradient information*;
- *Inherent capability to deal with both discrete and continuous DVs*;
- *Automated global search features to produce near-optimum solutions (if not the global optimum) for complicated problems*.

Algorithms with such capabilities are nature-inspired, and derivative-free methods. These algorithms simulate biological and physical systems in nature, for e.g. natural evolution, immune system, swarm intelligence, animal behaviour, etc. Taking the methodology example developed in this work, a FEM program is calculated several times and the result of a quantity is evaluated. Then, in each iteration, the optimization algorithm has to specify the next DVs to create new solutions. Now, the big difference between meta-heuristics and other types of optimization approaches, is that the former is able to explore or move around the design space, based on nature-inspired techniques. This kind of exploration, will increase the possibility of finding, faster, a global optimum in a non-linear problem.

At this point it is possible to understand that optimization algorithms are complex and vast. A considerable number of algorithms exist with different categories. Then, inside each main category, an immense variety of different methods and approaches exist; focusing on meta-heuristic optimization, Figure 1.26 shows different examples of algorithms.

In the present work, several smart structures were optimized, considering several objectives and DVs, using a nature-inspired guided random search method: the **H**ybrid-**B**at-**A**lgorithm (HBA), a non-linear meta-heuristic approach, mixing the traditional **B**at-**A**lgorithm (BA) with DE. The BA is an algorithm based on the behaviour of micro-bats, and DE is an optimization technique in a way related with GAs, which belong to the evolutionary algorithms. In Figure 1.27 is possible to see a time-line that illustrates the evolution of bio-inspired heuristic algorithms, showing the location of BA. At the moment, the optimization trend in terms of algorithms is the following: when the complexity of problems increases, the need to use bio-inspired heuristic algorithms increases too, as shown in Figure 1.28.

GAs are based on the mechanism of natural selection, which is supported by Darwin's principle, the *survival of the fittest* (Arora, 2015). As stated by Yang, X.-S. (2014), if several hunters are searching for a treasure in an extremely large area and some hunters are better than others, *we can only keep the better hunters and recruit new ones*, to take less time.

DE, developed by R. Storn and K. Price in 1996 and 1997, is a *vector-based evolutionary algorithm, considered as a further development to* GAs (Koziel and Yang, X.-S., 2011). This *is a stochastic search algorithm, with self-organizing tendency and does not use the information of derivatives*. Comparing traditional GA and DE, in the former mutation is carried out at one or multiple sites of a chromosome, whereas in the latter a difference vector of two randomly-chosen population vectors is used, by means of perturbation factors, to transform an existing solution vector. DE is supported by three steps, i.e. *mutation*, *crossover* and *selection*.

In sum, with a DE approach, it is possible to increase the BA's efficiency, by improving the best bats and replacing the worst ones. Since smart structures and multifunctional materials are bio-inspired, why not to optimize those structural systems using also a nature-inspired optimization algorithm? This work intends to evaluate the performance of that combination. The following subsection is only focused on bat-inspired optimization.

1.3.3.1 Bat-inspired optimization

Swarm intelligence theory considers the modelling of populations of interacting agents, where the local interactions between all the members may give an overall intelligent global behaviour. Examples

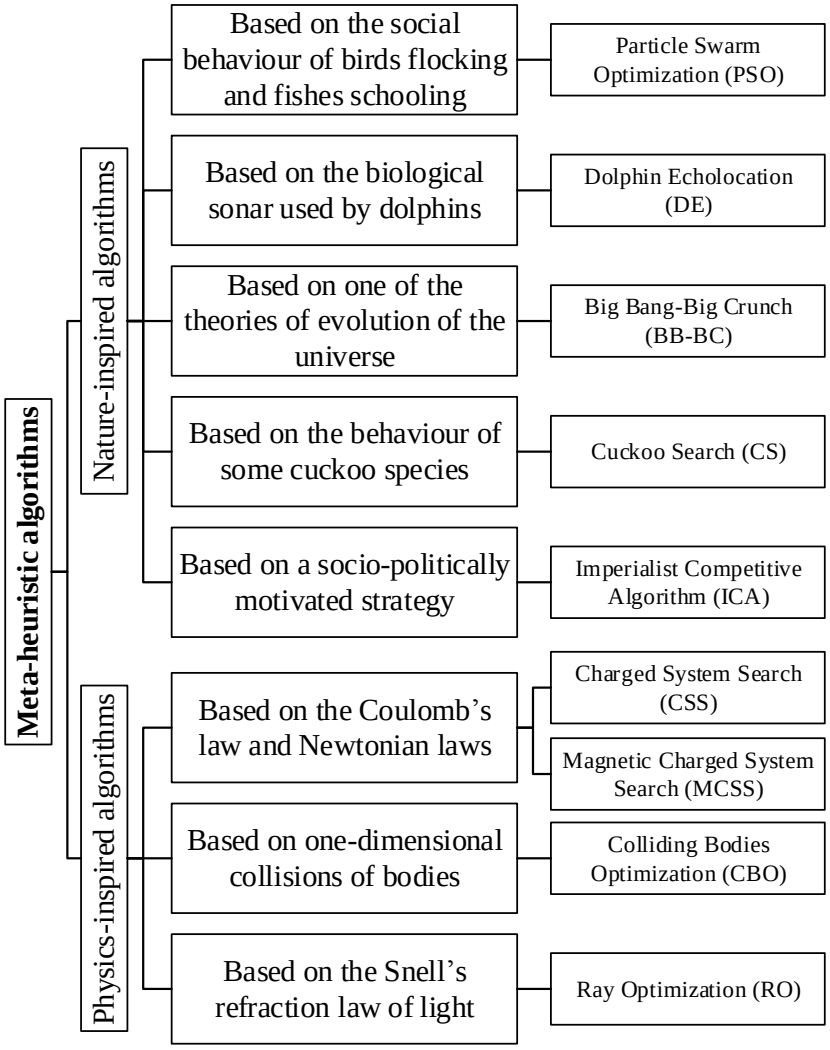

Figure 1.26: Classification of some meta-heuristic algorithms. Adapted from Kaveh (2014).

of swarm intelligence based algorithms are presented in Figure 1.26. The BA also belongs to this optimization family.

Xin-She Yang developed the traditional version of BA in 2010, which was found to be very efficient (Yang, X.-S., 2010). After that, as addressed in Section 2.2 with more detail, BA has been evolving and several versions of it were created, mixed up with other optimization methods and used in different applications.

BA mimics the behaviour of micro-bats which can find their prey and discriminate different types of insects, in complete darkness. This is done through the use of a type of sonar, called, *echolocation*, which enable them to detect prey and to avoid eventual obstacles. These bats emit very loud sound pulses and listen for the echo that bounces back from the surrounding objects, including preys. From the time delay between the emission and detection of these pulses/echoes, the time difference between their two ears and the loudness variations of the echoes, they can create a three-dimensional visualization of the surrounding environment (even in complete darkness) (Yang, X.-S., 2014). This echolocation behaviour can be formulated mathematically and associated with OFs to be optimized. The algorithm

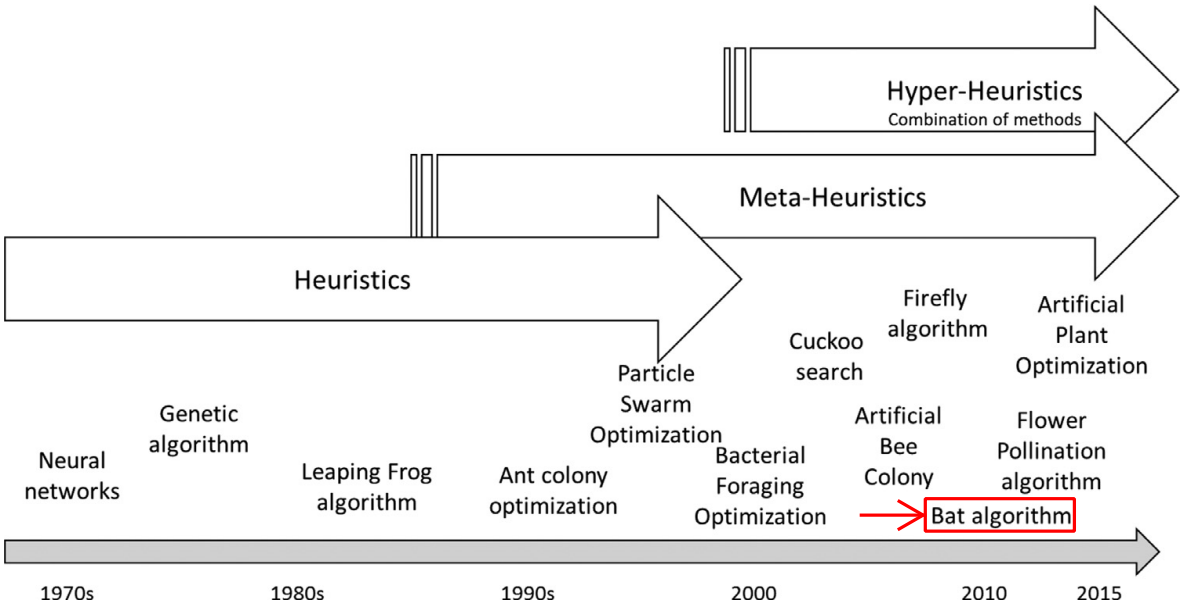

Figure 1.27: Time-line of bio-inspired algorithms' development. Adapted from Kar (2016).

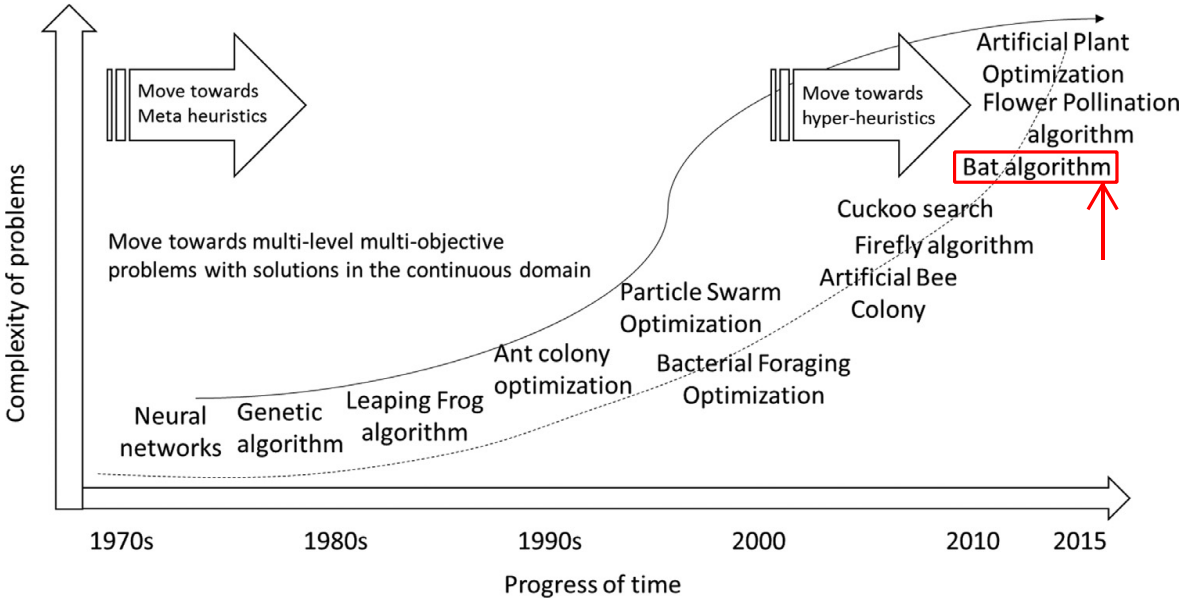

Figure 1.28: Paradigm of evolution of algorithms with increase of complexity of problems. Adapted from Kar (2016).

is then supported upon the following three main principles:

- Echolocation capacity of micro-bats (sense distances, preys, obstacles);
- Random flying capacity (characterized by velocity, frequency and loudness);
- Ability to vary frequency and loudness (depending on proximity of objects).

At this point, a legitimate question is: *why* BA *instead of other meta-heuristic approach?* In the first place, Yang, X.-S. (2010) compared BA with GA and PSO, comparing *the numbers of function evaluations for a given tolerance or accuracy*. In those studies, the algorithm was run a hundred times, with a fixed tolerance of $\epsilon \leq 10^{-5}$. For ten different benchmarking functions, the BA performed much better. Between the results of all those functions, GA achieved an average accuracy of $91.6\,\%$, PSO $94.6\,\%$ and BA $99.8\,\%$. Also in Gandomi et al. (2013a); Yang, X.-S. and Gandomi (2012) the performance of BA was evaluated with other benchmarking problems of constrained engineering optimization, revealing impressive results comparing to other algorithms. Figure 1.29 shows an example of BA's convergence with the *eggcrate* benchmark function.

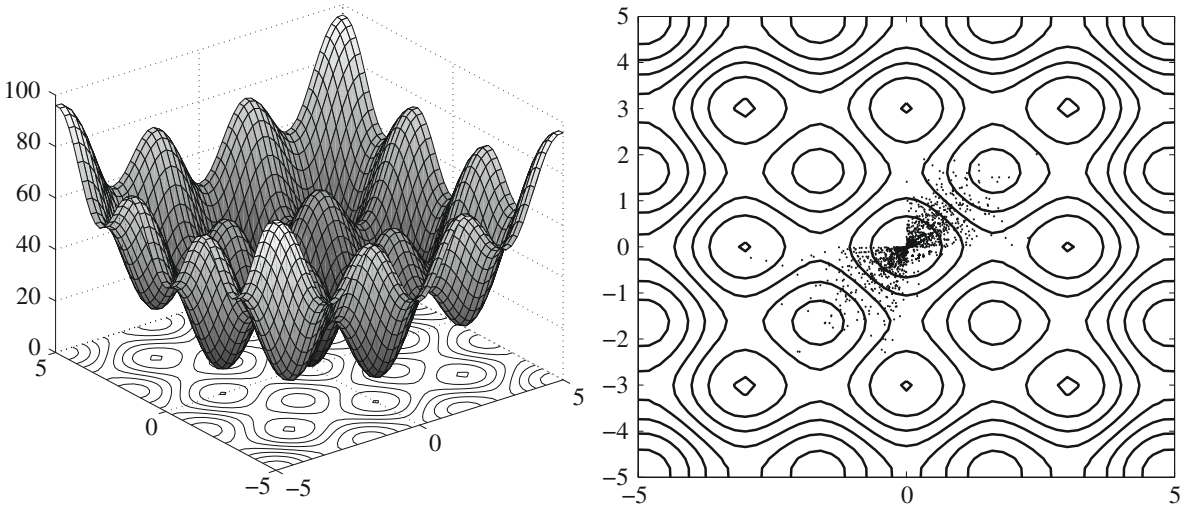

Figure 1.29: BA's convergence on *eggcrate* function (40 bats in the last 10 iterations). From Yang, X.-S. (2014).

Yang, X.-S. (2014) enumerates three main features in order to explain why BA is efficient, which are the following:

- ***Frequency tuning:*** *BA uses echolocation and frequency tuning to solve problems. Though echolocation is not directly used to mimic the true function in reality, frequency variations are used. This capability can provide some functionality that may be similar to the key feature used in PSO, SA, and HS. Therefore, BA possesses the advantages of other swarm-intelligence-based algorithms*;
- ***Automatic zooming:*** *BA has a distinct advantage over other meta-heuristic algorithms. That is, BA has a capability of automatically zooming into a region where promising solutions have been found. This zooming is accompanied by the automatic switch from explorative moves to local intensive exploitation. As a result, BA has a quick convergence rate, at least at early stages of the iterations, compared with other algorithms*;
- ***Parameter control****: Many meta-heuristic algorithms used fixed parameters by using some pre-tuned algorithm-dependent parameters. In contrast, BA uses parameter control, which can vary*

the values of parameters (loudness and rate of pulse emission) as the iterations proceed. This provides a way to automatically switch from exploration to exploitation when the optimal solution is approaching. This gives another advantage of BA over other meta-heuristic algorithms.

So, the *first reason* to use BA is its efficiency, already proved by other references. The *second reason* is because no smart structural problems were found to be optimized using BA, in the literature, specially by a FEM algorithm that also models Kriging elements. Finally, the *third reason* is related to the fact that both candidate and supervisor of this thesis implemented this algorithm previously, in a very different context: optimization of desalination heat exchanger's geometries (Costa et al., 2015b).

Then, *how would a nature-inspired optimization algorithm perform, when optimizing a nature-inspired smart structure?*

1.4 Thesis structure

After the present *Introduction* chapter, a *Literature Review* or *State-of-the-Art* is carried out in Chapter 2, concerning the main topics of the present work. It would make sense to open Chapter 2 with *smart structures and materials*, but the developed FEM algorithm covers more than that. So, for that reason, the first subsection is called *advanced structures*. This way, it is possible to address structural design, including smart structures (and not only), all materials already mentioned and FEM. Afterwards, one focuses on *bat-inspired optimization* only.

The overall thesis can be divided, essentially in four main phases, where each of them corresponds to scientific journal publications and international conference talks, resulting from this thesis. Those phases, all carried out with the same programmed algorithms that evolved continuously since this work started, are the following:

1. The modelling of static behaviour of hybrid CNT-metal-ceramic composite structures, where several validations of FGM models and new studies are carried out (deflections, stresses, etc.), by means of static parametric studies and comparison with external references (Costa, 2016b; Costa and Loja, 2016a);

2. New parametric case studies, in a way related to the materials from the last item, but focused on the characterization of free vibrational dynamic behaviour of multiscale composite structures, also with FGM considerations (different distributions of micro and nano-inclusions) (Costa, 2016b; Costa and Loja, 2016c);

3. The modelling and validation of several types of smart structures constituted by different passive and active layers/materials, both statics and dynamics (free vibrations). New parametric case studies concerning the static and dynamic behaviour of functionally graded active composite structures (Costa, 2016b; Costa and Loja, 2016b);

4. Finally, several case studies to model, study and optimize the mechanical behaviour of adaptive structures, assessing the interaction of both FEM and BA; different optimization objectives and DVs are modelled, considering other optimization techniques, i.e. from hybridization of the standard BA using DE, to micro approaches based on micro-GAs (Costa, 2016b; Costa and Loja, 2016b). The research carried out in this topic was already submitted to the scientific *Journal of Composite Structures* and *Journal of Composites Part B: Engineering*.

The previous topics are only a general guideline and additional studies may arise between them. For e.g. convergence studies comparing Lagrange and Kriging elements, comparisons and/or validations with AMAPDL and other references.

All topics are presented in Chapters 3 and 4, the *Methodology* and *Case Studies*, respectively. The former has the objective of explaining mathematically the approach used to model all case studies, i.e. modelling of materials and finite elements, as well as bat-inspired optimization and the definition, structure and computational implementation of algorithms. The latter, defines the validation, parametric and optimization case studies, as well as their respective results and discussion.

Finally, Chapter 5 summarizes the most important, relevant and interesting *Conclusions* from the whole work, as well as the specification of future work. To complement everything from the present thesis' main-matter, a set of Appendices was created; they integrate figures, tables and equations.

1.5 Remarks to the reader

The virtual package of the present work contains a lot more data than the printed one.

Each interactive element of the present pdf, i.e. animation or video, is identified in its respective caption; instructions are given to the reader, in order to avoid misinterpretations. All elements were tested using the Adobe Acrobat® pdf viewer, on operating system Windows® 8.1; all worked properly.

In this pdf, all clickable *hyper-refs* are formatted with blue text color (e.g. chapters, sections, figures, tables, equations cross-references, etc.), *bibliographic citations* with red and *units* with ForestGreen.

In the *Bibliography* chapter, each reference has in front of it one or more *hyper-refs* with numbers, corresponding to the pages where that particular reference was cited previously along the pdf.

After clicking any *hyper-ref*, probably the pdf is going to change page to go to that specific reference page. However, the reader might want to return to the previous page. To swap between the previous and following pages, the reader can press, respectively the keystrokes Alt + ← and Alt + → . This methodology works in the most commonly used pdf readers and facilitates the navigation a lot, throughout large documents.

NOTE: This document contains **299 Figures**, **100 Tables**, **214 Equations** and **182 Cited References**.

- **Chapter 1 – *Introduction*** contains pages from 1 to 30 **(30 TOTAL)**;
- **Chapter 2 – *Literature Review*** contains pages from 31 to 44 **(14 TOTAL)**;
- **Chapter 3 – *Methodology*** contains pages from 45 to 100 **(56 TOTAL)**;
- **Chapter 4 – *Case Studies*** contains pages from 101 to 142 **(42 TOTAL)**;
- **Chapter 5 – *Conclusions*** contains pages from 143 to 148 **(6 TOTAL)**.

The number of pages from **Chapter 1** to **Chapter 5** is **148**.

Chapter 2

Literature Review

In this chapter, a literature review about the main subjects addressed in this work is carried out. First, advanced structures are approached, which include passive and active ones, constituted by composites, multiscale, hierarchical and hybrid composites. Both smart and traditional materials are addressed, as well as FGMs and CNTs. It is intended to review innovative applications and FEM models. Afterwards, the literature about the bat-inspired optimization topic is also reviewed, mentioning range of applications, types of BA variations, optimization techniques, and so on.
NOTE: This chapter contains pages 31 to 44, which is 14 in total.

2.1 Advanced structures

Nowadays, the traditional approach of structural design does not fulfil all requirements and is not fully compatible with certain innovative structural applications. As explained and reviewed in this chapter, the state-of-the-art in structural design goes far beyond conventional passive structures. Applications in several fields such as aerospace, aeronautics, automotive and medical must comply with several strict requirements and restrictions that are only possible to achieve, efficiently, using smart structures and state-of-the-art materials. Multifunctional materials, smart, composites, FGMs and CNTs are helping the goal pursuit of achieving structures with enhanced performances and improved material characteristics, where tailoring different constituent phases at different scale levels is crucial.

There is a significant number of research works on composite materials, with a particular focus on its micro and macro mechanics aspects, ranging from the different materials interaction analysis to the structural performance assessment. Among these works, in a more global perspective, examples are the reviews of Gibson (2010); Lau, K.-t. et al. (2006); Singh and Chauhan (2016), among others.

In his review work, Gibson (2010) tried to identify the most relevant topics in multifunctional composite materials and structures. He considered mechanical properties, such as strength, stiffness, fracture toughness, and damping, but also other factors, namely, electrical and/or thermal conductivity, sensing and actuation, energy harvesting/storage, self-healing capability, electromagnetic interference shielding, recyclability and biodegradability. According to the conclusions of this review, the majority of these recent developments are associated with polymeric composite materials and corresponding advances in nano-materials and nano-structures. The review also concludes with a discussion of recent

applications of multifunctional materials and structures, such as morphing aircraft wings, structurally integrated electronic components, biomedical nano-particles for dispensing drugs and diagnostics, and optically transparent impact absorbing structures.

Another review paper is due to Singh and Chauhan (2016), and it is focused on the analysis of the feasibility and viability of developing low cost, high performance hybrid aluminium matrix composites for automotive and aerospace applications. This study considers fabrication characteristics and the mechanical behaviour of this type of composites. These parameters' appreciation takes into account the distribution of the reinforcing particles in the matrix alloy and the porosity levels. The authors concluded that the density, hardness, tensile behaviour and fracture toughness of these metal matrix composites were comparable or superior to the ceramic reinforced composites.

As another review work, with different characteristics from the previous two, is the one carried out by Lau, K.-t. et al. (2006), which made a critical review on recent research related to nano-tube/polymer composites, discussing as well recently-adopted coiled nano-tubes to enhance the interfacial bonding strength of nano-composites and the growth of nano-tubes from nano-clay substrates to form exfoliated nano-tube/nano-clay polymer composites.

Concerning to the study of the mechanical performance of functionally graded structural elements, there are many published works, but a much less number incorporating CNTs. Among other works on these hybrid advanced composites, Heshmati et al. (2015) studied the effects of CNT length, waviness, agglomeration and distribution on the vibration behaviour of functionally graded nano-composite beams reinforced by SWCNTs. To this purpose, and to determine the effective elastic properties of wavy CNTs they have used Monte-Carlo simulation method. For the prediction of the elastic properties of the nano-composite, a two-scale micro-mechanical model was developed. The numerical solutions were obtained using the FEM and the Timoshenko beam formulation. The authors concluded that the parameters studied have a significant influence on the vibrational behaviour of the functionally graded nano-composite beams.

Other works in this context of the nano-composites are due to He et al. (2015); Kamarian et al. (2016); Mareishi et al. (2015); Rafiee et al. (2014b) among others. Mareishi et al. (2015), presented an analytical solution for the non-linear free and forced vibration response of smart laminated nano-composite beams resting on non-linear elastic foundation and under external harmonic excitation. They have studied the effects of the applied voltage, temperature change, beam geometry, volume fraction and distribution of the CNTs on the non-linear natural frequencies and frequency-response curves.

Another work focused on the characterization of the influence of the applied voltage, plate geometry, volume fraction of fibres and weight percentage of SWCNTs and MWCNTs on the linear and non-linear natural frequencies of piezoelectric nano-tubes/fibre/polymer multiscale composite plate, was carried out by Rafiee et al. (2014b). This study was based on FSDT and considered von Kármán geometrical non-linearity.

He et al. (2015) presented an analytical formulation combined with a fractional-order time derivative damping model in order to study the large amplitude free and forced vibration response of CNTs/-fibre/polymer laminated multiscale composite beams. That study was based on the Euler-Bernoulli beam theory and von Kármán geometric non-linearity. The bulk material properties of the multiscale nano-composite were predicted using Halpin-Tsai equations and fibre micro-mechanics.

More recently, Kamarian et al. (2016) carried out a parametric study to investigate the influences of CNTs volume fraction and agglomeration, fibre volume fraction, geometrical parameters and laminate lay-up on the natural frequencies of multiscale nano-composite plates, with a polymeric matrix phase. The authors have also considered the stacking sequence optimization of these plates to maximize their fundamental frequency using the firefly algorithm.

A recent work devoted to the analysis of functionally graded plates, was carried out by Bernardo et al. (2016). They presented a study on the characterization of the mechanical behaviour of functionally graded plates, using a meshless approach and Kriging-based FEM. On their work they considered the influence of using a discrete stacking of layers to approximate the continuous variation, as well as using different distributions of the reinforcement particles through the plate thickness. Different sandwich configurations and the effect of diverse material and geometrical parameters in the static and free vibrations behaviour of plates are also studied.

Also in the context of the FGMs, particularly on a study focused on the static bending and free vibration behaviour of functionally graded beams resting on Winkler foundation, Akbaş, Ş.D. (2015) used a Navier-type solution for simply-supported **B**oundary **C**onditions (BCs), and proposed exact formulas for the static deflections and the fundamental frequencies. He considered the material properties varying through the thickness according to power law distribution and Euler-Bernoulli and Timoshenko beam theories.

García-Macías et al. (2016) also presented results associated to static and dynamic numerical simulations of thin and moderately thick functionally graded skew plates with uniaxially aligned reinforcements. To this study, a shell element based on FSDT was formulated in oblique coordinates. According to the authors, the four-noded skew element presents a good performance. Parametric studies were carried out to explain the influences of the skew angle and other plate geometrical characteristics as well as the CNTs volume fraction. The fibre orientation was also analysed.

The effect of a sudden transverse dynamic load produced in quadrilateral plates made with functionally graded composites reinforced with CNTs, was studied by Zhang et al. (2016). These authors considered the use of the FSDT and the element-free IMLS-Ritz method. The numerical time integration is performed using the Newmark-b method. Numerical simulations were carried out to assess the effect of CNTs volume fraction and distribution type. The plate characteristics such as side angles, area and aspect ratios were also analysed.

Also a recent work presented by Lei et al. (2016) is related to the buckling behaviour of functionally graded composite laminated plate reinforced with CNTs. The authors have used the FSDT, implemented through the meshless kp-Ritz method. Parametric studies were developed for various types of nanotubes distributions, volume fraction and other geometrical characteristics. The number of layers and lamination angles were also considered.

At this point, is evident that several contributions were published considering the addition of CNTs to polymeric and ceramic matrices, making the multiscale reinforcement a current research field (Ferreira et al., 2016). To illustrate this, it is possible to enumerate among others, works orientated to characterize material properties of composites with these types of matrices (Hussain et al., 2006; Ramakrishna et al., 2001; Zok and Levi, 2001). Comparatively, a minor visibility was given to the metal matrix composites (Davim, 2014; Esawi et al., 2010; Neubauer et al., 2010).

Engineers are also trying to use regular microscale fibres and CNTs to reinforce composites (Garcia et al., 2008; Khan and Kim, J.-K., 2011; Qian et al., 2008), where CNTs may even be dispersed along carbon fibres themselves.

The use of CNTs to reinforce FGMs, as a promising research target, has its reasons; e.g. due to their improvement in *weight*, *electrical conductivity*, *dimensional stability*, *flame retardancy* and *strength* (Udupa et al., 2012). In consequence, these materials are suitable for applications such as *gas adsorbents*, *actuators*, *catalyst supports*, *probes*, *chemical sensors*, *nano-pipes*, *nano-reactors*, etc. (Bharti et al., 2013). In addition, FGMs can improve environmental resistance and reduce crack driving in interfacial zones, i.e. increasing bonding strength (Di and Yang, Y.-C., 2012).

The use of ceramic materials as reinforcement particles and as agents of a thermal performance improvement is a more common solution in the context of particle composites (Bernardo et al., 2016;

Ferreira et al., 2005; Kadoli et al., 2008; Loja et al., 2012; Nguyen, T.-K. et al., 2007, 2008; Qian et al., 2004). These solutions may assume that the weight or volume fraction remains constant in the whole composite or admit that they may vary in the 3D domain of the composite structural element. FGMs are typical examples of this last case, where the mixture composition of the constituent phases depends on the space coordinates of the composite (Birman and Byrd, 2007; Miyamoto et al., 1999).

The structural analysis of components or systems made of these materials was carried out by several researchers mainly considering polymeric or ceramic matrices with ceramic reinforcement particles (Fazzolari, 2015; Ferreira et al., 2005; Loja et al., 2012, 2015; Qian et al., 2004; Tornabene et al., 2014; Viola et al., 2014). It is important to note that these works focused from the mechanical to thermal analysis of beams, plates and shell structures, using a diverse range of numerical approaches.

The possibility of using nano-particles to enhance material characteristics, has deserved the attention of many researchers, and it has been possible to find a number of review studies in the nano-composites field, focusing processing techniques, nano-tube dispersion, interface, strengthening mechanisms and mechanical properties, and on its use as a reinforcement agent in composites (Ajayan et al., 2000; Bartolucci et al., 2011; Coleman et al., 2006; Du, J.-H. et al., 2007; Hu et al., 2006; Kim et al., 2009; Kuilla et al., 2010; Liew et al., 2006; Rashad et al., 2015; Salvetat, J.-P. et al., 1999; Thostenson et al., 2005; Zapata-Solvas et al., 2012).

Concerning to the analysis of structures made of materials that somehow include nano-composites (Rafiee et al., 2014a; Zhu et al., 2012), and particularly in the case of FGMs that incorporate nano-particles (Alibeigloo and Liew, 2013; Liew et al., 2015; Tornabene et al., 2016) it is possible to perceive a research field that is currently in expansion. It is however understood that further research will be needed for a more comprehensive understanding of the response of these structures from nano to macroscale, as well as in what concerns to the multiscale interaction.

Ferreira et al. (2016) enumerate several main fields where the FGMs research is focused on, with associated references:

- FGMs *subjected to thermal and mechanical loading* (Beena and Byju, 2013; Wang et al., 2013);
- *Fracture properties and crack propagation/analysis* (Di and Yang, Y.-C., 2012; Shin et al., 2013);
- *Improving and discovering better manufacturing processes* (Jha et al., 2013; Kieback et al., 2003);
- *Modelling and numerical simulation of loading parts made of* FGMs (Birman and Byrd, 2007; Yu and Kidane, 2014);
- *Using piezoelectric materials and* CNTs *along with* FGMs (Bharti et al., 2013; Udupa et al., 2012).

The same authors state that FGMs manufacturing-related characteristics still have a major impact on cost issues. Jha et al. (2013) support this idea by reviewing the state-of-the-art on fabrication processes, concluding that more focus is required on improving the most promising fabrication method, i.e. *solid freeform*.

In terms of smart materials, as stated by Ferreira et al. (2016), the most commonly used piezoelectrics, at the moment, are polycrystalline ceramic (PZT, $PbTiO_3$, $BaTiO_3$), single crystals (SiO_2, $LiNbO_3$, $LiTaO_3$) and polymeric (PVDF, co-polymer) taking the form of monolithic, thin films, wafers and (nano)fibres/wires, which can be hollow and arranged as **M**acro **F**ibre **C**omposites (MFCs) and **A**ctive **F**ibre **C**omposites (AFCs). The authors also report that monolithic piezoelectric materials have several handicaps, i.e. *they do not contribute to the load bearing capacity of the structure and may actually diminish it because of stress concentrations generated in the structure by their inclusion*. In contrast, researchers have been focusing on fibre-based piezoelectric materials, which are better options

to integrate in composites. It is important to note that the FEM algorithm here developed is prepared to model both ceramic and fibre-based piezoelectric materials, with both isotropic and orthotropic (monoclinic) material approaches, respectively.

The authors enumerate several references with multiscale analysis (Cook and Vel, 2012) and finite element analysis (Liu, Y.-g. et al., 2010; Ray and Mallik, 2004; Shen et al., 2009) to model smart structures containing piezoelectric fibre-reinforced composite actuators. Still, these types of actuators are fragile and are preferred for sensing and energy harvesting applications. There are other smart materials more suitable for actuation purposes, such as SMAs.

SMAs *are metallic alloys that can reversibly recover permanent strains when subjected to a specific stimulus, which happens when the* SMA *goes back from the malleable martensite phase to the very stiff austenite phase* (Ferreira et al., 2016). This type of stimulus can be thermal, pressure and magnetic field. SMAs are already being used in several state-of-the-art smart structures, with efficient actuation capabilities. Sun et al. (2012) reviewed these materials, in terms of applications and working mechanisms. Recently, Sun et al. (2016) carried out a relevant state-of-the-art review concerning smart materials and structures on morphing aircraft applications, also showing evidence that SMAs are being incorporated on structures in this field. In fact, Ferreira et al. (2016) state that SMAs are extensively used throughout morphing aerospace structures.

An interesting example of this technology is the shape morphing aircraft wing developed by Sofla et al. (2010), which uses an antagonistically positioned SMA material, in order to flex the wing (see Figure 2.1). These innovative actuation designs reduce the weight penalty and are excellent concerning power/weight ratio, in comparison with traditional ones based on hydraulics, pneumatics or motor-based (Ferreira et al., 2016).

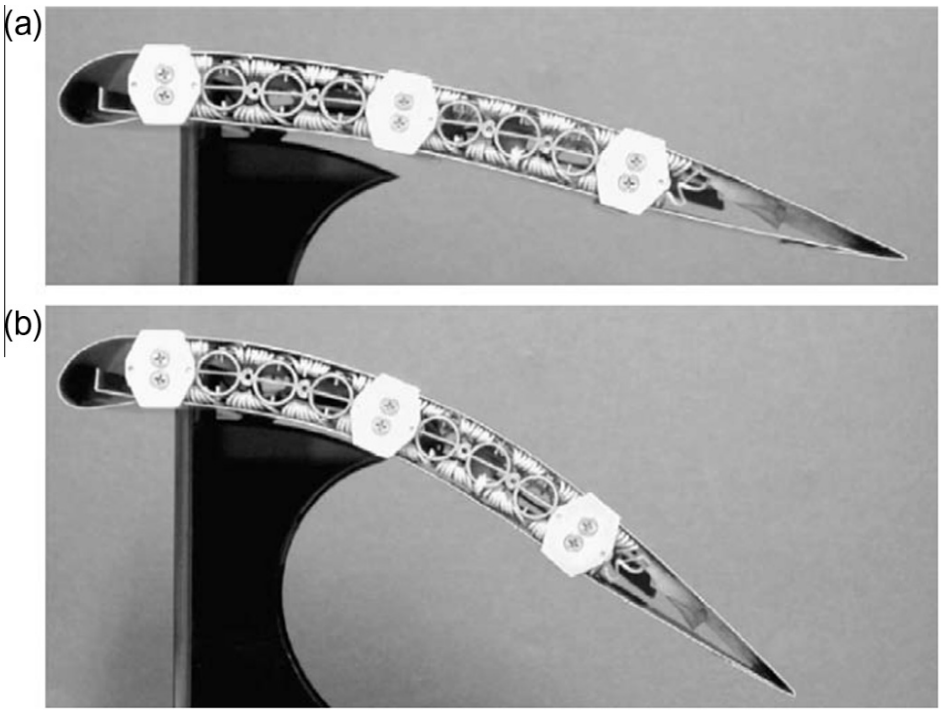

Figure 2.1: Bending achieved in a prototype aircraft wing by heating of SMA strips. (a) Un-morphed and (b) morphed. From Ferreira et al. (2016).

Another example are the well-known NiTi SMAs flexures used in engine nozzles (trailing-edges)

of a Boeing commercial airplane (Ferreira et al., 2016; Sun et al., 2016). These chevrons, shown in Figure 2.2, enable geometry variation by means of actuation, reducing jet noise during takeoff and increasing cruise efficiency. In addition, they also improve the mixing of the freestream air and the fan stream. Sun et al. (2016) also report other SMAs actuators in jet engines, such as a morphing inlet internal wall tested in a wind tunnel, morphing intake and morphing nozzle.

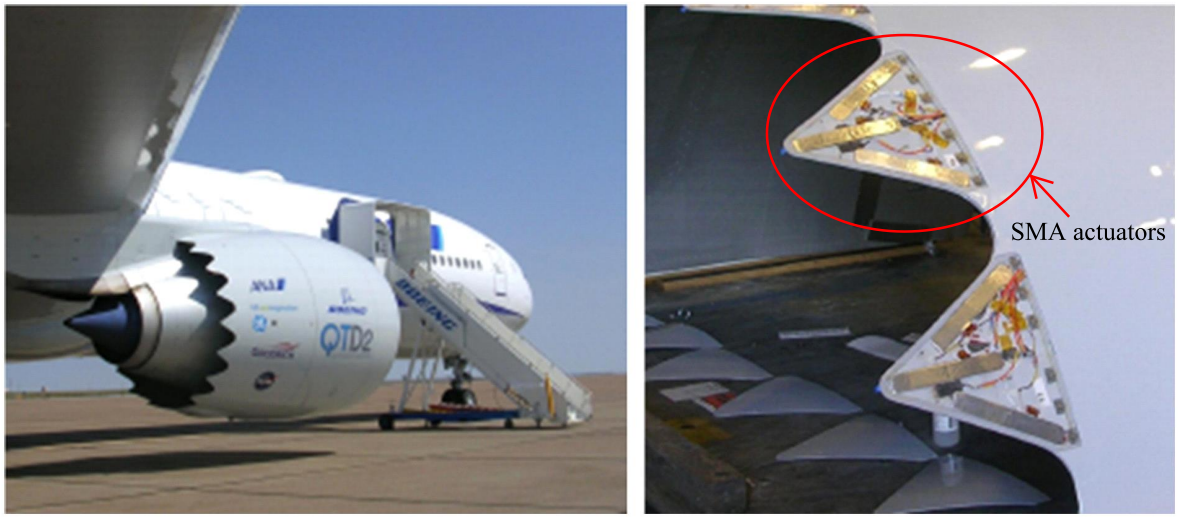

Figure 2.2: Full-scale flight tests of SMA-actuated variable-geometry chevrons on a Boeing 777-300ER with GE-115B engines. Adapted from Sun et al. (2016).

According to these authors, SMA actuators are also used to change the wing geometry itself. For example, variable-sweep wing controlled by SMA ribbons on the spar, SMA wire used to create a morphing trailing-edge to enhance lift, several segmented morphing trailing-edge concepts to produce larger trailing-edge angle, and others.

Other relevant examples are the piezoelectric materials used in linear actuators in helicopter rotor systems to improve vibration, noise and aerodynamic performance (Sun et al., 2016). Among others, X-type actuators were successfully tested in a BK117 S7045 prototype, shown in Figure 2.3. The authors reported remarkable results, where vibrations were reduced up to 90 % (i.e. to less than 0.05 g), when the active-flap rotor was installed (Jaenker et al., 2008; Konstanzer et al., 2008).

It is possible to understand from this literature review that smart materials are evolving and successfully being integrated in structures. Micro air vehicles, unmanned aerial vehicles, and full-size aircraft are only few examples of this field application. This suggests that smart materials have huge potential in state-of-the-art advanced structures. However, Sun et al. (2016) concluded that smart materials and structures are not currently suitable for production aircraft, proposing the following five main challenges, in order to understand the full potential of these devices:

1. **Material modification:** *At the molecular scale, amputation, grafting, or recombination technology could be used to improve the performance of current smart materials*;
2. **Functional additives:** *Additives (e.g. CNTs, carbon black, graphite, ferrous powders, and nickel powders) could be incorporated into smart composites to make them multifunctional. For example, shape memory materials can be heated electrically by incorporating conductive additives*;



Figure 2.3: BK117 S7045 flight test with active rotor trailing-edge flaps actuated by piezoelectric actuators. From Sun et al. (2016).

3. **Structure optimization:** *Optimized structures can be designed using topology optimization methods. Moreover, novel structures may be discovered by applying new concepts*;
4. **Hybrid applications:** *Novel structures can be constructed using various smart materials; for example, honeycombs constructed using SMAs, bi-stablestructure actuators constructed from MFCs and hybrid linear step actuators driven by magnetostrictive or piezoelectric materials*;
5. **Novel smart materials:** *Many types of novel smart materials are required, and efforts should be made to create and investigate them.*

Finally, Figures 2.4 and 2.5 show interesting videos about shape-morphing aircraft and automotive wings, respectively. These smart structures were developed by a company called FlexSys Inc., founded in 2000 by Dr. Sridhar Kota to develop and commercialize his patented design of a shape-morphing adaptive control surface of an airfoil. More information in `http://www.flxsys.com/`. In the following section, a literature review about the bat-inspired optimization is carried out.

2.2 Bat-inspired optimization

As already explained in Chapter 1, BA is an innovative and recent nature-inspired meta-heuristic optimization algorithm, which is inspired by the micro-bats' sonar capabilities (echolocation). The algorithm solves both single and multi-objective optimization problems. The bats emit sounds/pulses, which are reflected by the surrounding objects. Then, through several relations and characteristics of the sound echoes, bats are able to identify preys and obstacles in complete darkness. In the process, bats adjust continuously several parameters, such as velocity, frequency and loudness of the pulses, to accomplish their objectives. When bats come closer to their preys, loudness and rate of pulse emission decreases and increases, respectively. Those remarkable features were put together in an optimization iterative algebra-based algorithm, by Yang, X.-S. (2010).

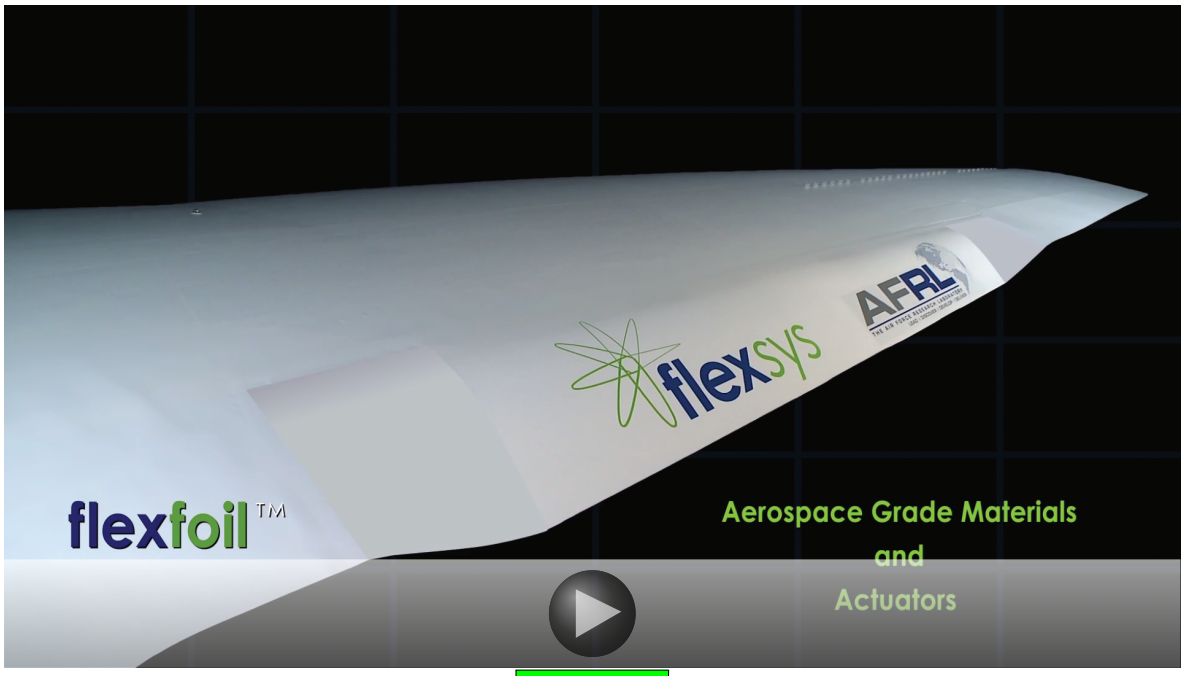

Figure 2.4: "*At last, a shape-morphing aircraft wing is here – no flaps*". From https://www.youtube.com/watch?v=9ZpAHxMj5lU. Please click 2 times on the button above this caption to start the video. After clicking the video use Spacebar (play/pause), Home / End (go to start/end), ← / → (seek backwards/forwards) and m (mute/unmute).

Kar (2016) made an excellent work by reviewing bio-inspired computational algorithms, addressing their scope of applications, as well as their quantity distribution throughout the literature – this includes BA. In order to start this chapter, it is convenient to show the amount of papers about BA found in Scopus, in comparison with other nature-inspired algorithms. Figure 2.6 presents search results carried out by this author, showing that BA was the third least found, with only $0.16\,\%$ of the whole results. In addition, Figure 2.7 supports this information by saying that there were found only 170 BA-related papers, which in comparison with, for instance, neural networks (62,500), GA (23,000) or PSO (8,500), is a very small number. These conclusions were expected, since this algorithm is relatively recent. This way, BA becomes an interesting approach to test in this type of structural analysis, searching for innovation.

This reference classifies BA as an algorithm suitable to solve *non-linear and multimodal problems, especially suitable for complex high-dimensional problems where convergence is a challenge* (Yang, X.-S. and Gandomi, 2012). In consequence, this type of algorithm has been used in a wide range of applications, such as:

- Adaptive learning problems;
- Association rule mining;
- Classification;
- Effort estimation;
- Environmental/economic dispatch;
- Multi-constrained operations;



Figure 2.5: "*Morphing automotive wing*". Please notice the red arrows region in the video wing. From https://www.youtube.com/watch?v=RhuB1TDp67A. Please click 2 times on the button above this caption to start the video. After clicking the video use Spacebar (play/pause), Home / End (go to start/end), ← / → (seek backwards/forwards) and m (mute/unmute).

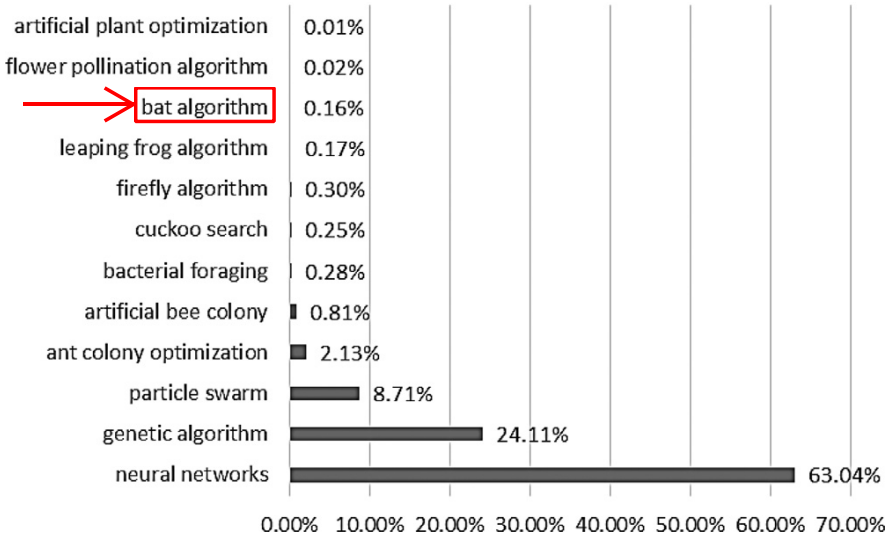

Figure 2.6: Scopus search results of bio-inspired optimization algorithms, in percentages. Adapted from Kar (2016).

Algorithms	Dominant contributors	Dominant subject areas	Articles	Conference
Neural networks	Cao, J; Melin, P; Wang, J; Oh, SK; Pedrycz, W.	Engineering, Computer Science, Mathematics, Physics and Astronomy, Materials Science	62,490	53,651
Genetic algorithm	Gen, M; Goldberg, DE; Chakraborti, N; Sakawa, M, Castillo, O.	Engineering, Computer Science, Mathematics, Physics and Astronomy, Materials Science	22,939	22,112
Particle swarm	Sun, J.; Engelbrecht, AP; Xu, W; Abraham, A; Zeng, J.	Computer science, Engineering, Mathematics, Energy, Physics and Astronomy	8386	7907
Ant colony optimization	Blum, C; Zhang, J; Dorigo, M; Stutzle, T; Kaveh, A.	Computer science, Engineering, Mathematics, Decision Sciences, Social Sciences	1858	2114
Artificial bee colony	Karaboga, D; Pant, M; Ozturk, C; Vega-Rodriguez, MA; Akay, B.	Computer science, Engineering, Mathematics, Energy, Decision sciences	866	633
Bacterial foraging	Niu, B; Abraham, A; Chen, H; Zhu, Y; Das, S.	Computer science, Engineering, Mathematics, Energy, Physics and Astronomy	284	237
Cuckoo search	Yang, XS; Deb, S; khan, A; Rehman, MZ; Zhou, Y.	Computer science, Engineering, Mathematics, Energy, Environmental Sciences	292	162
Firefly algorithm	Yang, XS; Shareef, H; Mohamed, A; Tuba, M; Horng, MH.	Computer science, Engineering, Mathematics, Energy, Physics and Astronomy	315	232
Leaping frog algorithm	Hosseinian, SH; Chen, MR; Li, X; Zhao, L; Wang, L.	Engineering, Computer Science, Mathematics, Energy, Social Science	199	117
Bat algorithm	Yang, XS; Zhou, Y; Tsai, PW; Nguyen, TT; Dao, TK	Computer science, Engineering, Mathematics, Energy, Materials science	169	113
Flower pollination algorithm	Abdelaziz, AY; Ali, ES; Yang, XS; Abd Elazim, SM; Dubey, HM	Computer science, Engineering, Mathematics, Energy, Neuroscience	21	15
Artificial plant optimization	Cui, Z; Shi, Z; Zeng, J; Liu, D; Cai, X.	Engineering, Physics and Astronomy, Mathematics, Computer science, Materials science	16	8

Figure 2.7: Scopus search results of bio-inspired optimization algorithms, in discrete numbers. Adapted from Kar (2016).

- Multi-objective optimization;
- Network path analysis;
- Numerical optimization problems;
- Scheduling;
- Structural design optimization;
- Vector matching.

It was also mentioned by Kar (2016), that the application of hybrid algorithms and hyper-heuristics involving BA would be of interest to the academic community and such approach is carried out in this work. The author also emphasizes that, for constrained optimization tasks, BA's performance was reported to be higher than other nature-inspired methods, e.g. GA and PSO (Gandomi et al., 2013b). This supports the information already found in other references, such as Hasançebi et al. (2013).

Concerning several concrete examples, Svečko and Kusić (2015) published a paper entitled ***F**eedforward **N**eural **N**etwork (FNN) position control of a piezoelectric actuator based on a BAT search algorithm*. In fact, this was the most related publication found to the present work, but still it is not about smart structures FEM optimization using BA. These authors used BA to improve the positional control of piezoelectric actuators and also to train the FNN. They reported that BA improves the optimization results much better, comparing to the classical FNN control approach.

The optimization of desalination heat exchanger's geometries was carried out in Costa et al. (2015b), where BA proved to be efficient in the heat transfer optimization case studies.

Another example is the one in Rodrigues et al. (2014), where the authors created a novel feature selection algorithm based on BA and **O**ptimum **P**ath **F**orest (OPF). They modelled the problem of feature selection as an binary-based optimization technique, guided by BA using the OPF accuracy over a validating set as the fitness function to be maximized. The results showed improvements in the classification effectiveness.

Meng, X.-B. et al. (2015) developed a new BA with habitat selection and Doppler effect in echoes for optimization, featuring the quantum search operator and mechanical search operator, as well as self-adaptive local search. This approach enabled significant performance in comparison with more

than twenty methods. The authors used BA to optimize a *cantilever beam design*, *welded beam design* and *coil compression spring design*.

Another algorithm inspired on the bat behaviour was proposed by Liu et al. (2012) being designated as **D**oppler **E**ffect **B**at **A**lgorithm (DEBA) as it combines BA with the Doppler effect. In their work the authors proposed a new frequency equation, as well as the velocities and locations updating where inertia weights are considered. The performance of this approach is evaluated with benchmark functions.

Another study on the performance of BA optimization technique was carried out by Fister Jr. et al. (2013), where standard benchmark functions were used to achieve comparative evaluations. These authors hybridized BA with DE to improve the local search step, and concluded on a significant improvement of the original bat technique. The HBA implemented in the present work, is based on this particular variant.

Now, in terms of structural optimization, Hasançebi et al. (2013) is a relevant example concerning this engineering approach. The authors used BA to evaluate its performance using one benchmark example, as well as three practical truss structures that are sized for minimum weight subject to stress, stability and displacement constraints according to American Institute of Steel Construction-Allowable Stress Design (AISC-ASD) specification. In addition, the authors related in a very interesting way the BA with structural design optimization, explaining every detail. Four complex truss structures were optimized, i.e. (i) 25-bar truss with 8 DVs, (ii) 354-bar braced dome with 22 DVs, (iii) 693-bar braced barrel vault with 23 DVs and (iv) 942-bar truss tower with 59 DVs. They optimized these structures to minimize weight, selecting the members from a set of discrete sections, comparing the results with other optimization approaches, i.e. simulated annealing, evolution strategies, PSO, ant colony optimization, tabu search, harmony search, simple GA and big bang-big crunch. It is important to point out that for structures (i) and (ii) the BA converged to similar optimum results, comparing to the remaining approaches. However, in structures (iii) and (iv) their BA approach obtained the best solution, i.e. minimum structure weights. Figure 2.8 shows the truss structure number (iv) in question. Finally, the authors also reported that, in addition to the improved effectiveness of BA in comparison with other meta-heuristic approaches, this algorithm also shows favourable convergence speed. Once again, as pointed out by Yang, X.-S. (2014), the BA's robustness has to do with a trade-off between two contradictory requirements: *exploration* and *exploitation*, directly related to *random flying* and *local search*, respectively.

Yang published four references that include detailed literature reviews about BA (Yang, X.-S., 2013, 2014; Yang, X.-S. et al., 2013; Yang, X.-S. and He, 2013), reporting other case studies of structural BA optimization, including *pressure vessel design, car side design, spring and beam design, truss systems, tower and tall building design, brushless DC wheel motors and others* (Yang, X.-S., 2014).

So far, BA proves to be an outstanding algorithm to research about. However, nothing is perfect and this algorithm is no exception. From this reference is possible to understand that the standard BA may lead to *stagnation* after some initial stage, i.e. no better solutions are found along several iterations. This may be caused when the user allows, by means of inputs, the algorithm to switch to exploitation stage too fast, i.e. varying both loudness and pulse rate too quickly. Because of this, a considerable amount of BA variants can be found in literature, attempting to increase performance. The HBA implemented in this work, gathering DE and micro-GAs techniques, is one of those attempts: the **M**icro-**H**ybrid-**B**at-**A**lgorithm (MHBA). Yang, X.-S. and He (2013) enumerate other variants:

- **B**inary **B**at **A**lgorithm (BBA): *Nakamura et al. (2012) developed a discrete version of BA to solve classifications and feature selection problems (Nakamura et al., 2012)*;

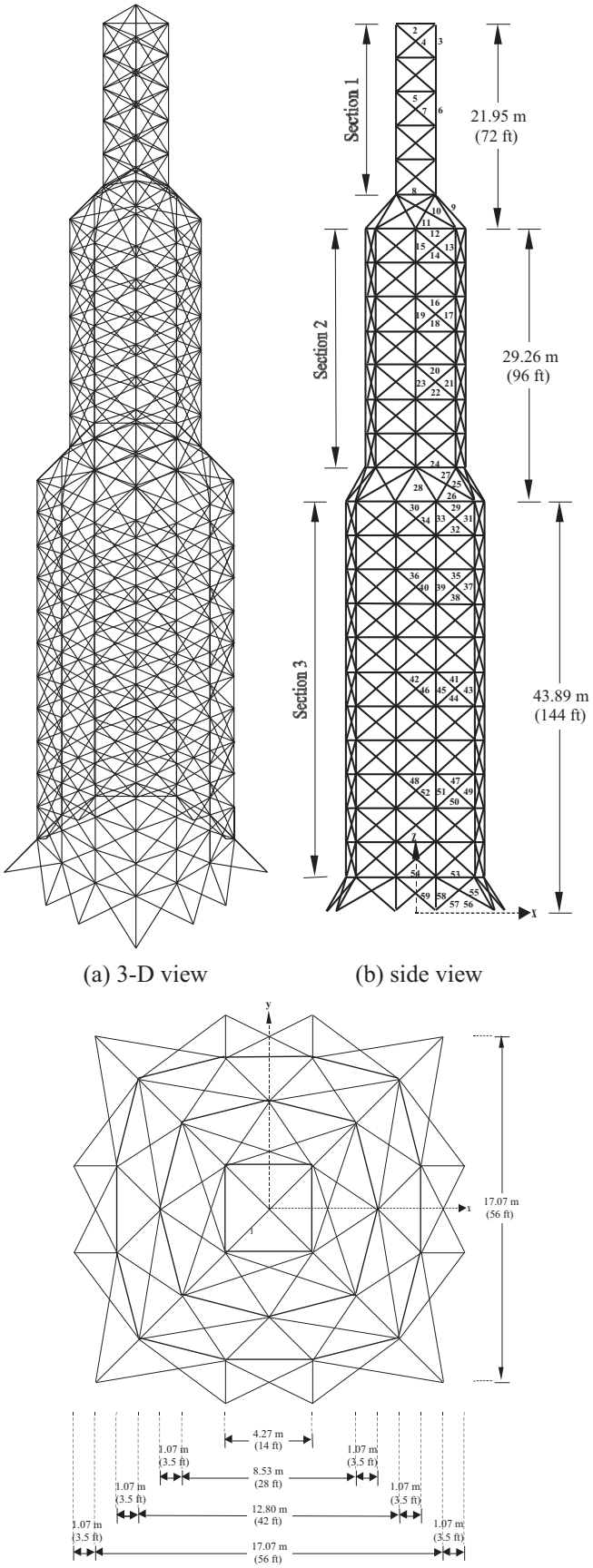

(a) 3-D view (b) side view

(c) top view

Figure 2.8: 26-Story, 942-bar space truss tower. From Hasançebi et al. (2013).

- **C**haotic **B**at **A**lgorithm (CBA): *Lin et al. (2012) presented a chaotic BA using Lévy flights and chaotic maps to carry out parameter estimation in dynamic biological systems (Lin et al., 2012). Gandomi and Yang, X.-S. (2014) proposed another CBA using various iterative maps (Gandomi and Yang, X.-S., 2014)*;
- **F**uzzy **L**ogic **B**at **A**lgorithm (FLBA): *Khan and Sahai (2012) presented a variant by introducing fuzzy logic into BA. They called their variant FLBA (Khan and Sahai, 2012)*;
- **I**mproved **B**at **A**lgorithm (IBA): *Jamil et al. (2013) extended BA with a good combination of Lévy flights and subtle variations of loudness and pulse emission rates. They tested the IBA versus more than 70 different test functions, and IBA proved to be very efficient (Jamil et al., 2013)*;
- **K** **M**eans **B**at **A**lgorithm (KMBA): *Komarasamy and Wahi (2012) presented a combination of K-means and bat algorithm (KMBA) for efficient clustering (Komarasamy and Wahi, 2012)*;
- **M**odified **B**at **A**lgorithm (MBA): *Huang et al. (2013) developed this invariant by using orthogonal Latin square sampling as the initial population and incorporating autonomous danger-averting behaviour. The researchers proved that MBA has guaranteed global convergence (Huang et al., 2013)*;
- **M**ulti **O**bjective **B**at **A**lgorithm (MOBA): *Yang, X.-S. (2011) extended BA to deal with multi-objective optimization, which has demonstrated its effectiveness for solving a few design benchmarks in engineering (Yang, X.-S., 2011)*.

The following chapter addresses the methodology carried out to develop this work.

Chapter 3

Methodology

As already stated, the present chapter has the objective of briefly explaining how the work presented in this thesis was carried out, using a physical and mathematical approach. Both plate and optimization theories are here assessed, as well as material and finite element modelling. In addition, a brief explanation about the computational implementation is also included, i.e. both FEM and bat algorithms. Since the present chapter deals with a considerable amount of mathematics and engineering/physical quantities, The International System of Units (SI) was adopted and the references Cohen et al. (2007); Cohen and Giacomo (2010); Taylor and Thompson (2008) used to support units' definition/description. **NOTE:** This chapter contains pages 45 to 100, which is 56 in total.

3.1 Plate theories

Concerning plate theories, several authors explain them in detail and this work is supported on that. Among others, e.g. of these references are Carrera et al. (2011); Ferreira (2009); Reddy (2004, 2006).

Carrera et al. (2011) enumerate several approaches to analyse plates and shells, such as *three-dimensional*, *continuum-based methods*, *axiomatic* and *asymptotic two-dimensional theories*.

Here, the objective is to model multilayered structures, with an **E**quivalent **S**ingle **L**ayer (ESL) approach, i.e. the several layers are seen as only one equivalent plate. According to Reddy (2004), *in addition to their inherent simplicity and low computational cost, the* ESL *models often provide a sufficiently accurate description of global response for thin to moderately thick laminates, e.g., gross deflections, critical buckling loads, and fundamental vibration frequencies and associated mode shapes*.

Due to computational simplification, a two-dimensional plate model is suitable to simplify the three-dimensional problem. This simplification is possible, and extensively implemented throughout the literature, because plates are by definition 2D structures, i.e. one dimension, normally the *thickness* h, is at least one order of magnitude lower than the other two, *length* a and *width* b. The latter two are the in-plane dimensions, whereas the former can be interpreted as the transversal one, regarding the structure's (beam/plate) reference mid-surface Ω. In the present work, a standard Cartesian coordinate system is always used, where the *thickness* h corresponds to the z-direction, the *length* a to x-direction and *width* b to y-direction. This coordinate system is here denoted by the *problem reference coordinate system*, defined with the previous Cartesian coordinates (x, y, z); this coordinate system can be interpreted as

the *global* one. Further ahead, another coordinate system must be defined, to support the materials' directions, called *principal material coordinate system*, where the Cartesian coordinates are numeric, i.e. $(x, y, z) \Rightarrow (x_1, y_2, z_3) \Rightarrow (1, 2, 3)$ (see Figure 3.8); this coordinate system can be interpreted as a *local* one. The SI unit associated with these quantities is [m] (metre). Such notation is illustrated in Figure 3.1.

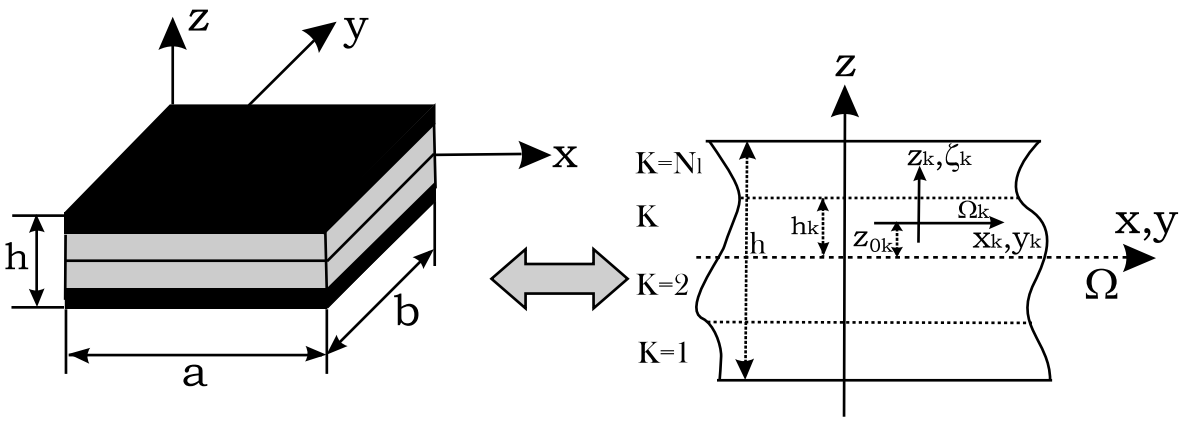

Figure 3.1: Geometrical notations of a multilayered plate. From Carrera et al. (2011).

So, this approach simplifies the problem of the 3D continuum, where each structure point Pt becomes defined in this reference plate surface Ω, depending on both x and y-coordinates $Pt_\Omega = (x, y)$. This idealized surface is always defined in the middle z-coordinate between the top and bottom surfaces of the multilayered structure, i.e. half of the whole structure's thickness exist above $(h/2)$ and below $(-h/2)$ this surface. It can correspond to an interface between two different layers, or not, depending on the layers thickness disposition. In addition, each layer k is defined by a specific thickness h_k and middle surface Ω_k. The numbering of the layers is made from the bottom up, in the z-coordinate; for instance, considering the generic stacking sequence represented in Figure 3.1, the bottom layer is the first, $k = 1$ (number one), and the top one is the last, $k = 4$ (number four).

In these 2D problems, the z-coordinate in often eliminated on the integration of the equilibrium equations, compatibility equations and physical constitutive relations (Carrera et al., 2011), according to several methodologies, leading to several possible approaches and techniques.

To carry out this work, one focuses on a theory that belongs to the group of **L**ove **S**econd **A**pproximation **T**heories (LSATs), which takes into consideration the effects of transverse shear stresses: the FSDT. This theory is addressed in the following subsection and is well known because, *of the* ESL *theories, the* FSDT *with transverse extensibility appears to provide the best compromise of solution accuracy, economy, and simplicity* (Reddy, 2004). However, due to the type of structures that will be studied in this work, the transverse extensibility will be neglected, without a significant compromise of the results' accuracy.

3.1.1 First-Order Shear Deformation Theory (FSDT)

This theory, as described in the literature, is based upon the removal of the third part of the Kirchoff hypotheses, i.e. *transverse normals do not remain perpendicular to the mid-surface after deformation*. In consequence, transverse shear strains are included in the theory, but the *inextensibility of transverse normals* remains, meaning that displacement w is constant along the thickness. According to Carrera et al. (2011), FSDT is *an extension of the so-called Reissner-Mindlin model to multilayered structures*.

One important aspect to keep in mind, associated with this theory, is the fact that it is not suitable to cover *the whole spectrum of composite laminate problems*, since *the accuracy of the global response predicted by the* ESL *models deteriorates as the laminate becomes thicker* and *are often incapable of accurately describing the state of stress and strain at the ply level near geometric and material discontinuities or near regions of intense loading* (Reddy, 2004).

In any case, the studies developed in this work are not incompatible with these theory's "handicaps", making this an efficient and suitable choice to implement, to model plate-type multilayered structures.

The following subsections specify the displacement and strain fields, as well as the considered constitutive equations, for both passive and active structures.

3.1.1.1 Displacement and strain fields

Figure 3.2 shows the FSDT hypotheses, in which the displacement field has five unknowns, i.e. the mid-surface displacements in the x-, y- and z-direction and the rotations of a transverse normal around x- and y-axis. The following set of equations specifies the displacement field of this theory, considering the time t dependency, in the dynamic case (Carrera et al., 2011; Reddy, 2004):

$$\begin{aligned} u(x,y,z,t) &= u^0(x,y,0,t) + z\theta_x(x,y,z,t) \\ v(x,y,z,t) &= v^0(x,y,0,t) + z\theta_y(x,y,z,t) \\ w(x,y,z,t) &= w^0(x,y,0,t) \end{aligned} \tag{3.1.1}$$

here, both u^0 and v^0 represent the mid-surface membrane displacements (along x- and y-direction, respectively) and w^0 the mid-surface transverse displacement (along z-direction) – meaning that superscript 0 is used to identify quantities associated with the structure's mid-surface, i.e. on the reference plane $z_\Omega = 0$. The previous displacements, without superscript 0, correspond to the resultant ones at any structure's point, considering the coordinates (x, y, z). θ_x and θ_y are the rotations of a transverse normal around the y- and x-axis of the considered coordinate system, respectively; these can also be described as functions of the resultant membrane displacements, u and v:

$$\begin{aligned} \theta_x &= \frac{\partial u}{\partial z} \\ \theta_y &= \frac{\partial v}{\partial z} \end{aligned} \tag{3.1.2}$$

note that these rotations do not follow the right-hand-rule, since θ_x describes the rotation around the y-axis and θ_y around the x-axis. In any case, as explained in Reddy (2004); Wang (2004), this notation is preferred because it may greatly simplify the algebra involved. The SI units associated with time, displacement and rotation are, respectively, [s] (second), [m] (metre) and [rad] (radian).

The in-plane displacement components assume a linear and ESL behaviour through the thickness direction of the multilayered structure, whereas the out-of-plane displacement component is constant, as shown in Figure 3.3.

In this case, due to thickness inextensibility, the z-direction normal strain is neglected $\epsilon_{zz} = 0$. However, transverse shear stresses τ_{yz} and τ_{xz} are different from zero and constant along each layer's thickness (see Figure 3.4). The nomenclature and respective SI units associated with both strains and stresses are explained in the following subsection.

Omitting dependencies, for simplicity, the strain field is obtained by applying the elasticity kinematical relations for small deformations, resulting in the following:

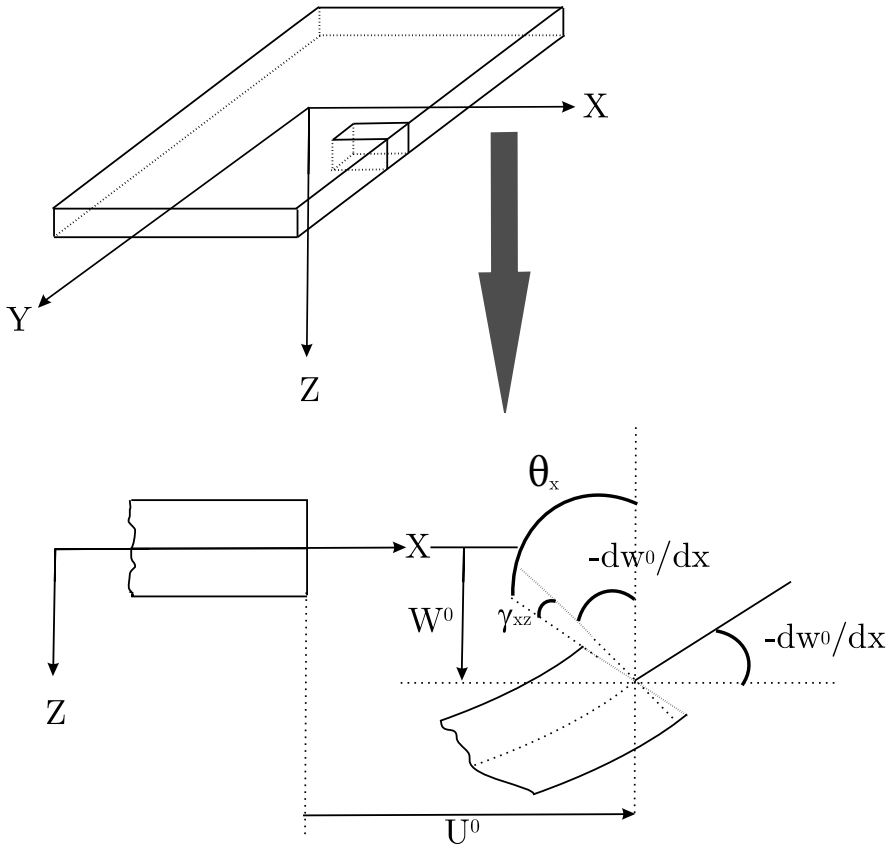

Figure 3.2: Undeformed and deformed geometries of a plate according to the Reissner-Mindlin hypotheses. Adapted from Carrera et al. (2011).

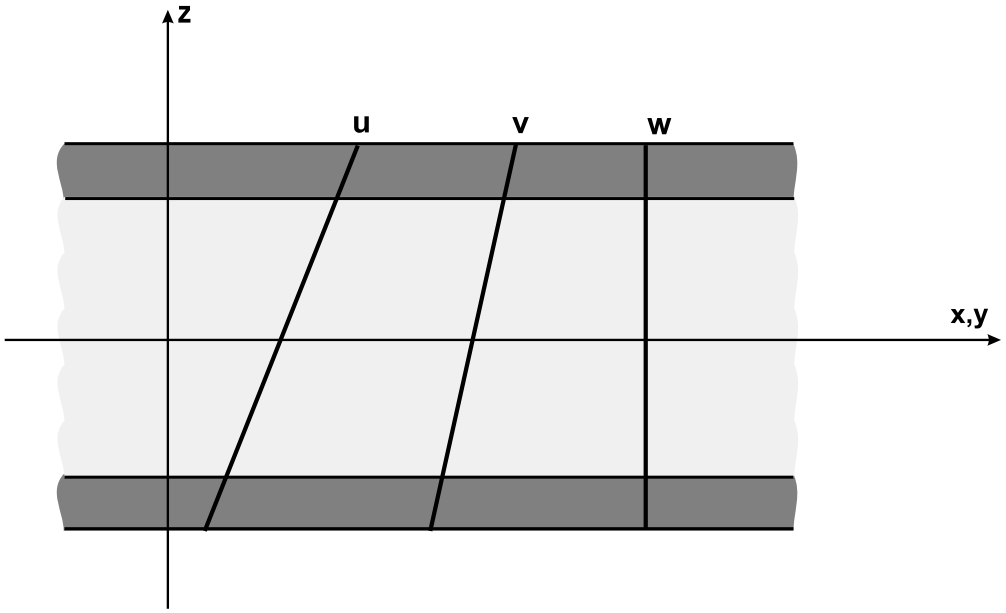

Figure 3.3: Displacement components through the thickness direction. Adapted from Carrera et al. (2011).

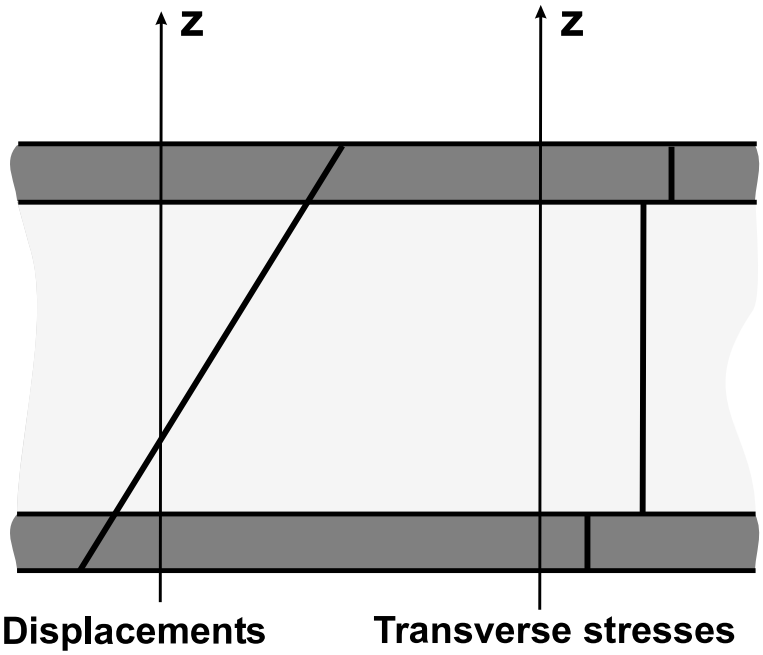

Figure 3.4: In-plane displacement components and transverse shear stresses through the thickness direction. Adapted from Carrera et al. (2011).

$$\begin{Bmatrix} \epsilon_{xx} \\ \epsilon_{yy} \\ \gamma_{xy} \end{Bmatrix} = \begin{Bmatrix} \frac{\partial u}{\partial x} \\ \frac{\partial v}{\partial y} \\ \frac{\partial u}{\partial y} + \frac{\partial v}{\partial x} \end{Bmatrix} = \begin{Bmatrix} \epsilon_{xx}^{(0)} \\ \epsilon_{yy}^{(0)} \\ \gamma_{xy}^{(0)} \end{Bmatrix} + z \begin{Bmatrix} \epsilon_{xx}^{(1)} \\ \epsilon_{yy}^{(1)} \\ \gamma_{xy}^{(1)} \end{Bmatrix} = \begin{Bmatrix} \frac{\partial u^0}{\partial x} \\ \frac{\partial v^0}{\partial y} \\ \frac{\partial u^0}{\partial y} + \frac{\partial v^0}{\partial x} \end{Bmatrix} + z \begin{Bmatrix} \frac{\partial \theta_x}{\partial x} \\ \frac{\partial \theta_y}{\partial y} \\ \frac{\partial \theta_x}{\partial y} + \frac{\partial \theta_y}{\partial x} \end{Bmatrix}$$
$$\begin{Bmatrix} \gamma_{yz} \\ \gamma_{xz} \end{Bmatrix} = \begin{Bmatrix} \frac{\partial w}{\partial y} + \frac{\partial v}{\partial z} \\ \frac{\partial w}{\partial x} + \frac{\partial u}{\partial z} \end{Bmatrix} = \begin{Bmatrix} \gamma_{yz}^{(0)} \\ \gamma_{xz}^{(0)} \end{Bmatrix} + z \begin{Bmatrix} \gamma_{yz}^{(1)} \\ \gamma_{xz}^{(1)} \end{Bmatrix} = \begin{Bmatrix} \frac{\partial w^0}{\partial y} + \theta_y \\ \frac{\partial w^0}{\partial x} + \theta_x \end{Bmatrix} + z \begin{Bmatrix} 0 \\ 0 \end{Bmatrix} \tag{3.1.3}$$

where the first three strains are the in-plane normal and shear ones; the last two are the interlaminar transverse shear strains. Strains are divided into two subtypes, which are here identified by superscripts (0) and (1), denoting *membrane* and *flexural (bending)* strains, respectively. The latter are also commonly known as *curvatures*.

Due to the fact that the transverse normal strain ϵ_{zz} is zero, a phenomena called (*Poisson* or *shear*) *locking* occurs, which can induce erroneous results for the generalized displacements solution. This effect, explained in Reddy (2004, 2006), is most likely to be verified when the structure is too thin $(a/h \geq 100)$, because in this case the transverse shear strains γ_{yz} and γ_{xz} are required to vanish, and the FSDT-based finite elements become excessively stiff – this results in displacements too small compared to the true solution. From Reddy (2004), an e.g. of shear locking definition is the following:

Definition 3.1.1. **Shear Locking** *"Shear locking is due to the inability of shear deformable elements to accurately model the bending within an element under a state of zero transverse shearing strain. The spurious shear stiffness phenomenon is caused by an interpolation inconsistency that prevents the finite element from modelling a state of zero transverse shear stress in the presence of general non-zero bending strains. As the plate's span-to-thickness ratio approaches the thin plate limit, the*

transverse shear deformation must tend toward zero relative to the bending deformation (i.e., the Kirchhoff condition). The degree to which a particular finite element fails in approximating this condition determines the amount of spurious shear stiffness the element will exhibit while deforming in a bending mode. Thus elements that are poor approximators of this condition are known to exhibit shear locking while elements which are better approximators of this condition may simply exhibit a slight overstiffness."

In terms of finite element implementation, there are specific techniques to minimize or overcome this problem, as explained further ahead in this work.

The FSDT can be extended to smart structures, where a new component is added to the displacement field described in Eq. (3.1.1): the electric potential ϕ^k. This variable depends on the active layer k, since each one can be excited with or return different electric potentials; for instance, considering a piezoelectric material. The SI unit associated with electric potential is $[\mathrm{V}]$ (Volt) and, throughout this work, an electric potential difference $\Delta\phi$ is denoted by *voltage*, having the same SI unit.

Similarly to the shear locking phenomena, classical theories, such as FSDT, when extended to smart structures, also exhibit electrical locking (Carrera et al., 2011). This type of limitation occurs due to the approximation/assumption of constant/linear electric potentials through the thickness, which also results in constant electric fields. In addition, it is important to note that such theories do not include higher-order terms to model the electromechanical coupling. To avoid this issue, several approaches are being used throughout the literature; among other examples, Wang (2004) further discretizes each piezoelectric layer into finite sub-layers along the thickness direction; such methodology shows an evident non-linear behaviour of the electric potentials in this direction.

In the present methodology, differently from shear locking, the electrical one is not avoided, i.e. the electric potentials associated with each active layer are assumed to be constant, always with polarization only in the thickness z-direction; this approach is similar to the one described in Loja et al. (2001), proved to be sufficient to model the present case studies.

3.1.1.2 Constitutive equations

Since the objective is to relate both mechanical and electrical fields, in order to model smart structures, constitutive equations must be defined to account that physical coupling. These equations describe the material reaction to applied loads (Carrera et al., 2011).

Accounting for both mechanical and electrical effects of active materials (inclusions, layers, mixtures, particles, patches, etc.) in a generic multilayered structure, the following constitutive relations apply:

$$\begin{aligned} \{\sigma\}^k &= \left[\overline{Q}(x,y,z)\right]^k \{\epsilon\} - \left([\overline{e}(x,y,z)]^k\right)^{\mathrm{T}} \{\mathcal{E}\}^k \quad \text{(converse effect)} \\ \{\mathcal{D}\}^k &= [\overline{e}(x,y,z)]^k \{\epsilon\} + [\overline{\varepsilon}(x,y,z)]^k \{\mathcal{E}\}^k \quad \text{(direct effect)} \end{aligned} \tag{3.1.4}$$

where T is the transpose operator (linear algebra), vectors $\{\sigma\}^k$, $\{\epsilon\}$, $\{\mathcal{E}\}^k$ and $\{\mathcal{D}\}^k$ contain components associated with different directions of, respectively, stresses, strains, electric field and electric displacement. Considering the same order, the respective SI units are $[\mathrm{Pa}]$ (Pascal), $\left[\mathrm{m}\cdot\mathrm{m}^{-1}\right]$ (dimensionless), $\left[\mathrm{V}\cdot\mathrm{m}^{-1}\right]$ (Volt per metre) and $\left[\mathrm{C}\cdot\mathrm{m}^{-2}\right]$ (Coulomb per square metre). $\left[\overline{Q}(x,y,z)\right]^k$, $[\overline{e}(x,y,z)]^k$ and $[\overline{\varepsilon}(x,y,z)]^k$ are, respectively, the transformed plane stress-reduced elastic, stress-charge piezoelectric and permittivity coefficients matrices. Once again, with the same order, the SI units associated with these material quantities are $[\mathrm{Pa}]$ (Pascal), $\left[\mathrm{C}\cdot\mathrm{m}^{-2}\right]$ (Coulomb per square metre)

and $\left[\mathrm{F}\cdot\mathrm{m}^{-1}\right]$ (Farad per metre). Note that vectors are always defined using *curly brackets* $\{...\}$ and matrices using *square brackets* $[...]$; in certain cases, due to space optimization, vectors and matrices can also be identified using **bold** math format.

Also note that all these material coefficients have an overline $\overline{...}$, which means that they are *transformed* coefficients, to account eventual fibre orientations in the xy-plane, different from zero, characteristic from certain types of monoclinic/orthotropic materials. At the same time, these coefficients are *reduced*, because FSDT considers a plane state of stress (imposing $\sigma_{zz}=0$), meaning that the original material matrices must be modified to account this effect (Reddy, 2004). This is why the majority of quantities' components in the z-direction (components zz), disappeared from the following constitutive relations; such simplification, associated with FSDT, reduces the vectors' and tensors' maximum dimension from 6 to 5. The only two pure quantities in the z-direction that remain are associated with the electric field and electric displacement, respectively $\mathcal{E}_z$ and $\mathcal{D}_z$; these components shall be used because the considered piezoelectric materials are polarized in their thickness direction, as already explained.

In addition, all material coefficients can depend on x-, y- and z-direction, because the present algorithm is able to model FGMs concerning spatial variation in length, width and thickness directions (individually or at the same time, considering different material layers).

Individually and generically, vectors $\{\sigma\}^k$, $\{\epsilon\}$, $\{\mathcal{E}\}^k$, $\{\mathcal{D}\}^k$ and matrices $\left[\overline{Q}\right]^k$, $[\overline{e}]^k$, $[\overline{\varepsilon}]^k$ can be described, with the same order, by the following equations:

$$\{\sigma\}^k=\begin{Bmatrix}\sigma_{xx}\\ \sigma_{yy}\\ \tau_{xy}\\ \tau_{yz}\\ \tau_{xz}\end{Bmatrix}^k,\quad \{\sigma\}^k_b=\begin{Bmatrix}\sigma_{xx}\\ \sigma_{yy}\\ \tau_{xy}\end{Bmatrix}^k,\quad \{\sigma\}^k_s=\begin{Bmatrix}\tau_{yz}\\ \tau_{xz}\end{Bmatrix}^k \tag{3.1.5}$$

$$\{\epsilon\}=\begin{Bmatrix}\epsilon_{xx}\\ \epsilon_{yy}\\ \gamma_{xy}\\ \gamma_{yz}\\ \gamma_{xz}\end{Bmatrix},\quad \{\epsilon\}_b=\begin{Bmatrix}\epsilon_{xx}\\ \epsilon_{yy}\\ \gamma_{xy}\end{Bmatrix},\quad \{\epsilon\}_s=\begin{Bmatrix}\gamma_{yz}\\ \gamma_{xz}\end{Bmatrix} \tag{3.1.6}$$

$$\begin{gathered}\{\epsilon\}=\left\{\epsilon^{(0)}\right\}+z\left\{\epsilon^{(1)}\right\},\quad \left\{\epsilon^{(0)}\right\}=\begin{Bmatrix}\epsilon^{(0)}_{xx}\\ \epsilon^{(0)}_{yy}\\ \gamma^{(0)}_{xy}\\ \gamma^{(0)}_{yz}\\ \gamma^{(0)}_{xz}\end{Bmatrix},\quad \left\{\epsilon^{(1)}\right\}=\begin{Bmatrix}\epsilon^{(1)}_{xx}\\ \epsilon^{(1)}_{yy}\\ \gamma^{(1)}_{xy}\\ 0\\ 0\end{Bmatrix}\\ \left\{\epsilon^{(0)}_b\right\}=\begin{Bmatrix}\epsilon^{(0)}_{xx}\\ \epsilon^{(0)}_{yy}\\ \gamma^{(0)}_{xy}\end{Bmatrix},\quad \left\{\epsilon^{(0)}_s\right\}=\begin{Bmatrix}\gamma^{(0)}_{yz}\\ \gamma^{(0)}_{xz}\end{Bmatrix},\quad \left\{\epsilon^{(1)}_b\right\}=\begin{Bmatrix}\epsilon^{(1)}_{xx}\\ \epsilon^{(1)}_{yy}\\ \gamma^{(1)}_{xy}\end{Bmatrix}\end{gathered} \tag{3.1.7}$$

where the stress and strain vectors, respectively $\{\sigma\}^k$ and $\{\epsilon\}$, are subdivided into bending b and shear s components. Note that greek letters σ and ϵ are used for normal components, whereas τ and γ for shear ones, where the former ones are stresses and the latter ones are strains. $\left\{\epsilon^{(0)}\right\}$ and $\left\{\epsilon^{(1)}\right\}$ are the

vectors of membrane and flexural (bending) strains, respectively. Once again, the latter are also known as curvatures.

$$\{\mathcal{E}\}^k = -\nabla\phi^k(x,y,z,t) = -\begin{Bmatrix} \frac{\partial}{\partial x} \\ \frac{\partial}{\partial y} \\ \frac{\partial}{\partial z} \end{Bmatrix} \phi^k(x,y,z,t) = \begin{Bmatrix} \mathcal{E}_x \\ \mathcal{E}_y \\ \mathcal{E}_z \end{Bmatrix}^k \tag{3.1.8}$$

$$\{\mathcal{D}\}^k = \begin{Bmatrix} \mathcal{D}_x \\ \mathcal{D}_y \\ \mathcal{D}_z \end{Bmatrix}^k \tag{3.1.9}$$

where both electric field $\{\mathcal{E}\}^k$ and electric displacement $\{\mathcal{D}\}^k$ vectors have three different components, x, y and z, corresponding to the 3D Cartesian coordinates of the problem reference coordinate system. The electric field can be related to the electric potential by using the gradient vector ∇, considering the present linear piezoelectric constitutive behaviour. This way, retrieving the methodology from Loja et al. (2001) and considering polarization only in the thickness direction, i.e. $\mathcal{E}_x = \mathcal{E}_y = 0$, the electric field component associated with the z-direction can be defined according to the following equation:

$$\mathcal{E}_z{}^k = -\frac{\phi^k}{h_k} \tag{3.1.10}$$

this way, each electric field associated with each different layer k is a function of its thickness h_k; note that this relation considers, as reference, the null electric potential. Similarly to the strains and stresses, also the material matrices can be divided into bending and shear components:

$$\left[\overline{Q}(x,y,z)\right]^k = \begin{bmatrix} \overline{Q}_{11}(x,y,z) & \overline{Q}_{12}(x,y,z) & \overline{Q}_{16}(x,y,z) & 0 & 0 \\ \overline{Q}_{12}(x,y,z) & \overline{Q}_{22}(x,y,z) & \overline{Q}_{26}(x,y,z) & 0 & 0 \\ \overline{Q}_{16}(x,y,z) & \overline{Q}_{26}(x,y,z) & \overline{Q}_{66}(x,y,z) & 0 & 0 \\ 0 & 0 & 0 & \overline{Q}_{44}(x,y,z) & \overline{Q}_{45}(x,y,z) \\ 0 & 0 & 0 & \overline{Q}_{45}(x,y,z) & \overline{Q}_{55}(x,y,z) \end{bmatrix}^k \tag{3.1.11}$$

$$\left[\overline{Q}(x,y,z)\right]_b^k = \begin{bmatrix} \overline{Q}_{11}(x,y,z) & \overline{Q}_{12}(x,y,z) & \overline{Q}_{16}(x,y,z) \\ \overline{Q}_{12}(x,y,z) & \overline{Q}_{22}(x,y,z) & \overline{Q}_{26}(x,y,z) \\ \overline{Q}_{16}(x,y,z) & \overline{Q}_{26}(x,y,z) & \overline{Q}_{66}(x,y,z) \end{bmatrix}^k \tag{3.1.12}$$

$$\left[\overline{Q}(x,y,z)\right]_s^k = \begin{bmatrix} \overline{Q}_{44}(x,y,z) & \overline{Q}_{45}(x,y,z) \\ \overline{Q}_{45}(x,y,z) & \overline{Q}_{55}(x,y,z) \end{bmatrix}^k \tag{3.1.13}$$

where $\left[\overline{Q}(x,y,z)\right]^k$ is the transformed plane stress-reduced elastic matrix, containing each coefficient for a generic monoclinic/orthotropic material. The definition and distinction between monoclinic, orthotropic, isotropic... and all the other materials supported by the present algorithm are addressed with more detail in Section 3.2. In any case, a monoclinic material is basically a rotated orthotropic one

$$[\overline{e}(x,y,z)]^k = \begin{bmatrix} 0 & 0 & 0 & \overline{e}_{14}(x,y,z) & \overline{e}_{15}(x,y,z) \\ 0 & 0 & 0 & \overline{e}_{24}(x,y,z) & \overline{e}_{25}(x,y,z) \\ \overline{e}_{31}(x,y,z) & \overline{e}_{32}(x,y,z) & \overline{e}_{36}(x,y,z) & 0 & 0 \end{bmatrix}^k \tag{3.1.14}$$

$$[\overline{e}(x,y,z)]_b^k = \begin{bmatrix} 0 & 0 & 0 \\ 0 & 0 & 0 \\ \overline{e}_{31}(x,y,z) & \overline{e}_{32}(x,y,z) & \overline{e}_{36}(x,y,z) \end{bmatrix}^k \tag{3.1.15}$$

$$[\overline{e}(x,y,z)]_s^k = \begin{bmatrix} \overline{e}_{14}(x,y,z) & \overline{e}_{15}(x,y,z) \\ \overline{e}_{24}(x,y,z) & \overline{e}_{25}(x,y,z) \\ 0 & 0 \end{bmatrix}^k \tag{3.1.16}$$

where $[\overline{e}(x,y,z)]^k$ is the transformed plane stress-reduced stress-charge piezoelectric matrix

$$[\overline{\varepsilon}(x,y,z)]^k = \begin{bmatrix} \overline{\varepsilon}_{11}(x,y,z) & \overline{\varepsilon}_{12}(x,y,z) & 0 \\ \overline{\varepsilon}_{12}(x,y,z) & \overline{\varepsilon}_{22}(x,y,z) & 0 \\ 0 & 0 & \overline{\varepsilon}_{33}(x,y,z) \end{bmatrix}^k \tag{3.1.17}$$

where $[\overline{\varepsilon}(x,y,z)]^k$ is the transformed plane stress-reduced permittivity matrix. Based on Eq. (3.1.4) yields the following transformed stress-strain relations (considering a plane state of stress), for the bending contributions:

$$\begin{aligned} &\{\sigma\}_b^k = \left[\overline{Q}(x,y,z)\right]_b^k \{\epsilon\}_b + \left([\overline{e}(x,y,z)]_b^k\right)^{\mathrm{T}} \{\mathcal{E}\}^k \Leftrightarrow \\ &\Leftrightarrow \begin{Bmatrix} \sigma_{xx} \\ \sigma_{yy} \\ \tau_{xy} \end{Bmatrix}^k = \begin{bmatrix} \overline{Q}_{11}(x,y,z) & \overline{Q}_{12}(x,y,z) & \overline{Q}_{16}(x,y,z) \\ \overline{Q}_{12}(x,y,z) & \overline{Q}_{22}(x,y,z) & \overline{Q}_{26}(x,y,z) \\ \overline{Q}_{16}(x,y,z) & \overline{Q}_{26}(x,y,z) & \overline{Q}_{66}(x,y,z) \end{bmatrix}^k \begin{Bmatrix} \epsilon_{xx} \\ \epsilon_{yy} \\ \gamma_{xy} \end{Bmatrix} + \begin{bmatrix} 0 & 0 & \overline{e}_{31}(x,y,z) \\ 0 & 0 & \overline{e}_{32}(x,y,z) \\ 0 & 0 & \overline{e}_{36}(x,y,z) \end{bmatrix}^k \begin{Bmatrix} \mathcal{E}_x \\ \mathcal{E}_y \\ \mathcal{E}_z \end{Bmatrix}^k \end{aligned} \tag{3.1.18}$$

and shear contributions

$$\begin{aligned} &\{\sigma\}_s^k = \chi_k \left[\overline{Q}(x,y,z)\right]_s^k \{\epsilon\}_s + \left([\overline{e}(x,y,z)]_s^k\right)^{\mathrm{T}} \{\mathcal{E}\}^k \Leftrightarrow \\ &\Leftrightarrow \begin{Bmatrix} \tau_{yz} \\ \tau_{xz} \end{Bmatrix}^k = \chi_k \begin{bmatrix} \overline{Q}_{44}(x,y,z) & \overline{Q}_{45}(x,y,z) \\ \overline{Q}_{45}(x,y,z) & \overline{Q}_{55}(x,y,z) \end{bmatrix}^k \begin{Bmatrix} \gamma_{yz} \\ \gamma_{xz} \end{Bmatrix} + \begin{bmatrix} \overline{e}_{14}(x,y,z) & \overline{e}_{24}(x,y,z) & 0 \\ \overline{e}_{15}(x,y,z) & \overline{e}_{25}(x,y,z) & 0 \end{bmatrix}^k \begin{Bmatrix} \mathcal{E}_x \\ \mathcal{E}_y \\ \mathcal{E}_z \end{Bmatrix}^k \end{aligned} \tag{3.1.19}$$

$$\begin{aligned} &\{\mathcal{D}\}^k = [\overline{e}(x,y,z)]^k \{\epsilon\} + [\overline{\varepsilon}(x,y,z)]^k \{\mathcal{E}\}^k \Leftrightarrow \\ &\Leftrightarrow \{\mathcal{D}\}^k = \left[[\overline{e}(x,y,z)]_b \quad [\overline{e}(x,y,z)]_s\right]^k \begin{Bmatrix} \{\epsilon\}_b \\ \{\epsilon\}_s \end{Bmatrix} + [\overline{\varepsilon}(x,y,z)]^k \{\mathcal{E}\}^k \Leftrightarrow \\ &\Leftrightarrow \begin{Bmatrix} \mathcal{D}_x \\ \mathcal{D}_y \\ \mathcal{D}_z \end{Bmatrix}^k = \begin{bmatrix} 0 & 0 & 0 & \overline{e}_{14}(x,y,z) & \overline{e}_{15}(x,y,z) \\ 0 & 0 & 0 & \overline{e}_{24}(x,y,z) & \overline{e}_{25}(x,y,z) \\ \overline{e}_{31}(x,y,z) & \overline{e}_{32}(x,y,z) & \overline{e}_{36}(x,y,z) & 0 & 0 \end{bmatrix}^k \begin{Bmatrix} \epsilon_{xx} \\ \epsilon_{yy} \\ \gamma_{xy} \\ \gamma_{yz} \\ \gamma_{xz} \end{Bmatrix} + \\ &+ \begin{bmatrix} \overline{\varepsilon}_{11}(x,y,z) & \overline{\varepsilon}_{12}(x,y,z) & 0 \\ \overline{\varepsilon}_{12}(x,y,z) & \overline{\varepsilon}_{22}(x,y,z) & 0 \\ 0 & 0 & \overline{\varepsilon}_{33}(x,y,z) \end{bmatrix}^k \begin{Bmatrix} \mathcal{E}_x \\ \mathcal{E}_y \\ \mathcal{E}_z \end{Bmatrix}^k \end{aligned} \tag{3.1.20}$$

here, the interlaminar transverse shear components are affected by the shear correction factor χ. This constant is normally denoted by k, but since this letter is already being used to specify the layers, χ is adopted. Such factor is used because, with the FSDT, the transverse shear strains are represented as constant through the laminate thickness, which also results in constant transverse shear

stresses. However, in composite laminated plates, these stresses vary at least quadratically through layer thickness (Reddy, 2004). This is an important discrepancy to take into consideration, which is often minimized by using this factor; normally it is set to $5/6 \approx 0.8333$. Other possibilities exist, such as the coefficients' calculation using other theories (Ferreira, 2009; Nguyen, T.-K. et al., 2007), which can depend on the laminate layers' thickness, materials, etc.; these are not used throughout this work.

3.1.1.3 Governing equations of motion

The governing equations of motion to describe the behaviour of a smart structure are obtained by means of a variational approach. This kind of methodology is well known and extensively used, so for that reason it will be described very briefly in this subsection. Detailed mathematical descriptions about this subject can be found in Carrera et al. (2011); Reddy (2004, 2006), among others.

Essentially, the motion equations for the electro-elastic medium are deducted using the **P**rinciple of **V**irtual **D**isplacements (PVD), which can be derived from the Hamilton's variational principle (Carrera et al., 2011). Variational principles are very useful, since they are applicable to both linear and non-linear theories, in order to derive governing equations and BCs for complicated systems. This way, approximate solutions are obtained by variational methods, such as the PVD or by seeking the minimum of the total potential energy of the system (Reddy, 2004). In this work, one focuses on the PVD, as shown below.

According to Reddy (2004), the PVD can be stated as the following (considering only the mechanical effect): *if a continuous body is in equilibrium, the virtual work of all actual forces in moving through a virtual displacement is zero:*

$$\delta U + \delta V \equiv \delta W = 0 \tag{3.1.21}$$

where δ is the variational operator, δU the *internal virtual work* and δV the *external virtual work*, which is equivalent to the *virtual work done by the applied (actual) forces* δW; all these three quantities are work (energies), having the SI unit of $[\mathrm{J}]$ (Joule). Note that the work done by the actual forces moving through virtual displacements is called *virtual work*. In the same reference, it is explained that the virtual work done by actual forces $\mathbf{F}$ per unit volume, with SI units of $\left[\mathrm{N \cdot m^{-3}}\right]$ (Newton per cubic metre), in a solid body or volume V, in moving through the virtual displacements $\delta\mathbf{u}$, in $[\mathrm{m}]$ (metre), is given by:

$$\delta W = \int_V \mathbf{F} \cdot \delta\mathbf{u} \, \mathrm{d}V \tag{3.1.22}$$

where $\mathrm{d}V$ denotes the volume element $\mathrm{d}V = \mathrm{d}x_1\mathrm{d}y_2\mathrm{d}z_3$ in the material of the body, associated with the volume integral $\int_V$; all volumetric quantities are in $\left[\mathrm{m^3}\right]$ (cubic metre); $\mathrm{d}x_1$, $\mathrm{d}y_2$ and $\mathrm{d}z_3$ are the element dimensions in the x_1, y_2 and z_3 directions, respectively, in the principal material coordinate system. Then, the external virtual work done due to virtual displacements $\delta\mathbf{u}$ in a solid body V subjected to body forces $\mathbf{F_b}$ per unit volume, in $\left[\mathrm{N \cdot m^{-3}}\right]$ (Newton per cubic metre), and surface tractions $\mathbf{F_s}$ per unit area, in $\left[\mathrm{N \cdot m^{-2}}\right]$ (Newton per square metre), of the boundary Γ_σ is given by:

$$\delta V = -\left(\int_V \mathbf{F_b} \cdot \delta\mathbf{u} \, \mathrm{d}V + \int_{\Gamma_\sigma} \mathbf{F_s} \cdot \delta\mathbf{u} \, \mathrm{d}S \right) \tag{3.1.23}$$

where $\mathrm{d}S$ denotes an area or surface element and Γ_σ the portion of the boundary on which stresses are specified, i.e. the external mechanical loading surface; $\int_\Gamma$ is a boundary integral; the SI unit of area quantity is $\left[\mathrm{m^2}\right]$ (square metre). Note that subscripts b and s denote *body* and *surface*, respectively,

to properly identify the different load types (in the constitutive equations these were used to identify *bending* and *shear* components). In addition, also note that surface loads are merely pressures, which can also be denoted by P in this work, with SI units of $[\mathrm{Pa}] = \left[\mathrm{N \cdot m^{-2}}\right]$ (Pascal). The total internal virtual work done by virtual strains $\delta\epsilon_{ij}$ in moving through the actual stresses σ_{ij} is given by:

$$\delta U = \int_V \sigma_{ij}\delta\epsilon_{ij}\,\mathrm{d}V \tag{3.1.24}$$

to sum up, in terms of Cartesian rectangular components, the PVD can be expressed as:

$$\int_V \sigma_{ij}\delta\epsilon_{ij}\,\mathrm{d}V - \int_V F_{b,i}\delta u_i\,\mathrm{d}V - \int_{\Gamma_\sigma} F_{s,i}\delta u_i\,\mathrm{d}S = 0 \tag{3.1.25}$$

In order to obtain the equations of motion for the electromechanical dynamic case, one considers the Hamilton's principle, which is a generalization of the PVD to dynamics of systems. The principle considers that the system is characterized by two energy functions, i.e. kinetic energy E_c and potential energy E_p. The following time-dependent virtual work expressions apply, considering an infinitesimal time instant $\mathrm{d}t$ (Carrera et al., 2011):

$$\delta \int_{t_i}^{t_f} (E_c - E_p)\,\mathrm{d}t = 0 \Leftrightarrow \delta \int_{t_i}^{t_f} (U + V - E_c)\,\mathrm{d}t = 0 \tag{3.1.26}$$

where t_i and t_f are the initial and final time instants, δU and δV remain the *internal virtual work* and the *(external) virtual work done by the applied forces*, respectively. A new term is included to consider the dynamic behaviour, i.e. *virtual kinetic energy* δE_c. Note that the internal virtual work δU can also be represented by the summation of *virtual strain energy* δU_m and *virtual electrical internal work* δU_e:

$$\delta U = \delta U_m + \delta U_e \tag{3.1.27}$$

where all energy and work quantities, once again, are associated with SI units of $[\mathrm{J}]$ (Joule). The previously mentioned virtual quantities are described by the following equations (Wang, 2004):

$$U = \frac{1}{2}\int_V \left(\boldsymbol{\sigma}^{\mathrm{T}}\boldsymbol{\epsilon} - \boldsymbol{\mathcal{E}}^{\mathrm{T}}\boldsymbol{\mathcal{D}}\right)\mathrm{d}V \tag{3.1.28}$$

$$\begin{aligned} V &= W_b + W_s + W_c - W_\phi \\ W_b &= \int_V \mathbf{u}^{\mathrm{T}}\mathbf{F_b}\,\mathrm{d}V \\ W_s &= \int_{\Gamma_\sigma} \mathbf{u}^{\mathrm{T}}\mathbf{F_s}\,\mathrm{d}\Gamma_\sigma \\ W_c &= \sum_i \left(\mathbf{u}_i^{\mathrm{T}}\mathbf{F_{c},}_i\right) \\ W_\phi &= \int_{\Gamma_\phi} \phi q_0\,\mathrm{d}\Gamma_\phi \end{aligned} \tag{3.1.29}$$

$$E_c = \frac{1}{2}\int_V \dot{\mathbf{u}}^{\mathrm{T}}\rho\dot{\mathbf{u}}\,\mathrm{d}V \tag{3.1.30}$$

where $\mathbf{u}$ is the displacement field vector in $[\mathrm{m}]$ (metre), $\dot{\mathbf{u}}$ is the velocity field vector in $\left[\mathrm{m \cdot s^{-1}}\right]$ (metre per second) and ρ is the material (mass) density in $\left[\mathrm{kg \cdot m^{-3}}\right]$ (kilogram per cubic metre). In terms of loads, two more are here considered, described by the concentrated force vector $\mathbf{F_c}$ in $[\mathrm{N}]$ (Newton)

and the multiplication between both electric potential ϕ in [V] (Volt) and surface charge density q_0 in $\left[\mathrm{C}\cdot\mathrm{m}^{-2}\right]$ (Coulomb per square metre). This way, the external virtual work δV is the summation of the virtual work generated by each load type (both mechanical and electrical contributions), i.e. the virtual works done by the mechanical *body* δW_b, *surface* δW_s and *concentrated* δW_c forces, as well as by the applied *surface electrical charge* δW_ϕ. Note that the electrical loads are integrated over the portion of the boundary on which they are applied, i.e. the external electrical loading surface Γ_ϕ.

Considering the constitutive equations already described in Eq. (3.1.4), the previous equations concerning the Hamilton's principle and other mathematical manipulations found in the referred literature, the following variational expression is obtained (Loja et al., 2001):

$$\iiint_V \left\{\left(\delta\boldsymbol{\epsilon}^{\mathrm{T}}\overline{\mathbf{Q}}\boldsymbol{\epsilon} - \delta\boldsymbol{\epsilon}^{\mathrm{T}}\overline{\mathbf{e}}\boldsymbol{\mathcal{E}} - \delta\boldsymbol{\mathcal{E}}^{\mathrm{T}}\overline{\mathbf{e}}^{\mathrm{T}}\boldsymbol{\epsilon} - \delta\boldsymbol{\mathcal{E}}^{\mathrm{T}}\overline{\boldsymbol{\varepsilon}}\boldsymbol{\mathcal{E}}\right) + \left(\rho\delta\mathbf{u}^{\mathrm{T}}\ddot{\mathbf{u}}\right)\right\}\mathrm{d}V - \delta V = 0 \tag{3.1.31}$$

the equations of motion are then obtained (considering both static and dynamic behaviours, with electromechanical coupling):

$$\begin{aligned}\left[M_{uu}\right]\{\ddot{u}\} + \left[K_{uu}\right]\{u\} + \left[K_{u\phi}\right]\{\phi\} &= \{F_u(t)\}\\ \left[K_{\phi u}\right]\{u\} + \left[K_{\phi\phi}\right]\{\phi\} &= \{F_\phi(t)\}\end{aligned} \tag{3.1.32}$$

where $[M_{uu}]$ is the mass matrix in [kg] (kilogram), $[K_{uu}]$ in $\left[\mathrm{N}\cdot\mathrm{m}^{-1}\right]$ (Newton per metre), both $[K_{u\phi}]$ and $[K_{\phi u}]$ in $\left[\mathrm{C}\cdot\mathrm{m}^{-1}\right]$ (Coulomb per metre) and $[K_{\phi\phi}]$ in [F] (Farad) are, respectively, the stiffness components of the pure mechanical, coupling between mechanical/electrical and pure electrical contributions. The vectors $\{u\}$ and $\{\phi\}$ contain the generalized electromechanical response of the structure, to be determined, with SI units of [m] (metre) and [V] (Volt), respectively. $\{F_u(t)\}$ and $\{F_\phi(t)\}$ are the generalized time-dependent electromechanical load vectors, applied to the structure, with SI units of [N] (Newton) and [C] (Coulomb), respectively.

Another essential way of writing the governing equations of motion is in terms of force and moment resultants. In result, the following integrals in the z-direction of the multilayered structure are defined:

$$\begin{aligned}\begin{Bmatrix}N_{xx}\\N_{yy}\\N_{xy}\end{Bmatrix} &= \int_{-h/2}^{h/2}\begin{Bmatrix}\sigma_{xx}\\\sigma_{yy}\\\sigma_{xy}\end{Bmatrix}^k \mathrm{d}z\\ \begin{Bmatrix}Q_x\\Q_y\end{Bmatrix} &= \int_{-h/2}^{h/2}\begin{Bmatrix}\sigma_{xz}\\\sigma_{yz}\end{Bmatrix}^k \mathrm{d}z\\ \begin{Bmatrix}M_{xx}\\M_{yy}\\M_{xy}\end{Bmatrix} &= \int_{-h/2}^{h/2} z\begin{Bmatrix}\sigma_{xx}\\\sigma_{yy}\\\sigma_{xy}\end{Bmatrix}^k \mathrm{d}z\end{aligned} \tag{3.1.33}$$

where N_{ij} are the in-plane force resultants per unit length in $\left[\mathrm{N}\cdot\mathrm{m}^{-1}\right]$ (Newton per metre), M_{ij} the moment resultants per unit length in [N] (Newton) and Q_i the transverse force resultants per unit length also in $\left[\mathrm{N}\cdot\mathrm{m}^{-1}\right]$ (Newton per metre). Considering the constitutive relations previously defined in Eq. (3.1.4), the previous resultants become the following, for a generic multilayered structure

constituted by a total number of layers N_l (Carrera et al., 2011):

$$\begin{Bmatrix} N_{xx} \\ N_{yy} \\ N_{xy} \end{Bmatrix} = \sum_{k=1}^{N_l} \left\{ \int_{z_k}^{z_{k+1}} \begin{Bmatrix} \sigma_{xx} \\ \sigma_{yy} \\ \sigma_{xy} \end{Bmatrix}^k \mathrm{d}z \right\} = \sum_{k=1}^{N_l} \left\{ \int_{z_k}^{z_{k+1}} \left(\left[\overline{Q}(x,y,z) \right]_b^k \{\epsilon\}_b - \left(\left[\overline{e}(x,y,z) \right]_b^k \right)^{\mathrm{T}} \{\mathcal{E}\}^k \right) \mathrm{d}z \right\} =$$

$$= \sum_{k=1}^{N_l} \left\{ \int_{z_k}^{z_{k+1}} \left(\begin{bmatrix} \overline{Q}_{11}(x,y,z) & \overline{Q}_{12}(x,y,z) & \overline{Q}_{16}(x,y,z) \\ \overline{Q}_{12}(x,y,z) & \overline{Q}_{22}(x,y,z) & \overline{Q}_{26}(x,y,z) \\ \overline{Q}_{16}(x,y,z) & \overline{Q}_{26}(x,y,z) & \overline{Q}_{66}(x,y,z) \end{bmatrix}^k \begin{Bmatrix} \epsilon_{xx}^{(0)} + z\epsilon_{xx}^{(1)} \\ \epsilon_{yy}^{(0)} + z\epsilon_{yy}^{(1)} \\ \gamma_{xy}^{(0)} + z\gamma_{xy}^{(1)} \end{Bmatrix} - \right.$$

$$\left. - \begin{bmatrix} 0 & 0 & \overline{e}_{31}(x,y,z) \\ 0 & 0 & \overline{e}_{32}(x,y,z) \\ 0 & 0 & \overline{e}_{36}(x,y,z) \end{bmatrix}^k \begin{Bmatrix} \mathcal{E}_x^{(0)} + z\mathcal{E}_x^{(1)} \\ \mathcal{E}_y^{(0)} + z\mathcal{E}_y^{(1)} \\ \mathcal{E}_z^{(0)} + z0 \end{Bmatrix}^k \right) \mathrm{d}z \right\} \tag{3.1.34}$$

$$\begin{Bmatrix} Q_x \\ Q_y \end{Bmatrix} = \sum_{k=1}^{N_l} \left\{ \int_{z_k}^{z_{k+1}} \begin{Bmatrix} \sigma_{xz} \\ \sigma_{yz} \end{Bmatrix}^k \mathrm{d}z \right\} = \sum_{k=1}^{N_l} \left\{ \int_{z_k}^{z_{k+1}} \left(\chi_k \left[\overline{Q}(x,y,z) \right]_s^k \{\epsilon\}_s - \left(\left[\overline{e}(x,y,z) \right]_s^k \right)^{\mathrm{T}} \{\mathcal{E}\}^k \right) \mathrm{d}z \right\} =$$

$$= \sum_{k=1}^{N_l} \left\{ \int_{z_k}^{z_{k+1}} \left(\chi_k \begin{bmatrix} \overline{Q}_{44}(x,y,z) & \overline{Q}_{45}(x,y,z) \\ \overline{Q}_{45}(x,y,z) & \overline{Q}_{55}(x,y,z) \end{bmatrix}^k \begin{Bmatrix} \gamma_{yz}^{(0)} \\ \gamma_{xz}^{(0)} \end{Bmatrix} - \right.$$

$$\left. - \begin{bmatrix} \overline{e}_{14}(x,y,z) & \overline{e}_{24}(x,y,z) & 0 \\ \overline{e}_{15}(x,y,z) & \overline{e}_{25}(x,y,z) & 0 \end{bmatrix}^k \begin{Bmatrix} \mathcal{E}_x^{(0)} + z\mathcal{E}_x^{(1)} \\ \mathcal{E}_y^{(0)} + z\mathcal{E}_y^{(1)} \\ \mathcal{E}_z^{(0)} + z0 \end{Bmatrix}^k \right) \mathrm{d}z \right\} \tag{3.1.35}$$

$$\begin{Bmatrix} M_{xx} \\ M_{yy} \\ M_{xy} \end{Bmatrix} = \sum_{k=1}^{N_l} \left\{ \int_{z_k}^{z_{k+1}} z \begin{Bmatrix} \sigma_{xx} \\ \sigma_{yy} \\ \sigma_{xy} \end{Bmatrix}^k \mathrm{d}z \right\} = \sum_{k=1}^{N_l} \left\{ \int_{z_k}^{z_{k+1}} z \left(\left[\overline{Q}(x,y,z) \right]_b^k \{\epsilon\}_b - \left(\left[\overline{e}(x,y,z) \right]_b^k \right)^{\mathrm{T}} \{\mathcal{E}\}^k \right) \mathrm{d}z \right\} =$$

$$= \sum_{k=1}^{N_l} \left\{ \int_{z_k}^{z_{k+1}} z \left(\begin{bmatrix} \overline{Q}_{11}(x,y,z) & \overline{Q}_{12}(x,y,z) & \overline{Q}_{16}(x,y,z) \\ \overline{Q}_{12}(x,y,z) & \overline{Q}_{22}(x,y,z) & \overline{Q}_{26}(x,y,z) \\ \overline{Q}_{16}(x,y,z) & \overline{Q}_{26}(x,y,z) & \overline{Q}_{66}(x,y,z) \end{bmatrix}^k \begin{Bmatrix} \epsilon_{xx}^{(0)} + z\epsilon_{xx}^{(1)} \\ \epsilon_{yy}^{(0)} + z\epsilon_{yy}^{(1)} \\ \gamma_{xy}^{(0)} + z\gamma_{xy}^{(1)} \end{Bmatrix} - \right.$$

$$\left. - \begin{bmatrix} 0 & 0 & \overline{e}_{31}(x,y,z) \\ 0 & 0 & \overline{e}_{32}(x,y,z) \\ 0 & 0 & \overline{e}_{36}(x,y,z) \end{bmatrix}^k \begin{Bmatrix} \mathcal{E}_x^{(0)} + z\mathcal{E}_x^{(1)} \\ \mathcal{E}_y^{(0)} + z\mathcal{E}_y^{(1)} \\ \mathcal{E}_z^{(0)} + z0 \end{Bmatrix}^k \right) \mathrm{d}z \right\} \tag{3.1.36}$$

note that the shear correction factor χ was recalled. Then, it is possible to define the *extensional stiffnesses* A_{ij} in $\left[\mathrm{N} \cdot \mathrm{m}^{-1}\right]$ (Newton per metre), *bending-extensional coupling stiffnesses* B_{ij} in $[\mathrm{N}]$ (Newton) and *bending stiffnesses* D_{ij} in $[\mathrm{N} \cdot \mathrm{m}]$ (Newton metre), neglecting the electrical stiffnesses, as the following:

$$\begin{Bmatrix} \{N\} \\ \{Q\} \\ \{M\} \end{Bmatrix} = \begin{bmatrix} [A(x,y,z)] & 0 & [B(x,y,z)] \\ 0 & \chi\,[A_s(x,y,z)] & 0 \\ [B(x,y,z)] & 0 & [D(x,y,z)] \end{bmatrix} \begin{Bmatrix} \{\epsilon_b^{(0)}\} \\ \{\epsilon_s^{(0)}\} \\ \{\epsilon_b^{(1)}\} \end{Bmatrix} \tag{3.1.37}$$

where

$$\begin{Bmatrix} N_{xx} \\ N_{yy} \\ N_{xy} \end{Bmatrix} = \begin{bmatrix} A_{11}(x,y,z) & A_{12}(x,y,z) & A_{16}(x,y,z) \\ A_{12}(x,y,z) & A_{22}(x,y,z) & A_{26}(x,y,z) \\ A_{16}(x,y,z) & A_{26}(x,y,z) & A_{66}(x,y,z) \end{bmatrix} \begin{Bmatrix} \epsilon_{xx}^{(0)} \\ \epsilon_{yy}^{(0)} \\ \gamma_{xy}^{(0)} \end{Bmatrix} + \\ + \begin{bmatrix} B_{11}(x,y,z) & B_{12}(x,y,z) & B_{16}(x,y,z) \\ B_{12}(x,y,z) & B_{22}(x,y,z) & B_{26}(x,y,z) \\ B_{16}(x,y,z) & B_{26}(x,y,z) & B_{66}(x,y,z) \end{bmatrix} \begin{Bmatrix} \epsilon_{xx}^{(1)} \\ \epsilon_{yy}^{(1)} \\ \gamma_{xy}^{(1)} \end{Bmatrix} \tag{3.1.38}$$

$$\begin{Bmatrix} Q_x \\ Q_y \end{Bmatrix} = \chi \begin{bmatrix} A_{44}(x,y,z) & A_{45}(x,y,z) \\ A_{45}(x,y,z) & A_{55}(x,y,z) \end{bmatrix} \begin{Bmatrix} \gamma_{yz}^{(0)} \\ \gamma_{xz}^{(0)} \end{Bmatrix} \tag{3.1.39}$$

$$\begin{Bmatrix} M_{xx} \\ M_{yy} \\ M_{xy} \end{Bmatrix} = \begin{bmatrix} B_{11}(x,y,z) & B_{12}(x,y,z) & B_{16}(x,y,z) \\ B_{12}(x,y,z) & B_{22}(x,y,z) & B_{26}(x,y,z) \\ B_{16}(x,y,z) & B_{26}(x,y,z) & B_{66}(x,y,z) \end{bmatrix} \begin{Bmatrix} \epsilon_{xx}^{(0)} \\ \epsilon_{yy}^{(0)} \\ \gamma_{xy}^{(0)} \end{Bmatrix} + \\ + \begin{bmatrix} D_{11}(x,y,z) & D_{12}(x,y,z) & D_{16}(x,y,z) \\ D_{12}(x,y,z) & D_{22}(x,y,z) & D_{26}(x,y,z) \\ D_{16}(x,y,z) & D_{26}(x,y,z) & D_{66}(x,y,z) \end{bmatrix} \begin{Bmatrix} \epsilon_{xx}^{(1)} \\ \epsilon_{yy}^{(1)} \\ \gamma_{xy}^{(1)} \end{Bmatrix} \tag{3.1.40}$$

individually, for each layer, the stiffness matrices are calculated by the following integrals, along z-direction:

$$\begin{aligned} \Big[A(x,y,z)\Big]^k &= \int_{z_k}^{z_{k+1}} \Big[\overline{Q}(x,y,z)\Big]_b^k \,\mathrm{d}z \\ \Big[A_s(x,y,z)\Big]^k &= \int_{z_k}^{z_{k+1}} \Big[\overline{Q}(x,y,z)\Big]_s^k \,\mathrm{d}z \\ \Big[B(x,y,z)\Big]^k &= \int_{z_k}^{z_{k+1}} z\,\Big[\overline{Q}(x,y,z)\Big]_b^k \,\mathrm{d}z \\ \Big[D(x,y,z)\Big]^k &= \int_{z_k}^{z_{k+1}} z^2\,\Big[\overline{Q}(x,y,z)\Big]_b^k \,\mathrm{d}z \end{aligned} \tag{3.1.41}$$

then, resultant stiffness matrices for the whole multilayered structure, are given by the following summation operators:

$$\begin{aligned} \Big[A(x,y,z)\Big] &= \sum_{k=1}^{N_l} \left(\Big[A(x,y,z)\Big]^k\right) \\ \Big[A_s(x,y,z)\Big] &= \sum_{k=1}^{N_l} \left(\Big[A_s(x,y,z)\Big]^k\right) \\ \Big[B(x,y,z)\Big] &= \sum_{k=1}^{N_l} \left(\Big[B(x,y,z)\Big]^k\right) \\ \Big[D(x,y,z)\Big] &= \sum_{k=1}^{N_l} \left(\Big[D(x,y,z)\Big]^k\right) \end{aligned} \tag{3.1.42}$$

or simply:

$$\{A_{ij}(x,y,z), B_{ij}(x,y,z), D_{ij}(x,y,z)\} = \sum_{k=1}^{N_l} \left\{ \int_{z_k}^{z_{k+1}} \overline{Q}_{ij}(x,y,z)^k \cdot \left(1, z, z^2\right) \mathrm{d}z \right\} \tag{3.1.43}$$

The governing equations of motion are once more addressed in Section 3.3 with a finite element modelling perspective, for the whole discretized domain. The methodology to calculate all previous quantities is then described.

3.2 Material models

In the previous section, material matrices and respective coefficients were mentioned; these must be defined. To accomplish this, the present section is intended to summarize the modelling theories for all the materials used in this work, including passive and smart ones.

3.2.1 Piezoelectrics and monoclinics

As explained in Section 1.3.1.1, piezoelectric materials are polarized to enhance their electric field. The first important aspect to be defined is the coordinate system of this field, which can be seen in Figure 3.5. The considered active materials are assumed to be polarized in direction 3, i.e. along thickness. This point is relevant because, depending on this polarization field, piezoelectric materials have different coupling between electrical and mechanical deformations/stresses (Carrera et al., 2011).

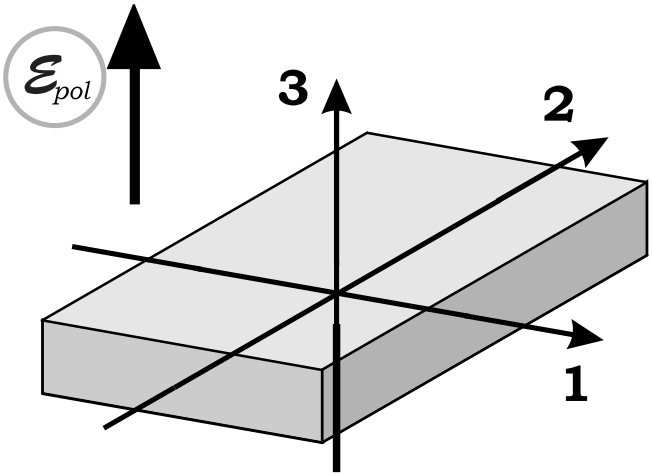

Figure 3.5: Reference system for polarization of a piezoelectric material in transverse direction. From Carrera et al. (2011).

As already assessed before, piezoelectrics are characterized by having a *converse/inverse* and *direct effect*. In the former one, the electric field induces an effect in the mechanical field, whereas in the latter one the opposite is verified. This interaction is assumed to be linear and for that reason it can be described using coupling factors/coefficients, which are also linear. As included in the constitutive equations from the previous section, the piezoelectric matrix contains these coefficients. This way it is possible to define the coupling between several variables associated with these two systems, i.e. stresses $\boldsymbol{\sigma}$ and strains $\boldsymbol{\epsilon}$ (mechanical system), electric field $\boldsymbol{\mathcal{E}}$ and electric displacement $\boldsymbol{\mathcal{D}}$ (electrical system); such relations can be seen in Figures 3.6 and 3.7.

Detailed information about piezoelectric constitutive relations and coefficients can be found in Balmes and Deraemaeker (2001); Emery (1997); Jaffe et al. (1971); Mainprice et al. (2014); Tichý et al. (2010); Zieliński (2016).

Piezoelectric coefficient	Converse effect	Direct effect
$\boldsymbol{a}$	$\boldsymbol{\sigma} = \boldsymbol{a}^T \boldsymbol{\mathcal{D}}$	$\boldsymbol{\mathcal{E}} = \boldsymbol{a}\, \boldsymbol{\epsilon}$
$\boldsymbol{d}$	$\boldsymbol{\epsilon} = \boldsymbol{d}^T \boldsymbol{\mathcal{E}}$	$\boldsymbol{\mathcal{D}} = \boldsymbol{d}\, \boldsymbol{\sigma}$
$\boldsymbol{b}$	$\boldsymbol{\epsilon} = \boldsymbol{b}^T \boldsymbol{\mathcal{D}}$	$\boldsymbol{\mathcal{E}} = \boldsymbol{b}\, \boldsymbol{\sigma}$
$\boldsymbol{e}$	$\boldsymbol{\sigma} = \boldsymbol{e}^T \boldsymbol{\mathcal{E}}$	$\boldsymbol{\mathcal{D}} = \boldsymbol{e}\, \boldsymbol{\epsilon}$

Figure 3.6: Piezoelectric coefficients. Coupling between mechanical and electrical fields. From Carrera et al. (2011).

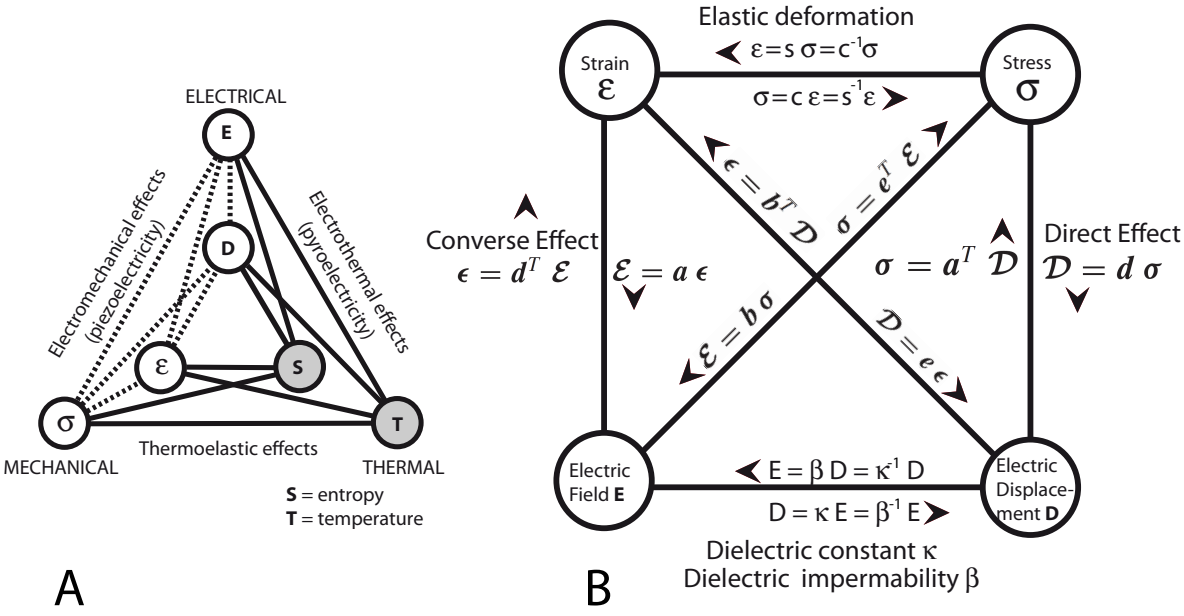

Figure 3.7: Interaction between variables: A) The Heckmann triangle (left) shows the complete set of thermodynamical variables; the variables chosen for constitutive equations are in white circles and the constant variables (entropy and temperature) in circles with grey shading. B) The interaction square (right) with strain, stress, electric displacement and electric field variables at constant entropy and temperature. The piezoelectric tensors $\mathbf{a}$, $\mathbf{d}$, $\mathbf{b}$ and $\mathbf{e}$ in the direct effect are marked with arrows towards bottom and in the converse effect towards to top. Adapted from Mainprice et al. (2014).

From all tensors of constitutive piezoelectric coefficients mentioned in Figures 3.6 and 3.7, i.e. $\mathbf{a}$, $\mathbf{d}$, $\mathbf{b}$ and $\mathbf{e}$, both $\mathbf{e}$ and $\mathbf{d}$ are of special interest. Respectively, these contain the *piezoelectric coefficients for* ***Stress-Charge*** *and* ***Strain-Charge*** *form*, characterized by the SI units of $\left[\mathrm{C}\cdot\mathrm{m}^{-2}\right]$ (Coulomb per square metre) and $\left[\mathrm{C}\cdot\mathrm{N}^{-1}\right]$ (Coulomb per Newton) (Zieliński, 2016). In the literature, the piezoelectric coefficients are usually given in the form of either $\mathbf{e}$ or $\mathbf{d}$, so it is important to consider the following equation, relating both by means of the elastic coefficients (Emery, 1997):

$$[e]^k = \left([Q]^k \left([d]^k\right)^{\mathrm{T}}\right)^{\mathrm{T}} \tag{3.2.1}$$

where $[Q]^k$, in $[\mathrm{Pa}]$ (Pascal), is the elastic coefficients matrix associated with the material of the active layer k in question. The present material modelling methodology starts with the "most complex" of the individual materials included in the present FEM algorithm, i.e. with the highest number of material constants: the monoclinic material, with 13 material constants. Then this material can be simplified according to the user's inputs, where the number of material constants gradually becomes smaller, i.e. resulting in materials such as orthotropic (9 material constants), transversely isotropic (5 material constants) and finally, the "less complex" of the individual materials, isotropic (2 material constants) (Barbero, 2014). Starting with the monoclinic material, the following stress-strain relation apply, where $[Q]^k$ becomes defined as:

$$\{\sigma\}^k = [Q]^k \{\epsilon\} \Leftrightarrow \begin{Bmatrix}\sigma_1\\ \sigma_2\\ \sigma_3\\ \tau_4\\ \tau_5\\ \tau_6\end{Bmatrix}^k = \begin{bmatrix}Q_{11} & Q_{12} & Q_{13} & 0 & 0 & Q_{16}\\ Q_{12} & Q_{22} & Q_{23} & 0 & 0 & Q_{26}\\ Q_{13} & Q_{23} & Q_{33} & 0 & 0 & Q_{36}\\ 0 & 0 & 0 & Q_{44} & Q_{45} & 0\\ 0 & 0 & 0 & Q_{45} & Q_{55} & 0\\ Q_{16} & Q_{26} & Q_{36} & 0 & 0 & Q_{66}\end{bmatrix}^k \begin{Bmatrix}\epsilon_1\\ \epsilon_2\\ \epsilon_3\\ \gamma_4\\ \gamma_5\\ \gamma_6\end{Bmatrix} \tag{3.2.2}$$

the stress or strain components, i.e. 11, 22, 33, 23, 13 and 12, are represented by the numbers 1 to 6, with the same order. Considering an orthotropic material, with 9 material constants:

$$\{\sigma\}^k = [Q]^k \{\epsilon\} \Leftrightarrow \begin{Bmatrix}\sigma_1\\ \sigma_2\\ \sigma_3\\ \tau_4\\ \tau_5\\ \tau_6\end{Bmatrix}^k = \begin{bmatrix}Q_{11} & Q_{12} & Q_{13} & 0 & 0 & 0\\ Q_{12} & Q_{22} & Q_{23} & 0 & 0 & 0\\ Q_{13} & Q_{23} & Q_{33} & 0 & 0 & 0\\ 0 & 0 & 0 & Q_{44} & 0 & 0\\ 0 & 0 & 0 & 0 & Q_{55} & 0\\ 0 & 0 & 0 & 0 & 0 & Q_{66}\end{bmatrix}^k \begin{Bmatrix}\epsilon_1\\ \epsilon_2\\ \epsilon_3\\ \gamma_4\\ \gamma_5\\ \gamma_6\end{Bmatrix} \tag{3.2.3}$$

note that a monoclinic material is a transformed orthotropic one, for instance a composite lamina, constituted by matrix and fibres, where the latter assume orientations different from 0° (throughout this work, the non-SI unit $[^\circ]$ (degree) can be sometimes used, instead of the SI unit $[\mathrm{rad}]$ (radian) to define plane angles). This means that, considering the generic monoclinic material from Eq. (3.2.2), if the material orientation in the xy-plane is $\theta = 0^\circ$, the elastic coefficients Q_{ij} with $ij = \{16, 26, 36, 45\}$ are also zero, reducing to a conventional orthotropic material (9 material constants). Considering a

transversely isotropic material (isotropy along yz-plane), with 5 material constants:

$$\{\sigma\}^k = [Q]^k \{\epsilon\} \Leftrightarrow \begin{Bmatrix} \sigma_1 \\ \sigma_2 \\ \sigma_3 \\ \tau_4 \\ \tau_5 \\ \tau_6 \end{Bmatrix}^k = \begin{bmatrix} Q_{11} & Q_{12} & Q_{12} & 0 & 0 & 0 \\ Q_{12} & Q_{22} & Q_{23} & 0 & 0 & 0 \\ Q_{12} & Q_{23} & Q_{22} & 0 & 0 & 0 \\ 0 & 0 & 0 & \frac{(Q_{22}-Q_{23})}{2} & 0 & 0 \\ 0 & 0 & 0 & 0 & Q_{66} & 0 \\ 0 & 0 & 0 & 0 & 0 & Q_{66} \end{bmatrix}^k \begin{Bmatrix} \epsilon_1 \\ \epsilon_2 \\ \epsilon_3 \\ \gamma_4 \\ \gamma_5 \\ \gamma_6 \end{Bmatrix} \tag{3.2.4}$$

and finally, considering an isotropic material, with 2 material constants:

$$\{\sigma\}^k = [Q]^k \{\epsilon\} \Leftrightarrow \begin{Bmatrix} \sigma_1 \\ \sigma_2 \\ \sigma_3 \\ \tau_4 \\ \tau_5 \\ \tau_6 \end{Bmatrix}^k = \begin{bmatrix} Q_{11} & Q_{12} & Q_{12} & 0 & 0 & 0 \\ Q_{12} & Q_{11} & Q_{12} & 0 & 0 & 0 \\ Q_{12} & Q_{12} & Q_{11} & 0 & 0 & 0 \\ 0 & 0 & 0 & \frac{(Q_{11}-Q_{12})}{2} & 0 & 0 \\ 0 & 0 & 0 & 0 & \frac{(Q_{11}-Q_{12})}{2} & 0 \\ 0 & 0 & 0 & 0 & 0 & \frac{(Q_{11}-Q_{12})}{2} \end{bmatrix}^k \begin{Bmatrix} \epsilon_1 \\ \epsilon_2 \\ \epsilon_3 \\ \gamma_4 \\ \gamma_5 \\ \gamma_6 \end{Bmatrix} \tag{3.2.5}$$

The present FEM algorithm receives the material inputs in two different possibilities, i.e. by means of the standard material elastic constants Q_{ij}, or in terms of engineering constants. This approach is very useful, since in literature the material information can appear in these two ways. Then, it is important to specify how the engineering constants are obtained, by means of the following equations. Here, the generic constants for an orthotropic material are specified (monoclinic ones are obtained further, by means of angular transformation operations), which are functions of elastic moduli E_i in $[\mathrm{Pa}]$ (Pascal), shear moduli G_{ij} also in $[\mathrm{Pa}]$ (Pascal) and Poisson's ratios ν_{ij}, which are $\left[\mathrm{m} \cdot \mathrm{m}^{-1}\right]$ (dimensionless):

$$\begin{aligned} Q_{11} &= \frac{1-\nu_{23}\nu_{32}}{E_2 E_3 \Delta} \\ Q_{12} &= \frac{\nu_{12}+\nu_{32}\nu_{13}}{E_1 E_3 \Delta} \\ Q_{13} &= \frac{\nu_{13}+\nu_{12}\nu_{23}}{E_1 E_2 \Delta} \\ Q_{22} &= \frac{1-\nu_{13}\nu_{31}}{E_1 E_3 \Delta} \\ Q_{23} &= \frac{\nu_{32}+\nu_{12}\nu_{31}}{E_1 E_3 \Delta} \\ Q_{33} &= \frac{1-\nu_{12}\nu_{21}}{E_1 E_2 \Delta} \\ Q_{44} &= G_{23} \\ Q_{55} &= G_{13} \\ Q_{66} &= G_{12} \end{aligned} \tag{3.2.6}$$

where the relations between Poisson's ratios are given by:

$$\begin{aligned}\nu_{21} &= \nu_{12}\frac{E_2}{E_1}\\ \nu_{31} &= \nu_{13}\frac{E_3}{E_1}\\ \nu_{32} &= \nu_{23}\frac{E_3}{E_2}\end{aligned} \tag{3.2.7}$$

and the auxiliary constant Δ by:

$$\Delta = \frac{1-\nu_{12}\nu_{21}-\nu_{23}\nu_{32}-\nu_{31}\nu_{13}-2\left(\nu_{21}\nu_{32}\nu_{13}\right)}{E_1E_2E_3} \tag{3.2.8}$$

retrieving the stress-strain relation of the generic orthotropic material from Eq. (3.2.3), in order to impose the condition of plane state of stress, all components associated with σ_3 are eliminated, as shown in the following equations:

$$\sigma_3 = Q_{13}\epsilon_1 + Q_{23}\epsilon_2 + Q_{33}\epsilon_3 = 0 \Leftrightarrow \epsilon_3 = -\frac{Q_{13}\epsilon_1 + Q_{23}\epsilon_2}{Q_{33}} \tag{3.2.9}$$

$$\begin{aligned}\{\sigma\}^k = [Q]^k\{\epsilon\} \Leftrightarrow \begin{Bmatrix}\sigma_1\\ \sigma_2\\ \sigma_3\\ \tau_4\\ \tau_5\\ \tau_6\end{Bmatrix}^k &= \begin{bmatrix}Q_{11} & Q_{12} & Q_{13} & 0 & 0 & 0\\ Q_{12} & Q_{22} & Q_{23} & 0 & 0 & 0\\ Q_{13} & Q_{23} & Q_{33} & 0 & 0 & 0\\ 0 & 0 & 0 & Q_{44} & 0 & 0\\ 0 & 0 & 0 & 0 & Q_{55} & 0\\ 0 & 0 & 0 & 0 & 0 & Q_{66}\end{bmatrix}^k \begin{Bmatrix}\epsilon_1\\ \epsilon_2\\ \epsilon_3\\ \gamma_4\\ \gamma_5\\ \gamma_6\end{Bmatrix} \Rightarrow\\ \Rightarrow \begin{Bmatrix}\sigma_1\\ \sigma_2\\ \boxed{\sigma_3 = 0}\\ \tau_4\\ \tau_5\\ \tau_6\end{Bmatrix}^k &= \begin{bmatrix}Q_{11} & Q_{12} & \cancel{Q_{13}} & 0 & 0 & 0\\ Q_{12} & Q_{22} & \cancel{Q_{23}} & 0 & 0 & 0\\ \cancel{Q_{13}} & \cancel{Q_{23}} & \cancel{Q_{33}} & 0 & 0 & 0\\ 0 & 0 & 0 & Q_{44} & 0 & 0\\ 0 & 0 & 0 & 0 & Q_{55} & 0\\ 0 & 0 & 0 & 0 & 0 & Q_{66}\end{bmatrix}^k \begin{Bmatrix}\epsilon_1\\ \epsilon_2\\ \epsilon_3\\ \gamma_4\\ \gamma_5\\ \gamma_6\end{Bmatrix} \Rightarrow\end{aligned} \tag{3.2.10}$$

however, when such modification is carried out, to simplify the stress-strain relations by neglecting direction 3, the remaining elastic coefficients must also be modified (note that in Eq. (3.2.9), when the plane state of stress condition is imposed, $\sigma_3 = 0$, the normal strain in that direction remains different from zero, $\epsilon_3 \neq 0$), becoming *plane stress-reduced* ones (identified by the temporary[1] asterisk $*$ superscript), as shown in the following equations:

$$\Rightarrow \begin{Bmatrix}\sigma_1\\ \sigma_2\\ \tau_4\\ \tau_5\\ \tau_6\end{Bmatrix}^k = \begin{bmatrix}Q^*_{11} & Q^*_{12} & 0 & 0 & 0\\ Q^*_{12} & Q^*_{22} & 0 & 0 & 0\\ 0 & 0 & Q^*_{44} & 0 & 0\\ 0 & 0 & 0 & Q^*_{55} & 0\\ 0 & 0 & 0 & 0 & Q^*_{66}\end{bmatrix}^k \begin{Bmatrix}\epsilon_1\\ \epsilon_2\\ \gamma_4\\ \gamma_5\\ \gamma_6\end{Bmatrix} \Rightarrow \tag{3.2.11}$$

[1] The "temporary" asterisk designation is used because throughout literature it is not commonly seen a distinction between *standard*, *plane stress-reduced* and *transformed plane stress-reduced* material coefficients, i.e. in terms of nomenclature, it goes straight from standard to transformed plane stress-reduced, where the latter is simply denoted by an overline $Q_{ij} \Rightarrow \overline{Q}_{ij}$.

This way, in order to stick to the common approach, the *plane stress-reduced* coefficients are identified by a "temporary" asterisk superscript, only to specify their equations.

rearranging the stress-strain relation and writing all components considering the normal strain obtained in Eq. (3.2.9), each plane stress-reduced elastic coefficient is found and given by:

$$\begin{aligned} Q_{11}^{*} &= Q_{11} - \frac{{Q_{13}}^2}{Q_{33}} \\ Q_{12}^{*} &= Q_{12} - \frac{Q_{13}Q_{23}}{Q_{33}} \\ Q_{22}^{*} &= Q_{22} - \frac{{Q_{23}}^2}{Q_{33}} \\ Q_{44}^{*} &= Q_{44} \\ Q_{55}^{*} &= Q_{55} \\ Q_{66}^{*} &= Q_{66} \end{aligned} \tag{3.2.12}$$

note that only components $\{11, 12, 22\}$ are modified. Finally, the transformed plane stress-reduced stress-strain relation becomes:

$$\Rightarrow \{\sigma\}^k = \left[\overline{Q}\right]^k \{\epsilon\} \Leftrightarrow \begin{Bmatrix} \sigma_1 \\ \sigma_2 \\ \tau_6 \\ \tau_4 \\ \tau_5 \end{Bmatrix}^k = \begin{bmatrix} \overline{Q}_{11} & \overline{Q}_{12} & \overline{Q}_{16} & 0 & 0 \\ \overline{Q}_{12} & \overline{Q}_{22} & \overline{Q}_{26} & 0 & 0 \\ \overline{Q}_{16} & \overline{Q}_{26} & \overline{Q}_{66} & 0 & 0 \\ 0 & 0 & 0 & \overline{Q}_{44} & \overline{Q}_{45} \\ 0 & 0 & 0 & \overline{Q}_{45} & \overline{Q}_{55} \end{bmatrix}^k \begin{Bmatrix} \epsilon_1 \\ \epsilon_2 \\ \gamma_6 \\ \gamma_4 \\ \gamma_5 \end{Bmatrix} \tag{3.2.13}$$

where the transformed plane stress-reduced elastic coefficients are obtained by the following angular transformations:

$$\begin{aligned} \overline{Q}_{11} &= Q_{11}^{*}m^4 + \left(2\left(Q_{12}^{*} + 2Q_{66}^{*}\right)\right)n^2m^2 + Q_{22}^{*}n^4 \\ \overline{Q}_{12} &= \left(Q_{11}^{*} + Q_{22}^{*} - 4Q_{66}^{*}\right)n^2m^2 + Q_{12}^{*}\left(m^4 + n^4\right) \\ \overline{Q}_{22} &= Q_{11}^{*}n^4 + \left(2\left(Q_{12}^{*} + 2Q_{66}^{*}\right)\right)n^2m^2 + Q_{22}^{*}m^4 \\ \overline{Q}_{16} &= \left(Q_{11}^{*} - Q_{12}^{*} - 2Q_{66}^{*}\right)nm^3 + \left(Q_{12}^{*} - Q_{22}^{*} + 2Q_{66}^{*}\right)n^3m \\ \overline{Q}_{26} &= \left(Q_{11}^{*} - Q_{12}^{*} - 2Q_{66}^{*}\right)n^3m + \left(Q_{12}^{*} - Q_{22}^{*} + 2Q_{66}^{*}\right)nm^3 \\ \overline{Q}_{66} &= \left(Q_{11}^{*} + Q_{22}^{*} - 2Q_{12}^{*} - 2Q_{66}^{*}\right)n^2m^2 + Q_{66}^{*}\left(m^4 + n^4\right) \\ \overline{Q}_{44} &= Q_{44}^{*}m^2 + Q_{55}^{*}n^2 \\ \overline{Q}_{45} &= \left(Q_{55}^{*} - Q_{44}^{*}\right)mn \\ \overline{Q}_{55} &= Q_{55}^{*}m^2 + Q_{44}^{*}n^2 \end{aligned} \tag{3.2.14}$$

where m and n are auxiliary variables to denote cosine and sine functions of the material angular orientation θ (visually explained in Figure 3.8, where in the material coordinate system the x_1-axis assumes the longitudinal direction of the fibres, y_2-axis is perpendicular to the fibres and z_3-axis is perpendicular to the lamina/layer, coinciding with z-axis), in the xy-plane:

$$\begin{aligned} m &= \cos(\theta) \\ n &= \sin(\theta) \end{aligned} \tag{3.2.15}$$

note, once again, that when $\theta = 0^{\circ}$ the transformed plane stress-reduced elastic coefficients components $\{16, 26, 45\}$ become equal to zero (analysing Eq. (3.2.14)); this is the condition that distinguishes monoclinic from orthotropic materials.

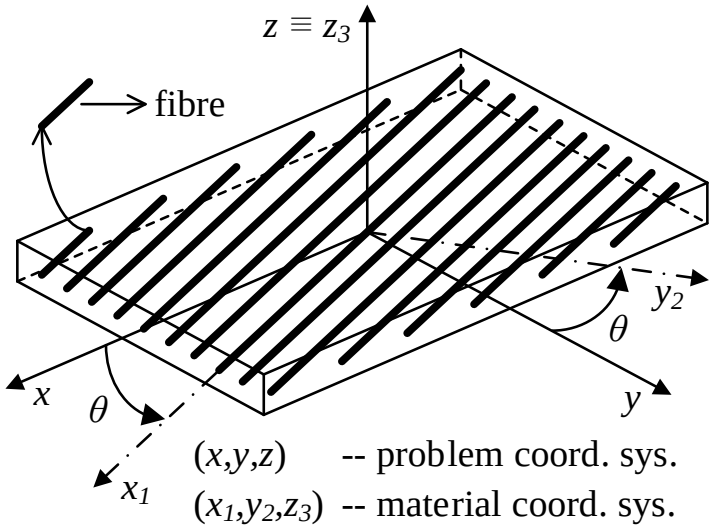

Figure 3.8: A lamina with problem and material coordinate systems. Adapted from Reddy (2004).

The strain-charge piezoelectric coefficients matrix $[d]^k$ is given by 8 material constants:

$$[d]^k = \begin{bmatrix} 0 & 0 & 0 & d_{14} & d_{15} & 0 \\ 0 & 0 & 0 & d_{24} & d_{25} & 0 \\ d_{31} & d_{32} & d_{33} & 0 & 0 & d_{36} \end{bmatrix}^k \tag{3.2.16}$$

as well as the stress-charge piezoelectric coefficients matrix $[e]^k$:

$$[e]^k = \begin{bmatrix} 0 & 0 & 0 & e_{14} & e_{15} & 0 \\ 0 & 0 & 0 & e_{24} & e_{25} & 0 \\ e_{31} & e_{32} & e_{33} & 0 & 0 & e_{36} \end{bmatrix}^k \tag{3.2.17}$$

using the present methodology, it is possible to input the piezoelectric coefficients using the stress-charge or strain-charge form, where the conversion of the latter to the former is carried out automatically.

All the previously defined material matrices can be simplified, depending on the particular material that one intends to model. For instance, if the piezoelectric material is a polarized polycrystalline ceramic, with the crystal symmetry associated to the crystallographic class, the strain-charge piezoelectric coefficients matrix only considers 5 material constants, since $d_{14} = d_{25} = d_{36} = 0$ (Carrera et al., 2011). In any case, the methodology is here described using a generic approach and each possibility of material modelling is then customized inside the FEM algorithm, setting specific coefficients to zero or changing certain material equations.

In terms of the piezoelectric coefficients physical meaning, the different components are distinguished by means of subscripts. According to Carrera et al. (2011), assuming for instance the strain-charge form d_{ij}, i refers to the *electric field direction* and j to the *stress or strain components*. The electric field directions, once again, can be 1, 2 or 3, and the stress or strain components, i.e. 11, 22, 33, 23, 13 and 12, are represented by the numbers 1 to 6, with the same order. To support this definition, Figure 3.9 illustrates the meaning and effects of some piezoelectric coefficients, corresponding to the 33, 31 and 15 components.

Similarly to the methodology presented for the elastic coefficients (Eqs. (3.2.9) to (3.2.15)), the same procedure is carried out to find the transformed plane stress-reduced piezoelectric ones,

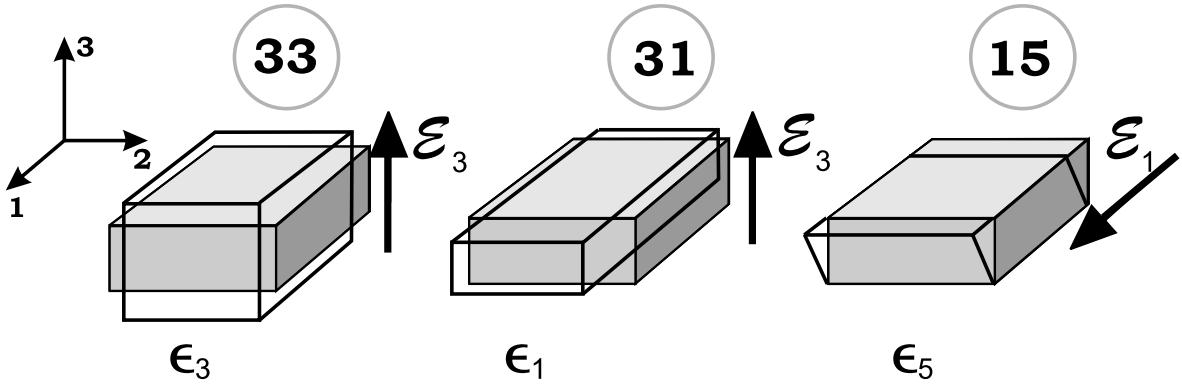

Figure 3.9: Meaning and effects of some piezoelectric coefficients. From Carrera et al. (2011).

considering the electromechanical constitutive relations from Eq. (3.1.4):

$$[e]^k = \begin{bmatrix} 0 & 0 & 0 & e_{14} & e_{15} & 0 \\ 0 & 0 & 0 & e_{24} & e_{25} & 0 \\ e_{31} & e_{32} & \cancel{e_{33}} & 0 & 0 & e_{36} \end{bmatrix}^k \Rightarrow \begin{bmatrix} 0 & 0 & e_{14}^* & e_{15}^* & 0 \\ 0 & 0 & e_{24}^* & e_{25}^* & 0 \\ e_{31}^* & e_{32}^* & 0 & 0 & e_{36}^* \end{bmatrix}^k \Rightarrow$$
$$\Rightarrow [\overline{e}]^k = \begin{bmatrix} 0 & 0 & 0 & \overline{e}_{14} & \overline{e}_{15} \\ 0 & 0 & 0 & \overline{e}_{24} & \overline{e}_{25} \\ \overline{e}_{31} & \overline{e}_{32} & \overline{e}_{36} & 0 & 0 \end{bmatrix}^k \tag{3.2.18}$$

where the piezoelectric coefficients are defined as, with m and n from Eq. (3.2.15):

$$\begin{aligned} e_{31}^* &= e_{31} - e_{33}\frac{Q_{13}}{Q_{33}} \\ e_{32}^* &= e_{32} - e_{33}\frac{Q_{23}}{Q_{33}} \\ e_{36}^* &= e_{36} \\ e_{15}^* &= e_{15} \\ e_{25}^* &= e_{25} \\ e_{14}^* &= e_{14} \\ e_{24}^* &= e_{24} \end{aligned} \tag{3.2.19}$$

note that only components $\{31, 32\}$ are modified

$$\begin{aligned} \overline{e}_{31} &= e_{31}^* m^2 + e_{32}^* n^2 \\ \overline{e}_{32} &= e_{31}^* n^2 + e_{32}^* m^2 \\ \overline{e}_{36} &= (e_{31}^* - e_{32}^*)\, nm \\ \overline{e}_{15} &= e_{15}^* m^2 + e_{24}^* n^2 \\ \overline{e}_{25} &= (e_{15}^* - e_{24}^*)\, nm \\ \overline{e}_{14} &= (e_{15}^* - e_{24}^*)\, nm \\ \overline{e}_{24} &= e_{24}^* m^2 + e_{15}^* n^2 \end{aligned} \tag{3.2.20}$$

The last material property to specify, from constitutive relations, is permittivity, whose coefficients are given by:

$$[\varepsilon]^k = \begin{bmatrix} \varepsilon_{11} & \varepsilon_{12} & 0 \\ \varepsilon_{12} & \varepsilon_{22} & 0 \\ 0 & 0 & \varepsilon_{33} \end{bmatrix}^k \Rightarrow \begin{bmatrix} \varepsilon^*_{11} & \varepsilon^*_{12} & 0 \\ \varepsilon^*_{12} & \varepsilon^*_{22} & 0 \\ 0 & 0 & \varepsilon^*_{33} \end{bmatrix}^k \Rightarrow [\overline{\varepsilon}]^k = \begin{bmatrix} \overline{\varepsilon}_{11} & \overline{\varepsilon}_{12} & 0 \\ \overline{\varepsilon}_{12} & \overline{\varepsilon}_{22} & 0 \\ 0 & 0 & \overline{\varepsilon}_{33} \end{bmatrix}^k \tag{3.2.21}$$

where each coefficient is defined as, with m and n from Eq. (3.2.15):

$$\begin{aligned} \varepsilon^*_{11} &= \varepsilon_{11} \\ \varepsilon^*_{22} &= \varepsilon_{22} \\ \varepsilon^*_{33} &= \varepsilon_{33} + \frac{{e_{33}}^2}{Q_{33}} \\ \varepsilon^*_{12} &= \varepsilon_{12} \end{aligned} \tag{3.2.22}$$

note that only component 33 is modified

$$\begin{aligned} \overline{\varepsilon}_{11} &= \varepsilon^*_{11} m^2 + \varepsilon^*_{22} n^2 \\ \overline{\varepsilon}_{22} &= \varepsilon^*_{11} n^2 + \varepsilon^*_{22} m^2 \\ \overline{\varepsilon}_{33} &= \varepsilon^*_{33} \\ \overline{\varepsilon}_{12} &= (\varepsilon^*_{11} - \varepsilon^*_{22})\, nm \end{aligned} \tag{3.2.23}$$

In sum, an individual material, which is associated with a layer k of the multilayered structure, is defined with $\boxed{9} + \boxed{7} + \boxed{4} = 20$ transformed plane-stress reduced material constants (or less), corresponding to the *elastic*, *piezoelectric* and *permittivity* coefficients, respectively. The previously defined equations are used for both passive and active (piezoelectric) materials; when the layer is constituted by the former type, piezoelectric coefficients are zero, vanishing the electrical contribution; on the other hand, elastic coefficients are always calculated for all types of materials.

It is also important to note that the piezoelectric shear contributions are not considered in this work, i.e. $\overline{e}_{ij}(x, y, z)$ with $ij = \{14, 15, 24, 25\}$ are always zero. In addition, polarization of the active patches was considered only in their thickness direction, also reducing permittivity coefficients $\overline{\varepsilon}_{ij}(x, y, z)$ with $ij = \{11, 22, 12\}$ to zero.

To carry out validation studies, examples of materials are: Polyvinylidene Fluoride (PVDF) $(C_2H_2F_2)_n$, Lead Zirconate Titanate (PZT) $Pb[Zr_xTi_{1-x}]O_3$ (type -4), **Al**uminium **O**xide (AO) Al_2O_3, Aluminium Al, Adhesive and **Gr**aphite (Gr) C / Epoxy. Concerning present case studies, among others, one passive and two active materials were chosen for comparison purposes, being respectively, **La**ngley **R**esearch **C**enter-**S**oluble **I**mide (LaRC-Si), PVDF and PZT-7A. According to several references (the material sources), Tables 3.1 and 3.2 summarize some material properties used in both validation and present studies. In these tables, references were shortened to the following notation: $R_1 \Rightarrow$ Loja et al. (2001), $R_2 \Rightarrow$ Odegard (2004), $R_3 \Rightarrow$ Wang (2004), $R_4 \Rightarrow$ Saravanos and Heyliger (1995), $R_5 \Rightarrow$ Saravanos et al. (1997), $R_6 \Rightarrow$ Farsangi et al. (2013).

In addition to the previously defined properties, since the dynamic behaviour is also considered and as evidenced by Eqs. (3.1.26), (3.1.30) and (3.1.31), for each layer k it is necessary to calculate two types of inertias, i.e. the *translational inertia* (to describe the translation motion effects) I_0 and the *rotational inertia* (to describe the rotation motion effects) I_2, with SI units of $\left[\mathrm{kg \cdot m^{-2}}\right]$ (kilogram

Table 3.1: Passive and active materials' properties used in case studies, from several references (continues in Table 3.2).

material	PVDF	PVDF	LaRC-Si	PZT-7A	PZT-4	PZT-4
reference	R_1	R_2	R_2	R_2	R_3	R_4
purpose	validations	present	present	present	validations	validations
			material properties			
Q_{11} [GPa]	2.0	3.8	8.1	148.0	139.0	108.9
Q_{12} [GPa]	0.0	1.9	5.4	76.2	77.8	45.6
Q_{13} [GPa]	0.0	1.0	5.4	74.2	74.3	38.1
Q_{22} [GPa]	2.0	3.2	8.1	148.0	139.0	108.9
Q_{23} [GPa]	0.0	0.9	5.4	74.2	74.3	38.1
Q_{33} [GPa]	2.0	1.2	8.1	131.0	115.0	84.8
Q_{44} [GPa]	1.0	0.7	1.4	25.4	25.6	31.0
Q_{55} [GPa]	1.0	0.9	1.4	25.4	25.6	31.0
Q_{66} [GPa]	1.0	0.9	1.4	35.9	30.6	31.0
e_{31} $[\mathrm{C \cdot m^{-2}}]$	0.046	0.024	–	-2.100	-5.200	-2.435
e_{32} $[\mathrm{C \cdot m^{-2}}]$	0.046	0.001	–	-2.100	-5.200	5.295
e_{33} $[\mathrm{C \cdot m^{-2}}]$	0.000	-0.027	–	9.500	15.100	19.515
ε_{11} $[\mathrm{F \cdot m^{-1}}]$	0.0000E+00	6.5490E-11	2.4780E-11	4.0710E-09	1.3060E-08	0.0000E+00
ε_{22} $[\mathrm{F \cdot m^{-1}}]$	0.0000E+00	8.2305E-11	2.4780E-11	4.0710E-09	1.3060E-08	0.0000E+00
ε_{33} $[\mathrm{F \cdot m^{-1}}]$	1.0620E-10	6.7260E-11	2.4780E-11	2.0798E-09	1.1510E-08	1.1530E-08
operating voltage [V]	–	$\pm$ 750	–	-200 to +1000	–	–
ρ $[\mathrm{kg \cdot m^{-3}}]$	1800	1800	1376	7900	7600	7600

per square metre) and [kg] (kilogram), respectively. These are given in Eq. (3.2.24).

$$\begin{aligned} I_0^k(x,y,z) &= \int_{z_k}^{z_{k+1}} \rho_k(x,y,z)\,\mathrm{d}z \\ I_2^k(x,y,z) &= \int_{z_k}^{z_{k+1}} z^2 \rho_k(x,y,z)\,\mathrm{d}z \end{aligned} \tag{3.2.24}$$

The next subsection addresses FGMs.

3.2.2 Functionally Graded Materials (FGMs)

In the present work, the objective is to model and predict the mechanical behaviour of structures constituted by, not only passive materials, but also smart ones. Different kinds of piezoelectric particles are mixed up with passive matrices, to put together the advantages of FGMs and smart/adaptive materials. This material approach can be interesting to achieve specific and complex results in structural design, since it is possible to optimize the electric potentials applied to each active patch (or structure's region), as well as the volume fraction behaviour along a specific structure's direction.

Another interesting possibility is to consider functionally graded layers, with material variations in their thickness direction, by modelling material mixtures made of metal and ceramic phases, or even

Table 3.2: Passive and active materials' properties used in case studies, from several references (continued from Table 3.1).

material	PZT-4	PZT-4	Al_2O_3	Al	Adhesive	Gr/Epoxy
reference	R_5	R_6	R_6	R_4	R_4	R_5
purpose	validations					
material properties						
Q_{11} [GPa]	138.5	132.0	460.2	82.7	14.8	134.9
Q_{12} [GPa]	77.4	71.0	174.7	27.6	9.9	5.2
Q_{13} [GPa]	73.6	73.0	127.4	27.6	9.9	5.2
Q_{22} [GPa]	138.5	132.0	460.2	82.7	14.8	14.4
Q_{23} [GPa]	73.6	73.0	127.4	27.6	9.9	7.1
Q_{33} [GPa]	114.7	115.0	509.5	82.7	14.8	14.4
Q_{44} [GPa]	30.6	26.0	126.9	27.6	2.5	5.7
Q_{55} [GPa]	25.6	26.0	126.9	27.6	2.5	5.7
Q_{66} [GPa]	25.6	26.0	126.9	27.6	2.5	3.6
e_{31} $\left[\mathrm{C \cdot m^{-2}}\right]$	-47.324	-4.100	–	–	–	–
e_{32} $\left[\mathrm{C \cdot m^{-2}}\right]$	-47.324	-4.100	–	–	–	–
e_{33} $\left[\mathrm{C \cdot m^{-2}}\right]$	-50.671	14.100	–	–	–	–
ε_{11} $\left[\mathrm{F \cdot m^{-1}}\right]$	0.0000E+00	7.1240E-09	0.0000E+00	0.0000E+00	0.0000E+00	0.0000E+00
ε_{22} $\left[\mathrm{F \cdot m^{-1}}\right]$	0.0000E+00	0.0000E+00	0.0000E+00	0.0000E+00	0.0000E+00	0.0000E+00
ε_{33} $\left[\mathrm{F \cdot m^{-1}}\right]$	1.1505E-08	5.8410E-09	0.0000E+00	0.0000E+00	0.0000E+00	0.0000E+00
operating voltage [V]	–	–	–	–	–	–
ρ $\left[\mathrm{kg \cdot m^{-3}}\right]$	7600	7500	4000	2769	1662	1578

more complex reinforcement options, such as CNTs; nano-, multiscale and hybrid composites are also modelled and addressed in present case studies.

The concept of FGMs is to create mixtures of two or more different materials, where each one can be a passive individual one (monoclinic, orthotropic, transversely isotropic or isotropic), active one (piezoelectric), or a pre-modelled mixture. This way, in the present FEM algorithm it is possible to model "mixtures of mixtures", using different types of both volume fraction distribution *directions* and *approximation approaches*, as well as *homogenization methods*, which makes possible the modelling of multiscale (including CNTs, for example), hybrid materials, etc.

Figure 3.10 shows a few examples of various possibilities according to FGMs modelling in the present work. Volume fraction distributions can be defined along z-direction (thickness) or in the xy-plane (length/width); here, these two approaches are explained separately.

In the former one, Voigt's Rule of Mixtures or Mori-Tanaka's homogenization schemes are available, to mix-up different materials; the defined volume fraction distribution can be modelled using a discrete approximation, where a user-defined number of sub-layers N_{sl} (where each one is identified by the sub-layer number sk) is used to discretize the FGM layer k in the z-direction, or continuous approximation, where the material properties are integrated analytically over thickness.

In the case of the direction being in the xy-plane, the effective material distribution is discrete, since finite element discretization is always carried out in this plane Ω (the FGM spatial variation would be continuous, only if an infinite number of finite elements was created, which is impossible

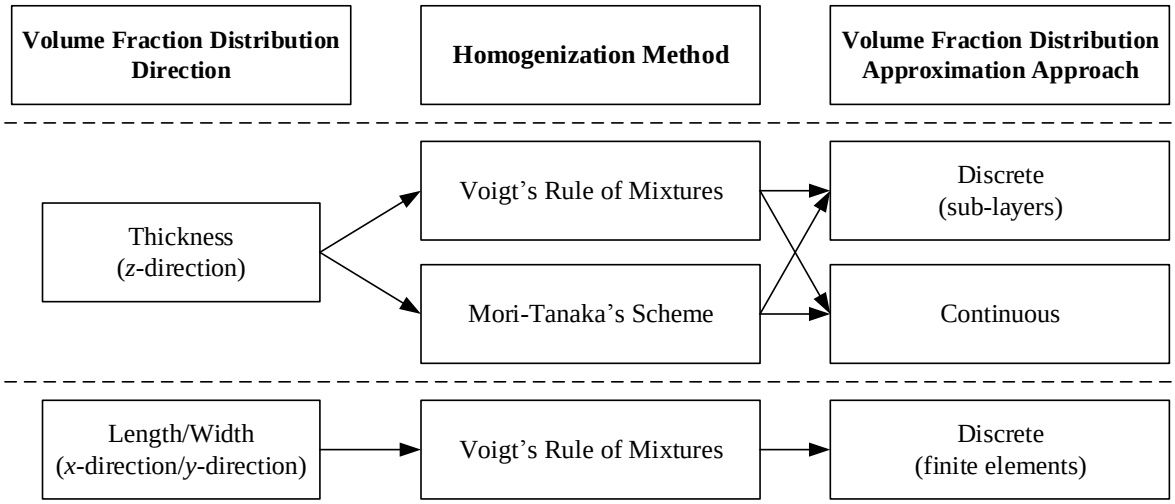

Figure 3.10: FGMs possibilities in terms of both volume fraction distribution directions and approximation approaches, as well as homogenization methods.

using this method); in this case, the homogenization method is always Voigt's Rule of Mixtures.

The following two subsections describe the mathematical approach used to model the FGMs along thickness and length directions.

3.2.2.1 Along thickness (z-direction)

For the FGMs with variations along thickness, two materials must be considered, which in this work are the *matrix* m (e.g. metallic material) and *reinforcement* r (e.g. ceramic material) phases. To model this material variation, the following volume fraction power law is defined (along thickness), considering the volume percentage of reinforcement particles dispersed in a continuous phase, the matrix:

$$V_f = \left(\frac{1}{2} + sp \cdot \frac{z}{h_k}\right)^p, \quad \text{with } sp = \{-1, 1\} \text{ and } z = [z_k, z_{k+1}] \tag{3.2.25}$$

where V_f stands for the volume fraction power law; if multiplied per 100 has units of $[\%]$ (percent), otherwise is $\left[\mathrm{m} \cdot \mathrm{m}^{-1}\right]$ (dimensionless); sp means "surface position" and is an auxiliary variable that can be either -1 or 1, to control which FGM's phase is on the bottom or top surfaces of the FGM layer k, z the coordinate in the transversal thickness direction (from the layer's bottom to top surface z-coordinate, i.e. from z_k to z_{k+1}) in $[\mathrm{m}]$ (metre), h_k the thickness of the FGM layer k (given by $z_{k+1} - z_k$) also in $[\mathrm{m}]$ (metre) and p the exponent of the volume fraction power law, which defines the way the reinforcement particles' volume fraction varies through the FGM's thickness. This exponent permits an adjustment on the fastness the particles are incorporated closer to the bottom or top surfaces of the composite. This ability to vary the phases' mixture in a continuous way, may result in a composite more able to respond to specific requirements. It has additionally significant advantages concerning the minimization of stresses concentrations and may act as a thermal barrier when using ceramics.

The influence of this last parameter on the volume fraction power law can be seen in Figure 3.11, considering a continuous approximation; only exponents $p = \{0, 0.5, 1, 2, 5, +\inf\}$ are considered because these were used in several case studies of the present work, to model metal-ceramic FGMs in the thickness direction.

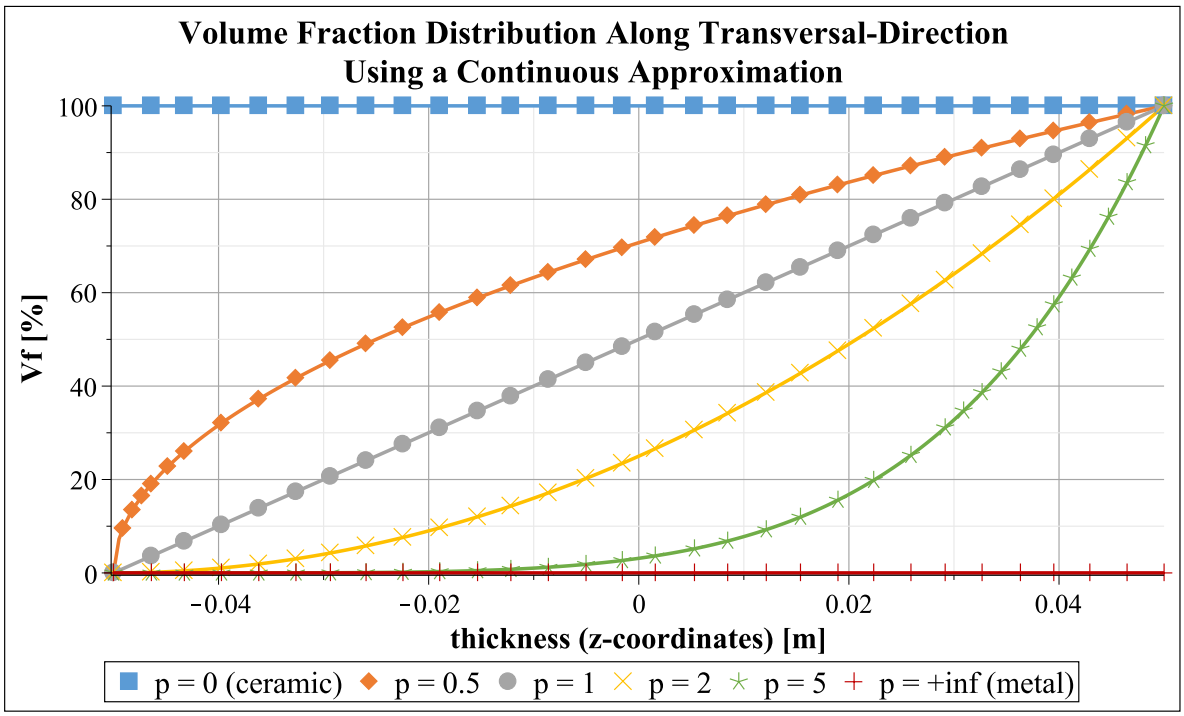

Figure 3.11: Plot of the volume fraction power law along transversal direction, with continuous approximation, considering several p exponents and thickness from -50 to $50\,\mathrm{mm}$.

To generate this plot, a layer span-to-thickness ratio of $a/h_k = 10$ was considered, with $a = 1\,\mathrm{m}$, resulting in a total layer thickness of $h_k = 100\,\mathrm{mm}$; this is why the volume fraction distribution is plotted from $z = -50$ to $z = 50\,\mathrm{mm}$. Note that when $p = 0$, all thickness is constituted by $100\,\%$ of ceramic particles (constant percentage) because V_f becomes always 1, whereas when $p = +\inf$, V_f tends to $0\,\%$ of ceramic particles (meaning that only exists the metallic matrix). Analysing this plot, it is possible to conclude that when $sp = 1$, the ceramic phase is located in the layer's top surface, because for all p-exponents, $100\,\%$ of ceramic particles exist when $z = 50\,\mathrm{mm}$; i.e. the mixture gradient goes from a *bottom* to *top* surface, with ideally $100\,\%$ of *matrix* and *reinforcement*, respectively.

Plots of the same p-exponents are presented in Appendix A, but considering discrete approximations. Figures A.1 to A.3 show, in the same order, discrete distributions in the thickness direction for $N_{sl} = \{5, 10, 50\}$ sub-layers.

After defining the volume fraction power law over thickness coordinates, it is necessary to specify the homogenization methods (Ferreira et al., 2005; Loja et al., 2012) in order to determine the effective material properties (average, macroscopic values) that result from the mixture of both phases.

Starting with Voigt's Rule of Mixtures, the effective properties of the graded material are only based on the volume fraction of the different phases (neglecting voids). Considering the metal-ceramic dual-phase composite as an example, the following equations apply:

$$\begin{aligned} V_{f,r} &= \left(\frac{1}{2} + sp \cdot \frac{z}{h_k}\right)^p \\ V_{f,m} &= 1 - V_{f,r} \\ P_{\mathit{eff}} &= P_r V_{f,r} + P_m V_{f,m} \end{aligned} \tag{3.2.26}$$

where $V_{f,r}$ and $V_{f,m}$ are the volume fraction distributions of the reinforcement r (ceramic particles) and

matrix m (metallic) phases, respectively; P denotes a generic material property (e.g. elastic modulus E, Poisson's ratio ν, shear modulus G or density ρ); subscript eff identifies the resulting material effective properties. The following set of equations specifies these properties' distributions along thickness, considering that the metal-ceramic composite is the mixture between two isotropic materials:

$$\begin{aligned} E_{\mathit{eff}} &= E_r V_{f,r} + E_m V_{f,m} \\ \nu_{\mathit{eff}} &= \nu_r V_{f,r} + \nu_m V_{f,m} \\ G_{\mathit{eff}} &= \frac{E_{\mathit{eff}}}{2\left(1+\nu_{\mathit{eff}}\right)} \\ \rho_{\mathit{eff}} &= \rho_r V_{f,r} + \rho_m V_{f,m} \end{aligned} \tag{3.2.27}$$

where all effective properties, as well as the subsequent elastic coefficients, inertias, material matrices (stiffnesses), etc. are function of the z-coordinate; these are then analytically integrated over thickness, when the continuous approximation is considered. In the case of discrete approximation, each sub-layer will possess constant effective properties (evaluated at their mid-surface z-coordinate $z_{\Omega_{sk}}$); then, the FGM layer's final properties will consider the properties of each sub-layer, by means of discrete summations (stiffness matrices A, B and D, as well as inertias I_0 and I_2); each sub-layer's contribution is distinguished, from the others, by means of the z-coordinates of each bottom and top surfaces, associated with each individual sub-layer (z_{sk} and z_{sk+1}).

Note that the present FEM algorithm is not restricted to isotropic mixtures, but for case studies with the metal-ceramic FGMs in the thickness direction, isotropic materials are considered. In any case, the material mixture can be modelled considering all elastic Q_{ij}, piezoelectric e_{ij} and permittivity ε_{ij} coefficients (if at least one of the phases is piezoelectric, otherwise piezoelectric and permittivity coefficients are null and only elastic ones are modelled), where the generic properties P from Eq. (3.2.26) become these coefficients themselves, instead of engineering constants.

In Mori-Tanaka's homogenization scheme, which is a micro-mechanics' based model, the interaction of the elastic fields among neighbouring inclusions is considered, and the elastic properties are estimated by solving the following equations:

$$\begin{aligned} \frac{K_{\mathit{eff}} - K_m}{K_r - K_m} &= \frac{V_{f,r}}{1 + V_{f,m}\left(\frac{K_r - K_m}{K_m + \frac{4}{3}G_m}\right)} \\ \frac{G_{\mathit{eff}} - G_m}{G_r - G_m} &= \frac{V_{f,r}}{1 + V_{f,m}\left(\frac{G_r - G_m}{G_m + f_m}\right)} \end{aligned} \tag{3.2.28}$$

where K_i and G_i denote, respectively, the bulk and shear moduli associated with subscript i, which can be reinforcement r, matrix m or effective eff; all quantities in [Pa] (Pascal) given by:

$$K_r = \frac{E_r}{3\left(1-2\nu_r\right)}, \quad K_m = \frac{E_m}{3\left(1-2\nu_m\right)}, \quad G_r = \frac{E_r}{2\left(1+\nu_r\right)}, \quad G_m = \frac{E_m}{2\left(1+\nu_m\right)} \tag{3.2.29}$$

f_m is an auxiliary variable associated with matrix's m bulk and shear moduli relations:

$$f_m = \frac{G_m\left(9K_m + 8G_m\right)}{6\left(K_m + 2G_m\right)} \tag{3.2.30}$$

solving Eq. (3.2.28), the effective bulk and shear moduli of the graded composite are obtained:

$$\begin{aligned} K_{\mathit{eff}} &= \frac{4G_mK_m + 3K_mK_r - 4G_mK_mV_{f,r} + 4G_mK_rV_{f,r}}{4G_m + 3K_r + 3K_mV_{f,r} - 3K_rV_{f,r}} \\ G_{\mathit{eff}} &= \frac{G_mf_m + G_mG_r - G_mV_{f,r}f_m + G_rV_{f,r}f_m}{G_r + f_m + G_mV_{f,r} - G_rV_{f,r}} \end{aligned} \tag{3.2.31}$$

the effective elastic modulus E_{eff} and Poisson's ratio ν_{eff} thickness distributions, according to Mori-Tanaka's approach, are given by:

$$E_{\mathit{eff}} = \frac{9K_{\mathit{eff}}G_{\mathit{eff}}}{3K_{\mathit{eff}} + G_{\mathit{eff}}}, \quad \nu_{\mathit{eff}} = \frac{3K_{\mathit{eff}} - 2G_{\mathit{eff}}}{2\left(3K_{\mathit{eff}} + G_{\mathit{eff}}\right)} \tag{3.2.32}$$

and, finally, the effective density distribution along thickness is always calculated using Voigt's Rule of Mixtures, Eq. (3.2.27), even when the remaining properties are obtained using Mori-Tanaka's scheme:

$$\rho_{\mathit{eff}} = \rho_r V_{f,r} + \rho_m V_{f,m} \tag{3.2.33}$$

In sum, the present FEM algorithm predicts the behaviour of FGM layers in the thickness direction, where the average material properties are obtained by means of two different homogenization methods and approximation approaches.

The example of metal-ceramic dual-phase composite was addressed; several case studies in this work consider nano-composites as the matrix (instead of a conventional homogeneous metallic one), which is obtained by the dispersion of CNTs in the metal. Ceramic particles can afterwards be dispersed in that nano-composite, resulting in a multiscale one. The methodology used to estimate CNTs' properties is addressed further ahead.

The next subsection describes the methodology used to model FGMs along length direction (which is the same for width direction).

3.2.2.2 Along length (x-direction)

Concerning FGMs with variations along x-direction, smart materials are mixed-up with passive ones. To model this type of active functionally graded composites, by means of a volume fraction distribution, piezoelectric particles (smart/adaptive reinforcement) are dispersed in a passive continuous phase (matrix). Most research works in this area focus the FGM variation in the plates' thickness direction, but the present algorithm enables one to put together several layers, with material variations along different directions, i.e. (x, y, z). So, as an example, the longitudinal direction is considered (e.g. along a beam's or plate's length), as modelled by the following equation:

$$V_f = \left(\frac{x}{L}\right)^p, \quad \text{with } x = [0, a] \tag{3.2.34}$$

where, again, V_f is the volume fraction power law, x is the coordinate in the longitudinal length direction (assuming values between 0 and the total structure's length a) in $[\mathrm{m}]$ (metre), L is the total length of the FGM layer k considered in the same x-direction (can be, or not, equal to the whole structure's length a) also in $[\mathrm{m}]$ (metre) and p the exponent of the volume fraction power law, which defines the way the piezoelectric particles' volume fraction varies through the FGM's length.

The influence of this last parameter on the volume fraction power law can be seen in Figure 3.12, similarly to the thickness case in Figure 3.11, considering a continuous approximation; only exponents $p = \{0, 0.1, 0.5, 1, 2, 5\}$ are considered because these were used in several case studies of the present work, to model functionally graded active composites along length direction.

A layer with a maximum length of $L = 100\,\mathrm{mm}$ was considered, i.e. the volume fraction distribution is plotted from $x = 0$ to $x = 100\,\mathrm{mm}$. Note that when $p = 0$, all length is constituted by $100\,\%$ of piezoelectric particles (constant percentage) because V_f becomes always 1, whereas when $p > 0$, V_f exhibits the behaviours shown in this plot; for the FGMs along length, the $p = +\inf$ was not considered because it would result in a fully passive structure, whose behaviour is not so

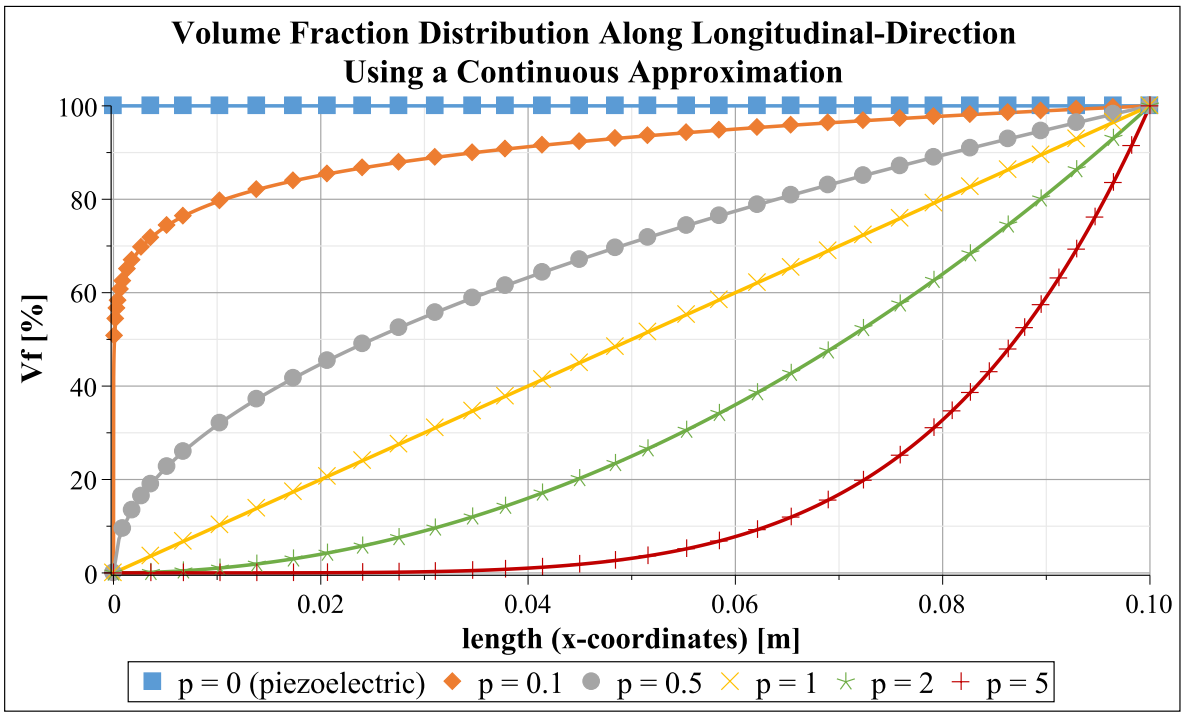

Figure 3.12: Plot of the volume fraction power law along longitudinal direction, with continuous approximation, considering several p exponents and length from 0 to 100 mm.

interesting to study. Analysing this plot, it is possible to conclude that, when using the volume fraction distribution from Eq. (3.2.34), piezoelectric particles' percentages tend to be higher when the x-coordinate increases.

Similarly to FGMs along thickness, plots of the same p-exponents are presented in Appendix A, but considering discrete approximations. Figures A.4 to A.6 show, in the same order, discrete distributions in the length direction for, $N_{ex} = \{6, 10, 16\}$ finite elements in the x-direction .

Both passive and active materials are theoretically mixed-up according to the Voigt's Rule of Mixtures. The macroscopic, averaged values of several effective properties, e.g. density, elastic, piezoelectric and permittivity coefficients can be obtained according to the following expressions:

$$\begin{aligned} V_{f,r}^{ex} &= \left(\frac{x_{cn}^{ex}}{L}\right)^{p} \\ V_{f,m}^{ex} &= 1 - V_{f,r}^{ex} \\ P_{eff}^{ex} &= P_r V_{f,r}^{ex} + P_m V_{f,m}^{ex} \end{aligned} \tag{3.2.35}$$

where $V_{f,r}^{ex}$ and $V_{f,m}^{ex}$ are the volume fraction distributions of the reinforcement r (piezoelectric particles) and matrix m (passive material) phases, for each finite element along x-direction ex, respectively; x_{cn}^{ex} is the centre x-coordinate of each finite element. P denotes a generic material property: for the density distribution, P_i are engineering constants (ρ_r, ρ_m), but for the remaining ones, are directly all elastic Q_{ij}, piezoelectric e_{ij} and permittivity ε_{ij} coefficients of each phase r and m.

In terms of metal-ceramic materials properties, several were used in order to carry out both validations and present case studies; Table 3.3 summarizes them, with their references (sources) shortened to the following notation: $R_1 \Rightarrow$ Ferreira et al. (2005), $R_2 \Rightarrow$ Qian et al. (2004), $R_3 \Rightarrow$

Bernardo et al. (2016). One metallic matrix, made of Aluminium Al, and two ceramic reinforcements, made of **Z**irconium **D**ioxide (ZD) (Zirconia) ZrO_2 and **A**luminium **O**xide (AO) Al_2O_3 were used.

Table 3.3: Material properties of metal-ceramic FGMs.

material	Al	ZrO_2	Al_2O_3
phase subscript i	m	$c1$	$c2$
reference	R_1; R_2	R_1; R_2	R_3
purpose	validations/present	validations/present	present
material properties			
E_i [GPa]	70	151 – 200	380
ν_i	0.3	0.3	0.3
$\rho_i \left[\mathrm{kg \cdot m^{-3}}\right]$	2700 – 2702	5700	3800

The following subsection focuses on the methodology used for CNTs' modelling.

3.2.3 Carbon Nano-Tubes (CNTs)

If one considers the inclusion or dispersion of CNTs in a homogeneous metallic matrix, then it is necessary to estimate the properties of this nano-composite, which is done by using the Halpin-Tsai equations (Halpin and Kardos, 1976). It is globally a hierarchical process, with the objective of modelling the behaviour of hybrid CNT-metal-ceramic composites.

In result, the structural performance of the metal-ceramic functionally graded plates may be improved by considering a multiscale hierarchical composite which can be achieved by hybridizing the mentioned continuous phase, the matrix, through the dispersion of CNTs. In such conditions, and considering the present work, the overall homogenization process can be split into two phases: one wherein the dispersed CNTs in the metallic matrix phase yields a nano-composite with its own material characteristics, and a second one where this nano-composite will receive ceramic inclusions in a graded manner, and finally achieving the graded CNT-metal-ceramic multiscale composite.
The following two subsections describe the mathematics of both phases, or hybridization stages.

3.2.3.1 1st hybridization stage: nano-composite

At the first stage, the reinforcement r and matrix m are, respectively, CNTs (identified by the subscript CNT) and homogeneous metallic phase m.

To estimate the effective material properties of this nano-particle composite, one have used Halpin-Tsai equations (Halpin and Kardos, 1976). Assuming a perfect CNT dispersion within the matrix, the nano-composite can be considered to be an isotropic material, which enables to write the following equations, concerning the elastic modulus:

$$E_{NC} = \frac{E_m}{8}\left\{5\left(\frac{1+2\beta_{dd}V_{f,CNT}}{1-\beta_{dd}V_{f,CNT}}\right)+3\left(\frac{1+2\left(\frac{l_{CNT}}{d_{CNT}}\right)\beta_{dl}V_{f,CNT}}{1-\beta_{dl}V_{f,CNT}}\right)\right\} \tag{3.2.36}$$

with:

$$\beta_{dd} = \frac{\left(\frac{E_{CNT}}{E_m}\right) - \left(\frac{d_{CNT}}{4t_{CNT}}\right)}{\left(\frac{E_{CNT}}{E_m}\right) + \left(\frac{d_{CNT}}{2t_{CNT}}\right)}, \quad \beta_{dl} = \frac{\left(\frac{E_{CNT}}{E_m}\right) - \left(\frac{d_{CNT}}{4t_{CNT}}\right)}{\left(\frac{E_{CNT}}{E_m}\right) + \left(\frac{l_{CNT}}{2t_{CNT}}\right)} \tag{3.2.37}$$

where subscript NC stands for nano-composite. Auxiliary variables β_{dd} and β_{dl} consist of relations between the elastic moduli of the CNTs E_{CNT} and metallic matrix E_m, outer diameter d_{CNT}, length l_{CNT} and thickness t_{CNT} of the CNTs. $V_{f,CNT}$ and $V_{f,m}$ are, respectively, the volume fraction distribution of the reinforcement r (dispersed CNTs) and matrix m (metallic material) phases, given by (Rafiee et al., 2014a):

$$\begin{aligned} V_{f,CNT} &= \frac{w_{CNT}}{w_{CNT} + \left(\frac{\rho_{CNT}}{\rho_m}\right)(1 - w_{CNT})} \\ V_{f,m} &= 1 - V_{f,CNT} \end{aligned} \tag{3.2.38}$$

with w_{CNT} as the CNT weight fraction, which if multiplied per 100 has units of $[\%]$ (percent), otherwise is $\left[\mathrm{m} \cdot \mathrm{m}^{-1}\right]$ (dimensionless). ρ_{CNT} and ρ_m denote the density of CNTs and metallic matrix, respectively. The remaining effective properties of the nano-composite, i.e. Poisson's ratio ν_{NC}, shear modulus G_{NC} and density ρ_{NC}, are obtained using Voigt's Rule of Mixtures:

$$\begin{aligned} \nu_{NC} &= \nu_{CNT} V_{f,CNT} + \nu_m V_{f,m} \\ G_{NC} &= \frac{E_{NC}}{2\,(1 + \nu_{NC})} \\ \rho_{NC} &= \rho_{CNT} V_{f,CNT} + \rho_m V_{f,m} \end{aligned} \tag{3.2.39}$$

Considering a determined CNT's weight fraction, it is then possible to obtain the corresponding volume fraction through Eq. (3.2.38). Using then the estimation expression given in Eq. (3.2.36), where characteristic CNTs' material and geometrical parameters β_{dd} and β_{dl}, are explicitly given in Eq. (3.2.37), it is finally possible to obtain the elastic modulus prediction for the nano-composite.

This prediction is supported by the assumption that a good dispersion of the CNTs is guaranteed. The effectiveness of the dispersion is a very important issue and it has been studied by many researchers. Among others, see refs. Hu et al. (2006); Thostenson et al. (2005); Tornabene et al. (2016). From the studies carried out upon this topic, it can be said that a good dispersion of the CNTs is indispensable for the improvement of the mechanical response of a composite material. However this dispersion is difficult to obtain because, due to Van der Waals forces among the nano-inclusions and the surrounding matrix, the CNTs tend to agglomerate and form bundles or ropes. These agglomerates possess lower aspect ratios and these contribute to a more limited capacity to carry and transfer the loads. According to the experiments carried out by Ajayan et al. (2000) and Salvetat, J.-P. et al. (1999) using SWCNTs, as the bundles grow in diameter, this aspect ratio diminishes and the axial and shear moduli decrease drastically, suggesting that individual CNTs are slipping within the bundle and decreasing the load required to deform the bundle. Nevertheless, depending on the application, these bundles may have advantages. As result of other studies (Suhr et al., 2005), it was concluded that the sliding mechanism within bundles may provide high mechanical damping. Generally speaking, it is important to break these agglomerates into individual CNTs in order to take full advantage of their reinforcement effect. From the literature review, one concludes that an intense effort has been developed in order to modify the surface properties of the CNTs, to minimize this agglomeration trend, focusing on chemical functionalization and on physical methods. Comprehensive reviews on the methods used to this purpose, are given in Balasubramanian and Burghard (2005); Ma, P.-C. et al. (2010); Sinnott (2002).

Because of these aspects, and not to compromise the assumption of a perfect dispersion of the CNTs in the matrix, which underlies the isotropic assumption for the nano-composites used in this study, one has then considered low values of CNT weight fraction/volume fraction (Rafiee et al., 2014a).

Note that the CNTs can either be single-walled, SWCNTs, or multi-walled, MWCNTs, depending on the engineering constants inputs. The geometrical and material properties of the CNTs used to hybridize the metallic aluminium matrix correspond to the ones used by Kim et al. (2009) and Rafiee et al. (2014a), among others, and are shown in Table 3.4.

Table 3.4: Material and geometrical properties of CNTs (Kim et al., 2009; Rafiee et al., 2014a).

CNT type	material properties					
	E_{CNT} [GPa]	ν_{CNT}	l_{CNT} [µm]	d_{CNT} [nm]	t_{CNT} [nm]	ρ_{CNT} $\left[\text{kg}\cdot\text{m}^{-3}\right]$
SWCNT	640	0.33	25	1.4	0.34	1350
MWCNT	400	0.33	50	20	0.34	1350

It is worth mentioning here that according to Al-Rub et al. (2012); Salvetat, J.-P. et al. (1999) the diameter here considered for the MWCNTs is expected to provide a worse performance to the nano-composite, as its aspect ratio is much lower than the one corresponding to the SWCNTs, which in the present case are respectively equal to $l_{CNT}/d_{CNT} = \left(50\times10^{-6}\right)/\left(20\times10^{-9}\right) = 2500$ and to $l_{CNT}/d_{CNT} = \left(25\times10^{-6}\right)/\left(1.4\times10^{-9}\right) \approx 17857$.

3.2.3.2 2nd hybridization stage: multiscale composite

At the second stage, the reinforcement r and matrix m are, respectively, ceramic particles c and nano-composite NC from the first hybridization stage. The resulting properties of the graded CNT-metal-ceramic multiscale composite are obtained using Voigt's Rule of Mixtures, considering a graded variation along z-direction (thickness), similarly to the methodology explained in Eq. (3.2.26):

$$\begin{aligned} V_{f,c} &= \left(\frac{1}{2} + sp\cdot\frac{z}{h_k}\right)^p \\ V_{f,NC} &= 1 - V_{f,c} \\ P_{\mathit{eff}} &= P_c V_{f,c} + P_{NC} V_{f,NC} \end{aligned} \tag{3.2.40}$$

where $V_{f,c}$ and $V_{f,NC}$ are, respectively, the volume fraction distribution of the reinforcement r (ceramic particles) and matrix m (nano-composite) phases. This results in the following effective distributions along thickness:

$$\begin{aligned} E_{MC} &= E_c V_{f,c} + E_{NC} V_{f,NC} \\ \nu_{MC} &= \nu_c V_{f,c} + \nu_{NC} V_{f,NC} \\ G_{MC} &= \frac{E_{MC}}{2\left(1+\nu_{MC}\right)} \\ \rho_{MC} &= \rho_c V_{f,c} + \rho_{NC} V_{f,NC} \end{aligned} \tag{3.2.41}$$

where subscript MC stands for multiscale composite.

At this point, all remaining material quantities, matrices, etc. can be computed, similarly to a conventional FGM, which in this case are function of the z-coordinate; multiscale FGMs based on

CNT-reinforcements were only considered along thickness direction. In any case, for xy-directions, the methodology is similar to the one described in Section 3.2.2.2.
The next section briefly explains the methodology used for finite element modelling.

3.3 Finite element modelling

The main objective of the present section is to describe the methodology used to obtain the FEM governing equations of multilayered structures (beams and plates), considering both static and dynamic electromechanical coupling. In addition, it is also intended to briefly address the finite element implementation, i.e. the algorithmic aspects, as well as the interaction between different software.

The present approach, to solve these engineering problems, is a *discrete* one, involving several finite elements with a limited number of **D**egrees **O**f **F**reedom (DOFs). The continuous structures are discretized and the problem becomes expressed in terms of a finite number of discrete variables, associated to a finite number of DOFs (Carrera et al., 2011). This is a valid mathematical approximation of the continuous problem, extensively used throughout engineering design, by solving the discrete one. It is also well known that the error due to discretization can be reduced by increasing the number of discrete variables, where convergence tests enable one to analyse the approximation accuracy.

It is convenient to state that, since the structures modelled in this work have always a rectangular/squared geometric configuration, the continuous problem is simply discretized using quadrilateral elements; the implemented methodology only generates meshes where their elements have the same uniform dimensions, i.e. refinements and mesh transitions were not programmed, to simplify the work.

In sum, according to Carrera et al. (2011), the finite element process can be described as *a method of approximation to continuous problems so that*:

- *the continuum is divided into a finite number of parts (elements), the behaviour of which is specified by a finite number of parameters; and*
- *the solution of the complete system, as an assembly of its elements, follows precisely the same rules as those applicable to standard discrete problems*.

This section starts with the finite element discretization, as illustrated in the following subsection.

3.3.1 Finite element discretization

Using such approach, the PVD described in Eq. (3.1.26) can be solved by the FEM, where the structure is discretized in several *generic elements*, associated with the surface Ω (structure's mesh) (Carrera et al., 2011). These elements, at every instant, can be transformed into a *master element*, identified by $\hat{\Omega}$, as shown in Figure 3.13; such element, which in this work is always quadrilateral, can be constituted by several nodes.

For comparison purposes and in order to create a more versatile FEM program, three types of finite quadrilateral elements were considered, in terms of number of nodes: the 4-Node Quadrilateral (Q4), 9-Node Quadrilateral (Q9) and 16-Node Quadrilateral (Q16); the node enumeration adopted can be seen in Figure 3.14.

Note that these master elements $\hat{\Omega}$ are represented in a new coordinate system, where the conventional x and y directions are replaced by ξ and η, respectively; the origin of the referential is located at the element's centre position $(\xi, \eta) = (0, 0)$, where each variable is defined between -1 and $+1$; the $\xi\eta$-coordinates of each node, for all the mentioned elements, are summarized in Table 3.5.

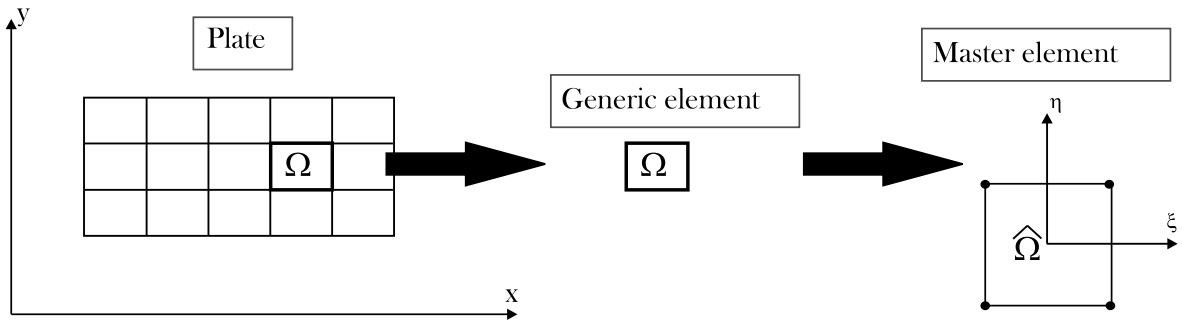

Figure 3.13: Mesh for a generic plate by means of several master elements. From Carrera et al. (2011).

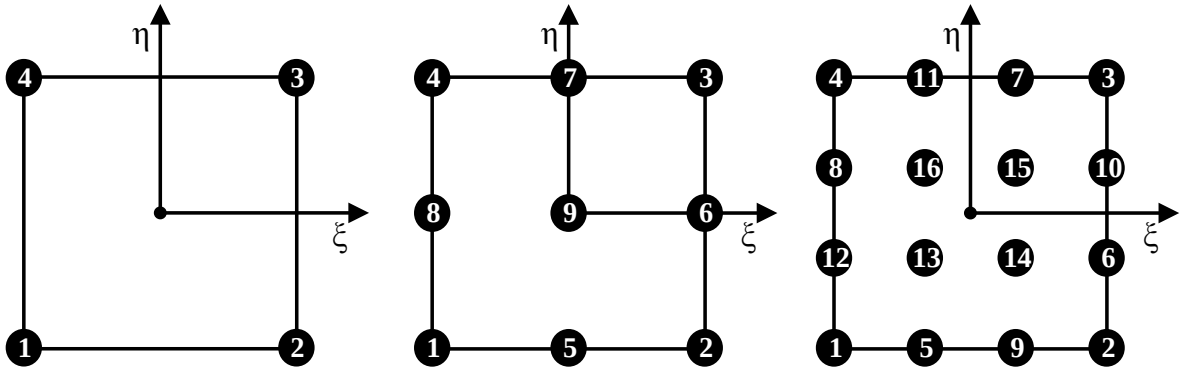

a) 4-Node Quadrilateral (Q4)

b) 9-Node Quadrilateral (Q9)

c) 16-Node Quadrilateral (Q16)

Figure 3.14: The quadrilateral master elements' enumeration with natural coordinate system.

The finite element discretization results in the generation of several elements, constituted by nodes, connected to each other in a specific manner. After discretizing a continuous squared plate, as an example, its mesh becomes numbered with a specific order, as shown in Figure 3.15.

This figure considers a mesh of one-hundred Q4 elements, i.e. 10 elements along both xy-directions, N_{ex} and N_{ey}. Throughout this work, different meshes are denoted using the following notation: $(N_{ex} \times N_{ey})$; for instance, a mesh that is constituted by 10 elements along x-direction and 5 elements along y-direction is defined as (10×5). The present algorithm is able to generate meshes automatically for all the considered element types, Q4, Q9 and Q16, depending on user-defined inputs, such as the number of elements along both directions (can be different), the structures' length/width, etc. Note that, considering the global coordinate system presented in Figure 3.15, its origin is always located at the first node, where the numbering of nodes (black circles) and elements (white-filled rectangles) increment along x and y directions.

At this point, the two finite element formulations implemented in this work, i.e. Lagrange and Kriging, are addressed separately, as explained in the following two subsections.

3.3.2 Lagrange formulation

The elements from Figure 3.14 are well known as the Lagrangian ones, which belong to the Lagrange family (Enes, 2009); the shape functions $N_i(\xi, \eta)$ associated with this type of elements are obtained

Table 3.5: Nodes coordinates on local element natural coordinate system.

node no.	nodes natural coordinates					
	Q4		Q9		Q16	
	ξ	η	ξ	η	ξ	η
1	-1	-1	-1	-1	-1	-1
2	1	-1	1	-1	1	-1
3	1	1	1	1	1	1
4	-1	1	-1	1	-1	1
5			0	-1	$-1/3$	-1
6			1	0	1	$-1/3$
7			0	1	$1/3$	1
8			-1	0	-1	$1/3$
9			0	0	$1/3$	-1
10	–	–			1	$1/3$
11					$-1/3$	1
12					-1	$-1/3$
13			–	–	$-1/3$	$-1/3$
14					$1/3$	$-1/3$
15					$1/3$	$1/3$
16					$-1/3$	$1/3$

by means of products between Lagrange interpolation polynomials in both directions, ξ and η. These functions assume unit values in the elements' nodes, enabling the discrete nodal unknowns to be expressed at points that are different from the nodes, like interpolations (Carrera et al., 2011):

$$\mathbf{a}_\tau(x,y) = N_i(\xi,\eta)\cdot\mathbf{q}_{\tau,i}, \quad \delta\mathbf{a}_s(x,y) = N_j(\xi,\eta)\cdot\delta\mathbf{q}_{s,j}, \quad \text{with } i,j = 1,2,...,N_n \tag{3.3.1}$$

where $\mathbf{a}_\tau$ is a generic variable defined in the xy-plane, $\delta\mathbf{a}_s$ its virtual variation, expressed in terms of nodal values $\mathbf{q}_{\tau,i}$ and $\mathbf{q}_{s,j}$, via shape functions $N_i(\xi,\eta)$ and $N_j(\xi,\eta)$; N_n is the total number of nodes of the considered element (in this work can either be 4, 9 or 16).

As explained before, the displacement field of the FSDT comprises 5 different DOFs per node, i.e. w, θ_x, θ_y, u and v. In consequence, Q4, Q9 and Q16 elements are described by, in the same order, $4\times5 = 20$, $9\times5 = 45$ and $16\times5 = 80$ DOFs. These DOFs are interpolated by the following relations, similarly to the ones from Eq. (3.3.1):

$$\begin{aligned} w &= \sum_{i=1}^{N_n}\left\{N_i(\xi,\eta)\,w_i\right\}, \quad \theta_x = \sum_{i=1}^{N_n}\left\{N_i(\xi,\eta)\,\theta_{xi}\right\} \\ \theta_y &= \sum_{i=1}^{N_n}\left\{N_i(\xi,\eta)\,\theta_{y_i}\right\}, \quad u = \sum_{i=1}^{N_n}\left\{N_i(\xi,\eta)\,u_i\right\} \\ v &= \sum_{i=1}^{N_n}\left\{N_i(\xi,\eta)\,v_i\right\}, \quad \text{with } i = 1,2,...,N_n \end{aligned} \tag{3.3.2}$$

In result, for all generated elements the following equations apply:

$$\mathbf{u} = \mathbf{Z}\mathbf{u}^0 \tag{3.3.3}$$

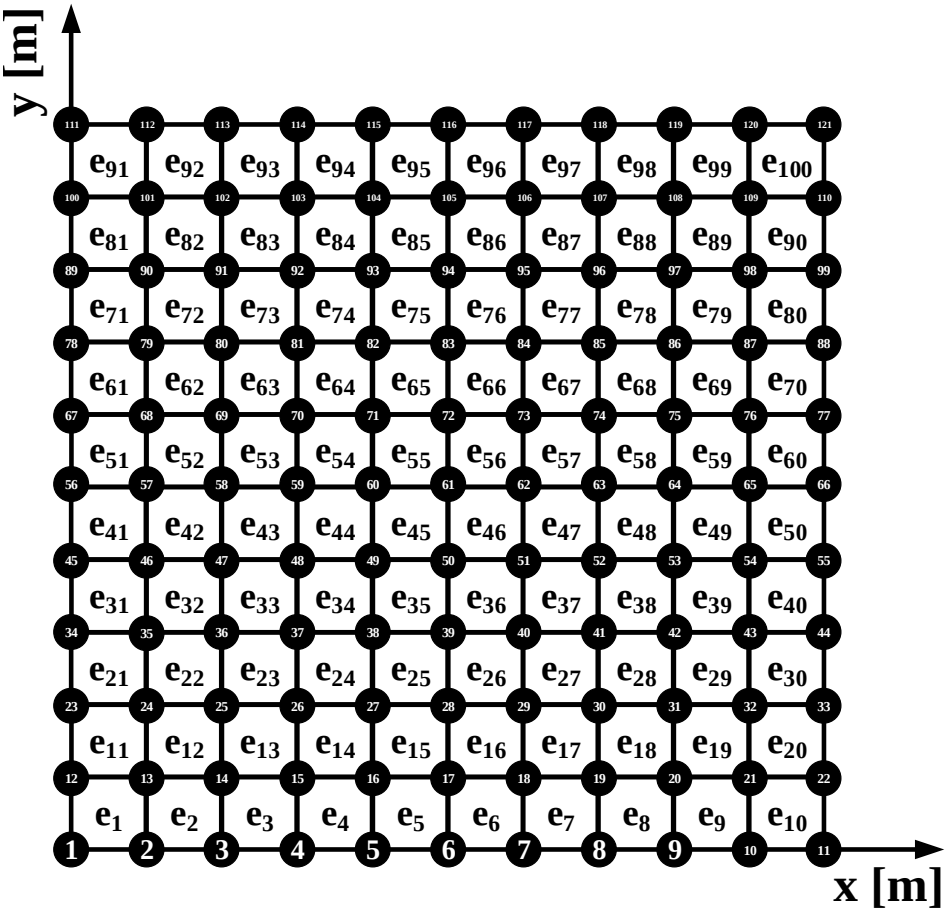

Figure 3.15: Mesh numbering order, considering ten Q4 elements in each xy-direction (10×10).

$$\mathbf{u}(x,y,z,t) = \begin{Bmatrix} u(x,y,z,t) & v(x,y,z,t) & w(x,y,z,t) \end{Bmatrix}^{\mathrm{T}} \tag{3.3.4}$$

$$\mathbf{Z} = \begin{bmatrix} 1 & 0 & 0 & z & 0 \\ 0 & 1 & 0 & 0 & z \\ 0 & 0 & 1 & 0 & 0 \end{bmatrix} \tag{3.3.5}$$

$$\mathbf{u}^0 = \begin{Bmatrix} u^0(x,y,0,t) & v^0(x,y,0,t) & w^0(x,y,0,t) & \theta_x(x,y,z,t) & \theta_y(x,y,z,t) \end{Bmatrix}^{\mathrm{T}} \tag{3.3.6}$$

The vector of generalized mechanical displacements is considered to have the following organization in terms of DOFs, per finite element:

$$\mathbf{q}^e = \begin{Bmatrix} w_1^0 \cdots w_{N_n}^0 & \theta_{x_1} \cdots \theta_{x_{N_n}} & \theta_{y_1} \cdots \theta_{y_{N_n}} & u_1^0 \cdots u_{N_n}^0 & v_1^0 \cdots v_{N_n}^0 \end{Bmatrix}^{\mathrm{T}} \tag{3.3.7}$$

Of course that one more DOF exists, the electric potential ϕ. According to the methodology here implemented, each active element comprises only one electrical DOF, instead of one per node. As explained further ahead, the mechanical and electrical displacements are obtained separately.

This type of approach is known as the *isoparametric approach*, where the elements are normally denominated *isoparametric quadrilaterals*. It is well known throughout the literature that it is more convenient to recover the shape functions from the natural coordinates (ξ, η), rather than from the global

ones (x, y). All shape functions used in this work concerning the presented elements were obtained symbolically, according to specific FEM literature, for both element formulations implemented in this work, i.e. Lagrange[2] and Kriging[3]; these are summarized in Appendix B, function of variables ξ and η, and illustrated by means of several plots in Appendix C. These shape functions are an essential part of the methodology in order to implement the FEM, since their derivatives are used to form strain-displacement matrices, to describe the structures' mechanical behaviour.

Depending on the finite element's number of nodes, formulation and shape functions' polynomial degree, it is possible to identify several elements with different names and respective abbreviations:

- **Lagrange elements:**
  - o **4**-Node **Bi**__**lin**__ear **Lag**range Quadrilateral (4BlinLag);
  - o **9**-Node **Biquad**ratic **Lag**range Quadrilateral (9BquadLag);
  - o **16**-Node **Bicub**ic **Lag**range Quadrilateral (16BcubLag).
- **Kriging elements:**
  - o **4**-Node **Bi**__**lin**__ear **Krig**ing Quadrilateral (4BlinKrig);
  - o **9**-Node **Bi**__**lin**__ear **Krig**ing Quadrilateral (9BlinKrig);
  - o **9**-Node **Biquad**ratic **Krig**ing Quadrilateral (9BquadKrig);
  - o **16**-Node **Bi**__**lin**__ear **Krig**ing Quadrilateral (16BlinKrig);
  - o **16**-Node **Biquad**ratic **Krig**ing Quadrilateral (16BquadKrig);
  - o **16**-Node **Bicub**ic **Krig**ing Quadrilateral (16BcubKrig).

Note that the designation of "bi"(linear, quadratic or cubic) is used because the quadrilateral elements possess two different directions that must be characterized by the shape functions, that is why the word "bi" is commonly used before the polynomial degree.

In order to compute the shape functions, the following geometrical relations must be considered, where natural coordinates ξ and η become function of global x and y, respectively; note that x_1 and y_1 denote global coordinates of the first node of the element, a and b are the lateral dimensions of the element along x and y global coordinates, respectively:

$$\xi = \frac{2\,(x - x_1) - a}{a}, \quad \eta = \frac{2\,(y - y_1) - b}{b} \tag{3.3.8}$$

then, the relations between both global and natural coordinate systems become defined as the following:

$$x = \sum_{i=1}^{N_n} \{x_i N_i(\xi, \eta)\}, \quad y = \sum_{i=1}^{N_n} \{y_i N_i(\xi, \eta)\} \tag{3.3.9}$$

At this point it is convenient to state that, when the Lagrange formulation is used, the quantities associated with the governing equations of motion are integrated along the in-plane directions, by means of the well known Gauss quadrature method; for this reason, everything must be expressed in terms of natural coordinates in order to create an efficient computational model. This way, the

[2]The finite elements based on Lagrange formulation are described by shape functions that consider Lagrange polynomials (only).

[3]The finite elements based on Kriging formulation are described by shape functions that consider both Lagrange polynomials and Gaussian functions.

following equations apply:

$$\begin{aligned}\frac{\partial N_i(x(\xi,\eta),y(\xi,\eta))}{\partial \xi} &= \frac{\partial N_i(\xi,\eta)}{\partial x}\frac{\partial x}{\partial \xi} + \frac{\partial N_i(\xi,\eta)}{\partial y}\frac{\partial y}{\partial \xi} \\ \frac{\partial N_i(x(\xi,\eta),y(\xi,\eta))}{\partial \eta} &= \frac{\partial N_i(\xi,\eta)}{\partial x}\frac{\partial x}{\partial \eta} + \frac{\partial N_i(\xi,\eta)}{\partial y}\frac{\partial y}{\partial \eta}\end{aligned} \tag{3.3.10}$$

which in matrix notation becomes:

$$\begin{Bmatrix}\dfrac{\partial N_i(\xi,\eta)}{\partial \xi} \\ \dfrac{\partial N_i(\xi,\eta)}{\partial \eta}\end{Bmatrix} = \begin{bmatrix}\dfrac{\partial x}{\partial \xi} & \dfrac{\partial y}{\partial \xi} \\ \dfrac{\partial x}{\partial \eta} & \dfrac{\partial y}{\partial \eta}\end{bmatrix} \begin{Bmatrix}\dfrac{\partial N_i(\xi,\eta)}{\partial x} \\ \dfrac{\partial N_i(\xi,\eta)}{\partial y}\end{Bmatrix} \tag{3.3.11}$$

the Jacobian matrix is defined as:

$$\boldsymbol{\mathcal{J}} = \begin{bmatrix}\dfrac{\partial x}{\partial \xi} & \dfrac{\partial y}{\partial \xi} \\ \dfrac{\partial x}{\partial \eta} & \dfrac{\partial y}{\partial \eta}\end{bmatrix} \tag{3.3.12}$$

and the relation from Eq. (3.3.11) can be inverted, using the inverse operation (linear algebra) of the Jacobian matrix:

$$\begin{Bmatrix}\dfrac{\partial N_i(\xi,\eta)}{\partial x} \\ \dfrac{\partial N_i(\xi,\eta)}{\partial y}\end{Bmatrix} = [\boldsymbol{\mathcal{J}}]^{-1} \begin{Bmatrix}\dfrac{\partial N_i(\xi,\eta)}{\partial \xi} \\ \dfrac{\partial N_i(\xi,\eta)}{\partial \eta}\end{Bmatrix} \tag{3.3.13}$$

Afterwards, to carry out the integrations along in-plane directions, it is possible to consider the master element $\hat{\Omega}$ in natural coordinates (ξ,η) or the generic element Ω in global coordinates (x,y). Both elements' infinitesimal areas are related by the following equation:

$$\mathrm{d}\Omega = \mathrm{d}x\,\mathrm{d}y = \det(\boldsymbol{\mathcal{J}})\,\mathrm{d}\xi\,\mathrm{d}\eta \tag{3.3.14}$$

note the use of the linear algebra determinant operator $\det$; $\mathrm{d}\xi$ and $\mathrm{d}\eta$ denote, respectively, the infinitesimal dimension along natural directions ξ and η, in the natural coordinate system of the master element.

Gauss quadrature rule is a numerical integration approach, often carried out over isoparametric element domains, since it uses a *minimal number of sample points to achieve a desired level of accuracy* (Felippa, 2016a). In comparison with analytical integration methodologies, this one evaluates matrices products at each sample point, increasing the computation efficiency. In result, depending on the number of integration points, several Gauss points weights $\mathcal{G}_w^i$ and Gauss points natural coordinates $\mathcal{G}_{\xi\eta}^i$ must be defined; associated with these, there are several Gauss rules, which in the case of isoparametric quadrilaterals are denoted as following: rule $p=1$ means that (1×1) integration points are used (for both in-plane directions of the elements), $p=2$ is (2×2), $p=3$ is (3×3), $p=4$ is (4×4) and so on; in this work only these rules are needed, since the maximum polynomial degree of the shape functions is bicubic. The first four two-dimensional Gauss product rules are illustrated in Figure 3.16. Appendix D summarizes the Gauss points natural coordinates and respective weights.

It is also well known that shear locking can be minimized when selective/mixed integration schemes are used, i.e. when bending and membrane stiffness components are integrated using full p rules and shear ones using reduced p rules. The present FEM algorithm enables one to control the different types

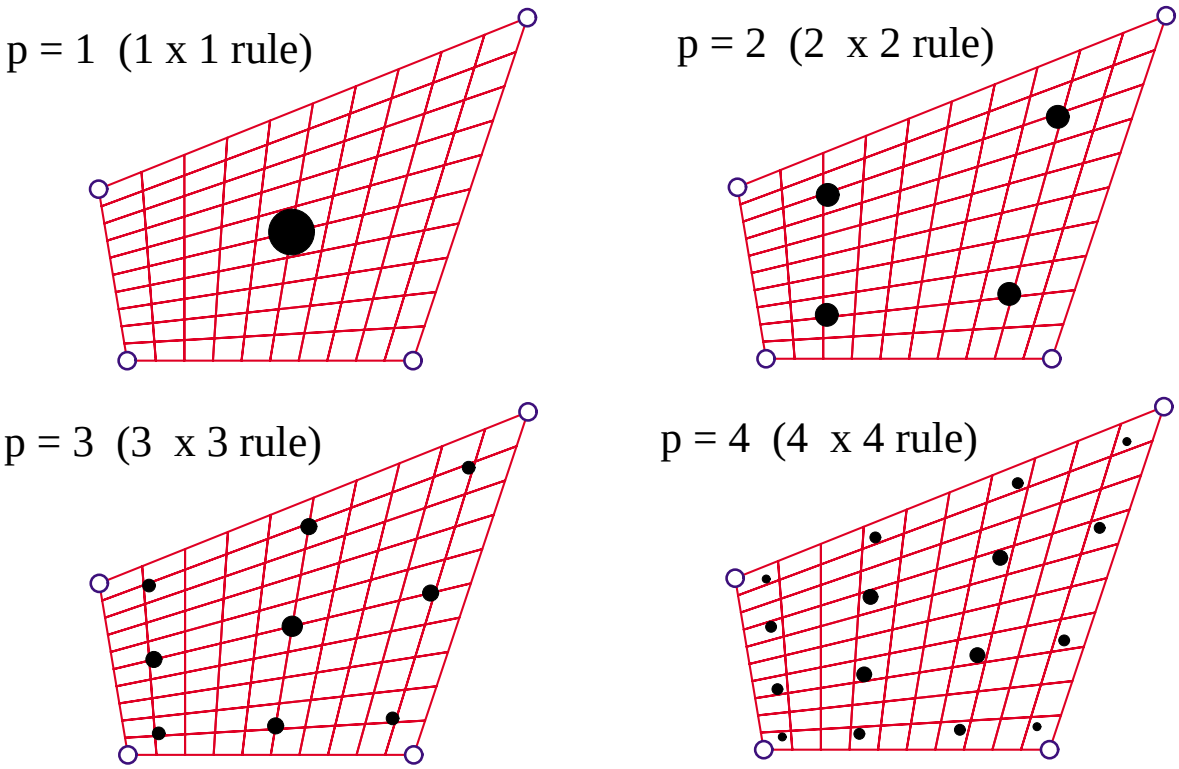

Figure 3.16: The first four two-dimensional Gauss product rules $p = 1, 2, 3, 4$ depicted over a straight-sided quadrilateral region. Sample points are marked with black circles. The areas of these circles are proportional to the integration weights. From Felippa (2016a).

Table 3.6: Different integration schemes for Lagrangian elements and respective quadrature rules. Adapted from Bocskai and Nagy (2013).

integration scheme	**stiffness component**	**Lagrangian element**		
		bilinear Q4	biquadratic Q9	bicubic Q16
		quadrature rule		
full	bending & membrane	(2×2)	(3×3)	(4×4)
	shear	(2×2)	(3×3)	(4×4)
selective/mixed	bending & membrane	(2×2)	(3×3)	(4×4)
	shear	(1×1)	(2×2)	(3×3)
reduced	bending & membrane	(1×1)	(2×2)	(3×3)
	shear	(1×1)	(2×2)	(3×3)

of integration schemes to use (full, selective/mixed and reduced), associated with the different stiffness components; this information is summarized in Table 3.6, for the implemented Lagrangian elements.

Of course that selective/mixed integration scheme gives more accurate results (due to shear locking minimization), but full and reduced were also implemented for comparison and validation purposes; this approach is often used by Reddy (2004, 2006).
The following subsection addresses Kriging formulation.

3.3.3 Kriging formulation

According to Loja et al. (2015), Kriging *is a form of generalized regression for the formulation of an optimal estimator, in a similar sense to that corresponding to the least squares method*. Krige (1951) introduced this geostatistical technique focused on spatial interpolation in mining and geology. However, there are other types of applications where such approach has being used, e.g. surfaces modelling in reverse engineering – in this work, this interpolation technique is applied to the FEM, in parallel with Lagrange formulation.

Comparatively to the Lagrange formulation, the Kriging one has small differences; while in the former the shape functions are constituted by Lagrange polynomials (only), to interpolate DOFs, and Gauss quadrature is used to compute stiffness and mass matrices, in the latter the shape functions are also constituted by Gaussian functions (derived from the Kriging interpolation technique) and all integrations are computed analytically. Similarly to the Lagrange shape functions, Kriging ones are also symbolically summarized in Appendix B and plotted in Appendix C.

Recalling the relation from Eq. (3.3.1), instead of the conventional Lagrange shape functions $N_i(\xi,\eta)$, a different linear combination of functions $\varphi_i(\xi,\eta)$ is used to interpolate DOFs. Such methodology *is based on the assumption that to closer locations correspond similar data results, and considering that any unknown node value can be then interpolated by using neighbour scattered points* (Loja et al., 2015). In order to obtain these shape functions, the following equations apply:

$$\begin{aligned} \mathbf{a}_\tau(x,y) &= \varphi_i(\xi,\eta)\cdot\mathbf{q}_{\tau,i}, \quad \text{with } i=1,2,...,N_n \\ \varphi_i(\xi,\eta) &= \{p(\xi,\eta)\}^{\mathrm{T}}[A] + \{r(\xi,\eta)\}^{\mathrm{T}}[B] \end{aligned} \tag{3.3.15}$$

where matrices $[A]$ and $[B]$ are given by:

$$\begin{aligned} [A] &= \left([P]^{\mathrm{T}}[R]^{-1}[P]\right)^{-1}[P]^{\mathrm{T}}[R]^{-1} \\ [B] &= [R]^{-1}\left(I-[P][A]\right) \end{aligned} \tag{3.3.16}$$

with $[P]$ and $[R]$ as:

$$\begin{aligned} [P] &= \begin{bmatrix} p_1(\xi_1,\eta_1) & \cdots & p_M(\xi_1,\eta_1) \\ \vdots & \ddots & \vdots \\ p_1(\xi_N,\eta_N) & \cdots & p_M(\xi_N,\eta_N) \end{bmatrix} \\ [R] &= \begin{bmatrix} \mathcal{R}((\xi_1,\eta_1),(\xi_1,\eta_1)) & \cdots & \mathcal{R}((\xi_1,\eta_1),(\xi_N,\eta_N)) \\ \vdots & \ddots & \vdots \\ \mathcal{R}((\xi_N,\eta_N),(\xi_1,\eta_1)) & \cdots & \mathcal{R}((\xi_N,\eta_N),(\xi_N,\eta_N)) \end{bmatrix} \end{aligned} \tag{3.3.17}$$

matrix $[P]$ is a rectangular matrix, M represents the order of the polynomial basis considered. Considering $M=1$, it results in $\{p(\xi,\eta)\}^{\mathrm{T}} = \begin{Bmatrix} 1 & (\xi,\eta) & (\xi,\eta)^2 \end{Bmatrix}$, $M=2$ in $\{p(\xi,\eta)\}^{\mathrm{T}} =$

$\left\{1 \quad (\xi,\eta) \quad (\xi,\eta)^2 \quad (\xi,\eta)^3\right\}$ and $M = 3$ in $\{p(\xi,\eta)\}^{\mathrm{T}} = \left\{1 \quad (\xi,\eta) \quad (\xi,\eta)^2 \quad (\xi,\eta)^3 \quad (\xi,\eta)^4\right\}$. This way, Kriging shape functions are obtained for bilinear, biquadratic and bicubic elements. Here, N is a parameter that represents the number of points in the shape functions' domain. $R((\xi_i,\eta_i),(\xi_j,\eta_j))$ are covariance coefficients, gathered in the correlation matrix $[R]$; these were computed using the Gaussian function $\exp\left(-\theta \cdot r_{i,j}^2\right)$, where $r_{i,j}$ is the Euclidean distance between two given points. θ is a generic variable, considered to be equal to 2.

Lagrangian elements, depending on their number of nodes, are constrained in terms of polynomial degree, i.e. Q4 are always bilinear, Q9 biquadratic and Q16 bicubic. Using Kriging's approach, Q9 can also be bilinear and Q16 bilinear and biquadratic. Such characteristic is possible to achieve because Kriging's shape functions have more than one solution.

Finally, comparing all shape functions presented in Appendices B and C, it is possible to verify that Kriging's shape functions are more complex than Lagrange ones. Convergence case studies are presented further ahead to compare both Lagrange and Kriging methodologies, where conclusions about computational time are also drawn.

The following subsection focuses on the elementary governing equations of motion, where the calculation of crucial quantities for the method is described (stiffness and mass matrices, etc.).

3.3.4 Elementary governing equations of motion

Recalling the governing equations of motion from Eq. (3.1.32), for the whole discretized plate domain yields the following, in terms of matrix notation:

$$\begin{bmatrix}[M_{uu}] & 0\\ 0 & 0\end{bmatrix}\begin{Bmatrix}\{\ddot{u}\}\\ \{\ddot{\phi}\}\end{Bmatrix}+\begin{bmatrix}[K_{uu}] & [K_{u\phi}]\\ [K_{\phi u}] & [K_{\phi\phi}]\end{bmatrix}\begin{Bmatrix}\{u\}\\ \{\phi\}\end{Bmatrix}=\begin{Bmatrix}\{F_u(t)\}\\ \{F_\phi(t)\}\end{Bmatrix} \tag{3.3.18}$$

From this point on, since this work deals with multilayered structures, the computations of all quantities are carried out for each layer k and element e. The generic mass matrix $[M_{uu}]$, considering the mechanical contribution uu, is given by the following relation:

$$[M_{uu}]^{k,e} = \int_{V_e} \{N(\xi,\eta)\}^{\mathrm{T}} \mathbf{Z}^{\mathrm{T}} \rho_k(x,y,z)\, \mathbf{Z}\, \{N(\xi,\eta)\}\, \mathrm{d}V_e \tag{3.3.19}$$

The elemental mass matrix is calculated by the following set of equations, subdivided in each

contribution associated with each DOF, i.e. $\{w, \theta_x, \theta_y, u, v\}$:

$$
\begin{aligned}
[M^{w}_{uu}]^{k,e} &= \int_{\Omega_e} \{N(\xi,\eta)\}^{\mathrm{T}} I_0^k(x,y,z) \{N(\xi,\eta)\} \,\mathrm{d}\Omega_e = \\
&= \sum_{i=1}^{N_{\mathcal{G}_{w,b}}} \left(\left(\{N(\xi,\eta)\}_i\right)^{\mathrm{T}} I_0^k(x,y,z) \{N(\xi,\eta)\}_i \mathcal{G}^i_{w,b} \det(\boldsymbol{\mathcal{J}}_e) \right) \\
\left[M^{\theta_x}_{uu}\right]^{k,e} &= \int_{\Omega_e} \{N(\xi,\eta)\}^{\mathrm{T}} I_2^k(x,y,z) \{N(\xi,\eta)\} \,\mathrm{d}\Omega_e = \\
&= \sum_{i=1}^{N_{\mathcal{G}_{w,b}}} \left(\left(\{N(\xi,\eta)\}_i\right)^{\mathrm{T}} I_2^k(x,y,z) \{N(\xi,\eta)\}_i \mathcal{G}^i_{w,b} \det(\boldsymbol{\mathcal{J}}_e) \right) \\
\left[M^{\theta_y}_{uu}\right]^{k,e} &= \int_{\Omega_e} \{N(\xi,\eta)\}^{\mathrm{T}} I_2^k(x,y,z) \{N(\xi,\eta)\} \,\mathrm{d}\Omega_e = \\
&= \sum_{i=1}^{N_{\mathcal{G}_{w,b}}} \left(\left(\{N(\xi,\eta)\}_i\right)^{\mathrm{T}} I_2^k(x,y,z) \{N(\xi,\eta)\}_i \mathcal{G}^i_{w,b} \det(\boldsymbol{\mathcal{J}}_e) \right) \\
[M^{u}_{uu}]^{k,e} &= \int_{\Omega_e} \{N(\xi,\eta)\}^{\mathrm{T}} I_0^k(x,y,z) \{N(\xi,\eta)\} \,\mathrm{d}\Omega_e = \\
&= \sum_{i=1}^{N_{\mathcal{G}_{w,b}}} \left(\left(\{N(\xi,\eta)\}_i\right)^{\mathrm{T}} I_0^k(x,y,z) \{N(\xi,\eta)\}_i \mathcal{G}^i_{w,b} \det(\boldsymbol{\mathcal{J}}_e) \right) \\
[M^{v}_{uu}]^{k,e} &= \int_{\Omega_e} \{N(\xi,\eta)\}^{\mathrm{T}} I_0^k(x,y,z) \{N(\xi,\eta)\} \,\mathrm{d}\Omega_e = \\
&= \sum_{i=1}^{N_{\mathcal{G}_{w,b}}} \left(\left(\{N(\xi,\eta)\}_i\right)^{\mathrm{T}} I_0^k(x,y,z) \{N(\xi,\eta)\}_i \mathcal{G}^i_{w,b} \det(\boldsymbol{\mathcal{J}}_e) \right)
\end{aligned}
\tag{3.3.20}
$$

these are calculated using the vector of shape functions associated with the finite element type, which are functions of natural coordinates ξ and η, $\{N(\xi,\eta)\}$. Note that, for the Lagrange formulation, the integrals are converted in summations (considering the associated Gauss points), whereas for the Kriging formulation these are computed analytically. Here, each Gauss weight $\mathcal{G}^i_w$ has one additional subscript, which can either be b, s or ϕ; such nomenclature is used because the present FEM algorithm, by means of user-defined inputs, enables one to control the quadrature rule to use (individually) for all components of bending b / membrane m, shear s and electrical ϕ.
The elemental stiffness matrices can be written as:

$$
\begin{aligned}
[K_{uu}]^{k,e} &= \int_{V_e} \left([B_u]_e\right)^{\mathrm{T}} \mathbf{Z}^{\mathrm{T}} \left[\overline{Q}(x,y,z)\right]^k \mathbf{Z} \left[B_u\right]_e \mathrm{d}V_e \\
[K_{u\phi}]^{k,e} &= \int_{V_e} \left([B_u]_e\right)^{\mathrm{T}} \mathbf{Z}^{\mathrm{T}} \left[\overline{e}(x,y,z)\right]^k\Big)^{\mathrm{T}} \left[B_\phi\right]_k \mathrm{d}V_e \\
[K_{\phi u}]^{k,e} &= \left([K_{u\phi}]^{k,e}\right)^{\mathrm{T}} \\
[K_{\phi\phi}]^{k,e} &= \int_{V_e} \left([B_\phi]_k\right)^{\mathrm{T}} \left[\overline{\varepsilon}(x,y,z)\right]^k \left[B_\phi\right]_k \mathrm{d}V_e
\end{aligned}
\tag{3.3.21}
$$

the pure mechanical contribution is subdivided into bending-bending, membrane-membrane, bending-membrane, membrane-bending and shear-shear, respectively identified using the subscripts bb, mm, bm, mb and ss; these are not integrated over thickness because, at this point, matrices $[A(x,y,z)]^k$,

$[A_s(x,y,z)]^k$, $[B(x,y,z)]^k$ and $[D(x,y,z)]^k$ already carry this contribution (since the pre-processing phase). The electromechanical coupling contributions are identified using subscripts $u\phi$ and ϕu; the pure electrical contribution with $\phi\phi$. The following equations apply:

$$
\begin{aligned}
[K_{bb}]^{k,e} &= \int_{\Omega_e} ([B_b]_e)^{\mathrm{T}} \, [D(x,y,z)]^k \, [B_b]_e \, \mathrm{d}\Omega_e = \\
&= \sum_{i=1}^{N_{\mathcal{G}_{w,b}}} \left\{ \left([B_b]_{e,i} \right)^{\mathrm{T}} \, [D(x,y,z)]^k \, [B_b]_{e,i} \, \mathcal{G}^i_{w,b} \det(\boldsymbol{\mathcal{J}}_e) \right\} \\
[K_{mm}]^{k,e} &= \int_{\Omega_e} ([B_m]_e)^{\mathrm{T}} \, [A(x,y,z)]^k \, [B_m]_e \, \mathrm{d}\Omega_e = \\
&= \sum_{i=1}^{N_{\mathcal{G}_{w,b}}} \left\{ \left([B_m]_{e,i} \right)^{\mathrm{T}} \, [A(x,y,z)]^k \, [B_m]_{e,i} \, \mathcal{G}^i_{w,b} \det(\boldsymbol{\mathcal{J}}_e) \right\} \\
[K_{bm}]^{k,e} &= \int_{\Omega_e} ([B_b]_e)^{\mathrm{T}} \, [B(x,y,z)]^k \, [B_m]_e \, \mathrm{d}\Omega_e = \\
&= \sum_{i=1}^{N_{\mathcal{G}_{w,b}}} \left\{ \left([B_b]_{e,i} \right)^{\mathrm{T}} \, [B(x,y,z)]^k \, [B_m]_{e,i} \, \mathcal{G}^i_{w,b} \det(\boldsymbol{\mathcal{J}}_e) \right\} \\
[K_{mb}]^{k,e} &= \int_{\Omega_e} ([B_m]_e)^{\mathrm{T}} \, [B(x,y,z)]^k \, [B_b]_e \, \mathrm{d}\Omega_e = \\
&= \sum_{i=1}^{N_{\mathcal{G}_{w,b}}} \left\{ \left([B_m]_{e,i} \right)^{\mathrm{T}} \, [B(x,y,z)]^k \, [B_b]_{e,i} \, \mathcal{G}^i_{w,b} \det(\boldsymbol{\mathcal{J}}_e) \right\} \\
[K_{ss}]^{k,e} &= \int_{\Omega_e} ([B_s]_e)^{\mathrm{T}} \, \chi \, [A_s(x,y,z)]^k \, [B_s]_e \, \mathrm{d}\Omega_e = \\
&= \sum_{i=1}^{N_{\mathcal{G}_{w,s}}} \left\{ \left([B_s]_{e,i} \right)^{\mathrm{T}} \, \chi \, [A_s(x,y,z)]^k \, [B_s]_{e,i} \, \mathcal{G}^i_{w,s} \det(\boldsymbol{\mathcal{J}}_e) \right\}
\end{aligned}
\tag{3.3.22}
$$

$$
\begin{aligned}
[K_{u\phi}]^{k,e} &= \int_{V_e} ([B_u]_e)^{\mathrm{T}} \left([\overline{e}(x,y,z)]^k_{[3,1..3]} \right)^{\mathrm{T}} \, [B_\phi]_k \, \mathrm{d}\Omega_e \, \mathrm{d}z = \\
&= \int_{z_k}^{z_{k+1}} \sum_{i=1}^{N_{\mathcal{G}_{w,\phi}}} \left\{ \left([B_u]_{e,i} \right)^{\mathrm{T}} \left([\overline{e}(x,y,z)]^k_{[3,1..3]} \right)^{\mathrm{T}} \, [B_\phi]_{k,i} \, \mathcal{G}^i_{w,\phi} \det(\boldsymbol{\mathcal{J}}_e) \right\} \mathrm{d}z \\
[K_{\phi u}]^{k,e} &= \int_{V_e} ([B_\phi]_k)^{\mathrm{T}} \left([\overline{e}(x,y,z)]^k_{[3,1..3]} \right)^{\mathrm{T}} \, [B_u]_e \, \mathrm{d}\Omega_e \, \mathrm{d}z = \\
&= \int_{z_k}^{z_{k+1}} \sum_{i=1}^{N_{\mathcal{G}_{w,\phi}}} \left\{ [B_\phi]^{\mathrm{T}}_{k,i} \left([\overline{e}(x,y,z)]^k_{[3,1..3]} \right)^{\mathrm{T}} \, [B_u]_{e,i} \, \mathcal{G}^i_{w,\phi} \det(\boldsymbol{\mathcal{J}}_e) \right\} \mathrm{d}z \\
[K_{\phi\phi}]^{k,e} &= -\int_{V_e} ([B_\phi]_k)^{\mathrm{T}} \, [\overline{\varepsilon}(x,y,z)]^k_{[3,3]} \, [B_\phi]_k \, \mathrm{d}\Omega_e \, \mathrm{d}z = \\
&= -\int_{z_k}^{z_{k+1}} ([B_\phi]_k)^{\mathrm{T}} \, [\overline{\varepsilon}(x,y,z)]^k_{[3,3]} \, [B_\phi]_k \, 4 \det(\boldsymbol{\mathcal{J}}_e) \, \mathrm{d}z
\end{aligned}
\tag{3.3.23}
$$

The strain-displacement matrix $[B_u]_e$ is subdivided into bending $[B_b]_e$ and membrane $[B_m]_e$ contributions, as the following:

$$
[B_u]_e = z \, [B_b]_e + [B_m]_e \tag{3.3.24}
$$

where each strain-displacement coupling matrix is given by (Ferreira, 2009):

$$[B_b]_e = \begin{bmatrix} \text{same order} \Rightarrow w_1^0 \cdots w_n^0 & \theta_{x_1}^0 \cdots \theta_{x_n}^0 & \theta_{y_1}^0 \cdots \theta_{y_n}^0 & u_1^0 \cdots u_n^0 & v_1^0 \cdots v_n^0 \\ 0_{(3\times1)_1} \cdots 0_{(3\times1)_n} & \begin{matrix} \frac{\partial N_1(\xi,\eta)}{\partial x} & \frac{\partial N_n(\xi,\eta)}{\partial x} \\ 0 \quad \cdots \quad 0 \\ \frac{\partial N_1(\xi,\eta)}{\partial y} & \frac{\partial N_n(\xi,\eta)}{\partial y} \end{matrix} & \begin{matrix} 0 & 0 \\ \frac{\partial N_1(\xi,\eta)}{\partial y} & \cdots \; \frac{\partial N_n(\xi,\eta)}{\partial y} \\ \frac{\partial N_1(\xi,\eta)}{\partial x} & \frac{\partial N_n(\xi,\eta)}{\partial x} \end{matrix} & 0_{(3\times2)_1} \cdots 0_{(3\times2)_n} \end{bmatrix} \tag{3.3.25}$$

$$[B_m]_e = \begin{bmatrix} \text{same order} \Rightarrow w_1^0 \cdots w_n^0 & \theta_{x_1}^0 \cdots \theta_{x_n}^0 & \theta_{y_1}^0 \cdots \theta_{y_n}^0 & u_1^0 \cdots u_n^0 & v_1^0 \cdots v_n^0 \\ 0_{(3\times3)_1} \cdots 0_{(3\times3)_n} & \begin{matrix} \frac{\partial N_1(\xi,\eta)}{\partial x} & \frac{\partial N_n(\xi,\eta)}{\partial x} \\ 0 \quad \cdots \quad 0 \\ \frac{\partial N_1(\xi,\eta)}{\partial y} & \frac{\partial N_n(\xi,\eta)}{\partial y} \end{matrix} & \begin{matrix} 0 & 0 \\ \frac{\partial N_1(\xi,\eta)}{\partial y} & \cdots \; \frac{\partial N_n(\xi,\eta)}{\partial y} \\ \frac{\partial N_1(\xi,\eta)}{\partial x} & \frac{\partial N_n(\xi,\eta)}{\partial x} \end{matrix} & \end{bmatrix} \tag{3.3.26}$$

$$[B_s]_e = \begin{bmatrix} \text{same order} \Rightarrow w_1^0 \cdots w_n^0 & \theta_{x_1}^0 \cdots \theta_{x_n}^0 & \theta_{y_1}^0 \cdots \theta_{y_n}^0 & u_1^0 \cdots u_n^0 & v_1^0 \cdots v_n^0 \\ \begin{matrix} \frac{\partial N_1(\xi,\eta)}{\partial x} & \cdots & \frac{\partial N_n(\xi,\eta)}{\partial x} \\ \frac{\partial N_1(\xi,\eta)}{\partial y} & & \frac{\partial N_n(\xi,\eta)}{\partial y} \end{matrix} & \begin{matrix} N_1(\xi,\eta) & \cdots & N_n(\xi,\eta) \\ 0 & & 0 \end{matrix} & \begin{matrix} 0 & \cdots & 0 \\ N_1(\xi,\eta) & & N_n(\xi,\eta) \end{matrix} & 0_{(2\times2)_1} \cdots 0_{(2\times2)_n} \end{bmatrix} \tag{3.3.27}$$

where $[B_u]$, $[B_b]$, $[B_m]$ and $[B_s]$ are, respectively, the strain-displacement coupling matrix of mechanical (bending plus membrane), bending, membrane and shear contributions. The electric potential matrix $[B_\phi]$ is given by (Loja et al., 2001):

$$[B_\phi] = \begin{bmatrix} 1/h_1 & \cdots & 0 \\ \vdots & \ddots & \vdots \\ 0 & \cdots & 1/h_{N_{pl}} \end{bmatrix} \tag{3.3.28}$$

where each electric potential matrix for each piezoelectric layer pl, $[B_\phi]_k$, corresponds to the diagonal positions of this matrix, i.e. $1/h_1 \cdots 1/h_{N_{pl}}$, which in this case are constants (inverse of the piezoelectric layer thickness).

Moving on to the load vectors, it is possible to define mechanical and electrical components. The former can be concentrated loads or distributed pressures along the surface Ω and the latter electric potentials/voltages applied to piezoelectric layers. Considering the concentrated loads, mechanical forces or moments, are applied directly onto the mechanical force vector $\{F_u\}$ (depending on the DOFs

locations). However, considering pressures' modelling, in-plane integration must be carried out as:

$$\begin{aligned}\{F_u\}^e &= \int_{\Omega_e} \{N(\xi,\eta)\}\, P\, \mathrm{d}\Omega_e = \\ &= \sum_{i=1}^{N_{\mathcal{G}_{w,b}}} \left\{\{N(\xi,\eta)\}\, P\, \mathcal{G}^i_{w,b} \det(\boldsymbol{\mathcal{J}}_e)\right\}\end{aligned} \tag{3.3.29}$$

where P is the specified pressure in [Pa] (Pascal). Once again, the same integration rules apply for Lagrange and Kriging formulations.
The electrical load vector $\{F_\phi\}$ is given by:

$$\{F_\phi\}^{k,e} = [K_{u\phi}]^{k,e}\, \phi^k \tag{3.3.30}$$

The finite element static analyses are carried out using the usual equilibrium equation after the imposition of the adequate set of **M**echanical **B**oundary **C**onditions (MBCs):

$$[K_{uu}]\,\{q\} = \{\{F_u\} - \{F_\phi\}\} \Leftrightarrow \{q\} = [K_{uu}]^{-1}\,\{\{F_u\} - \{F_\phi\}\} \tag{3.3.31}$$

from this equation, it is possible to obtain the solution of mechanical DOFs, the generalized nodal displacements vector $\{q\}$. Then, the electrical DOFs are obtained by the following relation (Wang, 2004):

$$\{\phi\} = -\,[K_{\phi\phi}]^{-1}\left([K_{\phi u}]\,\{q\} + [K_{\phi\phi}]_{[..,1]}\,\{V\}^k\right) \tag{3.3.32}$$

where $[K_{\phi\phi}]_{[..,1]}$ is the first column of the corresponding sub-matrix $[K_{\phi\phi}]$ and $\{V\}^k$ contains the electric voltages applied to each layer. Rewriting Eq. (3.3.18) for free harmonic vibrations, yields:

$$\begin{aligned}&\left([K_{uu}] - \{\omega_n\}^2\,[M_{uu}]\right)\{u\} + [K_{u\phi}]\,\{\phi\} = 0 \\ &[K_{\phi u}]\,\{u\} + [K_{\phi\phi}]\,\{\phi\} = 0\end{aligned} \tag{3.3.33}$$

where ω_n corresponds to each natural frequency in $\left[\mathrm{rad}\cdot\mathrm{s}^{-1}\right]$ (radian per second), associated to mode n; throughout this work, natural frequencies can also be presented in [Hz] (Hertz). This eigenvalue/vector problem can be solved considering two different **E**lectric **B**oundary **C**onditions (EBCs), either closed or open-circuit. In terms of condensation of electrical DOFs, by matrix algebra, the following equations apply (Wang, 2004):

$$\left([K^*] - \{\omega_n\}^2\,[M_{uu}]\right)\{u\} = 0 \quad \text{with} \quad [K^*] = \begin{cases} [K_{uu}] & \text{if } \textit{closed} \\ [K_{uu}] - [K_{u\phi}]\,[K_{\phi\phi}]^{-1}\,[K_{\phi u}] & \text{if } \textit{open} \end{cases} \tag{3.3.34}$$

Closed-circuit (or sensory) conditions only consider the mechanical contribution of the structure's behaviour, where electric potentials at external surfaces of the piezoelectric patches are imposed to be zero. In addition, open-circuit (or active) conditions, besides the mechanical contribution, also consider the electrical one, making the electric potentials free at the external surfaces. For the latter conditions, the electric potential field is less constrained, which increases the induced stiffness, also increasing the structure's natural frequencies (Wang, 2004).

3.3.5 Strains and stresses computation

Strains and stresses are computed for all elements and evaluated at user-defined z-coordinates, $z^k_{\epsilon\sigma}$, for each layer; these are, by default, calculated at the Gauss points global coordinates, $[\mathcal{G}_{xy}]$, associated to the reduced p integration rule (depending on the finite element used, number of nodes).

There are numerous examples of authors who state that the strains and stresses are more accurate when computed at these points – among others, Reddy (2004) states that *stresses computed at the Gauss points associated with the Gauss rule used to evaluate the stiffness matrix of an element are the most accurate*; stress averaging methodologies were not implemented, in order to simplify the work. In any case, the user is able to compute these quantities wherever desired, e.g. at elements' nodes, etc. The following equations apply:

$$\begin{aligned}
\{\epsilon\}_b^{k,e}(z) &= \begin{Bmatrix}\epsilon_{xx}\\ \epsilon_{yy}\\ \gamma_{xy}\end{Bmatrix}^{k,e} = [B_u]_e\,\mathbf{u}^e = (z\,[B_b]_e + [B_m]_e)\,\mathbf{u}^e \\
\{\sigma\}_b^{k,e}(z) &= \begin{Bmatrix}\sigma_{xx}\\ \sigma_{yy}\\ \tau_{xy}\end{Bmatrix}^{k,e} = \left(\left[\overline{Q}(x,y,z)\right]^k_{[1..3,1..3]}\right)\{\epsilon\}_b^{k,e}(z) \\
\{\epsilon\}_s^{k,e} &= \begin{Bmatrix}\gamma_{yz}\\ \gamma_{xz}\end{Bmatrix}^{k,e} = [B_s]_e\,\mathbf{u}^e \\
\{\sigma\}_s^{k,e} &= \begin{Bmatrix}\tau_{yz}\\ \tau_{xz}\end{Bmatrix}^{k,e} = \chi^k\left(\left[\overline{Q}(x,y,z)\right]^k_{[4..5,4..5]}\right)\{\epsilon\}_s^{k,e}
\end{aligned} \tag{3.3.35}$$

note that it is also possible to user-define different shear correction factors for each layer, χ^k. Finally, for each layer, the in-plane strains and stresses are evaluated (or not) at the user-defined z-coordinates:

$$\left(\{\epsilon\}_b^{k,e}(z)\right)\Big|_{z=z^k_{\epsilon\sigma}} = \{\epsilon\}_b^{k,e}\left(z^k_{\epsilon\sigma}\right), \quad \left(\{\sigma\}_b^{k,e}(z)\right)\Big|_{z=z^k_{\epsilon\sigma}} = \{\sigma\}_b^{k,e}\left(z^k_{\epsilon\sigma}\right) \tag{3.3.36}$$

In addition to the main stress components, the algorithm also computes the Von Mises stress (identified using subscript VM), which is given by:

$$\begin{aligned}
sc &= 6\left\{\left(\{\sigma_{xy}\}^{k,e}\right)^2 + \left(\{\sigma_{yz}\}^{k,e}\right)^2 + \left(\{\sigma_{xz}\}^{k,e}\right)^2\right\} \\
\{\sigma_{VM}\}^{k,e} &= \sqrt{\frac{1}{2}\left\{\left(\{\sigma_{xx}\}^{k,e} - \{\sigma_{yy}\}^{k,e}\right)^2 + \left(\{\sigma_{yy}\}^{k,e}\right)^2 - \left(\{\sigma_{xx}\}^{k,e}\right)^2 + sc\right\}}
\end{aligned} \tag{3.3.37}$$

where sc denotes "shear components", but it is only an auxiliary variable to avoid space constraints. Of course that this yield criterion is mostly used when the material is isotropic, but it has been implemented. The following subsection addresses finite element implementation, regarding software.

3.3.6 Finite element implementation

In terms of a generic overview concerning the main software used to carry out the present work, a general sequence was followed, as illustrated in Figure 3.17.

All files associated with this work are stored inside a cloud, i.e. Dropbox®, with the objective of maximizing security and backup capabilities.

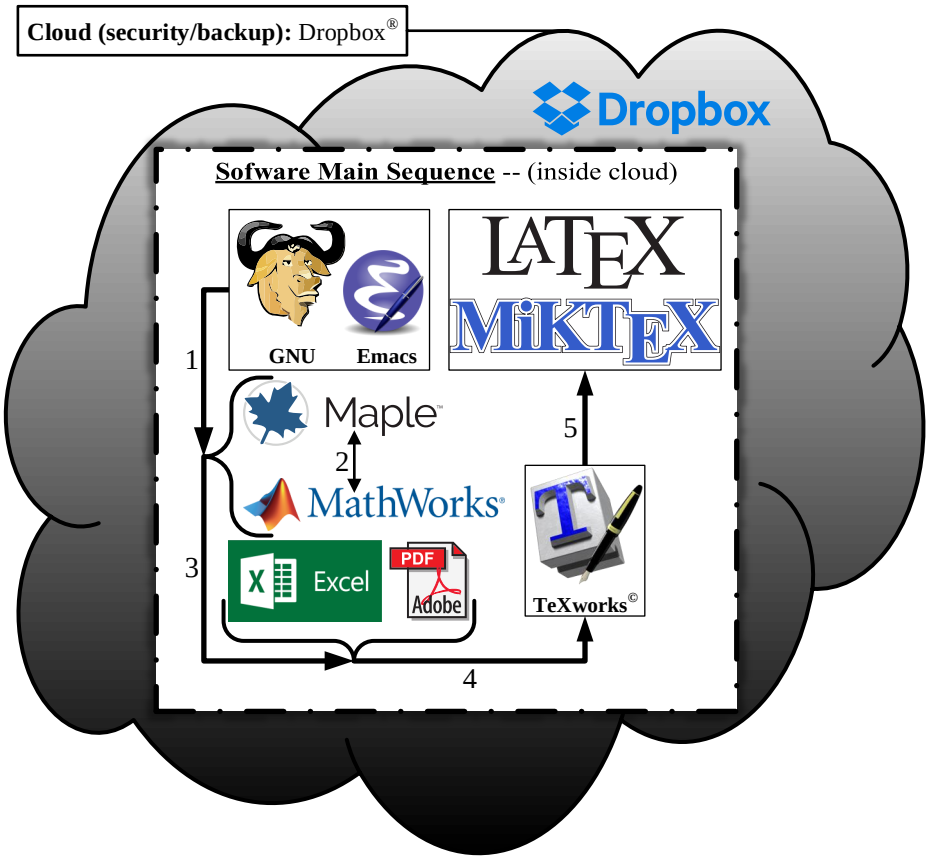

Figure 3.17: Software main sequence scheme, inside the chosen cloud.

More specifically, the first step is to use GNU Emacs, a free-ware code editor, to program all Maple® procedures and MATLAB® functions. This way, user-defined FEM and optimization case studies are solved inside Maple® and MATLAB® batches, considering an automatic interaction between both, by means of symbolic and numerical computation; the algorithms were programmed in a certain way, to put together the advantages of these two programs: for instance, Maple® can be stronger concerning symbolic operations, whereas MATLAB® offers more advanced graphical tools and faster eigen computations when both stiffness and mass matrices are considerably big. Of course that more efficient programming languages could have been used, e.g. Fortran, Python, C+... but taking into account the available time and experience, at this moment, Maple® and MATLAB® together seemed to be a fair choice, in terms of computational efficiency and graphical output.

The outputs are saved and gather as Excel® files (tabular format), as well as .pdf Portable Document format (figures, plots, graphics, etc.). Finally, all results can be gathered, edited and compiled using TEXworks©, in order to write all presentations (preliminary, conferences and final), papers and the final document; all .pdf presentations/documents are obtained by means of MiKTEX and LATEX capabilities.

In sum, an efficient, automatic/generalized and integrated symbolic-numerical-graphical package devoted to the analysis of plate-type structures and its non-linear meta-heuristic optimization was implemented, where all outputs are pre-programmed with a methodical approach, minimizing the struggle between raw data and document writing – with tables, interactive plots and animations, results become dynamic with the objective of achieving innovation inside .pdf documents.

In Figure 3.18 a global computational scheme for both FEM and bat algorithms is presented. The interaction between FEM algorithm and MHBA starts with an user-defined Array structure, where each position corresponds to one case study – this file is called inputs.mpl. Inside each position, a matrix is stored and gathers all the needed information to fully define each case study: e.g. geometry (different layers, stacking sequences, etc.), MBCs and EBCs, mechanical and electrical loads, mesh (element types, formulation/interpolation types, etc.), materials (multilayered approach, engineering constants, properties, etc.), processing options (integration schemes, etc.), FEM analysis options (static, dynamic, etc.), optimization options (MHBA inputs, variables, DE and micro characteristics, DVs' bounds, control points, etc.), numerical and graphical outputs options (post-processor), formatting inside Excel® (fonts, colours, etc.).

Using such methodology, the user is able to create an Array with n positions (e.g. using fast copy paste and changing details), leaving several PCs or servers solving the n FEM plus (or not) optimization problems. The results are saved and organized automatically inside specific folders (see Appendix E for one example of directory tree with outputs). In a work such as this one, the only way to obtain this amount of results is by programming both algorithms using this efficient methodology; otherwise, it would be very time consuming, specially when meta-heuristics is involved, where several inputs must be pre-tested in order to maximize the optimizations' results.

This inputs file is read by main.mw, which is the Maple® GUI interface, where the algorithms are run. This file contains information about innovative research ideas to implement in the future, information about the current version of the program (capabilities, etc.), also reads Maple® procedures and MATLAB® functions, and the main procedure, called main.mpl.

Note that the arrow between inputs.mpl and main.mw is bidirectional, because in certain optimization case studies, the MHBA needs to inject new inputs values inside the current case study input data (inside inputs.mpl), along optimization iterations.

The main.mpl file is the brain of the package. It contains a considerable amount of code, to control everything, starting with inputs assignments, calling every single procedure and function about FEM and optimization, ending with outputs storage.

The FEM algorithm general architecture, for multilayered smart structures, can be analysed in Figure 3.19. A conventional FEM nomenclature was adopted, dividing the program into Pre-Processor, Processor and Post-Processor. Inside each one, several procedures and functions are stored, which are called when needed; almost all of them possess self-explanatory names. Pseudo-code should be written for all of them, but due to their complexity, size and available time, such task is not viable.

3.4 Micro-Hybrid-Bat-Algorithm (MHBA)

The BA is supported upon the following main three principles: the echolocation capacity, used to sense distances and to differentiate between prey and barriers; the random flying capacity, characterized by velocity, frequency and loudness; the ability to vary frequency and loudness, depending on the proximity of the object. From Yang, X.-S. (2014), the following assumptions (idealized rules) about echolocation characteristics of micro-bats apply:

1. *All bats use echolocation to sense distance, and they also "know" the difference between food/prey and background barriers*;
2. *Bats fly randomly with velocity v_i at position x_i. They can automatically adjust the frequency (or wavelength) of their emitted pulses and adjust the rate of pulse emission $r \in [0, 1]$, depending on the proximity of their target*;

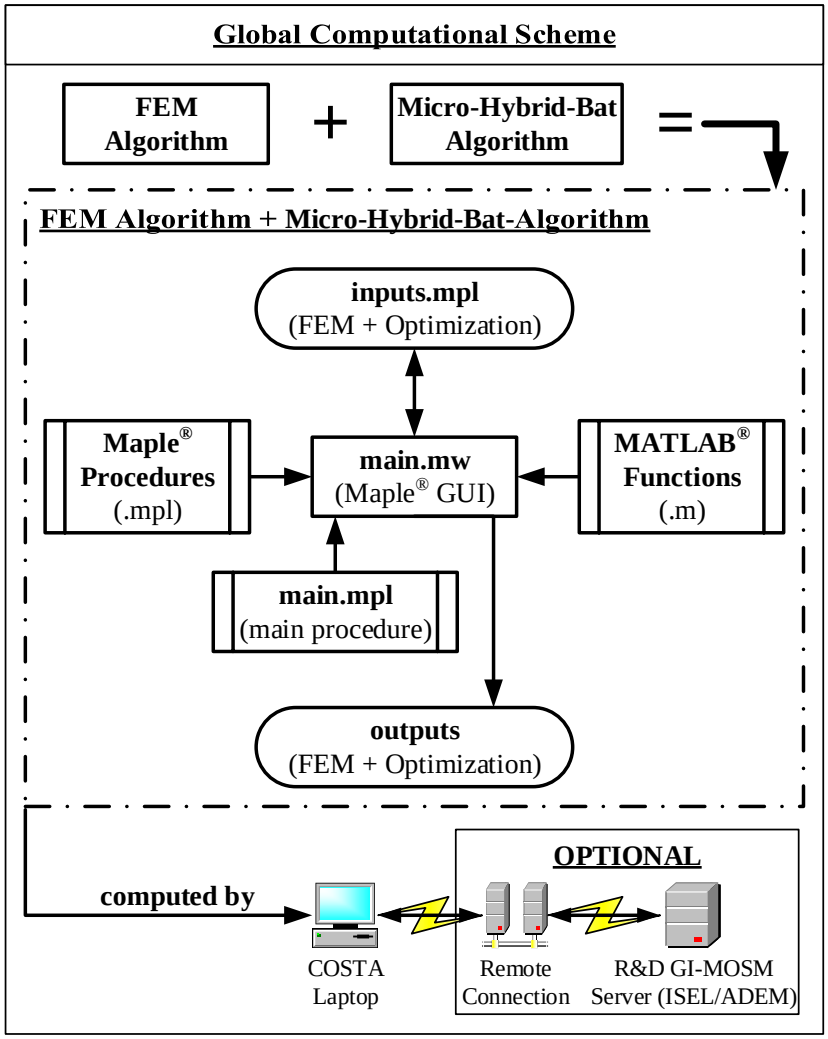

Figure 3.18: Global computational scheme for both FEM and bat algorithms.

3. *Although the loudness can vary in many ways, we assume that the loudness varies from a large (positive) A_0 to a minimum value A_{min}.*

To this purpose, in BA each bat in a population of n individuals is initialized with a starting position, rate of pulse, loudness and frequency, which evolute during the number of iterations/generations necessary to meet the stopping criteria.

Each new generation of bats is updated through the movement of the existing ones, according to the relations:

$$\begin{aligned} f_i^t &= f_{min} + (f_{max} - f_{min})\,\beta \\ v_i^{t+1} &= v_i^t + \left(x_i^t - best\right) f_i^t \\ x_i^{t+1} &= x_i^t + v_i^t \end{aligned} \tag{3.4.1}$$

where $\beta \in [0,1]$, f_i^t is the pulse frequency of the i-th bat at an instant t. The lateral bounds of the pulse frequency are f_{min} and f_{max}. The position and velocity of the i-th bat at the instant t are denoted by x_i^t and v_i^t respectively. $best$ stands for the best solution until the current instant.

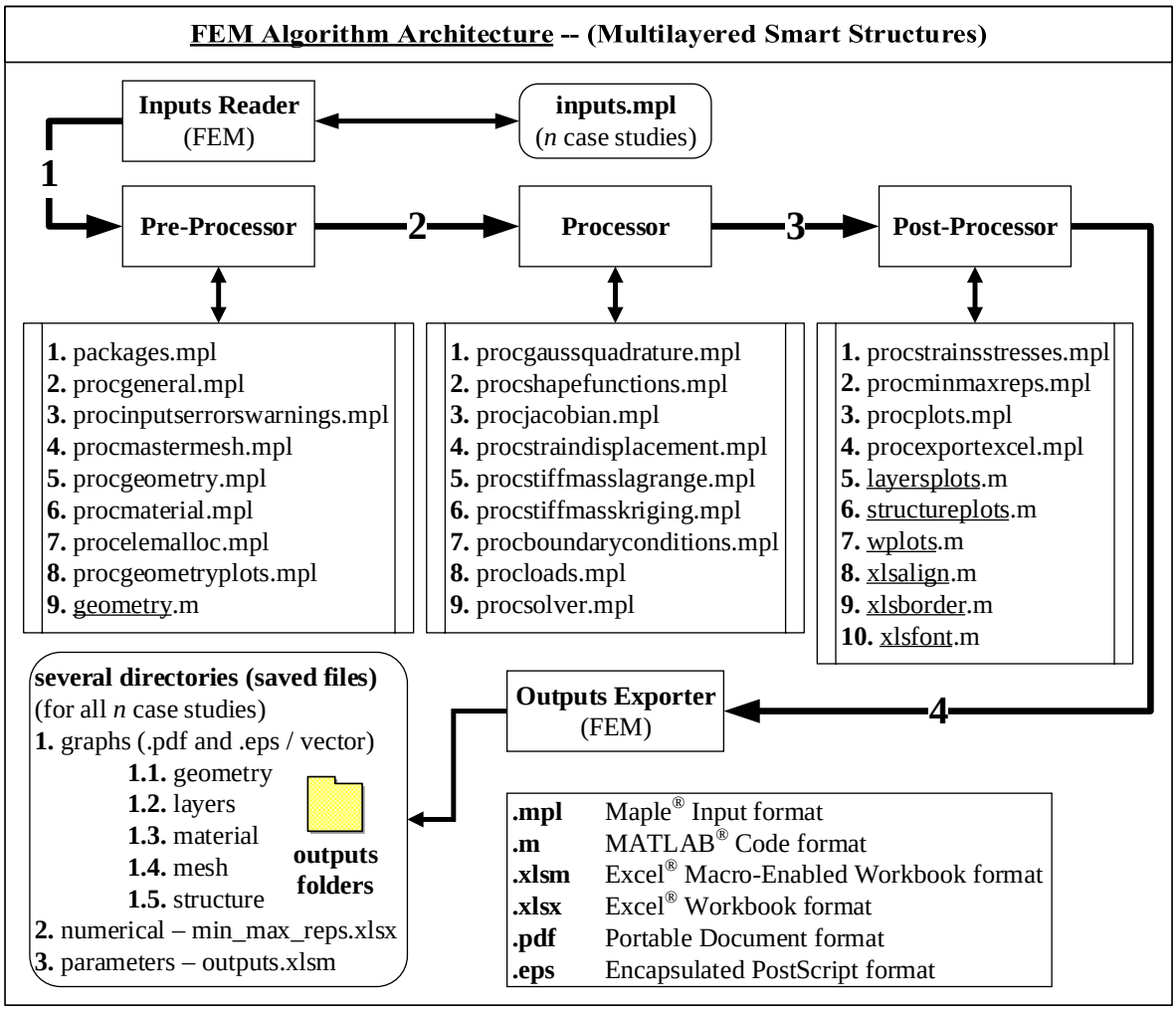

Figure 3.19: FEM algorithm architecture scheme.

The local search that starts depending on the proximity of the pulse rate of each bat r_i^t, to a randomly generated rate, will modify the current global best solution as follows:

$$x^t = best + \epsilon A_i^t \left(2\beta - 1\right) \tag{3.4.2}$$

which differs from the original BA, as in this latter the loudness was an average quantity, considering the contribution of all the bats in the population. In the present case, an improved local search proposed by Fister Jr. et al. (2013) was adopted (the HBA). The parameters involved on the updating of the i-th bat position are the position of the global best solution, a scaling factor ϵ and the loudness of each bat A_i^t at that generic instant t. Again β is a random value in $[0, 1]$.

Pulse rate and loudness parameters closely mimetic the behaviour of bats, as the first increases when the bat finds a prey and at the same time the loudness decreases. These relations are established according to:

$$\begin{aligned} A_i^{t+1} &= \alpha A_i^t \\ r_i^t &= r_i^0 \left(1 - e^{(-\gamma\epsilon)}\right) \end{aligned} \tag{3.4.3}$$

with α and γ being constants that enable a progressive variation of loudness and pulse rate. These constants have a similar effect to the cooling schedule parameter present in simulated annealing method (Loja et al., 2002). As in other optimization techniques, the current iteration best is registered along with the corresponding DVs, maintaining a log that allows tracing the evolution of the whole process.

Since BA is a meta-heuristic optimization algorithm, resulting in a certain level of randomness when generating new solutions, the input parameters can have a huge impact on its convergence capabilities (Yang, X.-S., 2010). More specifically, the lower and upper bounds of the echolocation parameters, i.e. *frequency* f, *pulse rate* r and *loudness* A, are crucial. In the present work, before every optimization case study, several random combinations of these parameters are pre-tested using low numbers of iterations (number of generations N_{gen} and population sizes n); then, the best inputs are selected to exploit the case studies with more iterations, and hopefully reach good results (this is important in terms of computational efficiency). It is also well known from literature that there is not a standard "recipe" of inputs, associated with case studies' categories; i.e. every case study is different, and for that reason, different MHBA's inputs must be tested for each one; among others, Hasançebi et al. (2013) state that "*each optimization problem has unique features of its own, and in most cases a problem-wise reformulation is necessary to achieve the best performance of an algorithm for a particular class of problems*".

Hasançebi et al. (2013) give an excellent review and methodology concerning BA's implementation to solve structural optimization problems, as well as descriptions about the influence of each input variable on BA's convergence performance. The present approach enables one to specify several different DVs, either continuous or discrete, inside the same optimization case study; these are specified using lower and upper bounds, or discrete values.

As already stated before, a hybridized version of BA is also implemented in this work, where the local search is performed according to DE technique (Fister Jr. et al., 2013; Loja et al., 2014). At each generation, new bat positions are achieved by differential mutation wherein it is possible to adopt either one or two scaled differences of trial solutions. In both cases, the mutation is based on the global best solution so far, so DE schemes used can be in short designated by DE/best/1 and DE/best/2. Considering the recombination/crossover operator, an arithmetic recombination is used, wherein an adaptive or not, perturbation factor can be selected. This is also used in other evolutionary approaches for other particular parameters, such as in the case of the PSO (Loja, 2014; Salerno, 1997).

Finally, the optimization algorithm here developed, also includes a micro-GA technique. This "micro" technique, is defined by Senecal (2000) as *a "small population"* GA *that operates on the principles of natural selection or "survival of the fittest" to evolve the best potential solution (i.e., design) over a number of generations to the most-fit, or optimal, solution*. This approach, enables one to considerably reduce the number of individuals in each bat population, increasing the computational efficiency for particular optimization case studies here developed (e.g. optimization of patches xy-coordinates and electric potentials to minimize plates' deflections). According to Alvarez (2002), a *micro genetic algorithm evolves a very small population that must be restarted whenever the population loses its genetic diversity*. This author also states that a micro-GA is more efficient in terms of improved rate of converge, especially in the first few generations.

In sum, the MHBA mixes together the original BA, the *hybrid* technique associated with DE (perturbation factors, etc.) and *micro* technique from GAs (populations' reinitializations, etc.).

The following subsection addresses the optimization implementation, very briefly.

3.4.1 Optimization implementation

In order to understand the optimization implementation of the MHBA it is convenient to start with both original BA and HBA. This subject is addressed by several authors, e.g. Fister Jr. et al. (2013); Hasançebi et al. (2013); Yang, X.-S. (2010, 2014).

From Fister Jr. et al. (2013), the pseudo-codes are obtained for both original BA and HBA, illustrated in Figures 3.20 and 3.21, respectively.

Similarly to Hasançebi et al. (2013), by employing the fundamental principles of echolocation behaviour of bats, the present MHBA is also characterized by similarities with both original BA and HBA. However, "*a major adaptation of the technique is carried out in its formulation and outline to generate an algorithm that performs efficiently for structural optimization problems*" (in the present case, multilayered smart structures).

Firstly, bat populations are initialized, as well as pulse rates and loudness. Then, the main optimization process starts (iterations), where new solutions are generated by adjusting frequency, updating velocities and locations/solutions and flying randomly.

Note that, in this work, OFs are the minimization or maximization of some discrete FEM output variables, instead of symbolic functions; this means that each set of DVs origins a particular OF value (solution), which is compared with the remaining ones.

Comparing both original BA and HBA, the only difference is on point number 9 (*modify the solution using "DE/rand/1/bin"*). This notation is often used to identify DE techniques, where crossover and mutation can be performed in many ways; according to Fister Jr. et al. (2013), this *denotes that the base vector is randomly selected, 1 vector difference is added to it, and the number of modified parameters in mutation vector follows binomial distribution*. Here, perturbation factors are used to modify the current solutions, $Fper_i$ and $Fper_f$.

When one uses HBA or MHBA, since hybrid is activated, it is possible to use either fixed or adaptive perturbation factors $Fper$. These factors modify the bat-solutions in order to optimize the problem iteratively and are defined by the following equations:

$$\begin{aligned} &\Delta F = \frac{Fper_f - Fper_i}{N_{gen}} \Rightarrow F_{per} = Fper_i + \Delta F\,(t-2)\,, \quad \text{if Adaptive = TRUE} \\ &Fper = Fper_i, \quad \text{if Adaptive = FALSE} \end{aligned} \tag{3.4.4}$$

where t is the generations' cycle variable, from 2 to N_{gen}.

Regarding the current optimization implementation, Figure 3.22 shows the general MHBA architecture. In comparison with the FEM algorithm, this one is constituted by less procedures, i.e. only 3; it was also subdivided into Pre-Processor, Processor and Post-Processor, associated with the procedures procpopini.mpl, procbat.mpl and procoptimizationplots.mpl, respectively.

The MHBA's implementation is similar to the ones illustrated in Figures 3.20 and 3.21, with particular differences and changes to enable the interaction with the FEM algorithm. Concerning the micro approach, the user is able to specify one vector containing bats' generations numbers, in which the bats' populations are going to be randomly reinitialized; for instance, considering one optimization case study with 5 generations, $N_{gen} = 5$, it is possible to automatically reinitialize the populations at generations number 2 and 4, by defining a vector such as $\{2, 4\}$.

In sum, three types of BAs were programmed in the same optimization algorithm, which the user controls by means of several inputs. The first one is the traditional BA, which was not used in any optimization case study in this work; the second one, the HBA, considers DE characteristics; and finally the third one, the MHBA, adds to the HBA the micro-GA approach. In order to identify the optimization algorithm's mode used in each case study, a specific notation was created:

Algorithm 1 Original Bat Algorithm

Objective function $f(x)$, $x = (x_1, ..., x_d)^T$
Initialize the bat population x_i and v_i for $i = 1 \dots n$
Define pulse frequency $Q_i \in [Q_{min}, Q_{max}]$
Initialize pulse rates r_i and the loudness A_i
while $(t < T_{max})$ // number of iterations
  Generate new solutions by adjusting frequency, and
  updating velocities and locations/solutions [Eq.(2) to (4)]
  if($rand(0,1) > r_i$)
    Select a solution among the best solutions
    Generate a local solution around the best solution
  end if
  Generate a new solution by flying randomly
  if($rand(0,1) < A_i$ *and* $f(x_i) < f(x)$)
    Accept the new solutions
    Increase r_i and reduce A_i
  end if
  Rank the bats and find the current best
end while
Postprocess results and visualization

Figure 3.20: Original BA pseudo-code. From Fister Jr. et al. (2013).

Algorithm 2 Hybrid Bat Algorithm

Objective function $f(x)$, $x = (x_1, ..., x_d)^T$
Initialize the bat population x_i and v_i for $i = 1 \dots n$
Define pulse frequency $Q_i \in [Q_{min}, Q_{max}]$
Initialize pulse rates r_i and the loudness A_i
while $(t < T_{max})$ // number of iterations
  Generate new solutions by adjusting frequency, and
  updating velocities and locations/solutions [Eq.(2) to (4)]
  if($rand(0,1) > r_i$)
    Modify the solution using "DE/rand/1/bin"
  end if
  Generate a new solution by flying randomly
  if($rand(0,1) < A_i$ *and* $f(x_i) < f(x)$)
    Accept the new solutions
    Increase r_i and reduce A_i
  end if
  Rank the bats and find the current best
end while
Postprocess results and visualization

Figure 3.21: HBA pseudo-code. From Fister Jr. et al. (2013).

(1.) BA → **not** used;

(2.) HBA → Hybrid (BA+DE) → **always** used;

(3.) MHBA → MicroHybrid (BA+DE+micro-GA) → **sometimes** used.

Hybrid (BA+DE) mode is always active throughout all optimization case studies in this work, as well as the Adaptive mode, meaning that the perturbation factors are adaptive. This approach was adopted because due to previously carried out numerical tests, the optimization algorithm showed much higher performance comparing to Hybrid (BA+DE) = Adaptive = FALSE. However, some case studies are computed with MicroHybrid (BA+DE+micro-GA) = TRUE, and others with FALSE.

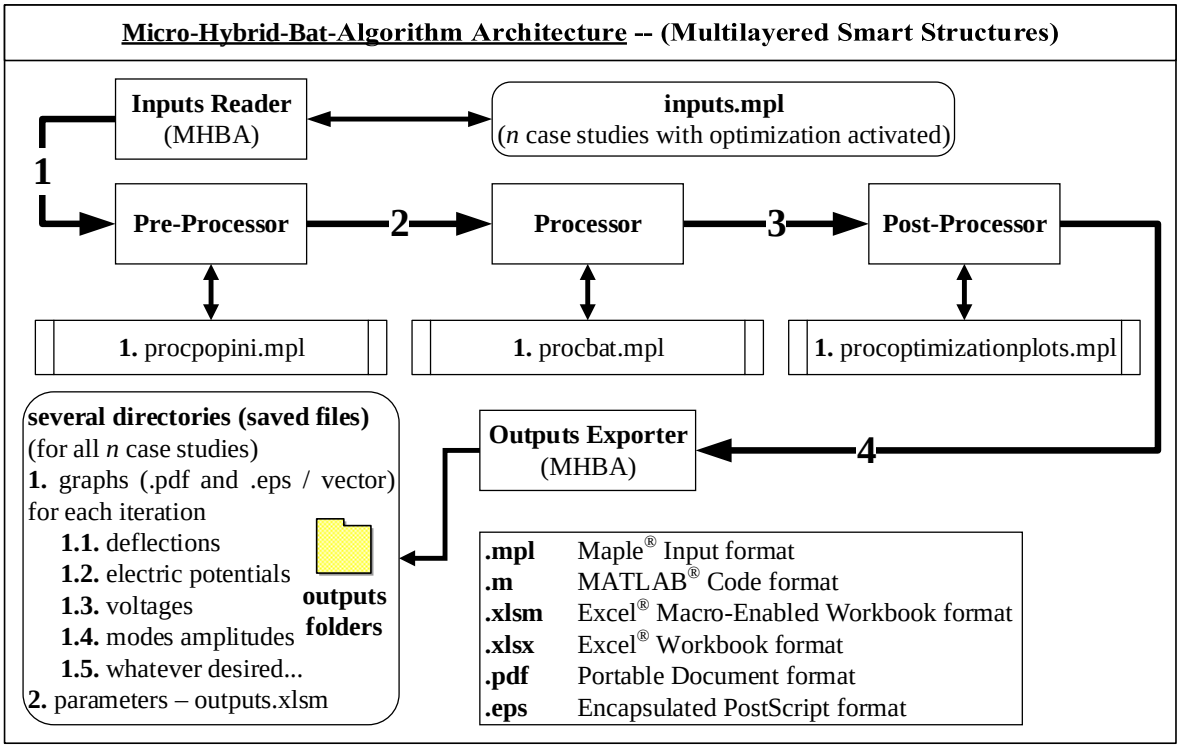

Figure 3.22: MHBA architecture scheme.

The following chapter specifies, shows the results and their respective discussion, associated with all case studies developed in this work, using both present FEM and bat algorithms. The case studies are categorized into **validation**, **parametric** and **optimization**, in order to follow a logic sequence.

Chapter 4

Case Studies

In the following sections, several case studies are presented, categorized into **validation**, **parametric** and **optimization**. Some of these case studies originated several scientific communications/talks at both national and international **conferences** (**proceedings**), as well as publications in international scientific **journals**. These are cited along the present chapter, in the subsections associated with each published case study; the following list summarizes all scientific products associated with this thesis:

- **National scientific conference / proceedings:**
  1. 4th Workshop on Mechanical Engineering and Maintenance Engineering (WEMEM). Took place in 02 November 2016, at Lisbon Superior Engineering Institute (ISEL), Lisbon, Portugal. Title is "*Mechanical Behaviour of Adaptive Structures*" (Costa, 2016b).
- **International scientific conference / proceedings:**
  2. 2nd International Conference on **Mech**anics of **Comp**osites (MECHCOMP2). Took place in 11-14 July 2016, at University of Porto (FEUP), Oporto, Portugal. The communication is entitled "*Bat-Inspired Optimization of Adaptive FGM Plates*" (Costa and Loja, 2016b).
- **International scientific journals (published):**
  3. *AIMS Materials Science Journal*. Pub. in 05 July 2016. The pub. is entitled "*Assessing the static behavior of hybrid CNT-metal-ceramic composite plates*" (Costa and Loja, 2016a);
  4. ***R**esearch on **E**ngineering **S**tructures and **M**aterials* (RESM) Journal. Published in 01 September 2016 (online first). The publication is entitled "*On the characterization of the free vibrations behavior of multiscale composite plates*" (Costa and Loja, 2016c).
- **International scientific journals (submitted):**
  5. *Journal of Composite Structures*. The publication is entitled "*Bat-inspired optimization of multilayered adaptive structures*";
  6. *Journal of Composites Part B: Engineering*. The publication is entitled "*Optimal design of smart composite structures using a refined bat-algorithm*".

NOTE: This chapter contains pages 101 to 142, which is 42 in total.

4.1 Validation studies

The validation studies' organization follows a logic sequence, from the less to the most complex ones, in terms of modelled materials and type of structures. First of all, a straightforward case study is carried out to validate different integration schemes. Afterwards, all outputs resulting from this same structure are compared with a model programmed using the commercial FEM software, AMAPDL. Then, after ensuring the correct implementation of the method, by comparing DOFs, natural frequencies, strains and stresses, functionally graded structures along thickness direction are addressed. Finally, to end the validations' section, several multilayered smart structures are modelled, considering both static and dynamic (free vibrations) behaviours, where different EBCs are validated (closed and open-circuit), smart materials combined with orthotropic ones, both actuation and sensor configurations, and so on. All validations are carried out and the respective results compared with scientific references, such as relevant books and papers about these subjects.

Before starting the case studies themselves, it is relevant to note that the following notation was used to specify MBCs: (x_0, x_1, y_0, y_1) are the beams' or plates' edges corresponding, respectively, to the coordinates $(x = x_{min}, x = x_{max}, y = y_{min}, y = y_{max})$. Finally, with the same coordinates' order, four letters are defined to specify the MBCs, assigned to each edge, where "C" means clamped, "S" simply-supported and "F" free. For instance, recalling the global coordinate system shown in Figure 3.15: if that plate was subjected to MBCs described by the nomenclature (CFFF), it would mean that the edge at $x = x_{min}$ was clamped and the remaining three, $x = x_{max}, y = y_{min}, y = y_{max}$, were free – all combinations of MBCs are modelled by the present algorithm, in which the user is able to control the constraints applied to each DOF, individually, at different in-plane coordinates of the mesh. Note that, for all case studies in this work, the same coordinate systems described in Chapter 3 apply, because the present FEM algorithm was programmed this way – this facilitates the creation of each case study concerning the inputs, as well as the interpretation of results.

In addition, note that sometimes the words "**C**ase **S**tudy" are abbreviated to simply "CS"; this nomenclature is often used in the present work to optimize figures'/tables' sizes.

All relative deviations throughout this work were calculated with $|(pre - ref)|/ref \times 100$, where pre is the present result and ref is the "target" from other reference.

The first validation example, shown in the next subsection, consists of a simply-supported, square plate subjected to an uniformly distributed transverse load, from Reddy (2006). Similarly to this one, other small case studies were also programmed along the whole process, in order to validate several programming details, such as coordinates transformations for orthotropic materials and so on. To this purpose, among others, references Reddy (2004, 2006) were very useful; it is not important to mention and specify in detail those smaller validation case studies, because throughout the present section more complex multilayered structures are validated, mixing different materials, BCs, mesh sizes, etc. and proving the accuracy of the present programming methodology. Only the most important validation studies are presented, providing a general overview. This way, the present parametric and optimization case studies are supported by these validations, minimizing eventual mistakes or non-compliances.

4.1.1 Standard, benchmarking study: Reddy, J.N.

This is a very simple example, suitable to start this section, with the objective of validating the implemented FEM, considering different Lagrangian elements and integration schemes. In addition, it also enables (indirectly) the validation of mesh sizes and convergence, stress computation, isotropic

material modelling, MBCs, load application, etc. This proved to be a good benchmarking case study due to its simplicity, since the beginning and throughout the present FEM programming.

The author investigates the *effect of reduced integration, thickness, and mesh on the centre deflection and normal stress* σ_{xx}. The displacement and stress are non-dimensionalized according to the following equations:

$$\overline{w} = \frac{w(0,0)\, Eh^3 \times 10^2}{q_0 a^4}, \quad \overline{\sigma}_{xx} = \frac{\sigma_{xx}\left(A, A, \pm\frac{h}{2}\right)}{q_0}\left(\frac{h}{a}\right)^2 \tag{4.1.1}$$

where $\overline{w}$ is the non-dimensionalized deflection, $w(0,0)$ the centre deflection of the plate, E the elastic modulus, h the plate's thickness, q_0 the uniform transverse pressure applied on top of the plate's surface, a the side dimension. In addition, $\overline{\sigma}_{xx}$ is the non-dimensionalized xx-component normal stress, which depends on the obtained stress σ_{xx} evaluated at the coordinates $\left(A, A, \pm\frac{h}{2}\right)$; these correspond to Gauss points' locations, with respect to the global xy-coordinates and vary accordingly with the element type and mesh size:

$$\begin{aligned} &A = \frac{1}{4}a \rightarrow (1 \times 1)\ \text{linear}, \quad A = \frac{1}{8}a \rightarrow (2 \times 2)\ \text{linear}, \quad A = \frac{1}{16}a \rightarrow (4 \times 4)\ \text{linear}, \\ &A = 0.05283 \cdot a \rightarrow (2 \times 2)\ \text{quadratic} \end{aligned} \tag{4.1.2}$$

Note that the overline $\overline{\cdots}$ is also used to identify non-dimensionalized quantities, since this nomenclature is commonly seen throughout literature (different from the meaning of the overline to identify transformed material coefficients). Reddy (2006) considers biaxial symmetry, so in the present FEM algorithm the mesh must be duplicated; the previously defined coordinates in Eq. (4.1.2) are associated with a different coordinate system, as explained in the same reference. The author specifies the Poisson's ratio as $\nu = 0.25$, in order to model an isotropic material. The remaining geometrical and material properties were assumed to be $E = 200\,\text{GPa}$, $q_0 = -1000\,\text{Pa}$, $a = b = 1\,\text{m}$. Due to the specified side-to-thickness ratios a/h, several thickness were considered, i.e. $h = \{1/10, 1/20, 1/40, 1/50, 1/100\}\,[\text{m}]$. In terms of MBCs, the plate is simply-supported along all edges (SSSS).

The results are summarized in Table F.1, considering both Q4 (linear) and Q9 (quadratic) finite elements, with meshes of (2×2), (4×4) and (8×8). The present non-dimensionalized results are followed by a number, inside parentheses, which are the relative deviations in $[\%]$ (percent), between both present and reference results. In addition, each cell is formatted using a coloured scale (conditional formatting), from green (minimum deviation, "good") to red (maximum deviation, "bad"). This approach is very efficient to use when analysing the results and useful to spot outliers.

At this point, generally speaking, it is possible to conclude that the present FEM algorithm reproduces the same results as this reference – negligible deviations are obtained, below $1\,\%$. However, two specific values are worth of comment. First, considering a side-to-thickness ratio of $a/h = 50$, a $800\,\%$ deviation is obtained; this is most likely to be a mistake from the book edition, since it does not follow the deflection trend shown by the remaining values for other side-to-thickness ratios. Then, another deviation stands out, $2.35\,\%$ $(a/h = 40)$; there is no apparent justification for this one, because this table was obtained using a programming cycle, for each different thickness; so, since the deviations are below $1\,\%$ for the remaining column's values, this does not make sense (the thickness used was in fact $h = 1/40\,\text{m}$). In sum, this case study reveals that everything seems to be fine at this point.

4.1.2 Standard, benchmarking study: AMAPDL

The same plate from the previous subsection was modelled using the commercial FEM software AMAPDL, only for comparison purposes, considering both static and dynamic (free vibrations)

behaviours. In Reddy (2006) only deflections w and stresses σ_{xx} are available; using a FEM software, it is possible to compare every output of the present FEM algorithm, to find major mistakes or bugs.

The results were obtained using the following inputs: $E = 200\,\mathrm{GPa}$, $\nu = 0.25$, $q_0 = -1000\,\mathrm{Pa}$, $a = b = 1\,\mathrm{m}$. A side-to-thickness ratio of $a/h = 1000$ was considered, resulting in a thickness $h = 1/1000\,\mathrm{m}$. In addition, a density of $\rho = 2000\,\mathrm{kg \cdot m^{-3}}$ was assumed, to compute natural frequencies. MBCs were the same, (SSSS). In terms of mesh, everything was computed using 4BlinLag elements; convergence was ensured by an increasing mesh, from (2×2) by (2×2) to (30×30) (15 different meshes in total). The results were organized separately, as the following: **5 DOFs** $(\max|w|, \max|\theta_x|, \max|\theta_y|, \max|u|, \max|v|)$, **5 strains** $(\max|\epsilon_{xx}|, \max|\epsilon_{yy}|, \max|\gamma_{xy}|, \max|\gamma_{xz}|, \max|\gamma_{yz}|)$, **6 stresses** (including Von Mises) $(\max|\sigma_{xx}|, \max|\sigma_{yy}|, \max|\tau_{xy}|, \max|\tau_{xz}|, \max|\tau_{yz}|, \max|\sigma_{VM}|)$ and **5 natural frequencies** (the first 5 modes) $(\omega_1, \omega_2, \omega_3, \omega_4, \omega_5)$. The absolute maximum values were compared and deviations calculated; in the same order, the results are summarized in Tables F.2 to F.5; note that, strains and stresses were computed at the plate's top surface, because that is the maximum location, i.e. $z^1_{\epsilon\sigma} = +h/2 = +1/2000\,\mathrm{m}$.

However, this approach is not enough to achieve a proper validation. So, taking advantage of the present algorithm's capabilities, the distributions of all these results along the plate's mesh were generated and summarized in Figure F.2; these are then compared with the distributions from AMAPDL, in Figure F.1. Note that, the plots were only generated for the (30×30) mesh.

The FEM algorithm saves all these plots automatically, and organizes them in folders, as already shown in Appendix E; these are plotted using xy-axes with different Data Aspect Ratios (inside MATLAB®), in order to summarize them all together in A4 sheet format. However, it is not shown here, but the algorithm also saves every sub-plot, individually, using equal Data Aspect Ratios in separate folders. This way, it seems that the plates in Figure F.2 are rectangular, but they are not, because $a = b = 1\,\mathrm{m}$. Each of these figures shows the same structure, considering different views (2D and 3D plots, from different orientations around z-axis). Also note that, each title summarizes important information about each result, such as minimum and maximum values and respective xy-coordinates. The algorithm identifies all minima and maxima, displaying them in the same plots – this is interesting when analysing post-processor results, specially when the structures are more complex; such approach minimizes the probability of misjudgement concerning same values locations. Since this is a single-layer structure, strains' and stresses' distributions are only generated one time, otherwise the algorithm would create plots for every single layer, considering the user-defined evaluation z-coordinates, $z^k_{\epsilon\sigma}$.

Analysing the results from Tables F.2 to F.5, it is possible to conclude that deviations are very acceptable, almost zero for the majority of results. However, there are some details to discuss.

Firstly, in Tables F.3 and F.4, shear components present slightly higher deviations, in comparison with the in-plane ones. This could be due to different shear correction factors, between AMAPDL and the present FEM algorithm; however, it was confirmed that both programs were using $\chi = 5/6$. Then, there is the integration scheme issue, but both programs were using selective integration, otherwise all remaining quantities would have higher deviations. This deviations' behaviour is most likely to be associated with strains' and stresses' averaging procedures carried by AMAPDL, because in the present FEM algorithm the quantities are evaluated at the reduced Gauss points' locations, and that is it. In any case, it is visible that the deviations decrease when the mesh size increases, proving that the present methodology is correct (also note that the deviations associated with Von Mises stress are negligible in Table F.4).

Secondly, and this is only a detail, in Table F.5, very high deviations are observed for the (2×2) mesh (second to fifth mode); this must be associated with numerical issues, due to this coarse mesh. For meshes bigger than this, deviations are negligible.

Finally, by visually comparing the distributions from Figures F.1 and F.2 one concludes that

they comply with each other. However, it is worth to note that AMAPDL does not consider the same convention of rotations as the implemented FSDT, that is why θ_x and θ_y are swapped. Both displacements u and v are zero in this case study. In addition, both strains and stresses are symmetric when comparing the distributions, because the AMAPDL plots were obtained using *element solutions*; when this approach is carried out, the plots are shown in the element coordinate system, which is different from the global coordinate system of the present FEM algorithm; this detail is explained in the software's help page (ANSYS® Documentation → Mechanical APDL → Element Reference → I. Element Library → SHELL181): "*stresses, total strains, plastic strains, elastic strains, creep strains, and thermal strains in the element coordinate system are available for output (at all section points through thickness)*" (ANSYS®, Inc., 2016). Figure 4.1 shows the ANSYS® element stress output coordinate system, SHELL181:

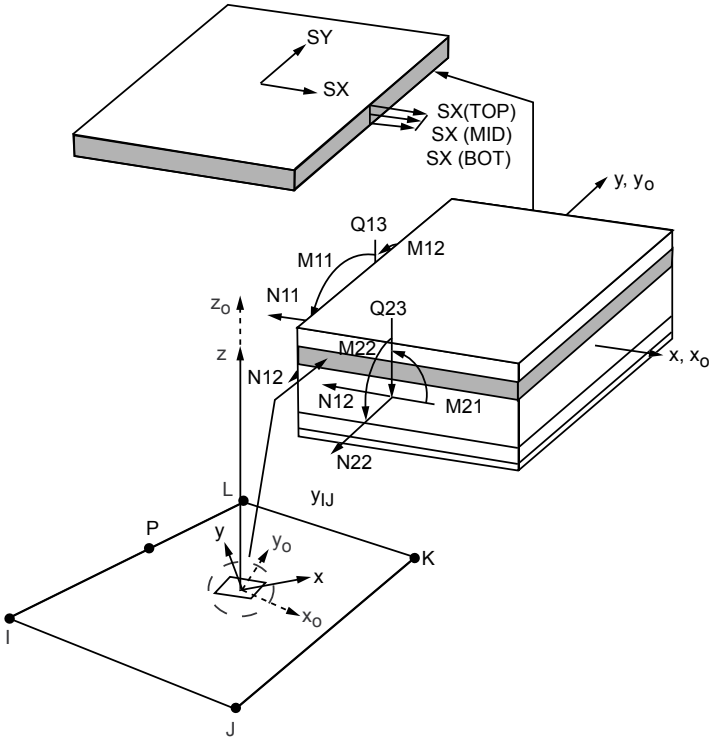

Figure 4.1: SHELL181 stress output. From ANSYS®, Inc. (2016).

4.1.3 Functionally graded plates

The present subsection addresses the validation of functionally graded plates, along thickness, in order to validate FGMs' modelling. This subsection is subdivided into statics and dynamics (free vibrations); the former studies were published in Costa and Loja (2016a) and the latter in Costa and Loja (2016c).

The implementation of the models developed, considered the coding of two quadrilateral finite element plate models, using 4BlinLag and 9BquadLag elements. Concerning to other implementation options, it is worth to mention that a selective integration scheme was used to minimize shear locking effects, and a shear correction factor χ characteristic of FSDT was also considered, and set to $5/6$.

4.1.3.1 Statics

Concerning the static behaviour of functionally graded plates and to enable the validation of the finite element models implemented, one has considered a first study where the present models' results are compared with other authors' alternative solutions. This comparison is carried out for the maximum transverse displacement of a plate, and for normal in-plane stresses in its outer surfaces. To this purpose, a functionally graded square plate with a unit edge length $a = b = 1\,\mathrm{m}$ and an aspect ratio $a/h = 20$, is assumed to be simply-supported (SSSS) and submitted to an uniform pressure, applied in its whole top surface. The material properties of the phases are summarized in Table 3.3 – Al metallic matrix with $E_m = 70\,\mathrm{GPa}$ and $\nu_m = 0.3$; ZrO_2 ceramic particles with $E_{c1} = 151\,\mathrm{GPa}$ and $\nu_{c1} = 0.3$.

The plate was discretized using a (18×18) mesh and the effective elastic modulus was estimated using both Voigt's and Mori-Tanaka's method. The maximum transverse displacements obtained for different values of exponent of the volume fraction distribution, and for different homogenization schemes, are presented in Tables 4.1 and 4.2, in a non-dimensional form, using $\overline{w} = w/h$. The external load applied to this first case, equals $P_z = E_m h^4$ to correspond to a unit parameter load.

Table 4.1: Non-dimensional maximum deflection $\overline{w}$. 4BlinLag elements.

p $(a/h = 20)$	Voigt		Mori-Tanaka	
	Ferreira et al. (2005)	present	Ferreira et al. (2005)	present
0 (ceramic)	0.0208	0.0208	0.0208	0.0208
0.5	0.0265	0.0265	0.0279	0.0279
1	0.0297	0.0297	0.0309	0.0309
2	0.0324	0.0324	0.0333	0.0334
$+\infty$ (metal)	0.0448	0.0448	0.0448	0.0449

Table 4.2: Non-dimensional maximum deflection $\overline{w}$. 9BquadLag elements.

p $(a/h = 20)$	Voigt		Mori-Tanaka	
	Ferreira et al. (2005)	present	Ferreira et al. (2005)	present
0 (ceramic)	0.0208	0.0208	0.0208	0.0208
0.5	0.0265	0.0266	0.0279	0.0279
1	0.0297	0.0297	0.0309	0.0309
2	0.0324	0.0325	0.0333	0.0334
$+\infty$ (metal)	0.0448	0.0449	0.0448	0.0449

As can be observed in Tables 4.1 and 4.2, both plate models provide a good agreement with the reference solutions (Ferreira et al., 2005).

A thicker plate, with an aspect ratio of $a/h = 5$ and submitted to an uniformly distributed force $P_z = 10^4\,\mathrm{Pa}$ was then considered for the in-plane normal stresses σ_{xx}, for comparison purposes. These stresses, obtained at the lower and upper surface centroids are presented in a non-dimensional form, in Tables 4.3 and 4.4 for both meshes. This is carried out using the multiplier $\overline{\sigma}_{xx} = \sigma_{xx}\,(h^2/P_z)$. Mori-Tanaka's scheme was used to calculate the effective material properties.

From the results obtained it is also possible to understand that the present models denote a better agreement with Qian et al. (2004), when a graded variation of the properties is present. In the other

Table 4.3: Non-dimensional stress $\overline{\sigma}_{xx}$ at plate outer surfaces' centroids. 4BlinLag elements.

p $(a/h = 5)$	Qian et al. (2004)		Ferreira et al. (2005)		present	
	$\overline{\sigma}_{xx}(-h/2)$	$\overline{\sigma}_{xx}(+h/2)$	$\overline{\sigma}_{xx}(-h/2)$	$\overline{\sigma}_{xx}(+h/2)$	$\overline{\sigma}_{xx}(-h/2)$	$\overline{\sigma}_{xx}(+h/2)$
0 (ceramic)	0.29175	–0.29200	0.28650	–0.28650	0.28645	–0.28645
1	0.22617	–0.37875	0.17815	–0.38428	0.22214	–0.37142
2	0.24497	–0.40650	0.21278	–0.45899	0.24066	–0.39867
$+\infty$ (metal)	0.29175	–0.29200	0.28650	–0.28650	0.28645	–0.28645

Table 4.4: Non-dimensional stress $\overline{\sigma}_{xx}$ at plate outer surfaces' centroids. 9BquadLag elements.

p $(a/h = 5)$	Qian et al. (2004)		Ferreira et al. (2005)		present	
	$\overline{\sigma}_{xx}(-h/2)$	$\overline{\sigma}_{xx}(+h/2)$	$\overline{\sigma}_{xx}(-h/2)$	$\overline{\sigma}_{xx}(+h/2)$	$\overline{\sigma}_{xx}(-h/2)$	$\overline{\sigma}_{xx}(+h/2)$
0 (ceramic)	0.29175	–0.29200	0.28650	–0.28650	0.28737	–0.28737
1	0.22617	–0.37875	0.17815	–0.38428	0.22285	–0.37262
2	0.24497	–0.40650	0.21278	–0.45899	0.24144	–0.39995
$+\infty$ (metal)	0.29175	–0.29200	0.28650	–0.28650	0.28737	–0.28737

cases of a single constituent material, the agreement with Ferreira et al. (2005) is closer. Similar conclusions can be drawn if one uses a similar mesh of 9BquadLag plate finite elements, as can be observed in Table 4.4. It is worth noting that the reference solutions are based on higher order theories implemented through meshless methods.

4.1.3.2 Dynamics (free vibrations)

Again, to validate the dynamic behaviour of the Lagrange quadrilateral plate finite element models implemented, another comparison of the present results with other authors' alternative solutions was carried out (Qian et al., 2004). This comparison is made for the first eight natural frequencies of a simply-supported (SSSS), functionally graded square plate with a unit edge length $a = b = 1\,\mathrm{m}$ and an aspect ratio $a/h = 5$. The material properties are given in Table 3.3 – Al metallic matrix with $E_m = 70\,\mathrm{GPa}$, $\nu_m = 0.3$ and $\rho_m = 2702\,\mathrm{kg \cdot m^{-3}}$; ZrO_2 ceramic particles with $E_{c1} = 200\,\mathrm{GPa}$, $\nu_{c1} = 0.3$ and $\rho_{c1} = 5700\,\mathrm{kg \cdot m^{-3}}$.

Similarly to the static case studies from the previous subsection, the plate was discretized in (18×18) quadrilateral Lagrangian elements, with four and nine nodes. The average elastic modulus was estimated using Mori-Tanaka's method; the Poisson's ratio and the density were estimated through Voigt's Rule of Mixtures. The first eight natural frequencies, obtained for different values of exponent of the volume fraction distribution power law, are presented in Table 4.5 in a non-dimensional form. The multiplier used to obtain these non-dimensional frequencies was $\overline{\omega} = \omega h \sqrt{\rho_m / E_m}$.

To enable an easier appreciation of the deviations between the present results and the alternative solutions, the [%] (percent) deviations are also included in the table, using cell coloured scale (conditional formatting). These frequencies were obtained for ceramic-rich and for metal-rich materials, as well as for other exponent values of the exponent p. From the results in Table 4.5, it is possible to conclude on the low percent deviations between the present results and the reference solutions (Qian et al., 2004) and therefore on the good agreement between them, despite the low aspect ratio. To mention also that

Table 4.5: Non-dimensional natural frequencies ϖ. 4BlinLag / 9BquadLag elements (same results).

p	**data**	**frequency modes**							
$(a/h = 5)$	**type / source**	1	2	3	4	5	6	7	8
0 (ceramic)	Qian et al. (2004)	0.2469	0.4535	0.4535	0.5441	0.5441	0.6418	0.7881	0.9076
	present	0.2465	0.4541	0.4541	0.5421	0.5421	0.6429	0.7825	0.9116
	deviation [%]	0.16	0.13	0.13	0.37	0.37	0.17	0.71	0.44
1	Qian et al. (2004)	0.2152	0.4114	0.4114	0.4761	0.4761	0.5820	0.6914	0.8192
	present	0.2187	0.4114	0.4114	0.4821	0.4821	0.5815	0.6971	0.8216
	deviation [%]	1.63	0.00	0.00	1.26	1.26	0.09	0.82	0.29
2	Qian et al. (2004)	0.2153	0.4034	0.4034	0.4720	0.4720	0.5709	0.6817	0.8056
	present	0.2198	0.4035	0.4035	0.4821	0.4821	0.5702	0.6949	0.8053
	deviation [%]	2.09	0.02	0.02	2.14	2.14	0.12	1.94	0.04
5	Qian et al. (2004)	0.2194	0.3964	0.3964	0.4760	0.4760	0.5611	0.6832	0.7928
	present	0.2233	0.3967	0.3967	0.4866	0.4866	0.5610	0.6988	0.7936
	deviation [%]	1.78	0.08	0.08	2.23	2.23	0.02	2.28	0.10
$+\infty$ (metal)	Qian et al. (2004)	0.2122	0.3897	0.3897	0.4675	0.4675	0.5517	0.6772	0.7615
	present	0.2118	0.3902	0.3902	0.4658	0.4658	0.5524	0.6724	0.7833
	deviation [%]	0.19	0.13	0.13	0.36	0.36	0.13	0.71	2.86

both elements 4BlinLag and 9BquadLag gave similar results with the discretization used, thus one just presents one table.

4.1.4 Multilayered smart structures

The present subsection addresses the validation of multilayered smart structures. This subsection is subdivided into statics, dynamics (free vibrations) and optimization; all static and dynamic studies were presented at Costa (2016b) and Costa and Loja (2016b), as well as submitted to *Journal of Composite Structures* and *Journal of Composites Part B: Engineering*. Although the optimization studies were not presented at the conferences, they were submitted to these scientific journals.

4.1.4.1 Statics

Actuation configuration: The first validation case study concerning the static behaviour of multilayered smart structures is represented in Figure 4.2. This represents a bimorph cantilever beam (constituted by two active layers), subjected to a constant voltage equal to $+1\,\mathrm{V}$ along its whole length, i.e. electric potentials ϕ of $-0.5\,\mathrm{V}$ at the top layer and $+0.5\,\mathrm{V}$ at the bottom one. This is a very well known case study, commonly used throughout the literature, for validation purposes. Both layers are made of PVDF and the material properties are shown in Table 3.1. The resulting deflection values (see Figure 4.3), considering 5, 10 and 15 elements along the x-direction, were compared with several references, showing negligible deviations (almost $0\,\%$). One example of this comparison can be analysed in Table 4.6.

Sensing configuration: The same procedure was carried out in sensing conditions, in which a nodal tip concentrated load was applied to the beam, in order to generate a tip deflection of $10\,\mathrm{mm}$, for comparison purposes – see Figure F.3. Note that this nodal load was divided equally by the two tip

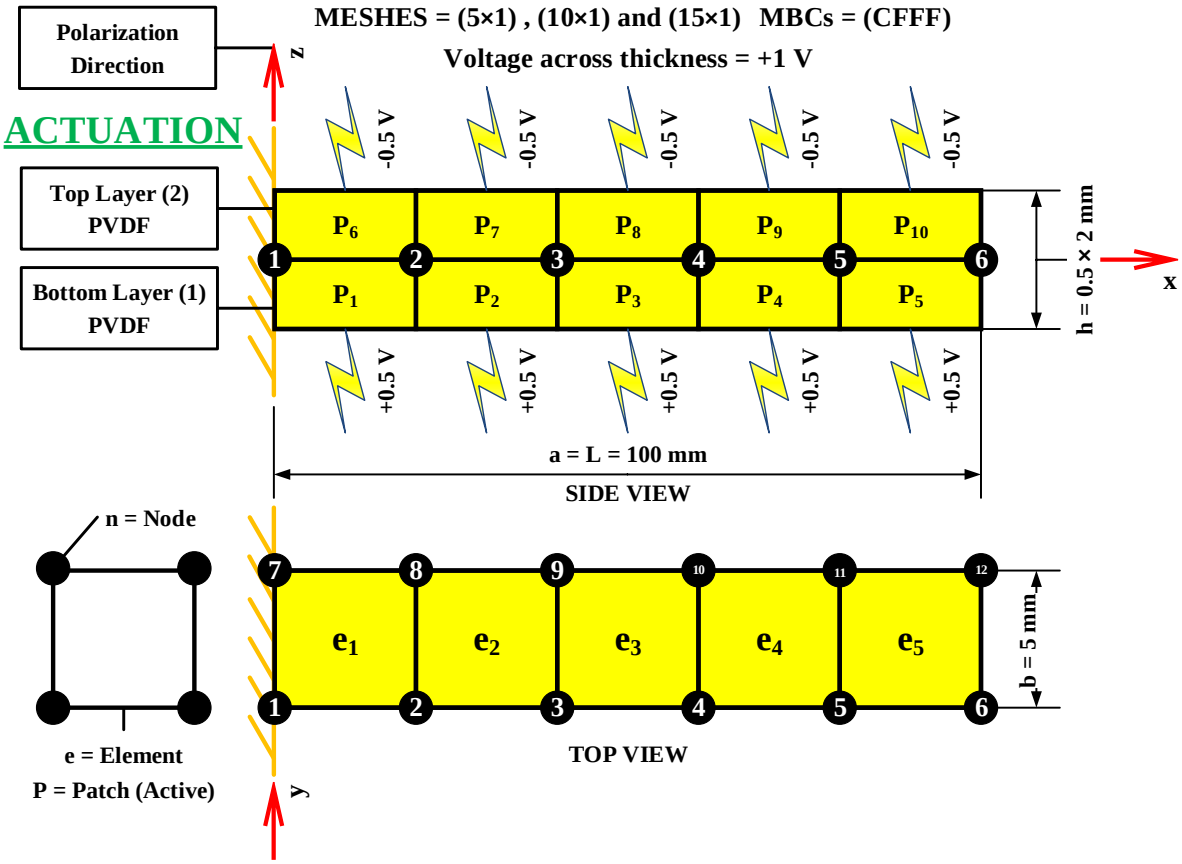

Figure 4.2: Validation case study scheme of bimorph beam (actuation (CFFF)).

Figure 4.3: Deflections obtained in the validation case study of bimorph beam (actuation (CFFF)).

Table 4.6: Comparison of deflections' deviations obtained in the validation case study of bimorph beam (actuation (CFFF)), with Loja et al. (2001).

x [mm]	**Loja et al. (2001)** [m]	**present** [m]	**deviation** [%]
20	1.38E-08	1.38E-08	0.00
40	5.52E-08	5.52E-08	0.00
60	1.24E-07	1.24E-07	0.00
80	2.21E-07	2.21E-07	0.00
100	3.45E-07	3.45E-07	0.00

nodes, since one is using 4-noded quadrangular elements (4BlinLag). For all sensing case studies here presented, this load was found iteratively (automatically, by the FEM algorithm), until the $10\,\mathrm{mm}$ tip deflection was reached (approximately). After solving the FEM problem, the electric potentials generated by the bottom layer were subtracted to the top ones (not forgetting that to each element corresponds a different electrical DOF), generating the voltage distribution plotted in Figure F.4. From this plot it is possible to observe a decreasing linear behaviour of the voltage along beam's length, as it was supposed to, as well as the maximum voltage near the clamped edge (and almost zero at the free tip). Results of this nature were compared with several references, summarized in Tables F.6 and F.7. From these two tables one observes that the maximum and minimum deviations are, respectively, 10.9 and $0.0\,\%$. These voltages are likely to vary according to different references. In any case, specially when comparing to the same FSDT theory, deviations below $2\,\%$ occur, being acceptable.

In addition to the (CFFF) MBCs, (CCFF) were also considered, in order to understand the structure's behaviour in terms of voltage distribution along the beam's length – see Figure F.5. For all beams' case studies with (CCFF) MBCs, in contrast with the (CFFF) ones, the structures were discretized with 6, 10 and 16 elements along length. This approach was performed due to the need of having midspan nodes, to apply midspan nodal loads, generating midspan deflections of $10\,\mathrm{mm}$ (to compare with other MBCs). In terms of results, symmetric voltage distribution along length was obtained, as shown in Figure F.6. Here, two equal absolute maxima occur near the two clamped edges, instead of the same location where the load was applied. In comparison with (CFFF), the voltages' magnitudes are considerably higher. This can be explained by the new MBCs, since (CCFF) constrain the model a lot more (stiffer) and in consequence a higher load is required to generate the same midspan deflection.

4.1.4.2 Dynamics (free vibrations)

In the present subsection, natural frequencies associated with several vibrational modes of active structures are obtained and compared with other references, considering closed and open-circuit EBCs.

1st structure: The first structure is a piezoelectric bimorph, rectangular plate, subjected to cylindrical MBCs (SSFF) from Wang (2004) (see Figure F.7). Two identical PZT-4 piezoelectric ceramic layers are bonded together, considering a slenderness ratio of $L/h = 10$, being $L = 25\,\mathrm{mm}$ (length along x-direction), $l = 12.5\,\mathrm{mm}$ (width along y-direction) and h the whole plate's thickness (along z-direction) – the properties of this material are summarized in Table 3.1. For this validation study, natural frequencies associated with the first six vibrational modes were calculated and summarized for closed and open-circuit in Tables F.8 and F.9, respectively. The present results are here compared with four approaches referred in Wang (2004), namely 3D FEM (ANSYS Multi-Physics®), Wang $nsub = 2$, Wang $nsub = 1$ and 2D Analytical (2D plane strain model from Fernandes and Pouget (2003)), where

$nsub$ is the number of finite sub-layers, in Wang (2004), to discretize the electric potential field of each active layer in the plate's thickness direction (layerwise approximation). In terms of results, as previously expected, open-circuit natural frequencies are always higher comparing to closed-circuit ones. From these two tables, it is possible to conclude that deviations are similar between closed and open-circuit, and acceptable for all modes, excepting the fourth. This higher discrepancy (with a maximum deviation of $34.82\,\%$) can be explained by *"the fact that this mode is an in-plane shear mode and the transversally isotropic PZT cannot produce shear deformations to affect this mode"*, as explained in Wang (2004). Since the present natural frequencies were obtained without considering the shear effect of the active patches, this discrepancy occurs. In addition, it is important to remind that the present methodology does not discretizes each active layer to approximate electric potentials along thickness. Comparing to the remaining approaches, the deviations associated with the 2D Analytical are higher, in general. The fundamental natural frequency has deviations between 2 to $3\,\%$ in closed-circuit, and less than $1\,\%$ in open-circuit – these are acceptable deviations.

2nd structure: The second structure, from Farsangi et al. (2013), is a hybrid rectangular plate made of a transversely isotropic, homogeneous and linear elastic core (Al_2O_3) and face sheets composed of piezoelectric material (PZT-4) (see Figure F.9) – material properties in Table 3.2. Similarly to the previous validation case study, free vibrations analysis is carried out for the first three vibrational modes, considering both closed and open-circuit, for several different piezoelectric layer thickness and plate aspect ratio, as well as MBCs ((SSSS), (SSFF) and (SSFC)). The results are shown in Table F.10, where acceptable deviations were obtained (in general below $2\,\%$). The maximum deviation was found in the second vibrational mode, when considering (SSFF) MBCs, with a value of $3.40\,\%$. Again, the deviations between closed and open-circuit frequencies are similar and acceptable.

3rd structure: Saravanos and Heyliger (1995) analysed a three-layer active/sensory cantilever composite beam, $152.4\,\mathrm{mm}$ long (see Figure F.8). The first thick layer (bottom) is made of Al (see Table 3.2) and the third thick layer (top) of PZT-4 (see Table 3.1), bonded together using an adhesive layer (see Table 3.2) – in the same order, layers' thickness are 15.24, 1.524 and $0.254\,\mathrm{mm}$. The fundamental frequency of this structure was calculated and compared with this reference, for closed and open-circuit EBCs, considering three different meshes. From the results presented in Table 4.7 one concludes that minimum deviations are acceptable and found for the coarser mesh (10×1), with values below $1\,\%$. Maximum deviations occur for the remaining meshes (20×1) and (30×1), with values of around $4\,\%$, meaning that by using the present element, the method converges with higher frequency values.

Table 4.7: Comparison of closed and open-circuit natural frequencies' deviations, for several meshes (10×1), (20×1) and (30×1), obtained in the validation case study of three-layer active/sensory cantilever composite beam, with Saravanos and Heyliger (1995).

Saravanos and Heyliger (1995)							
		EBCs					
		closed			open		
mode no.	**mesh**	**target** [Hz]	**present** [Hz]	**deviation** [%]	**target** [Hz]	**present** [Hz]	**deviation** [%]
1	(10×1)	557.8	561.5	0.667	567.1	567.4	0.051
	(20×1)	538.2	560.9	4.225	544.2	566.8	4.152
	(30×1)	538.1	560.8	4.224	544.1	566.7	4.151

4th structure: Finally, the last validation case study of dynamics, from Saravanos et al. (1997), consists in the free-vibration response of a 5-ply $[p/0°/90°/0°/p]$ laminated simply-supported square plate, where p identifies the piezoelectric layers in this stacking sequence, whereas the remaining ones are composite plies with different fibre in-plane orientations (see Figure F.10). The piezoelectric layers are made of PZT-4 and the composite plies of Gr/Epoxy (see Table 3.2). Results were obtained considering two main aspect ratios (see Table 4.8), in order to simulate a thin ($a/h = 50$) and thick plate ($a/h = 4$), being important to note that all layers were assumed to have equal density of $\rho = 1\,\mathrm{kg \cdot m^{-3}}$, as explained in the cited reference. It was assumed lateral dimensions of $a = b = 1\,\mathrm{m}$, where composite plies are $0.267h$ thick and piezoelectric layers $0.1h$, each. Only to numerically illustrate the thickness differences, $a/h = 4$ results in $h_p = 25\,\mathrm{mm}$ and $h_l = 66.75\,\mathrm{mm}$, whereas $a/h = 50$ results in $h_p = 2\,\mathrm{mm}$ and $h_l = 5.34\,\mathrm{mm}$. In addition, meshes of (4×4), (8×8) and (12×12) were considered. The calculated frequencies are non-dimensionalized according to the equation $\overline{\omega} = \omega a^2/(h\sqrt{\rho} \times 10^3)$. As it was expected, the overall deviations are higher for the thick plate, with values between $10\,\%$ to $19\,\%$, since the present methodology is based on the FSDT. On the other hand, for the thin plate the deviations are lower and it is possible to observe that open-circuit frequencies have higher deviations (around $7\,\%$) comparing to closed-circuit ones ($\approx 1\,\%$).

Table 4.8: Comparison of closed and open-circuit non-dimensional natural frequencies' deviations, for several aspect ratios, obtained in the validation case study of a 5-ply $[p/0°/90°/0°/p]$ laminated simply-supported square plate, with Saravanos et al. (1997).

Saravanos et al. (1997)										
			EBCs							
			closed				open			
a/h	w type	mesh	target	present	deviation target [%]	deviation exact [%]	target	present	deviation target [%]	deviation exact [%]
4	constant	(4×4)	148.154	170.679	15.20	17.44	153.720	172.684	12.34	18.78
		(8×8)	145.323	166.322	14.45	14.44	151.222	168.437	11.38	15.86
		(12×12)	144.768	165.492	14.32	13.87	150.727	167.626	11.21	15.30
	variable	(4×4)	149.310	–	14.31	–	154.591	–	11.70	–
		(8×8)	146.269	–	13.71	–	151.964	–	10.84	–
		(12×12)	145.675	–	13.60	–	151.531	–	10.62	–
	exact				145.339				145.377	
50	constant	(4×4)	249.860	250.301	0.18	1.77	272.860	255.871	6.23	4.04
		(8×8)	236.833	237.190	0.15	3.56	259.173	242.642	6.38	1.34
		(12×12)	234.533	234.877	0.15	4.50	256.765	240.305	6.41	2.29
	variable	(4×4)	253.670	–	1.33	–	276.185	–	7.36	–
		(8×8)	239.628	–	1.02	–	261.703	–	7.28	–
		(12×12)	237.158	–	0.96	–	259.655	–	7.45	–
	exact				245.941				245.942	

4.1.4.3 Optimization

After validating both static and dynamic (free vibrations) behaviours of multilayered structures, it is convenient to test the implementation and performance of MHBA; to this purpose, one optimization case study from Correia et al. (2016, 2001) was chosen, for comparison purposes.

This case study intends to find the optimal fibre orientations of a composite skew plate with piezoelectric layers, in order to maximize its fundamental frequency ω_1. This single optimization problem is summarized in Figure F.11, in terms of geometry, mesh, BCs, materials, optimization objective and DVs' bounds. The structure is clamped along y_0 edge, i.e. MBCs are (FFCF). The DVs consist of fibre in-plane orientation angles θ_k of each ply, from -90 to $+90°$ each, along thickness direction; this laminate is built up by four layers of unidirectional Gr/Epoxy (each $h_l = 1\,\mathrm{mm}$ thick), the substrate, as well as two surface bonded PZT-5H piezoelectric layers (each $h_p = 0.5\,\mathrm{mm}$

thick). The former material is modelled as an orthotropic one, considering the following properties: $E_1 = 145\,\text{GPa}$, $E_2 = E_3 = 10\,\text{GPa}$, $G_{12} = G_{23} = G_{13} = 4.8\,\text{GPa}$, $\nu_{12} = \nu_{23} = \nu_{13} = 0.25$ and $\rho = 1580\,\text{kg} \cdot \text{m}^{-3}$. The piezoceramic layers are modelled in open-circuit EBCs (free electric potentials), using $E_1 = E_2 = 69\,\text{GPa}$, $E_3 = 106\,\text{GPa}$, $G_{12} = G_{23} = G_{13} = 26.3\,\text{GPa}$, $\nu_{12} = \nu_{23} = \nu_{13} = 0.31$ and $\rho = 7700\,\text{kg} \cdot \text{m}^{-3}$, concerning mechanical properties; electrical ones are strain-charge piezoelectric coefficients $d_{31} = d_{32} = -171 \times 10^{-12}\,\text{C} \cdot \text{N}^{-1}$, $d_{33} = 374 \times 10^{-12}\,\text{C} \cdot \text{N}^{-1}$ and permittivity $\varepsilon_{33} = 1.505 \times 10^{-8}\,\text{F} \cdot \text{m}^{-1}$. A (4×4) mesh was used, which had to be transformed in the xy-plane, by means of the following x-direction shear transformation matrix:

$$[T] = \begin{bmatrix} 1 & \tan(\alpha) \\ 0 & 1 \end{bmatrix}, \quad \begin{Bmatrix} x \\ y \end{Bmatrix}_{sk}^{n} = [T] \begin{Bmatrix} x \\ y \end{Bmatrix}_{nsk}^{n} \tag{4.1.3}$$

where α denotes skew angle, which is, due to the specified geometry, $\approx 26.57°$ (see Figure F.11). The skewed sk xy-coordinates of each node n, are obtained by the multiplication between the transformation matrix and each non-skewed nsk xy-coordinates of each node n, as shown in Eq. (4.1.3).

Before starting the optimization process itself, the structure was validated (dynamic free vibrations behaviour) considering both available stacking sequences, for the substrate plies, from the references, i.e. $[0°/0°/0°/0°]$ and $[70°/70°/70°/70°]$. The obtained natural frequencies associated with both first and second vibrational modes are summarized in Table 4.9, as well as the computed deviations.

Table 4.9: Validation of both first and second modes' natural frequencies, considering ply angles of $[0°/0°/0°/0°]$ and $[70°/70°/70°/70°]$ (substrate). Comparison between the present FEM 4BlinLag elements and the ones from Correia et al. (2001) (Q9-HSDT 11P, Q9-HSDT 9P and Q9-FSDT 5P).

	natural frequencies $[\text{rad} \cdot \text{s}^{-1}]$		
	Q9-HSDT 11P (Correia et al., 2001)	Q9-HSDT 9P (Correia et al., 2001)	Q9-FSDT 5P (Correia et al., 2001)
angles	$[0°/0°/0°/0°]$	$[0°/0°/0°/0°]$	$[0°/0°/0°/0°]$
1st mode	206.894	209.849	209.880
2nd mode	449.867	450.524	450.769
angles	$[70°/70°/70°/70°]$	$[70°/70°/70°/70°]$	$[70°/70°/70°/70°]$
1st mode	312.960	314.493	314.614
2nd mode	497.724	498.180	498.621
	4BlinLag (present)		
angles		$[0°/0°/0°/0°]$	
1st mode		206.575	
2nd mode		461.712	
deviation [%]	0.15	1.56	1.57
	2.63	2.48	2.43
angles		$[70°/70°/70°/70°]$	
1st mode		314.026	
2nd mode		507.901	
deviation [%]	0.34	0.15	0.19
	2.04	1.95	1.86

Deviations are smaller in the 1st mode, comparing to the 2nd one. Note that 4BlinLag was used instead of 9BquadLag only to speed up the following MHBA optimization; in any case, the fundamental natural frequency has very acceptable deviations, enabling to proceed to the optimization phase.

Several MHBA optimization trials, or "case studies" (79 in total), were run and the results are summarized in Table F.11, including each input of the optimization algorithm; in the present work,

concerning optimization, one run of both FEM and bat algorithms is called "case study", since each position of the inputs' array specifies independent case studies, with (or not) different inputs.

Note that OF Best is the OF result, fundamental natural frequency ω_1 in $\left[\text{rad} \cdot \text{s}^{-1}\right]$ (radian per second), found in all generations N_{gen} of each case study; to this best result, correspond best DVs, in this case the ply angles DV1 (θ_1), DV2 (θ_2), DV3 (θ_3) and DV4 (θ_4), in $[°]$ (degree). Since the single optimization objective is maximization, for each OF Best the **P**ercentage **I**ncrease (PI) was computed, i.e. the percent increase when comparing both optimal and initial designs, in $[\%]$ (percent). When the micro approach is TRUE, the reinitializations of bats' populations were carried out after 10 generations, continuously, until the 50; this approach is denoted as "Reinits Step 10 Gens". Note that, even when $N_{gen} = 150$, the same approach was used, i.e. from the 51st to the last 150th no reinitializations were performed, to force the algorithm's convergence.

Analysing the results from Table F.11, the best result was found in the last trial, i.e. 79th case study. The best 6 trials were obtained using micro mode activated; in fact, the populations' reinitializations enable a wider exploration in the solutions' domain, avoiding local optima. The best 4 trials correspond to the highest combinations of $N_{gen} = 150$ and $n = 20$, because comparing to $N_{gen} = 50$ and $n = 10$, the algorithm has more iterations to converge with the former.

In Figure F.12, the most important data from Table F.11 was plotted, i.e. best OF solution, PI of fundamental natural frequency regarding the initial state one, best 25 DVs and best 10 perturbation factors. Since the present algorithms have capabilities to record everything specified by the user along computation time, Figure F.13 shows all fundamental modes along the best iterations of the best overall case study (79th); note that in the title of each frame the current natural frequency and DVs are shown, to understand the optimization evolution. The present MHBA enables one to specify both discrete and continuous DVs, but for this case study the latter were used. Table 4.10 compares the present optimization results with the reference Correia et al. (2001).

Table 4.10: Optimal ply angles for maximum natural frequency of first vibration mode. Comparison between results obtained using the simulated annealing method and gradient-based optimization method from Correia et al. (2001), and the present MHBA, considering an initial design of $[0°/0°/0°/0°]$.

		natural frequencies $\left[\text{rad} \cdot \text{s}^{-1}\right]$ (**P**ercentage **I**ncrease (**PI**) $[\%]$)		
		Q9-HSDT 11P (Correia et al., 2001)	Q9-HSDT 9P (Correia et al., 2001)	Q9-FSDT 5P (Correia et al., 2001)
initial design	**angles**	$[0°/0°/0°/0°]$	$[0°/0°/0°/0°]$	$[0°/0°/0°/0°]$
	1st mode	206.894	209.849	209.880
simulated annealing optimal design	**angles**	$[70°/70°/70°/70°]$	$[70°/70°/70°/70°]$	$[70°/70°/70°/70°]$
	1st mode	312.960 (51.27)	314.493 (49.87)	314.614 (49.90)
gradient-based optimal design	**angles**	$[71.7°/10.6°/10.6°/71.7°]$	$[71.6°/10.8°/10.8°/71.6°]$	$[71.0°/10.0°/10.0°/71.0°]$
	1st mode	303.062 (46.48)	304.652 (45.18)	304.706 (45.18)
		4BlinLag (present)		
initial design	**angles**		$[0°/0°/0°/0°]$	
	1st mode		206.575	
MHBA optimal design	**angles**		$[70.3°/71.2°/70.4°/70.5°]$	
	1st mode		314.045 (52.02)	

Since all MHBA trials started with an initial design of $[0°/0°/0°/0°]$, the same results of simulated annealing and gradient-based optimization were retrieved from the reference. MHBA converged to an optimal design, where each ply would have orientations of about $70°$, like the other approaches; in Table 4.10, PIs between initial and optimal designs are inside parentheses, for all algorithms. Gradient-based optimization achieved $46.48\,\%$, simulated annealing $51.27\,\%$ and MHBA $52.02\,\%$.

It is also interesting to point out the following detail: the present algorithm found a better solution

comparing to the one from Table 4.9, with $[70°/70°/70°/70°]$, i.e. $314.045 > 314.026\,\mathrm{rad \cdot s^{-1}}$; although this being a minor difference, this supports the fact that discrete DVs sometimes can lead to local optima; even with continuous DVs, MHBA reveals to be efficient. Nothing is perfect and MHBA requires testing of several inputs before exploiting with more iterations – micro approach helps increasing the convergence rate of this preliminary phase, while decreasing the computational time by using smaller populations. The present interaction between both FEM and bat algorithms is validated.

4.2 Parametric studies

Parametric case studies are useful to intensively test the performance of the present FEM algorithm, without considering optimization yet. Such studies enable one to model innovative materials and multilayered structures, with the objective of describing their static and dynamic behaviours.

Before addressing more interesting structures, the first step of parametric studies has to do with the analysis of finite element convergence. Here, the same structure modelled in Section 4.1.2 is computed with all different finite elements supported by this algorithm; both Lagrange and Kriging formulations are briefly addressed in terms of computational efficiency, considering Q4, Q9 and Q16 elements.

Afterwards, it is intended to analyse the static behaviour of hybrid CNT-metal-ceramic composite structures, as well as the free vibrational dynamic behaviour of multiscale composite structures; these are plate-type structures mostly constituted by FGMs with spatial variations along thickness direction, considering distributions of both micro and nano-inclusions.

Finally, the most extensive subsection of parametric studies is analysed, about multilayered smart structures; here, present case studies are modelled with the objective of describing the electromechanical behaviour of functionally graded active composite structures, considering several materials' variations along in-plane direction. Different passive and active materials' combinations are considered, with several piezoelectric configurations, BCs, load conditions, etc.

4.2.1 Finite element convergence

As already mentioned, all numerical results presented in the present subsection are associated with the same simply-supported, isotropic, square plate under an uniform pressure addressed in Section 4.1.2.

Tables G.1 to G.15 contain the finite element convergence results, including computation time in [s] (second) for each different mesh. The standard results in these tables are the ones obtained using AMAPDL (SHELL181) and 4BlinLag with meshes from (2×2) by (2×2) to (30×30); note that the results using 4BlinKrig were the only ones, besides AMAPDL and 4BlinLag, to be computed using these meshes – such approach was adopted due to the exponential growth of computation time associated with the remaining elements, whose results were computed using smaller meshes from (2×2) by (2×2) to (10×10). Strains and stresses were, again, evaluated at the plate's top surface. DOF $\max|\theta_y|$ is not included because is equal to $\max|\theta_x|$, both DOFs $\max|u|$ and $\max|v|$ are always zero in this case study, strain $\max|\epsilon_{yy}|$ equals to $\max|\epsilon_{xx}|$, strain $\max|\gamma_{yz}|$ equals to $\max|\gamma_{xz}|$, stress $\max|\sigma_{yy}|$ equals to $\max|\sigma_{xx}|$ and stress $\max|\tau_{yz}|$ equals to $\max|\tau_{xz}|$.

With the same order as Tables G.1 to G.15, Figures G.1 to G.15 illustrate plots of this data along mesh size; in order to compare different elements' convergence rates, logarithmic scales were used in y-axes. These figures contain several frames, where the user is able to toggle between all results, Lagrange elements only, Kriging elements only, bilinear, biquadratic or bicubic elements only. This way, it is possible to minimize results' misinterpretation. Then, similarly to Figure F.2 for 4BlinLag element, Figures G.16 to G.23 show plots of all variables' results for the remaining elements, considering

the maximum mesh for each one, either (10×10) or (30×30); these are presented to illustrate that the algorithm's methodology saves all results, no matter what element chosen by the user. Finally, Figure G.24 shows the results of Von Mises stress, considering 4BlinLag with meshes from (2×2) by (2×2) to (30×30), to understand the mesh size influence; this stress was chosen because, from all the remaining variables of this case study, this one is the most interesting to visualize.

Lagrange elements have a faster convergence rate towards AMAPDL results, comparing with Kriging. In addition, 16BcubLag is the fastest (due to its number of nodes), then 9BquadLag and finally 4BlinLag. Bilinear elements are slower than biquadratic, which are slower than bicubic. Concerning Kriging elements and the meshes used, 16BcubKrig is the only one that reaches AMAPDL results.

Generally, all variables converge to the expected results, with the exception of shear components in biquadratic Kriging elements; a possible justification of this phenomena is the shape functions associated with these elements, or the coordinates evaluation of these components (at the reduced Gauss points coordinates, for both Lagrange and Kriging elements). Concerning computation time, bicubic elements take more time to compute, then biquadratic and then bilinear (due to shape functions complexity and consequent integration times). Since Kriging elements are integrated analytically, a higher computation time is expected, comparing with Lagrangian ones (Gauss quadrature).

With all this being concluded, one decided to proceed with 4BlinLag elements towards the parametric and optimization studies, due to its computational efficiency. Since the main focus of this work is not to compare numerical differences between different elements/formulations, this Q4 is a fair choice to start describing both static and dynamic behaviours of multilayered smart structures. In addition, since meta-heuristics requires a considerable amount of FEM evaluations, this faster element gives an excellent starting point to test both FEM and bat algorithms.

4.2.2 Functionally graded, multiscale & hybrid composite structures

The present subsection addresses functionally graded, multiscale and hybrid composite structures, along thickness. This subsection is subdivided into statics and dynamics (free vibrations); the former studies were published in Costa and Loja (2016a) and the latter in Costa and Loja (2016c).

4.2.2.1 Statics

In the present subsection, one proceeds to the characterization of the static response of moderately thick plates made of dual-phase FGMs, where the continuous phase is metallic and the discontinuous one are ceramic particles. Additionally these metal-ceramic graded composites may be enriched with CNTs. Parametric studies are developed, to characterize the influence of some parameters on the transverse displacements of the plates as well as the inherent states of stress.

In order to enable a parametric study related to the static response of a FGM plate, a set of studies was developed. To this purpose, a simply-supported (SSSS) plate with a varying composition of a metallic matrix and different ceramic inclusions was considered. The effective average properties were determined using Voigt's Rule of Mixtures, and it was also considered the possibility of first hybridizing the metallic matrix with CNTs with different weight fractions on that response. In all the cases considered, the plate was submitted to an uniformly distributed pressure of $P_z = 10^4\,\mathrm{Pa}$.

The material properties of the metallic and the ceramic phases, used in this subsection, are given in Table 3.3; Al metallic matrix with $E_m = 70\,\mathrm{GPa}$ and $\nu_m = 0.3$; ceramic material 1 (ZrO_2) with $E_{c1} = 200\,\mathrm{GPa}$ and $\nu_{c1} = 0.3$; ceramic material 2 (Al_2O_3) with $E_{c2} = 380\,\mathrm{GPa}$ and $\nu_{c2} = 0.3$. For simplicity, FGM1 denotes the mixture of the aluminium matrix with the zirconia, and FGM2 the mixture of the aluminium matrix with alumina. CNTs' material properties in Table 3.4. The meshes

used are the same as in Section 4.1.3.1, i.e. (18×18), considering both 4BlinLag and 9BquadLag elements. The results continue to be presented in a non-dimensional form.

Influence of finite element model: In a first stage it was considered the evaluation of the performance of the plate finite element models (4BlinLag and 9BquadLag elements) used in the present work. To achieve this goal, one considered that the plate was made of FGM1 and possesses an aspect ratio $a/h = 20$. It was also allowed the possibility of hybridizing the matrix with MWCNTs. The fraction volumes of the constituents were assumed to vary continuously. The results obtained for the maximum transverse displacement for different values of exponent p, are presented in Table 4.11.

Table 4.11: Non-dimensional maximum deflections, $\overline{w}$ (MWCNTs).

p	$w_{CNT} = 0\,\%$		$w_{CNT} = 2.5\,\%$		$w_{CNT} = 5\,\%$	
	4BlinLag	9BquadLag	4BlinLag	9BquadLag	4BlinLag	9BquadLag
0.5	4.90E-04	4.90E-04	4.94E-04	4.94E-04	4.98E-04	4.98E-04
1	5.74E-04	5.74E-04	5.82E-04	5.82E-04	5.88E-04	5.90E-04
2	6.52E-04	6.54E-04	6.66E-04	6.66E-04	6.78E-04	6.78E-04
5	7.22E-04	7.22E-04	7.38E-04	7.38E-04	7.54E-04	7.54E-04

As it is possible to confirm, under the present conditions, both elements give a similar response. Because of this, one continues using one or other of these elements in further studies. However Q4 has a lower computational cost, which may be a selection parameter in order to make the more adequate selection for a certain approach. Concerning to the magnitude of the response, it is additionally possible to conclude that from the first case where the FGM1 does not include CNTs to the other two cases where increasing weight fraction contents w_{CNT} of MWCNTs are considered, one obtains an increasing maximum transverse deflection. This is an expected trend in this case, as the present MWCNTs' properties, contribute with a negative strengthening effect to this metallic matrix and therefore to the overall hybrid material. This negative effect, already identified by other authors (Al-Rub et al., 2012), may be explained through the close relation to the CNT diameter, which has a very important effect on the resulting properties of the nano-composite. In fact, there are research works that reported the conclusion that larger diameters (Salvetat, J.-P. et al., 1999) lead to lower effective modulus, thus explaining the trend that is visible in the present study.

Just as an academic example one considered two additional situations. A first one, where one simplistically supposed that all the remaining characteristics of the MWCNT would be maintained, except its outer diameter which one considers to be lower, e.g. $4\,\mathrm{nm}$. In the other case, one has considered other MWCNTs from U.S. Research Nanomaterials Inc. (U.S. Research Nanomaterials, Inc., 2016). The information provided by this company was then used to determine the estimated properties for the nano-composite. The properties for these CNTs are presented in Table 4.12.

Table 4.12: Properties of MWCNTs (U.S. Research Nanomaterials, Inc., 2016).

CNT type	**material properties**				
	$E_{CNT}\,[\mathrm{GPa}]$	$l_{CNT}\,[\mu\mathrm{m}]$	$d_{CNT}\,[\mathrm{nm}]$	$t_{CNT}\,[\mathrm{nm}]$	$\rho_{CNT}\left[\mathrm{kg}\cdot\mathrm{m}^{-3}\right]$
MWCNT	1200	30	7	2	2600

In Figure 4.4, it is possible to observe the predicted nano-composite elastic moduli considering SWCNTs and different MWCNTs. These cases are respectively identified as MWCNT*, MWCNT** and MWCNT***. As one may see, particularly for the MWCNTs, when a lower diameter (MWCNT**) is considered and assuming that all the remaining parameters would be the same, an increasing trend is verified with the CNTs weight fraction. If one considers a more realistic situation (MWCNT***) the improvement in the predicted elastic modulus is quite notorious, even when compared to SWCNTs.

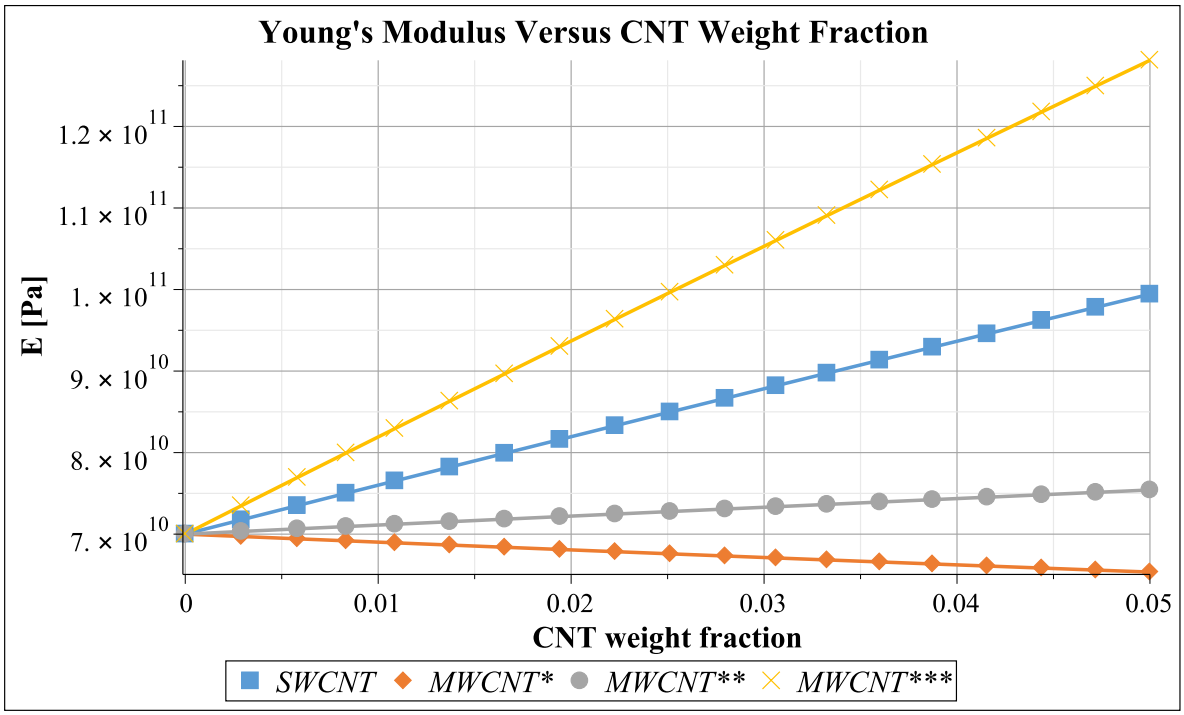

Figure 4.4: Evolution of elastic moduli E versus CNT weight fractions w_{CNT}, for nano-composites.

Influence of continuous and discrete approach: Another aspect that was considered important to analyse is related to the continuous or discrete approach of these hybrid functionally graded composites. To this, one has considered three different numbers of sub-layers, namely five, ten and fifty. Figure G.25 illustrates the results obtained as function of MWCNT weight fractions w_{CNT} and power law exponent p, for five and fifty sub-layers. The plate finite element used was 9BquadLag. Generically, one can conclude from this figure, that the growing pattern of the maximum transverse deflection referred in the previous case is also here confirmed, independently of the no. sub-layers used in the discrete approach.

Figure G.25, allows to conclude that when the power law exponent p increases from 0.5 to 5, the discrepancy among the results obtained using 5 or 50 sub-layers also increases, which may be explained by the mixture evolution rate through the thickness (see Figure 3.11). This is also visible for lower values of p, i.e. $p =]0, 1[$, taking as reference the situation $p = 1$. The way the convergence occurs for exponent values greater or minor than the unit one is different and is quantified in Table 4.13; in this table, the deviations between the results of continuous and the remaining sub-layers are within parentheses in [%] (percent), with associated cell colours (conditional formatting).

Due to symmetry reasons, only one of the in-plane normal stresses, corresponding to this case study, is presented in Tables 4.14 and 4.15. In the first table the functionally graded composite does not incorporate CNTs and on the second table, a 5 % weight fraction of these nano-inclusions is considered.

Table 4.13: Non-dimensional maximum deflections, $\overline{w} \times 10^{-4}$ (MWCNTs).

p	$w_{CNT} = 5\,\%$			
	continuous	NL=5	NL=10	NL=50
0	3.59	3.59 (0.00)	3.59 (0.00)	3.59 (0.00)
0.5	4.98	4.87 (2.21)	4.94 (0.80)	4.97 (0.20)
1	5.89	5.85 (0.68)	5.88 (0.17)	5.89 (0.00)
2	6.78	6.85 (1.03)	6.80 (0.29)	6.78 (0.00)
5	7.54	7.81 (3.58)	7.61 (0.93)	7.54 (0.00)

Table 4.14: Non-dimensional stress $\overline{\sigma}_{xx}$ at plate outer surfaces' centroids ($w_{CNT} = 0$).

p	**NL=5**		**NL=10**		**NL=50**	
	$\overline{\sigma}_{xx}(-h/2)$	$\overline{\sigma}_{xx}(+h/2)$	$\overline{\sigma}_{xx}(-h/2)$	$\overline{\sigma}_{xx}(+h/2)$	$\overline{\sigma}_{xx}(-h/2)$	$\overline{\sigma}_{xx}(+h/2)$
0	–0.28645	0.28645	–0.28645	0.28645	–0.28645	0.28645
0.5	–0.23988	0.33337	–0.21822	0.34127	–0.18483	0.34698
1	–0.22363	0.36155	–0.20813	0.37320	–0.19459	0.38259
2	–0.22828	0.37912	–0.22437	0.39809	–0.22311	0.41641
5	–0.24688	0.37391	–0.24290	0.41591	–0.24160	0.46326

Table 4.15: Non-dimensional stress $\overline{\sigma}_{xx}$ at plate outer surfaces' centroids ($w_{CNT} = 0.05$, SWCNTs).

p	**NL=5**		**NL=10**		**NL=50**	
	$\overline{\sigma}_{xx}(-h/2)$	$\overline{\sigma}_{xx}(+h/2)$	$\overline{\sigma}_{xx}(-h/2)$	$\overline{\sigma}_{xx}(+h/2)$	$\overline{\sigma}_{xx}(-h/2)$	$\overline{\sigma}_{xx}(+h/2)$
0	–0.28645	0.28645	–0.28645	0.28645	–0.28645	0.28645
0.5	–0.25469	0.31933	–0.24013	0.32472	–0.21765	0.32867
1	–0.24585	0.33595	–0.23610	0.34375	–0.22761	0.35018
2	–0.25005	0.34520	–0.24742	0.35806	–0.24657	0.37046
5	–0.26265	0.34206	–0.25962	0.36995	–0.25861	0.40120

As expected, there is no symmetry between the values found in the lower and upper surfaces, due to the fact that on these surfaces there exist different materials mixture compositions. In the lower and upper surfaces exist $100\,\%$ of, respectively, metallic matrix (with or without nano-inclusions) and ceramic mixture. Also, greater stress values are verified on the upper surface, with the exception of the situation when $p = 0$, where the structure is constituted by a whole ceramic homogeneous composition.

Influence of CNTs: Considering now the same plate with an aspect ratio $a/h = 10$, and assuming that the volume fraction of the metal and ceramic varies continuously, it is important to understand the effect the present SWCNTs and MWCNTs have on the FGM. The FGM used to this purpose continues to be the first one, FGM1. The results were obtained using the same mesh as in the previous case, for the different hybrid nano-composites and are depicted in Figures G.26 and G.27.

From Figure G.26 it is possible to observe again that incorporating SWCNTs in the FGM1 provide a clear stiffening effect. Also, when one increases the weight fraction of the SWCNTs, decreasing

maximum transverse displacements are obtained, which is contrary to what happens in the case of MWCNTs inclusion. It is worth noting that this happens with the present materials, because of their relative orders of magnitude. In addition, one can observe that the greater the exponent p of the power law is, the greater this effect also is. Figure G.27 enables a more detailed observation concerning the evolution trend of the plate deflection when the FGM1 includes SWCNTs or MWCNTs.

The slopes associated with the non-dimensional deflection of the hybrid SWCNT nano-composites are negative whereas the slopes of the MWCNT nano-composites are positive. The in-plane non-dimensional stress $\overline{\sigma}_{xx}$ at the plates outer surfaces' centroids can be seen in Tables 4.16 and 4.17, for different SWCNT and MWCNT weight fractions.

Table 4.16: Non-dimensional stress $\overline{\sigma}_{xx}$ at plate outer surfaces' centroids (SWCNTs).

p	$w_{CNT} = 0\,\%$		$w_{CNT} = 2.5\,\%$		$w_{CNT} = 5\,\%$	
	$\overline{\sigma}_{xx}(-h/2)$	$\overline{\sigma}_{xx}(+h/2)$	$\overline{\sigma}_{xx}(-h/2)$	$\overline{\sigma}_{xx}(+h/2)$	$\overline{\sigma}_{xx}(-h/2)$	$\overline{\sigma}_{xx}(+h/2)$
0	–0.28645	0.28645	–0.28645	0.28645	–0.28645	0.28645
0.5	–0.15611	0.34819	–0.17858	0.33825	–0.19822	0.32953
1	–0.19106	0.38495	–0.20986	0.36681	–0.22539	0.35182
2	–0.22305	0.42147	–0.23597	0.39497	–0.24654	0.37388
5	–0.24154	0.47738	–0.25078	0.44037	–0.25857	0.41045

Table 4.17: Non-dimensional stress $\overline{\sigma}_{xx}$ at plate outer surfaces' centroids (MWCNTs).

p	$w_{CNT} = 2.5\,\%$		$w_{CNT} = 5\,\%$	
	$\overline{\sigma}_{xx}(-h/2)$	$\overline{\sigma}_{xx}(+h/2)$	$\overline{\sigma}_{xx}(-h/2)$	$\overline{\sigma}_{xx}(+h/2)$
0	–0.28645	0.28645	–0.28645	0.28645
0.5	–0.15233	0.34985	–0.14871	0.35144
1	–0.18778	0.38812	–0.18461	0.39118
2	–0.22077	0.42623	–0.21855	0.43088
5	–0.23995	0.48396	–0.23842	0.49035

Similar conclusions concerning to the trend evolution depending on the exponent of the volume fraction power law and on the CNT weight fraction, can be taken from these tables. To note that the results associated to the null MWCNT weight fraction were omitted because that situation is already contemplated in the null SWCNT weight fraction case, i.e. there are no nano-inclusions.

The non-dimensional normal stress distribution can be observed in Figure G.28 (3D) and Figure G.29 (2D). A symmetric distribution profile is visible as it was expected, and the places where the minimum and maximum values occur are respectively identified by red or blue triangles. This extrema identification is not taken in absolute value but instead considers the real mathematical relation among the values. Due to symmetry reasons only the non-dimensional in-plane shear stress and one of the interlaminar shear stresses, $\overline{\tau}_{xy}$ and $\overline{\tau}_{xz}$, are presented in Tables 4.18 to 4.20.

If the FGM1 includes CNTs either multi-walled or single-walled, then the structural response for the set of weight fractions considered can be observed in Tables 4.19 and 4.20, respectively. From these tables, it is possible to understand that the shear stresses present higher values in the case of MWCNTs, for a similar weight fraction, which is expected and already seen for transverse displacements.

Table 4.18: Non-dimensional maximum shear stresses, $\overline{\tau}_{xy}$ and $\overline{\tau}_{xz}$.

p	$w_{CNT} = 0\,\%$			
	$\overline{\tau}_{xy}(-h/2)$	$\overline{\tau}_{xy}(+h/2)$	$\overline{\tau}_{xz}(-h/2)$	$\overline{\tau}_{xz}(+h/2)$
0	–0.19038	0.19038	–0.03108	0.03108
0.5	–0.09707	0.23141	–0.01348	0.04003
1	–0.11880	0.25585	–0.01572	0.04668
2	–0.13869	0.28012	–0.01883	0.05592
5	–0.15019	0.31728	–0.02346	0.06967

Table 4.19: Non-dimensional maximum shear stresses, $\overline{\tau}_{xy}$ and $\overline{\tau}_{xz}$ (MWCNTs).

p	$w_{CNT} = 2.5\,\%$				$w_{CNT} = 5\,\%$			
	$\overline{\tau}_{xy}(-h/2)$	$\overline{\tau}_{xy}(+h/2)$	$\overline{\tau}_{xz}(-h/2)$	$\overline{\tau}_{xz}(+h/2)$	$\overline{\tau}_{xy}(-h/2)$	$\overline{\tau}_{xy}(+h/2)$	$\overline{\tau}_{xz}(-h/2)$	$\overline{\tau}_{xz}(+h/2)$
0	–0.19038	0.19038	–0.03108	0.03108	–0.19038	0.19038	–0.03108	0.03108
0.5	–0.09472	0.23252	–0.01309	0.04023	–0.09247	0.23358	–0.01272	0.04042
1	–0.11676	0.25796	–0.01532	0.04709	–0.11479	0.25999	–0.01494	0.04747
2	–0.13727	0.28329	–0.01845	0.05670	–0.13590	0.28638	–0.01807	0.05745
5	–0.14920	0.32165	–0.02316	0.07119	–0.14825	0.32590	–0.02286	0.07268

Table 4.20: Non-dimensional maximum shear stresses, $\overline{\tau}_{xy}$ and $\overline{\tau}_{xz}$ (SWCNTs).

p	$w_{CNT} = 2.5\,\%$				$w_{CNT} = 5\,\%$			
	$\overline{\tau}_{xy}(-h/2)$	$\overline{\tau}_{xy}(+h/2)$	$\overline{\tau}_{xz}(-h/2)$	$\overline{\tau}_{xz}(+h/2)$	$\overline{\tau}_{xy}(-h/2)$	$\overline{\tau}_{xy}(+h/2)$	$\overline{\tau}_{xz}(-h/2)$	$\overline{\tau}_{xz}(+h/2)$
0	–0.19038	0.19038	–0.03108	0.03108	–0.19038	0.19038	–0.03108	0.03108
0.5	–0.11104	0.22481	–0.01589	0.03881	–0.12325	0.21901	–0.01810	0.03768
1	–0.13049	0.24379	–0.01811	0.04425	–0.14015	0.23383	–0.02022	0.04211
2	–0.14673	0.26251	–0.02105	0.05142	–0.15330	0.24849	–0.02290	0.04768
5	–0.15594	0.29269	–0.02511	0.06133	–0.16078	0.27280	–0.02637	0.05492

To note also that the positive stresses are also higher in this last case due to a cross effect with the elastic properties of the ceramic-rich mixture. Figures G.30 and G.31 and Figures G.32 and G.33 depict non-dimensional shear stresses for the FGM1 case without inclusion of any type of CNTs.

Influence of plate's aspect ratio: The aspect ratio of the plate structure is an important geometrical parameter, because it is commonly considered as a first selection indicator of the shear deformation theory to use. It may also enable a preliminary perception of expectable deformations, in connection with the BCs to which the plate is submitted. To see its influence, two aspect ratios were chosen, $a/h = 10$ and $a/h = 20$. The FGM1 continues to be considered with continuous variation. The non-dimensional deflections, with the dispersion or not, of SWCNTs can be observed in Table 4.21. Accordingly to these results, several stress components are presented in Tables 4.22 to 4.24.

It is possible to see that the non-dimensional in-plane shear stress is not affected by the aspect ratio, while in the case of the interlaminar shear stress, which are known to increase when the plate becomes thicker, this trend is verified by the corresponding non-dimensional quantity.

From Figures G.34 and G.35, although the nature of the distribution surface is preserved, the magnitude of the non-dimensional stress is higher for the minor aspect ratio. The response pattern

Table 4.21: Non-dimensional maximum deflections, $\overline{w}$ (SWCNTs).

p	$w_{CNT} = 0\,\%$		$w_{CNT} = 2.5\,\%$		$w_{CNT} = 5\,\%$	
	$a/h = 10$	$a/h = 20$	$a/h = 10$	$a/h = 20$	$a/h = 10$	$a/h = 20$
0	2.33E-05	3.60E-04	2.33E-05	3.60E-04	2.33E-05	3.60E-04
0.5	3.17E-05	4.90E-04	3.03E-05	4.60E-04	2.91E-05	4.48E-04
1	3.72E-05	5.74E-04	3.44E-05	5.28E-04	3.22E-05	4.96E-04
2	4.23E-05	6.52E-04	3.80E-05	5.92E-04	3.48E-05	5.36E-04
5	4.70E-05	7.22E-04	4.15E-05	6.54E-04	3.74E-05	5.74E-04

Table 4.22: Non-dimensional maximum in-plane stresses, $\overline{\sigma}_{xx}$ (SWCNTs).

p	$w_{CNT} = 0\,\%$		$w_{CNT} = 2.5\,\%$		$w_{CNT} = 5\,\%$	
	$a/h = 10$	$a/h = 20$	$a/h = 10$	$a/h = 20$	$a/h = 10$	$a/h = 20$
0	0.28645	0.28645	0.28645	0.28645	0.28645	0.28645
0.5	0.34819	0.34819	0.33825	0.33825	0.32953	0.32953
1	0.38495	0.38495	0.36681	0.36681	0.35182	0.35182
2	0.42147	0.42147	0.39497	0.39497	0.37388	0.37388
5	0.47738	0.47738	0.44037	0.44037	0.41045	0.41045

Table 4.23: Non-dimensional maximum shear stresses, $\overline{\tau}_{xy}$ and $\overline{\tau}_{xz}$ ($w_{CNT} = 0$, SWCNTs).

p	$\overline{\tau}_{xy}(+h/2)$		$\overline{\tau}_{xz}(+h/2)$	
	$a/h = 10$	$a/h = 20$	$a/h = 10$	$a/h = 20$
0	0.19038	0.19038	0.03108	0.01554
0.5	0.23141	0.23141	0.04003	0.02002
1	0.25585	0.25585	0.04668	0.02334
2	0.28012	0.28012	0.05592	0.02796
5	0.31728	0.31728	0.06967	0.03483

Table 4.24: Non-dimensional maximum shear stresses, $\overline{\tau}_{xy}$ and $\overline{\tau}_{xz}$ (SWCNTs).

p	$w_{CNT} = 2.5\,\%$				$w_{CNT} = 5\,\%$			
	$\overline{\tau}_{xy}(+h/2)$		$\overline{\tau}_{xz}(+h/2)$		$\overline{\tau}_{xy}(+h/2)$		$\overline{\tau}_{xz}(+h/2)$	
	$a/h = 10$	$a/h = 20$	$a/h = 10$	$a/h = 20$	$a/h = 10$	$a/h = 20$	$a/h = 10$	$a/h = 20$
0	0.19038	0.19038	0.03108	0.01554	0.19038	0.19038	0.03108	0.01554
0.5	0.22481	0.22481	0.03881	0.01940	0.21901	0.21901	0.03768	0.01884
1	0.24379	0.24379	0.04425	0.02212	0.23383	0.23383	0.04211	0.02105
2	0.26251	0.26251	0.05142	0.02571	0.24849	0.24849	0.04768	0.02384
5	0.29269	0.29269	0.06133	0.03066	0.27280	0.27280	0.05492	0.02746

identified is also extensive to the cases where CNTs are dispersed in the metallic constituent phase.

Influence of ceramic materials: Structures made of different materials will potentially behave differently, so in this case one will consider both FGM1 and FGM2 and the hybridization of these FGMs with SWCNTs. An aspect ratio $a/h = 10$ is chosen and the volume fractions continue to vary continuously. Similar meshes were used as well as the external load applied. The non-dimensional maximum transverse displacements are presented in Table 4.25.

Table 4.25: Non-dimensional maximum deflections, $\overline{w}$ (SWCNTs).

p	FGM1			FGM2		
	$w_{CNT} = 0\,\%$	$w_{CNT} = 2.5\,\%$	$w_{CNT} = 5\,\%$	$w_{CNT} = 0\,\%$	$w_{CNT} = 2.5\,\%$	$w_{CNT} = 5\,\%$
0	2.33E-05	2.33E-05	2.33E-05	1.23E-05	1.23E-05	1.23E-05
0.5	3.17E-05	3.03E-05	2.91E-05	1.87E-05	1.82E-05	1.77E-05
1	3.72E-05	3.44E-05	3.22E-05	2.43E-05	2.29E-05	2.17E-05
2	4.23E-05	3.80E-05	3.48E-05	3.12E-05	2.82E-05	2.60E-05
5	4.70E-05	4.15E-05	3.74E-05	3.72E-05	3.29E-05	2.97E-05

The maximum deflections become minor for FGM2 when compared with the ones obtained using FGM1. This is an expected pattern, as the second material (due to its elastic properties), has a higher strengthening effect. Also, within the range of the SWCNTs' contents considered (not to compromise the CNTs dispersion) the higher the weight fraction, the stiffer the plate becomes.

Concerning to the non-dimensional normal stress $\overline{\sigma}_{xx}$ and shear stresses $\overline{\tau}_{xy}$ and $\overline{\tau}_{xz}$, Tables 4.26 to 4.28 illustrate the influence of the ceramic material used. In these cases, it is possible to verify that the increase of the SWCNT weight fraction produces minor magnitude non-dimensional stresses. This effect was already identified in previous subsections.

Table 4.26: Non-dimensional maximum in-plane stresses, $\overline{\sigma}_{xx}$ (SWCNTs).

p	FGM1			FGM2		
	$w_{CNT} = 0\,\%$	$w_{CNT} = 2.5\,\%$	$w_{CNT} = 5\,\%$	$w_{CNT} = 0\,\%$	$w_{CNT} = 2.5\,\%$	$w_{CNT} = 5\,\%$
0	0.28645	0.28645	0.28645	0.28645	0.28645	0.28645
0.5	0.34819	0.33825	0.32953	0.37465	0.36760	0.36120
1	0.38495	0.36681	0.35182	0.44106	0.42477	0.41088
2	0.42147	0.39497	0.37388	0.51499	0.48541	0.46197
5	0.47738	0.44037	0.41045	0.60378	0.56412	0.53264

Additionally, the FGM2 plate when compared to the FGM1 one, presents higher non-dimensional stresses, which is due to the magnitude of its elastic stiffness coefficients.

4.2.2.2 Dynamics (free vibrations)

Considering the importance to analyse and characterize the response of structures made of these types of multiscale materials, the present subsection addresses the study of moderately thick plates made of hybrid FGMs. Here, the continuous phase is a nano-composite of aluminium and CNTs, and the micro inclusions, ceramic particles, are incorporated in a graded manner. Parametric studies are developed, to

Table 4.27: Non-dimensional maximum shear stresses, $\overline{\tau}_{xy}$ (SWCNTs).

p	FGM1			FGM2		
	$w_{CNT} = 0\,\%$	$w_{CNT} = 2.5\,\%$	$w_{CNT} = 5\,\%$	$w_{CNT} = 0\,\%$	$w_{CNT} = 2.5\,\%$	$w_{CNT} = 5\,\%$
0	0.19038	0.19038	0.19038	0.19038	0.19038	0.19038
0.5	0.23141	0.22481	0.21901	0.24900	0.24432	0.24006
1	0.25585	0.24379	0.23383	0.29314	0.28231	0.27308
2	0.28012	0.26251	0.24849	0.34227	0.32262	0.30704
5	0.31728	0.29269	0.27280	0.40129	0.37493	0.35401

Table 4.28: Non-dimensional maximum shear stresses, $\overline{\tau}_{xz}$ (SWCNTs).

p	FGM1			FGM2		
	$w_{CNT} = 0\,\%$	$w_{CNT} = 2.5\,\%$	$w_{CNT} = 5\,\%$	$w_{CNT} = 0\,\%$	$w_{CNT} = 2.5\,\%$	$w_{CNT} = 5\,\%$
0	0.03108	0.03108	0.03108	0.03108	0.03108	0.03108
0.5	0.04003	0.03881	0.03768	0.04301	0.04226	0.04155
1	0.04668	0.04425	0.04211	0.05309	0.05139	0.04985
2	0.05592	0.05142	0.04768	0.06922	0.06549	0.06222
5	0.06967	0.06133	0.05492	0.09932	0.09012	0.08266

characterize the influence of diverse material and geometrical parameters on the natural frequencies of this type of plates.

With the present work it is intended to characterize the free vibrations response of a FGM plate, namely by analysing the influence of a set of material and geometrical parameters. To achieve this goal, a simply-supported (SSSS) FGM plate, with the same unit edge length $a = b = 1\,\mathrm{m}$ was considered in most of the case studies. The exception is the case devoted to identify the influence of MBCs. The average properties were determined using Voigt's Rule of Mixtures, and it was also considered the possibility of first hybridizing the metallic matrix with CNTs with different weight fractions.

Similarly to the static case studies in the previous subsection, the material properties of the metallic and the ceramic phases are given in Table 3.3; Al metallic matrix with $E_m = 70\,\mathrm{GPa}$, $\nu_m = 0.3$ and $\rho_m = 2700\,\mathrm{kg \cdot m^{-3}}$; ceramic material 1 ($ZrO_2$) with $E_{c1} = 200\,\mathrm{GPa}$, $\nu_{c1} = 0.3$ and $\rho_{c1} = 5700\,\mathrm{kg \cdot m^{-3}}$; ceramic material 2 ($Al_2O_3$) with $E_{c2} = 380\,\mathrm{GPa}$, $\nu_{c2} = 0.3$ and $\rho_{c2} = 3800\,\mathrm{kg \cdot m^{-3}}$. For simplicity, FGM1 denotes the mixture of the aluminium matrix with the zirconia, and FGM2 the mixture of the aluminium matrix with alumina. CNTs' material properties in Table 3.4.

Influence of continuous and discrete approach: The first study carried out is related to the possibility of considering a layered stacking scheme to approximate the continuous variation intrinsically associated to the FGM concept. To this goal one has analysed two different situations, one where the mixture composition varied continuously and the other where a different number of sub-layers were used. In this case, one has considered three different numbers of sub-layers, namely five, ten and fifty.

Figure G.36 illustrates the results obtained as function of MWCNT weight fractions w_{CNT} and power law exponent p, for five and fifty sub-layers. The plate finite element used was 9BquadLag. In a global appreciation, one may conclude that the evolution pattern of the fundamental frequency for different MWCNT weight fractions and for different values of the exponent p, is clearly influenced by the number of sub-layers considered in the discrete approach. From this figure, it is also conclusive

that the fundamental frequency decreases with the increase of the weight fraction.

It is important to note that this behaviour is expected, considering the geometrical characteristics of the MWCNTs, namely its aspect ratio, as shown in Costa and Loja (2016a) although in the scope of the linear static analysis. It is also possible to understand that for exponent values lower or equal to one, a minor no. of sub-layers gives higher values of frequency. If the exponent is higher than unity, a lower no. of sub-layers provides lower values of frequency. This illustrates the different ways, convergence to the continuous solutions occurs, as one may also see in Table 4.29 for the case of $w_{CNT} = 5\,\%$.

Table 4.29: Natural frequencies ω in [Hz] (Hertz) (MWCNTs, $w_{CNT} = 5\,\%$).

p	number of	frequency modes				
$(a/h = 20)$	sub-layers	1	2	3	4	5
0.5	5	265	654	654	1033	1281
	10	263	650	650	1027	1274
	50	262	648	648	1024	1270
	continuous	262	648	648	1024	1270
1	5	257	634	634	1002	1242
	10	256	632	632	999	1239
	50	256	632	632	998	1238
	continuous	256	631	631	998	1238
2	5	254	627	627	990	1228
	10	255	629	629	993	1231
	50	255	629	629	994	1232
	continuous	255	629	629	994	1232
5	5	258	636	636	1003	1243
	10	261	642	642	1013	1254
	50	261	644	644	1016	1258
	continuous	261	644	644	1016	1258

Through Table 4.29 one can see that considering a number superior to ten sub-layers already gives good predictions when compared to continuous ones. Complementing the previous results with deviations, taking as reference the continuous solutions, it is possible to observe in Table 4.30, the convergence patterns, qualitatively identified in Figure G.36 and jointly commented with Table 4.29.

Influence of plate's aspect ratio: The influence of the aspect ratio is now considered. Two aspect ratios were chosen, $a/h = 10$ and $a/h = 20$ and the material used was the FGM1 with a continuous mixture variation. The predicted fundamental frequencies, considering the dispersion or not, of MWCNTs can be observed in Table 4.31. From this table, it is possible to see what was already expected; maintaining all the other characteristics, thicker plates possess higher fundamental frequencies when compared to thinner ones. It is also possible to observe that for exponent values greater than unity, the increasing dispersion of MWCNTs, lowers, although slightly, the fundamental frequency. Figure G.41 (3D) and Figure G.42 (2D) depict the fundamental vibrational mode for a FGM1 plate with $p = 0$. The evolution trend as a function of p, identified in previous cases, can also be verified here.

Table 4.30: Deviations in [%], from continuous approach, of nat. freqs. ω (MWCNTs, $w_{CNT} = 5\,\%$).

p	number of	frequency modes				
$(a/h = 20)$	sub-layers	1	2	3	4	5
0.5	5	1.15	0.93	0.93	0.88	0.87
	10	0.38	0.31	0.31	0.29	0.31
	50	0.00	0.00	0.00	0.00	0.00
1	5	0.39	0.48	0.48	0.40	0.32
	10	0.00	0.16	0.16	0.10	0.08
	50	0.00	0.16	0.16	0.00	0.00
2	5	0.39	0.32	0.32	0.40	0.32
	10	0.00	0.00	0.00	0.10	0.08
	50	0.00	0.00	0.00	0.00	0.00
5	5	1.15	1.24	1.24	1.28	1.19
	10	0.00	0.31	0.31	0.30	0.32
	50	0.00	0.00	0.00	0.00	0.00

Table 4.31: Fundamental natural frequency ω_1 in [Hz] (Hertz) (MWCNTs).

p	$w_{CNT} = 0\,\%$		$w_{CNT} = 2.5\,\%$		$w_{CNT} = 5\,\%$	
	$a/h = 10$	$a/h = 20$	$a/h = 10$	$a/h = 20$	$a/h = 10$	$a/h = 20$
0	546	280	546	280	546	280
0.5	515	264	514	264	514	263
1	503	258	502	257	501	257
2	502	258	500	257	498	256
5	512	264	511	263	510	262

Influence of MBCs: To enable a conclusion on the influence of the plates' MBCs, a set of cases was considered. The material and geometrical characteristics of the plate are the same as in the previous case study, considering additionally a SWCNT $w_{CNT} = 4\,\%$. As expected, stiffer boundaries yield higher frequencies and less stiff ones correspond to lower values of the natural frequencies. For illustrative purposes, Figures G.43 and G.44 (CFFF) and Figures G.45 and G.46 (CCSF) present two of the fundamental frequency mode shapes, corresponding to Table 4.32; in this table, a coloured cell scale was adopted (conditional formatting), where smaller and higher values are associated with colours blue and red, respectively.

Influence of ceramic materials: Now, one considers both FGM1 and FGM2 and the hybridization of these materials with SWCNTs. An aspect ratio $a/h = 10$ is chosen and the volume fraction continues to vary continuously. Similar meshes were used to this purpose. The fundamental frequencies obtained are presented in Table 4.33, for different values of the exponent p and CNTs weight fraction w_{CNT}.

In Table 4.33, the fundamental frequencies allow concluding that the increase of SWCNTs weight fraction, produces higher values of frequencies no matter the FGM used. The other aspect that one can observe is that FGM2, due to its material properties, yields higher values of fundamental frequencies. It

Table 4.32: Natural frequencies ω in [Hz] (Hertz) (SWCNTs, $w_{CNT} = 4\,\%$, $p = 5$).

MBCs	**frequency modes**				
$(a/h = 10)$	1	2	3	4	5
CFFF	102	238	595	622	757
SSSS	569	1351	1351	1830	1830
CCFF	613	710	1138	1554	1670
CCSF	641	950	1591	1725	1753
CCSS	792	1456	1748	1830	2322
CCCC	965	1830	1830	2556	3004

Table 4.33: Fundamental natural frequency ω_1 in [Hz] (Hertz) (SWCNTs).

p	**FGM1**			**FGM2**		
	$w_{CNT} = 0\,\%$	$w_{CNT} = 2.5\,\%$	$w_{CNT} = 5\,\%$	$w_{CNT} = 0\,\%$	$w_{CNT} = 2.5\,\%$	$w_{CNT} = 5\,\%$
0	546	546	546	921	921	921
0.5	515	528	541	784	798	812
1	503	525	545	707	732	756
2	502	533	560	642	680	714
5	512	550	584	606	651	692

is also possible to understand from Table 4.33 and to see in Figure G.37, that the fundamental frequency varies differently when CNTs are incorporated in the matrix. For the FGM2 a monotonic decreasing curve is always obtained. This is not the case for the FGM1 case, which may be explained by the trade-off between the elastic and mass properties of the different constituents (see Table 4.30). This pattern was previously identified in another authors' work (Loja et al., 2015).

Table 4.34 presents the five first frequencies for FGM1 and FGM2, with and without SWCNTs. In both cases, frequencies increase with the inclusion of SWCNTs, no matter the frequency mode.

Table 4.34: Natural frequencies ω in [Hz] (Hertz) (SWCNTs, $p = 5$).

material	w_{CNT} [%]	**frequency modes**				
		1	2	3	4	5
FGM1	0	263	647	647	1021	1265
	2.5	282	695	695	1096	1358
	5	300	738	738	1165	1443
FGM2	0	606	1449	1449	1991	1991
	2.5	651	1558	1558	2111	2111
	5	692	1654	1654	2226	2226

Influence of CNTs: In this study, one intends to illustrate the influence of the different types of CNTs. To that purpose, one has considered plates made of both FGMs and with an aspect ratio $a/h = 10$, and assumed the volume fraction of the metal and ceramic to be varying in a continuous way. The

results for the different hybrid nano-composites are firstly depicted in Figure G.38 for a FGM1 plate. A first qualitative observation is related to the fact that SWCNTs provide a stiffening effect more visible when compared to the MWCNTs, being the fundamental frequencies higher in the first case. To note a decreasing region associated to lower exponent values, as identified in previous cases. These observations, given for the cases where SWCNTs were introduced, are complemented with the higher order frequencies evolution in Table 4.35.

Table 4.35: Natural frequencies ω in [Hz] (Hertz) (FGM1 with SWCNTs).

p	w_{CNT} [%]	frequency modes				
		1	2	3	4	5
0 (ceramic)	0	546	1312	1312	1839	1839
	2.5	546	1312	1312	1839	1839
	5	546	1312	1312	1839	1839
0.5	0	515	1240	1240	1784	1784
	2.5	528	1272	1272	1817	1817
	5	541	1301	1301	1848	1848
1	0	503	1212	1212	1748	1748
	2.5	525	1264	1264	1802	1802
	5	545	1311	1311	1855	1855
2	0	502	1205	1205	1701	1701
	2.5	533	1279	1279	1785	1785
	5	560	1345	1345	1864	1864
5	0	512	1224	1224	1639	1639
	2.5	550	1315	1315	1762	1762
	5	584	1398	1398	1878	1878

For illustrative purposes, in Figure G.47 (3D) and Figure G.48 (2D) one can observe the second free vibrational mode for a FGM1 plate. As one may conclude from Table 4.35, the frequencies increase with both SWCNTs weight fraction and power law exponent. In Figures G.39 and G.40 it is shown the fundamental frequency for FGM2 plates with increasing SWCNTs or MWCNTs weight fractions.

When one considers the inclusion of SWCNTs, it is possible to verify that for higher exponent values the increasing trends are higher, which is visible through the slope of those trends. To note also that in all the cases considered in Figure G.39, the evolution is positive.

The effect of the MWCNTs considered, follows a different trend as the one shown in Figure G.40, particularly in the case of higher exponent values, where although small in the analysed range, a decreasing trend of the frequencies is observed when the weight fraction of the CNTs increases. This situation was already identified in a previous case study. This latter evidence is also found for the higher frequencies, as one can see in Table 4.36.

4.2.3 Multilayered smart structures

The present subsection addresses parametric studies concerning multilayered smart structures. These were presented at Costa (2016b) and Costa and Loja (2016b).

Table 4.36: Natural frequencies ω in [Hz] (Hertz) (MWCNTs).

p	w_{CNT} [%]	frequency modes				
		1	2	3	4	5
0 (ceramic)	2.5	546	1312	1312	1839	1839
	5	546	1312	1312	1839	1839
0.5	2.5	514	1239	1239	1784	1784
	5	514	1237	1237	1784	1784
1	2.5	502	1208	1208	1747	1747
	5	501	1205	1205	1746	1746
2	2.5	500	1201	1201	1699	1699
	5	498	1197	1197	1698	1698
5	2.5	511	1221	1221	1635	1635
	5	510	1218	1218	1632	1632

This subsection is also subdivided into statics and dynamics (free vibrations), of several types of bimorph beams, considering longitudinal material distributions. Here, several beams are modelled with different meshes, loads, BCs and materials' parameters, to understand the behaviour of these smart structures, when considering distinct mixtures of passive matrices and active particles. Deflection and voltage results along the structures' length are analysed, considering both actuation and sensor configurations, as well as natural frequencies and free vibrational modes in closed and open-circuit.

4.2.3.1 Statics

Similarly to the beams analysed in Section 4.1.4 (multilayered smart structures validation), parametric studies were carried out with bimorphs having the same dimensions in terms of geometry. Two types of MBCs were modelled, i.e. (CFFF) and (CCFF); for the former, one has used meshes of (5×1), (10×1) and (15×1), whereas for the latter (6×1), (10×1) and (16×1). Two active configurations were considered, i.e. actuation and sensing. For the actuation configurations, voltage across thickness equal to $+1\,\mathrm{V}$ was considered, meaning that the top layer patches were charged with $-0.5\,\mathrm{V}$ and the bottom ones with $+0.5\,\mathrm{V}$. On the other hand, sensing configurations require mechanical loads (to generate responses with associated electric potentials) and for that reason nodal tip and midspan loads are applied when MBCs are (CFFF) and (CCFF), respectively, imposing tip and midspan deflections of $10\,\mathrm{mm}$; this is why different MBCs, (CFFF) and (CCFF), were computed using different meshes, (5 and 15) or (6 and 16) elements along longitudinal direction. On top of all the previous modelling characteristics, all structures are constituted by FGMs with properties' variation along length (x-direction), mixing up two different materials (longitudinal FGM passive + active mixture): LaRC-Si (passive matrix) + PVDF (active reinforcement) and LaRC-Si (passive matrix) + PZT-7A (active reinforcement) – see Table 3.1. For comparison purposes, six different p-exponents of the FGM volume fraction power law were considered, i.e. 0 (piezoelectric), 0.1, 0.5, 1, 2 and 5 (see Figure 3.12). Note that, when $p = 0$, the material is not functionally graded, since it sets $V_{f,r}^{ex} = 1$ (or $100\,\%$), completely removing the passive material from the mixture. This variety of exponents was chosen to enhance this study and understand the mechanical behaviour of the beams, when constituted only by piezoelectric material,

but also with exponents below, equal to and above the unit value. Again, from Figure 3.12 it is possible to understand the volume fraction differences between curves.

In generic terms, there are four main static case study templates, i.e. actuation and sensing configurations, divided into (CFFF) and (CCFF) MBCs. Since a considerable amount of information is here presented, related to all case study combinations, graphical results are separated in p-exponents "below" and "above" the unit value, maintaining always both $p = 0$ and $p = 1$ as references, i.e. the "below" set is $p = \{0, 0.1, 0.5, 1\}$ and the "above" set is $p = \{0, 1, 2, 5\}$. From this point on, the reader can virtually interact with certain plots, by means of buttons, with the objective of changing the plotted results, enhancing the analysis. This methodology helps refining the information displayed in each plot, minimizing the possibility of having plots too much "crowded"; those are identified in their caption.

In addition, it is important to note that the magnitudes of all results do not matter so much; in this work, it is more important to compare them in relative terms. For example, in some actuation and sensing case studies, one obtains extremely low deflections and high voltages, respectively; it is only a matter of inputs associated with each modelled structure; these are preliminary academic examples.

Actuation configuration: Figures G.49 and G.50 represent schemes of actuation structural configurations used in static parametric studies, specifying type, geometry, mesh, loads, MBCs and materials aspects. Deflection plots, along length dimension, considering "below" and "above" p-exponent sets, are illustrated in Figures G.53 to G.56 and Figures G.57 to G.60, respectively. Then, Figures G.61 to G.64 summarize the results obtained using the biggest considered meshes, i.e. (15×1) and (16×1), for all p-exponents (hiding the intermediate meshes). To support the graphical results presented in Figures G.61 to G.64, with the same order, Tables G.16 to G.19 summarize them in tabular form; here the intermediate meshes' tabular results are omitted due to space constraints – in these tables, a coloured cell scale was adopted (conditional formatting), where smaller and higher values are associated with colours blue and red, respectively. To enhance even more these parametric studies, animations containing 251 frames, each, corresponding to 251 different p-exponents from 0 by 0.02 to 5, were created to minimize the possibility of misinterpretation of the deflections' distributions between the 6 p-exponents selected – see Figures G.65 to G.68. Following paragraphs are results' discussions.

Firstly, one compares the material properties of the passive and active materials used. Generically, in terms of elastic, piezoelectric and permittivity coefficients, the following relations apply:

$$Q_{ij}^{\text{PZT-7A}} \gg \left(Q_{ij}^{\text{LaRC-Si}} > Q_{ij}^{\text{PVDF}}\right), \quad e_{ij}^{\text{PZT-7A}} \gg e_{ij}^{\text{PVDF}}, \quad \varepsilon_{ij}^{\text{PZT-7A}} \gg \left(\varepsilon_{ij}^{\text{PVDF}} \gg \varepsilon_{ij}^{\text{LaRC-Si}}\right) \tag{4.2.1}$$

From Figures G.61 to G.64 and Tables G.16 to G.19 one concludes that, in terms of overall absolute maximum deflections, the highest values are obtained using (CFFF) MBCs and the active material PZT-7A. This trend was expectable, since with (CCFF) the structure becomes more constrained, reducing deflections (keeping in mind that the applied actuation voltages were always the same); then, due to the fact that PZT-7A has higher material coefficients comparing to PVDF, the FGM containing the former has more actuation power. The following relation applies, in order to compare maximum absolute deflections of all conditions: $8.12 \times 10^{-7}\,\text{m}$ (PZT-7A (CFFF)) > $2.27 \times 10^{-7}\,\text{m}$ (PVDF (CFFF)) > $8.17 \times 10^{-8}\,\text{m}$ (PZT-7A (CCFF)) > $3.03 \times 10^{-9}\,\text{m}$ (PVDF (CCFF)).

Deflection distributions are coherent with both (CFFF) and (CCFF) MBCs. In the former, concerning the curves' shapes, the deflection is always zero at $x = 0\,\text{m}$ (clamped edge) gradually decreasing or increasing towards the global minimum or maximum deflection at $x = 0.1\,\text{m}$ (free tip end); this behaviour is verified for both active materials, PVDF and PZT-7A, but deflections have opposite signals due to the materials coefficients from literature; when using PVDF, (CFFF) deflections are always negative, whereas when using PZT-7A are positive. In these conditions, no matter the active material

in the mixture, when the p-exponent increases, the absolute maximum deflection tends to decrease towards zero; this happens because when p increases, the mixture contains less piezoelectric particles distributed along the beam's length (they tend to accumulate near the free tip end). Also note that the deflection gradient is more accentuated near the free tip end, specially for higher p-exponents; this effect is visible in Tables G.16 and G.18, by the gradient colours. So, when p increases from zero to five, the (CFFF) beam loses actuation power and the deflection distributions follow a predictable path, as shown in Figures G.65 and G.67, for both materials.

Analysing the (CCFF) MBCs, deflection is always zero at both $x = 0\,\mathrm{m}$ (clamped edge) and $x = 0.1\,\mathrm{m}$ (clamped edge), as it should be. In addition, the general behaviour of the curves is similar for both materials. However, comparing to the (CFFF) MBCs, deflection distributions are not so predictable when p increases. First of all, minima and maxima occur at different locations along the beams' length, depending on the material distribution behaviour (p-exponent). Once again, (CCFF) deflection distributions, as in the (CFFF) ones, possess opposite signal for both active materials. However, when p increases, deflections are not always negative of positive; (CCFF) MBCs result in a more interesting behaviour, which can be observed from these figures and specially the animations in Figures G.66 and G.68; when p-exponents are below the unit value, a non-linear behaviour is obtained, where the deflection initially increases (or decreases, depending on the active material), but then around $p = [0.4, 0.6]$ this trend completely inverts, and the overall distribution starts to increase (or decreasing, again) towards some value. This behaviour is completely different from the previous one and it is possible to conclude the following: whereas the increase of p makes the (CFFF) beam to reduce actuation power, when MBCs are (CCFF) the opposite is verified, i.e. when the piezoelectric particles accumulate near a clamped edge, the beam gains actuation power $(p > 1)$ – in terms of structural design, using this methodology, one can optimize the FGM mixture in order to fulfil certain requirements. Also note that, for (CCFF) MBCs, when $p = 0$ (piezoelectric only), the maximum deflection occurs at the midspan x-coordinate $(x = 0.05\,\mathrm{m})$ and its distribution is symmetric along beam's length, as it should be (for both active materials).

In Figures G.53 to G.60, different meshes result in different deflections, as expected. Since to each element a discrete $V_{f,r}^{ex}$ value is allocated, the deviations between results when using different meshes increase, because each mesh will result in a different structure (the material distribution along x-direction varies, function of the number of elements). The conventional FEM convergence analysis of the same structure, associated to each specific p-exponent, would only be possible to carry out if a non-linear distribution of the elements along the beam's length (according to each p-exponent) was considered, otherwise, if one only increases the mesh (as done here), maintaining the linear discretization, different material distributions are obtained. If one was able to use an infinite number of elements along length, the continuous volume fraction distributions would be fully modelled. However, the manufacturing aspect is also important to discuss, where the mesh must be adequately selected (trade-off between number and distribution of elements, concerning each p-exponent), because the real objective can either be using discrete sections or to fully reproduce the continuous variation along length; in these case studies, the objective is only to understand the influence of different meshes, when maintaining the linear discretization (see Appendix A.2). Comparing this analysis between (CFFF) and (CCFF) MBCs, the differences are higher in the latter because in this case the structure is considerably more constrained by the two clamped ends, and any slightly variation of the piezoelectric particles' percentage along the beam's length will result in higher deviations between deflections. Analysing the results of each p individually, for different meshes, it is evident that the curves are further apart from each other when (CCFF) is used, in contrast with (CFFF). This enables one to conclude that the relation between meshes and p-exponents must be considered to obtain the desired results, specially when the stiffer structures are being modelled. In sum, to predict the behaviour of these structures

using FEM, one must consider an adequate number of elements, depending on the real objective in terms of material distribution, because for each element a discrete material mixture is calculated.

Again, manufacturing aspects of these passive/active FGMs are interesting to address. Some kind of electrical insulation/separation technique would be required to control each region of the structures independently, otherwise the electric charges would propagate to other sections along length; maybe in the future this subject can be more addressed, not in the present thesis.

Sensing configuration: Figures G.51 and G.52 represent schemes of sensing structural configurations used in static parametric studies, specifying type, geometry, mesh, loads, MBCs and materials aspects. Voltage plots, along length dimension, considering "below" and "above" p-exponent sets, are illustrated in Figures G.69 to G.72 and Figures G.73 to G.76, respectively. Then, Figures G.77 to G.80 summarize the results obtained using the biggest considered meshes, i.e. (15×1) and (16×1), for all p-exponents (hiding the intermediate meshes). To support the graphical results presented in Figures G.77 to G.80, with the same order, Tables G.20 to G.23 summarize them in tabular form; here the intermediate meshes' tabular results are omitted due to space constraints – in these tables, a coloured cell scale was adopted (conditional formatting), where smaller and higher values are associated with colours blue and red, respectively. To enhance even more these parametric studies, animations containing 251 frames, each, corresponding to 251 different p-exponents from 0 by 0.02 to 5, were created to minimize the possibility of misinterpretation of the voltages' distributions between the 6 p-exponents selected – see Figures G.81 to G.84. Following paragraphs are results' discussions.

From Figures G.77 to G.80 and Tables G.20 to G.23 one concludes that, in terms of overall absolute maximum voltages, the highest values are obtained using (CCFF) MBCs and the active material PZT-7A. This trend was expectable, since PZT-7A possesses higher material coefficients, i.e. the structure becomes stiffer comparing to the usage of PVDF; then, in order to generate the required $10\,\mathrm{mm}$ tip and midspan deflections, higher nodal tip and midspan loads are required; because of this, higher stresses are generated, resulting in higher voltages. In addition, it is also important to remind that both PZT-7A's piezoelectric and permittivity coefficients are higher than PVDF's ones. The following relation applies, in order to compare maximum absolute voltages of all conditions: $24\,792\,\mathrm{V}$ (PZT-7A (CCFF)) > $3677\,\mathrm{V}$ (PZT-7A (CFFF)) > $3322\,\mathrm{V}$ (PVDF (CCFF)) > $409\,\mathrm{V}$ (PVDF (CFFF)). Note that these voltage trends are different from the deflection ones in terms of materials and MBCs order.

Considering (CFFF) MBCs, in terms of voltage distributions' shapes, when $p = 0$ one obtains a decreasing or increasing behaviour (depending on the active material), approximately linear, from a global minimum or maximum near the clamped edge, towards zero near the free tip end. On the other hand, (CCFF) MBCs with $p = 0$ show a symmetric voltage behaviour along length, with global minima and maxima near the two clamped edges. As previously shown in the validation case studies, these two behaviours are expected, for these MBCs. Now, while deflection distributions showed similar shapes between the two active materials, voltages do not. These start with $p = 0$, with a similar shape, but when p-exponent increases, trends assume very distinct behaviours between different active materials and MBCs. At the first sight, the most curious detail about the shapes associated with different exponents, is that when this variable p increases, each (CCFF) case study seems to have two "pivot points" in specific length x-coordinates, which the curves rotate about – see Figures G.78 and G.80 and animations in Figures G.82 and G.84. Finally, with the increase of p, it is evident (specially by the animations) that at the length coordinates where the piezoelectric percentage gradually tends to zero, the generated voltage also tends to zero at those elements.

4.2.3.2 Dynamics (free vibrations)

In this subsection the same beam structures from the previous one are studied, but now considering dynamics (free vibrations) analysis (eigen-values/vectors problem solution), with closed and open-circuit EBCs. Figures G.85 and G.86 represent schemes of these dynamic parametric studies, specifying type, geometry, mesh, loads, BCs (both MBCs and EBCs) and materials aspects. Natural frequencies plots associated with the first five free vibrational modes, considering "below" and "above" p-exponent sets, are illustrated in Figures G.87 to G.90 and Figures G.91 to G.94, respectively; these plots were obtained using the biggest considered meshes, i.e. (15×1) and (16×1), for all p-exponents (hiding the intermediate meshes). In order to better understand the behaviour of the fundamental natural frequency, Figures G.95 and G.96 ("below" p-exponent set) and Figures G.97 and G.98 ("above" p-exponent set) show them, for each p-exponent. Note that these plots contain the absolute differences between closed and open-circuit natural frequencies in [Hz] (Hertz), i.e. $\omega_{difference} = \omega_{open} - \omega_{closed}$, for comparison purposes. To support the graphical results presented in Figures G.87 to G.98, Tables G.24 to G.27 summarize them in tabular form; here the intermediate meshes' tabular results are not omitted, only to show their convergence behaviour. In addition, using conditional formatting from cell colours green to red, associated with minimum and maximum values, respectively, Tables G.28 to G.31 show the absolute differences between all closed and open-circuit natural frequencies. Finally, Figures G.99 to G.102 show the first five free vibrational modes for the 2 active materials (PVDF and PZT-7A) mixed with the passive LaRC-Si, for the 6 p-exponents (0, 0.1, 0.5, 1, 2 and 5) and 2 MBCs analysed.

Note that natural frequencies in all tables related to these dynamic parametric studies are formatted with 4 decimal places, which is too much. This format was applied on purpose, or otherwise, in some case studies, no differences between closed and open-circuit natural frequencies would be noticed.

From Tables G.28 to G.31, it is observed that open-circuit natural frequencies are always higher than closed-circuit ones, as already predicted before (in these four tables $\omega_{difference} > 0$). Then, from Tables G.24 to G.27 one concludes that the highest fundamental natural frequencies ω_1 are obtained when using PZT-7A $(p = 0)$ with (CCFF) MBCs. In fact, focusing only on the fundamental natural frequency, the following relation applies, in order to compare maximum ω_1 of all conditions (biggest meshes and open-circuit EBCs): 377 Hz (PZT-7A, $p = 0$, (CCFF)) > 165 Hz (PVDF, $p = 5$, (CCFF)) > 58 Hz (PZT-7A, $p = 0$, (CFFF)) > 25 Hz (PVDF, $p = 5$, (CFFF)). From this analysis, it is evident that (CCFF) MBCs are always associated with higher frequencies due to the higher constraint in comparison with (CFFF); then, structures containing PZT-7A possess higher frequencies. However, it is important to understand that when p increases, the natural frequencies decrease and increase when the structure contains PZT-7A and PVDF, respectively. This trend is expectable, because for higher p-exponents the percentage of active material decreases along the beams' length; recalling that $Q_{ij}^{\text{PZT-7A}} \gg \left(Q_{ij}^{\text{LaRC-Si}} > Q_{ij}^{\text{PVDF}}\right)$, less PZT-7A means less stiffness (reduces ω) and less PVDF means more stiffness (increases ω), explaining this trend (see Figures G.95 to G.98).

Tables G.28 to G.31 show that, in general, differences between closed and open-circuit natural frequencies tend to increase when the structure's stiffness also increases, with the same tables' order. So, higher differences are associated with (CCFF) MBCs and PZT-7A active material, which possesses higher piezoelectric and permittivity coefficients (see Eq. (4.2.1) and Table G.31). When the mesh increases, differences tend to decrease; the same happens when p-exponent increases, which is expectable, since this results in less piezoelectric material along length (less electric contributions).

From Figures G.87 to G.94 and Tables G.28 to G.31 one observes that, depending on MBCs, there are vibrational modes with associated frequencies' differences always equal to zero (at least with the present meshes); e.g. when the material is PVDF and MBCs are (CFFF) modes number 2, 4 and 5 (Table G.28), or when the material is PZT-7A and MBCs are (CCFF), modes number 2 and 4

(Table G.31). Analysing these particular modes in Figures G.99 and G.102, respectively, it is possible to conclude that these correspond to modes without any vibrational waves along length x-direction (remembering that only one element exists in the mesh along y-direction). It is important to recall that only in-plane piezoelectric coefficients' components are being considered $\{31, 32, 36\}$, and shear ones neglected $\{14, 15, 24, 25\}$; this fact is most likely the motive to explain these observations.

Finally, another aspect that is worth to mention is the influence that p-exponents have on vibrational modes; e.g. analysing Figure G.102, more specifically the 2D plots, the modes' amplitudes are considerably shifted towards $x = 0\,\mathrm{m}$, i.e. the opposite way of the higher piezoelectric percentage. In this figure, since PZT-7A is the analysed material with highest elastic coefficients, makes sense that the vibrational oscillations with greater amplitudes tend to occur where the structure is less stiff.

4.3 Optimization studies

Optimization case studies are the last ones of the present work. Here, the performance, efficiency and behaviour of the interaction between both FEM and bat algorithms are evaluated. In this section, multilayered smart structures are modelled and one develops several different case studies, static and dynamic (free vibrations), in order to accomplish design objectives by means of DVs' sets.

In order to diversify the presented studies, one subdivided this section using a logic sequence. Firstly, the objective is to minimize both beams' and plates' overall deflections, by means of controlling the electric potentials applied to the structures' active materials; here, the micro behaviour of the MHBA is intensively tested, to enhance the performance of the patches locations' optimization (plates).

Then, with a structural design perspective, shape morphing, beams' deflections are approximated to 2 and 3 user-defined control points, controlling electric potentials and material distributions.

Finally, after completing the static optimization case studies, one modelled the dynamic ones, where the objective is the maximization of the fundamental natural frequency; here, multilayered smart structures also constituted by fibre-reinforced orthotropic (monoclinic) materials are addressed, in order to find the optimal fibre angles. The first structure is a non-skewed beam, the second one is a skewed beam and finally, the third one is a skewed plate.

The first two optimization studies' categories, i.e. minimization of deflections and approximation of deflections to control points, were presented at Costa (2016b) and Costa and Loja (2016b), as well as submitted to *Journal of Composite Structures* and *Journal of Composites Part B: Engineering*. Although the last dynamic optimization studies were not presented at the conferences, they were submitted to these scientific journals.

4.3.1 Multilayered smart structures

The present subsection addresses optimization studies concerning multilayered smart structures. The first category is the minimization of beams' deflections, as presented next.

4.3.1.1 Minimization of beams' deflections

Figure H.1 is the case study scheme associated with the modelled bimorph beam, for deflections' minimization; this figure specifies the geometry, mesh, loads, MBCs, materials, optimization objectives and DVs. The geometry of this structure is equal to the (CCFF) ones analysed in the parametric studies.

This beam is constituted by two FGM active layers (bimorph), along length x-direction, mixing LaRC-Si with PVDF. Concerning the optimization process and due to computational efficiency, the

structure was discretized in (6×1). Since the optimization objective is the minimization of overall deflections, a midspan nodal load was imposed to generate an initial deflection. By means of 12 DVs, i.e. the electric potentials applied to each active patch (6 from the bottom layer and 6 from the top one), the optimization algorithm searches for the optimum combination of voltages along length, in order to minimize the initial deflection. For comparison purposes, one considered two p-exponents, i.e. 1 and 5, in order to obtain different piezoelectric distributions along length. The lower and upper bounds of all DVs were assumed to be from -750 to $750\,\mathrm{V}$; this is an adequate range for PVDF.

The present optimization case study was computed using HBA, i.e. with Micro technique disabled; the inputs used in this optimization process are summarized in Table H.1. One can observe the optimization problem definition, parameters associated with echolocation, solution modification and constants. Note that variable d is the total number of DVs used in the optimization case study. All remaining variables were described previously. In order to understand the behaviour of the HBA when dealing with this type of structural optimization problem, one has randomly chosen 25 different combinations of DE perturbation factors, to run the interaction between both algorithms 25 times (FEM and HBA). Using this methodology, considering a small number of generations and bats' population sizes (50 for both), it is possible to understand which factors lead to better results; Table H.2 summarizes those factors, as well as the best deflection results obtained with each of them.

For each case study, the **P**ercentage **R**eduction (PR) was computed, i.e. the percent reduction when comparing both optimal and initial maximum absolute deflections, in $[\%]$ (percent). Figure H.2 shows the optimization results from these 25 case studies, considering the best OF solution, PR regarding the initial state deflection, DVs and perturbation factors' evolutions. In relation to the initial state, it was possible to reduce the maximum absolute deflection in about $93.88\,\%$, corresponding to perturbation factors $Fper_i = 1.5$ and $Fper_f = 0$ (see Table H.2).

From Figure H.2, it is possible to understand that the PR curve starts to increase after case study number 17; this means that, in all case studies after this one, the best OF result was higher than the initial state deflection. This is why bat-inspired optimization requires a preliminary study considering several combinations of inputs (in this case perturbation factors). So, in these worst cases, there is a "percentage increase" instead of a "percentage reduction", from the point that the OF best curve is higher than the initial state one (see Figure H.2); this behaviour shows that certain perturbation factors are not suitable for this particular optimization case study, where the algorithm is not able to converge towards the objective. Keeping in mind that bat-inspired optimization has a level of randomness associated to itself, it is difficult to perceive a particular trend on these perturbation factors from Table H.2. In any case, the top combinations are the most viable to exploit; when using this type of optimization, one needs to start somewhere, otherwise it would be a shot in the dark.

To understand the convergence rate of the HBA, Figure H.3 shows the optimization results, for all generations, from the best case study found in Table H.2. From this figure it is possible to observe that the HBA started already with a better solution in comparison with the initial design; no best was found from generation 1 to 23; suddenly a jump occurs and the algorithm converges towards the best result after generation 30 or so. This behaviour illustrates the capabilities of this algorithm, where exploitation and random flights enable one to escape from local optima; it is also important to note that a low number of generations and population size were considered in this preliminary case study.

In order to take advantage from the present algorithms' capabilities, associated with this best case study Figures H.4 to H.7 show, respectively, the record along all best optimization generations of parametric deflection plots, 3D and 2D deflection plots, electric potentials of both layers and voltages along beam's length – note that these plots' titles contain interesting information along animations' frames, such as best OF and PR values of each best iteration.

After this preliminary analysis, the optimization case study considering $n = 50$, $p = 1$, $Fper_i = 1.5$

and $Fper_f = 0$ was exploited using a higher number of generations, i.e. $N_{gen} = 100$ (which is still reduced). Similarly to the plots in Figures H.3 to H.7 for the initial computations using $N_{gen} = 50$, Figures H.8 to H.12 show the same plots but for the computations using $N_{gen} = 100$. These results are shown here on purpose, in order to point out the meta-heuristics behaviour associated with HBA; first of all, the "most promising" perturbation factors were found using the available time; after that, it would be fair to think that increasing the number of generations, a better result could be found. However, with $N_{gen} = 50$ the algorithm reached a PR of $93.88\,\%$, whereas $N_{gen} = 100$ resulted in PR of $90.06\,\%$. Since there are not perfect algorithms, this illustrates the complexity of HBA, which requires a proper preliminary input study, tailored-made for each particular optimization problem. In any case, the obtained PRs are satisfactory; in order to increase PR even more, one could increase generations and population sizes, enable Micro technique and test other HBA inputs. Figures H.4 and H.9 illustrate the deflections' minimization evolution along best iterations, where it is possible to see their significant reduction in comparison with the initial state.

Afterwards, only for comparison purposes, the same approach was carried out using $p = 5$ (results in Figures H.13 to H.17). Similarly to the previous study with $p = 1$, this one was computed with $N_{gen} = 100$, $n = 50$, $Fper_i = 1.5$ and $Fper_f = 0$. The major differences to report between results with $p = 1$ and $p = 5$ are the voltages' distributions along length, because in the latter there are less piezoelectric particles along length (see Figures H.12 and H.17). In any case, without apparent motive, the HBA found a better result in this case of $p = 5$, where PR is equal to $98.58\,\%$.

4.3.1.2 Minimization of plates' deflections

In the present subsection one considers the plate illustrated in Figure H.18, which consists of one bottom passive layer made of LaRC-Si, with PZT-7A patches on top of it (either 1, 2, 3 or 4 patches); this scheme specifies the geometry, mesh, loads, MBCs, materials, optimization objectives and DVs. This plate is simply-supported along all edges (SSSS) and is supporting an uniform transverse pressure distributed on the whole mesh, which is (10×10). The optimization objective is to minimize the overall deflection caused by that pressure, using the top patches' locations and respective electric potentials. This scheme only reflects the visualization of 1 patch on top of the passive layer, however the same methodology applies for 2, 3 and 4 patches, keeping in mind that during optimization all patches assume independent and different locations between each other; note that the patches were assumed to have lateral dimensions equal to the dimensions of each quadrilateral mesh's element.

In addition, it is possible to see two different possibilities of DVs' combinations. Concerning electric potentials' DVs (one per each active patch, individually and independently), the first approach considers that these DVs can be from -1000 to $1000\,\mathrm{V}$, whereas the second approach only considers positive electric potentials from 0 to $1000\,\mathrm{V}$; this is an adequate range for PZT-7A. Then, concerning locations' DVs, also one per patch independently, the first approach considers the locations of each patch to be defined by minimum coordinates in the xy-plane (continuous variables, floats, from 0 to $0.45\,\mathrm{m}$), whereas the second one selects an element from the plate's mesh directly (discrete variables, integers, from 1 to 100). The second approach makes the bat-inspired algorithm more efficient, because it reduces the total number of possible DVs and sets the values of the locations' DVs closer to the electric potentials. Several case studies were run using the first set of DVs and the bat-inspired algorithm was not able to explore wide ranges of patches locations, because when the locations' DVs are float numbers, the increment on each DV's updating may not be high enough to select the next element inside the mesh (each layer has allocated elements, which are selected based upon their centre xy-coordinates). In contrast, by forcing the algorithm to pick up integers from 1 to 100, the universe of possibilities becomes smaller, making the algorithm exploring more locations. In addition, in the second approach

the bounds' range of the electric potentials DVs were reduced and became non-negative, eliminating the useless negative electric potentials; since the uniform pressure is negative, only positive electric potentials applied to the patches will contribute to minimize deflections (tested before).

On top of this, three types of solutions' reinitializations were tested and compared, to understand the effect of the Micro technique on the results, i.e. Reinits All Gens (reinitializations before each generation), Reinits Step 5 Gens (reinitializations from 5 to 5 generations) and Reinits Step 10 Gens (reinitializations from 10 to 10 generations). All case studies with reinitializations before each generation (Reinits All Gens) were computed using the first approach of DVs and the remaining ones with the second approach, for comparison purposes. So, in all these case studies to minimize plates' deflections, Micro technique was always active, to force a wider exploration of design space; note that one reinitialization means that all DVs, i.e. both electric potentials and locations, are randomly re-generated inside their respective bounds. It is not shown here, but in the first tests of these case studies, when using the first set of DVs (continuous locations) with Micro technique disabled, the algorithm's performance used to be very very poor; it would change between only one or two different locations (converging to local optima), and only electric potentials would be optimized, fixing the location (the successive solutions' updating were not able to inflict perturbations high enough to test new locations throughout the mesh); after testing the second set of DVs and enabling the Micro technique, the behaviour of the algorithm became a lot more different, enabling huge exploration of locations (and electric potentials), to minimize deflections.

If these changes still did not improve the bat-inspired algorithm's performance (which was not the case), one could have used a *multilevel approach*, dividing the problem into two separate steps, i.e. first step to optimize locations only and second step to optimize electric potentials only; this solution would be less comfortable to the user, and less efficient. In addition, another solution would be the normalization of all DVs to be from 0 to 1, in order to work with different DVs' categories (electric potentials or locations), with equal bounds; this way, the algorithm would be able to explore more locations because any slightly perturbation on the DVs between 0 to 1, would result in a different element position.

Again, PR was always computed to compare both initial and "optimal" deflections (before and after optimization). However, in some plots here presented, it is possible to see "increasing percentage reductions". In those cases, similarly to the previous case studies (minimization of beams' deflections), it means that the optimization algorithm converged to a worse result comparing to the initial one, but in terms of plot label it is still called a "PR". For instance, analysing Figure H.19 and keeping in mind that the results were sorted from the best (lowest) to the worst (highest) deflection result in the y-axis, it is possible to conclude that somewhere between case studies no. 44 and 20 PR stops decreasing and starts increasing. This only means that from this point on, the OF solution was always higher than the initial state deflection caused by the uniform pressure, i.e. the algorithm, with those particular DE perturbation factors was not able to minimize the original deflection.

Similarly to the previous beams' examples, 50 combinations of perturbation factors were tested for these plates, using 1 patch only and Micro type of Reinits All Gens (see Table H.4); after this, only the 25 best combinations (left side of this table) were used to compute the remaining case studies. These 25 trials were computed to each number of patches (1, 2, 3 and 4), divided into the 3 types of Micro reinitializations. Note that a (10×10) plate takes more time to solve then the previous (6×1) beams; it is important to remember that when one uses, for example, $N_{gen} = 50$ generations with $n = 10$ bats each, it means that $50 \times 10 = 500$ FEM problems will be solved. Doing the maths, only to optimize these plates' problems, $25 \times 4 \times 3 = 300$ trials (or case studies) were computed; assuming the previous number of generations and bats, this results in $500 \times 300 = 150{,}000$ FEM evaluations; these thoughts apply to every case study here presented.

The inputs used in this optimization process are summarized in Table H.3. The results are organized in the following manner: Reinits All Gens (1, 2, 3 and 4 patches), Reinits Step 5 Gens (1, 2, 3 and 4 patches) and Reinits Step 10 Gens (1, 2, 3 and 4 patches), i.e. from the most to the less frequent number of reinitializations per case study. All these results are presented in Figures H.19 to H.47; note that in this .pdf document, in these animations, one can toggle between OF best, PR, DVs and perturbation factors' evolutions along all case studies. In figures such as Figure H.20, in the fourth sub-plot (bottom right side) it is possible to see the mesh of the plate, as well as the active mesh (where the active patches are) in each frame of the animation; this type of visualization is extremely interesting to see, in order to understand both behaviour and performance of the present algorithms' interaction. In certain animations, such as Figure H.19, DVs are separated into separate frames, in order to analyse data of electric potentials and patches' locations separately. Figures H.43 to H.47 are animations that summarize the most important data, to compare results between 1, 2, 3 and 4 patches, for all types of Micro reinitializations; Table H.5 summarizes these results in tabular form, enhancing the comparison of the first five top results for each case study type (averages and standard deviations of the top five PRs are also shown). Inside each cell of this table, one can observe both deflection and respective PR, separated by /.

From Table H.4 it is possible to notice that worse deflection results were mostly obtained with higher perturbation factors (right side of the table). From Table H.5, several interesting facts must be mentioned. Tendentiously and intuitively, the higher the number of patches, the higher the PRs should be, with this particular plate set-up (MBCs, load distribution, etc.). From this table, focusing on the first line, it is possible to understand this trend, i.e. more patches, higher PRs. However, the highest PR out of all was obtained using 3 patches and Reinits All Gens ($60\,\%$); this only happened because the number of generations and population sizes were constant for all case studies, and since the complexity/number of possibilities increases with the number of patches, the case studies with 4 patches did not have enough iterations to fully converge. In contrast, it is fair to say that both 1 and 2 patches converged, specially the former – standard deviations help understanding this fact, and it is obvious that this variable increases with the increase of number of patches (from 1.00 to 6.84). Of course that for higher number of patches, 3 and 4, one should have used more iterations; however, due to time constraints such was not possible, maybe in the future. In any case, these results already enable one to extract several interesting conclusions.

Analysing the PRs' averages, from 1 to 4 patches, one obtained $46.29\,\%$, $48.66\,\%$, $47.61\,\%$ and $47.48\,\%$ – these results show an evident lack of convergence, because this trend should increase; instead, it decreases between 2 and 3 patches. To support even more this conclusion, associated with 1 and 2 patches, animations in Figures H.20 and H.30 show that the algorithm found a specific trend in the patches' locations; the best solution is to put one patch in the centre coordinates of the plate (elements 45, 46, 55 or 56), whereas when using two patches a symmetric solution is found (elements number 34 and 67). In contrast, in these plots for 3 and 4 patches a specific trend is not so evident.

In any case, from Table H.5, the Micro effect is visualized. Focusing on the separate averages for each number of patches and reinitializations type (line associated with "average of above PRs"), analysing each number of patch individually, the highest average trend is the following: $46.75\,\%$ (1 patch, Reinits Step 10 Gens), $51.06\,\%$ (2 patches, Reinits Step 5 Gens), $51.67\,\%$ (3 patches, Reinits Step All Gens) and $48.95\,\%$ (4 patches, Reinits Step All Gens) – one concludes that when the number of patches increases (maintaining the number of generations and population individuals), better results (in average) are obtained using more reinitializations (the present Micro technique); this behaviour makes sense because when the number of patches is low (1 or 2), the algorithm converges to the right locations and then optimizes electric potentials (so here Micro effect reduces the performance because instead of optimizing the electric potentials at the right locations, it forces the algorithm to explore other

worse locations); whereas for higher number of patches (3 or 4) the number of locations' combinations increases very much, and in these latter cases Micro technique helps the algorithm to explore more locations and runaway from local optima. From a mesh of 100 elements, 1, 2, 3 and 4 patches can assume, respectively, 100, $\approx$4950, $\approx$161700 and $\approx$3921225 combinations. Again, it is obvious that 3 and 4 patches needed more iterations in order to find better results.

In sum, from this particular optimization case study, MHBA reveals to be useful when dealing with more complex problems, because the issue here is to find optimal patches' positions. When less number of patches are used, a lot of reinitializations give worse results (in average), because here the algorithm converges very fast towards the optimal solution; however, if the Micro was disabled, HBA would require more iterations to find the optimal locations, because it would have less exploration capabilities.

4.3.1.3 Approximation of beams' deflections to 2 control points

The present subsection describes a set of case studies that consider the same beam structures as in Section 4.3.1.1 and Figure H.1 – geometry, mesh, loads, MBCs, materials and FGM behaviour are exactly the same, before optimization (initial state). However, these ones (illustrated in Figure H.48), possess different optimization objectives and some details about DVs. As shown in this figure, instead of minimizing the overall deflection, one intends to approximate the beams' deflection to two user-defined control points. As before, a midspan nodal load is imposed to this (CCFF) beam, in order to start with a negative deflection. Afterwards, the user specifies four points by means of xz-coordinates (y-coordinate is by default equal to zero, since this is a beam); in this case, these points possess the same x-coordinates as the nodes number 1, 3, 5 and 7; then, the points number 1 and 4 have z-coordinates equal to $0\,\mathrm{m}$, whereas points number 2 and 3 equal to $1.5 \times 10^{-6}\,\mathrm{m}$. Using these four points (here called "polynomial interpolation points"), the algorithm creates a polynomial interpolation, obtaining the function that intersects each of them. Finally, the user specifies the number of control points to consider, which in this case is two; by means of two x-coordinates, one for each control point, the evaluation of those coordinates in the previously interpolated polynomial curve gives the z-coordinate of each control point. In sum, one specifies each control point indirectly, by means of four interpolated points – this type of methodology might be interesting to use in certain types of designs, where the deflection must be approximated to points belonging to some function. One has specified the x-coordinates of these control points to be equal to the ones of nodes number 2 and 6. With this being said, the optimization objective is to counteract completely the initial negative deflection and force the beams' deflection at nodes number 2 and 6 to be approximately equal to the specified control points; in the process, the algorithm has to find the optimal voltages' distribution along beam's length, in order to make that happen. Now, the discrete OF is the minimization of the sum of the squared deviations, between the z-coordinates of nodes number 2 and 6, and z-coordinates of control points number 1 and 2, respectively. Still in this figure, one can observe two different sets of DVs; the first one is only the electric potentials of each patch (exactly the same as in the minimization of overall beams' deflections); the second one, considers additionally the p-exponents of patches number 1 and 7, as well as number 2 and 8; the motive of considering these two possibilities is explained further ahead, along with the optimization results. Note that in this figure CP means **C**ontrol **P**oint, $\overline{w}_{CP}$ is the z-coordinate of each control point CP and w (without overline) is the deflection (z-coordinate DOF) of the nodes (in this case, number 2 and 6), both in $[\mathrm{m}]$ (metre).

The first optimization trial was carried out considering the same HBA parameters as in Figure H.8, i.e. $N_{gen} = 100$, $n = 50$, $Fper_i = 1.5$, $Fper_f = 0$ and $p = 1$. In all case studies about approximation of beams' deflections to control points, the Micro technique was disabled, i.e. HBA was used.

The optimization results are shown in Figure H.49, for all generations of this trial. Instead of the measurement parameters previously described PR and PI, now one created another one: the **P**ercent **D**eviation (PD), which is basically the deviation between the nodes' deflections w and the control points' z-coordinates (the targets) $\overline{w}_{CP}$. From this figure, one concludes that both PDs associated with both control points tend to $0\,\%$ – the HBA successfully solves this problem. In order to take advantage, again, from the programmed package in the present work, Figures H.50 to H.53 show the record of this case study, concerning the evolutions of deflections, PDs and DVs. From Figure H.50, in the last best iteration, the PDs associated with control points number 1 and 2 were, respectively $0.09\,\%$ and $0.12\,\%$ – these are acceptable and one concludes that using $p = 1$, both control points are very well approximated.

After this, the exact same case study was computed, but considering $p = 5$, i.e. less active material (PVDF) along beam's length. The same results are presented in Figures H.54 to H.58. Analysing these results, it is possible to conclude that the HBA converges towards optimum, but higher deviations between the optimized and control points z-coordinates occur, i.e. $50.73\,\%$ and $17.80\,\%$; these higher percentages were expected and are not a result of HBA's inefficiency, but instead are due to the material constraints themselves. With such low percentages of PVDF, specially the left side control point becomes compromised. At this point, in a real design situation, a viable solution would be optimizing the p-exponent associated with left side patches; in order to do that, the following case study considers as DVs the same electric potentials for the 12 patches and additionally two more, i.e. one p-exponent equal for both patches numbers 1 and 7, and another one p for both patches numbers 2 and 8.

The new results, considering these two p-exponent DVs, are shown in Figures H.59 to H.63. Analysing the results, as expected, the HBA easily founds the optimum solution, setting $100\,\%$ and $0\,\%$ of piezoelectric particles at, respectively, patches numbers (1 and 7) and (2 and 8). The final PDs are equal to $0.01\,\%$ and $0.02\,\%$, which are acceptable.

4.3.1.4 Approximation of beams' deflections to 3 control points

The exact same procedure from the previous subsection (2 control points), was developed considering 3 control points (see Figure H.64); same beam conditions, same HBA inputs, same everything (except the discrete OF, because now it considers one more control point in the sum of the squared deviations). In the present subsection, the results concerning this latter case are addressed and discussed.

The first step considers $p = 1$ and only electric potentials as DVs – the results are shown in Figures H.65 to H.69. From these, one concludes that the algorithm found a very efficient solution, with PDs equal to $7.96\,\%$, $0.64\,\%$ and $0.47\,\%$. It is evident that the first control point (left side) possesses a higher PD, around $7.96\,\%$, because at that length there are only $8\,\%$ and $25\,\%$ of piezoelectric particles. Comparing to the previous results of 2 control points, the major differences are only the final deflection shape, as well as the voltages' distributions along length (because 3 control points add one more constraint to the problem).

After this, results of the computation considering $p = 5$ are shown in Figures H.70 to H.74. Again, PDs are higher and equal to $63.48\,\%$, $8.73\,\%$ and $7.37\,\%$. Note that both control points numbers 2 (middle) and 3 (right side) possess lower deviations, due to the higher piezoelectric particles' percentages at those length coordinates.

Finally, and to end the control points' case studies, two p-exponents were added to the DVs' set (as in the previous subsection). The results are shown in Figures H.75 to H.79. The HBA set $89\,\%$ and $68\,\%$ of piezoelectric particles at, respectively, patches numbers (1 and 7) and (2 and 8). The final PDs are equal to $7.75\,\%$, $3.74\,\%$ and $12.49\,\%$ – this solution is acceptable, but better results could be obtained if one had increased the number of generations and population individuals (in order to

increase the number of available iterations and time to converge), or even tested other HBA's inputs (because the initial best perturbation factors were not found/chosen based on this particular case study).

4.3.1.5 Maximization of fundamental natural frequencies (non-skewed beams)

Following the sequence of the optimization validation studies in Section 4.1.4.3, from the present subsection on, several present optimization studies are developed. These three case studies have the optimization objective on maximizing the fundamental natural frequency ω_1 of a beam or plate structure; this way, the present bat-inspired algorithm can also be tested in dynamics (free vibrations) behaviour. The first structure, illustrated in Figure H.80, is a non-skewed beam with (FFCC) MBCs and constituted by five layers: the bottom one is a piezoelectric layer made of PZT-5H ($h_p = 0.5\,\mathrm{mm}$ thick) and covers the whole mesh; then, four independent fibre-reinforced orthotropic (monoclinic) layers ($h_l = 1\,\mathrm{mm}$ thick, each) are glued on top of the bottom one. To each of these orthotropic layers, made of Gr/Epoxy, only one mesh's element is allocated to it, along y-direction – a mesh (1×4) was considered, due to computational available resources (note that in these cases additional processing is necessary in order to solve the eigen-values/vectors problem). Since the top four layers are independent from each other, the objective is to find the optimal set of fibre orientations θ_k in $[^\circ]$ (degree), to maximize ω_1; these four angles have lower and upper bounds of, respectively, -90 and $+90^\circ$. One considered open-circuit EBCs for the piezoelectric layer, i.e. free electric potentials. In the initial design (before optimization), all fibre angles are equal to 0°, i.e. the orientation sequence is $[\theta_{e_1}, \theta_{e_2}, \theta_{e_3}, \theta_{e_4}] = [0^\circ, 0^\circ, 0^\circ, 0^\circ]$ at the beginning (θ_{e_i} means fibre angle of element number i).

Only one trial/case study was computed to optimize this beam, because the results were already the expected ones. Micro technique was enabled, considering Reinits Step 10 Gens (only from generation numbers 1 to 50); this means that reinitializations occur only in generation numbers 11, 21, 31 and 41. The remaining MHBA inputs are presented in Table H.6. Comparing to the initial state $\omega_1 = 469\,\mathrm{Hz}$, the algorithm found the optimum solution with orientation sequence of $[90^\circ, -90^\circ, 90^\circ, 90^\circ]$ (as expected); this optimized design results in a new $\omega_1 = 1043\,\mathrm{Hz}$, with PI of $122.35\,\%$. In Figures H.81 and H.82, respectively, it is possible to observe the record along this optimization trial, concerning the DVs evolution and fundamental free vibrational mode amplitude's distributions.

4.3.1.6 Maximization of fundamental natural frequencies (skewed beams)

The present subsection addresses the maximization of the fundamental natural frequency ω_1 of the same beam modelled in the previous one (illustrated in Figure H.80), but now considering a skew angle equal to 30° along x-direction (see Figure H.83). Eight trials were computed considering different MHBA inputs, as shown in Table H.7. Note that the length of the beam is the same, $100\,\mathrm{mm}$, in order to see if this skew angle influences or not the optimal solution concerning the maximization of ω_1.

Analysing this table, the best result was found in case study number 7. Before and after optimization, the fundamental natural frequency was equal to $\omega_1 = 470\,\mathrm{Hz}$ and $\omega_1 = 1017\,\mathrm{Hz}$, respectively, corresponding to PI equal to $116.27\,\%$. While when the skew angle was 0° the optimal orientation sequence was $[90^\circ, 90^\circ, 90^\circ, 90^\circ]$, now considering skew angle of 30° the optimal sequence becomes around $[60^\circ, 60^\circ, 60^\circ, 60^\circ]$. One concludes that the skew angle has a considerable influence on the optimal design solution. In order to complement the present results, Figures H.84 and H.85 show the animations about this case study.

4.3.1.7 Maximization of fundamental natural frequencies (skewed plates)

The last case study of the present thesis is similar to the previous ones, but now one has the objective of maximizing the fundamental natural frequency ω_1 of a skewed plate. The case study scheme of this structure is presented in Figure H.86. In terms of the skewed geometry, one considered the same as the one in the optimization validation example from Correia et al. (2016, 2001) (already addressed in Section 4.1.4.3). One considered a mesh of (4×4), where each element row along y-direction has the same DV (fibre angle θ); for instance, DV number 1 is equal for all element numbers 1 to 4, until DV number 4 that is associated with element numbers 13 to 16. Once again, the initial design is $[0°, 0°, 0°, 0°]$, concerning the fibres' orientations sequence; before optimization $\omega_1 = 51.509\,\text{Hz}$.

This model was optimized considering the same eight trials from the previous subsection and the results are shown in Table H.8. The best result found is around $\omega_1 = 114.334\,\text{Hz}$, with orientations sequence of $[-87.8°, 80.9°, 78.2°, 90.0°]$; PI is equal to $121.97\,\%$. Analysing results one can suppose that the optimum design is around this best present result, but there are no external references to compare with. So, only to create two reference points, the FEM algorithm was run considering the orientations sequences of $[90°, 90°, 90°, 90°]$ and $[80°, 80°, 80°, 80°]$; with the same order, the results were $\omega_1 = 112.545\,\text{Hz}$ with PI equal to $118.50\,\%$, and $\omega_1 = 112.679\,\text{Hz}$ with PI equal to $118.76\,\%$.

These two reference points enable one to conclude that the present result of $\omega_1 = 114.334\,\text{Hz}$ with PI is equal to $121.97\,\%$ is in fact better than these two, with a non-linear fibres' orientations sequence along the elements' rows of the plate. To visualize the best results' animations see Figures H.87 and H.88.

Chapter 5

Conclusions

NOTE: This chapter contains pages 143 to 148, which is 6 in total.

5.1 General overview

Throughout the present work, an integrated symbolic-numerical-graphical package devoted to the analysis of plate-type structures and its bat-inspired optimization was implemented. Several validation case studies were developed to prove the accuracy of the present interaction between FEM and bat-algorithms. In addition, present parametric and optimization studies were carried out, to study in detail both static and dynamic (free vibrations) behaviours of multilayered smart structures, as well as functionally graded, multiscale and hybrid composite structures. The majority of the work documented here, was already presented and published internationally in several scientific conferences and journals.

Concerning the implementation of FEM, one considered the FSDT (5 DOFs per node), capable of modelling 2D beam/plate type structures (quadrilateral skewed and non-skewed meshes in the xy-plane). The algorithm supports several types of materials, including passive and active ones: isotropic, orthotropic (monoclinic), FGMs along several spacial directions (two types of homogenization schemes and approximation approaches), CNTs (SWCNTs and MWCNTs), piezoelectrics. This way, it is possible to model complex multilayered smart structures, considering several configurations in terms of materials' combinations, ranging from piezoelectric materials to graded mixtures of piezoelectric particles and non-active materials along different directions, hybrid, multiscale composite structures, etc. In terms of FEM processing, both Lagrangian and Kriging elements are available.

The non-linear meta-heuristics bat-inspired algorithm interacts automatically with the FEM one, being possible to specify several different types of optimization objectives, as well as DVs. Two upgraded versions of the traditional BA were implemented, in order to optimize these innovative types of structures: the HBA and MHBA. The performance of both algorithms was tested and compared, for different sets of optimization case studies: minimization of both beams' and plates' overall deflections, approximation of beams' deflections to several control points and maximization of structures' fundamental natural frequencies. A considerable amount of results are automatically organized and exported by both algorithms, to make the post-processing analysis easier. It is also possible to specify several case studies and leave the computer/server handling everything automatically.

5.2 Most relevant conclusions by main topic

Finite element convergence: Concerning to the finite element convergence carried out, one concludes that Lagrangian elements are more efficient in comparison with Kriging ones, at least in the present convergence case study; the latter require analytical integration, which compared to numerical Gauss quadrature are computationally heavier; the Kriging shape functions are also more complex. Faster convergence rates are associated with bicubic elements, followed by biquadratic and bilinear ones (in general). Since 4BlinLag element proved to be the most efficient in term of processing resources, this one was used throughout most case studies.

Functionally graded, multiscale and hybrid composite structures (static behaviour): In terms of more specific conclusions, about the modelling of static behaviour of hybrid CNT-metal-ceramic composite structures (addressed in Section 4.2.2.1), the following lines apply: this work presents a characterization study of the static response of moderately thick plates made of dual-phase metal-ceramic FGMs, where it was also considered the possibility of dispersing CNTs in the metallic matrix. The resulting hybrid multiscale composites were then used in order to predict the response of a plate structure and its dependence on a set of selected parameters. The structural responses analysed were the maximum transverse displacement of the plates and normal and shear stress components. The parametric studies carried out allowed characterizing the influence of material and geometrical properties of the plates analysed. Summarizing the results obtained in the different parametric studies carried out, it is possible to conclude that for the discretization used there is no significant difference between the two plate finite elements implemented. It is also possible to say that using a sufficiently large number of discrete layers with a constant volume fraction one converges to the results associated to the continuous volume fraction variation through thickness. Concerning to the inclusion of CNTs one concludes that SWCNTs provide a clear stiffening effect visible either in the transverse deflection or on the stresses distributions. These patterns are verified for the weight fractions contents considered in this study. Because of the material properties, namely the aspect ratio considered for the MWCNTs, its inclusion produced an inverse contribution, when compared to the SWCNTs. However as it was illustrated, one can say that the inclusion of adequately selected MWCNTs may provide a significant improvement in the mechanical performance of the nano-composite and subsequently of the hybrid composite. The aspect ratio of the plates is also a relevant parameter. As one can conclude from the results obtained, thicker plates present lower transverse displacements, and thus stresses. However, it is possible to see that interlaminar shear stresses increase when the aspect ratio decreases. When the plate includes the higher modulus ceramic it is also visible the expected response of lower displacements and stresses. Globally, the results obtained from this parametric study are expected to contribute to the understanding of the static behaviour of metal-ceramic FGMs with dispersed CNTs.

Functionally graded, multiscale and hybrid composite structures (dynamic behaviour): In terms of more specific conclusions, about the characterization of free vibrational dynamic behaviour of multiscale composite structures, with different distributions of micro and nano inclusions, (addressed in Section 4.2.2.2), the following lines apply: this work presents a study on the free vibrations response of moderately thick plates made of metal-ceramic FGMs, where CNTs are dispersed in the metallic matrix. The parametric analyses carried out allowed characterizing the influence of material and geometrical properties of the plates analysed. Summarizing the results obtained in the different parametric studies carried out, it is possible to conclude that for the discretization used there is no

significant difference between the two plate finite elements implemented. It is also possible to say that using a sufficiently large number of discrete layers with a constant volume fraction one converges to the results associated to the continuous volume fraction variation through thickness. Concerning to the dispersion of CNTs one concludes that SWCNTs provide a clear stiffening effect visible in the higher frequencies' values. These patterns are verified for the weight fractions' contents considered in this study. The inclusion of MWCNTs presents an inverse contribution, due to the specific characteristics of the CNTs considered in the present study. The aspect ratio of the plates, as well as its MBCs, are also relevant parameters. As one may conclude from the results obtained, thicker plates present higher frequencies and stiffer boundaries as well. When the plate includes the higher modulus ceramic it is also visible the expected response of higher frequencies values. Globally, one considers that the results obtained in this parametric study contribute to the better understanding of the free vibrations behaviour of metal-ceramic FGMs with dispersed CNTs.

Multilayered smart structures (parametric studies): Concerning the parametric studies of multilayered smart structures, functionally graded active composites were modelled along several beams' length. A wide variety of different structural configurations and set-ups were addressed, considering both static and dynamic (free vibrations) behaviours, as well as actuation and sensing ones, being possible to achieve several findings. Animations concerning different exponents of the volume fraction power law enable one to understand the material influence on the structural behaviour of smart structures, revealing to be a useful FEM tool in terms of design; considering different distributions of piezoelectric particles within a passive matrix along these beams' length, unique shapes of both deflections (actuation configuration) and voltages (sensing configuration) are obtained. In fact, one has considered 251 different p-exponents, in order to fully understand these behaviours from $p = 0$ to $p = 5$. It is important to mention that stiffer structures need to be addressed carefully in terms of mesh characteristics; the certain types of mechanical constraints, MBCs, require a compromise between number of elements (and its distribution) and the p-exponent to use, otherwise the material behaviour can be modelled incorrectly using the present approach (i.e. discrete mixture in every element); to minimize this effect, non-linear meshes and adaptive mesh refinements can be implemented in the future, to address this problem automatically (upgrade). Manufacturing aspects concerning these types of structures are also important to address in the future, to understand the most efficient way of reproducing these types of functionally graded active beams in reality. Concerning the dynamic behaviour, one concludes that different EBCs might result in different structural responses; when structures are stiffer and the materials possess higher piezoelectric and permittivity coefficients, the deviations between closed and open-circuit fundamental natural frequencies are higher. In addition, concerning the free vibrational modes, assumptions about the smart materials might lead to erroneous results, for example when neglecting the shear components of these materials.

Multilayered smart structures (optimization studies): Optimization studies covered several different structural problems, ranging from the minimization of static quantities to the maximization of dynamic ones. The programming methodology here developed, enables one to change between different optimization objectives and DVs' specifications very easily; this is why the present algorithms explore both continuous and discrete DVs (separately or not); basically, any of the FEM variables can be used inside the optimization problems. Both 2D and 3D graphical outputs associated to the optimization process reveal to be very useful when analysing the structures' electromechanical response, where the user is able to see in real time the whole record of iterations, as well as the influence that DVs have on the optimization objective/targets. Considerably high (PRs and PIs) and low PDs were

obtained and the HBA/MHBA showed a very acceptable performance when optimizing multilayered smart structures.

Final remarks: The case studies considered, allow concluding from the global good performance of the implemented package, both on the modelling and analysis phase, as well as on the optimization one. The most relevant scientific contributes, in one's opinion, is the fact that one single algorithm, automatically, is able to cover such wide range of material models and types of structures' configurations; on top of that, the amount of post-processing results, for both FEM and bat-inspired optimization, is considerably interesting. With time, the present platform can evolute towards a GUI platform in order to enhance the quality of the present structural modelling approach. Based on the literature found, it is fair to state that multilayered smart structures were successfully modelled and designed, throughout a wide range of different optimization problems revealing accurate results. In addition, the present algorithms are able to reproduce the results of several international references, with small deviations (even tough considering only FSDT). The Micro technique here implemented showed that it is an efficient approach to enhance the performance of the bat-inspired optimization, when used at the same time as DE; the optimization problems can become lighter in terms of processing needs, the rate of convergence towards global optima increases and more local optima are avoided. For example, concerning the optimization of piezoelectric patches' locations, this Micro approach allowed for the use of smaller populations and thus for a "Micro-bat" optimization, useful in higher dimension problems; by restarting populations, a much wider range of possible locations was explored by the algorithm.

5.3 Future work

In terms of future work, several major ideas can be enumerated. All these came up in the beginning of this thesis, but due to budget and (mostly) time constraints, it was not possible to finish them.

In relation to the theoretical component of this work, the one presented here, it would be important to include in the present FEM algorithm some failure prediction concerning more complex models. Then, about the bat-inspired optimization, **P**rincipal **C**omponent **A**nalysis (PCA) (the statistical procedure) would also be interesting to implement, in order to improve the algorithms' efficiency; in fact, statistics in general could bring improvements to this work. It would be important to compare, in real time, the behaviour and performance of HBA/MHBA, when optimizing multilayered smart structures, with other optimization algorithms (of the heuristics family and others).

In addition, one intends to include the present algorithms in a **G**raphical **U**ser **I**nterface (GUI) platform, in order to enhance and create an easier user experience. This subject was already addressed in the past and one already possesses a very efficient and solid Maplet® GUI platform, which was presented in Costa et al. (2015a, 2016); Costa and Loja (2015); this work won a honourable mention award. This is basically a symbolic simulation platform to study the mechanics of homogeneous and non-homogeneous thin plates using Navier's Method, with educational purposes; the platform enables one to model isotropic, orthotropic and FGM materials, several types of loads, interact with results, etc. Figures I.1 to I.4 show some print screens of the software already programmed last year (2015). Note that Maplet® is a package that contains GUI tools inside Maple® software. The objective would be creating something similar, but now considering FEM and bat-inspired optimization.

More efficient programming languages, e.g. Fortran, Python, or something similar, in order to improve computational efficiency. However, keeping the interaction with Maple® and/or MATLAB® would be required (or other similar graphical software), since graphical visualization of results, in one's

opinion, really enhances the overall FEM work. Also, it would be valuable the improvement of 3D structures plots, maybe using more complex 3D graphical methodologies.

To complement the theoretical simulations here developed (at least the less complex), one intends to design, develop, build and test a "home-made" small workbench to instrument smart structures with piezoelectric sensors and actuators, in order to control them using micro-controllers or micro-computers, such as Arduino® (see Figure I.5) or Raspberry Pi® (see Figure I.6). This is more like a "geek hobby", but it also can be useful to make some comparisons with the present algorithm, in order to attenuate vibrations (using shaker sources), control the structures' shapes, etc. Certain parts and even structures could be built using 3D printing home-made technology for example; the amount of possibilities is huge, depending only on one's creativity. During the beginning of this work, several equipment and piezoelectric actuators/sensors were studied, even emails with specialized companies were exchanged (see Appendix I.2.2). However, one has decided to abandon this idea, at least before delivering this thesis, to not compromise time deadlines; it is also important to refer budget constraints, because more-less 500 € would be required initially. The actuators illustrated in Figure I.7 seemed to be a fair choice; the goal was to buy six of these P-876.SP1 DuraAct(TM) Patch Transducer $16 \times 13 \times 0.5\,\mathrm{mm}$, with a price of 306 € (see Figure I.9). In addition, one also would need a voltage amplifier; the DRV8662 Piezo Haptic Driver with Integrated Boost Converter chip (see Figure I.8) could be used to build the amplifier board. Finally, other general parts would be required too, e.g. accelerometers, strain gauges, potentiometers, etc.

One feels that the present work constitutes a solid base to model more complex problems in the future, considering other materials and geometries (e.g. shells, besides the 2D domain); in fact, even the present interaction between FEM and bat-algorithms is not fully explored yet. The amount of generalization carried out during the implementation process enables one to model a considerable amount of different case studies; the programming component exports results almost in their final form, ready to incorporate themselves directly into papers and presentations.

Bibliography

Ahmad, I. (1988). "Smart" structures and materials. In C.A. Rogers (ed.), *Proceedings of U. S. Army Research Office Workshop*, Smart Materials, Structures, and Mathematical Issues, 13–16. Virginia Polytechnic Institute and State University, Technomic Publishing Co., Inc., Blacksburg, Virginia. URL. (cit. in p. 3)

Airbus (2013). A350 XWB. *FAST (Flight, Airworthiness, Support, Technology): Airbus Technical Magazine*, Special Edition, 6. URL. (cit. in pp. ix, 12)

Ajayan, P.M., Schadler, L.S., Giannaris, C., and Rubio, A. (2000). Single-walled carbon nanotube–polymer composites: Strength and weakness. *Advanced Materials*, 12(10), 750–753. URL. (cit. in pp. 34, 76)

Akbaş, Ş.D. (2015). Free vibration and bending of functionally graded beams resting on elastic foundation. *Research on Engineering Structures and Materials*, 1(1), 25–37. URL. (cit. in p. 33)

Al-Rub, R.K.A., Ashour, A.I., and Tyson, B.M. (2012). On the aspect ratio effect of multi-walled carbon nanotube reinforcements on the mechanical properties of cementitious nanocomposites. *Construction and Building Materials*, 35, 647–655. URL. (cit. in pp. 77, 117)

Alibeigloo, A. and Liew, K.M. (2013). Thermoelastic analysis of functionally graded carbon nanotube-reinforced composite plate using theory of elasticity. *Composite Structures*, 106, 873–881. URL. (cit. in p. 34)

Alvarez, G. (2002). Can we make genetic algorithms work in high-dimensionality problems? *Genetic Algorithm Inversion, Stanford Exploration Project (SEP)*, 112, 195–212. URL. (cit. in p. 96)

ANSYS®, Inc. (2016). *ANSYS Mechanical APDL® Element Reference (SHELL181 Element Output Definitions)*. Software help page. (cit. in pp. xi, 105)

Arduino® (2016). Arduino® UNO. Accessed January 2016. URL. (cit. in pp. xxix, I-4)

Arora, R.K. (2015). *OPTIMIZATION: Algorithms and Applications*. Taylor and Francis Group LLC, 1st edition. URL. (cit. in pp. 24, 25)

Balasubramanian, K. and Burghard, M. (2005). Chemically functionalized carbon nanotubes. *Small*, 1(2), 180–192. URL. (cit. in p. 76)

Balmes, E. and Deraemaeker, A. (2001). *Modeling structures with piezoelectric materials: Theory and SDT Tutorial*. URL. (cit. in p. 59)

Barbero, E.J. (ed.) (2014). *Finite Element Analysis of Composite Materials Using ANSYS®*. CRC Press Taylor & Francis Group, 2nd edition. URL. (cit. in p. 61)

Bartolucci, S.F., Paras, J., Rafiee, M.A., Rafiee, J., Lee, S., Kapoor, D., and Koratkar, N. (2011). Graphene–aluminum nanocomposites. *Materials Science and Engineering: A*, 528(27), 7933–7937. URL. (cit. in p. 34)

Bathe, K.-J. (1996). *Finite Element Procedures*. Prentice-Hall, Inc., 1st edition. URL. (cit. in p. B-1)

Beena, K.P. and Byju, V. (2013). Analysis of buckling behaviour of functionally graded plates. Online presentation. URL. (cit. in p. 34)

Bernardo, G.M.S., Damásio, F.R., Silva, T.A.N., and Loja, M.A.R. (2016). A study on the structural behaviour of FGM plates static and free vibrations analyses. *Composite Structures*, 136, 124–138. URL. (cit. in pp. 33, 75)

Bharti, I., Gupta, N., and Gupta, K.M. (2013). Novel applications of functionally graded nano, optoelectronic and thermoelectric materials. *International Journal of Materials, Mechanics and Manufacturing*, 1(3), 221–224. URL. (cit. in pp. 33, 34)

Birman, V. and Byrd, L.W. (2007). Modeling and analysis of functionally graded materials and structures. *Applied Mechanics Reviews*, 60(5), 195–216. URL. (cit. in p. 34)

Bocskai, Z. and Nagy, R. (2013). Discussion of the numerical integration of the 9-node shell finite element. In *Proceedings of the Second Conference of Junior Researchers in Civil Engineering*. Budapest, Hungary. URL. (cit. in pp. xxxi, 84)

Brigante, D. (2014). *New Composite Materials: Selection, Design, and Application*. Springer International Publishing, 1st edition. URL. (cit. in pp. ix, 10, 11)

Carrera, E., Brischetto, S., and Nali, P. (2011). *Plates and Shells for Smart Structures: Classical and Advanced Theories for Modeling and Analysis*. John Wiley and Sons, Ltd., 1st edition. URL. (cit. in pp. ix, x, xi, 3, 4, 5, 6, 7, 8, 45, 46, 47, 48, 49, 50, 54, 55, 57, 59, 60, 65, 66, 78, 79, 80)

Chopra, I. and Sirohi, J. (2013). *Smart Structures Theory*. Cambridge Aerospace. Cambridge University Press, 1st edition. URL. (cit. in pp. 3, 4)

Cohen, E.R., Cvitaš, T., Frey, J.G., Holmström, B., Kuchitsu, K., Marquardt, R., Mills, I., Pavese, F., Quack, M., Stohner, J., Strauss, H.L., Takami, M., and Thor, A.J. (eds.) (2007). *Quantities, Units and Symbols in Physical Chemistry*. The Royal Society of Chemistry, 3rd edition. International Union of Pure and Applied Chemistry (IUPAC), URL. (cit. in p. 45)

Cohen, E.R. and Giacomo, P. (eds.) (2010). *Symbols, Units, Nomenclature and Fundamental Constants in Physics*. The Royal Society of Chemistry. International Union of Pure and Applied Physics (IUPAP), Commission C2, SUNAMCO, URL. (cit. in p. 45)

Coleman, J.N., Khan, U., Blau, W.J., and Gun'ko, Y.K. (2006). Small but strong: A review of the mechanical properties of carbon nanotube–polymer composites. *Carbon*, 44(9), 1624–1652. URL. (cit. in p. 34)

Cook, A.C. and Vel, S.S. (2012). Multiscale analysis of laminated plates with integrated piezoelectric fiber composite actuators. *Composite Structures*, 94(2), 322–336. URL. (cit. in p. 35)

Correia, V.M.F., Gomes, M.A.A., Suleman, A., Mota Soares, C.M., and Mota Soares, C.A. (2000). Modelling and design of adaptive composite structures. *Computer Methods in Applied Mechanics and Engineering*, 185(2–4), 325–346. URL. (cit. in p. F-10)

Correia, V.M.F., Madeira, J.F.A., Araújo, A.L., and Mota Soares, C.M. (2016). Multiobjective design optimization of laminated composite plates with piezoelectric layers. *Composite Structures*. Article in Press, URL. (cit. in pp. xiii, 112, 142, F-18)

Correia, V.M.F., Mota Soares, C.M., and Mota Soares, C.A. (2001). Refined models for the optimal design of adaptive structures using simulated annealing. *Composite Structures*, 54(2–3), 161–167. Third International Conference on Composite Science and Technology, URL. (cit. in pp. xiii, xxxi, xxxiii, 112, 113, 114, 142, F-19, F-20)

Costa, D.M.S. (2014). Design of an aerodynamic hybrid trailer to transport hunting dogs: CostaDT-Cruiser-4SAC Trailer. Academic work during Mechanical Design classes, B.Sc. in Mechanical Engineering, Lisbon Superior Engineering Institute (ISEL). Also presented at Workshop on Mechanical Engineering and Maintenance Engineering (WEMEM), October 2014. (cit. in pp. ix, 22)

Costa, D.M.S. (2015). Literature review on composite materials for aeronautics: fatigue behaviour. Academic work during Joining Processes of Materials classes, M.Sc. in Mechanical Engineering, Lisbon Superior Engineering Institute (ISEL). Also presented at Workshop on Mechanical Engineering and Maintenance Engineering (WEMEM), November 2015. (cit. in p. 12)

Costa, D.M.S. (2016a). Application of Lean management to aviation maintenance organizations: Limitations of its implementation. Paper during Total Productive Maintenance and Lean Management classes, M.Sc. in Mechanical Engineering, Lisbon Superior Engineering Institute (ISEL). (cit. in p. 4)

Costa, D.M.S. (2016b). Mechanical behaviour of adaptive structures. Conference presentation about the present Thesis. Presented at Workshop on Mechanical Engineering and Maintenance Engineering (WEMEM), 02 November, Lisbon Superior Engineering Institute (ISEL), Lisbon, Portugal. (cit. in pp. 29, 101, 108, 128, 134)

Costa, D.M.S. and Barbosa, J.I. (2015). Mechanical design improvement using symbolic and numerical computational tools. In M.A.R. Loja, J.I. Barbosa, and J.A. Rodrigues (eds.), *Proceedings of SYMCOMP 2015, 2nd International Conference on Numerical and Symbolic Computation: Developments and Applications*, 455–473. University of Algarve, Faro, Portugal. Conference Presentation and Paper, URL. (cit. in pp. ix, 22)

Costa, D.M.S., Bernardo, G.M.S., and Loja, M.A.R. (2015a). Functionally graded particulate composite plates: a didactical case study. In *exp.at'15, 3rd Experiment@ International Conference*. University of Azores, Ponta Delgada, São Miguel Island, Azores, Portugal. Conference Demonstration, URL. (cit. in p. 146)

Costa, D.M.S., Bernardo, G.M.S., and Loja, M.A.R. (2016). A symbolic simulator platform for the static analysis of thin plates. *International Journal of Online Engineering (iJOE)*, 12(4), 7–10. URL. (cit. in p. 146)

Costa, D.M.S. and Loja, M.A.R. (2015). Mechanics of homogeneous and non-homogeneous thin plates: a symbolic simulation platform. In *exp.at'15, 3rd Experiment@ International Conference*. University of Azores, Ponta Delgada, São Miguel Island, Azores, Portugal. Conference Presentation, Honorable Mention Award Winner, URL. (cit. in p. 146)

Costa, D.M.S. and Loja, M.A.R. (2016a). Assessing the static behavior of hybrid CNT-metal-ceramic composite plates. *AIMS Materials Science*, 3(3), 808–831. Paper publication about the present Thesis, Published in 05 July, URL. (cit. in pp. 29, 101, 105, 116, 125)

Costa, D.M.S. and Loja, M.A.R. (2016b). Bat-inspired optimization of adaptive FGM plates. In A. Ferreira, A. Neves, E. Viola, F. Tornabene, and N. Fantuzzi (eds.), *Proceedings of MECHCOMP2, 2nd International Conference on Mechanics of Composites*, Composite Structures, 11. Società Editrice Esculapio, 11-14 July, University of Porto (FEUP), Oporto, Portugal. Conference presentation about the present Thesis, URL. (cit. in pp. 29, 101, 108, 128, 134)

Costa, D.M.S. and Loja, M.A.R. (2016c). On the characterization of the free vibrations behavior of multiscale composite plates. *Research on Engineering Structures and Materials (RESM)*, Online First. Paper publication about the present Thesis, Published in 01 September (online first), URL. (cit. in pp. 29, 101, 105, 116)

Costa, D.M.S., Trindade, J.M.F., and Loja, M.A.R. (2015b). Optimization of desalination heat exchanger's geometries using bat-inspired techniques. In M.A.R. Loja, J.I. Barbosa, and J.A. Rodrigues (eds.), *Proceedings of SYMCOMP 2015, 2nd International Conference on Numerical and Symbolic Computation: Developments and Applications*, 275–300. University of Algarve, Faro, Portugal. Conference Presentation and Paper, URL. (cit. in pp. 29, 40)

Costa, D.M.S. and Venâncio, M.A.S. (2015). Stress-intensity factor calculation, using FEM, of two elliptical corner cracks at the edge of a hole in a finite three-dimensional plate. Academic work during Fracture Mechanics classes, M.Sc. in Mechanical Engineering, Lisbon Superior Engineering Institute (ISEL). (cit. in pp. x, 23)

Costa, D.M.S., Venâncio, M.A.S., Marques, M.A.G., and Loja, M.A.R. (2015c). Reverse engineering in automotive parts. Poster exhibition at The Day of Innovation and Competence: Innovation for Volkswagen. (cit. in pp. ix, 20)

Curie, J. and Curie, P. (1880). Développement, par pression, de l'électricité polaire dans les cristaux hémièdres à faces inclinées. *Comptes Rendus de l'Académie des Sciences*, 91, 294–295. (cit. in p. 7)

Davim, J.P. (ed.) (2014). *Metal Matrix Composites: Materials, Manufacturing and Engineering*. Walter de Gruyter GmbH. URL. (cit. in p. 33)

Di, K. and Yang, Y.-C. (2012). Modeling method for the crack problem of a functionally graded interfacial zone with arbitrary material properties. *Acta Mechanica*, 223(12), 2609–2620. URL. (cit. in pp. 33, 34)

Du, J.-H., Bai, J., and Cheng, H.-M. (2007). The present status and key problems of carbon nanotube based polymer composites. *eXPRESS Polymer Letters*, 1(5), 253–273. URL. (cit. in p. 34)

Emery, J.D. (1997). Piezoelectric theory for finite element analysis of ultrasonic motors. *Federal Manufacturing and Technologies*. URL. (cit. in pp. 59, 61)

Enes, S. (2009). Shape functions generation, requirements, etc. Student presentation. URL. (cit. in pp. 79, B-1)

Ermanni, P. (2009). Multidisciplinary Optimization of Morphing Wings with Distributed Compliance and Smart Actuation. Accessed July 2016. URL. (cit. in pp. ix, 5)

Esawi, A.M.K., Morsi, K., Sayed, A., Taher, M., and Lanka, S. (2010). Effect of carbon nanotube (CNT) content on the mechanical properties of CNT-reinforced aluminium composites. *Composites Science and Technology*, 70(16), 2237–2241. URL. (cit. in p. 33)

Farsangi, M.A.A., Saidi, A.R., and Batra, R.C. (2013). Analytical solution for free vibrations of moderately thick hybrid piezoelectric laminated plates. *Journal of Sound and Vibration*, 332(22), 5981–5998. URL. (cit. in pp. xiii, xxxiii, 67, 111, F-13, F-17)

Fazzolari, F.A. (2015). Natural frequencies and critical temperatures of functionally graded sandwich plates subjected to uniform and non-uniform temperature distributions. *Composite Structures*, 121, 197–210. URL. (cit. in p. 34)

Felippa, C. (2016a). *Introduction to Finite Element Methods (ASEN 5007): Chapter 17: Isoparametric Quadrilaterals*. Department of Aerospace Engineering Sciences, University of Colorado Boulder. Accessed May 2016. URL. (cit. in pp. xi, 83, 84, B-1)

Felippa, C. (2016b). *Introduction to Finite Element Methods (ASEN 5007): Chapter 18: Shape Function Magic*. Department of Aerospace Engineering Sciences, University of Colorado Boulder. Accessed May 2016. URL. (cit. in p. B-1)

Fernandes, A. and Pouget, J. (2003). Analytical and numerical approaches to piezoelectric bimorph. *International Journal of Solids and Structures*, 40(17), 4331–4352. URL. (cit. in p. 110)

Ferreira, A.J.M. (2009). *MATLAB Codes for Finite Element Analysis: Solids and Structures*, volume 157 of *Solid Mechanics and its Applications*. Springer Netherlands, 1st edition. URL. (cit. in pp. 45, 54, 89)

Ferreira, A.J.M., Batra, R.C., Roque, C.M.C., Qian, L.F., and Martins, P.A.L.S. (2005). Static analysis of functionally graded plates using third-order shear deformation theory and a meshless method. *Composite Structures*, 69(4), 449–457. URL. (cit. in pp. 34, 71, 74, 106, 107)

Ferreira, A.D.B.L., Nóvoa, P.R.O., and Marques, A.T. (2016). Multifunctional material systems: A state-of-the-art review. *Composite Structures*, 151, 3–35. *Smart composites and composite structures In honour of the 70th anniversary of Professor Carlos Alberto Mota Soares*. URL. (cit. in pp. ix, x, 14, 15, 33, 34, 35, 36)

Fister Jr., I., Fister, D., and Yang, X.-S. (2013). A hybrid bat algorithm. *Elektrotehniški Vestnik / Electrotechnical Review*, 80(1–2), 1–7. URL. (cit. in pp. xi, 41, 95, 96, 97, 98)

Gandomi, A.H. and Yang, X.-S. (2014). Chaotic bat algorithm. *Journal of Computational Science*, 5(2), 224–232. URL. (cit. in p. 43)

Gandomi, A.H., Yang, X.-S., Alavi, A.H., and Talatahari, S. (2013a). Bat algorithm for constrained optimization tasks. *Neural Computing and Applications*, 22(6), 1239–1255. URL. (cit. in p. 28)

Gandomi, A.H., Yun, G.J., Yang, X.-S., and Talatahari, S. (2013b). Chaos-enhanced accelerated particle swarm optimization. *Communications in Nonlinear Science and Numerical Simulation*, 18(2), 327–340. URL. (cit. in p. 40)

Garcia, E.J., Wardle, B.L., and Hart, A.J. (2008). Joining prepreg composite interfaces with aligned carbon nanotubes. *Composites Part A: Applied Science and Manufacturing*, 39(6), 1065–1070. URL. (cit. in p. 33)

García-Macías, E., Castro-Triguero, R., Flores, E.I.S., Friswell, M.I., and Gallego, R. (2016). Static and free vibration analysis of functionally graded carbon nanotube reinforced skew plates. *Composite Structures*, 140, 473–490. URL. (cit. in p. 33)

Gaudenzi, P. (2009). *Smart Structures: Physical Behaviour, Mathematical Modelling and Applications*. John Wiley and Sons, Ltd., 1st edition. URL. (cit. in p. 4)

Gibson, R.F. (2010). A review of recent research on mechanics of multifunctional composite materials and structures. *Composite Structures*, 92(12), 2793–2810. URL. (cit. in p. 31)

Halpin, J.C. and Kardos, J.L. (1976). The Halpin-Tsai equations: A review. *Polymer Engineering and Science*, 16(5), 344–352. URL. (cit. in p. 75)

Hasançebi, O., Teke, T., and Pekcan, O. (2013). A bat-inspired algorithm for structural optimization. *Computers and Structures*, 128, 77–90. URL. (cit. in pp. x, 24, 40, 41, 42, 96, 97)

He, X.Q., Rafiee, M., Mareishi, S., and Liew, K.M. (2015). Large amplitude vibration of fractionally damped viscoelastic CNTs/fiber/polymer multiscale composite beams. *Composite Structures*, 131, 1111–1123. URL. (cit. in p. 32)

Heshmati, M., Yas, M.H., and Daneshmand, F. (2015). A comprehensive study on the vibrational behavior of CNT-reinforced composite beams. *Composite Structures*, 125, 434–448. URL. (cit. in p. 32)

Hu, Y., Shenderova, O.A., Hu, Z., Padgett, C.W., and Brenner, D.W. (2006). Carbon nanostructures for advanced composites. *Reports on Progress in Physics*, 69(6), 1847–1895. URL. (cit. in pp. 34, 76)

Huang, G.Q., Zhao, W.J., and Lu, Q.Q. (2013). Bat algorithm with global convergence for solving large-scale optimization problem. *Application Research of Computers*, 30(5), 1323–1328. URL. (cit. in p. 43)

Hussain, F., Hojjati, M., Okamoto, M., and Gorga, R.E. (2006). Review article: Polymer-matrix nanocomposites, processing, manufacturing, and application: An overview. *Journal of Composite Materials*, 40(17), 1511–1575. URL. (cit. in p. 33)

Hwang, W.-S. and Park, H.C. (1993). Finite element modeling of piezoelectric sensors and actuators. *American Institute of Aeronautics and Astronautics Journal*, 31(5), 930–937. URL. (cit. in p. F-10)

Jaenker, P., Kloeppel, V., Konstanzer, P., and Maier, R. (2008). Piezo active vibration and noise control in helicopters. In *Proceedings of the 26th international congress of the aeronautical sciences*, 1–10. Anchorage, Alaska, USA. URL. (cit. in p. 36)

Jaffe, B., Cook, W.R., and Jaffe, H. (1971). Piezoelectric ceramics. In J.P. Roberts and P. Popper (eds.), *Non-Metallic Solids: A Series of Monographs*. Academic Press. URL. (cit. in p. 59)

Jamil, M., Zepernic, H.-J., and Yang, X.-S. (2013). Improved bat algorithm for global optimization. *Applied Soft Computing*. Submitted. (cit. in p. 43)

Janocha, H. (ed.) (2007). *Adaptronics and Smart Structures: Basics, Materials, Design and Applications*. Springer – Verlag Berlin Heidelberg, 2nd edition. URL. (cit. in pp. ix, 3, 16, 17)

Jha, D.K., Kant, T., and Singh, R.K. (2013). A critical review of recent research on functionally graded plates. *Composite Structures*, 96, 833–849. URL. (cit. in p. 34)

Kadoli, R., Akhtar, K., and Ganesan, N. (2008). Static analysis of functionally graded beams using higher order shear deformation theory. *Applied Mathematical Modelling*, 32(12), 2509–2525. URL. (cit. in p. 34)

Kamarian, S., Shakeri, M., and Yas, M.H. (2016). Natural frequency analysis and optimal design of CNT/fiber/polymer hybrid composites plates using Mori-Tanaka approach, GDQ technique, and firefly algorithm. *Polymer Composites*, 1–14. URL. (cit. in p. 32)

Kar, A.K. (2016). Bio inspired computing – a review of algorithms and scope of applications. *Expert Systems with Applications*, 59, 20–32. URL. (cit. in pp. x, 27, 37, 39, 40)

Kaveh, A. (2014). *Advances in Metaheuristic Algorithms for Optimal Design of Structures*. Springer International Publishing, 1st edition. URL. (cit. in pp. x, 26)

Khan, K. and Sahai, A. (2012). A comparison of ba, ga, pso, bp and lm for training feed forward neural networks in e-learning context. *International Journal of Intelligent Systems and Applications*, 4(7), 23–29. URL. (cit. in p. 43)

Khan, S.U. and Kim, J.-K. (2011). Impact and delamination failure of multiscale carbon nanotube-fiber reinforced polymer composites: A review. *International Journal of Aeronautical and Space Sciences*, 12(2), 115–133. URL. (cit. in p. 33)

Kieback, B., Neubrand, A., and Riedel, H. (2003). Processing techniques for functionally graded materials. *Materials Science and Engineering: A*, 362(1–2), 81–106. Papers from the German Priority Programme (Functionally Graded Materials). URL. (cit. in p. 34)

Kim, M., Park, Y.-B., Okoli, O.I., and Zhang, C. (2009). Processing, characterization, and modeling of carbon nanotube-reinforced multiscale composites. *Composites Science and Technology*, 69(3–4), 335–342. URL. (cit. in pp. xxxi, 34, 77)

Komarasamy, G. and Wahi, A. (2012). An optimized k-means clustering technique using bat algorithm. *European Journal of Scientific Research*, 84(2), 263–273. URL. (cit. in p. 43)

Konstanzer, P., Enenkl, B., Aubourg, P.-A., and Cranga, P. (2008). Recent advances in eurocopter's passive and active vibration control. In *Proceedings of the American helicopter society 64th annual forum*. Montreal, Quebec, Canada. URL. (cit. in p. 36)

Koziel, S. and Yang, X.-S. (eds.) (2011). *Computational Optimization, Methods and Algorithms*, volume 356 of *Studies in Computational Intelligence*. Springer-Verlag Berlin Heidelberg, 1st edition. URL. (cit. in p. 25)

Krige, D.G. (1951). A Statistical Approach to Some Basic Mine Valuation Problems on the Witwatersrand. *Journal of the Chemical, Metallurgical and Mining Society of South Africa*, 52(6), 119–139. URL. (cit. in p. 85)

Kuilla, T., Bhadra, S., Yao, D., Kim, N.H., Bose, S., and Lee, J.H. (2010). Recent advances in graphene based polymer composites. *Progress in Polymer Science*, 35(11), 1350–1375. URL. (cit. in p. 34)

Lau, K.-t., Gu, C., and Hui, D. (2006). A critical review on nanotube and nanotube/nanoclay related polymer composite materials. *Composites Part B: Engineering*, 37(6), 425–436. URL. (cit. in pp. 31, 32)

Lei, Z.X., Zhang, L.W., and Liew, K.M. (2016). Buckling analysis of CNT reinforced functionally graded laminated composite plates. *Composite Structures*, 152, 62–73. URL. (cit. in p. 33)

Liew, K.M., Lei, Z.X., and Zhang, L.W. (2015). Mechanical analysis of functionally graded carbon nanotube reinforced composites: A review. *Composite Structures*, 120, 90–97. URL. (cit. in p. 34)

Liew, K.M., Wong, C.H., and Tan, M.J. (2006). Tensile and compressive properties of carbon nanotube bundles. *Acta Materialia*, 54(1), 225–231. URL. (cit. in p. 34)

Lima Jr., J.J. (1999). *Modelagem de Sensores e Atuadores Piezelétricos com Aplicações em Controle Ativo de Estruturas*. Ph.D. thesis, Universidade Estadual de Campinas (UNICAMP). URL. (cit. in p. F-10)

Lin, J.H., Chou, C.W., Yang, C.H., and Tsai, H.L. (2012). A chaotic lévy flight bat algorithm for parameter estimation in nonlinear dynamic biological systems. *Journal of Computer and Information Technology*, 2(2), 56–63. URL. (cit. in p. 43)

Liu, G., Huang, H., Wang, S., and Chen, Z. (2012). An improved bat algorithm with doppler effect for stochastic optimization. *International Journal of Digital Content Technology and its Applications*, 6(21), 326–336. URL. (cit. in p. 41)

Liu, G.R. and Quek, S.S. (2014). *The Finite Element Method: A Practical Course*. Butterworth-Heinemann, Oxford, 2nd edition. URL. (cit. in pp. ix, 18, 19, 21)

Liu, Y.-g., Li, J.-s., Wang, X.-j., Tian, B., and Shen, X. (2010). The mechanical performance of piezoelectric fiber composite actuators. In *Electrical and Control Engineering (ICECE), 2010 International Conference on*, 2371–2374. URL. (cit. in p. 35)

Loja, M.A.R. (2014). On the use of particle swarm optimization to maximize bending stiffness of functionally graded structures. *Journal of Symbolic Computation*, 61–62(1), 12–30. URL. (cit. in p. 96)

Loja, M.A.R., Barbosa, J.I., and Mota Soares, C.M. (2012). A study on the modeling of sandwich functionally graded particulate composites. *Composite Structures*, 94(7), 2209–2217. URL. (cit. in pp. 34, 71)

Loja, M.A.R., Barbosa, J.I., and Mota Soares, C.M. (2015). Analysis of sandwich beam structures using Kriging based higher order models. *Composite Structures*, 119, 99–106. URL. (cit. in pp. 34, 85, 127)

Loja, M.A.R., Barbosa, J.I., Mota Soares, C.M., and Mota Soares, C.A. (2001). Analysis of piezolaminated plates by the spline finite strip method. *Computers and Structures*, 79(26–28), 2321–2333. URL. (cit. in pp. xxxi, 50, 52, 56, 67, 89, 110)

Loja, M.A.R., Mota Soares, C.M., and Barbosa, J.I. (2014). Optimization of magneto-electro-elastic composite structures using differential evolution. *Composite Structures*, 107(1), 276–287. URL. (cit. in p. 96)

Loja, M.A.R., Mota Soares, C.M., and Mota Soares, C.A. (2002). Modelling and design of adaptive structures using B-spline strip models. *Composite Structures*, 57(1–4), 245–251. URL. (cit. in p. 96)

Ma, P.-C., Siddiqui, N.A., Marom, G., and Kim, J.-K. (2010). Dispersion and functionalization of carbon nanotubes for polymer-based nanocomposites: A review. *Composites Part A: Applied Science and Manufacturing*, 41(10), 1345–1367. URL. (cit. in p. 76)

Mainprice, D., Bachmann, F., Hielscher, R., Schaeben, H., and Lloyd, G.E. (2014). Calculating anisotropic piezoelectric properties from texture data using the MTEX open source package. *Geological Society, London, Special Publications*, 409, 223–249. URL. (cit. in pp. xi, 59, 60)

Mareishi, S., Kalhori, H., Rafiee, M., and Hosseini, S.M. (2015). Nonlinear forced vibration response of smart two-phase nano-composite beams to external harmonic excitations. *Curved and Layered Structures*, 2(1), 150–161. URL. (cit. in p. 32)

Mazumdar, S.K. (2001). *Composites Manufacturing: Materials, Product, and Process Engineering*. CRC Press LLC, 1st edition. URL. (cit. in pp. 11, 12)

Meng, X.-B., Gao, X.Z., Liu, Y., and Zhang, H. (2015). A novel bat algorithm with habitat selection and doppler effect in echoes for optimization. *Expert Systems with Applications*, 42(17–18), 6350–6364. URL. (cit. in p. 40)

Miyamoto, Y., Kaysser, W.A., Rabin, B.H., Kawasaki, A., and Ford, R.G. (eds.) (1999). *Functionally Graded Materials: Design, Processing and Applications*, volume 5 of *Materials Technology Series*. Springer US. URL. (cit. in p. 34)

Nakamura, R.Y.M., Pereira, L.A.M., Costa, K.A., Rodrigues, D., Papa, J.P., and Yang, X.-S. (2012). BBA: A binary bat algorithm for feature selection. *Journal of Computer and Information Technology*, 291–297. URL. (cit. in p. 41)

Neubauer, E., Kitzmantel, M., Hulman, M., and Angerer, P. (2010). Potential and challenges of metal-matrix-composites reinforced with carbon nanofibers and carbon nanotubes. *Composites Science and Technology*, 70(16), 2228–2236. URL. (cit. in p. 33)

Nguyen, N. (2014). A framework for adaptive aeroelastic wing shaping control. National Aeronautics and Space Administration (NASA), Intelligent Systems Division NASA Ames Research Center, Moffett Field, CA 94035. URL. (cit. in pp. ix, 4)

Nguyen, T.-K., Sab, K., and Bonnet, G. (2007). Shear correction factors for functionally graded plates. *Mechanics of Advanced Materials and Structures*, 14(8), 567–575. URL. (cit. in pp. 34, 54)

Nguyen, T.-K., Sab, K., and Bonnet, G. (2008). First-order shear deformation plate models for functionally graded materials. *Composite Structures*, 83(1), 25–36. URL. (cit. in p. 34)

Odegard, G.M. (2004). Constitutive modeling of piezoelectric polymer composites. *Acta Materialia*, 52(18), 5315–5330. URL. (cit. in p. 67)

Pereira, C.B. (2003). *Técnicas de Otimização Discreto-Continuas Aplicadas ao Controle de Vibração de Estruturas Inteligentes*. Master's thesis, Universidade Federal de Uberlândia (UFU). (cit. in p. F-10)

PI-Ceramic® (2016a). Catalog: DuraAct Patch Transducer. Accessed September 2016. URL. (cit. in pp. ix, xxix, 9, I-5)

PI-Ceramic® (2016b). Catalog: PI Piezoelectric Ceramic Products: Fundamentals, Characteristics and Applications. Accessed September 2016. URL. (cit. in pp. ix, 9)

Qian, H., Bismarck, A., Greenhalgh, E.S., Kalinka, G., and Shaffer, M.S.P. (2008). Hierarchical composites reinforced with carbon nanotube grafted fibers: The potential assessed at the single fiber level. *Chemistry of Materials*, 20(5), 1862–1869. URL. (cit. in p. 33)

Qian, L.F., Batra, R.C., and Chen, L.M. (2004). Static and dynamic deformations of thick functionally graded elastic plates by using higher-order shear and normal deformable plate theory and meshless local Petrov–Galerkin method. *Composites Part B: Engineering*, 35(6–8), 685–697. URL. (cit. in pp. 34, 74, 106, 107, 108)

Rafiee, M., He, X.Q., Mareishi, S., and Liew, K.M. (2014a). Modeling and stress analysis of smart CNTs/fiber/polymer multiscale composite plates. *International Journal of Applied Mechanics*, 6(3), 1450025 (23 pages). URL. (cit. in pp. xxxi, 34, 76, 77)

Rafiee, M., Liu, X.F., He, X.Q., and Kitipornchai, S. (2014b). Geometrically nonlinear free vibration of shear deformable piezoelectric carbon nanotube/fiber/polymer multiscale laminated composite plates. *Journal of Sound and Vibration*, 333(14), 3236–3251. URL. (cit. in p. 32)

Rahmandoust, M. and Ayatollahi, M.R. (2016). *Characterization of Carbon Nanotube-Based Composites Under Consideration of Defects*, volume 39 of *Advanced Structured Materials*. Springer International Publishing. URL. (cit. in pp. ix, 16, 17)

Ramakrishna, S., Mayer, J., Wintermantel, E., and Leong, K.W. (2001). Biomedical applications of polymer-composite materials: A review. *Composites Science and Technology*, 61(9), 1189–1224. URL. (cit. in p. 33)

Rashad, M., Pan, F., Hu, H., Asif, M., Hussain, S., and She, J. (2015). Enhanced tensile properties of magnesium composites reinforced with graphene nanoplatelets. *Materials Science and Engineering: A*, 630, 36–44. URL. (cit. in p. 34)

Raspberry Pi® (2016). Raspberry Pi® 2 Model B V1.1. Accessed January 2016. URL. (cit. in pp. xxix, I-4)

Ray, M.C. and Mallik, N. (2004). Finite element analysis of smart structures containing piezoelectric fiber-reinforced composite actuator. *American Institute of Aeronautics and Astronautics Journal*, 42(7), 1398–1405. URL. (cit. in p. 35)

Reddy, J.N. (2004). *Mechanics of Laminated Composite Plates and Shells: Theory and Analysis*. CRC Press LLC, 2nd edition. URL. (cit. in pp. xi, 10, 23, 45, 46, 47, 49, 51, 54, 65, 85, 91, 102)

Reddy, J.N. (2006). *An Introduction to the Finite Element Method*. McGraw-Hill Education, 3rd edition. URL. (cit. in pp. xxxii, 45, 49, 54, 85, 102, 103, 104, F-2)

Rodrigues, D., Pereira, L.A.M., Nakamura, R.Y.M., Costa, K.A.P., Yang, X.-S., Souza, A.N., and Papa, J.P. (2014). A wrapper approach for feature selection based on bat algorithm and optimum-path forest. *Expert Systems with Applications*, 41(5), 2250–2258. URL. (cit. in p. 40)

Rogers, C.A. (1990). Intelligent material systems and structures. In I. Ahmad, A. Crowson, C.A. Rogers, and M. Aizawa (eds.), *Proceedings of U.S.-Japan Workshop on Smart/Intelligent Materials and Systems*, 11–33. Technomic Publishing Co., Inc., Honolulu, Hawaii. URL. (cit. in p. 3)

Rogers, C.A., Barker, D.K., and Jaeger, C.A. (1988). Introduction to smart materials and structures. In C.A. Rogers (ed.), *Proceedings of U. S. Army Research Office Workshop*, Smart Materials, Structures, and Mathematical Issues, 17–28. Virginia Polytechnic Institute and State University, Technomic Publishing Co., Inc., Blacksburg, Virginia. URL. (cit. in pp. 3, 6)

Salerno, J. (1997). Using the particle swarm optimization technique to train a recurrent neural model. In *Proceedings of the Ninth IEEE International Conference on Tools with Artificial Intelligence*, 45–49. URL. (cit. in p. 96)

Salvetat, J.-P., Briggs, G.A.D., Bonard, J.-M., Bacsa, R.R., Kulik, A.J., Stöckli, T., Burnham, N.A., and Forró, L. (1999). Elastic and shear moduli of single-walled carbon nanotube ropes. *Physical Review Letters*, 82(5), 944–947. URL. (cit. in pp. 34, 76, 77, 117)

Saravanos, D.A. and Heyliger, P.R. (1995). Coupled layerwise analysis of composite beams with embedded piezoelectric sensors and actuators. *Journal of Intelligent Material Systems and Structures*, 6(3), 350–363. URL. (cit. in pp. xiii, xxxi, 67, 111, F-12)

Saravanos, D.A., Heyliger, P.R., and Hopkins, D.A. (1997). Layerwise mechanics and finite element for the dynamic analysis of piezoelectric composite plates. *International Journal of Solids and Structures*, 34(3), 359–378. URL. (cit. in pp. xiii, xxxi, 67, 112, F-14)

Senecal, P.K. (2000). *Numerical optimization using the GEN4 micro-genetic algorithm code*. Engine Research Centre, University of Wisconsin-Madison. Draft manuscript, URL. (cit. in p. 96)

Shen, X., Liu, Y., and Zhang, J. (2009). Study of piezoelectric fiber composite actuators applied in the flapping wing. In *2009 18th IEEE International Symposium on the Applications of Ferroelectrics*, 1–4. URL. (cit. in p. 35)

Shin, J.W., Lee, Y.-S., and Kim, S.J. (2013). An interface crack in a functionally graded piezoelectric bi-layer under anti-plane shear impact. *Acta Mechanica*, 224(4), 867–879. URL. (cit. in p. 34)

Singh, J. and Chauhan, A. (2016). Characterization of hybrid aluminum matrix composites for advanced applications – A review. *Journal of Materials Research and Technology*, 5(2), 159–169. URL. (cit. in pp. 31, 32)

Sinnott, S.B. (2002). Chemical functionalization of carbon nanotubes. *Journal of Nanoscience and Nanotechnology*, 2(2), 113–123. URL. (cit. in p. 76)

Sofla, A.Y.N., Meguid, S.A., Tan, K.T., and Yeo, W.K. (2010). Shape morphing of aircraft wing: Status and challenges. *Materials and Design*, 31(3), 1284–1292. URL. (cit. in p. 35)

Soh, C.-K., Yang, Y., and Bhalla, S. (eds.) (2012). *Smart Materials in Structural Health Monitoring, Control and Biomechanics*. Advanced Topics in Science and Technology in China. Springer Berlin Heidelberg, 1st edition. URL. (cit. in pp. ix, 3, 6, 7)

Srinivasan, A.V. and McFarland, D.M. (2001). *Smart Structures: Analysis and Design*. Cambridge University Press, 1st edition. URL. (cit. in pp. 6, 7, 23)

Suhr, J., Koratkar, N., Keblinski, P., and Ajayan, P.M. (2005). Viscoelasticity in carbon nanotube composites. *Nature Materials*, 4(2), 134–137. URL. (cit. in p. 76)

Sun, J., Guan, Q., Liu, Y., and Leng, J. (2016). Morphing aircraft based on smart materials and structures: A state-of-the-art review. *Journal of Intelligent Material Systems and Structures*, 27(17), 2289–2312. URL. (cit. in pp. x, 35, 36, 37)

Sun, L., Huang, W.M., Ding, Z., Zhao, Y., Wang, C.C., Purnawali, H., and Tang, C. (2012). Stimulus-responsive shape memory materials: A review. *Materials and Design*, 33, 577–640. URL. (cit. in p. 35)

Svečko, R. and Kusić, D. (2015). Feedforward neural network position control of a piezoelectric actuator based on a bat search algorithm. *Expert Systems with Applications*, 42(13), 5416–5423. URL. (cit. in p. 40)

Takagi, K., Li, J.-F., Yokoyama, S., Watanabe, R., Almajid, A., and Taya, M. (2002). Design and fabrication of functionally graded PZT/Pt piezoelectric bimorph actuator. *Science and Technology of Advanced Materials*, 3(2), 217–224. URL. (cit. in pp. ix, 14)

Taylor, B.N. and Thompson, A. (eds.) (2008). *The International System of Units (SI)*. National Institute of Standards and Technology (NIST) Special Publication 330, 8th edition. URL. (cit. in p. 45)

Texas Instruments® (2016). Catalog: DRV8662 Piezo Haptic Driver with Integrated Boost Converter. Accessed January 2016. URL. (cit. in pp. xxix, I-5)

Thostenson, E.T., Li, C., and Chou, T.-W. (2005). Review: Nanocomposites in context. *Composites Science and Technology*, 65(3–4), 491–516. URL. (cit. in pp. 34, 76)

Tichý, J., Erhart, J., Kittinger, E., and Prívratská, J. (2010). *Fundamentals of Piezoelectric Sensorics: Mechanical, Dielectric, and Thermodynamical Properties of Piezoelectric Materials*. Springer-Verlag Berlin Heidelberg, 1st edition. URL. (cit. in p. 59)

Tornabene, F., Fantuzzi, N., and Bacciocchi, M. (2014). Free vibrations of free-form doubly-curved shells made of functionally graded materials using higher-order equivalent single layer theories. *Composites Part B: Engineering*, 67, 490–509. URL. (cit. in p. 34)

Tornabene, F., Fantuzzi, N., Bacciocchi, M., and Viola, E. (2016). Effect of agglomeration on the natural frequencies of functionally graded carbon nanotube-reinforced laminated composite doubly-curved shells. *Composites Part B: Engineering*, 89, 187–218. URL. (cit. in pp. 34, 76)

Udupa, G., rao, S.S., and Gangadharan, K.V. (2012). Future applications of carbon nanotube reinforced functionally graded composite materials. In *Advances in Engineering, Science and Management (ICAESM), 2012 International Conference on*, 399–404. URL. (cit. in pp. 33, 34)

U.S. Research Nanomaterials, Inc. (2016). MWCNTs (>95%, OD: <7nm). URL http://us-nano.com/inc/sdetail/215. Accessed June 2016. (cit. in pp. xxxi, 117)

Vepa, D.R. (2010). *Dynamics of Smart Structures*. John Wiley and Sons, Ltd., 1st edition. URL. (cit. in pp. ix, 7, 10)

Viola, E., Rossetti, L., Fantuzzi, N., and Tornabene, F. (2014). Static analysis of functionally graded conical shells and panels using the generalized unconstrained third order theory coupled with the stress recovery. *Composite Structures*, 112, 44–65. URL. (cit. in p. 34)

Wang, M., Lempke, M., Wong, T., and Kwon, P. (2013). Perspirable skin: Thermal buckling achieved by complex functionally graded materials. *Journal of Manufacturing Processes*, 15(1), 121–126. URL. (cit. in p. 34)

Wang, S.Y. (2004). A finite element model for the static and dynamic analysis of a piezoelectric bimorph. *International Journal of Solids and Structures*, 41(15), 4075–4096. URL. (cit. in pp. xiii, xxxiii, 47, 50, 55, 67, 90, 110, 111, F-12, F-15, F-16)

Wehrle, E.J. (2015). *Design optimization of lightweight space frame structures considering crashworthiness and parameter uncertainty*. Dr.-ing. diss., Lehrstuhl für Leichtbau, Technische Universität München. URL. (cit. in pp. ix, 19, 20, 21)

Yang, X.-S. (2010). A new metaheuristic bat-inspired algorithm. In J.R. González, D.A. Pelta, C. Cruz, G. Terrazas, and N. Krasnogor (eds.), *Nature Inspired Cooperative Strategies for Optimization (NICSO 2010)*, volume 284 of *Studies in Computational Intelligence*, 65–74. Springer Berlin, Heidelberg. URL. (cit. in pp. 26, 28, 37, 96, 97)

Yang, X.-S. (2011). Bat algorithm for multi-objective optimisation. *International Journal of Bio-Inspired Computation*, 3(5), 267–274. URL. (cit. in p. 43)

Yang, X.-S. (2013). *Bat Algorithm and Cuckoo Search: A Tutorial*, volume 427 of *Studies in Computational Intelligence*. Springer Berlin Heidelberg, 1st edition. URL. (cit. in p. 41)

Yang, X.-S. (2014). *Nature-Inspired Optimization Algorithms*. Elsevier, 1st edition. URL. (cit. in pp. x, 25, 26, 28, 41, 93, 97)

Yang, X.-S., Cui, Z., Xiao, R., Gandomi, A.H., and Karamanoglu, M. (eds.) (2013). *Swarm Intelligence and Bio-Inspired Computation: Theory and Applications*. Elsevier. URL. (cit. in p. 41)

Yang, X.-S. and Gandomi, A.H. (2012). Bat algorithm: a novel approach for global engineering optimization. *Engineering Computations*, 29(5), 464–483. URL. (cit. in pp. 28, 38)

Yang, X.-S. and He, X. (2013). Bat algorithm: Literature review and applications. *International Journal of Bio-Inspired Computation (IJBIC)*, 5(3), 141–149. URL. (cit. in p. 41)

Yu, J. and Kidane, A. (2014). Modeling functionally graded materials containing multiple heterogeneities. *Acta Mechanica*, 225(7), 1931–1943. URL. (cit. in p. 34)

Zapata-Solvas, E., Gómez-García, D., and Domínguez-Rodríguez, A. (2012). Towards physical properties tailoring of carbon nanotubes-reinforced ceramic matrix composites. *Journal of the European Ceramic Society*, 32(12), 3001–3020. URL. (cit. in p. 34)

Zhang, L.W., Xiao, L.N., Zou, G.L., and Liew, K.M. (2016). Elastodynamic analysis of quadrilateral CNT-reinforced functionally graded composite plates using FSDT element-free method. *Composite Structures*, 148, 144–154. URL. (cit. in p. 33)

Zhu, P., Lei, Z.X., and Liew, K.M. (2012). Static and free vibration analyses of carbon nanotube-reinforced composite plates using finite element method with first order shear deformation plate theory. *Composite Structures*, 94(4), 1450–1460. URL. (cit. in p. 34)

Zieliński, T.G. (2016). Fundamentals of piezoelectricity: Introductory course on multiphysics modelling. Online presentation. URL. (cit. in pp. 7, 59, 61)

Zienkiewicz, O.C., Taylor, R.L., and Zhu, J.Z. (eds.) (2013). *The Finite Element Method: Its Basis and Fundamentals*. Butterworth-Heinemann, 7th edition. URL. (cit. in p. B-1)

Zok, F.W. and Levi, C.G. (2001). Mechanical properties of porous-matrix ceramic composites. *Advanced Engineering Materials*, 3(1–2), 15–23. URL. (cit. in p. 33)

APPENDICES

Appendix A

FGMs Discrete Distributions

In this appendix, several plots are presented, considering several FGMs discrete distributions along thickness (z-direction) and length (x-direction), as examples. For the former, distributions were generated using $N_{sl} = \{5, 10, 50\}$ sub-layers in the z-direction, whereas in the latter using $N_{ex} = \{6, 10, 16\}$ finite elements in the x-direction. In these figures, the discrete approximation is plotted over the continuous V_f curves (for all considered p-exponents), using horizontal red lines.

A.1 Along thickness (z-direction)

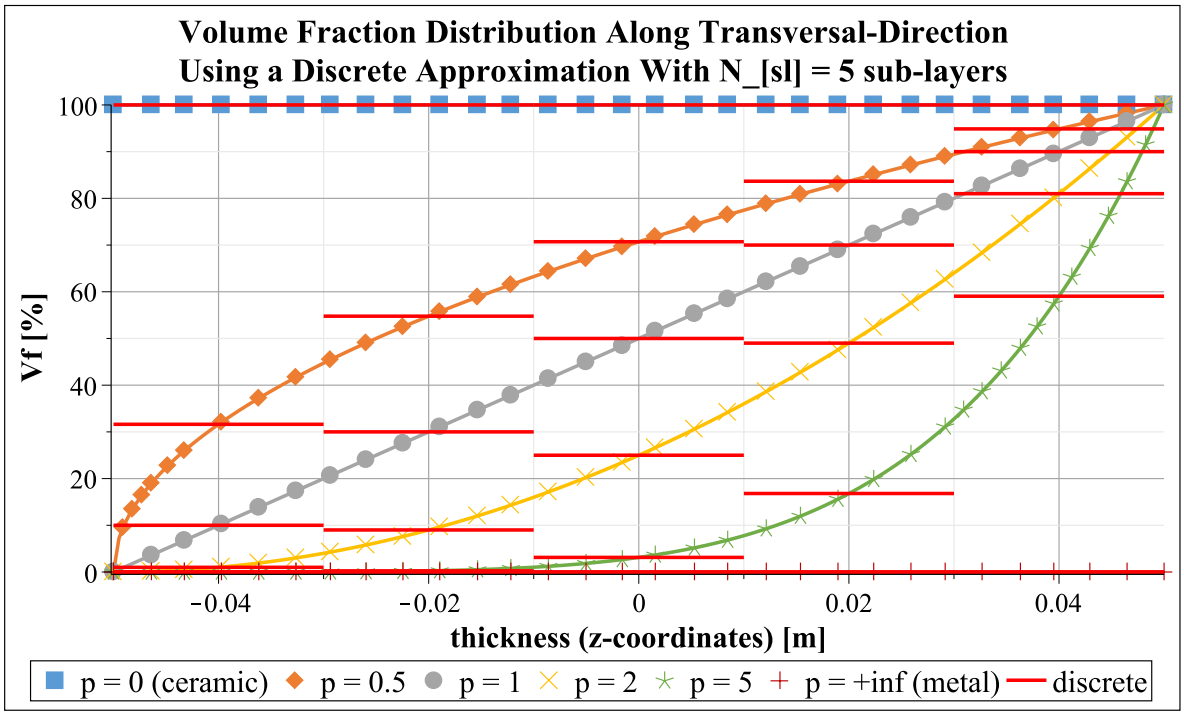

Figure A.1: Plot of the volume fraction power law along transversal direction, with discrete approximation ($N_{sl} = 5$ sub-layers), considering several p exponents and thickness from -50 to $50\,\mathrm{mm}$.

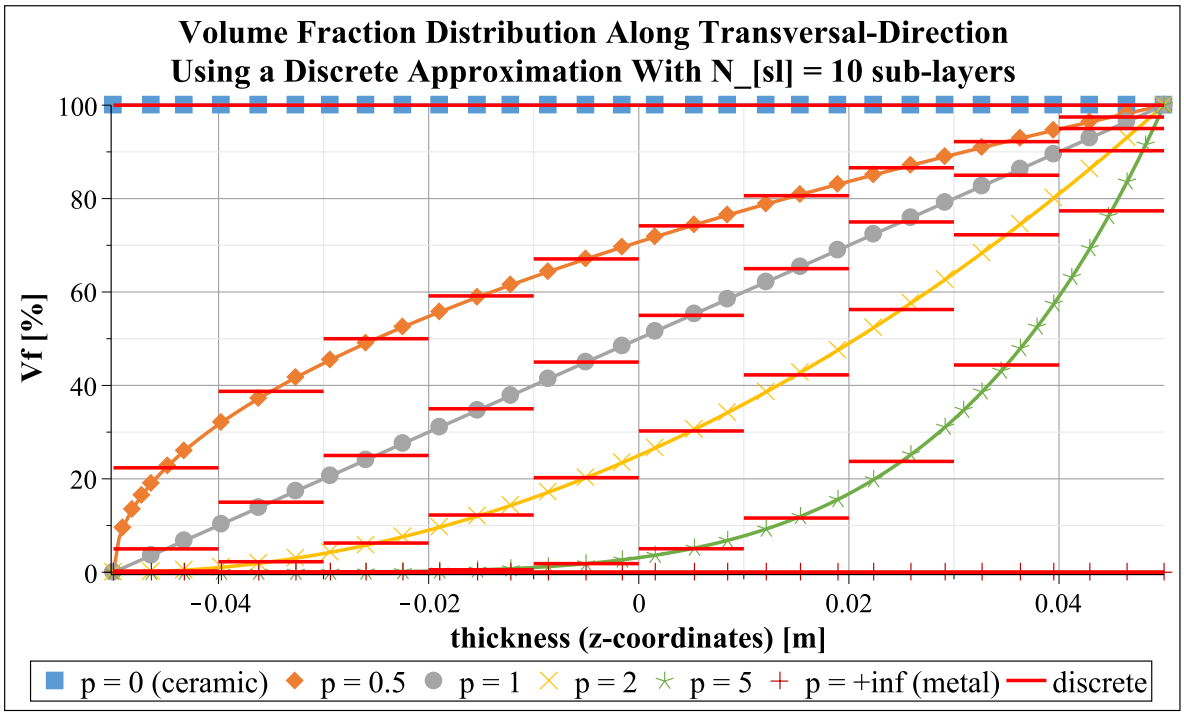

Figure A.2: Plot of the volume fraction power law along transversal direction, with discrete approximation ($N_{sl} = 10$ sub-layers), considering several p exponents and thickness from -50 to $50\,\mathrm{mm}$.

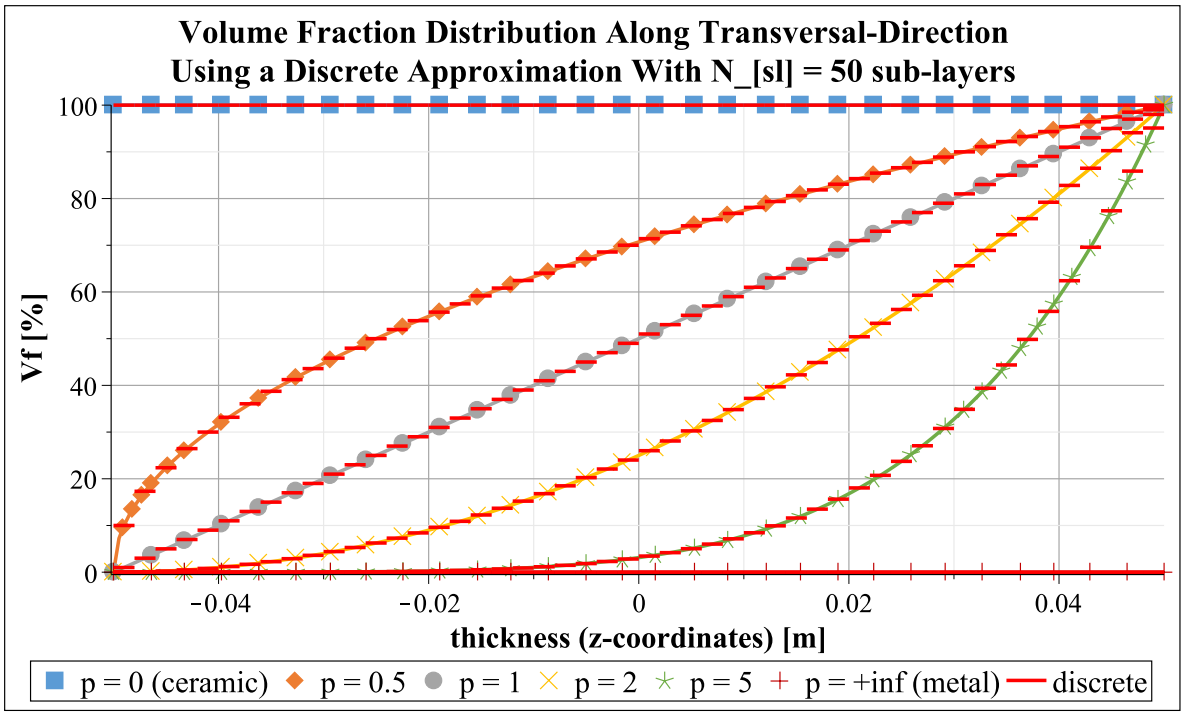

Figure A.3: Plot of the volume fraction power law along transversal direction, with discrete approximation ($N_{sl} = 50$ sub-layers), considering several p exponents and thickness from -50 to $50\,\mathrm{mm}$.

A.2 Along length (x-direction)

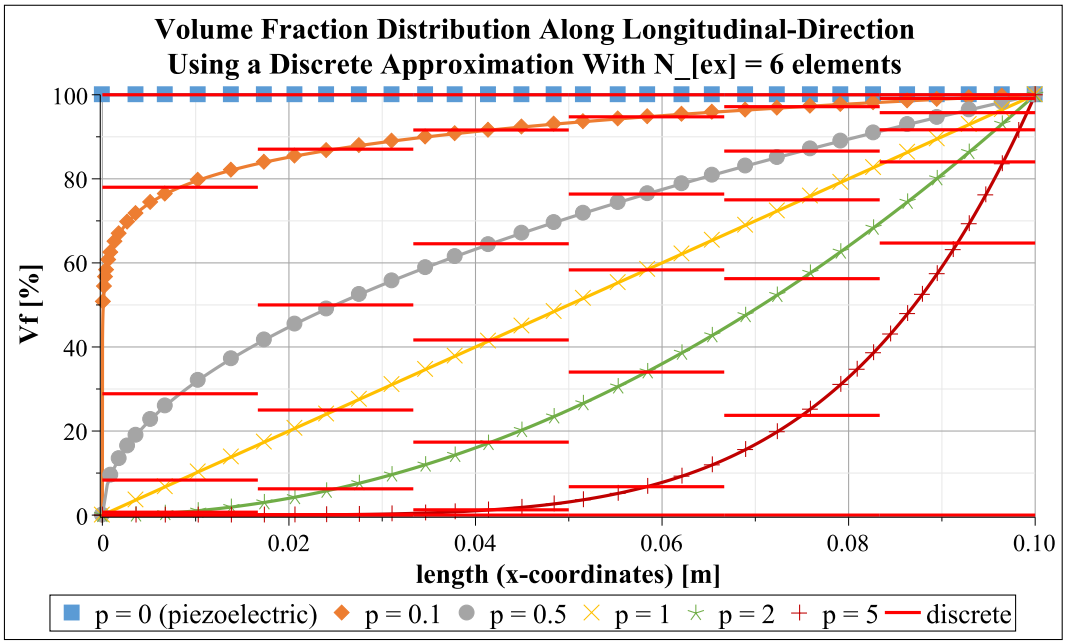

Figure A.4: Plot of the volume fraction power law along longitudinal direction, with discrete approximation ($N_{ex} = 6$ elements), considering several p exponents and length from 0 to 100 mm.

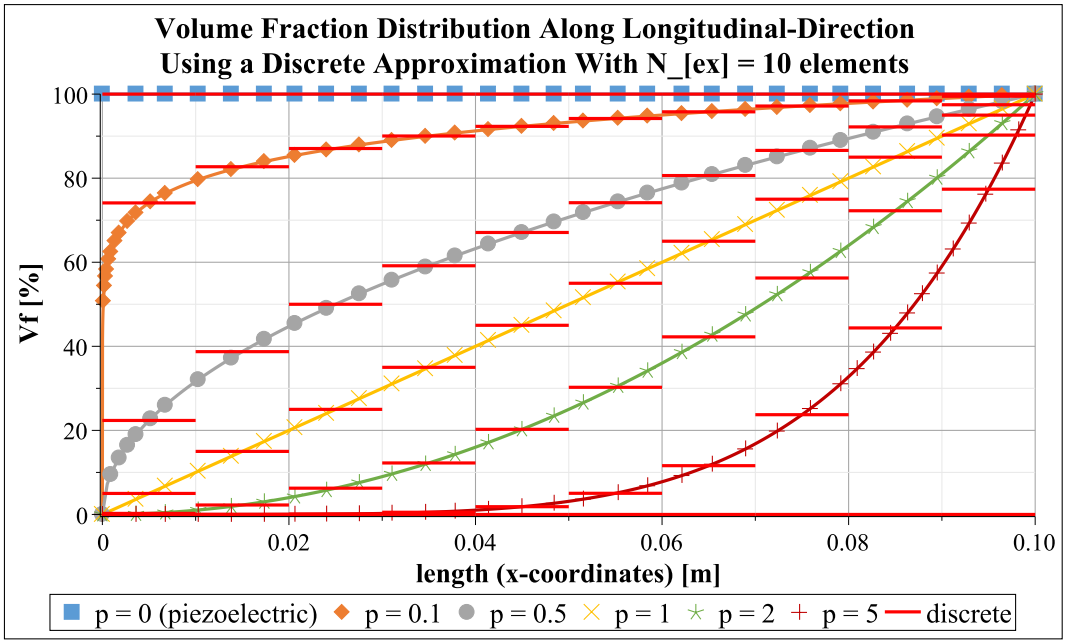

Figure A.5: Plot of the volume fraction power law along longitudinal direction, with discrete approximation ($N_{ex} = 10$ elements), considering several p exponents and length from 0 to 100 mm.

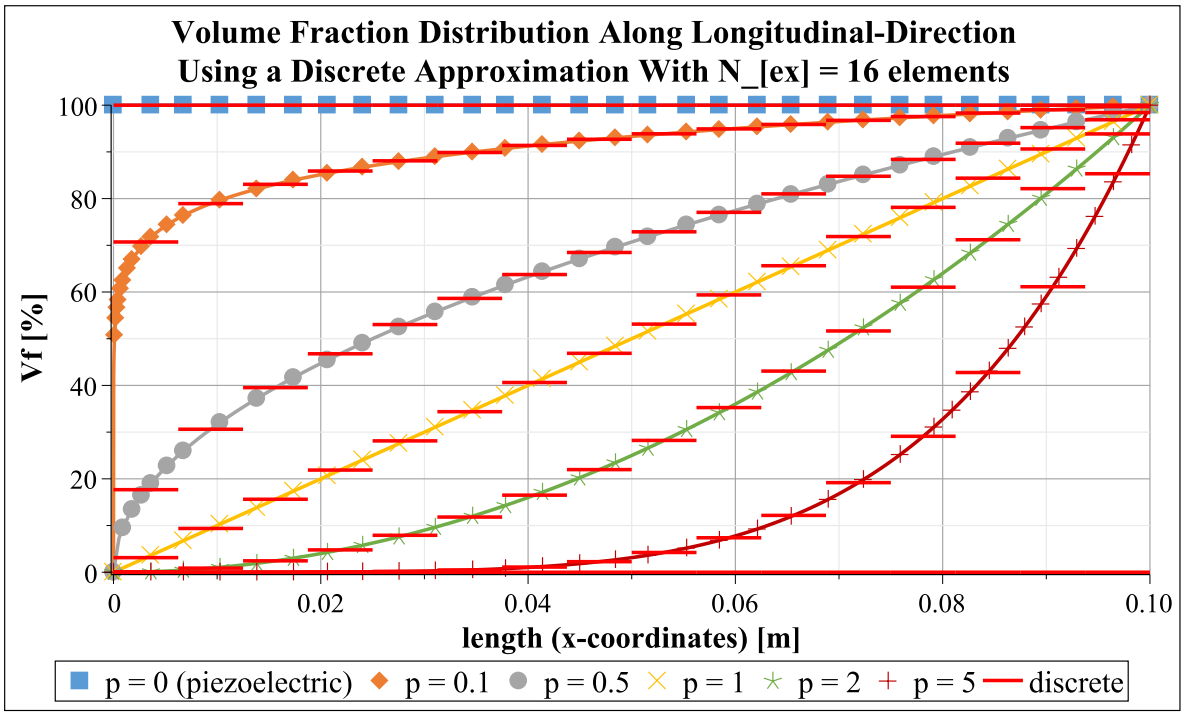

Figure A.6: Plot of the volume fraction power law along longitudinal direction, with discrete approximation ($N_{ex} = 16$ elements), considering several p exponents and length from 0 to 100 mm.

Appendix B

Shape Functions

The present appendix summarizes the symbolic equations associated with all computed shape functions, for Q4, Q9 and Q16 elements, considering both Lagrange and Kriging element formulations. Examples of relevant references about this subject are Bathe, K.-J. (1996); Enes (2009); Felippa (2016a,b); Zienkiewicz et al. (2013).

B.1 Lagrange elements

B.1.1 4-Node Bilinear Quadrilateral (4BlinLag)

$$\left\{\begin{array}{c} N_1(\xi,\eta) \\ N_2(\xi,\eta) \\ N_3(\xi,\eta) \\ N_4(\xi,\eta) \end{array}\right\} = \left\{\begin{array}{c} 1/4\,(-1+\xi)\,(-1+\eta) \\ -1/4\,(1+\xi)\,(-1+\eta) \\ 1/4\,(1+\xi)\,(1+\eta) \\ -1/4\,(-1+\xi)\,(1+\eta) \end{array}\right\} \tag{B.1.1}$$

B.1.2 9-Node Biquadratic Quadrilateral (9BquadLag)

$$\left\{\begin{array}{c} N_1(\xi,\eta) \\ N_2(\xi,\eta) \\ N_3(\xi,\eta) \\ N_4(\xi,\eta) \\ N_5(\xi,\eta) \\ N_6(\xi,\eta) \\ N_7(\xi,\eta) \\ N_8(\xi,\eta) \\ N_9(\xi,\eta) \end{array}\right\} = \left\{\begin{array}{c} 1/4\,\xi\,\eta - 1/4\,\eta^2\xi - 1/4\,\eta\,\xi^2 + 1/4\,\eta^2\xi^2 \\ -1/4\,\xi\,\eta - 1/4\,\eta\,\xi^2 + 1/4\,\eta^2\xi + 1/4\,\eta^2\xi^2 \\ 1/4\,\xi\,\eta + 1/4\,\eta^2\xi + 1/4\,\eta\,\xi^2 + 1/4\,\eta^2\xi^2 \\ -1/4\,\xi\,\eta + 1/4\,\eta\,\xi^2 - 1/4\,\eta^2\xi + 1/4\,\eta^2\xi^2 \\ 1/2\,\eta\,\xi^2 - \eta/2 - 1/2\,\eta^2\xi^2 + 1/2\,\eta^2 \\ -1/2\,\eta^2\xi + \xi/2 - 1/2\,\eta^2\xi^2 + 1/2\,\xi^2 \\ -1/2\,\eta\,\xi^2 + \eta/2 - 1/2\,\eta^2\xi^2 + 1/2\,\eta^2 \\ 1/2\,\eta^2\xi - \xi/2 - 1/2\,\eta^2\xi^2 + 1/2\,\xi^2 \\ (\xi^2-1)\,(\eta^2-1) \end{array}\right\} \tag{B.1.2}$$

B.1.3 16-Node Bicubic Quadrilateral (16BcubLag)

$$N_1(\xi,\eta) = -\frac{9\,\eta^3\xi}{256} - \frac{9\,\eta\,\xi^3}{256} + \frac{81\,\eta^3\xi^3}{256} - \frac{81\,\eta^3\xi^2}{256} - \frac{81\,\eta^2\xi^3}{256} + \frac{81\,\eta^2\xi^2}{256} - \frac{9\,\xi^2}{256} - \frac{9\,\eta^2}{256} - \frac{\xi}{256} - \frac{\eta}{256} + \frac{\xi\,\eta}{256} + \frac{9\,\eta^3}{256} + \frac{9\,\xi^3}{256} + \frac{1}{256} + \frac{9\,\eta^2\xi}{256} + \frac{9\,\eta\,\xi^2}{256} \tag{B.1.3}$$

$$N_2(\xi,\eta) = \frac{9\,\eta^3\xi}{256} + \frac{9\,\eta\,\xi^3}{256} - \frac{81\,\eta^3\xi^3}{256} - \frac{81\,\eta^3\xi^2}{256} + \frac{81\,\eta^2\xi^3}{256} + \frac{81\,\eta^2\xi^2}{256} - \frac{9\,\xi^2}{256} - \frac{9\,\eta^2}{256} + \frac{\xi}{256} - \frac{\eta}{256} - \frac{\xi\,\eta}{256} + \frac{9\,\eta^3}{256} - \frac{9\,\xi^3}{256} + \frac{1}{256} - \frac{9\,\eta^2\xi}{256} + \frac{9\,\eta\,\xi^2}{256} \tag{B.1.4}$$

$$N_3(\xi,\eta) = -\frac{9\,\eta^3\xi}{256} - \frac{9\,\eta\,\xi^3}{256} + \frac{81\,\eta^3\xi^3}{256} + \frac{81\,\eta^3\xi^2}{256} + \frac{81\,\eta^2\xi^3}{256} + \frac{81\,\eta^2\xi^2}{256} - \frac{9\,\xi^2}{256} - \frac{9\,\eta^2}{256} + \frac{\xi}{256} + \frac{\eta}{256} + \frac{\xi\,\eta}{256} - \frac{9\,\eta^3}{256} - \frac{9\,\xi^3}{256} + \frac{1}{256} - \frac{9\,\eta^2\xi}{256} - \frac{9\,\eta\,\xi^2}{256} \tag{B.1.5}$$

$$N_4(\xi,\eta) = \frac{9\,\eta^3\xi}{256} + \frac{9\,\eta\,\xi^3}{256} - \frac{81\,\eta^3\xi^3}{256} + \frac{81\,\eta^3\xi^2}{256} - \frac{81\,\eta^2\xi^3}{256} + \frac{81\,\eta^2\xi^2}{256} - \frac{9\,\xi^2}{256} - \frac{9\,\eta^2}{256} - \frac{\xi}{256} + \frac{\eta}{256} - \frac{\xi\,\eta}{256} - \frac{9\,\eta^3}{256} + \frac{9\,\xi^3}{256} + \frac{1}{256} + \frac{9\,\eta^2\xi}{256} - \frac{9\,\eta\,\xi^2}{256} \tag{B.1.6}$$

$$N_5(\xi,\eta) = \frac{243\,\eta^3\xi}{256} + \frac{27\,\eta\,\xi^3}{256} - \frac{243\,\eta^3\xi^3}{256} + \frac{81\,\eta^3\xi^2}{256} + \frac{243\,\eta^2\xi^3}{256} - \frac{81\,\eta^2\xi^2}{256} + \frac{9\,\xi^2}{256} + \frac{81\,\eta^2}{256} + \frac{27\,\xi}{256} + \frac{9\,\eta}{256} - \frac{27\,\xi\,\eta}{256} - \frac{81\,\eta^3}{256} - \frac{27\,\xi^3}{256} - \frac{9}{256} - \frac{243\,\eta^2\xi}{256} - \frac{9\,\eta\,\xi^2}{256} \tag{B.1.7}$$

$$N_6(\xi,\eta) = -\frac{27\,\eta^3\xi}{256} - \frac{243\,\eta\,\xi^3}{256} + \frac{243\,\eta^3\xi^3}{256} + \frac{243\,\eta^3\xi^2}{256} - \frac{81\,\eta^2\xi^3}{256} - \frac{81\,\eta^2\xi^2}{256} + \frac{81\,\xi^2}{256} + \frac{9\,\eta^2}{256} - \frac{9\,\xi}{256} + \frac{27\,\eta}{256} + \frac{27\,\xi\,\eta}{256} - \frac{27\,\eta^3}{256} + \frac{81\,\xi^3}{256} - \frac{9}{256} + \frac{9\,\eta^2\xi}{256} - \frac{243\,\eta\,\xi^2}{256} \tag{B.1.8}$$

$$N_7(\xi,\eta) = \frac{243\,\eta^3\xi}{256} + \frac{27\,\eta\,\xi^3}{256} - \frac{243\,\eta^3\xi^3}{256} - \frac{81\,\eta^3\xi^2}{256} - \frac{243\,\eta^2\xi^3}{256} - \frac{81\,\eta^2\xi^2}{256} + \frac{9\,\xi^2}{256} + \frac{81\,\eta^2}{256} - \frac{27\,\xi}{256} - \frac{9\,\eta}{256} - \frac{27\,\xi\,\eta}{256} + \frac{81\,\eta^3}{256} + \frac{27\,\xi^3}{256} - \frac{9}{256} + \frac{243\,\eta^2\xi}{256} + \frac{9\,\eta\,\xi^2}{256} \tag{B.1.9}$$

$$N_8(\xi,\eta) = -\frac{27\,\eta^3\xi}{256} - \frac{243\,\eta\,\xi^3}{256} + \frac{243\,\eta^3\xi^3}{256} - \frac{243\,\eta^3\xi^2}{256} + \frac{81\,\eta^2\xi^3}{256} - \frac{81\,\eta^2\xi^2}{256} + \frac{81\,\xi^2}{256} + \frac{9\,\eta^2}{256} + \frac{9\,\xi}{256} - \frac{27\,\eta}{256} + \frac{27\,\xi\,\eta}{256} + \frac{27\,\eta^3}{256} - \frac{81\,\xi^3}{256} - \frac{9}{256} - \frac{9\,\eta^2\xi}{256} + \frac{243\,\eta\,\xi^2}{256} \tag{B.1.10}$$

$$N_9(\xi,\eta) = -\frac{243\,\eta^3\xi}{256} - \frac{27\,\eta\,\xi^3}{256} + \frac{243\,\eta^3\xi^3}{256} + \frac{81\,\eta^3\xi^2}{256} - \frac{243\,\eta^2\xi^3}{256} - \frac{81\,\eta^2\xi^2}{256} + \frac{9\,\xi^2}{256} + \frac{81\,\eta^2}{256} - \frac{27\,\xi}{256} + \frac{9\,\eta}{256} + \frac{27\,\xi\,\eta}{256} - \frac{81\,\eta^3}{256} + \frac{27\,\xi^3}{256} - \frac{9}{256} + \frac{243\,\eta^2\xi}{256} - \frac{9\,\eta\,\xi^2}{256} \tag{B.1.11}$$

$$N_{10}(\xi,\eta) = \frac{27\,\eta^3\xi}{256} + \frac{243\,\eta\,\xi^3}{256} - \frac{243\,\eta^3\xi^3}{256} - \frac{243\,\eta^3\xi^2}{256} - \frac{81\,\eta^2\xi^3}{256} - \frac{81\,\eta^2\xi^2}{256} + \frac{81\,\xi^2}{256} + \frac{9\,\eta^2}{256} - \frac{9\,\xi}{256} - \frac{27\,\eta}{256} - \frac{27\,\xi\,\eta}{256} + \frac{27\,\eta^3}{256} + \frac{81\,\xi^3}{256} - \frac{9}{256} + \frac{9\,\eta^2\xi}{256} + \frac{243\,\eta\,\xi^2}{256} \tag{B.1.12}$$

$$N_{11}(\xi,\eta) = -\frac{243\,\eta^3\xi}{256} - \frac{27\,\eta\,\xi^3}{256} + \frac{243\,\eta^3\xi^3}{256} - \frac{81\,\eta^3\xi^2}{256} + \frac{243\,\eta^2\xi^3}{256} - \frac{81\,\eta^2\xi^2}{256} + \frac{9\,\xi^2}{256} + \frac{81\,\eta^2}{256} + \frac{27\,\xi}{256} - \frac{9\,\eta}{256} + \frac{27\,\xi\,\eta}{256} + \frac{81\,\eta^3}{256} - \frac{27\,\xi^3}{256} - \frac{9}{256} - \frac{243\,\eta^2\xi}{256} + \frac{9\,\eta\,\xi^2}{256} \tag{B.1.13}$$

$$N_{12}(\xi,\eta) = \frac{27\,\eta^3\xi}{256} + \frac{243\,\eta\,\xi^3}{256} - \frac{243\,\eta^3\xi^3}{256} + \frac{243\,\eta^3\xi^2}{256} + \frac{81\,\eta^2\xi^3}{256} - \frac{81\,\eta^2\xi^2}{256} + \frac{81\,\xi^2}{256} + \frac{9\,\eta^2}{256} + \frac{9\,\xi}{256} + \frac{27\,\eta}{256} - \frac{27\,\xi\,\eta}{256} - \frac{27\,\eta^3}{256} - \frac{81\,\xi^3}{256} - \frac{9}{256} - \frac{9\,\eta^2\xi}{256} - \frac{243\,\eta\,\xi^2}{256} \tag{B.1.14}$$

$$\left\{\begin{array}{c} N_{13}(\xi,\eta) \\ N_{14}(\xi,\eta) \\ N_{15}(\xi,\eta) \\ N_{16}(\xi,\eta) \end{array}\right\} = \left\{\begin{array}{c} \frac{\left(81\,\xi^2-81\right)(-1+3\,\xi)\left(\eta^2-1\right)(-1+3\,\eta)}{256} \\ -\frac{\left(81\,\xi^2-81\right)(1+3\,\xi)\left(\eta^2-1\right)(-1+3\,\eta)}{256} \\ \frac{\left(81\,\xi^2-81\right)(1+3\,\xi)\left(\eta^2-1\right)(1+3\,\eta)}{256} \\ -\frac{\left(81\,\xi^2-81\right)(-1+3\,\xi)\left(\eta^2-1\right)(1+3\,\eta)}{256} \end{array}\right\} \tag{B.1.15}$$

B.2 Kriging elements

B.2.1 4-Node Bilinear Quadrilateral (4BlinKrig)

$$N_1(\xi,\eta) = 0.25 - 0.25\,\xi - 0.25\,\eta + 0.25941570\,\mathrm{e}^{-\eta^2-\xi^2-2.0\,\eta-2.0\,\xi-2.0} - 0.25941570\,\mathrm{e}^{-\eta^2-\xi^2-2.0\,\eta+2.0\,\xi-2.0} - 0.25941570\,\mathrm{e}^{-\eta^2-\xi^2+2.0\,\eta-2.0\,\xi-2.0} + 0.25941570\,\mathrm{e}^{-\eta^2-\xi^2+2.0\,\eta+2.0\,\xi-2.0} \tag{B.2.1}$$

$$N_2(\xi,\eta) = 0.25 + 0.25\,\xi - 0.25\,\eta - 0.25941570\,\mathrm{e}^{-\eta^2-\xi^2-2.0\,\eta-2.0\,\xi-2.0} + 0.25941570\,\mathrm{e}^{-\eta^2-\xi^2-2.0\,\eta+2.0\,\xi-2.0} + 0.25941570\,\mathrm{e}^{-\eta^2-\xi^2+2.0\,\eta-2.0\,\xi-2.0} - 0.25941570\,\mathrm{e}^{-\eta^2-\xi^2+2.0\,\eta+2.0\,\xi-2.0} \tag{B.2.2}$$

$$\begin{aligned} N_3(\xi,\eta) = {} & 0.25 + 0.25\,\xi + 0.25\,\eta + 0.25941570\,\mathrm{e}^{-\eta^2-\xi^2-2.0\,\eta-2.0\,\xi-2.0} \\ & - 0.25941570\,\mathrm{e}^{-\eta^2-\xi^2-2.0\,\eta+2.0\,\xi-2.0} - 0.25941570\,\mathrm{e}^{-\eta^2-\xi^2+2.0\,\eta-2.0\,\xi-2.0} \\ & + 0.25941570\,\mathrm{e}^{-\eta^2-\xi^2+2.0\,\eta+2.0\,\xi-2.0} \end{aligned} \tag{B.2.3}$$

$$\begin{aligned} N_4(\xi,\eta) = {} & 0.25 - 0.25\,\xi + 0.25\,\eta - 0.25941570\,\mathrm{e}^{-\eta^2-\xi^2-2.0\,\eta-2.0\,\xi-2.0} \\ & + 0.25941570\,\mathrm{e}^{-\eta^2-\xi^2-2.0\,\eta+2.0\,\xi-2.0} + 0.25941570\,\mathrm{e}^{-\eta^2-\xi^2+2.0\,\eta-2.0\,\xi-2.0} \\ & - 0.25941570\,\mathrm{e}^{-\eta^2-\xi^2+2.0\,\eta+2.0\,\xi-2.0} \end{aligned} \tag{B.2.4}$$

B.2.2 9-Node Bilinear Quadrilateral (9BlinKrig)

$$\begin{aligned} N_1(\xi,\eta) = {} & 0.16701 - 0.20433\,\xi - 0.20433\,\eta + 0.91656\,\mathrm{e}^{-\eta^2-\xi^2-2.0\,\eta-2.0\,\xi-2.0} \\ & - 0.71171\,\mathrm{e}^{-\eta^2-\xi^2-2.0\,\eta-1.0} + 0.06845\,\mathrm{e}^{-\eta^2-\xi^2-2.0\,\eta+2.0\,\xi-2.0} \\ & - 0.71171\,\mathrm{e}^{-\eta^2-\xi^2-2.0\,\xi-1.0} + 0.21826\,\mathrm{e}^{-1.0\,\eta^2-1.0\,\xi^2} \\ & - 0.05315\,\mathrm{e}^{-\eta^2-\xi^2+2.0\,\xi-1.0} + 0.06845\,\mathrm{e}^{-\eta^2-\xi^2+2.0\,\eta-2.0\,\xi-2.0} \\ & - 0.05315\,\mathrm{e}^{-\eta^2-\xi^2+2.0\,\eta-1.0} + 0.25800\,\mathrm{e}^{-\eta^2-\xi^2+2.0\,\eta+2.0\,\xi-2.0} \end{aligned} \tag{B.2.5}$$

$$\begin{aligned} N_2(\xi,\eta) = {} & 0.16701 + 0.20433\,\xi - 0.20433\,\eta + 0.06845\,\mathrm{e}^{-\eta^2-\xi^2-2.0\,\eta-2.0\,\xi-2.0} \\ & - 0.71171\,\mathrm{e}^{-\eta^2-\xi^2-2.0\,\eta-1.0} + 0.91656\,\mathrm{e}^{-\eta^2-\xi^2-2.0\,\eta+2.0\,\xi-2.0} \\ & - 0.05315\,\mathrm{e}^{-\eta^2-\xi^2-2.0\,\xi-1.0} + 0.21826\,\mathrm{e}^{-1.0\,\eta^2-1.0\,\xi^2} \\ & - 0.71171\,\mathrm{e}^{-\eta^2-\xi^2+2.0\,\xi-1.0} + 0.25800\,\mathrm{e}^{-\eta^2-\xi^2+2.0\,\eta-2.0\,\xi-2.0} \\ & - 0.05315\,\mathrm{e}^{-\eta^2-\xi^2+2.0\,\eta-1.0} + 0.06845\,\mathrm{e}^{-\eta^2-\xi^2+2.0\,\eta+2.0\,\xi-2.0} \end{aligned} \tag{B.2.6}$$

$$\begin{aligned} N_3(\xi,\eta) = {} & 0.16701 + 0.20433\,\xi + 0.20433\,\eta + 0.25800\,\mathrm{e}^{-\eta^2-\xi^2-2.0\,\eta-2.0\,\xi-2.0} \\ & - 0.05315\,\mathrm{e}^{-\eta^2-\xi^2-2.0\,\eta-1.0} + 0.06845\,\mathrm{e}^{-\eta^2-\xi^2-2.0\,\eta+2.0\,\xi-2.0} \\ & - 0.05315\,\mathrm{e}^{-\eta^2-\xi^2-2.0\,\xi-1.0} + 0.21826\,\mathrm{e}^{-1.0\,\eta^2-1.0\,\xi^2} \\ & - 0.71171\,\mathrm{e}^{-\eta^2-\xi^2+2.0\,\xi-1.0} + 0.06845\,\mathrm{e}^{-\eta^2-\xi^2+2.0\,\eta-2.0\,\xi-2.0} \\ & - 0.71171\,\mathrm{e}^{-\eta^2-\xi^2+2.0\,\eta-1.0} + 0.91656\,\mathrm{e}^{-\eta^2-\xi^2+2.0\,\eta+2.0\,\xi-2.0} \end{aligned} \tag{B.2.7}$$

$$\begin{aligned} N_4(\xi,\eta) = {} & 0.16701 - 0.20433\,\xi + 0.20433\,\eta + 0.06845\,\mathrm{e}^{-\eta^2-\xi^2-2.0\,\eta-2.0\,\xi-2.0} \\ & - 0.05315\,\mathrm{e}^{-\eta^2-\xi^2-2.0\,\eta-1.0} + 0.25800\,\mathrm{e}^{-\eta^2-\xi^2-2.0\,\eta+2.0\,\xi-2.0} \\ & - 0.71171\,\mathrm{e}^{-\eta^2-\xi^2-2.0\,\xi-1.0} + 0.21826\,\mathrm{e}^{-1.0\,\eta^2-1.0\,\xi^2} \\ & - 0.05315\,\mathrm{e}^{-\eta^2-\xi^2+2.0\,\xi-1.0} + 0.91656\,\mathrm{e}^{-\eta^2-\xi^2+2.0\,\eta-2.0\,\xi-2.0} \\ & - 0.71171\,\mathrm{e}^{-\eta^2-\xi^2+2.0\,\eta-1.0} + 0.06845\,\mathrm{e}^{-\eta^2-\xi^2+2.0\,\eta+2.0\,\xi-2.0} \end{aligned} \tag{B.2.8}$$

$$\begin{aligned} N_5(\xi,\eta) = {} & 0.07465 + 1.0\times10^{-17}\,\xi - 0.09134\,\eta - 0.71171\,\mathrm{e}^{-\eta^2-\xi^2-2.0\,\eta-2.0\,\xi-2.0} \\ & + 1.54559\,\mathrm{e}^{-\eta^2-\xi^2-2.0\,\eta-1.0} - 0.71171\,\mathrm{e}^{-\eta^2-\xi^2-2.0\,\eta+2.0\,\xi-2.0} \\ & + 0.21826\,\mathrm{e}^{-\eta^2-\xi^2-2.0\,\xi-1.0} - 0.68085\,\mathrm{e}^{-1.0\,\eta^2-1.0\,\xi^2} \\ & + 0.21826\,\mathrm{e}^{-\eta^2-\xi^2+2.0\,\xi-1.0} - 0.05315\,\mathrm{e}^{-\eta^2-\xi^2+2.0\,\eta-2.0\,\xi-2.0} \\ & + 0.22847\,\mathrm{e}^{-\eta^2-\xi^2+2.0\,\eta-1.0} - 0.05315\,\mathrm{e}^{-\eta^2-\xi^2+2.0\,\eta+2.0\,\xi-2.0} \end{aligned} \tag{B.2.9}$$

$$\begin{aligned} N_6(\xi,\eta) = {} & 0.07465 + 0.09134\,\xi - 1.0\times10^{-16}\,\eta - 0.05315\,\mathrm{e}^{-\eta^2-\xi^2-2.0\,\eta-2.0\,\xi-2.0} \\ & + 0.21826\,\mathrm{e}^{-\eta^2-\xi^2-2.0\,\eta-1.0} - 0.71171\,\mathrm{e}^{-\eta^2-\xi^2-2.0\,\eta+2.0\,\xi-2.0} \\ & + 0.22847\,\mathrm{e}^{-\eta^2-\xi^2-2.0\,\xi-1.0} - 0.68085\,\mathrm{e}^{-1.0\,\eta^2-1.0\,\xi^2} \\ & + 1.54559\,\mathrm{e}^{-\eta^2-\xi^2+2.0\,\xi-1.0} - 0.05315\,\mathrm{e}^{-\eta^2-\xi^2+2.0\,\eta-2.0\,\xi-2.0} \\ & + 0.21826\,\mathrm{e}^{-\eta^2-\xi^2+2.0\,\eta-1.0} - 0.71171\,\mathrm{e}^{-\eta^2-\xi^2+2.0\,\eta+2.0\,\xi-2.0} \end{aligned} \tag{B.2.10}$$

$$\begin{aligned} N_7(\xi,\eta) = {} & 0.07465 + 1.0\times10^{-16}\,\xi + 0.09134\,\eta - 0.05315\,\mathrm{e}^{-\eta^2-\xi^2-2.0\,\eta-2.0\,\xi-2.0} \\ & + 0.22847\,\mathrm{e}^{-\eta^2-\xi^2-2.0\,\eta-1.0} - 0.05315\,\mathrm{e}^{-\eta^2-\xi^2-2.0\,\eta+2.0\,\xi-2.0} \\ & + 0.21826\,\mathrm{e}^{-\eta^2-\xi^2-2.0\,\xi-1.0} - 0.68085\,\mathrm{e}^{-1.0\,\eta^2-1.0\,\xi^2} \\ & + 0.21826\,\mathrm{e}^{-\eta^2-\xi^2+2.0\,\xi-1.0} - 0.71171\,\mathrm{e}^{-\eta^2-\xi^2+2.0\,\eta-2.0\,\xi-2.0} \\ & + 1.54559\,\mathrm{e}^{-\eta^2-\xi^2+2.0\,\eta-1.0} - 0.71171\,\mathrm{e}^{-\eta^2-\xi^2+2.0\,\eta+2.0\,\xi-2.0} \end{aligned} \tag{B.2.11}$$

$$\begin{aligned} N_8(\xi,\eta) = {} & 0.07465 - 0.09134\,\xi - 1.4\times10^{-16}\,\eta - 0.71171\,\mathrm{e}^{-\eta^2-\xi^2-2.0\,\eta-2.0\,\xi-2.0} \\ & + 0.21826\,\mathrm{e}^{-\eta^2-\xi^2-2.0\,\eta-1.0} - 0.05315\,\mathrm{e}^{-\eta^2-\xi^2-2.0\,\eta+2.0\,\xi-2.0} \\ & + 1.54559\,\mathrm{e}^{-\eta^2-\xi^2-2.0\,\xi-1.0} - 0.68085\,\mathrm{e}^{-1.0\,\eta^2-1.0\,\xi^2} \\ & + 0.22847\,\mathrm{e}^{-\eta^2-\xi^2+2.0\,\xi-1.0} - 0.71171\,\mathrm{e}^{-\eta^2-\xi^2+2.0\,\eta-2.0\,\xi-2.0} \\ & + 0.21826\,\mathrm{e}^{-\eta^2-\xi^2+2.0\,\eta-1.0} - 0.05315\,\mathrm{e}^{-\eta^2-\xi^2+2.0\,\eta+2.0\,\xi-2.0} \end{aligned} \tag{B.2.12}$$

$$\begin{aligned} N_9(\xi,\eta) = {} & 0.03337 + 1.1\times10^{-16}\,\xi + 9.0\times10^{-17}\,\eta + 0.21826\,\mathrm{e}^{-\eta^2-\xi^2-2.0\,\eta-2.0\,\xi-2.0} \\ & - 0.68085\,\mathrm{e}^{-\eta^2-\xi^2-2.0\,\eta-1.0} + 0.21826\,\mathrm{e}^{-\eta^2-\xi^2-2.0\,\eta+2.0\,\xi-2.0} \\ & - 0.68085\,\mathrm{e}^{-\eta^2-\xi^2-2.0\,\xi-1.0} + 1.85036\,\mathrm{e}^{-1.0\,\eta^2-1.0\,\xi^2} \\ & - 0.68085\,\mathrm{e}^{-\eta^2-\xi^2+2.0\,\xi-1.0} + 0.21826\,\mathrm{e}^{-\eta^2-\xi^2+2.0\,\eta-2.0\,\xi-2.0} \\ & - 0.68085\,\mathrm{e}^{-\eta^2-\xi^2+2.0\,\eta-1.0} + 0.21826\,\mathrm{e}^{-\eta^2-\xi^2+2.0\,\eta+2.0\,\xi-2.0} \end{aligned} \tag{B.2.13}$$

B.2.3 9-Node Biquadratic Quadrilateral (9BquadKrig)

$$\begin{aligned} N_1(\xi,\eta) = {} & -0.16701 - 0.20433\,\xi - 0.20433\,\eta + 0.20433\,\xi^2 + 0.20433\,\eta^2 \\ & + 0.25000\,\xi\,\eta + 0.43377\,\mathrm{e}^{-\eta^2-\xi^2-2.0\,\eta-2.0\,\xi-2.0} - 0.53826\,\mathrm{e}^{-\eta^2-\xi^2-2.0\,\eta-1.0} \\ & + 0.10449\,\mathrm{e}^{-\eta^2-\xi^2-2.0\,\eta+2.0\,\xi-2.0} - 0.53826\,\mathrm{e}^{-\eta^2-\xi^2-2.0\,\xi-1.0} + 0.41796\,\mathrm{e}^{-1.0\,\eta^2-1.0\,\xi^2} \\ & + 0.12030\,\mathrm{e}^{-\eta^2-\xi^2+2.0\,\xi-1.0} + 0.10449\,\mathrm{e}^{-\eta^2-\xi^2+2.0\,\eta-2.0\,\xi-2.0} \\ & + 0.12030\,\mathrm{e}^{-\eta^2-\xi^2+2.0\,\eta-1.0} - 0.22479\,\mathrm{e}^{-\eta^2-\xi^2+2.0\,\eta+2.0\,\xi-2.0} \end{aligned} \tag{B.2.14}$$

$$
\begin{aligned}
N_2(\xi,\eta) = &-0.16701 + 0.20433\,\xi - 0.20433\,\eta + 0.20433\,\xi^2 + 0.20433\,\eta^2 \\
&- 0.25000\,\xi\,\eta + 0.10449\,\mathrm{e}^{-\eta^2-\xi^2-2.0\,\eta-2.0\,\xi-2.0} - 0.53826\,\mathrm{e}^{-\eta^2-\xi^2-2.0\,\eta-1.0} \\
&+ 0.43377\,\mathrm{e}^{-\eta^2-\xi^2-2.0\,\eta+2.0\,\xi-2.0} + 0.12030\,\mathrm{e}^{-\eta^2-\xi^2-2.0\,\xi-1.0} + 0.41796\,\mathrm{e}^{-1.0\,\eta^2-1.0\,\xi^2} \\
&- 0.53826\,\mathrm{e}^{-\eta^2-\xi^2+2.0\,\xi-1.0} - 0.22479\,\mathrm{e}^{-\eta^2-\xi^2+2.0\,\eta-2.0\,\xi-2.0} \\
&+ 0.12030\,\mathrm{e}^{-\eta^2-\xi^2+2.0\,\eta-1.0} + 0.10449\,\mathrm{e}^{-\eta^2-\xi^2+2.0\,\eta+2.0\,\xi-2.0}
\end{aligned}
\tag{B.2.15}
$$

$$
\begin{aligned}
N_3(\xi,\eta) = &-0.16701 + 0.20433\,\xi + 0.20433\,\eta + 0.20433\,\xi^2 + 0.20433\,\eta^2 \\
&+ 0.25000\,\xi\,\eta - 0.22479\,\mathrm{e}^{-\eta^2-\xi^2-2.0\,\eta-2.0\,\xi-2.0} + 0.12030\,\mathrm{e}^{-\eta^2-\xi^2-2.0\,\eta-1.0} \\
&+ 0.10449\,\mathrm{e}^{-\eta^2-\xi^2-2.0\,\eta+2.0\,\xi-2.0} + 0.12030\,\mathrm{e}^{-\eta^2-\xi^2-2.0\,\xi-1.0} + 0.41796\,\mathrm{e}^{-1.0\,\eta^2-1.0\,\xi^2} \\
&- 0.53826\,\mathrm{e}^{-\eta^2-\xi^2+2.0\,\xi-1.0} + 0.10449\,\mathrm{e}^{-\eta^2-\xi^2+2.0\,\eta-2.0\,\xi-2.0} \\
&- 0.53826\,\mathrm{e}^{-\eta^2-\xi^2+2.0\,\eta-1.0} + 0.43377\,\mathrm{e}^{-\eta^2-\xi^2+2.0\,\eta+2.0\,\xi-2.0}
\end{aligned}
\tag{B.2.16}
$$

$$
\begin{aligned}
N_4(\xi,\eta) = &-0.16701 - 0.20433\,\xi + 0.20433\,\eta + 0.20433\,\xi^2 + 0.20433\,\eta^2 \\
&- 0.25000\,\xi\,\eta + 0.10449\,\mathrm{e}^{-\eta^2-\xi^2-2.0\,\eta-2.0\,\xi-2.0} + 0.12030\,\mathrm{e}^{-\eta^2-\xi^2-2.0\,\eta-1.0} \\
&- 0.22479\,\mathrm{e}^{-\eta^2-\xi^2-2.0\,\eta+2.0\,\xi-2.0} - 0.53826\,\mathrm{e}^{-\eta^2-\xi^2-2.0\,\xi-1.0} + 0.41796\,\mathrm{e}^{-1.0\,\eta^2-1.0\,\xi^2} \\
&+ 0.12030\,\mathrm{e}^{-\eta^2-\xi^2+2.0\,\xi-1.0} + 0.43377\,\mathrm{e}^{-\eta^2-\xi^2+2.0\,\eta-2.0\,\xi-2.0} \\
&- 0.53826\,\mathrm{e}^{-\eta^2-\xi^2+2.0\,\eta-1.0} + 0.10449\,\mathrm{e}^{-\eta^2-\xi^2+2.0\,\eta+2.0\,\xi-2.0}
\end{aligned}
\tag{B.2.17}
$$

$$
\begin{aligned}
N_5(\xi,\eta) = &\,0.33401 + 1.0\times10^{-17}\,\xi - 0.09134\,\eta - 0.40866\,\xi^2 + 0.09134\,\eta^2 \\
&+ 1.0\times10^{-17}\,\xi\,\eta - 0.53826\,\mathrm{e}^{-\eta^2-\xi^2-2.0\,\eta-2.0\,\xi-2.0} + 1.07652\,\mathrm{e}^{-\eta^2-\xi^2-2.0\,\eta-1.0} \\
&- 0.53826\,\mathrm{e}^{-\eta^2-\xi^2-2.0\,\eta+2.0\,\xi-2.0} + 0.41796\,\mathrm{e}^{-\eta^2-\xi^2-2.0\,\xi-1.0} - 0.83592\,\mathrm{e}^{-1.0\,\eta^2-1.0\,\xi^2} \\
&+ 0.41796\,\mathrm{e}^{-\eta^2-\xi^2+2.0\,\xi-1.0} + 0.12030\,\mathrm{e}^{-\eta^2-\xi^2+2.0\,\eta-2.0\,\xi-2.0} \\
&- 0.24060\,\mathrm{e}^{-\eta^2-\xi^2+2.0\,\eta-1.0} + 0.12030\,\mathrm{e}^{-\eta^2-\xi^2+2.0\,\eta+2.0\,\xi-2.0}
\end{aligned}
\tag{B.2.18}
$$

$$
\begin{aligned}
N_6(\xi,\eta) = &\,0.33401 + 0.09134\,\xi + 0.09134\,\xi^2 - 0.40866\,\eta^2 + 0.12030\,\mathrm{e}^{-\eta^2-\xi^2-2.0\,\eta-2.0\,\xi-2.0} \\
&+ 0.41796\,\mathrm{e}^{-\eta^2-\xi^2-2.0\,\eta-1.0} - 0.53826\,\mathrm{e}^{-\eta^2-\xi^2-2.0\,\eta+2.0\,\xi-2.0} \\
&- 0.24060\,\mathrm{e}^{-\eta^2-\xi^2-2.0\,\xi-1.0} - 0.83592\,\mathrm{e}^{-1.0\,\eta^2-1.0\,\xi^2} \\
&+ 1.07652\,\mathrm{e}^{-\eta^2-\xi^2+2.0\,\xi-1.0} + 0.12030\,\mathrm{e}^{-\eta^2-\xi^2+2.0\,\eta-2.0\,\xi-2.0} \\
&+ 0.41796\,\mathrm{e}^{-\eta^2-\xi^2+2.0\,\eta-1.0} - 0.53826\,\mathrm{e}^{-\eta^2-\xi^2+2.0\,\eta+2.0\,\xi-2.0}
\end{aligned}
\tag{B.2.19}
$$

$$
\begin{aligned}
N_7(\xi,\eta) = &\,0.33401 - 1.0\times10^{-16}\,\xi + 0.09134\,\eta - 0.40866\,\xi^2 + 0.09134\,\eta^2 \\
&+ 0.12030\,\mathrm{e}^{-\eta^2-\xi^2-2.0\,\eta-2.0\,\xi-2.0} - 0.24060\,\mathrm{e}^{-\eta^2-\xi^2-2.0\,\eta-1.0} \\
&+ 0.12030\,\mathrm{e}^{-\eta^2-\xi^2-2.0\,\eta+2.0\,\xi-2.0} + 0.41796\,\mathrm{e}^{-\eta^2-\xi^2-2.0\,\xi-1.0} \\
&- 0.83592\,\mathrm{e}^{-1.0\,\eta^2-1.0\,\xi^2} + 0.41796\,\mathrm{e}^{-\eta^2-\xi^2+2.0\,\xi-1.0} - 0.53826\,\mathrm{e}^{-\eta^2-\xi^2+2.0\,\eta-2.0\,\xi-2.0} \\
&+ 1.07652\,\mathrm{e}^{-\eta^2-\xi^2+2.0\,\eta-1.0} - 0.53826\,\mathrm{e}^{-\eta^2-\xi^2+2.0\,\eta+2.0\,\xi-2.0}
\end{aligned}
\tag{B.2.20}
$$

$$
\begin{aligned}
N_8(\xi,\eta) = {} & 0.33401 - 0.09134\,\xi - 1.9\times10^{-16}\,\eta + 0.09134\,\xi^2 - 0.40866\,\eta^2 \\
& + 6.00\times10^{-17}\,\xi\,\eta - 0.53826\,\mathrm{e}^{-\eta^2-\xi^2-2.0\,\eta-2.0\,\xi-2.0} + 0.41796\,\mathrm{e}^{-\eta^2-\xi^2-2.0\,\eta-1.0} \\
& + 0.12030\,\mathrm{e}^{-\eta^2-\xi^2-2.0\,\eta+2.0\,\xi-2.0} + 1.07652\,\mathrm{e}^{-\eta^2-\xi^2-2.0\,\xi-1.0} - 0.83592\,\mathrm{e}^{-1.0\,\eta^2-1.0\,\xi^2} \\
& - 0.24060\,\mathrm{e}^{-\eta^2-\xi^2+2.0\,\xi-1.0} - 0.53826\,\mathrm{e}^{-\eta^2-\xi^2+2.0\,\eta-2.0\,\xi-2.0} \\
& + 0.41796\,\mathrm{e}^{-\eta^2-\xi^2+2.0\,\eta-1.0} + 0.12030\,\mathrm{e}^{-\eta^2-\xi^2+2.0\,\eta+2.0\,\xi-2.0}
\end{aligned}
\tag{B.2.21}
$$

$$
\begin{aligned}
N_9(\xi,\eta) = {} & 0.33198 + 1.1\times10^{-16}\,\xi + 6.00\times10^{-17}\,\eta - 0.18267\,\xi^2 - 0.18267\,\eta^2 \\
& - 1.1\times10^{-16}\,\xi\,\eta + 0.41796\,\mathrm{e}^{-\eta^2-\xi^2-2.0\,\eta-2.0\,\xi-2.0} - 0.83592\,\mathrm{e}^{-\eta^2-\xi^2-2.0\,\eta-1.0} \\
& + 0.41796\,\mathrm{e}^{-\eta^2-\xi^2-2.0\,\eta+2.0\,\xi-2.0} - 0.83592\,\mathrm{e}^{-\eta^2-\xi^2-2.0\,\xi-1.0} + 1.67183\,\mathrm{e}^{-1.0\,\eta^2-1.0\,\xi^2} \\
& - 0.83592\,\mathrm{e}^{-\eta^2-\xi^2+2.0\,\xi-1.0} + 0.41796\,\mathrm{e}^{-\eta^2-\xi^2+2.0\,\eta-2.0\,\xi-2.0} \\
& - 0.83592\,\mathrm{e}^{-\eta^2-\xi^2+2.0\,\eta-1.0} + 0.41796\,\mathrm{e}^{-\eta^2-\xi^2+2.0\,\eta+2.0\,\xi-2.0}
\end{aligned}
\tag{B.2.22}
$$

B.2.4 16-Node Bilinear Quadrilateral (16BlinKrig)

$$
\begin{aligned}
N_1(\xi,\eta) = {} & 0.15988446 - 0.26301070\,\xi - 0.26301070\,\eta \\
& + 4.04460403\,\mathrm{e}^{-\eta^2-\xi^2-2.0\,\eta-2.0\,\xi-2.0} - 4.75566300\,\mathrm{e}^{-1.1-0.67\,\xi-\xi^2-2.0\,\eta-\eta^2} \\
& + 2.78065321\,\mathrm{e}^{-1.1+0.67\,\xi-\xi^2-2.0\,\eta-\eta^2} - 1.37847871\,\mathrm{e}^{-\eta^2-\xi^2-2.0\,\eta+2.0\,\xi-2.0} \\
& - 4.75566300\,\mathrm{e}^{-1.1-2.0\,\xi-\xi^2-0.67\,\eta-\eta^2} + 5.06461879\,\mathrm{e}^{-0.2-0.67\,\xi-\xi^2-0.67\,\eta-\eta^2} \\
& - 3.18083906\,\mathrm{e}^{-0.2+0.67\,\xi-\xi^2-0.67\,\eta-\eta^2} + 1.58656463\,\mathrm{e}^{-1.1+2.0\,\xi-\xi^2-0.67\,\eta-\eta^2} \\
& + 2.78065321\,\mathrm{e}^{-1.1-2.0\,\xi-\xi^2+0.67\,\eta-\eta^2} - 3.18083906\,\mathrm{e}^{-0.2-0.67\,\xi-\xi^2+0.67\,\eta-\eta^2} \\
& + 1.90753594\,\mathrm{e}^{-0.2+0.67\,\xi-\xi^2+0.67\,\eta-\eta^2} - 1.01005937\,\mathrm{e}^{-1.1+2.0\,\xi-\xi^2+0.67\,\eta-\eta^2} \\
& - 1.37847871\,\mathrm{e}^{-\eta^2-\xi^2+2.0\,\eta-2.0\,\xi-2.0} + 1.58656463\,\mathrm{e}^{-1.1-0.67\,\xi-\xi^2+2.0\,\eta-\eta^2} \\
& - 1.01005937\,\mathrm{e}^{-1.1+0.67\,\xi-\xi^2+2.0\,\eta-\eta^2} + 0.89888586\,\mathrm{e}^{-\eta^2-\xi^2+2.0\,\eta+2.0\,\xi-2.0}
\end{aligned}
\tag{B.2.23}
$$

$$
\begin{aligned}
N_2(\xi,\eta) = {} & 0.15988446 + 0.26301070\,\xi - 0.26301070\,\eta \\
& - 1.37847871\,\mathrm{e}^{-\eta^2-\xi^2-2.0\,\eta-2.0\,\xi-2.0} + 2.78065321\,\mathrm{e}^{-1.1-0.67\,\xi-\xi^2-2.0\,\eta-\eta^2} \\
& - 4.75566300\,\mathrm{e}^{-1.1+0.67\,\xi-\xi^2-2.0\,\eta-\eta^2} + 4.04460403\,\mathrm{e}^{-\eta^2-\xi^2-2.0\,\eta+2.0\,\xi-2.0} \\
& + 1.58656463\,\mathrm{e}^{-1.1-2.0\,\xi-\xi^2-0.67\,\eta-\eta^2} - 3.18083906\,\mathrm{e}^{-0.2-0.67\,\xi-\xi^2-0.67\,\eta-\eta^2} \\
& + 5.06461879\,\mathrm{e}^{-0.2+0.67\,\xi-\xi^2-0.67\,\eta-\eta^2} - 4.75566300\,\mathrm{e}^{-1.1+2.0\,\xi-\xi^2-0.67\,\eta-\eta^2} \\
& - 1.01005937\,\mathrm{e}^{-1.1-2.0\,\xi-\xi^2+0.67\,\eta-\eta^2} + 1.90753594\,\mathrm{e}^{-0.2-0.67\,\xi-\xi^2+0.67\,\eta-\eta^2} \\
& - 3.18083906\,\mathrm{e}^{-0.2+0.67\,\xi-\xi^2+0.67\,\eta-\eta^2} + 2.78065321\,\mathrm{e}^{-1.1+2.0\,\xi-\xi^2+0.67\,\eta-\eta^2} \\
& + 0.89888586\,\mathrm{e}^{-\eta^2-\xi^2+2.0\,\eta-2.0\,\xi-2.0} - 1.01005937\,\mathrm{e}^{-1.1-0.67\,\xi-\xi^2+2.0\,\eta-\eta^2} \\
& + 1.58656463\,\mathrm{e}^{-1.1+0.67\,\xi-\xi^2+2.0\,\eta-\eta^2} - 1.37847871\,\mathrm{e}^{-\eta^2-\xi^2+2.0\,\eta+2.0\,\xi-2.0}
\end{aligned}
\tag{B.2.24}
$$

$$
\begin{aligned}
N_3(\xi,\eta) = {} & 0.15988446 + 0.26301070\,\xi + 0.26301070\,\eta \\
& + 0.89888586\,\mathrm{e}^{-\eta^2-\xi^2-2.0\,\eta-2.0\,\xi-2.0} - 1.01005937\,\mathrm{e}^{-1.1-0.67\,\xi-\xi^2-2.0\,\eta-\eta^2} \\
& + 1.58656463\,\mathrm{e}^{-1.1+0.67\,\xi-\xi^2-2.0\,\eta-\eta^2} - 1.37847871\,\mathrm{e}^{-\eta^2-\xi^2-2.0\,\eta+2.0\,\xi-2.0} \\
& - 1.01005937\,\mathrm{e}^{-1.1-2.0\,\xi-\xi^2-0.67\,\eta-\eta^2} + 1.90753594\,\mathrm{e}^{-0.2-0.67\,\xi-\xi^2-0.67\,\eta-\eta^2} \\
& - 3.18083906\,\mathrm{e}^{-0.2+0.67\,\xi-\xi^2-0.67\,\eta-\eta^2} + 2.78065321\,\mathrm{e}^{-1.1+2.0\,\xi-\xi^2-0.67\,\eta-\eta^2} \\
& + 1.58656463\,\mathrm{e}^{-1.1-2.0\,\xi-\xi^2+0.67\,\eta-\eta^2} - 3.18083906\,\mathrm{e}^{-0.2-0.67\,\xi-\xi^2+0.67\,\eta-\eta^2} \\
& + 5.06461879\,\mathrm{e}^{-0.2+0.67\,\xi-\xi^2+0.67\,\eta-\eta^2} - 4.75566300\,\mathrm{e}^{-1.1+2.0\,\xi-\xi^2+0.67\,\eta-\eta^2} \\
& - 1.37847871\,\mathrm{e}^{-\eta^2-\xi^2+2.0\,\eta-2.0\,\xi-2.0} + 2.78065321\,\mathrm{e}^{-1.1-0.67\,\xi-\xi^2+2.0\,\eta-\eta^2} \\
& - 4.75566300\,\mathrm{e}^{-1.1+0.67\,\xi-\xi^2+2.0\,\eta-\eta^2} + 4.04460403\,\mathrm{e}^{-\eta^2-\xi^2+2.0\,\eta+2.0\,\xi-2.0}
\end{aligned}
\tag{B.2.25}
$$

$$
\begin{aligned}
N_4(\xi,\eta) = {} & 0.15988446 - 0.26301070\,\xi + 0.26301070\,\eta \\
& - 1.37847871\,\mathrm{e}^{-\eta^2-\xi^2-2.0\,\eta-2.0\,\xi-2.0} + 1.58656463\,\mathrm{e}^{-1.1-0.67\,\xi-\xi^2-2.0\,\eta-\eta^2} \\
& - 1.01005937\,\mathrm{e}^{-1.1+0.67\,\xi-\xi^2-2.0\,\eta-\eta^2} + 0.89888586\,\mathrm{e}^{-\eta^2-\xi^2-2.0\,\eta+2.0\,\xi-2.0} \\
& + 2.78065321\,\mathrm{e}^{-1.1-2.0\,\xi-\xi^2-0.67\,\eta-\eta^2} - 3.18083906\,\mathrm{e}^{-0.2-0.67\,\xi-\xi^2-0.67\,\eta-\eta^2} \\
& + 1.90753594\,\mathrm{e}^{-0.2+0.67\,\xi-\xi^2-0.67\,\eta-\eta^2} - 1.01005937\,\mathrm{e}^{-1.1+2.0\,\xi-\xi^2-0.67\,\eta-\eta^2} \\
& - 4.75566300\,\mathrm{e}^{-1.1-2.0\,\xi-\xi^2+0.67\,\eta-\eta^2} + 5.06461879\,\mathrm{e}^{-0.2-0.67\,\xi-\xi^2+0.67\,\eta-\eta^2} \\
& - 3.18083906\,\mathrm{e}^{-0.2+0.67\,\xi-\xi^2+0.67\,\eta-\eta^2} + 1.58656463\,\mathrm{e}^{-1.1+2.0\,\xi-\xi^2+0.67\,\eta-\eta^2} \\
& + 4.04460403\,\mathrm{e}^{-\eta^2-\xi^2+2.0\,\eta-2.0\,\xi-2.0} - 4.75566300\,\mathrm{e}^{-1.1-0.67\,\xi-\xi^2+2.0\,\eta-\eta^2} \\
& + 2.78065321\,\mathrm{e}^{-1.1+0.67\,\xi-\xi^2+2.0\,\eta-\eta^2} - 1.37847871\,\mathrm{e}^{-\eta^2-\xi^2+2.0\,\eta+2.0\,\xi-2.0}
\end{aligned}
\tag{B.2.26}
$$

$$
\begin{aligned}
N_5(\xi,\eta) = {} & 0.04004332 + 0.18924880\,\xi - 0.06587145\,\eta \\
& - 4.75566300\,\mathrm{e}^{-\eta^2-\xi^2-2.0\,\eta-2.0\,\xi-2.0} + 9.23664333\,\mathrm{e}^{-1.1-0.67\,\xi-\xi^2-2.0\,\eta-\eta^2} \\
& - 7.08854256\,\mathrm{e}^{-1.1+0.67\,\xi-\xi^2-2.0\,\eta-\eta^2} + 2.78065321\,\mathrm{e}^{-\eta^2-\xi^2-2.0\,\eta+2.0\,\xi-2.0} \\
& + 5.06461879\,\mathrm{e}^{-1.1-2.0\,\xi-\xi^2-0.67\,\eta-\eta^2} - 9.59222786\,\mathrm{e}^{-0.2-0.67\,\xi-\xi^2-0.67\,\eta-\eta^2} \\
& + 7.38653803\,\mathrm{e}^{-0.2+0.67\,\xi-\xi^2-0.67\,\eta-\eta^2} - 3.18083906\,\mathrm{e}^{-1.1+2.0\,\xi-\xi^2-0.67\,\eta-\eta^2} \\
& - 3.18083906\,\mathrm{e}^{-1.1-2.0\,\xi-\xi^2+0.67\,\eta-\eta^2} + 6.07075359\,\mathrm{e}^{-0.2-0.67\,\xi-\xi^2+0.67\,\eta-\eta^2} \\
& - 4.67290322\,\mathrm{e}^{-0.2+0.67\,\xi-\xi^2+0.67\,\eta-\eta^2} + 1.90753594\,\mathrm{e}^{-1.1+2.0\,\xi-\xi^2+0.67\,\eta-\eta^2} \\
& + 1.58656463\,\mathrm{e}^{-\eta^2-\xi^2+2.0\,\eta-2.0\,\xi-2.0} - 2.64724107\,\mathrm{e}^{-1.1-0.67\,\xi-\xi^2+2.0\,\eta-\eta^2} \\
& + 2.09500767\,\mathrm{e}^{-1.1+0.67\,\xi-\xi^2+2.0\,\eta-\eta^2} - 1.01005937\,\mathrm{e}^{-\eta^2-\xi^2+2.0\,\eta+2.0\,\xi-2.0}
\end{aligned}
\tag{B.2.27}
$$

$$
\begin{aligned}
N_6(\xi,\eta) = {} & 0.04004332 + 0.06587145\,\xi + 0.18924880\,\eta \\
& + 1.58656463\,\mathrm{e}^{-\eta^2-\xi^2-2.0\,\eta-2.0\,\xi-2.0} - 3.18083906\,\mathrm{e}^{-1.1-0.67\,\xi-\xi^2-2.0\,\eta-\eta^2} \\
& + 5.06461879\,\mathrm{e}^{-1.1+0.67\,\xi-\xi^2-2.0\,\eta-\eta^2} - 4.75566300\,\mathrm{e}^{-\eta^2-\xi^2-2.0\,\eta+2.0\,\xi-2.0} \\
& - 2.64724107\,\mathrm{e}^{-1.1-2.0\,\xi-\xi^2-0.67\,\eta-\eta^2} + 6.07075359\,\mathrm{e}^{-0.2-0.67\,\xi-\xi^2-0.67\,\eta-\eta^2} \\
& - 9.59222786\,\mathrm{e}^{-0.2+0.67\,\xi-\xi^2-0.67\,\eta-\eta^2} + 9.23664333\,\mathrm{e}^{-1.1+2.0\,\xi-\xi^2-0.67\,\eta-\eta^2} \\
& + 2.09500767\,\mathrm{e}^{-1.1-2.0\,\xi-\xi^2+0.67\,\eta-\eta^2} - 4.67290322\,\mathrm{e}^{-0.2-0.67\,\xi-\xi^2+0.67\,\eta-\eta^2} \\
& + 7.38653803\,\mathrm{e}^{-0.2+0.67\,\xi-\xi^2+0.67\,\eta-\eta^2} - 7.08854256\,\mathrm{e}^{-1.1+2.0\,\xi-\xi^2+0.67\,\eta-\eta^2} \\
& - 1.01005937\,\mathrm{e}^{-\eta^2-\xi^2+2.0\,\eta-2.0\,\xi-2.0} + 1.90753594\,\mathrm{e}^{-1.1-0.67\,\xi-\xi^2+2.0\,\eta-\eta^2} \\
& - 3.18083906\,\mathrm{e}^{-1.1+0.67\,\xi-\xi^2+2.0\,\eta-\eta^2} + 2.78065321\,\mathrm{e}^{-\eta^2-\xi^2+2.0\,\eta+2.0\,\xi-2.0}
\end{aligned}
\tag{B.2.28}
$$

$$
\begin{aligned}
N_7(\xi,\eta) = {} & 0.04004332 - 0.18924880\,\xi + 0.06587145\,\eta \\
& - 1.01005937\,\mathrm{e}^{-\eta^2-\xi^2-2.0\,\eta-2.0\,\xi-2.0} + 2.09500767\,\mathrm{e}^{-1.1-0.67\,\xi-\xi^2-2.0\,\eta-\eta^2} \\
& - 2.64724107\,\mathrm{e}^{-1.1+0.67\,\xi-\xi^2-2.0\,\eta-\eta^2} + 1.58656463\,\mathrm{e}^{-\eta^2-\xi^2-2.0\,\eta+2.0\,\xi-2.0} \\
& + 1.90753594\,\mathrm{e}^{-1.1-2.0\,\xi-\xi^2-0.67\,\eta-\eta^2} - 4.67290322\,\mathrm{e}^{-0.2-0.67\,\xi-\xi^2-0.67\,\eta-\eta^2} \\
& + 6.07075359\,\mathrm{e}^{-0.2+0.67\,\xi-\xi^2-0.67\,\eta-\eta^2} - 3.18083906\,\mathrm{e}^{-1.1+2.0\,\xi-\xi^2-0.67\,\eta-\eta^2} \\
& - 3.18083906\,\mathrm{e}^{-1.1-2.0\,\xi-\xi^2+0.67\,\eta-\eta^2} + 7.38653803\,\mathrm{e}^{-0.2-0.67\,\xi-\xi^2+0.67\,\eta-\eta^2} \\
& - 9.59222786\,\mathrm{e}^{-0.2+0.67\,\xi-\xi^2+0.67\,\eta-\eta^2} + 5.06461879\,\mathrm{e}^{-1.1+2.0\,\xi-\xi^2+0.67\,\eta-\eta^2} \\
& + 2.78065321\,\mathrm{e}^{-\eta^2-\xi^2+2.0\,\eta-2.0\,\xi-2.0} - 7.08854256\,\mathrm{e}^{-1.1-0.67\,\xi-\xi^2+2.0\,\eta-\eta^2} \\
& + 9.23664333\,\mathrm{e}^{-1.1+0.67\,\xi-\xi^2+2.0\,\eta-\eta^2} - 4.75566300\,\mathrm{e}^{-\eta^2-\xi^2+2.0\,\eta+2.0\,\xi-2.0}
\end{aligned}
\tag{B.2.29}
$$

$$
\begin{aligned}
N_8(\xi,\eta) = {} & 0.04004332 - 0.06587145\,\xi - 0.18924880\,\eta \\
& + 2.78065321\,\mathrm{e}^{-\eta^2-\xi^2-2.0\,\eta-2.0\,\xi-2.0} - 3.18083906\,\mathrm{e}^{-1.1-0.67\,\xi-\xi^2-2.0\,\eta-\eta^2} \\
& + 1.90753594\,\mathrm{e}^{-1.1+0.67\,\xi-\xi^2-2.0\,\eta-\eta^2} - 1.01005937\,\mathrm{e}^{-\eta^2-\xi^2-2.0\,\eta+2.0\,\xi-2.0} \\
& - 7.08854256\,\mathrm{e}^{-1.1-2.0\,\xi-\xi^2-0.67\,\eta-\eta^2} + 7.38653803\,\mathrm{e}^{-0.2-0.67\,\xi-\xi^2-0.67\,\eta-\eta^2} \\
& - 4.67290322\,\mathrm{e}^{-0.2+0.67\,\xi-\xi^2-0.67\,\eta-\eta^2} + 2.09500767\,\mathrm{e}^{-1.1+2.0\,\xi-\xi^2-0.67\,\eta-\eta^2} \\
& + 9.23664333\,\mathrm{e}^{-1.1-2.0\,\xi-\xi^2+0.67\,\eta-\eta^2} - 9.59222786\,\mathrm{e}^{-0.2-0.67\,\xi-\xi^2+0.67\,\eta-\eta^2} \\
& + 6.07075359\,\mathrm{e}^{-0.2+0.67\,\xi-\xi^2+0.67\,\eta-\eta^2} - 2.64724107\,\mathrm{e}^{-1.1+2.0\,\xi-\xi^2+0.67\,\eta-\eta^2} \\
& - 4.75566300\,\mathrm{e}^{-\eta^2-\xi^2+2.0\,\eta-2.0\,\xi-2.0} + 5.06461879\,\mathrm{e}^{-1.1-0.67\,\xi-\xi^2+2.0\,\eta-\eta^2} \\
& - 3.18083906\,\mathrm{e}^{-1.1+0.67\,\xi-\xi^2+2.0\,\eta-\eta^2} + 1.58656463\,\mathrm{e}^{-\eta^2-\xi^2+2.0\,\eta+2.0\,\xi-2.0}
\end{aligned}
\tag{B.2.30}
$$

$$
\begin{aligned}
N_9(\xi,\eta) = {} & 0.04004332 - 0.18924880\,\xi - 0.06587145\,\eta \\
& + 2.78065321\,\mathrm{e}^{-\eta^2-\xi^2-2.0\,\eta-2.0\,\xi-2.0} - 7.08854256\,\mathrm{e}^{-1.1-0.67\,\xi-\xi^2-2.0\,\eta-\eta^2} \\
& + 9.23664333\,\mathrm{e}^{-1.1+0.67\,\xi-\xi^2-2.0\,\eta-\eta^2} - 4.75566300\,\mathrm{e}^{-\eta^2-\xi^2-2.0\,\eta+2.0\,\xi-2.0} \\
& - 3.18083906\,\mathrm{e}^{-1.1-2.0\,\xi-\xi^2-0.67\,\eta-\eta^2} + 7.38653803\,\mathrm{e}^{-0.2-0.67\,\xi-\xi^2-0.67\,\eta-\eta^2} \\
& - 9.59222786\,\mathrm{e}^{-0.2+0.67\,\xi-\xi^2-0.67\,\eta-\eta^2} + 5.06461879\,\mathrm{e}^{-1.1+2.0\,\xi-\xi^2-0.67\,\eta-\eta^2} \\
& + 1.90753594\,\mathrm{e}^{-1.1-2.0\,\xi-\xi^2+0.67\,\eta-\eta^2} - 4.67290322\,\mathrm{e}^{-0.2-0.67\,\xi-\xi^2+0.67\,\eta-\eta^2} \\
& + 6.07075359\,\mathrm{e}^{-0.2+0.67\,\xi-\xi^2+0.67\,\eta-\eta^2} - 3.18083906\,\mathrm{e}^{-1.1+2.0\,\xi-\xi^2+0.67\,\eta-\eta^2} \\
& - 1.01005937\,\mathrm{e}^{-\eta^2-\xi^2+2.0\,\eta-2.0\,\xi-2.0} + 2.09500767\,\mathrm{e}^{-1.1-0.67\,\xi-\xi^2+2.0\,\eta-\eta^2} \\
& - 2.64724107\,\mathrm{e}^{-1.1+0.67\,\xi-\xi^2+2.0\,\eta-\eta^2} + 1.58656463\,\mathrm{e}^{-\eta^2-\xi^2+2.0\,\eta+2.0\,\xi-2.0}
\end{aligned}
\tag{B.2.31}
$$

$$
\begin{aligned}
N_{10}(\xi,\eta) = {} & 0.04004332 + 0.06587145\,\xi - 0.18924880\,\eta \\
& - 1.01005937\,\mathrm{e}^{-\eta^2-\xi^2-2.0\,\eta-2.0\,\xi-2.0} + 1.90753594\,\mathrm{e}^{-1.1-0.67\,\xi-\xi^2-2.0\,\eta-\eta^2} \\
& - 3.18083906\,\mathrm{e}^{-1.1+0.67\,\xi-\xi^2-2.0\,\eta-\eta^2} + 2.78065321\,\mathrm{e}^{-\eta^2-\xi^2-2.0\,\eta+2.0\,\xi-2.0} \\
& + 2.09500767\,\mathrm{e}^{-1.1-2.0\,\xi-\xi^2-0.67\,\eta-\eta^2} - 4.67290322\,\mathrm{e}^{-0.2-0.67\,\xi-\xi^2-0.67\,\eta-\eta^2} \\
& + 7.38653803\,\mathrm{e}^{-0.2+0.67\,\xi-\xi^2-0.67\,\eta-\eta^2} - 7.08854256\,\mathrm{e}^{-1.1+2.0\,\xi-\xi^2-0.67\,\eta-\eta^2} \\
& - 2.64724107\,\mathrm{e}^{-1.1-2.0\,\xi-\xi^2+0.67\,\eta-\eta^2} + 6.07075359\,\mathrm{e}^{-0.2-0.67\,\xi-\xi^2+0.67\,\eta-\eta^2} \\
& - 9.59222786\,\mathrm{e}^{-0.2+0.67\,\xi-\xi^2+0.67\,\eta-\eta^2} + 9.23664333\,\mathrm{e}^{-1.1+2.0\,\xi-\xi^2+0.67\,\eta-\eta^2} \\
& + 1.58656463\,\mathrm{e}^{-\eta^2-\xi^2+2.0\,\eta-2.0\,\xi-2.0} - 3.18083906\,\mathrm{e}^{-1.1-0.67\,\xi-\xi^2+2.0\,\eta-\eta^2} \\
& + 5.06461879\,\mathrm{e}^{-1.1+0.67\,\xi-\xi^2+2.0\,\eta-\eta^2} - 4.75566300\,\mathrm{e}^{-\eta^2-\xi^2+2.0\,\eta+2.0\,\xi-2.0}
\end{aligned}
\tag{B.2.32}
$$

$$
\begin{aligned}
N_{11}(\xi,\eta) = {} & 0.04004332 + 0.18924880\,\xi + 0.06587145\,\eta \\
& + 1.58656463\,\mathrm{e}^{-\eta^2-\xi^2-2.0\,\eta-2.0\,\xi-2.0} - 2.64724107\,\mathrm{e}^{-1.1-0.67\,\xi-\xi^2-2.0\,\eta-\eta^2} \\
& + 2.09500767\,\mathrm{e}^{-1.1+0.67\,\xi-\xi^2-2.0\,\eta-\eta^2} - 1.01005937\,\mathrm{e}^{-\eta^2-\xi^2-2.0\,\eta+2.0\,\xi-2.0} \\
& - 3.18083906\,\mathrm{e}^{-1.1-2.0\,\xi-\xi^2-0.67\,\eta-\eta^2} + 6.07075359\,\mathrm{e}^{-0.2-0.67\,\xi-\xi^2-0.67\,\eta-\eta^2} \\
& - 4.67290322\,\mathrm{e}^{-0.2+0.67\,\xi-\xi^2-0.67\,\eta-\eta^2} + 1.90753594\,\mathrm{e}^{-1.1+2.0\,\xi-\xi^2-0.67\,\eta-\eta^2} \\
& + 5.06461879\,\mathrm{e}^{-1.1-2.0\,\xi-\xi^2+0.67\,\eta-\eta^2} - 9.59222786\,\mathrm{e}^{-0.2-0.67\,\xi-\xi^2+0.67\,\eta-\eta^2} \\
& + 7.38653803\,\mathrm{e}^{-0.2+0.67\,\xi-\xi^2+0.67\,\eta-\eta^2} - 3.18083906\,\mathrm{e}^{-1.1+2.0\,\xi-\xi^2+0.67\,\eta-\eta^2} \\
& - 4.75566300\,\mathrm{e}^{-\eta^2-\xi^2+2.0\,\eta-2.0\,\xi-2.0} + 9.23664333\,\mathrm{e}^{-1.1-0.67\,\xi-\xi^2+2.0\,\eta-\eta^2} \\
& - 7.08854256\,\mathrm{e}^{-1.1+0.67\,\xi-\xi^2+2.0\,\eta-\eta^2} + 2.78065321\,\mathrm{e}^{-\eta^2-\xi^2+2.0\,\eta+2.0\,\xi-2.0}
\end{aligned}
\tag{B.2.33}
$$

$$
\begin{aligned}
N_{12}(\xi,\eta) = {} & 0.04004332 - 0.06587145\,\xi + 0.18924880\,\eta \\
& - 4.75566300\,\mathrm{e}^{-\eta^2-\xi^2-2.0\,\eta-2.0\,\xi-2.0} + 5.06461879\,\mathrm{e}^{-1.1-0.67\,\xi-\xi^2-2.0\,\eta-\eta^2} \\
& - 3.18083906\,\mathrm{e}^{-1.1+0.67\,\xi-\xi^2-2.0\,\eta-\eta^2} + 1.58656463\,\mathrm{e}^{-\eta^2-\xi^2-2.0\,\eta+2.0\,\xi-2.0} \\
& + 9.23664333\,\mathrm{e}^{-1.1-2.0\,\xi-\xi^2-0.67\,\eta-\eta^2} - 9.59222786\,\mathrm{e}^{-0.2-0.67\,\xi-\xi^2-0.67\,\eta-\eta^2} \\
& + 6.07075359\,\mathrm{e}^{-0.2+0.67\,\xi-\xi^2-0.67\,\eta-\eta^2} - 2.64724107\,\mathrm{e}^{-1.1+2.0\,\xi-\xi^2-0.67\,\eta-\eta^2} \\
& - 7.08854256\,\mathrm{e}^{-1.1-2.0\,\xi-\xi^2+0.67\,\eta-\eta^2} + 7.38653803\,\mathrm{e}^{-0.2-0.67\,\xi-\xi^2+0.67\,\eta-\eta^2} \\
& - 4.67290322\,\mathrm{e}^{-0.2+0.67\,\xi-\xi^2+0.67\,\eta-\eta^2} + 2.09500767\,\mathrm{e}^{-1.1+2.0\,\xi-\xi^2+0.67\,\eta-\eta^2} \\
& + 2.78065321\,\mathrm{e}^{-\eta^2-\xi^2+2.0\,\eta-2.0\,\xi-2.0} - 3.18083906\,\mathrm{e}^{-1.1-0.67\,\xi-\xi^2+2.0\,\eta-\eta^2} \\
& + 1.90753594\,\mathrm{e}^{-1.1+0.67\,\xi-\xi^2+2.0\,\eta-\eta^2} - 1.01005937\,\mathrm{e}^{-\eta^2-\xi^2+2.0\,\eta+2.0\,\xi-2.0}
\end{aligned}
\tag{B.2.34}
$$

$$
\begin{aligned}
N_{13}(\xi,\eta) = {} & 0.01002891 + 0.04739766\,\xi + 0.04739766\,\eta \\
& + 5.06461879\,\mathrm{e}^{-\eta^2-\xi^2-2.0\,\eta-2.0\,\xi-2.0} - 9.59222786\,\mathrm{e}^{-1.1-0.67\,\xi-\xi^2-2.0\,\eta-\eta^2} \\
& + 7.38653803\,\mathrm{e}^{-1.1+0.67\,\xi-\xi^2-2.0\,\eta-\eta^2} - 3.18083906\,\mathrm{e}^{-\eta^2-\xi^2-2.0\,\eta+2.0\,\xi-2.0} \\
& - 9.59222786\,\mathrm{e}^{-1.1-2.0\,\xi-\xi^2-0.67\,\eta-\eta^2} + 18.44798981\,\mathrm{e}^{-0.2-0.67\,\xi-\xi^2-0.67\,\eta-\eta^2} \\
& - 14.15814810\,\mathrm{e}^{-0.2+0.67\,\xi-\xi^2-0.67\,\eta-\eta^2} + 6.07075359\,\mathrm{e}^{-1.1+2.0\,\xi-\xi^2-0.67\,\eta-\eta^2} \\
& + 7.38653803\,\mathrm{e}^{-1.1-2.0\,\xi-\xi^2+0.67\,\eta-\eta^2} - 14.15814810\,\mathrm{e}^{-0.2-0.67\,\xi-\xi^2+0.67\,\eta-\eta^2} \\
& + 10.87350869\,\mathrm{e}^{-0.2+0.67\,\xi-\xi^2+0.67\,\eta-\eta^2} - 4.67290322\,\mathrm{e}^{-1.1+2.0\,\xi-\xi^2+0.67\,\eta-\eta^2} \\
& - 3.18083906\,\mathrm{e}^{-\eta^2-\xi^2+2.0\,\eta-2.0\,\xi-2.0} + 6.07075359\,\mathrm{e}^{-1.1-0.67\,\xi-\xi^2+2.0\,\eta-\eta^2} \\
& - 4.67290322\,\mathrm{e}^{-1.1+0.67\,\xi-\xi^2+2.0\,\eta-\eta^2} + 1.90753594\,\mathrm{e}^{-\eta^2-\xi^2+2.0\,\eta+2.0\,\xi-2.0}
\end{aligned}
\tag{B.2.35}
$$

$$
\begin{aligned}
N_{14}(\xi,\eta) = {} & 0.01002891 - 0.04739766\,\xi + 0.04739766\,\eta \\
& - 3.18083906\,\mathrm{e}^{-\eta^2-\xi^2-2.0\,\eta-2.0\,\xi-2.0} + 7.38653803\,\mathrm{e}^{-1.1-0.67\,\xi-\xi^2-2.0\,\eta-\eta^2} \\
& - 9.59222786\,\mathrm{e}^{-1.1+0.67\,\xi-\xi^2-2.0\,\eta-\eta^2} + 5.06461879\,\mathrm{e}^{-\eta^2-\xi^2-2.0\,\eta+2.0\,\xi-2.0} \\
& + 6.07075359\,\mathrm{e}^{-1.1-2.0\,\xi-\xi^2-0.67\,\eta-\eta^2} - 14.15814810\,\mathrm{e}^{-0.2-0.67\,\xi-\xi^2-0.67\,\eta-\eta^2} \\
& + 18.44798981\,\mathrm{e}^{-0.2+0.67\,\xi-\xi^2-0.67\,\eta-\eta^2} - 9.59222786\,\mathrm{e}^{-1.1+2.0\,\xi-\xi^2-0.67\,\eta-\eta^2} \\
& - 4.67290322\,\mathrm{e}^{-1.1-2.0\,\xi-\xi^2+0.67\,\eta-\eta^2} + 10.87350869\,\mathrm{e}^{-0.2-0.67\,\xi-\xi^2+0.67\,\eta-\eta^2} \\
& - 14.15814810\,\mathrm{e}^{-0.2+0.67\,\xi-\xi^2+0.67\,\eta-\eta^2} + 7.38653803\,\mathrm{e}^{-1.1+2.0\,\xi-\xi^2+0.67\,\eta-\eta^2} \\
& + 1.90753594\,\mathrm{e}^{-\eta^2-\xi^2+2.0\,\eta-2.0\,\xi-2.0} - 4.67290322\,\mathrm{e}^{-1.1-0.67\,\xi-\xi^2+2.0\,\eta-\eta^2} \\
& + 6.07075359\,\mathrm{e}^{-1.1+0.67\,\xi-\xi^2+2.0\,\eta-\eta^2} - 3.18083906\,\mathrm{e}^{-\eta^2-\xi^2+2.0\,\eta+2.0\,\xi-2.0}
\end{aligned}
\tag{B.2.36}
$$

$$
\begin{aligned}
N_{15}(\xi,\eta) = {} & 0.01002891 - 0.04739766\,\xi - 0.04739766\,\eta \\
& + 1.90753594\,\mathrm{e}^{-\eta^2-\xi^2-2.0\,\eta-2.0\,\xi-2.0} - 4.67290322\,\mathrm{e}^{-1.1-0.67\,\xi-\xi^2-2.0\,\eta-\eta^2} \\
& + 6.07075359\,\mathrm{e}^{-1.1+0.67\,\xi-\xi^2-2.0\,\eta-\eta^2} - 3.18083906\,\mathrm{e}^{-\eta^2-\xi^2-2.0\,\eta+2.0\,\xi-2.0} \\
& - 4.67290322\,\mathrm{e}^{-1.1-2.0\,\xi-\xi^2-0.67\,\eta-\eta^2} + 10.87350869\,\mathrm{e}^{-0.2-0.67\,\xi-\xi^2-0.67\,\eta-\eta^2} \\
& - 14.15814810\,\mathrm{e}^{-0.2+0.67\,\xi-\xi^2-0.67\,\eta-\eta^2} + 7.38653803\,\mathrm{e}^{-1.1+2.0\,\xi-\xi^2-0.67\,\eta-\eta^2} \\
& + 6.07075359\,\mathrm{e}^{-1.1-2.0\,\xi-\xi^2+0.67\,\eta-\eta^2} - 14.15814810\,\mathrm{e}^{-0.2-0.67\,\xi-\xi^2+0.67\,\eta-\eta^2} \\
& + 18.44798981\,\mathrm{e}^{-0.2+0.67\,\xi-\xi^2+0.67\,\eta-\eta^2} - 9.59222786\,\mathrm{e}^{-1.1+2.0\,\xi-\xi^2+0.67\,\eta-\eta^2} \\
& - 3.18083906\,\mathrm{e}^{-\eta^2-\xi^2+2.0\,\eta-2.0\,\xi-2.0} + 7.38653803\,\mathrm{e}^{-1.1-0.67\,\xi-\xi^2+2.0\,\eta-\eta^2} \\
& - 9.59222786\,\mathrm{e}^{-1.1+0.67\,\xi-\xi^2+2.0\,\eta-\eta^2} + 5.06461879\,\mathrm{e}^{-\eta^2-\xi^2+2.0\,\eta+2.0\,\xi-2.0}
\end{aligned}
\tag{B.2.37}
$$

$$
\begin{aligned}
N_{16}(\xi,\eta) = {} & 0.01002891 + 0.04739766\,\xi - 0.04739766\,\eta \\
& - 3.18083906\,\mathrm{e}^{-\eta^2-\xi^2-2.0\,\eta-2.0\,\xi-2.0} + 6.07075359\,\mathrm{e}^{-1.1-0.67\,\xi-\xi^2-2.0\,\eta-\eta^2} \\
& - 4.67290322\,\mathrm{e}^{-1.1+0.67\,\xi-\xi^2-2.0\,\eta-\eta^2} + 1.90753594\,\mathrm{e}^{-\eta^2-\xi^2-2.0\,\eta+2.0\,\xi-2.0} \\
& + 7.38653803\,\mathrm{e}^{-1.1-2.0\,\xi-\xi^2-0.67\,\eta-\eta^2} - 14.15814810\,\mathrm{e}^{-0.2-0.67\,\xi-\xi^2-0.67\,\eta-\eta^2} \\
& + 10.87350869\,\mathrm{e}^{-0.2+0.67\,\xi-\xi^2-0.67\,\eta-\eta^2} - 4.67290322\,\mathrm{e}^{-1.1+2.0\,\xi-\xi^2-0.67\,\eta-\eta^2} \\
& - 9.59222786\,\mathrm{e}^{-1.1-2.0\,\xi-\xi^2+0.67\,\eta-\eta^2} + 18.44798981\,\mathrm{e}^{-0.2-0.67\,\xi-\xi^2+0.67\,\eta-\eta^2} \\
& - 14.15814810\,\mathrm{e}^{-0.2+0.67\,\xi-\xi^2+0.67\,\eta-\eta^2} + 6.07075359\,\mathrm{e}^{-1.1+2.0\,\xi-\xi^2+0.67\,\eta-\eta^2} \\
& + 5.06461879\,\mathrm{e}^{-\eta^2-\xi^2+2.0\,\eta-2.0\,\xi-2.0} - 9.59222786\,\mathrm{e}^{-1.1-0.67\,\xi-\xi^2+2.0\,\eta-\eta^2} \\
& + 7.38653803\,\mathrm{e}^{-1.1+0.67\,\xi-\xi^2+2.0\,\eta-\eta^2} - 3.18083906\,\mathrm{e}^{-\eta^2-\xi^2+2.0\,\eta+2.0\,\xi-2.0}
\end{aligned}
\tag{B.2.38}
$$

B.2.5 16-Node Biquadratic Quadrilateral (16BquadKrig)

$$
\begin{aligned}
N_{1}(\xi,\eta) = {} & -0.20986640 - 0.26301070\,\xi - 0.26301070\,\eta \\
& + 0.22491874\,\xi^2 + 0.22491874\,\eta^2 + 0.43265388\,\xi\,\eta \\
& + 2.67958949\,\mathrm{e}^{-\eta^2-\xi^2-2.0\,\eta-2.0\,\xi-2.0} - 3.88210695\,\mathrm{e}^{-1.1-0.67\,\xi-\xi^2-2.0\,\eta-\eta^2} \\
& + 2.14327786\,\mathrm{e}^{-1.1+0.67\,\xi-\xi^2-2.0\,\eta-\eta^2} - 0.64365885\,\mathrm{e}^{-\eta^2-\xi^2-2.0\,\eta+2.0\,\xi-2.0} \\
& - 3.88210695\,\mathrm{e}^{-1.1-2.0\,\xi-\xi^2-0.67\,\eta-\eta^2} + 4.59994167\,\mathrm{e}^{-0.2-0.67\,\xi-\xi^2-0.67\,\eta-\eta^2} \\
& - 2.55832869\,\mathrm{e}^{-0.2+0.67\,\xi-\xi^2-0.67\,\eta-\eta^2} + 0.94918929\,\mathrm{e}^{-1.1+2.0\,\xi-\xi^2-0.67\,\eta-\eta^2} \\
& + 2.14327786\,\mathrm{e}^{-1.1-2.0\,\xi-\xi^2+0.67\,\eta-\eta^2} - 2.55832869\,\mathrm{e}^{-0.2-0.67\,\xi-\xi^2+0.67\,\eta-\eta^2} \\
& + 1.44285882\,\mathrm{e}^{-0.2+0.67\,\xi-\xi^2+0.67\,\eta-\eta^2} - 0.13650332\,\mathrm{e}^{-1.1+2.0\,\xi-\xi^2+0.67\,\eta-\eta^2} \\
& - 0.64365885\,\mathrm{e}^{-\eta^2-\xi^2+2.0\,\eta-2.0\,\xi-2.0} + 0.94918929\,\mathrm{e}^{-1.1-0.67\,\xi-\xi^2+2.0\,\eta-\eta^2} \\
& - 0.13650332\,\mathrm{e}^{-1.1+0.67\,\xi-\xi^2+2.0\,\eta-\eta^2} - 0.46612868\,\mathrm{e}^{-\eta^2-\xi^2+2.0\,\eta+2.0\,\xi-2.0}
\end{aligned}
\tag{B.2.39}
$$

$$
\begin{aligned}
N_2(\xi,\eta) = & -0.20986640 + 0.26301070\,\xi - 0.26301070\,\eta \\
& + 0.22491874\,\xi^2 + 0.22491874\,\eta^2 - 0.43265388\,\xi\,\eta \\
& - 0.64365885\,\mathrm{e}^{-\eta^2-\xi^2-2.0\,\eta-2.0\,\xi-2.0} + 2.14327786\,\mathrm{e}^{-1.1-0.67\,\xi-\xi^2-2.0\,\eta-\eta^2} \\
& - 3.88210695\,\mathrm{e}^{-1.1+0.67\,\xi-\xi^2-2.0\,\eta-\eta^2} + 2.67958949\,\mathrm{e}^{-\eta^2-\xi^2-2.0\,\eta+2.0\,\xi-2.0} \\
& + 0.94918929\,\mathrm{e}^{-1.1-2.0\,\xi-\xi^2-0.67\,\eta-\eta^2} - 2.55832869\,\mathrm{e}^{-0.2-0.67\,\xi-\xi^2-0.67\,\eta-\eta^2} \\
& + 4.59994167\,\mathrm{e}^{-0.2+0.67\,\xi-\xi^2-0.67\,\eta-\eta^2} - 3.88210695\,\mathrm{e}^{-1.1+2.0\,\xi-\xi^2-0.67\,\eta-\eta^2} \\
& - 0.13650332\,\mathrm{e}^{-1.1-2.0\,\xi-\xi^2+0.67\,\eta-\eta^2} + 1.44285882\,\mathrm{e}^{-0.2-0.67\,\xi-\xi^2+0.67\,\eta-\eta^2} \\
& - 2.55832869\,\mathrm{e}^{-0.2+0.67\,\xi-\xi^2+0.67\,\eta-\eta^2} + 2.14327786\,\mathrm{e}^{-1.1+2.0\,\xi-\xi^2+0.67\,\eta-\eta^2} \\
& - 0.46612868\,\mathrm{e}^{-\eta^2-\xi^2+2.0\,\eta-2.0\,\xi-2.0} - 0.13650332\,\mathrm{e}^{-1.1-0.67\,\xi-\xi^2+2.0\,\eta-\eta^2} \\
& + 0.94918929\,\mathrm{e}^{-1.1+0.67\,\xi-\xi^2+2.0\,\eta-\eta^2} - 0.64365885\,\mathrm{e}^{-\eta^2-\xi^2+2.0\,\eta+2.0\,\xi-2.0}
\end{aligned}
\tag{B.2.40}
$$

$$
\begin{aligned}
N_3(\xi,\eta) = & -0.20986640 + 0.26301070\,\xi + 0.26301070\,\eta \\
& + 0.22491874\,\xi^2 + 0.22491874\,\eta^2 + 0.43265388\,\xi\,\eta \\
& - 0.46612868\,\mathrm{e}^{-\eta^2-\xi^2-2.0\,\eta-2.0\,\xi-2.0} - 0.13650332\,\mathrm{e}^{-1.1-0.67\,\xi-\xi^2-2.0\,\eta-\eta^2} \\
& + 0.94918929\,\mathrm{e}^{-1.1+0.67\,\xi-\xi^2-2.0\,\eta-\eta^2} - 0.64365885\,\mathrm{e}^{-\eta^2-\xi^2-2.0\,\eta+2.0\,\xi-2.0} \\
& - 0.13650332\,\mathrm{e}^{-1.1-2.0\,\xi-\xi^2-0.67\,\eta-\eta^2} + 1.44285882\,\mathrm{e}^{-0.2-0.67\,\xi-\xi^2-0.67\,\eta-\eta^2} \\
& - 2.55832869\,\mathrm{e}^{-0.2+0.67\,\xi-\xi^2-0.67\,\eta-\eta^2} + 2.14327786\,\mathrm{e}^{-1.1+2.0\,\xi-\xi^2-0.67\,\eta-\eta^2} \\
& + 0.94918929\,\mathrm{e}^{-1.1-2.0\,\xi-\xi^2+0.67\,\eta-\eta^2} - 2.55832869\,\mathrm{e}^{-0.2-0.67\,\xi-\xi^2+0.67\,\eta-\eta^2} \\
& + 4.59994167\,\mathrm{e}^{-0.2+0.67\,\xi-\xi^2+0.67\,\eta-\eta^2} - 3.88210695\,\mathrm{e}^{-1.1+2.0\,\xi-\xi^2+0.67\,\eta-\eta^2} \\
& - 0.64365885\,\mathrm{e}^{-\eta^2-\xi^2+2.0\,\eta-2.0\,\xi-2.0} + 2.14327786\,\mathrm{e}^{-1.1-0.67\,\xi-\xi^2+2.0\,\eta-\eta^2} \\
& - 3.88210695\,\mathrm{e}^{-1.1+0.67\,\xi-\xi^2+2.0\,\eta-\eta^2} + 2.67958949\,\mathrm{e}^{-\eta^2-\xi^2+2.0\,\eta+2.0\,\xi-2.0}
\end{aligned}
\tag{B.2.41}
$$

$$
\begin{aligned}
N_4(\xi,\eta) = & -0.20986640 - 0.26301070\,\xi + 0.26301070\,\eta \\
& + 0.22491874\,\xi^2 + 0.22491874\,\eta^2 - 0.43265388\,\xi\,\eta \\
& - 0.64365885\,\mathrm{e}^{-\eta^2-\xi^2-2.0\,\eta-2.0\,\xi-2.0} + 0.94918929\,\mathrm{e}^{-1.1-0.67\,\xi-\xi^2-2.0\,\eta-\eta^2} \\
& - 0.13650332\,\mathrm{e}^{-1.1+0.67\,\xi-\xi^2-2.0\,\eta-\eta^2} - 0.46612868\,\mathrm{e}^{-\eta^2-\xi^2-2.0\,\eta+2.0\,\xi-2.0} \\
& + 2.14327786\,\mathrm{e}^{-1.1-2.0\,\xi-\xi^2-0.67\,\eta-\eta^2} - 2.55832869\,\mathrm{e}^{-0.2-0.67\,\xi-\xi^2-0.67\,\eta-\eta^2} \\
& + 1.44285882\,\mathrm{e}^{-0.2+0.67\,\xi-\xi^2-0.67\,\eta-\eta^2} - 0.13650332\,\mathrm{e}^{-1.1+2.0\,\xi-\xi^2-0.67\,\eta-\eta^2} \\
& - 3.88210695\,\mathrm{e}^{-1.1-2.0\,\xi-\xi^2+0.67\,\eta-\eta^2} + 4.59994167\,\mathrm{e}^{-0.2-0.67\,\xi-\xi^2+0.67\,\eta-\eta^2} \\
& - 2.55832869\,\mathrm{e}^{-0.2+0.67\,\xi-\xi^2+0.67\,\eta-\eta^2} + 0.94918929\,\mathrm{e}^{-1.1+2.0\,\xi-\xi^2+0.67\,\eta-\eta^2} \\
& + 2.67958949\,\mathrm{e}^{-\eta^2-\xi^2+2.0\,\eta-2.0\,\xi-2.0} - 3.88210695\,\mathrm{e}^{-1.1-0.67\,\xi-\xi^2+2.0\,\eta-\eta^2} \\
& + 2.14327786\,\mathrm{e}^{-1.1+0.67\,\xi-\xi^2+2.0\,\eta-\eta^2} - 0.64365885\,\mathrm{e}^{-\eta^2-\xi^2+2.0\,\eta+2.0\,\xi-2.0}
\end{aligned}
\tag{B.2.42}
$$

$$
\begin{aligned}
N_5(\xi,\eta) = {} & 0.17861640 + 0.18924880\,\xi - 0.06587145\,\eta \\
& - 0.22491874\,\xi^2 + 0.05633126\,\eta^2 - 0.31131518\,\xi\,\eta \\
& - 3.88210695\,\mathrm{e}^{-\eta^2-\xi^2-2.0\,\eta-2.0\,\xi-2.0} + 8.52561852\,\mathrm{e}^{-1.1-0.67\,\xi-\xi^2-2.0\,\eta-\eta^2} \\
& - 6.71237988\,\mathrm{e}^{-1.1+0.67\,\xi-\xi^2-2.0\,\eta-\eta^2} + 2.14327786\,\mathrm{e}^{-\eta^2-\xi^2-2.0\,\eta+2.0\,\xi-2.0} \\
& + 4.59994167\,\mathrm{e}^{-1.1-2.0\,\xi-\xi^2-0.67\,\eta-\eta^2} - 9.23066205\,\mathrm{e}^{-0.2-0.67\,\xi-\xi^2-0.67\,\eta-\eta^2} \\
& + 6.96582039\,\mathrm{e}^{-0.2+0.67\,\xi-\xi^2-0.67\,\eta-\eta^2} - 2.55832869\,\mathrm{e}^{-1.1+2.0\,\xi-\xi^2-0.67\,\eta-\eta^2} \\
& - 2.55832869\,\mathrm{e}^{-1.1-2.0\,\xi-\xi^2+0.67\,\eta-\eta^2} + 5.65003594\,\mathrm{e}^{-0.2-0.67\,\xi-\xi^2+0.67\,\eta-\eta^2} \\
& - 4.31133740\,\mathrm{e}^{-0.2+0.67\,\xi-\xi^2+0.67\,\eta-\eta^2} + 1.44285882\,\mathrm{e}^{-1.1+2.0\,\xi-\xi^2+0.67\,\eta-\eta^2} \\
& + 0.94918929\,\mathrm{e}^{-\eta^2-\xi^2+2.0\,\eta-2.0\,\xi-2.0} - 2.27107839\,\mathrm{e}^{-1.1-0.67\,\xi-\xi^2+2.0\,\eta-\eta^2} \\
& + 1.38398286\,\mathrm{e}^{-1.1+0.67\,\xi-\xi^2+2.0\,\eta-\eta^2} - 0.13650332\,\mathrm{e}^{-\eta^2-\xi^2+2.0\,\eta+2.0\,\xi-2.0}
\end{aligned}
\tag{B.2.43}
$$

$$
\begin{aligned}
N_6(\xi,\eta) = {} & 0.17861640 + 0.06587145\,\xi + 0.18924880\,\eta \\
& + 0.05633126\,\xi^2 - 0.22491874\,\eta^2 + 0.31131518\,\xi\,\eta \\
& + 0.94918929\,\mathrm{e}^{-\eta^2-\xi^2-2.0\,\eta-2.0\,\xi-2.0} - 2.55832869\,\mathrm{e}^{-1.1-0.67\,\xi-\xi^2-2.0\,\eta-\eta^2} \\
& + 4.59994167\,\mathrm{e}^{-1.1+0.67\,\xi-\xi^2-2.0\,\eta-\eta^2} - 3.88210695\,\mathrm{e}^{-\eta^2-\xi^2-2.0\,\eta+2.0\,\xi-2.0} \\
& - 2.27107839\,\mathrm{e}^{-1.1-2.0\,\xi-\xi^2-0.67\,\eta-\eta^2} + 5.65003594\,\mathrm{e}^{-0.2-0.67\,\xi-\xi^2-0.67\,\eta-\eta^2} \\
& - 9.23066205\,\mathrm{e}^{-0.2+0.67\,\xi-\xi^2-0.67\,\eta-\eta^2} + 8.52561852\,\mathrm{e}^{-1.1+2.0\,\xi-\xi^2-0.67\,\eta-\eta^2} \\
& + 1.38398286\,\mathrm{e}^{-1.1-2.0\,\xi-\xi^2+0.67\,\eta-\eta^2} - 4.31133740\,\mathrm{e}^{-0.2-0.67\,\xi-\xi^2+0.67\,\eta-\eta^2} \\
& + 6.96582039\,\mathrm{e}^{-0.2+0.67\,\xi-\xi^2+0.67\,\eta-\eta^2} - 6.71237988\,\mathrm{e}^{-1.1+2.0\,\xi-\xi^2+0.67\,\eta-\eta^2} \\
& - 0.13650332\,\mathrm{e}^{-\eta^2-\xi^2+2.0\,\eta-2.0\,\xi-2.0} + 1.44285882\,\mathrm{e}^{-1.1-0.67\,\xi-\xi^2+2.0\,\eta-\eta^2} \\
& - 2.55832869\,\mathrm{e}^{-1.1+0.67\,\xi-\xi^2+2.0\,\eta-\eta^2} + 2.14327786\,\mathrm{e}^{-\eta^2-\xi^2+2.0\,\eta+2.0\,\xi-2.0}
\end{aligned}
\tag{B.2.44}
$$

$$
\begin{aligned}
N_7(\xi,\eta) = {} & 0.17861640 - 0.18924880\,\xi + 0.06587145\,\eta \\
& - 0.22491874\,\xi^2 + 0.05633126\,\eta^2 - 0.31131518\,\xi\,\eta \\
& - 0.13650332\,\mathrm{e}^{-\eta^2-\xi^2-2.0\,\eta-2.0\,\xi-2.0} + 1.38398286\,\mathrm{e}^{-1.1-0.67\,\xi-\xi^2-2.0\,\eta-\eta^2} \\
& - 2.27107839\,\mathrm{e}^{-1.1+0.67\,\xi-\xi^2-2.0\,\eta-\eta^2} + 0.94918929\,\mathrm{e}^{-\eta^2-\xi^2-2.0\,\eta+2.0\,\xi-2.0} \\
& + 1.44285882\,\mathrm{e}^{-1.1-2.0\,\xi-\xi^2-0.67\,\eta-\eta^2} - 4.31133740\,\mathrm{e}^{-0.2-0.67\,\xi-\xi^2-0.67\,\eta-\eta^2} \\
& + 5.65003594\,\mathrm{e}^{-0.2+0.67\,\xi-\xi^2-0.67\,\eta-\eta^2} - 2.55832869\,\mathrm{e}^{-1.1+2.0\,\xi-\xi^2-0.67\,\eta-\eta^2} \\
& - 2.55832869\,\mathrm{e}^{-1.1-2.0\,\xi-\xi^2+0.67\,\eta-\eta^2} + 6.96582039\,\mathrm{e}^{-0.2-0.67\,\xi-\xi^2+0.67\,\eta-\eta^2} \\
& - 9.23066205\,\mathrm{e}^{-0.2+0.67\,\xi-\xi^2+0.67\,\eta-\eta^2} + 4.59994167\,\mathrm{e}^{-1.1+2.0\,\xi-\xi^2+0.67\,\eta-\eta^2} \\
& + 2.14327786\,\mathrm{e}^{-\eta^2-\xi^2+2.0\,\eta-2.0\,\xi-2.0} - 6.71237988\,\mathrm{e}^{-1.1-0.67\,\xi-\xi^2+2.0\,\eta-\eta^2} \\
& + 8.52561852\,\mathrm{e}^{-1.1+0.67\,\xi-\xi^2+2.0\,\eta-\eta^2} - 3.88210695\,\mathrm{e}^{-\eta^2-\xi^2+2.0\,\eta+2.0\,\xi-2.0}
\end{aligned}
\tag{B.2.45}
$$

$$
\begin{aligned}
N_8(\xi,\eta) = {} & 0.17861640 - 0.06587145\,\xi - 0.18924880\,\eta \\
& + 0.05633126\,\xi^2 - 0.22491874\,\eta^2 + 0.31131518\,\xi\,\eta \\
& + 2.14327786\,\mathrm{e}^{-\eta^2-\xi^2-2.0\,\eta-2.0\,\xi-2.0} - 2.55832869\,\mathrm{e}^{-1.1-0.67\,\xi-\xi^2-2.0\,\eta-\eta^2} \\
& + 1.44285882\,\mathrm{e}^{-1.1+0.67\,\xi-\xi^2-2.0\,\eta-\eta^2} - 0.13650332\,\mathrm{e}^{-\eta^2-\xi^2-2.0\,\eta+2.0\,\xi-2.0} \\
& - 6.71237988\,\mathrm{e}^{-1.1-2.0\,\xi-\xi^2-0.67\,\eta-\eta^2} + 6.96582039\,\mathrm{e}^{-0.2-0.67\,\xi-\xi^2-0.67\,\eta-\eta^2} \\
& - 4.31133740\,\mathrm{e}^{-0.2+0.67\,\xi-\xi^2-0.67\,\eta-\eta^2} + 1.38398286\,\mathrm{e}^{-1.1+2.0\,\xi-\xi^2-0.67\,\eta-\eta^2} \\
& + 8.52561852\,\mathrm{e}^{-1.1-2.0\,\xi-\xi^2+0.67\,\eta-\eta^2} - 9.23066205\,\mathrm{e}^{-0.2-0.67\,\xi-\xi^2+0.67\,\eta-\eta^2} \\
& + 5.65003594\,\mathrm{e}^{-0.2+0.67\,\xi-\xi^2+0.67\,\eta-\eta^2} - 2.27107839\,\mathrm{e}^{-1.1+2.0\,\xi-\xi^2+0.67\,\eta-\eta^2} \\
& - 3.88210695\,\mathrm{e}^{-\eta^2-\xi^2+2.0\,\eta-2.0\,\xi-2.0} + 4.59994167\,\mathrm{e}^{-1.1-0.67\,\xi-\xi^2+2.0\,\eta-\eta^2} \\
& - 2.55832869\,\mathrm{e}^{-1.1+0.67\,\xi-\xi^2+2.0\,\eta-\eta^2} + 0.94918929\,\mathrm{e}^{-\eta^2-\xi^2+2.0\,\eta+2.0\,\xi-2.0}
\end{aligned}
\tag{B.2.46}
$$

$$
\begin{aligned}
N_9(\xi,\eta) = {} & 0.17861640 - 0.18924880\,\xi - 0.06587145\,\eta \\
& - 0.22491874\,\xi^2 + 0.05633126\,\eta^2 + 0.31131518\,\xi\,\eta \\
& + 2.14327786\,\mathrm{e}^{-\eta^2-\xi^2-2.0\,\eta-2.0\,\xi-2.0} - 6.71237988\,\mathrm{e}^{-1.1-0.67\,\xi-\xi^2-2.0\,\eta-\eta^2} \\
& + 8.52561852\,\mathrm{e}^{-1.1+0.67\,\xi-\xi^2-2.0\,\eta-\eta^2} - 3.88210695\,\mathrm{e}^{-\eta^2-\xi^2-2.0\,\eta+2.0\,\xi-2.0} \\
& - 2.55832869\,\mathrm{e}^{-1.1-2.0\,\xi-\xi^2-0.67\,\eta-\eta^2} + 6.96582039\,\mathrm{e}^{-0.2-0.67\,\xi-\xi^2-0.67\,\eta-\eta^2} \\
& - 9.23066205\,\mathrm{e}^{-0.2+0.67\,\xi-\xi^2-0.67\,\eta-\eta^2} + 4.59994167\,\mathrm{e}^{-1.1+2.0\,\xi-\xi^2-0.67\,\eta-\eta^2} \\
& + 1.44285882\,\mathrm{e}^{-1.1-2.0\,\xi-\xi^2+0.67\,\eta-\eta^2} - 4.31133740\,\mathrm{e}^{-0.2-0.67\,\xi-\xi^2+0.67\,\eta-\eta^2} \\
& + 5.65003594\,\mathrm{e}^{-0.2+0.67\,\xi-\xi^2+0.67\,\eta-\eta^2} - 2.55832869\,\mathrm{e}^{-1.1+2.0\,\xi-\xi^2+0.67\,\eta-\eta^2} \\
& - 0.13650332\,\mathrm{e}^{-\eta^2-\xi^2+2.0\,\eta-2.0\,\xi-2.0} + 1.38398286\,\mathrm{e}^{-1.1-0.67\,\xi-\xi^2+2.0\,\eta-\eta^2} \\
& - 2.27107839\,\mathrm{e}^{-1.1+0.67\,\xi-\xi^2+2.0\,\eta-\eta^2} + 0.94918929\,\mathrm{e}^{-\eta^2-\xi^2+2.0\,\eta+2.0\,\xi-2.0}
\end{aligned}
\tag{B.2.47}
$$

$$
\begin{aligned}
N_{10}(\xi,\eta) = {} & 0.17861640 + 0.06587145\,\xi - 0.18924880\,\eta \\
& + 0.05633126\,\xi^2 - 0.22491874\,\eta^2 - 0.31131518\,\xi\,\eta \\
& - 0.13650332\,\mathrm{e}^{-\eta^2-\xi^2-2.0\,\eta-2.0\,\xi-2.0} + 1.44285882\,\mathrm{e}^{-1.1-0.67\,\xi-\xi^2-2.0\,\eta-\eta^2} \\
& - 2.55832869\,\mathrm{e}^{-1.1+0.67\,\xi-\xi^2-2.0\,\eta-\eta^2} + 2.14327786\,\mathrm{e}^{-\eta^2-\xi^2-2.0\,\eta+2.0\,\xi-2.0} \\
& + 1.38398286\,\mathrm{e}^{-1.1-2.0\,\xi-\xi^2-0.67\,\eta-\eta^2} - 4.31133740\,\mathrm{e}^{-0.2-0.67\,\xi-\xi^2-0.67\,\eta-\eta^2} \\
& + 6.96582039\,\mathrm{e}^{-0.2+0.67\,\xi-\xi^2-0.67\,\eta-\eta^2} - 6.71237988\,\mathrm{e}^{-1.1+2.0\,\xi-\xi^2-0.67\,\eta-\eta^2} \\
& - 2.27107839\,\mathrm{e}^{-1.1-2.0\,\xi-\xi^2+0.67\,\eta-\eta^2} + 5.65003594\,\mathrm{e}^{-0.2-0.67\,\xi-\xi^2+0.67\,\eta-\eta^2} \\
& - 9.23066205\,\mathrm{e}^{-0.2+0.67\,\xi-\xi^2+0.67\,\eta-\eta^2} + 8.52561852\,\mathrm{e}^{-1.1+2.0\,\xi-\xi^2+0.67\,\eta-\eta^2} \\
& + 0.94918929\,\mathrm{e}^{-\eta^2-\xi^2+2.0\,\eta-2.0\,\xi-2.0} - 2.55832869\,\mathrm{e}^{-1.1-0.67\,\xi-\xi^2+2.0\,\eta-\eta^2} \\
& + 4.59994167\,\mathrm{e}^{-1.1+0.67\,\xi-\xi^2+2.0\,\eta-\eta^2} - 3.88210695\,\mathrm{e}^{-\eta^2-\xi^2+2.0\,\eta+2.0\,\xi-2.0}
\end{aligned}
\tag{B.2.48}
$$

$$
\begin{aligned}
N_{11}(\xi,\eta) = {} & 0.17861640 + 0.18924880\,\xi + 0.06587145\,\eta \\
& - 0.22491874\,\xi^2 + 0.05633126\,\eta^2 + 0.31131518\,\xi\,\eta \\
& + 0.94918929\,\mathrm{e}^{-\eta^2-\xi^2-2.0\,\eta-2.0\,\xi-2.0} - 2.27107839\,\mathrm{e}^{-1.1-0.67\,\xi-\xi^2-2.0\,\eta-\eta^2} \\
& + 1.38398286\,\mathrm{e}^{-1.1+0.67\,\xi-\xi^2-2.0\,\eta-\eta^2} - 0.13650332\,\mathrm{e}^{-\eta^2-\xi^2-2.0\,\eta+2.0\,\xi-2.0} \\
& - 2.55832869\,\mathrm{e}^{-1.1-2.0\,\xi-\xi^2-0.67\,\eta-\eta^2} + 5.65003594\,\mathrm{e}^{-0.2-0.67\,\xi-\xi^2-0.67\,\eta-\eta^2} \\
& - 4.31133740\,\mathrm{e}^{-0.2+0.67\,\xi-\xi^2-0.67\,\eta-\eta^2} + 1.44285882\,\mathrm{e}^{-1.1+2.0\,\xi-\xi^2-0.67\,\eta-\eta^2} \\
& + 4.59994167\,\mathrm{e}^{-1.1-2.0\,\xi-\xi^2+0.67\,\eta-\eta^2} - 9.23066205\,\mathrm{e}^{-0.2-0.67\,\xi-\xi^2+0.67\,\eta-\eta^2} \\
& + 6.96582039\,\mathrm{e}^{-0.2+0.67\,\xi-\xi^2+0.67\,\eta-\eta^2} - 2.55832869\,\mathrm{e}^{-1.1+2.0\,\xi-\xi^2+0.67\,\eta-\eta^2} \\
& - 3.88210695\,\mathrm{e}^{-\eta^2-\xi^2+2.0\,\eta-2.0\,\xi-2.0} + 8.52561852\,\mathrm{e}^{-1.1-0.67\,\xi-\xi^2+2.0\,\eta-\eta^2} \\
& - 6.71237988\,\mathrm{e}^{-1.1+0.67\,\xi-\xi^2+2.0\,\eta-\eta^2} + 2.14327786\,\mathrm{e}^{-\eta^2-\xi^2+2.0\,\eta+2.0\,\xi-2.0}
\end{aligned}
\tag{B.2.49}
$$

$$
\begin{aligned}
N_{12}(\xi,\eta) = {} & 0.17861640 - 0.06587145\,\xi + 0.18924880\,\eta \\
& + 0.05633126\,\xi^2 - 0.22491874\,\eta^2 - 0.31131518\,\xi\,\eta \\
& - 3.88210695\,\mathrm{e}^{-\eta^2-\xi^2-2.0\,\eta-2.0\,\xi-2.0} + 4.59994167\,\mathrm{e}^{-1.1-0.67\,\xi-\xi^2-2.0\,\eta-\eta^2} \\
& - 2.55832869\,\mathrm{e}^{-1.1+0.67\,\xi-\xi^2-2.0\,\eta-\eta^2} + 0.94918929\,\mathrm{e}^{-\eta^2-\xi^2-2.0\,\eta+2.0\,\xi-2.0} \\
& + 8.52561852\,\mathrm{e}^{-1.1-2.0\,\xi-\xi^2-0.67\,\eta-\eta^2} - 9.23066205\,\mathrm{e}^{-0.2-0.67\,\xi-\xi^2-0.67\,\eta-\eta^2} \\
& + 5.65003594\,\mathrm{e}^{-0.2+0.67\,\xi-\xi^2-0.67\,\eta-\eta^2} - 2.27107839\,\mathrm{e}^{-1.1+2.0\,\xi-\xi^2-0.67\,\eta-\eta^2} \\
& - 6.71237988\,\mathrm{e}^{-1.1-2.0\,\xi-\xi^2+0.67\,\eta-\eta^2} + 6.96582039\,\mathrm{e}^{-0.2-0.67\,\xi-\xi^2+0.67\,\eta-\eta^2} \\
& - 4.31133740\,\mathrm{e}^{-0.2+0.67\,\xi-\xi^2+0.67\,\eta-\eta^2} + 1.38398286\,\mathrm{e}^{-1.1+2.0\,\xi-\xi^2+0.67\,\eta-\eta^2} \\
& + 2.14327786\,\mathrm{e}^{-\eta^2-\xi^2+2.0\,\eta-2.0\,\xi-2.0} - 2.55832869\,\mathrm{e}^{-1.1-0.67\,\xi-\xi^2+2.0\,\eta-\eta^2} \\
& + 1.44285882\,\mathrm{e}^{-1.1+0.67\,\xi-\xi^2+2.0\,\eta-\eta^2} - 0.13650332\,\mathrm{e}^{-\eta^2-\xi^2+2.0\,\eta+2.0\,\xi-2.0}
\end{aligned}
\tag{B.2.50}
$$

$$
\begin{aligned}
N_{13}(\xi,\eta) = {} & 0.10263360 + 0.04739766\,\xi + 0.04739766\,\eta \\
& - 0.05633126\,\xi^2 - 0.05633126\,\eta^2 + 0.22400618\,\xi\,\eta \\
& + 4.59994167\,\mathrm{e}^{-\eta^2-\xi^2-2.0\,\eta-2.0\,\xi-2.0} - 9.23066205\,\mathrm{e}^{-1.1-0.67\,\xi-\xi^2-2.0\,\eta-\eta^2} \\
& + 6.96582039\,\mathrm{e}^{-1.1+0.67\,\xi-\xi^2-2.0\,\eta-\eta^2} - 2.55832869\,\mathrm{e}^{-\eta^2-\xi^2-2.0\,\eta+2.0\,\xi-2.0} \\
& - 9.23066205\,\mathrm{e}^{-1.1-2.0\,\xi-\xi^2-0.67\,\eta-\eta^2} + 18.14677981\,\mathrm{e}^{-0.2-0.67\,\xi-\xi^2-0.67\,\eta-\eta^2} \\
& - 13.89646769\,\mathrm{e}^{-0.2+0.67\,\xi-\xi^2-0.67\,\eta-\eta^2} + 5.65003594\,\mathrm{e}^{-1.1+2.0\,\xi-\xi^2-0.67\,\eta-\eta^2} \\
& + 6.96582039\,\mathrm{e}^{-1.1-2.0\,\xi-\xi^2+0.67\,\eta-\eta^2} - 13.89646769\,\mathrm{e}^{-0.2-0.67\,\xi-\xi^2+0.67\,\eta-\eta^2} \\
& + 10.57229869\,\mathrm{e}^{-0.2+0.67\,\xi-\xi^2+0.67\,\eta-\eta^2} - 4.31133740\,\mathrm{e}^{-1.1+2.0\,\xi-\xi^2+0.67\,\eta-\eta^2} \\
& - 2.55832869\,\mathrm{e}^{-\eta^2-\xi^2+2.0\,\eta-2.0\,\xi-2.0} + 5.65003594\,\mathrm{e}^{-1.1-0.67\,\xi-\xi^2+2.0\,\eta-\eta^2} \\
& - 4.31133740\,\mathrm{e}^{-1.1+0.67\,\xi-\xi^2+2.0\,\eta-\eta^2} + 1.44285882\,\mathrm{e}^{-\eta^2-\xi^2+2.0\,\eta+2.0\,\xi-2.0}
\end{aligned}
\tag{B.2.51}
$$

$$
\begin{aligned}
N_{14}(\xi,\eta) = {} & 0.10263360 - 0.04739766\,\xi + 0.04739766\,\eta \\
& - 0.05633126\,\xi^2 - 0.05633126\,\eta^2 - 0.22400618\,\xi\,\eta \\
& - 2.55832869\,\mathrm{e}^{-\eta^2-\xi^2-2.0\,\eta-2.0\,\xi-2.0} + 6.96582039\,\mathrm{e}^{-1.1-0.67\,\xi-\xi^2-2.0\,\eta-\eta^2} \\
& - 9.23066205\,\mathrm{e}^{-1.1+0.67\,\xi-\xi^2-2.0\,\eta-\eta^2} + 4.59994167\,\mathrm{e}^{-\eta^2-\xi^2-2.0\,\eta+2.0\,\xi-2.0} \\
& + 5.65003594\,\mathrm{e}^{-1.1-2.0\,\xi-\xi^2-0.67\,\eta-\eta^2} - 13.89646769\,\mathrm{e}^{-0.2-0.67\,\xi-\xi^2-0.67\,\eta-\eta^2} \\
& + 18.14677981\,\mathrm{e}^{-0.2+0.67\,\xi-\xi^2-0.67\,\eta-\eta^2} - 9.23066205\,\mathrm{e}^{-1.1+2.0\,\xi-\xi^2-0.67\,\eta-\eta^2} \\
& - 4.31133740\,\mathrm{e}^{-1.1-2.0\,\xi-\xi^2+0.67\,\eta-\eta^2} + 10.57229869\,\mathrm{e}^{-0.2-0.67\,\xi-\xi^2+0.67\,\eta-\eta^2} \\
& - 13.89646769\,\mathrm{e}^{-0.2+0.67\,\xi-\xi^2+0.67\,\eta-\eta^2} + 6.96582039\,\mathrm{e}^{-1.1+2.0\,\xi-\xi^2+0.67\,\eta-\eta^2} \\
& + 1.44285882\,\mathrm{e}^{-\eta^2-\xi^2+2.0\,\eta-2.0\,\xi-2.0} - 4.31133740\,\mathrm{e}^{-1.1-0.67\,\xi-\xi^2+2.0\,\eta-\eta^2} \\
& + 5.65003594\,\mathrm{e}^{-1.1+0.67\,\xi-\xi^2+2.0\,\eta-\eta^2} - 2.55832869\,\mathrm{e}^{-\eta^2-\xi^2+2.0\,\eta+2.0\,\xi-2.0}
\end{aligned}
\tag{B.2.52}
$$

$$
\begin{aligned}
N_{15}(\xi,\eta) = {} & 0.10263360 - 0.04739766\,\xi - 0.04739766\,\eta \\
& - 0.05633126\,\xi^2 - 0.05633126\,\eta^2 + 0.22400618\,\xi\,\eta \\
& + 1.44285882\,\mathrm{e}^{-\eta^2-\xi^2-2.0\,\eta-2.0\,\xi-2.0} - 4.31133740\,\mathrm{e}^{-1.1-0.67\,\xi-\xi^2-2.0\,\eta-\eta^2} \\
& + 5.65003594\,\mathrm{e}^{-1.1+0.67\,\xi-\xi^2-2.0\,\eta-\eta^2} - 2.55832869\,\mathrm{e}^{-\eta^2-\xi^2-2.0\,\eta+2.0\,\xi-2.0} \\
& - 4.31133740\,\mathrm{e}^{-1.1-2.0\,\xi-\xi^2-0.67\,\eta-\eta^2} + 10.57229869\,\mathrm{e}^{-0.2-0.67\,\xi-\xi^2-0.67\,\eta-\eta^2} \\
& - 13.89646769\,\mathrm{e}^{-0.2+0.67\,\xi-\xi^2-0.67\,\eta-\eta^2} + 6.96582039\,\mathrm{e}^{-1.1+2.0\,\xi-\xi^2-0.67\,\eta-\eta^2} \\
& + 5.65003594\,\mathrm{e}^{-1.1-2.0\,\xi-\xi^2+0.67\,\eta-\eta^2} - 13.89646769\,\mathrm{e}^{-0.2-0.67\,\xi-\xi^2+0.67\,\eta-\eta^2} \\
& + 18.14677981\,\mathrm{e}^{-0.2+0.67\,\xi-\xi^2+0.67\,\eta-\eta^2} - 9.23066205\,\mathrm{e}^{-1.1+2.0\,\xi-\xi^2+0.67\,\eta-\eta^2} \\
& - 2.55832869\,\mathrm{e}^{-\eta^2-\xi^2+2.0\,\eta-2.0\,\xi-2.0} + 6.96582039\,\mathrm{e}^{-1.1-0.67\,\xi-\xi^2+2.0\,\eta-\eta^2} \\
& - 9.23066205\,\mathrm{e}^{-1.1+0.67\,\xi-\xi^2+2.0\,\eta-\eta^2} + 4.59994167\,\mathrm{e}^{-\eta^2-\xi^2+2.0\,\eta+2.0\,\xi-2.0}
\end{aligned}
\tag{B.2.53}
$$

$$
\begin{aligned}
N_{16}(\xi,\eta) = {} & 0.10263360 + 0.04739766\,\xi - 0.04739766\,\eta \\
& - 0.05633126\,\xi^2 - 0.05633126\,\eta^2 - 0.22400618\,\xi\,\eta \\
& - 2.55832869\,\mathrm{e}^{-\eta^2-\xi^2-2.0\,\eta-2.0\,\xi-2.0} + 5.65003594\,\mathrm{e}^{-1.1-0.67\,\xi-\xi^2-2.0\,\eta-\eta^2} \\
& - 4.31133740\,\mathrm{e}^{-1.1+0.67\,\xi-\xi^2-2.0\,\eta-\eta^2} + 1.44285882\,\mathrm{e}^{-\eta^2-\xi^2-2.0\,\eta+2.0\,\xi-2.0} \\
& + 6.96582039\,\mathrm{e}^{-1.1-2.0\,\xi-\xi^2-0.67\,\eta-\eta^2} - 13.89646769\,\mathrm{e}^{-0.2-0.67\,\xi-\xi^2-0.67\,\eta-\eta^2} \\
& + 10.57229869\,\mathrm{e}^{-0.2+0.67\,\xi-\xi^2-0.67\,\eta-\eta^2} - 4.31133740\,\mathrm{e}^{-1.1+2.0\,\xi-\xi^2-0.67\,\eta-\eta^2} \\
& - 9.23066205\,\mathrm{e}^{-1.1-2.0\,\xi-\xi^2+0.67\,\eta-\eta^2} + 18.14677981\,\mathrm{e}^{-0.2-0.67\,\xi-\xi^2+0.67\,\eta-\eta^2} \\
& - 13.89646769\,\mathrm{e}^{-0.2+0.67\,\xi-\xi^2+0.67\,\eta-\eta^2} + 5.65003594\,\mathrm{e}^{-1.1+2.0\,\xi-\xi^2+0.67\,\eta-\eta^2} \\
& + 4.59994167\,\mathrm{e}^{-\eta^2-\xi^2+2.0\,\eta-2.0\,\xi-2.0} - 9.23066205\,\mathrm{e}^{-1.1-0.67\,\xi-\xi^2+2.0\,\eta-\eta^2} \\
& + 6.96582039\,\mathrm{e}^{-1.1+0.67\,\xi-\xi^2+2.0\,\eta-\eta^2} - 2.55832869\,\mathrm{e}^{-\eta^2-\xi^2+2.0\,\eta+2.0\,\xi-2.0}
\end{aligned}
\tag{B.2.54}
$$

B.2.6 16-Node Bicubic Quadrilateral (16BcubKrig)

$$
\begin{aligned}
N_1(\xi,\eta) = {} & 1.19705995\,\mathrm{e}^{-1.1-0.67\,\xi-\xi^2+2.0\,\eta-\eta^2} + 0.22491874\,\xi^2 \\
& + 0.22491874\,\eta^2 + 0.32911194\,\xi + 0.32911194\,\eta + 0.43265388\,\xi\,\eta \\
& + 0.75755679\,\mathrm{e}^{-\eta^2-\xi^2+2.0\,\eta+2.0\,\xi-2.0} - 0.64365885\,\mathrm{e}^{-\eta^2-\xi^2+2.0\,\eta-2.0\,\xi-2.0} \\
& - 0.64365885\,\mathrm{e}^{-\eta^2-\xi^2-2.0\,\eta+2.0\,\xi-2.0} - 0.22491874\,\eta^3 - 0.22491874\,\xi^3 \\
& + 1.45590403\,\mathrm{e}^{-\eta^2-\xi^2-2.0\,\eta-2.0\,\xi-2.0} - 1.31095789\,\mathrm{e}^{-1.1+0.67\,\xi-\xi^2+2.0\,\eta-\eta^2} \\
& - 2.70765238\,\mathrm{e}^{-1.1-2.0\,\xi-\xi^2-0.67\,\eta-\eta^2} - 0.20986640 \\
& + 1.19705995\,\mathrm{e}^{-1.1+2.0\,\xi-\xi^2-0.67\,\eta-\eta^2} + 1.89540719\,\mathrm{e}^{-1.1-2.0\,\xi-\xi^2+0.67\,\eta-\eta^2} \\
& - 1.31095789\,\mathrm{e}^{-1.1+2.0\,\xi-\xi^2+0.67\,\eta-\eta^2} - 0.36999242\,\eta^2\xi - 0.36999242\,\eta\,\xi^2 \\
& + 1.89540719\,\mathrm{e}^{-1.1+0.67\,\xi-\xi^2-2.0\,\eta-\eta^2} - 2.70765238\,\mathrm{e}^{-1.1-0.67\,\xi-\xi^2-2.0\,\eta-\eta^2} \\
& + 4.06892111\,\mathrm{e}^{-0.2-0.67\,\xi-\xi^2-0.67\,\eta-\eta^2} - 2.55832869\,\mathrm{e}^{-0.2+0.67\,\xi-\xi^2-0.67\,\eta-\eta^2} \\
& - 2.55832869\,\mathrm{e}^{-0.2-0.67\,\xi-\xi^2+0.67\,\eta-\eta^2} + 1.97387939\,\mathrm{e}^{-0.2+0.67\,\xi-\xi^2+0.67\,\eta-\eta^2}
\end{aligned}
\tag{B.2.55}
$$

$$
\begin{aligned}
N_2(\xi,\eta) = {} & -1.31095789\,\mathrm{e}^{-1.1-0.67\,\xi-\xi^2+2.0\,\eta-\eta^2} + 0.22491874\,\xi^2 \\
& + 0.22491874\,\eta^2 - 0.32911194\,\xi + 0.32911194\,\eta - 0.43265388\,\xi\,\eta \\
& - 0.64365885\,\mathrm{e}^{-\eta^2-\xi^2+2.0\,\eta+2.0\,\xi-2.0} + 0.75755679\,\mathrm{e}^{-\eta^2-\xi^2+2.0\,\eta-2.0\,\xi-2.0} \\
& + 1.45590403\,\mathrm{e}^{-\eta^2-\xi^2-2.0\,\eta+2.0\,\xi-2.0} - 0.22491874\,\eta^3 + 0.22491874\,\xi^3 \\
& - 0.64365885\,\mathrm{e}^{-\eta^2-\xi^2-2.0\,\eta-2.0\,\xi-2.0} + 1.19705995\,\mathrm{e}^{-1.1+0.67\,\xi-\xi^2+2.0\,\eta-\eta^2} \\
& + 1.19705995\,\mathrm{e}^{-1.1-2.0\,\xi-\xi^2-0.67\,\eta-\eta^2} - 0.20986640 \\
& - 2.70765238\,\mathrm{e}^{-1.1+2.0\,\xi-\xi^2-0.67\,\eta-\eta^2} - 1.31095789\,\mathrm{e}^{-1.1-2.0\,\xi-\xi^2+0.67\,\eta-\eta^2} \\
& + 1.89540719\,\mathrm{e}^{-1.1+2.0\,\xi-\xi^2+0.67\,\eta-\eta^2} + 0.36999242\,\eta^2\xi - 0.36999242\,\eta\,\xi^2 \\
& - 2.70765238\,\mathrm{e}^{-1.1+0.67\,\xi-\xi^2-2.0\,\eta-\eta^2} + 1.89540719\,\mathrm{e}^{-1.1-0.67\,\xi-\xi^2-2.0\,\eta-\eta^2} \\
& - 2.55832869\,\mathrm{e}^{-0.2-0.67\,\xi-\xi^2-0.67\,\eta-\eta^2} + 4.06892111\,\mathrm{e}^{-0.2+0.67\,\xi-\xi^2-0.67\,\eta-\eta^2} \\
& + 1.97387939\,\mathrm{e}^{-0.2-0.67\,\xi-\xi^2+0.67\,\eta-\eta^2} - 2.55832869\,\mathrm{e}^{-0.2+0.67\,\xi-\xi^2+0.67\,\eta-\eta^2}
\end{aligned}
\tag{B.2.56}
$$

$$
\begin{aligned}
N_3(\xi,\eta) = {} & 1.89540719\,\mathrm{e}^{-1.1-0.67\,\xi-\xi^2+2.0\,\eta-\eta^2} + 0.22491874\,\xi^2 \\
& + 0.22491874\,\eta^2 - 0.32911194\,\xi - 0.32911194\,\eta + 0.43265388\,\xi\,\eta \\
& + 1.45590403\,\mathrm{e}^{-\eta^2-\xi^2+2.0\,\eta+2.0\,\xi-2.0} - 0.64365885\,\mathrm{e}^{-\eta^2-\xi^2+2.0\,\eta-2.0\,\xi-2.0} \\
& - 0.64365885\,\mathrm{e}^{-\eta^2-\xi^2-2.0\,\eta+2.0\,\xi-2.0} + 0.22491874\,\eta^3 + 0.22491874\,\xi^3 \\
& + 0.75755679\,\mathrm{e}^{-\eta^2-\xi^2-2.0\,\eta-2.0\,\xi-2.0} - 2.70765238\,\mathrm{e}^{-1.1+0.67\,\xi-\xi^2+2.0\,\eta-\eta^2} \\
& - 1.31095789\,\mathrm{e}^{-1.1-2.0\,\xi-\xi^2-0.67\,\eta-\eta^2} - 0.20986640 \\
& + 1.89540719\,\mathrm{e}^{-1.1+2.0\,\xi-\xi^2-0.67\,\eta-\eta^2} + 1.19705995\,\mathrm{e}^{-1.1-2.0\,\xi-\xi^2+0.67\,\eta-\eta^2} \\
& - 2.70765238\,\mathrm{e}^{-1.1+2.0\,\xi-\xi^2+0.67\,\eta-\eta^2} + 0.36999242\,\eta^2\xi + 0.36999242\,\eta\,\xi^2 \\
& + 1.19705995\,\mathrm{e}^{-1.1+0.67\,\xi-\xi^2-2.0\,\eta-\eta^2} - 1.31095789\,\mathrm{e}^{-1.1-0.67\,\xi-\xi^2-2.0\,\eta-\eta^2} \\
& + 1.97387939\,\mathrm{e}^{-0.2-0.67\,\xi-\xi^2-0.67\,\eta-\eta^2} - 2.55832869\,\mathrm{e}^{-0.2+0.67\,\xi-\xi^2-0.67\,\eta-\eta^2} \\
& - 2.55832869\,\mathrm{e}^{-0.2-0.67\,\xi-\xi^2+0.67\,\eta-\eta^2} + 4.06892111\,\mathrm{e}^{-0.2+0.67\,\xi-\xi^2+0.67\,\eta-\eta^2}
\end{aligned}
\tag{B.2.57}
$$

$$
\begin{aligned}
N_4(\xi,\eta) = &-2.70765238\,\mathrm{e}^{-1.1-0.67\,\xi-\xi^2+2.0\,\eta-\eta^2} + 0.22491874\,\xi^2 \\
&+ 0.22491874\,\eta^2 + 0.32911194\,\xi - 0.32911194\,\eta - 0.43265388\,\xi\,\eta \\
&- 0.64365885\,\mathrm{e}^{-\eta^2-\xi^2+2.0\,\eta+2.0\,\xi-2.0} + 1.45590403\,\mathrm{e}^{-\eta^2-\xi^2+2.0\,\eta-2.0\,\xi-2.0} \\
&+ 0.75755679\,\mathrm{e}^{-\eta^2-\xi^2-2.0\,\eta+2.0\,\xi-2.0} + 0.22491874\,\eta^3 - 0.22491874\,\xi^3 \\
&- 0.64365885\,\mathrm{e}^{-\eta^2-\xi^2-2.0\,\eta-2.0\,\xi-2.0} + 1.89540719\,\mathrm{e}^{-1.1+0.67\,\xi-\xi^2+2.0\,\eta-\eta^2} \\
&+ 1.89540719\,\mathrm{e}^{-1.1-2.0\,\xi-\xi^2-0.67\,\eta-\eta^2} - 0.20986640 \\
&- 1.31095789\,\mathrm{e}^{-1.1+2.0\,\xi-\xi^2-0.67\,\eta-\eta^2} - 2.70765238\,\mathrm{e}^{-1.1-2.0\,\xi-\xi^2+0.67\,\eta-\eta^2} \\
&+ 1.19705995\,\mathrm{e}^{-1.1+2.0\,\xi-\xi^2+0.67\,\eta-\eta^2} - 0.36999242\,\eta^2\xi + 0.36999242\,\eta\,\xi^2 \\
&- 1.31095789\,\mathrm{e}^{-1.1+0.67\,\xi-\xi^2-2.0\,\eta-\eta^2} + 1.19705995\,\mathrm{e}^{-1.1-0.67\,\xi-\xi^2-2.0\,\eta-\eta^2} \\
&- 2.55832869\,\mathrm{e}^{-0.2-0.67\,\xi-\xi^2-0.67\,\eta-\eta^2} + 1.97387939\,\mathrm{e}^{-0.2+0.67\,\xi-\xi^2-0.67\,\eta-\eta^2} \\
&+ 4.06892111\,\mathrm{e}^{-0.2-0.67\,\xi-\xi^2+0.67\,\eta-\eta^2} - 2.55832869\,\mathrm{e}^{-0.2+0.67\,\xi-\xi^2+0.67\,\eta-\eta^2}
\end{aligned}
\tag{B.2.58}
$$

$$
\begin{aligned}
N_5(\xi,\eta) = &-3.09503465\,\mathrm{e}^{-1.1-0.67\,\xi-\xi^2+2.0\,\eta-\eta^2} + 0.17861640 - 0.22491874\,\xi^2 + 0.05633126\,\eta^2 \\
&- 0.89358583\,\xi - 0.29786194\,\eta - 0.31131518\,\xi\,\eta - 1.31095789\,\mathrm{e}^{-\eta^2-\xi^2+2.0\,\eta+2.0\,\xi-2.0} \\
&+ 1.19705995\,\mathrm{e}^{-\eta^2-\xi^2+2.0\,\eta-2.0\,\xi-2.0} + 1.89540719\,\mathrm{e}^{-\eta^2-\xi^2-2.0\,\eta+2.0\,\xi-2.0} \\
&- 0.05633126\,\eta^3 + 0.67475623\,\xi^3 - 2.70765238\,\mathrm{e}^{-\eta^2-\xi^2-2.0\,\eta-2.0\,\xi-2.0} \\
&+ 3.20893259\,\mathrm{e}^{-1.1+0.67\,\xi-\xi^2+2.0\,\eta-\eta^2} + 4.06892111\,\mathrm{e}^{-1.1-2.0\,\xi-\xi^2-0.67\,\eta-\eta^2} \\
&- 2.55832869\,\mathrm{e}^{-1.1+2.0\,\xi-\xi^2-0.67\,\eta-\eta^2} - 2.55832869\,\mathrm{e}^{-1.1-2.0\,\xi-\xi^2+0.67\,\eta-\eta^2} \\
&+ 1.97387939\,\mathrm{e}^{-1.1+2.0\,\xi-\xi^2+0.67\,\eta-\eta^2} + 0.26622726\,\eta^2\xi + 0.36999242\,\eta\,\xi^2 \\
&- 5.88842361\,\mathrm{e}^{-1.1+0.67\,\xi-\xi^2-2.0\,\eta-\eta^2} + 6.70066879\,\mathrm{e}^{-1.1-0.67\,\xi-\xi^2-2.0\,\eta-\eta^2} \\
&- 8.86604145\,\mathrm{e}^{-0.2-0.67\,\xi-\xi^2-0.67\,\eta-\eta^2} + 7.35544903\,\mathrm{e}^{-0.2+0.67\,\xi-\xi^2-0.67\,\eta-\eta^2} \\
&+ 5.26040730\,\mathrm{e}^{-0.2-0.67\,\xi-\xi^2+0.67\,\eta-\eta^2} - 4.67595800\,\mathrm{e}^{-0.2+0.67\,\xi-\xi^2+0.67\,\eta-\eta^2}
\end{aligned}
\tag{B.2.59}
$$

$$
\begin{aligned}
N_6(\xi,\eta) = &\,1.97387939\,\mathrm{e}^{-1.1-0.67\,\xi-\xi^2+2.0\,\eta-\eta^2} + 0.17861640 + 0.05633126\,\xi^2 - 0.22491874\,\eta^2 \\
&+ 0.29786194\,\xi - 0.89358583\,\eta + 0.31131518\,\xi\,\eta + 1.89540719\,\mathrm{e}^{-\eta^2-\xi^2+2.0\,\eta+2.0\,\xi-2.0} \\
&- 1.31095789\,\mathrm{e}^{-\eta^2-\xi^2+2.0\,\eta-2.0\,\xi-2.0} - 2.70765238\,\mathrm{e}^{-\eta^2-\xi^2-2.0\,\eta+2.0\,\xi-2.0} \\
&+ 0.67475623\,\eta^3 + 0.05633126\,\xi^3 + 1.19705995\,\mathrm{e}^{-\eta^2-\xi^2-2.0\,\eta-2.0\,\xi-2.0} \\
&- 2.55832869\,\mathrm{e}^{-1.1+0.67\,\xi-\xi^2+2.0\,\eta-\eta^2} - 3.09503465\,\mathrm{e}^{-1.1-2.0\,\xi-\xi^2-0.67\,\eta-\eta^2} \\
&+ 6.70066879\,\mathrm{e}^{-1.1+2.0\,\xi-\xi^2-0.67\,\eta-\eta^2} + 3.20893259\,\mathrm{e}^{-1.1-2.0\,\xi-\xi^2+0.67\,\eta-\eta^2} \\
&- 5.88842361\,\mathrm{e}^{-1.1+2.0\,\xi-\xi^2+0.67\,\eta-\eta^2} - 0.36999242\,\eta^2\xi + 0.26622726\,\eta\,\xi^2 \\
&+ 4.06892111\,\mathrm{e}^{-1.1+0.67\,\xi-\xi^2-2.0\,\eta-\eta^2} - 2.55832869\,\mathrm{e}^{-1.1-0.67\,\xi-\xi^2-2.0\,\eta-\eta^2} \\
&+ 5.26040730\,\mathrm{e}^{-0.2-0.67\,\xi-\xi^2-0.67\,\eta-\eta^2} - 8.86604145\,\mathrm{e}^{-0.2+0.67\,\xi-\xi^2-0.67\,\eta-\eta^2} \\
&- 4.67595800\,\mathrm{e}^{-0.2-0.67\,\xi-\xi^2+0.67\,\eta-\eta^2} + 7.35544903\,\mathrm{e}^{-0.2+0.67\,\xi-\xi^2+0.67\,\eta-\eta^2}
\end{aligned}
\tag{B.2.60}
$$

$$
\begin{aligned}
N_7(\xi,\eta) = &-5.88842361\,\mathrm{e}^{-1.1-0.67\,\xi-\xi^2+2.0\,\eta-\eta^2} + 0.17861640 - 0.22491874\,\xi^2 + 0.05633126\,\eta^2 \\
&+ 0.89358583\,\xi + 0.29786194\,\eta - 0.31131518\,\xi\,\eta - 2.70765238\,\mathrm{e}^{-\eta^2-\xi^2+2.0\,\eta+2.0\,\xi-2.0} \\
&+ 1.89540719\,\mathrm{e}^{-\eta^2-\xi^2+2.0\,\eta-2.0\,\xi-2.0} + 1.19705995\,\mathrm{e}^{-\eta^2-\xi^2-2.0\,\eta+2.0\,\xi-2.0} \\
&+ 0.05633126\,\eta^3 - 0.67475623\,\xi^3 - 1.31095789\,\mathrm{e}^{-\eta^2-\xi^2-2.0\,\eta-2.0\,\xi-2.0} \\
&+ 6.70066879\,\mathrm{e}^{-1.1+0.67\,\xi-\xi^2+2.0\,\eta-\eta^2} + 1.97387939\,\mathrm{e}^{-1.1-2.0\,\xi-\xi^2-0.67\,\eta-\eta^2} \\
&- 2.55832869\,\mathrm{e}^{-1.1+2.0\,\xi-\xi^2-0.67\,\eta-\eta^2} - 2.55832869\,\mathrm{e}^{-1.1-2.0\,\xi-\xi^2+0.67\,\eta-\eta^2} \\
&+ 4.06892111\,\mathrm{e}^{-1.1+2.0\,\xi-\xi^2+0.67\,\eta-\eta^2} - 0.26622726\,\eta^2\xi - 0.36999242\,\eta\,\xi^2 \\
&- 3.09503465\,\mathrm{e}^{-1.1+0.67\,\xi-\xi^2-2.0\,\eta-\eta^2} + 3.20893259\,\mathrm{e}^{-1.1-0.67\,\xi-\xi^2-2.0\,\eta-\eta^2} \\
&- 4.67595800\,\mathrm{e}^{-0.2-0.67\,\xi-\xi^2-0.67\,\eta-\eta^2} + 5.26040730\,\mathrm{e}^{-0.2+0.67\,\xi-\xi^2-0.67\,\eta-\eta^2} \\
&+ 7.35544903\,\mathrm{e}^{-0.2-0.67\,\xi-\xi^2+0.67\,\eta-\eta^2} - 8.86604145\,\mathrm{e}^{-0.2+0.67\,\xi-\xi^2+0.67\,\eta-\eta^2}
\end{aligned}
\tag{B.2.61}
$$

$$
\begin{aligned}
N_8(\xi,\eta) = &\ 4.06892111\,\mathrm{e}^{-1.1-0.67\,\xi-\xi^2+2.0\,\eta-\eta^2} + 0.17861640 + 0.05633126\,\xi^2 - 0.22491874\,\eta^2 \\
&- 0.29786194\,\xi + 0.89358583\,\eta + 0.31131518\,\xi\,\eta + 1.19705995\,\mathrm{e}^{-\eta^2-\xi^2+2.0\,\eta+2.0\,\xi-2.0} \\
&- 2.70765238\,\mathrm{e}^{-\eta^2-\xi^2+2.0\,\eta-2.0\,\xi-2.0} - 1.31095789\,\mathrm{e}^{-\eta^2-\xi^2-2.0\,\eta+2.0\,\xi-2.0} \\
&- 0.67475623\,\eta^3 - 0.05633126\,\xi^3 + 1.89540719\,\mathrm{e}^{-\eta^2-\xi^2-2.0\,\eta-2.0\,\xi-2.0} \\
&- 2.55832869\,\mathrm{e}^{-1.1+0.67\,\xi-\xi^2+2.0\,\eta-\eta^2} - 5.88842361\,\mathrm{e}^{-1.1-2.0\,\xi-\xi^2-0.67\,\eta-\eta^2} \\
&+ 3.20893259\,\mathrm{e}^{-1.1+2.0\,\xi-\xi^2-0.67\,\eta-\eta^2} + 6.70066879\,\mathrm{e}^{-1.1-2.0\,\xi-\xi^2+0.67\,\eta-\eta^2} \\
&- 3.09503465\,\mathrm{e}^{-1.1+2.0\,\xi-\xi^2+0.67\,\eta-\eta^2} + 0.36999242\,\eta^2\xi - 0.26622726\,\eta\,\xi^2 \\
&+ 1.97387939\,\mathrm{e}^{-1.1+0.67\,\xi-\xi^2-2.0\,\eta-\eta^2} - 2.55832869\,\mathrm{e}^{-1.1-0.67\,\xi-\xi^2-2.0\,\eta-\eta^2} \\
&+ 7.35544903\,\mathrm{e}^{-0.2-0.67\,\xi-\xi^2-0.67\,\eta-\eta^2} - 4.67595800\,\mathrm{e}^{-0.2+0.67\,\xi-\xi^2-0.67\,\eta-\eta^2} \\
&- 8.86604145\,\mathrm{e}^{-0.2-0.67\,\xi-\xi^2+0.67\,\eta-\eta^2} + 5.26040730\,\mathrm{e}^{-0.2+0.67\,\xi-\xi^2+0.67\,\eta-\eta^2}
\end{aligned}
\tag{B.2.62}
$$

$$
\begin{aligned}
N_9(\xi,\eta) = &\ 3.20893259\,\mathrm{e}^{-1.1-0.67\,\xi-\xi^2+2.0\,\eta-\eta^2} + 0.17861640 - 0.22491874\,\xi^2 + 0.05633126\,\eta^2 \\
&+ 0.89358583\,\xi - 0.29786194\,\eta + 0.31131518\,\xi\,\eta + 1.19705995\,\mathrm{e}^{-\eta^2-\xi^2+2.0\,\eta+2.0\,\xi-2.0} \\
&- 1.31095789\,\mathrm{e}^{-\eta^2-\xi^2+2.0\,\eta-2.0\,\xi-2.0} - 2.70765238\,\mathrm{e}^{-\eta^2-\xi^2-2.0\,\eta+2.0\,\xi-2.0} \\
&- 0.05633126\,\eta^3 - 0.67475623\,\xi^3 + 1.89540719\,\mathrm{e}^{-\eta^2-\xi^2-2.0\,\eta-2.0\,\xi-2.0} \\
&- 3.09503465\,\mathrm{e}^{-1.1+0.67\,\xi-\xi^2+2.0\,\eta-\eta^2} - 2.55832869\,\mathrm{e}^{-1.1-2.0\,\xi-\xi^2-0.67\,\eta-\eta^2} \\
&+ 4.06892111\,\mathrm{e}^{-1.1+2.0\,\xi-\xi^2-0.67\,\eta-\eta^2} + 1.97387939\,\mathrm{e}^{-1.1-2.0\,\xi-\xi^2+0.67\,\eta-\eta^2} \\
&- 2.55832869\,\mathrm{e}^{-1.1+2.0\,\xi-\xi^2+0.67\,\eta-\eta^2} - 0.26622726\,\eta^2\xi + 0.36999242\,\eta\,\xi^2 \\
&+ 6.70066879\,\mathrm{e}^{-1.1+0.67\,\xi-\xi^2-2.0\,\eta-\eta^2} - 5.88842361\,\mathrm{e}^{-1.1-0.67\,\xi-\xi^2-2.0\,\eta-\eta^2} \\
&+ 7.35544903\,\mathrm{e}^{-0.2-0.67\,\xi-\xi^2-0.67\,\eta-\eta^2} - 8.86604145\,\mathrm{e}^{-0.2+0.67\,\xi-\xi^2-0.67\,\eta-\eta^2} \\
&- 4.67595800\,\mathrm{e}^{-0.2-0.67\,\xi-\xi^2+0.67\,\eta-\eta^2} + 5.26040730\,\mathrm{e}^{-0.2+0.67\,\xi-\xi^2+0.67\,\eta-\eta^2}
\end{aligned}
\tag{B.2.63}
$$

$$
\begin{aligned}
N_{10}(\xi,\eta) = &-2.55832869\,\mathrm{e}^{-1.1-0.67\,\xi-\xi^2+2.0\,\eta-\eta^2} + 0.17861640 + 0.05633126\,\xi^2 - 0.22491874\,\eta^2 \\
&+ 0.29786194\,\xi + 0.89358583\,\eta - 0.31131518\,\xi\,\eta - 2.70765238\,\mathrm{e}^{-\eta^2-\xi^2+2.0\,\eta+2.0\,\xi-2.0} \\
&+ 1.19705995\,\mathrm{e}^{-\eta^2-\xi^2+2.0\,\eta-2.0\,\xi-2.0} + 1.89540719\,\mathrm{e}^{-\eta^2-\xi^2-2.0\,\eta+2.0\,\xi-2.0} \\
&- 0.67475623\,\eta^3 + 0.05633126\,\xi^3 - 1.31095789\,\mathrm{e}^{-\eta^2-\xi^2-2.0\,\eta-2.0\,\xi-2.0} \\
&+ 4.06892111\,\mathrm{e}^{-1.1+0.67\,\xi-\xi^2+2.0\,\eta-\eta^2} + 3.20893259\,\mathrm{e}^{-1.1-2.0\,\xi-\xi^2-0.67\,\eta-\eta^2} \\
&- 5.88842361\,\mathrm{e}^{-1.1+2.0\,\xi-\xi^2-0.67\,\eta-\eta^2} - 3.09503465\,\mathrm{e}^{-1.1-2.0\,\xi-\xi^2+0.67\,\eta-\eta^2} \\
&+ 6.70066879\,\mathrm{e}^{-1.1+2.0\,\xi-\xi^2+0.67\,\eta-\eta^2} - 0.36999242\,\eta^2\xi - 0.26622726\,\eta\,\xi^2 \\
&- 2.55832869\,\mathrm{e}^{-1.1+0.67\,\xi-\xi^2-2.0\,\eta-\eta^2} + 1.97387939\,\mathrm{e}^{-1.1-0.67\,\xi-\xi^2-2.0\,\eta-\eta^2} \\
&- 4.67595800\,\mathrm{e}^{-0.2-0.67\,\xi-\xi^2-0.67\,\eta-\eta^2} + 7.35544903\,\mathrm{e}^{-0.2+0.67\,\xi-\xi^2-0.67\,\eta-\eta^2} \\
&+ 5.26040730\,\mathrm{e}^{-0.2-0.67\,\xi-\xi^2+0.67\,\eta-\eta^2} - 8.86604145\,\mathrm{e}^{-0.2+0.67\,\xi-\xi^2+0.67\,\eta-\eta^2}
\end{aligned}
\tag{B.2.64}
$$

$$
\begin{aligned}
N_{11}(\xi,\eta) = &\;6.70066879\,\mathrm{e}^{-1.1-0.67\,\xi-\xi^2+2.0\,\eta-\eta^2} + 0.17861640 - 0.22491874\,\xi^2 + 0.05633126\,\eta^2 \\
&- 0.89358583\,\xi + 0.29786194\,\eta + 0.31131518\,\xi\,\eta + 1.89540719\,\mathrm{e}^{-\eta^2-\xi^2+2.0\,\eta+2.0\,\xi-2.0} \\
&- 2.70765238\,\mathrm{e}^{-\eta^2-\xi^2+2.0\,\eta-2.0\,\xi-2.0} - 1.31095789\,\mathrm{e}^{-\eta^2-\xi^2-2.0\,\eta+2.0\,\xi-2.0} \\
&+ 0.05633126\,\eta^3 + 0.67475623\,\xi^3 + 1.19705995\,\mathrm{e}^{-\eta^2-\xi^2-2.0\,\eta-2.0\,\xi-2.0} \\
&- 5.88842361\,\mathrm{e}^{-1.1+0.67\,\xi-\xi^2+2.0\,\eta-\eta^2} - 2.55832869\,\mathrm{e}^{-1.1-2.0\,\xi-\xi^2-0.67\,\eta-\eta^2} \\
&+ 1.97387939\,\mathrm{e}^{-1.1+2.0\,\xi-\xi^2-0.67\,\eta-\eta^2} + 4.06892111\,\mathrm{e}^{-1.1-2.0\,\xi-\xi^2+0.67\,\eta-\eta^2} \\
&- 2.55832869\,\mathrm{e}^{-1.1+2.0\,\xi-\xi^2+0.67\,\eta-\eta^2} + 0.26622726\,\eta^2\xi - 0.36999242\,\eta\,\xi^2 \\
&+ 3.20893259\,\mathrm{e}^{-1.1+0.67\,\xi-\xi^2-2.0\,\eta-\eta^2} - 3.09503465\,\mathrm{e}^{-1.1-0.67\,\xi-\xi^2-2.0\,\eta-\eta^2} \\
&+ 5.26040730\,\mathrm{e}^{-0.2-0.67\,\xi-\xi^2-0.67\,\eta-\eta^2} - 4.67595800\,\mathrm{e}^{-0.2+0.67\,\xi-\xi^2-0.67\,\eta-\eta^2} \\
&- 8.86604145\,\mathrm{e}^{-0.2-0.67\,\xi-\xi^2+0.67\,\eta-\eta^2} + 7.35544903\,\mathrm{e}^{-0.2+0.67\,\xi-\xi^2+0.67\,\eta-\eta^2}
\end{aligned}
\tag{B.2.65}
$$

$$
\begin{aligned}
N_{12}(\xi,\eta) = &-2.55832869\,\mathrm{e}^{-1.1-0.67\,\xi-\xi^2+2.0\,\eta-\eta^2} + 0.17861640 + 0.05633126\,\xi^2 - 0.22491874\,\eta^2 \\
&- 0.29786194\,\xi - 0.89358583\,\eta - 0.31131518\,\xi\,\eta - 1.31095789\,\mathrm{e}^{-\eta^2-\xi^2+2.0\,\eta+2.0\,\xi-2.0} \\
&+ 1.89540719\,\mathrm{e}^{-\eta^2-\xi^2+2.0\,\eta-2.0\,\xi-2.0} + 1.19705995\,\mathrm{e}^{-\eta^2-\xi^2-2.0\,\eta+2.0\,\xi-2.0} \\
&+ 0.67475623\,\eta^3 - 0.05633126\,\xi^3 - 2.70765238\,\mathrm{e}^{-\eta^2-\xi^2-2.0\,\eta-2.0\,\xi-2.0} \\
&+ 1.97387939\,\mathrm{e}^{-1.1+0.67\,\xi-\xi^2+2.0\,\eta-\eta^2} + 6.70066879\,\mathrm{e}^{-1.1-2.0\,\xi-\xi^2-0.67\,\eta-\eta^2} \\
&- 3.09503465\,\mathrm{e}^{-1.1+2.0\,\xi-\xi^2-0.67\,\eta-\eta^2} - 5.88842361\,\mathrm{e}^{-1.1-2.0\,\xi-\xi^2+0.67\,\eta-\eta^2} \\
&+ 3.20893259\,\mathrm{e}^{-1.1+2.0\,\xi-\xi^2+0.67\,\eta-\eta^2} + 0.36999242\,\eta^2\xi + 0.26622726\,\eta\,\xi^2 \\
&- 2.55832869\,\mathrm{e}^{-1.1+0.67\,\xi-\xi^2-2.0\,\eta-\eta^2} + 4.06892111\,\mathrm{e}^{-1.1-0.67\,\xi-\xi^2-2.0\,\eta-\eta^2} \\
&- 8.86604145\,\mathrm{e}^{-0.2-0.67\,\xi-\xi^2-0.67\,\eta-\eta^2} + 5.26040730\,\mathrm{e}^{-0.2+0.67\,\xi-\xi^2-0.67\,\eta-\eta^2} \\
&+ 7.35544903\,\mathrm{e}^{-0.2-0.67\,\xi-\xi^2+0.67\,\eta-\eta^2} - 4.67595800\,\mathrm{e}^{-0.2+0.67\,\xi-\xi^2+0.67\,\eta-\eta^2}
\end{aligned}
\tag{B.2.66}
$$

$$
\begin{aligned}
N_{13}(\xi,\eta) = {} & 5.26040730\,\mathrm{e}^{-1.1-0.67\,\xi-\xi^2+2.0\,\eta-\eta^2} - 0.05633126\,\xi^2 - 0.05633126\,\eta^2 + 0.04983583\,\xi \\
& + 0.04983583\,\eta + 0.22400618\,\xi\,\eta + 1.97387939\,\mathrm{e}^{-\eta^2-\xi^2+2.0\,\eta+2.0\,\xi-2.0} + 0.10263360 \\
& - 2.55832869\,\mathrm{e}^{-\eta^2-\xi^2+2.0\,\eta-2.0\,\xi-2.0} - 2.55832869\,\mathrm{e}^{-\eta^2-\xi^2-2.0\,\eta+2.0\,\xi-2.0} \\
& + 0.16899377\,\eta^3 + 0.16899377\,\xi^3 + 4.06892111\,\mathrm{e}^{-\eta^2-\xi^2-2.0\,\eta-2.0\,\xi-2.0} \\
& - 4.67595800\,\mathrm{e}^{-1.1+0.67\,\xi-\xi^2+2.0\,\eta-\eta^2} - 8.86604145\,\mathrm{e}^{-1.1-2.0\,\xi-\xi^2-0.67\,\eta-\eta^2} \\
& + 5.26040730\,\mathrm{e}^{-1.1+2.0\,\xi-\xi^2-0.67\,\eta-\eta^2} + 7.35544903\,\mathrm{e}^{-1.1-2.0\,\xi-\xi^2+0.67\,\eta-\eta^2} \\
& - 4.67595800\,\mathrm{e}^{-1.1+2.0\,\xi-\xi^2+0.67\,\eta-\eta^2} - 0.26622726\,\eta^2\xi - 0.26622726\,\eta\,\xi^2 \\
& + 7.35544903\,\mathrm{e}^{-1.1+0.67\,\xi-\xi^2-2.0\,\eta-\eta^2} - 8.86604145\,\mathrm{e}^{-1.1-0.67\,\xi-\xi^2-2.0\,\eta-\eta^2} \\
& + 17.50210183\,\mathrm{e}^{-0.2-0.67\,\xi-\xi^2-0.67\,\eta-\eta^2} - 13.89646769\,\mathrm{e}^{-0.2+0.67\,\xi-\xi^2-0.67\,\eta-\eta^2} \\
& - 13.89646769\,\mathrm{e}^{-0.2-0.67\,\xi-\xi^2+0.67\,\eta-\eta^2} + 11.21697667\,\mathrm{e}^{-0.2+0.67\,\xi-\xi^2+0.67\,\eta-\eta^2}
\end{aligned}
\tag{B.2.67}
$$

$$
\begin{aligned}
N_{14}(\xi,\eta) = {} & -4.67595800\,\mathrm{e}^{-1.1-0.67\,\xi-\xi^2+2.0\,\eta-\eta^2} - 0.05633126\,\xi^2 - 0.05633126\,\eta^2 - 0.04983583\,\xi \\
& + 0.04983583\,\eta - 0.22400618\,\xi\,\eta - 2.55832869\,\mathrm{e}^{-\eta^2-\xi^2+2.0\,\eta+2.0\,\xi-2.0} + 0.10263360 \\
& + 1.97387939\,\mathrm{e}^{-\eta^2-\xi^2+2.0\,\eta-2.0\,\xi-2.0} + 4.06892111\,\mathrm{e}^{-\eta^2-\xi^2-2.0\,\eta+2.0\,\xi-2.0} \\
& + 0.16899377\,\eta^3 - 0.16899377\,\xi^3 - 2.55832869\,\mathrm{e}^{-\eta^2-\xi^2-2.0\,\eta-2.0\,\xi-2.0} \\
& + 5.26040730\,\mathrm{e}^{-1.1+0.67\,\xi-\xi^2+2.0\,\eta-\eta^2} + 5.26040730\,\mathrm{e}^{-1.1-2.0\,\xi-\xi^2-0.67\,\eta-\eta^2} \\
& - 8.86604145\,\mathrm{e}^{-1.1+2.0\,\xi-\xi^2-0.67\,\eta-\eta^2} - 4.67595800\,\mathrm{e}^{-1.1-2.0\,\xi-\xi^2+0.67\,\eta-\eta^2} \\
& + 7.35544903\,\mathrm{e}^{-1.1+2.0\,\xi-\xi^2+0.67\,\eta-\eta^2} + 0.26622726\,\eta^2\xi - 0.26622726\,\eta\,\xi^2 \\
& - 8.86604145\,\mathrm{e}^{-1.1+0.67\,\xi-\xi^2-2.0\,\eta-\eta^2} + 7.35544903\,\mathrm{e}^{-1.1-0.67\,\xi-\xi^2-2.0\,\eta-\eta^2} \\
& - 13.89646769\,\mathrm{e}^{-0.2-0.67\,\xi-\xi^2-0.67\,\eta-\eta^2} + 17.50210183\,\mathrm{e}^{-0.2+0.67\,\xi-\xi^2-0.67\,\eta-\eta^2} \\
& + 11.21697667\,\mathrm{e}^{-0.2-0.67\,\xi-\xi^2+0.67\,\eta-\eta^2} - 13.89646769\,\mathrm{e}^{-0.2+0.67\,\xi-\xi^2+0.67\,\eta-\eta^2}
\end{aligned}
\tag{B.2.68}
$$

$$
\begin{aligned}
N_{15}(\xi,\eta) = {} & 7.35544903\,\mathrm{e}^{-1.1-0.67\,\xi-\xi^2+2.0\,\eta-\eta^2} - 0.05633126\,\xi^2 - 0.05633126\,\eta^2 - 0.04983583\,\xi \\
& - 0.04983583\,\eta + 0.22400618\,\xi\,\eta + 4.06892111\,\mathrm{e}^{-\eta^2-\xi^2+2.0\,\eta+2.0\,\xi-2.0} + 0.10263360 \\
& - 2.55832869\,\mathrm{e}^{-\eta^2-\xi^2+2.0\,\eta-2.0\,\xi-2.0} - 2.55832869\,\mathrm{e}^{-\eta^2-\xi^2-2.0\,\eta+2.0\,\xi-2.0} \\
& - 0.16899377\,\eta^3 - 0.16899377\,\xi^3 + 1.97387939\,\mathrm{e}^{-\eta^2-\xi^2-2.0\,\eta-2.0\,\xi-2.0} \\
& - 8.86604145\,\mathrm{e}^{-1.1+0.67\,\xi-\xi^2+2.0\,\eta-\eta^2} - 4.67595800\,\mathrm{e}^{-1.1-2.0\,\xi-\xi^2-0.67\,\eta-\eta^2} \\
& + 7.35544903\,\mathrm{e}^{-1.1+2.0\,\xi-\xi^2-0.67\,\eta-\eta^2} + 5.26040730\,\mathrm{e}^{-1.1-2.0\,\xi-\xi^2+0.67\,\eta-\eta^2} \\
& - 8.86604145\,\mathrm{e}^{-1.1+2.0\,\xi-\xi^2+0.67\,\eta-\eta^2} + 0.26622726\,\eta^2\xi + 0.26622726\,\eta\,\xi^2 \\
& + 5.26040730\,\mathrm{e}^{-1.1+0.67\,\xi-\xi^2-2.0\,\eta-\eta^2} - 4.67595800\,\mathrm{e}^{-1.1-0.67\,\xi-\xi^2-2.0\,\eta-\eta^2} \\
& + 11.21697667\,\mathrm{e}^{-0.2-0.67\,\xi-\xi^2-0.67\,\eta-\eta^2} - 13.89646769\,\mathrm{e}^{-0.2+0.67\,\xi-\xi^2-0.67\,\eta-\eta^2} \\
& - 13.89646769\,\mathrm{e}^{-0.2-0.67\,\xi-\xi^2+0.67\,\eta-\eta^2} + 17.50210183\,\mathrm{e}^{-0.2+0.67\,\xi-\xi^2+0.67\,\eta-\eta^2}
\end{aligned}
\tag{B.2.69}
$$

$$
\begin{aligned}
N_{16}(\xi,\eta) = &-8.86604145\,\mathrm{e}^{-1.1-0.67\,\xi-\xi^2+2.0\,\eta-\eta^2} - 0.05633126\,\xi^2 - 0.05633126\,\eta^2 + 0.04983583\,\xi \\
&- 0.04983583\,\eta - 0.22400618\,\xi\,\eta - 2.55832869\,\mathrm{e}^{-\eta^2-\xi^2+2.0\,\eta+2.0\,\xi-2.0} + 0.10263360 \\
&+ 4.06892111\,\mathrm{e}^{-\eta^2-\xi^2+2.0\,\eta-2.0\,\xi-2.0} + 1.97387939\,\mathrm{e}^{-\eta^2-\xi^2-2.0\,\eta+2.0\,\xi-2.0} \\
&- 0.16899377\,\eta^3 + 0.16899377\,\xi^3 - 2.55832869\,\mathrm{e}^{-\eta^2-\xi^2-2.0\,\eta-2.0\,\xi-2.0} \\
&+ 7.35544903\,\mathrm{e}^{-1.1+0.67\,\xi-\xi^2+2.0\,\eta-\eta^2} + 7.35544903\,\mathrm{e}^{-1.1-2.0\,\xi-\xi^2-0.67\,\eta-\eta^2} \\
&- 4.67595800\,\mathrm{e}^{-1.1+2.0\,\xi-\xi^2-0.67\,\eta-\eta^2} - 8.86604145\,\mathrm{e}^{-1.1-2.0\,\xi-\xi^2+0.67\,\eta-\eta^2} \\
&+ 5.26040730\,\mathrm{e}^{-1.1+2.0\,\xi-\xi^2+0.67\,\eta-\eta^2} - 0.26622726\,\eta^2\xi + 0.26622726\,\eta\,\xi^2 \\
&- 4.67595800\,\mathrm{e}^{-1.1+0.67\,\xi-\xi^2-2.0\,\eta-\eta^2} + 5.26040730\,\mathrm{e}^{-1.1-0.67\,\xi-\xi^2-2.0\,\eta-\eta^2} \\
&- 13.89646769\,\mathrm{e}^{-0.2-0.67\,\xi-\xi^2-0.67\,\eta-\eta^2} + 11.21697667\,\mathrm{e}^{-0.2+0.67\,\xi-\xi^2-0.67\,\eta-\eta^2} \\
&+ 17.50210183\,\mathrm{e}^{-0.2-0.67\,\xi-\xi^2+0.67\,\eta-\eta^2} - 13.89646769\,\mathrm{e}^{-0.2+0.67\,\xi-\xi^2+0.67\,\eta-\eta^2}
\end{aligned}
\tag{B.2.70}
$$

Appendix C

Shape Functions (Plots)

The shape functions summarized in Appendix B are 3D and 2D plotted in the present one, for comparison purposes. In each plot, the surfaces resultant from each shape function are presented, in the natural coordinate system element domain, i.e. $\xi = [-1, 1]$ and $\eta = [-1, 1]$. On top of this, the projections of each element node and Gauss points corresponding to both full and reduced quadrature rules are shown, in each surface.

These projections help visualizing the agreement to the Kronecker delta property, which states that *each node shape function must be equal to 1 at that node and 0 at all the remaining nodes*, ensuring the correct interpolation at each node.

Other requirement is the *compatibility* one, which is also ensured: *the interpolation is continual and derivable inside the element, and continual across the element boundaries*. These are *conforming or compatible* elements. Finally, *completeness* is also verified, i.e. *the sum of all element shape functions is equal to 1*.

C.1 Lagrange elements

C.1.1 4-Node Bilinear Quadrilateral (4BlinLag)

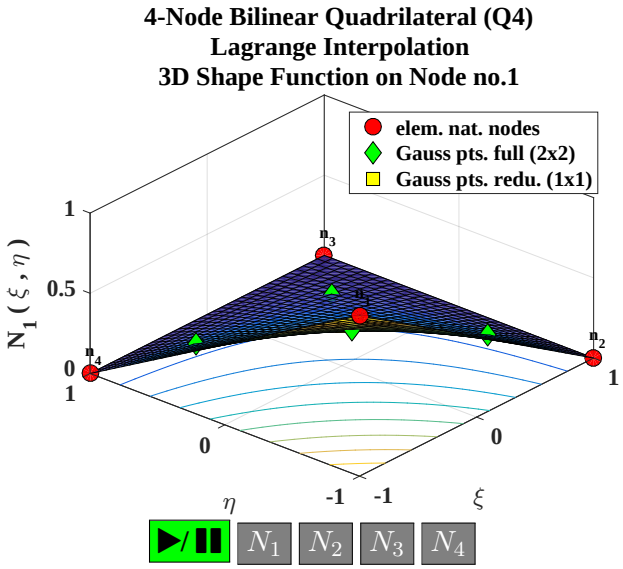

Figure C.1: 3D shape function plots of 4BlinLag element, including nodes and Gauss points spatial locations, on the local element natural coordinate system. Please click on the buttons above this caption to run the animation and toggle between plotted results.

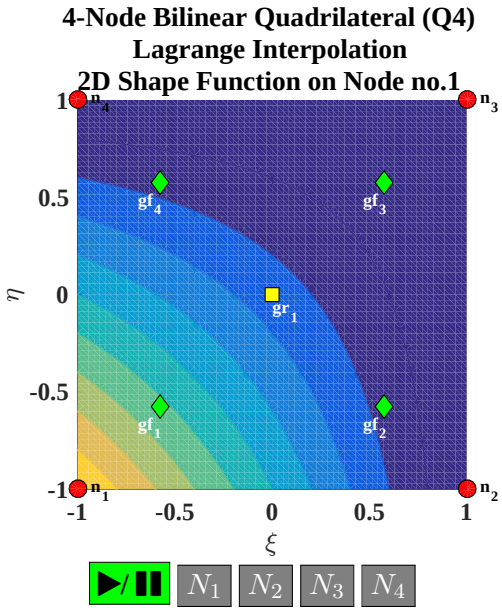

Figure C.2: 2D shape function plots of 4BlinLag element, including nodes and Gauss points spatial locations, on the local element natural coordinate system. Please click on the buttons above this caption to run the animation and toggle between plotted results.

C.1.2 9-Node Biquadratic Quadrilateral (9BquadLag)

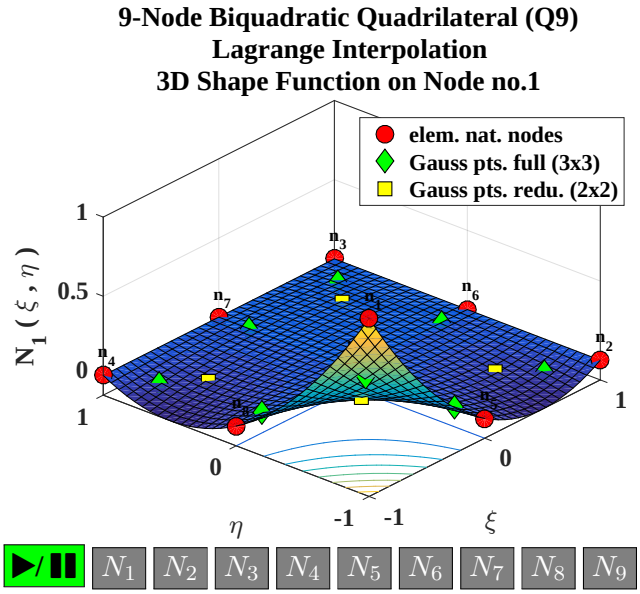

Figure C.3: 3D shape function plots of 9BquadLag element, including nodes and Gauss points spatial locations, on the local element natural coordinate system. Please click on the buttons above this caption to run the animation and toggle between plotted results.

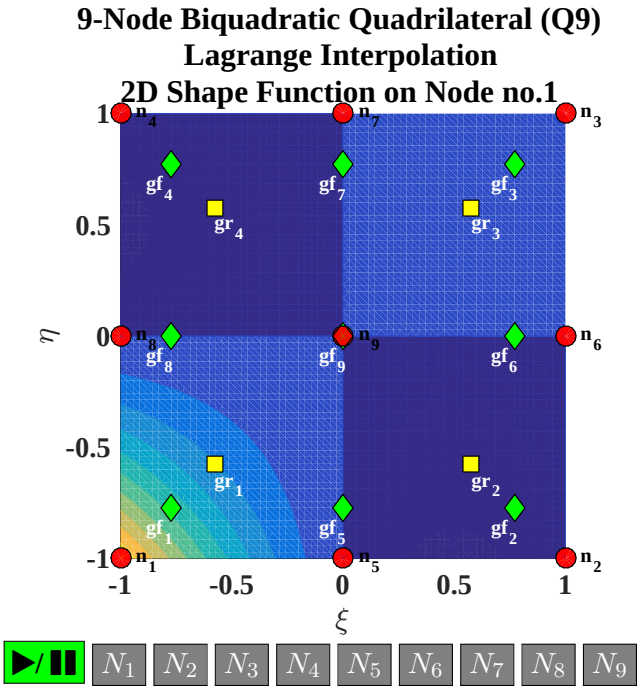

Figure C.4: 2D shape function plots of 9BquadLag element, including nodes and Gauss points spatial locations, on the local element natural coordinate system. Please click on the buttons above this caption to run the animation and toggle between plotted results.

C.1.3 16-Node Bicubic Quadrilateral (16BcubLag)

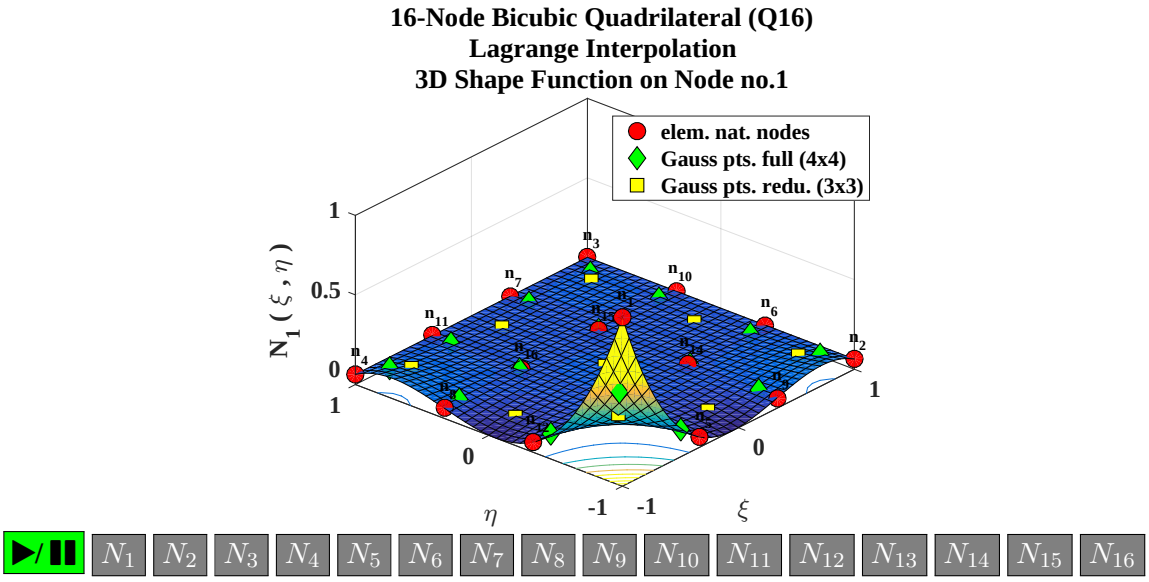

Figure C.5: 3D shape function plots of 16BcubLag element, including nodes and Gauss points spatial locations, on the local element natural coordinate system. Please click on the buttons above this caption to run the animation and toggle between plotted results.

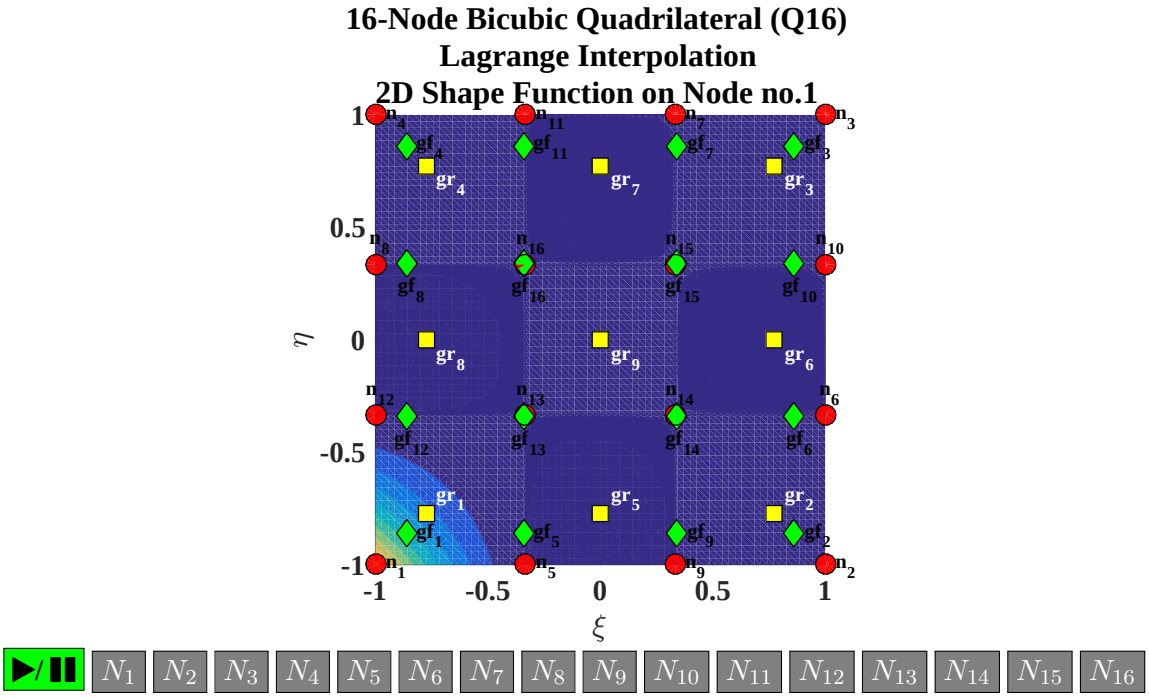

Figure C.6: 2D shape function plots of 16BcubLag element, including nodes and Gauss points spatial locations, on the local element natural coordinate system. Please click on the buttons above this caption to run the animation and toggle between plotted results.

C.2 Kriging elements

C.2.1 4-Node Bilinear Quadrilateral (4BlinKrig)

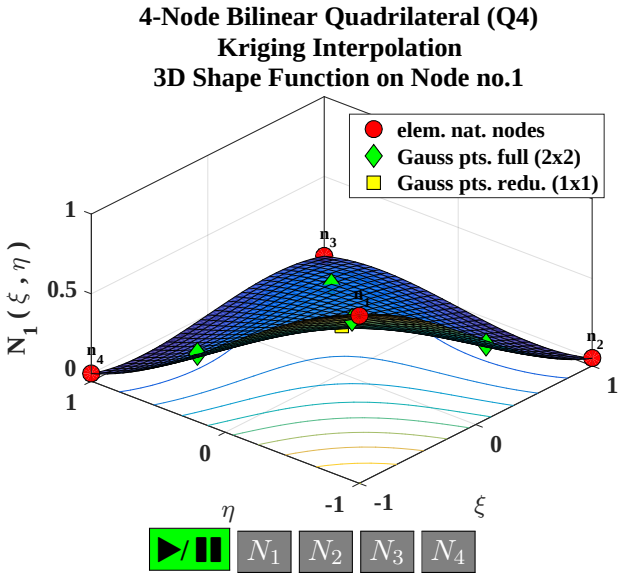

Figure C.7: 3D shape function plots of 4BlinKrig element, including nodes and Gauss points spatial locations, on the local element natural coordinate system. Please click on the buttons above this caption to run the animation and toggle between plotted results.

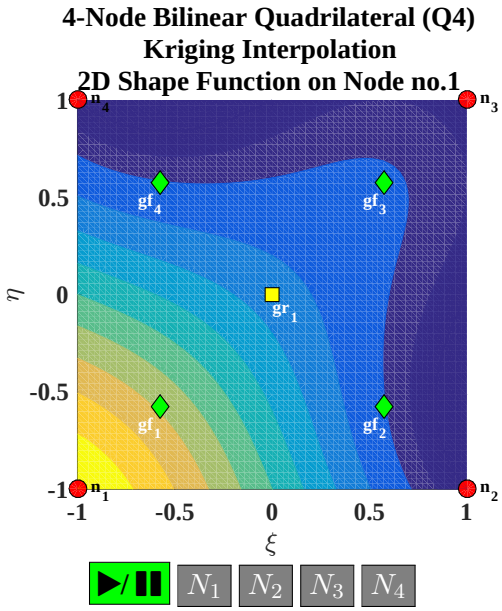

Figure C.8: 2D shape function plots of 4BlinKrig element, including nodes and Gauss points spatial locations, on the local element natural coordinate system. Please click on the buttons above this caption to run the animation and toggle between plotted results.

C.2.2 9-Node Bilinear Quadrilateral (9BlinKrig)

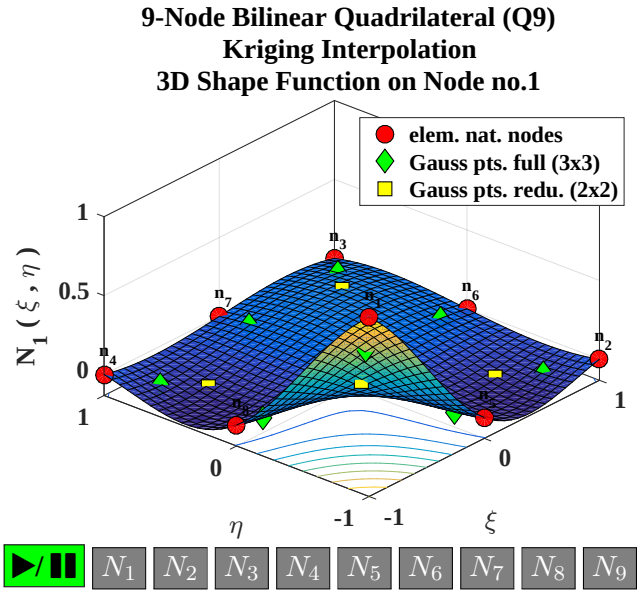

Figure C.9: 3D shape function plots of 9BlinKrig element, including nodes and Gauss points spatial locations, on the local element natural coordinate system. Please click on the buttons above this caption to run the animation and toggle between plotted results.

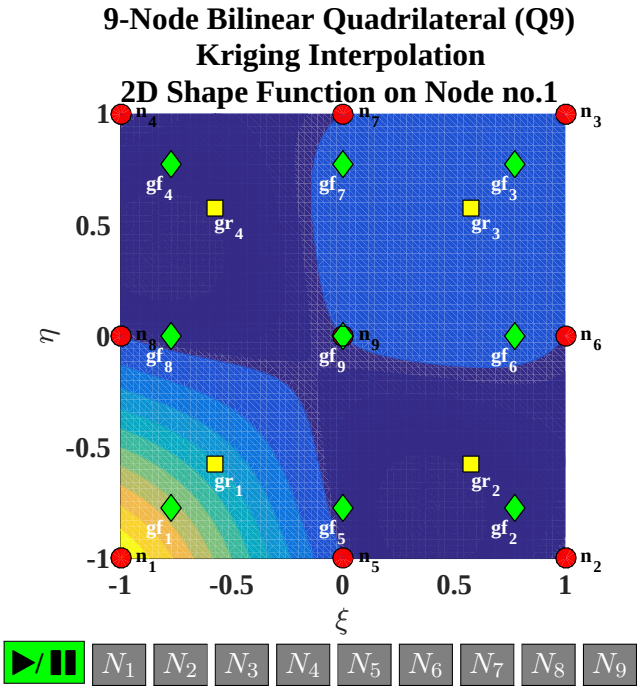

Figure C.10: 2D shape function plots of 9BlinKrig element, including nodes and Gauss points spatial locations, on the local element natural coordinate system. Please click on the buttons above this caption to run the animation and toggle between plotted results.

C.2.3 9-Node Biquadratic Quadrilateral (9BquadKrig)

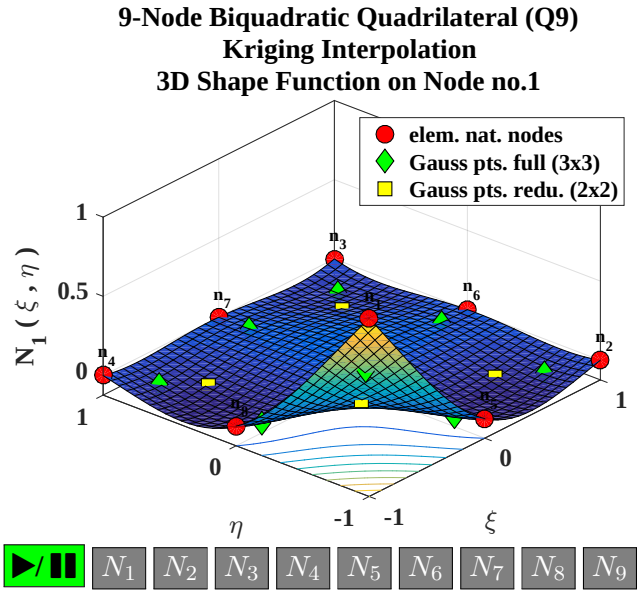

Figure C.11: 3D shape function plots of 9BquadKrig element, including nodes and Gauss points spatial locations, on the local element natural coordinate system. Please click on the buttons above this caption to run the animation and toggle between plotted results.

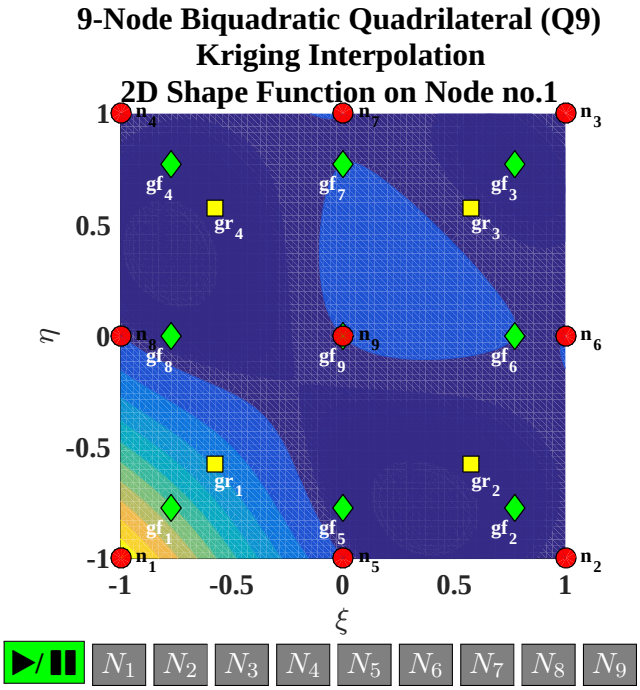

Figure C.12: 2D shape function plots of 9BquadKrig element, including nodes and Gauss points spatial locations, on the local element natural coordinate system. Please click on the buttons above this caption to run the animation and toggle between plotted results.

C.2.4 16-Node Bilinear Quadrilateral (16BlinKrig)

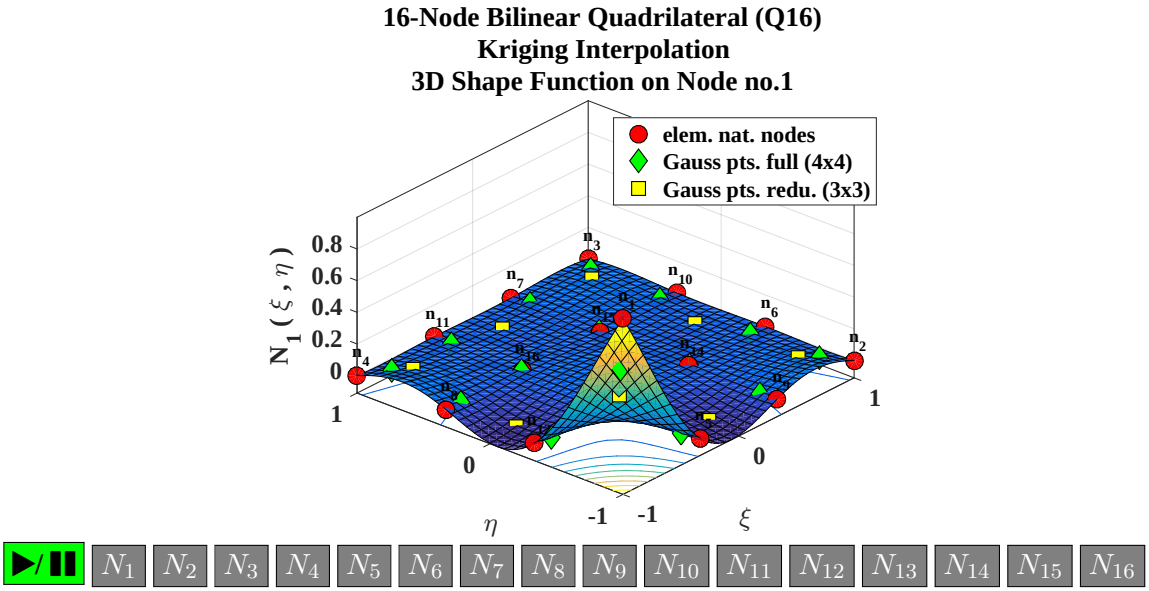

Figure C.13: 3D shape function plots of 16BlinKrig element, including nodes and Gauss points spatial locations, on the local element natural coordinate system. Please click on the buttons above this caption to run the animation and toggle between plotted results.

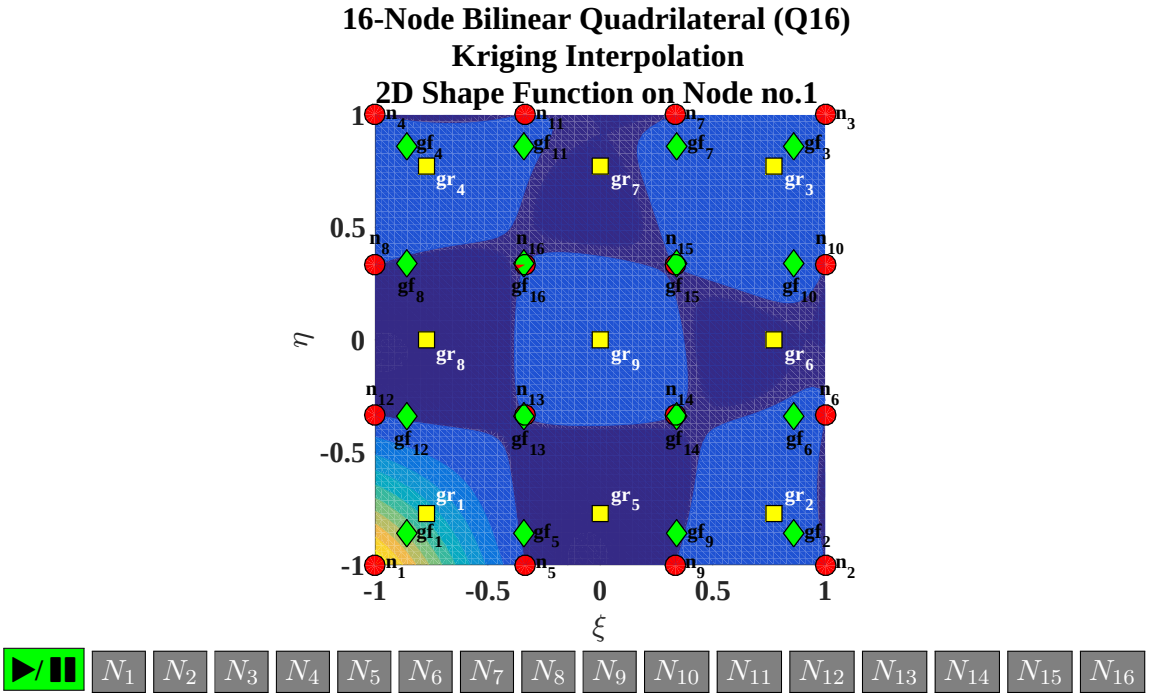

Figure C.14: 2D shape function plots of 16BlinKrig element, including nodes and Gauss points spatial locations, on the local element natural coordinate system. Please click on the buttons above this caption to run the animation and toggle between plotted results.

C.2.5 16-Node Biquadratic Quadrilateral (16BquadKrig)

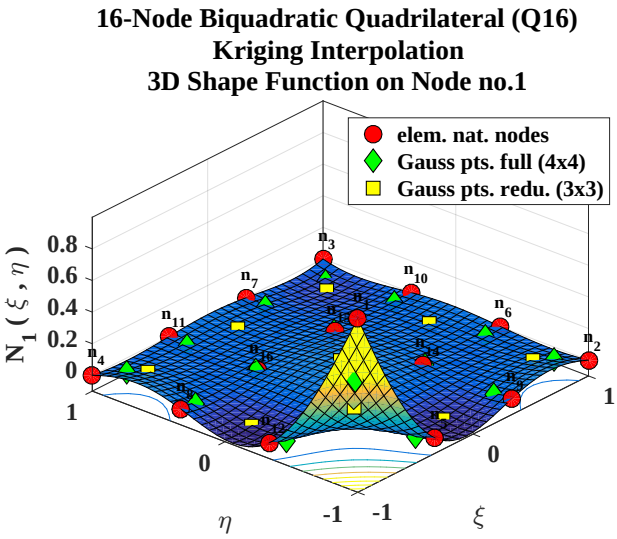

▶/⏸ N_1 N_2 N_3 N_4 N_5 N_6 N_7 N_8 N_9 N_{10} N_{11} N_{12} N_{13} N_{14} N_{15} N_{16}

Figure C.15: 3D shape function plots of 16BquadKrig element, including nodes and Gauss points spatial locations, on the local element natural coordinate system. Please click on the buttons above this caption to run the animation and toggle between plotted results.

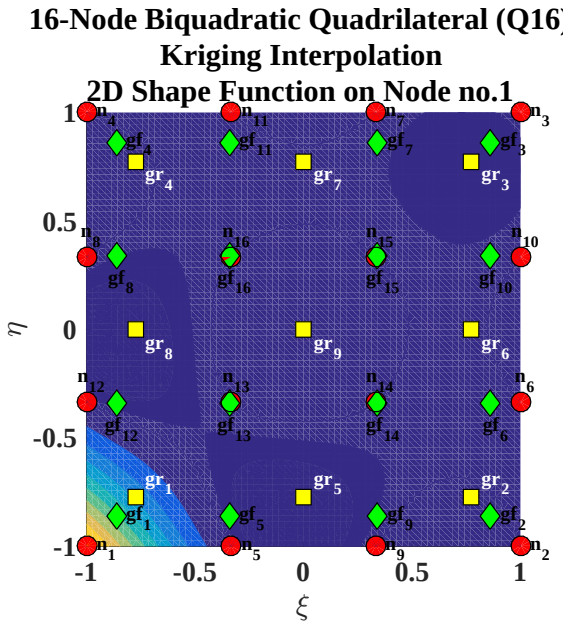

▶/⏸ N_1 N_2 N_3 N_4 N_5 N_6 N_7 N_8 N_9 N_{10} N_{11} N_{12} N_{13} N_{14} N_{15} N_{16}

Figure C.16: 2D shape function plots of 16BquadKrig element, including nodes and Gauss points spatial locations, on the local element natural coordinate system. Please click on the buttons above this caption to run the animation and toggle between plotted results.

C.2.6 16-Node Bicubic Quadrilateral (16BcubKrig)

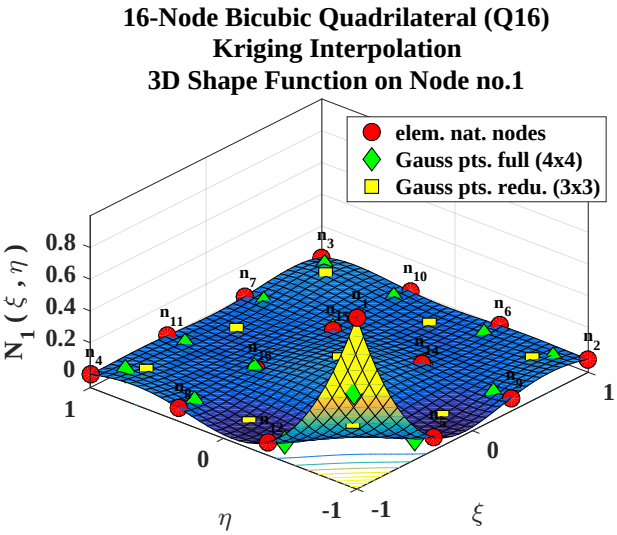

▶/⏸ N_1 N_2 N_3 N_4 N_5 N_6 N_7 N_8 N_9 N_{10} N_{11} N_{12} N_{13} N_{14} N_{15} N_{16}

Figure C.17: 3D shape function plots of 16BcubKrig element, including nodes and Gauss points spatial locations, on the local element natural coordinate system. Please click on the buttons above this caption to run the animation and toggle between plotted results.

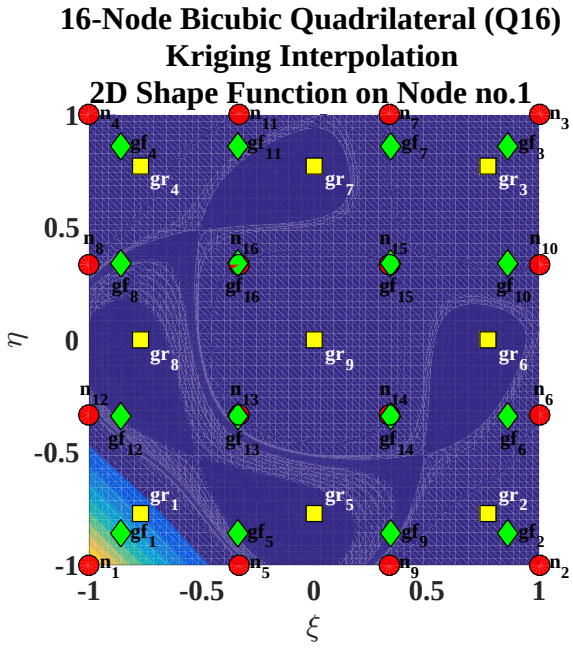

▶/⏸ N_1 N_2 N_3 N_4 N_5 N_6 N_7 N_8 N_9 N_{10} N_{11} N_{12} N_{13} N_{14} N_{15} N_{16}

Figure C.18: 2D shape function plots of 16BcubKrig element, including nodes and Gauss points spatial locations, on the local element natural coordinate system. Please click on the buttons above this caption to run the animation and toggle between plotted results.

Appendix D

Gauss Quadrature Rules

In this appendix, the Gauss points natural coordinates and respective weights are summarized, associated with the first four two-dimensional Gauss product rules $p = 1, 2, 3, 4$.

Table D.1: Gauss points natural coordinates associated with (1×1) two-dimensional product rule $(p = 1)$.

point no.	**Gauss points natural coordinates**	
	ξ	η
1	0	0

Table D.2: Gauss points integration weights associated with (1×1) two-dimensional product rule $(p = 1)$.

point no.	**Gauss points integration weights**
1	4

Table D.3: Gauss points natural coordinates associated with (2×2) two-dimensional product rule $(p = 2)$.

point no.	**Gauss points natural coordinates**			
	real		approximation	
	ξ	η	ξ	η
1	$-1/3\sqrt{3}$	$-1/3\sqrt{3}$	-0.5774	-0.5774
2	$1/3\sqrt{3}$	$-1/3\sqrt{3}$	0.5774	-0.5774
3	$1/3\sqrt{3}$	$1/3\sqrt{3}$	0.5774	0.5774
4	$-1/3\sqrt{3}$	$1/3\sqrt{3}$	-0.5774	0.5774

Table D.4: Gauss points integration weights associated with (2×2) two-dimensional product rule $(p = 2)$.

point no.	**Gauss points integration weights**
1	1
2	1
3	1
4	1

Table D.5: Gauss points natural coordinates associated with (3×3) two-dimensional product rule $(p = 3)$.

point no.	**Gauss points natural coordinates**			
	real		approximation	
	ξ	η	ξ	η
1	$-1/5\sqrt{15}$	$-1/5\sqrt{15}$	-0.7746	-0.7746
2	$1/5\sqrt{15}$	$-1/5\sqrt{15}$	0.7746	-0.7746
3	$1/5\sqrt{15}$	$1/5\sqrt{15}$	0.7746	0.7746
4	$-1/5\sqrt{15}$	$1/5\sqrt{15}$	-0.7746	0.7746
5	0	$-1/5\sqrt{15}$	0.0000	-0.7746
6	$1/5\sqrt{15}$	0	0.7746	0.0000
7	0	$1/5\sqrt{15}$	0.0000	0.7746
8	$-1/5\sqrt{15}$	0	-0.7746	0.0000
9	0	0	0.0000	0.0000

Table D.6: Gauss points integration weights associated with (3×3) two-dimensional product rule $(p = 3)$.

point no.	**Gauss points integration weights**	
	real	approximation
1	$25/81$	0.3086
2	$25/81$	0.3086
3	$25/81$	0.3086
4	$25/81$	0.3086
5	$40/81$	0.4938
6	$40/81$	0.4938
7	$40/81$	0.4938
8	$40/81$	0.4938
9	$64/81$	0.7901

Table D.7: Gauss points natural coordinates associated with (4×4) two-dimensional product rule $(p = 4)$.

point no.	**Gauss points natural coordinates**			
	real		approximation	
	ξ	η	ξ	η
1	$-1/35\sqrt{525+70\sqrt{30}}$	$-1/35\sqrt{525+70\sqrt{30}}$	-0.8611	-0.8611
2	$1/35\sqrt{525+70\sqrt{30}}$	$-1/35\sqrt{525+70\sqrt{30}}$	0.8611	-0.8611
3	$1/35\sqrt{525+70\sqrt{30}}$	$1/35\sqrt{525+70\sqrt{30}}$	0.8611	0.8611
4	$-1/35\sqrt{525+70\sqrt{30}}$	$1/35\sqrt{525+70\sqrt{30}}$	-0.8611	0.8611
5	$-1/35\sqrt{525-70\sqrt{30}}$	$-1/35\sqrt{525+70\sqrt{30}}$	-0.3400	-0.8611
6	$1/35\sqrt{525+70\sqrt{30}}$	$-1/35\sqrt{525-70\sqrt{30}}$	0.8611	-0.3400
7	$1/35\sqrt{525-70\sqrt{30}}$	$1/35\sqrt{525+70\sqrt{30}}$	0.3400	0.8611
8	$-1/35\sqrt{525+70\sqrt{30}}$	$1/35\sqrt{525-70\sqrt{30}}$	-0.8611	0.3400
9	$1/35\sqrt{525-70\sqrt{30}}$	$-1/35\sqrt{525+70\sqrt{30}}$	0.3400	-0.8611
10	$1/35\sqrt{525+70\sqrt{30}}$	$1/35\sqrt{525-70\sqrt{30}}$	0.8611	0.3400
11	$-1/35\sqrt{525-70\sqrt{30}}$	$1/35\sqrt{525+70\sqrt{30}}$	-0.3400	0.8611
12	$-1/35\sqrt{525+70\sqrt{30}}$	$-1/35\sqrt{525-70\sqrt{30}}$	-0.8611	-0.3400
13	$-1/35\sqrt{525-70\sqrt{30}}$	$-1/35\sqrt{525-70\sqrt{30}}$	-0.3400	-0.3400
14	$1/35\sqrt{525-70\sqrt{30}}$	$-1/35\sqrt{525-70\sqrt{30}}$	0.3400	-0.3400
15	$1/35\sqrt{525-70\sqrt{30}}$	$1/35\sqrt{525-70\sqrt{30}}$	0.3400	0.3400
16	$-1/35\sqrt{525-70\sqrt{30}}$	$1/35\sqrt{525-70\sqrt{30}}$	-0.3400	0.3400

Table D.8: Gauss points integration weights associated with (4×4) two-dimensional product rule $(p = 4)$.

point no.	Gauss points integration weights	
	real	approximation
1	$1/1296\left(-18+\sqrt{30}\right)^2$	0.1210
2	$1/1296\left(-18+\sqrt{30}\right)^2$	0.1210
3	$1/1296\left(-18+\sqrt{30}\right)^2$	0.1210
4	$1/1296\left(-18+\sqrt{30}\right)^2$	0.1210
5	$49/216$	0.2269
6	$49/216$	0.2269
7	$49/216$	0.2269
8	$49/216$	0.2269
9	$49/216$	0.2269
10	$49/216$	0.2269
11	$49/216$	0.2269
12	$49/216$	0.2269
13	$1/1296\left(18+\sqrt{30}\right)^2$	0.4253
14	$1/1296\left(18+\sqrt{30}\right)^2$	0.4253
15	$1/1296\left(18+\sqrt{30}\right)^2$	0.4253
16	$1/1296\left(18+\sqrt{30}\right)^2$	0.4253

Appendix E

Algorithms' Directory Trees

In this appendix, directory trees (in ASCII list format) are presented, considering both FEM and bat algorithms programmed along the present work, to illustrate the generic program architecture.

Only one case study was considered to create the following directory trees, due to space constraints; also, only one structure was considered, constituted by 2 layers (bimorph smart plate). In this example case study, the optimization mode was deactivated, because otherwise the amount of results would be extremely extensive to print. In any case, when any case study programmed inside the inputs file has the optimization mode activated, the algorithm is able to save user-defined results about optimization (e.g. the graphical frames from the animations presented here, every iteration results inside Excel®, etc.), and, in addition, all results for the structure in its states before and after optimization (results in both tabular and graphical formats!).

The programming methodology was carried out with the objective of saving every step of both FEM computations and optimization iterations, concerning the steps inside pre-processor, processor and post-processor.

```
E:\DROPBOX\THESIS\4_FEM\2_MAPLE_AND_MATLAB\2_NEW\MAIN
|     inputs.mpl
|     main.mpl
|     main.mw
|
+------fem
|     +------1_preprocessor
|     |     +------maple
|     |     |           packages.mpl
|     |     |           procelemalloc.mpl
|     |     |           procgeneral.mpl
|     |     |           procgeometry.mpl
|     |     |           procgeometryplots.mpl
|     |     |           procinputserrorswarnings.mpl
|     |     |           procmastermesh.mpl
|     |     |           procmaterial.mpl
|     |     |
|     |     \------matlab
|     |                 geometry.m
|     |
```

```
|    +------2_solution
|    |    \------maple
|    |              procboundaryconditions.mpl
|    |              procgaussquadrature.mpl
|    |              procjacobian.mpl
|    |              procloads.mpl
|    |              procshapefunctions.mpl
|    |              procsolver.mpl
|    |              procstiffmasskriging.mpl
|    |              procstiffmasslagrange.mpl
|    |              procstraindisplacement.mpl
|    |
|    \------3_postprocessor
|         +------maple
|         |         procexportexcel.mpl
|         |         procminmaxreps.mpl
|         |         procplots.mpl
|         |         procstrainsstresses.mpl
|         |
|         \------matlab
|                   layersplots.m
|                   structureplots.m
|                   wplots.m
|                   xlsalign.m
|                   xlsborder.m
|                   xlsfont.m
|
+------optimization
|    +------1_preprocessor
|    |    \------maple
|    |              procpopini.mpl
|    |
|    +------2_solution
|    |    \------maple
|    |              procbat.mpl
|    |
|    \------3_postprocessor
|         \------maple
|                   procoptimizationplots.mpl
|
\------outputs
     +------case_study_1
     |    +------graphs
     |    |    +------geometry
     |    |    |         geometry_adj.pdf
     |    |    |         geometry_input.pdf
     |    |    |
```

```
|   |   +------layers
|   |   |   +------layer_1
|   |   |   |   +------all_in_one_variables
|   |   |   |   |   \------a4_format
|   |   |   |   |           1_all_strains.pdf
|   |   |   |   |           2_all_stresses.pdf
|   |   |   |   |
|   |   |   |   \------individual_variables
|   |   |   |       +------a4_format
|   |   |   |       |       10_sigma_yz.pdf
|   |   |   |       |       11_sigma_vonmises.pdf
|   |   |   |       |       1_epsilon_x.pdf
|   |   |   |       |       2_epsilon_y.pdf
|   |   |   |       |       3_epsilon_xy.pdf
|   |   |   |       |       4_epsilon_xz.pdf
|   |   |   |       |       5_epsilon_yz.pdf
|   |   |   |       |       6_sigma_x.pdf
|   |   |   |       |       7_sigma_y.pdf
|   |   |   |       |       8_sigma_xy.pdf
|   |   |   |       |       9_sigma_xz.pdf
|   |   |   |       |
|   |   |   |       \------separated_format
|   |   |   |           +------10_sigma_yz
|   |   |   |           |       sigma_yz11.pdf
|   |   |   |           |       sigma_yz12.pdf
|   |   |   |           |       sigma_yz21.pdf
|   |   |   |           |       sigma_yz22.pdf
|   |   |   |           |       sigma_yz31.pdf
|   |   |   |           |       sigma_yz32.pdf
|   |   |   |           |       sigma_yz41.pdf
|   |   |   |           |       sigma_yz42.pdf
|   |   |   |           |       sigma_yz51.pdf
|   |   |   |           |       sigma_yz52.pdf
|   |   |   |           |       sigma_yz61.pdf
|   |   |   |           |       sigma_yz62.pdf
|   |   |   |           |
|   |   |   |           +------11_sigma_vonmises
|   |   |   |           |       sigma_vonmises11.pdf
|   |   |   |           |       sigma_vonmises12.pdf
|   |   |   |           |       sigma_vonmises21.pdf
|   |   |   |           |       sigma_vonmises22.pdf
|   |   |   |           |       sigma_vonmises31.pdf
|   |   |   |           |       sigma_vonmises32.pdf
|   |   |   |           |       sigma_vonmises41.pdf
|   |   |   |           |       sigma_vonmises42.pdf
|   |   |   |           |       sigma_vonmises51.pdf
|   |   |   |           |       sigma_vonmises52.pdf
```

```
|   |   |   |   |           |       sigma_vonmises61.pdf
|   |   |   |   |           |       sigma_vonmises62.pdf
|   |   |   |   |           |
|   |   |   |   |           +------1_epsilon_x
|   |   |   |   |           |       epsilon_x11.pdf
|   |   |   |   |           |       epsilon_x12.pdf
|   |   |   |   |           |       epsilon_x21.pdf
|   |   |   |   |           |       epsilon_x22.pdf
|   |   |   |   |           |       epsilon_x31.pdf
|   |   |   |   |           |       epsilon_x32.pdf
|   |   |   |   |           |       epsilon_x41.pdf
|   |   |   |   |           |       epsilon_x42.pdf
|   |   |   |   |           |       epsilon_x51.pdf
|   |   |   |   |           |       epsilon_x52.pdf
|   |   |   |   |           |       epsilon_x61.pdf
|   |   |   |   |           |       epsilon_x62.pdf
|   |   |   |   |           |
|   |   |   |   |           +------2_epsilon_y
|   |   |   |   |           |       epsilon_y11.pdf
|   |   |   |   |           |       epsilon_y12.pdf
|   |   |   |   |           |       epsilon_y21.pdf
|   |   |   |   |           |       epsilon_y22.pdf
|   |   |   |   |           |       epsilon_y31.pdf
|   |   |   |   |           |       epsilon_y32.pdf
|   |   |   |   |           |       epsilon_y41.pdf
|   |   |   |   |           |       epsilon_y42.pdf
|   |   |   |   |           |       epsilon_y51.pdf
|   |   |   |   |           |       epsilon_y52.pdf
|   |   |   |   |           |       epsilon_y61.pdf
|   |   |   |   |           |       epsilon_y62.pdf
|   |   |   |   |           |
|   |   |   |   |           +------3_epsilon_xy
|   |   |   |   |           |       epsilon_xy11.pdf
|   |   |   |   |           |       epsilon_xy12.pdf
|   |   |   |   |           |       epsilon_xy21.pdf
|   |   |   |   |           |       epsilon_xy22.pdf
|   |   |   |   |           |       epsilon_xy31.pdf
|   |   |   |   |           |       epsilon_xy32.pdf
|   |   |   |   |           |       epsilon_xy41.pdf
|   |   |   |   |           |       epsilon_xy42.pdf
|   |   |   |   |           |       epsilon_xy51.pdf
|   |   |   |   |           |       epsilon_xy52.pdf
|   |   |   |   |           |       epsilon_xy61.pdf
|   |   |   |   |           |       epsilon_xy62.pdf
|   |   |   |   |           |
|   |   |   |   |           +------4_epsilon_xz
|   |   |   |   |           |       epsilon_xz11.pdf
```

```
|   |   |   |           |       epsilon_xz12.pdf
|   |   |   |           |       epsilon_xz21.pdf
|   |   |   |           |       epsilon_xz22.pdf
|   |   |   |           |       epsilon_xz31.pdf
|   |   |   |           |       epsilon_xz32.pdf
|   |   |   |           |       epsilon_xz41.pdf
|   |   |   |           |       epsilon_xz42.pdf
|   |   |   |           |       epsilon_xz51.pdf
|   |   |   |           |       epsilon_xz52.pdf
|   |   |   |           |       epsilon_xz61.pdf
|   |   |   |           |       epsilon_xz62.pdf
|   |   |   |           |
|   |   |   |           +------5_epsilon_yz
|   |   |   |           |       epsilon_yz11.pdf
|   |   |   |           |       epsilon_yz12.pdf
|   |   |   |           |       epsilon_yz21.pdf
|   |   |   |           |       epsilon_yz22.pdf
|   |   |   |           |       epsilon_yz31.pdf
|   |   |   |           |       epsilon_yz32.pdf
|   |   |   |           |       epsilon_yz41.pdf
|   |   |   |           |       epsilon_yz42.pdf
|   |   |   |           |       epsilon_yz51.pdf
|   |   |   |           |       epsilon_yz52.pdf
|   |   |   |           |       epsilon_yz61.pdf
|   |   |   |           |       epsilon_yz62.pdf
|   |   |   |           |
|   |   |   |           +------6_sigma_x
|   |   |   |           |       sigma_x11.pdf
|   |   |   |           |       sigma_x12.pdf
|   |   |   |           |       sigma_x21.pdf
|   |   |   |           |       sigma_x22.pdf
|   |   |   |           |       sigma_x31.pdf
|   |   |   |           |       sigma_x32.pdf
|   |   |   |           |       sigma_x41.pdf
|   |   |   |           |       sigma_x42.pdf
|   |   |   |           |       sigma_x51.pdf
|   |   |   |           |       sigma_x52.pdf
|   |   |   |           |       sigma_x61.pdf
|   |   |   |           |       sigma_x62.pdf
|   |   |   |           |
|   |   |   |           +------7_sigma_y
|   |   |   |           |       sigma_y11.pdf
|   |   |   |           |       sigma_y12.pdf
|   |   |   |           |       sigma_y21.pdf
|   |   |   |           |       sigma_y22.pdf
|   |   |   |           |       sigma_y31.pdf
|   |   |   |           |       sigma_y32.pdf
```

```
|   |   |   |           |       sigma_y41.pdf
|   |   |   |           |       sigma_y42.pdf
|   |   |   |           |       sigma_y51.pdf
|   |   |   |           |       sigma_y52.pdf
|   |   |   |           |       sigma_y61.pdf
|   |   |   |           |       sigma_y62.pdf
|   |   |   |           |
|   |   |   |           +------8_sigma_xy
|   |   |   |           |       sigma_xy11.pdf
|   |   |   |           |       sigma_xy12.pdf
|   |   |   |           |       sigma_xy21.pdf
|   |   |   |           |       sigma_xy22.pdf
|   |   |   |           |       sigma_xy31.pdf
|   |   |   |           |       sigma_xy32.pdf
|   |   |   |           |       sigma_xy41.pdf
|   |   |   |           |       sigma_xy42.pdf
|   |   |   |           |       sigma_xy51.pdf
|   |   |   |           |       sigma_xy52.pdf
|   |   |   |           |       sigma_xy61.pdf
|   |   |   |           |       sigma_xy62.pdf
|   |   |   |           |
|   |   |   |           \------9_sigma_xz
|   |   |   |                   sigma_xz11.pdf
|   |   |   |                   sigma_xz12.pdf
|   |   |   |                   sigma_xz21.pdf
|   |   |   |                   sigma_xz22.pdf
|   |   |   |                   sigma_xz31.pdf
|   |   |   |                   sigma_xz32.pdf
|   |   |   |                   sigma_xz41.pdf
|   |   |   |                   sigma_xz42.pdf
|   |   |   |                   sigma_xz51.pdf
|   |   |   |                   sigma_xz52.pdf
|   |   |   |                   sigma_xz61.pdf
|   |   |   |                   sigma_xz62.pdf
|   |   |   |
|   |   |   \------layer_2
|   |   |          +------all_in_one_variables
|   |   |          |      \------a4_format
|   |   |          |                 1_all_strains.pdf
|   |   |          |                 2_all_stresses.pdf
|   |   |          |
|   |   |          \------individual_variables
|   |   |                 +------a4_format
|   |   |                 |       10_sigma_yz.pdf
|   |   |                 |       11_sigma_vonmises.pdf
|   |   |                 |       1_epsilon_x.pdf
|   |   |                 |       2_epsilon_y.pdf
```

```
|   |   |               |       3_epsilon_xy.pdf
|   |   |               |       4_epsilon_xz.pdf
|   |   |               |       5_epsilon_yz.pdf
|   |   |               |       6_sigma_x.pdf
|   |   |               |       7_sigma_y.pdf
|   |   |               |       8_sigma_xy.pdf
|   |   |               |       9_sigma_xz.pdf
|   |   |               |
|   |   |               \------separated_format
|   |   |                   +------10_sigma_yz
|   |   |                   |       sigma_yz11.pdf
|   |   |                   |       sigma_yz12.pdf
|   |   |                   |       sigma_yz21.pdf
|   |   |                   |       sigma_yz22.pdf
|   |   |                   |       sigma_yz31.pdf
|   |   |                   |       sigma_yz32.pdf
|   |   |                   |       sigma_yz41.pdf
|   |   |                   |       sigma_yz42.pdf
|   |   |                   |       sigma_yz51.pdf
|   |   |                   |       sigma_yz52.pdf
|   |   |                   |       sigma_yz61.pdf
|   |   |                   |       sigma_yz62.pdf
|   |   |                   |
|   |   |                   +------11_sigma_vonmises
|   |   |                   |       sigma_vonmises11.pdf
|   |   |                   |       sigma_vonmises12.pdf
|   |   |                   |       sigma_vonmises21.pdf
|   |   |                   |       sigma_vonmises22.pdf
|   |   |                   |       sigma_vonmises31.pdf
|   |   |                   |       sigma_vonmises32.pdf
|   |   |                   |       sigma_vonmises41.pdf
|   |   |                   |       sigma_vonmises42.pdf
|   |   |                   |       sigma_vonmises51.pdf
|   |   |                   |       sigma_vonmises52.pdf
|   |   |                   |       sigma_vonmises61.pdf
|   |   |                   |       sigma_vonmises62.pdf
|   |   |                   |
|   |   |                   +------1_epsilon_x
|   |   |                   |       epsilon_x11.pdf
|   |   |                   |       epsilon_x12.pdf
|   |   |                   |       epsilon_x21.pdf
|   |   |                   |       epsilon_x22.pdf
|   |   |                   |       epsilon_x31.pdf
|   |   |                   |       epsilon_x32.pdf
|   |   |                   |       epsilon_x41.pdf
|   |   |                   |       epsilon_x42.pdf
|   |   |                   |       epsilon_x51.pdf
```

```
|   |   |                   |       epsilon_x52.pdf
|   |   |                   |       epsilon_x61.pdf
|   |   |                   |       epsilon_x62.pdf
|   |   |                   |
|   |   |                   +------2_epsilon_y
|   |   |                   |       epsilon_y11.pdf
|   |   |                   |       epsilon_y12.pdf
|   |   |                   |       epsilon_y21.pdf
|   |   |                   |       epsilon_y22.pdf
|   |   |                   |       epsilon_y31.pdf
|   |   |                   |       epsilon_y32.pdf
|   |   |                   |       epsilon_y41.pdf
|   |   |                   |       epsilon_y42.pdf
|   |   |                   |       epsilon_y51.pdf
|   |   |                   |       epsilon_y52.pdf
|   |   |                   |       epsilon_y61.pdf
|   |   |                   |       epsilon_y62.pdf
|   |   |                   |
|   |   |                   +------3_epsilon_xy
|   |   |                   |       epsilon_xy11.pdf
|   |   |                   |       epsilon_xy12.pdf
|   |   |                   |       epsilon_xy21.pdf
|   |   |                   |       epsilon_xy22.pdf
|   |   |                   |       epsilon_xy31.pdf
|   |   |                   |       epsilon_xy32.pdf
|   |   |                   |       epsilon_xy41.pdf
|   |   |                   |       epsilon_xy42.pdf
|   |   |                   |       epsilon_xy51.pdf
|   |   |                   |       epsilon_xy52.pdf
|   |   |                   |       epsilon_xy61.pdf
|   |   |                   |       epsilon_xy62.pdf
|   |   |                   |
|   |   |                   +------4_epsilon_xz
|   |   |                   |       epsilon_xz11.pdf
|   |   |                   |       epsilon_xz12.pdf
|   |   |                   |       epsilon_xz21.pdf
|   |   |                   |       epsilon_xz22.pdf
|   |   |                   |       epsilon_xz31.pdf
|   |   |                   |       epsilon_xz32.pdf
|   |   |                   |       epsilon_xz41.pdf
|   |   |                   |       epsilon_xz42.pdf
|   |   |                   |       epsilon_xz51.pdf
|   |   |                   |       epsilon_xz52.pdf
|   |   |                   |       epsilon_xz61.pdf
|   |   |                   |       epsilon_xz62.pdf
|   |   |                   |
|   |   |                   +------5_epsilon_yz
```

```
|   |   |                   |       epsilon_yz11.pdf
|   |   |                   |       epsilon_yz12.pdf
|   |   |                   |       epsilon_yz21.pdf
|   |   |                   |       epsilon_yz22.pdf
|   |   |                   |       epsilon_yz31.pdf
|   |   |                   |       epsilon_yz32.pdf
|   |   |                   |       epsilon_yz41.pdf
|   |   |                   |       epsilon_yz42.pdf
|   |   |                   |       epsilon_yz51.pdf
|   |   |                   |       epsilon_yz52.pdf
|   |   |                   |       epsilon_yz61.pdf
|   |   |                   |       epsilon_yz62.pdf
|   |   |                   |
|   |   |                   +------6_sigma_x
|   |   |                   |       sigma_x11.pdf
|   |   |                   |       sigma_x12.pdf
|   |   |                   |       sigma_x21.pdf
|   |   |                   |       sigma_x22.pdf
|   |   |                   |       sigma_x31.pdf
|   |   |                   |       sigma_x32.pdf
|   |   |                   |       sigma_x41.pdf
|   |   |                   |       sigma_x42.pdf
|   |   |                   |       sigma_x51.pdf
|   |   |                   |       sigma_x52.pdf
|   |   |                   |       sigma_x61.pdf
|   |   |                   |       sigma_x62.pdf
|   |   |                   |
|   |   |                   +------7_sigma_y
|   |   |                   |       sigma_y11.pdf
|   |   |                   |       sigma_y12.pdf
|   |   |                   |       sigma_y21.pdf
|   |   |                   |       sigma_y22.pdf
|   |   |                   |       sigma_y31.pdf
|   |   |                   |       sigma_y32.pdf
|   |   |                   |       sigma_y41.pdf
|   |   |                   |       sigma_y42.pdf
|   |   |                   |       sigma_y51.pdf
|   |   |                   |       sigma_y52.pdf
|   |   |                   |       sigma_y61.pdf
|   |   |                   |       sigma_y62.pdf
|   |   |                   |
|   |   |                   +------8_sigma_xy
|   |   |                   |       sigma_xy11.pdf
|   |   |                   |       sigma_xy12.pdf
|   |   |                   |       sigma_xy21.pdf
|   |   |                   |       sigma_xy22.pdf
|   |   |                   |       sigma_xy31.pdf
```

```
|   |   |                   |       sigma_xy32.pdf
|   |   |                   |       sigma_xy41.pdf
|   |   |                   |       sigma_xy42.pdf
|   |   |                   |       sigma_xy51.pdf
|   |   |                   |       sigma_xy52.pdf
|   |   |                   |       sigma_xy61.pdf
|   |   |                   |       sigma_xy62.pdf
|   |   |                   |
|   |   |                   \------9_sigma_xz
|   |   |                           sigma_xz11.pdf
|   |   |                           sigma_xz12.pdf
|   |   |                           sigma_xz21.pdf
|   |   |                           sigma_xz22.pdf
|   |   |                           sigma_xz31.pdf
|   |   |                           sigma_xz32.pdf
|   |   |                           sigma_xz41.pdf
|   |   |                           sigma_xz42.pdf
|   |   |                           sigma_xz51.pdf
|   |   |                           sigma_xz52.pdf
|   |   |                           sigma_xz61.pdf
|   |   |                           sigma_xz62.pdf
|   |   |
|   |   +------material
|   |   |       phase1_E_distribution.eps
|   |   |       phase1_nu_distribution.eps
|   |   |       phase1_rho_distribution.eps
|   |   |       phase1_wcn_distribution.eps
|   |   |       phase2_E_distribution.eps
|   |   |       phase2_nu_distribution.eps
|   |   |       phase2_rho_distribution.eps
|   |   |
|   |   +------mesh
|   |   |       mesh.eps
|   |   |
|   |   \------structure
|   |       +------all_in_one_variables
|   |       |   \------a4_format
|   |       |           1_all_dofs.pdf
|   |       |           2_modes_1to5.pdf
|   |       |
|   |       \------individual_variables
|   |           +------a4_format
|   |           |       10_mode_4.pdf
|   |           |       11_mode_5.pdf
|   |           |       1_dof_w.pdf
|   |           |       2_dof_tx.pdf
|   |           |       3_dof_ty.pdf
```

```
|   |           |       4_dof_u.pdf
|   |           |       5_dof_v.pdf
|   |           |       6_dof_phi.pdf
|   |           |       7_mode_1.pdf
|   |           |       8_mode_2.pdf
|   |           |       9_mode_3.pdf
|   |           |
|   |           \------separated_format
|   |                  +------10_mode_4
|   |                  |       mode_411.pdf
|   |                  |       mode_412.pdf
|   |                  |       mode_421.pdf
|   |                  |       mode_422.pdf
|   |                  |       mode_431.pdf
|   |                  |       mode_432.pdf
|   |                  |       mode_441.pdf
|   |                  |       mode_442.pdf
|   |                  |       mode_451.pdf
|   |                  |       mode_452.pdf
|   |                  |       mode_461.pdf
|   |                  |       mode_462.pdf
|   |                  |
|   |                  +------11_mode_5
|   |                  |       mode_511.pdf
|   |                  |       mode_512.pdf
|   |                  |       mode_521.pdf
|   |                  |       mode_522.pdf
|   |                  |       mode_531.pdf
|   |                  |       mode_532.pdf
|   |                  |       mode_541.pdf
|   |                  |       mode_542.pdf
|   |                  |       mode_551.pdf
|   |                  |       mode_552.pdf
|   |                  |       mode_561.pdf
|   |                  |       mode_562.pdf
|   |                  |
|   |                  +------1_dof_w
|   |                  |       dof_w11.pdf
|   |                  |       dof_w12.pdf
|   |                  |       dof_w21.pdf
|   |                  |       dof_w22.pdf
|   |                  |       dof_w31.pdf
|   |                  |       dof_w32.pdf
|   |                  |       dof_w41.pdf
|   |                  |       dof_w42.pdf
|   |                  |       dof_w51.pdf
|   |                  |       dof_w52.pdf
```

```
|   |                   |       dof_w61.pdf
|   |                   |       dof_w62.pdf
|   |                   |
|   |                   +------2_dof_tx
|   |                   |       dof_tx11.pdf
|   |                   |       dof_tx12.pdf
|   |                   |       dof_tx21.pdf
|   |                   |       dof_tx22.pdf
|   |                   |       dof_tx31.pdf
|   |                   |       dof_tx32.pdf
|   |                   |       dof_tx41.pdf
|   |                   |       dof_tx42.pdf
|   |                   |       dof_tx51.pdf
|   |                   |       dof_tx52.pdf
|   |                   |       dof_tx61.pdf
|   |                   |       dof_tx62.pdf
|   |                   |
|   |                   +------3_dof_ty
|   |                   |       dof_ty11.pdf
|   |                   |       dof_ty12.pdf
|   |                   |       dof_ty21.pdf
|   |                   |       dof_ty22.pdf
|   |                   |       dof_ty31.pdf
|   |                   |       dof_ty32.pdf
|   |                   |       dof_ty41.pdf
|   |                   |       dof_ty42.pdf
|   |                   |       dof_ty51.pdf
|   |                   |       dof_ty52.pdf
|   |                   |       dof_ty61.pdf
|   |                   |       dof_ty62.pdf
|   |                   |
|   |                   +------4_dof_u
|   |                   |       dof_u11.pdf
|   |                   |       dof_u12.pdf
|   |                   |       dof_u21.pdf
|   |                   |       dof_u22.pdf
|   |                   |       dof_u31.pdf
|   |                   |       dof_u32.pdf
|   |                   |       dof_u41.pdf
|   |                   |       dof_u42.pdf
|   |                   |       dof_u51.pdf
|   |                   |       dof_u52.pdf
|   |                   |       dof_u61.pdf
|   |                   |       dof_u62.pdf
|   |                   |
|   |                   +------5_dof_v
|   |                   |       dof_v11.pdf
```

```
|   |                   |       dof_v12.pdf
|   |                   |       dof_v21.pdf
|   |                   |       dof_v22.pdf
|   |                   |       dof_v31.pdf
|   |                   |       dof_v32.pdf
|   |                   |       dof_v41.pdf
|   |                   |       dof_v42.pdf
|   |                   |       dof_v51.pdf
|   |                   |       dof_v52.pdf
|   |                   |       dof_v61.pdf
|   |                   |       dof_v62.pdf
|   |                   |
|   |                   +------6_dof_phi
|   |                   |       dof_phi11.pdf
|   |                   |       dof_phi12.pdf
|   |                   |       dof_phi21.pdf
|   |                   |       dof_phi22.pdf
|   |                   |       dof_phi31.pdf
|   |                   |       dof_phi32.pdf
|   |                   |       dof_phi41.pdf
|   |                   |       dof_phi42.pdf
|   |                   |       dof_phi51.pdf
|   |                   |       dof_phi52.pdf
|   |                   |       dof_phi61.pdf
|   |                   |       dof_phi62.pdf
|   |                   |
|   |                   +------7_mode_1
|   |                   |       mode_111.pdf
|   |                   |       mode_112.pdf
|   |                   |       mode_121.pdf
|   |                   |       mode_122.pdf
|   |                   |       mode_131.pdf
|   |                   |       mode_132.pdf
|   |                   |       mode_141.pdf
|   |                   |       mode_142.pdf
|   |                   |       mode_151.pdf
|   |                   |       mode_152.pdf
|   |                   |       mode_161.pdf
|   |                   |       mode_162.pdf
|   |                   |
|   |                   +------8_mode_2
|   |                   |       mode_211.pdf
|   |                   |       mode_212.pdf
|   |                   |       mode_221.pdf
|   |                   |       mode_222.pdf
|   |                   |       mode_231.pdf
|   |                   |       mode_232.pdf
```

```
|   |                   |       mode_241.pdf
|   |                   |       mode_242.pdf
|   |                   |       mode_251.pdf
|   |                   |       mode_252.pdf
|   |                   |       mode_261.pdf
|   |                   |       mode_262.pdf
|   |                   |
|   |                   \------9_mode_3
|   |                           mode_311.pdf
|   |                           mode_312.pdf
|   |                           mode_321.pdf
|   |                           mode_322.pdf
|   |                           mode_331.pdf
|   |                           mode_332.pdf
|   |                           mode_341.pdf
|   |                           mode_342.pdf
|   |                           mode_351.pdf
|   |                           mode_352.pdf
|   |                           mode_361.pdf
|   |                           mode_362.pdf
|   |
|   \------numerical
|               min_max_reps.xlsx
|
\------parameters
          outputs.xlsx
```

Appendix F

Validation Studies: Schemes & Results

This appendix gathers schemes and results about several validation case studies, in order to optimize the thesis' size.

F.1 Standard, benchmarking study: Reddy, J.N.

Results associated with Section 4.1.1.

Table F.1: The effect of reduced integration, thickness, and mesh refinement on the centre deflections and stresses of a simply-supported, isotropic, square plate under an uniform transverse load. Comparison between the results from Reddy (2006) and the present FEM algorithm.

		Reddy (2006)									
		mesh								**exact**	
		(1×1)		(2×2)		(4×4)		(2×2)			
		element									
		Linear Q4		Linear Q4		Linear Q4		Quadratic Q9			
a/h	**int. sch.**	$\overline{w}$	$\overline{\sigma}_{xx}$	$\overline{w}$	$\overline{\sigma}_{xx}$	$\overline{w}$	$\overline{\sigma}_{xx}$	$\overline{w}$	$\overline{\sigma}_{xx}$	$\overline{w}$	$\overline{\sigma}_{xx}$
10	full	0.964	0.018	2.474	0.119	3.883	0.216	4.770	0.290	4.791	0.276
	selective	3.950	0.095	4.712	0.235	4.773	0.266	4.799	0.272		
20	full	0.270	0.005	0.957	0.048	2.363	0.138	4.570	0.268	4.625	0.276
	selective	3.669	0.095	4.524	0.235	4.603	0.266	4.633	0.272		
40	full	0.070	0.001	0.279	0.014	0.944	0.056	4.505	0.270	4.584	0.276
	selective	3.599	0.095	4.375	0.235	4.560	0.266	4.592	0.271		
50	full	0.005	0.000	0.182	0.009	0.652	0.039	4.496	0.267	4.579	0.276
	selective	3.590	0.095	4.472	0.235	4.555	0.266	4.587	0.271		
100	full	0.011	0.000	0.047	0.002	0.182	0.011	4.482	0.266	4.572	0.276
	selective	3.579	0.095	4.465	0.235	4.548	0.266	4.580	0.272		

		present FEM (deviations [%])							
		mesh							
		(2×2)		(4×4)		(8×8)		(4×4)	
		element							
		4BlinLag		4BlinLag		4BlinLag		9BquadLag	
a/h	**int. sch.**	$\overline{w}$	$\overline{\sigma}_{xx}$	$\overline{w}$	$\overline{\sigma}_{xx}$	$\overline{w}$	$\overline{\sigma}_{xx}$	$\overline{w}$	$\overline{\sigma}_{xx}$
10	full	0.964 (0.00)	0.018 (0.00)	2.474 (0.00)	0.118 (0.84)	3.884 (0.03)	0.216 (0.00)	4.771 (0.02)	0.290 (0.00)
	selective	3.950 (0.00)	0.095 (0.00)	4.712 (0.00)	0.235 (0.00)	4.773 (0.00)	0.266 (0.00)	4.799 (0.00)	0.271 (0.37)
20	full	0.269 (0.37)	0.005 (0.00)	0.957 (0.00)	0.048 (0.00)	2.363 (0.00)	0.137 (0.72)	4.572 (0.04)	0.268 (0.00)
	selective	3.669 (0.00)	0.095 (0.00)	4.525 (0.02)	0.235 (0.00)	4.603 (0.00)	0.266 (0.00)	4.633 (0.00)	0.271 (0.37)
40	full	0.070 (0.00)	0.001 (0.00)	0.279 (0.00)	0.014 (0.00)	0.944 (0.00)	0.056 (0.00)	4.505 (0.00)	0.270 (0.00)
	selective	3.599 (0.00)	0.095 (0.00)	4.478 (2.35)	0.235 (0.00)	4.560 (0.00)	0.266 (0.00)	4.591 (0.02)	0.271 (0.00)
50	full	0.045 (800.00)	0.001 (0.00)	0.182 (0.00)	0.009 (0.00)	0.652 (0.00)	0.039 (0.00)	4.496 (0.00)	0.267 (0.00)
	selective	3.590 (0.00)	0.095 (0.00)	4.472 (0.00)	0.235 (0.00)	4.555 (0.00)	0.266 (0.00)	4.587 (0.00)	0.271 (0.00)
100	full	0.011 (0.00)	0.000 (0.00)	0.047 (0.00)	0.002 (0.00)	0.182 (0.00)	0.011 (0.00)	4.482 (0.00)	0.266 (0.00)
	selective	3.579 (0.00)	0.095 (0.00)	4.465 (0.00)	0.235 (0.00)	4.548 (0.00)	0.266 (0.00)	4.580 (0.00)	0.271 (0.37)

F.2 Standard, benchmarking study: AMAPDL

Results associated with Section 4.1.2.

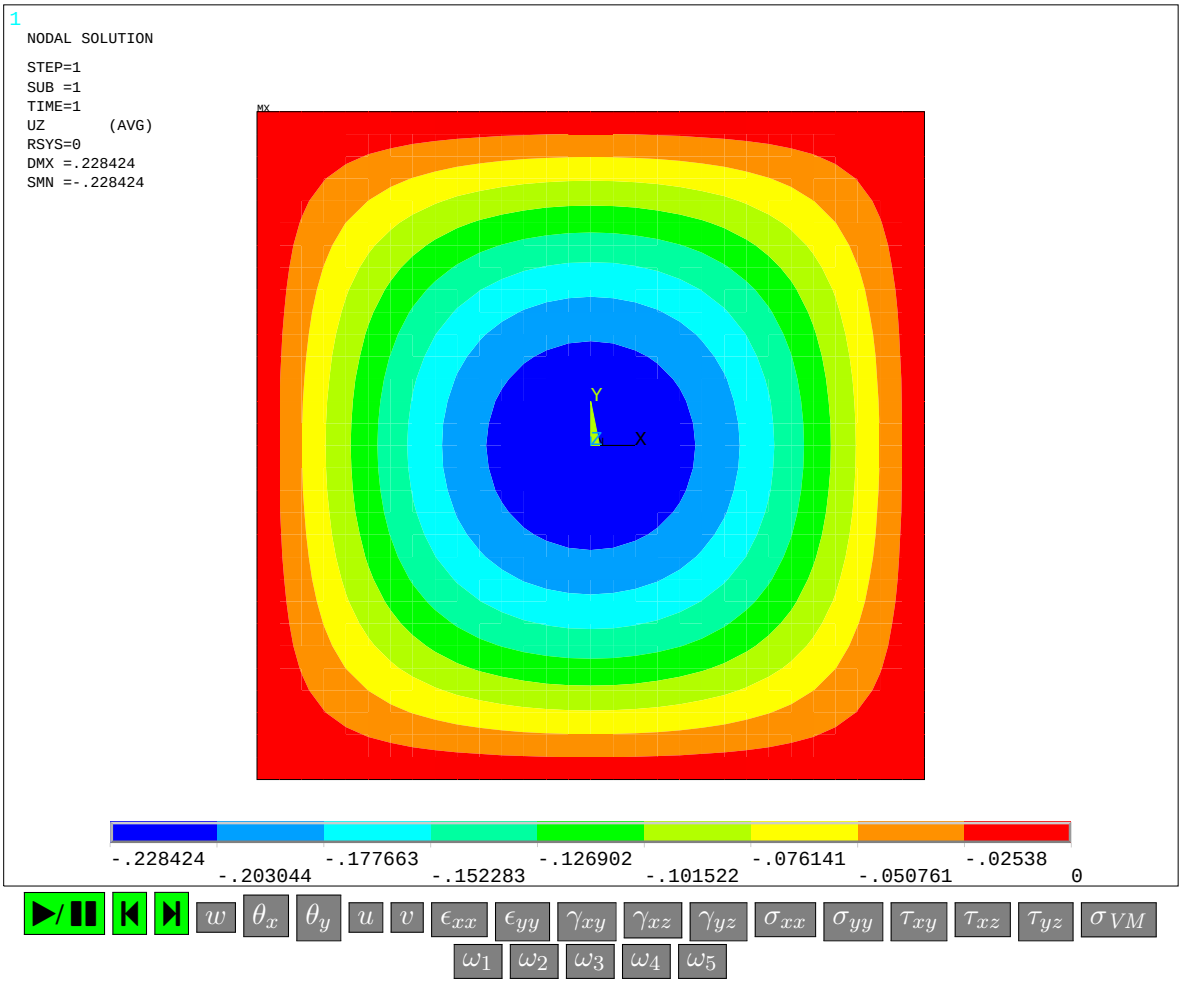

Figure F.1: Statics and dynamics (free vibrations) results obtained from the isotropic simply-supported plate validation model using AMAPDL, considering a (30×30) mesh. Please click on the buttons above this caption to run the animation and toggle between plotted results.

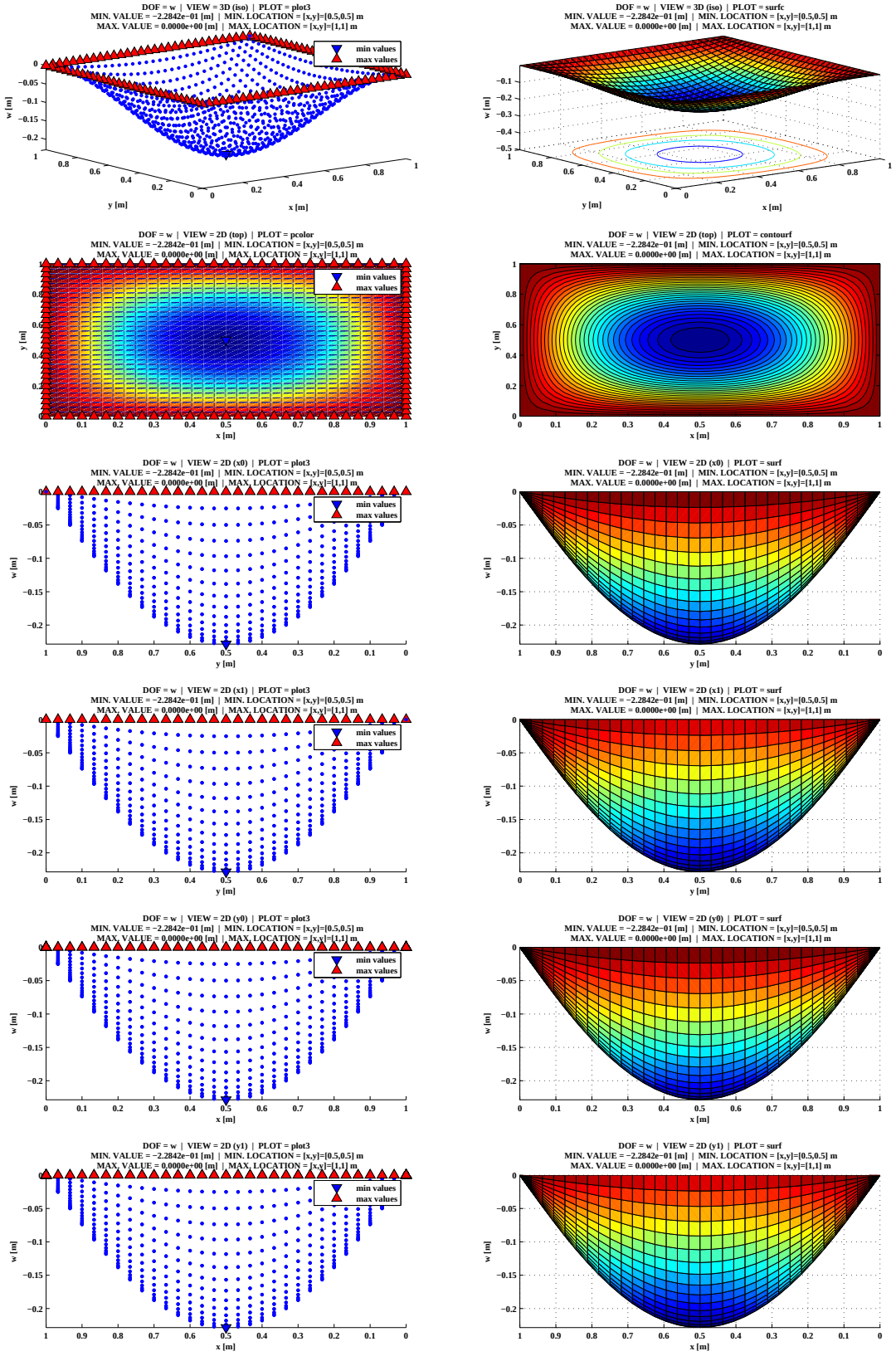

w θ_x θ_y u v ϵ_{xx} ϵ_{yy} γ_{xy} γ_{xz} γ_{yz} σ_{xx} σ_{yy} τ_{xy} τ_{xz} τ_{yz} σ_{VM}

ω_1 ω_2 ω_3 ω_4 ω_5

Figure F.2: Statics and dynamics (free vibrations) results obtained from the isotropic simply-supported plate validation model using the present FEM platform. 4BlinLag elements with a (30×30) mesh. Please click on the buttons above this caption to run the animation and toggle between plotted results.

Table F.2: Comparison of DOFs obtained from the isotropic simply-supported plate validation model using AMAPDL and the present FEM platform, considering 15 different meshes.

cs_no. (mesh)	DOFs AMAPDL				
	$\max\|w\|$ [m]	$\max\|\theta_x\|$ [rad]	$\max\|\theta_y\|$ [rad]	$\max\|u\|$ [m]	$\max\|v\|$ [m]
1 (2×2)	1.79E-01	7.15E-01	7.15E-01	4.78E-37	4.78E-37
2 (4×4)	2.23E-01	7.53E-01	7.53E-01	4.62E-37	4.62E-37
3 (6×6)	2.26E-01	7.56E-01	7.56E-01	3.96E-37	3.96E-37
4 (8×8)	2.27E-01	7.57E-01	7.57E-01	3.43E-37	3.43E-37
5 (10×10)	2.28E-01	7.57E-01	7.57E-01	3.03E-37	3.03E-37
6 (12×12)	2.28E-01	7.58E-01	7.58E-01	2.72E-37	2.72E-37
7 (14×14)	2.28E-01	7.58E-01	7.58E-01	2.47E-37	2.47E-37
8 (16×16)	2.28E-01	7.58E-01	7.58E-01	2.27E-37	2.27E-37
9 (18×18)	2.28E-01	7.58E-01	7.58E-01	2.10E-37	2.10E-37
10 (20×20)	2.28E-01	7.58E-01	7.58E-01	1.96E-37	1.96E-37
11 (22×22)	2.28E-01	7.58E-01	7.58E-01	1.83E-37	1.83E-37
12 (24×24)	2.28E-01	7.58E-01	7.58E-01	1.73E-37	1.73E-37
13 (26×26)	2.28E-01	7.58E-01	7.58E-01	1.63E-37	1.63E-37
14 (28×28)	2.28E-01	7.58E-01	7.58E-01	1.55E-37	1.55E-37
15 (30×30)	2.28E-01	7.58E-01	7.58E-01	1.47E-37	1.47E-37
cs_no. (mesh)	**DOFs 4BlinLag**				
	$\max\|w\|$ [m]	$\max\|\theta_x\|$ [rad]	$\max\|\theta_y\|$ [rad]	$\max\|u\|$ [m]	$\max\|v\|$ [m]
1 (2×2)	1.79E-01	7.15E-01	7.15E-01	0.00E+00	0.00E+00
2 (4×4)	2.23E-01	7.53E-01	7.53E-01	0.00E+00	0.00E+00
3 (6×6)	2.26E-01	7.56E-01	7.56E-01	0.00E+00	0.00E+00
4 (8×8)	2.27E-01	7.57E-01	7.57E-01	0.00E+00	0.00E+00
5 (10×10)	2.28E-01	7.57E-01	7.57E-01	0.00E+00	0.00E+00
6 (12×12)	2.28E-01	7.58E-01	7.58E-01	0.00E+00	0.00E+00
7 (14×14)	2.28E-01	7.58E-01	7.58E-01	0.00E+00	0.00E+00
8 (16×16)	2.28E-01	7.58E-01	7.58E-01	0.00E+00	0.00E+00
9 (18×18)	2.28E-01	7.58E-01	7.58E-01	0.00E+00	0.00E+00
10 (20×20)	2.28E-01	7.58E-01	7.58E-01	0.00E+00	0.00E+00
11 (22×22)	2.28E-01	7.58E-01	7.58E-01	0.00E+00	0.00E+00
12 (24×24)	2.28E-01	7.58E-01	7.58E-01	0.00E+00	0.00E+00
13 (26×26)	2.28E-01	7.58E-01	7.58E-01	0.00E+00	0.00E+00
14 (28×28)	2.28E-01	7.58E-01	7.58E-01	0.00E+00	0.00E+00
15 (30×30)	2.28E-01	7.58E-01	7.58E-01	0.00E+00	0.00E+00
cs_no. (mesh)	**DOFs deviations** [%]				
	$\max\|w\|$	$\max\|\theta_x\|$	$\max\|\theta_y\|$	$\max\|u\|$	$\max\|v\|$
1 (2×2)	8.57E-04	5.21E-05	5.21E-05	0.00E+00	0.00E+00
2 (4×4)	5.06E-05	7.61E-05	7.61E-05	0.00E+00	0.00E+00
3 (6×6)	3.75E-05	1.44E-05	1.44E-05	0.00E+00	0.00E+00
4 (8×8)	1.28E-04	6.04E-05	6.04E-05	0.00E+00	0.00E+00
5 (10×10)	4.57E-05	4.82E-06	4.82E-06	0.00E+00	0.00E+00
6 (12×12)	8.13E-05	4.21E-05	4.21E-05	0.00E+00	0.00E+00
7 (14×14)	9.97E-05	4.63E-05	4.63E-05	0.00E+00	0.00E+00
8 (16×16)	1.02E-04	5.81E-05	5.81E-05	0.00E+00	0.00E+00
9 (18×18)	5.14E-05	3.42E-05	3.42E-05	0.00E+00	0.00E+00
10 (20×20)	5.30E-07	2.82E-05	2.82E-05	0.00E+00	0.00E+00
11 (22×22)	6.91E-05	4.59E-05	4.59E-05	0.00E+00	0.00E+00
12 (24×24)	1.52E-04	1.97E-05	1.97E-05	0.00E+00	0.00E+00
13 (26×26)	2.97E-05	4.36E-05	4.35E-05	0.00E+00	0.00E+00
14 (28×28)	2.02E-04	3.50E-05	3.50E-05	0.00E+00	0.00E+00
15 (30×30)	7.76E-06	5.55E-05	5.55E-05	0.00E+00	0.00E+00

Table F.3: Comparison of strains obtained from the isotropic simply-supported plate validation model using AMAPDL and the present FEM platform, considering 15 different meshes.

cs_no. (mesh)	strains AMAPDL				
	$\max\|\epsilon_{xx}\|$	$\max\|\epsilon_{yy}\|$	$\max\|\gamma_{xy}\|$	$\max\|\gamma_{xz}\|$	$\max\|\gamma_{yz}\|$
1 (2×2)	3.58E-04	3.58E-04	7.15E-04	3.60E-06	3.60E-06
2 (4×4)	8.81E-04	8.81E-04	1.81E-03	4.56E-06	4.56E-06
3 (6×6)	9.68E-04	9.68E-04	2.15E-03	4.55E-06	4.55E-06
4 (8×8)	9.98E-04	9.98E-04	2.31E-03	4.57E-06	4.57E-06
5 (10×10)	1.01E-03	1.01E-03	2.40E-03	4.61E-06	4.61E-06
6 (12×12)	1.02E-03	1.02E-03	2.45E-03	4.65E-06	4.65E-06
7 (14×14)	1.02E-03	1.02E-03	2.49E-03	4.69E-06	4.69E-06
8 (16×16)	1.03E-03	1.03E-03	2.51E-03	4.72E-06	4.72E-06
9 (18×18)	1.03E-03	1.03E-03	2.53E-03	4.75E-06	4.75E-06
10 (20×20)	1.03E-03	1.03E-03	2.54E-03	4.77E-06	4.77E-06
11 (22×22)	1.03E-03	1.03E-03	2.55E-03	4.79E-06	4.79E-06
12 (24×24)	1.03E-03	1.03E-03	2.56E-03	4.81E-06	4.81E-06
13 (26×26)	1.03E-03	1.03E-03	2.57E-03	4.82E-06	4.82E-06
14 (28×28)	1.03E-03	1.03E-03	2.57E-03	4.84E-06	4.84E-06
15 (30×30)	1.03E-03	1.03E-03	2.58E-03	4.85E-06	4.85E-06
cs_no. (mesh)	**strains 4BlinLag**				
	$\max\|\epsilon_{xx}\|$	$\max\|\epsilon_{yy}\|$	$\max\|\gamma_{xy}\|$	$\max\|\gamma_{xz}\|$	$\max\|\gamma_{yz}\|$
1 (2×2)	3.58E-04	3.58E-04	7.15E-04	1.87E-06	1.87E-06
2 (4×4)	8.81E-04	8.81E-04	1.81E-03	3.44E-06	3.44E-06
3 (6×6)	9.68E-04	9.68E-04	2.15E-03	3.93E-06	3.93E-06
4 (8×8)	9.98E-04	9.98E-04	2.31E-03	4.20E-06	4.20E-06
5 (10×10)	1.01E-03	1.01E-03	2.40E-03	4.36E-06	4.36E-06
6 (12×12)	1.02E-03	1.02E-03	2.45E-03	4.47E-06	4.47E-06
7 (14×14)	1.02E-03	1.02E-03	2.49E-03	4.55E-06	4.55E-06
8 (16×16)	1.03E-03	1.03E-03	2.51E-03	4.61E-06	4.61E-06
9 (18×18)	1.03E-03	1.03E-03	2.53E-03	4.66E-06	4.66E-06
10 (20×20)	1.03E-03	1.03E-03	2.54E-03	4.70E-06	4.70E-06
11 (22×22)	1.03E-03	1.03E-03	2.55E-03	4.73E-06	4.73E-06
12 (24×24)	1.03E-03	1.03E-03	2.56E-03	4.76E-06	4.76E-06
13 (26×26)	1.03E-03	1.03E-03	2.57E-03	4.78E-06	4.78E-06
14 (28×28)	1.03E-03	1.03E-03	2.57E-03	4.80E-06	4.80E-06
15 (30×30)	1.03E-03	1.03E-03	2.58E-03	4.82E-06	4.82E-06
cs_no. (mesh)	**strains deviations** [%]				
	$\max\|\epsilon_{xx}\|$	$\max\|\epsilon_{yy}\|$	$\max\|\gamma_{xy}\|$	$\max\|\gamma_{xz}\|$	$\max\|\gamma_{yz}\|$
1 (2×2)	5.21E-05	5.21E-05	5.21E-05	47.97	47.97
2 (4×4)	3.11E-05	3.11E-05	2.02E-04	24.67	24.67
3 (6×6)	1.27E-05	1.27E-05	1.12E-04	13.70	13.70
4 (8×8)	2.62E-05	2.62E-05	9.62E-05	8.15	8.15
5 (10×10)	1.68E-04	1.68E-04	5.92E-05	5.44	5.44
6 (12×12)	6.95E-05	6.95E-05	1.77E-04	3.85	3.85
7 (14×14)	2.66E-04	2.66E-04	3.90E-05	2.87	2.87
8 (16×16)	2.48E-05	2.48E-05	1.66E-04	2.21	2.21
9 (18×18)	4.04E-04	4.04E-04	1.43E-04	1.76	1.76
10 (20×20)	4.45E-05	4.45E-05	7.06E-05	1.43	1.43
11 (22×22)	1.69E-04	1.69E-04	9.01E-05	1.19	1.19
12 (24×24)	1.13E-04	1.13E-04	3.13E-05	1.00	1.00
13 (26×26)	3.03E-04	3.03E-04	1.02E-06	0.85	0.85
14 (28×28)	4.67E-04	4.67E-04	6.07E-05	0.74	0.74
15 (30×30)	2.76E-04	2.76E-04	4.73E-05	0.64	0.64

Table F.4: Comparison of stresses obtained from the isotropic simply-supported plate validation model using AMAPDL and the present FEM platform, considering 15 different meshes.

cs_no. (mesh)	**stresses AMAPDL** [Pa]					
	$\max\|\sigma_{xx}\|$	$\max\|\sigma_{yy}\|$	$\max\|\tau_{xy}\|$	$\max\|\tau_{xz}\|$	$\max\|\tau_{yz}\|$	$\max\|\sigma_{VM}\|$
1 (2×2)	9.53E+07	9.53E+07	5.72E+07	9.38E+04	9.38E+04	1.38E+08
2 (4×4)	2.35E+08	2.35E+08	1.45E+08	2.19E+05	2.19E+05	2.55E+08
3 (6×6)	2.58E+08	2.58E+08	1.72E+08	2.59E+05	2.59E+05	3.00E+08
4 (8×8)	2.66E+08	2.66E+08	1.85E+08	2.77E+05	2.77E+05	3.21E+08
5 (10×10)	2.70E+08	2.70E+08	1.92E+08	2.89E+05	2.89E+05	3.33E+08
6 (12×12)	2.72E+08	2.72E+08	1.96E+08	2.97E+05	2.97E+05	3.40E+08
7 (14×14)	2.73E+08	2.73E+08	1.99E+08	3.03E+05	3.03E+05	3.45E+08
8 (16×16)	2.74E+08	2.74E+08	2.01E+08	3.07E+05	3.07E+05	3.48E+08
9 (18×18)	2.74E+08	2.74E+08	2.02E+08	3.10E+05	3.10E+05	3.50E+08
10 (20×20)	2.75E+08	2.75E+08	2.03E+08	3.13E+05	3.13E+05	3.52E+08
11 (22×22)	2.75E+08	2.75E+08	2.04E+08	3.15E+05	3.15E+05	3.54E+08
12 (24×24)	2.75E+08	2.75E+08	2.05E+08	3.17E+05	3.17E+05	3.55E+08
13 (26×26)	2.75E+08	2.75E+08	2.05E+08	3.19E+05	3.19E+05	3.56E+08
14 (28×28)	2.75E+08	2.75E+08	2.06E+08	3.20E+05	3.20E+05	3.56E+08
15 (30×30)	2.76E+08	2.76E+08	2.06E+08	3.21E+05	3.21E+05	3.57E+08
cs_no. (mesh)	**stresses 4BlinLag** [Pa]					
	$\max\|\sigma_{xx}\|$	$\max\|\sigma_{yy}\|$	$\max\|\tau_{xy}\|$	$\max\|\tau_{xz}\|$	$\max\|\tau_{yz}\|$	$\max\|\sigma_{VM}\|$
1 (2×2)	9.53E+07	9.53E+07	5.72E+07	1.25E+05	1.25E+05	1.38E+08
2 (4×4)	2.35E+08	2.35E+08	1.45E+08	2.29E+05	2.29E+05	2.55E+08
3 (6×6)	2.58E+08	2.58E+08	1.72E+08	2.62E+05	2.62E+05	3.00E+08
4 (8×8)	2.66E+08	2.66E+08	1.85E+08	2.80E+05	2.80E+05	3.21E+08
5 (10×10)	2.70E+08	2.70E+08	1.92E+08	2.91E+05	2.91E+05	3.33E+08
6 (12×12)	2.72E+08	2.72E+08	1.96E+08	2.98E+05	2.98E+05	3.40E+08
7 (14×14)	2.73E+08	2.73E+08	1.99E+08	3.03E+05	3.03E+05	3.45E+08
8 (16×16)	2.74E+08	2.74E+08	2.01E+08	3.08E+05	3.08E+05	3.48E+08
9 (18×18)	2.74E+08	2.74E+08	2.02E+08	3.11E+05	3.11E+05	3.50E+08
10 (20×20)	2.75E+08	2.75E+08	2.03E+08	3.13E+05	3.13E+05	3.52E+08
11 (22×22)	2.75E+08	2.75E+08	2.04E+08	3.16E+05	3.16E+05	3.54E+08
12 (24×24)	2.75E+08	2.75E+08	2.05E+08	3.17E+05	3.17E+05	3.55E+08
13 (26×26)	2.75E+08	2.75E+08	2.05E+08	3.19E+05	3.19E+05	3.56E+08
14 (28×28)	2.75E+08	2.75E+08	2.06E+08	3.20E+05	3.20E+05	3.56E+08
15 (30×30)	2.76E+08	2.76E+08	2.06E+08	3.21E+05	3.21E+05	3.57E+08
cs_no. (mesh)	**stresses deviations** [%]					
	$\max\|\sigma_{xx}\|$	$\max\|\sigma_{yy}\|$	$\max\|\tau_{xy}\|$	$\max\|\tau_{xz}\|$	$\max\|\tau_{yz}\|$	$\max\|\sigma_{VM}\|$
1 (2×2)	1.78E-05	1.78E-05	1.78E-05	33.33	33.33	1.29E-04
2 (4×4)	5.40E-05	5.40E-05	2.02E-04	4.76	4.76	9.44E-05
3 (6×6)	1.94E-04	1.94E-04	3.60E-06	1.28	1.28	1.15E-04
4 (8×8)	1.51E-04	1.51E-04	1.19E-05	0.82	0.82	1.26E-05
5 (10×10)	4.46E-05	4.46E-05	1.63E-04	0.46	0.46	8.68E-05
6 (12×12)	6.95E-05	6.95E-05	2.31E-04	0.33	0.33	1.84E-05
7 (14×14)	1.44E-04	1.44E-04	3.90E-05	0.23	0.23	2.54E-05
8 (16×16)	2.48E-05	2.48E-05	3.29E-05	0.18	0.18	8.07E-05
9 (18×18)	3.99E-05	3.99E-05	1.54E-04	0.14	0.14	8.01E-05
10 (20×20)	1.66E-04	1.66E-04	1.26E-04	0.11	0.11	6.78E-05
11 (22×22)	1.69E-04	1.69E-04	9.01E-05	0.09	0.09	3.42E-05
12 (24×24)	1.13E-04	1.13E-04	1.29E-04	0.08	0.08	1.18E-04
13 (26×26)	6.05E-05	6.05E-05	9.85E-05	0.06	0.06	9.36E-05
14 (28×28)	1.67E-05	1.67E-05	6.07E-05	0.06	0.06	9.61E-05
15 (30×30)	8.71E-05	8.71E-05	1.44E-04	0.05	0.05	8.12E-05

Table F.5: Comparison of natural freqs. obtained from the isotropic simply-supported plate validation model using AMAPDL and the present FEM platform, considering 15 different meshes.

cs_no. (mesh)	natural frequencies AMAPDL [Hz]				
	ω_1	ω_2	ω_3	ω_4	ω_5
1 (2×2)	12.63	2305.61	2561.59	2900.85	5015.82
2 (4×4)	10.05	30.96	30.96	50.50	107.17
3 (6×6)	9.66	26.30	26.30	42.53	63.63
4 (8×8)	9.53	24.96	24.96	40.20	55.18
5 (10×10)	9.47	24.39	24.39	39.18	51.89
6 (12×12)	9.44	24.08	24.08	38.64	50.25
7 (14×14)	9.42	23.90	23.90	38.32	49.30
8 (16×16)	9.41	23.79	23.79	38.12	48.70
9 (18×18)	9.40	23.71	23.71	37.98	48.30
10 (20×20)	9.39	23.65	23.65	37.88	48.01
11 (22×22)	9.39	23.61	23.61	37.81	47.81
12 (24×24)	9.38	23.58	23.58	37.75	47.65
13 (26×26)	9.38	23.55	23.55	37.71	47.52
14 (28×28)	9.38	23.54	23.54	37.68	47.43
15 (30×30)	9.38	23.52	23.52	37.65	47.35

cs_no. (mesh)	natural frequencies 4BlinLag [Hz]				
	ω_1	ω_2	ω_3	ω_4	ω_5
1 (2×2)	12.63	3486.91	3486.91	5420.62	7731.72
2 (4×4)	10.05	30.96	30.96	50.50	107.17
3 (6×6)	9.66	26.30	26.30	42.53	63.63
4 (8×8)	9.53	24.96	24.96	40.20	55.18
5 (10×10)	9.47	24.39	24.39	39.18	51.89
6 (12×12)	9.44	24.08	24.08	38.64	50.25
7 (14×14)	9.42	23.90	23.90	38.32	49.30
8 (16×16)	9.41	23.79	23.79	38.12	48.70
9 (18×18)	9.40	23.71	23.71	37.98	48.30
10 (20×20)	9.39	23.65	23.65	37.88	48.01
11 (22×22)	9.39	23.61	23.61	37.81	47.81
12 (24×24)	9.38	23.58	23.58	37.75	47.65
13 (26×26)	9.38	23.55	23.55	37.71	47.52
14 (28×28)	9.38	23.54	23.54	37.68	47.43
15 (30×30)	9.38	23.52	23.52	37.65	47.35

cs_no. (mesh)	natural frequencies deviations [%]				
	ω_1	ω_2	ω_3	ω_4	ω_5
1 (2×2)	7.92E-04	51.24	36.12	86.86	54.15
2 (4×4)	0.00E+00	3.23E-04	3.23E-04	1.98E-04	1.40E-03
3 (6×6)	2.07E-04	3.80E-04	3.80E-04	0.00E+00	3.14E-04
4 (8×8)	2.10E-04	0.00E+00	0.00E+00	0.00E+00	1.81E-04
5 (10×10)	2.11E-04	0.00E+00	0.00E+00	0.00E+00	1.93E-04
6 (12×12)	1.06E-04	0.00E+00	0.00E+00	0.00E+00	0.00E+00
7 (14×14)	3.18E-04	0.00E+00	0.00E+00	0.00E+00	2.03E-04
8 (16×16)	4.25E-04	0.00E+00	0.00E+00	0.00E+00	0.00E+00
9 (18×18)	2.13E-04	0.00E+00	0.00E+00	0.00E+00	0.00E+00
10 (20×20)	2.13E-04	0.00E+00	0.00E+00	0.00E+00	0.00E+00
11 (22×22)	1.07E-04	0.00E+00	0.00E+00	0.00E+00	0.00E+00
12 (24×24)	2.13E-04	0.00E+00	0.00E+00	0.00E+00	0.00E+00
13 (26×26)	2.13E-04	0.00E+00	0.00E+00	0.00E+00	0.00E+00
14 (28×28)	0.00E+00	0.00E+00	0.00E+00	0.00E+00	0.00E+00
15 (30×30)	0.00E+00	0.00E+00	0.00E+00	0.00E+00	0.00E+00

F.3 Multilayered smart structures

F.3.1 Statics

Schemes and results associated with Section 4.1.4.1.

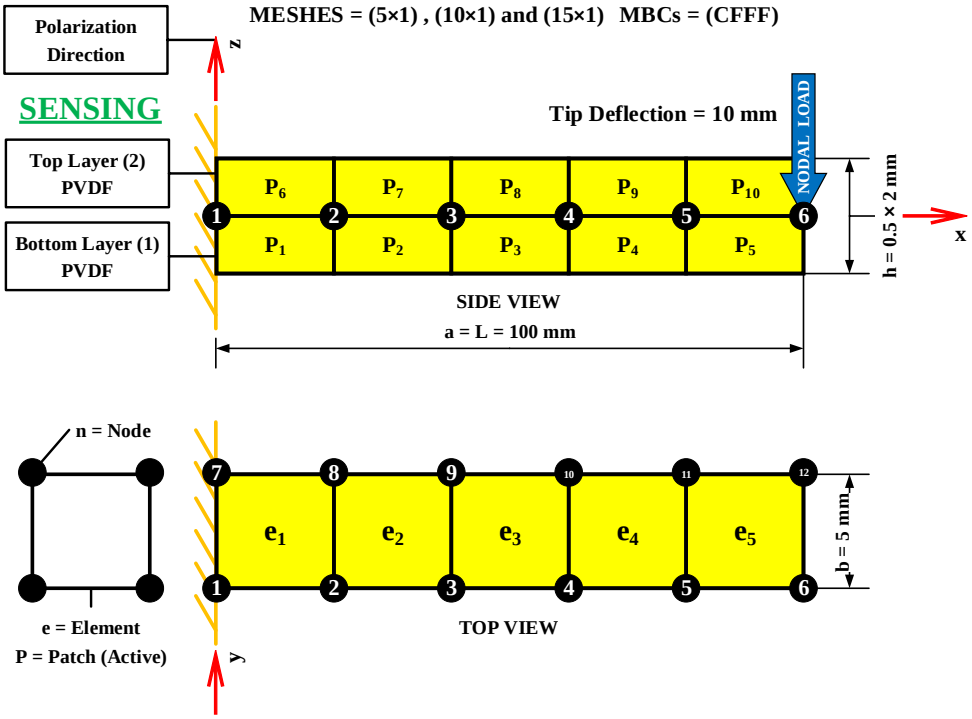

Figure F.3: Validation case study scheme of bimorph beam (sensing (CFFF)).

Figure F.4: Voltages obtained in the validation case study of bimorph beam (sensing (CFFF)).

Table F.6: Comparison of voltages' deviations, along x-coordinates, obtained in the validation case study of bimorph beam (sensing (CFFF)), with other references.

x [mm]	Hwang, W.-S. and Park (1993) [V]	present [V]	deviation [%]
10	298.8	286.1	4.3
30	200.6	222.5	10.9
50	149.4	158.9	6.4
70	93.9	95.4	1.6
90	29.9	31.8	6.4
x [mm]	Lima Jr. (1999) [V]	present [V]	deviation [%]
10	290.0	286.1	1.3
30	226.0	222.5	1.5
50	161.0	158.9	1.3
70	97.0	95.4	1.6
90	32.0	31.8	0.6
x [mm]	Pereira (2003) [V]	present [V]	deviation [%]
10	292.4	286.1	2.2
30	227.4	222.5	2.2
50	162.4	158.9	2.2
70	97.5	95.4	2.2
90	32.5	31.8	2.2

Table F.7: Comparison of voltages' deviations, for each element number, obtained in the validation case study of bimorph beam (sensing (CFFF)), with other references.

element	Q9-HSDT11P Correia et al. (2000) [V]	present [V]	deviation [%]
1	276	295	6.9
2	214	229	7.0
3	153	164	7.2
4	92	98	6.5
5	30	32	6.7
element	Q9-FSDT5P Correia et al. (2000) [V]	present [V]	deviation [%]
1	290	295	1.7
2	226	229	1.3
3	161	164	1.9
4	97	98	1.0
5	32	32	0.0

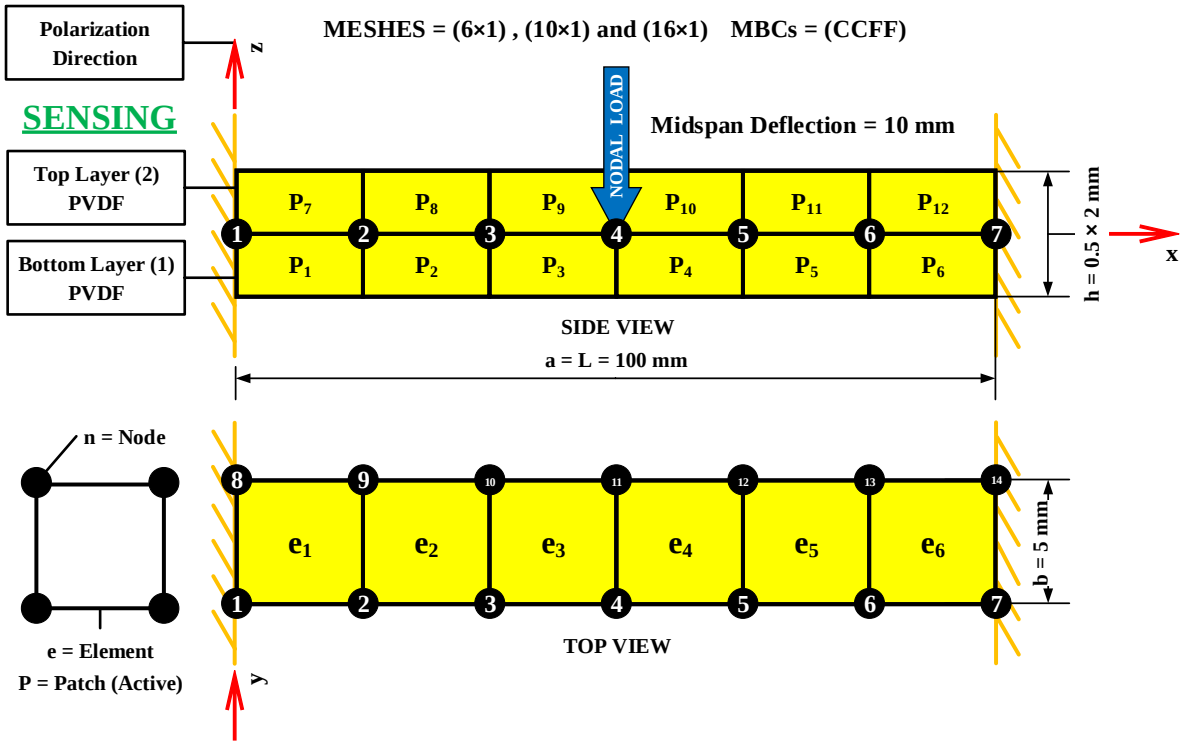

Figure F.5: Validation case study scheme of bimorph beam (sensing (CCFF)).

Figure F.6: Voltages obtained in the validation case study of bimorph beam (sensing (CCFF)).

F.3.2 Dynamics (free vibrations)

Schemes and results associated with Section 4.1.4.2.

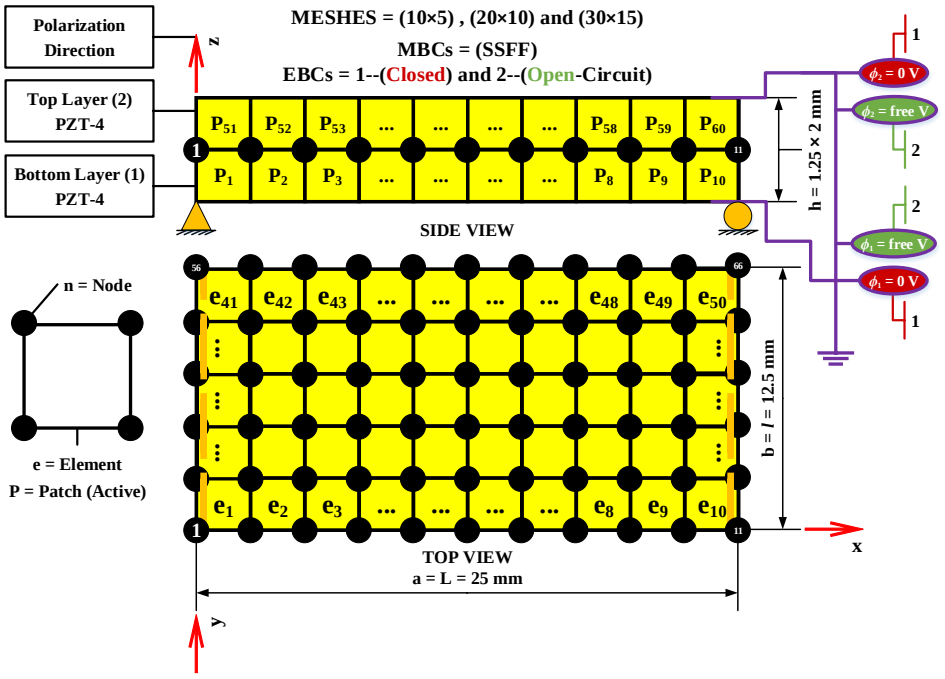

Figure F.7: Validation case study scheme of bimorph plate (dynamics (SSFF)) (Wang, 2004).

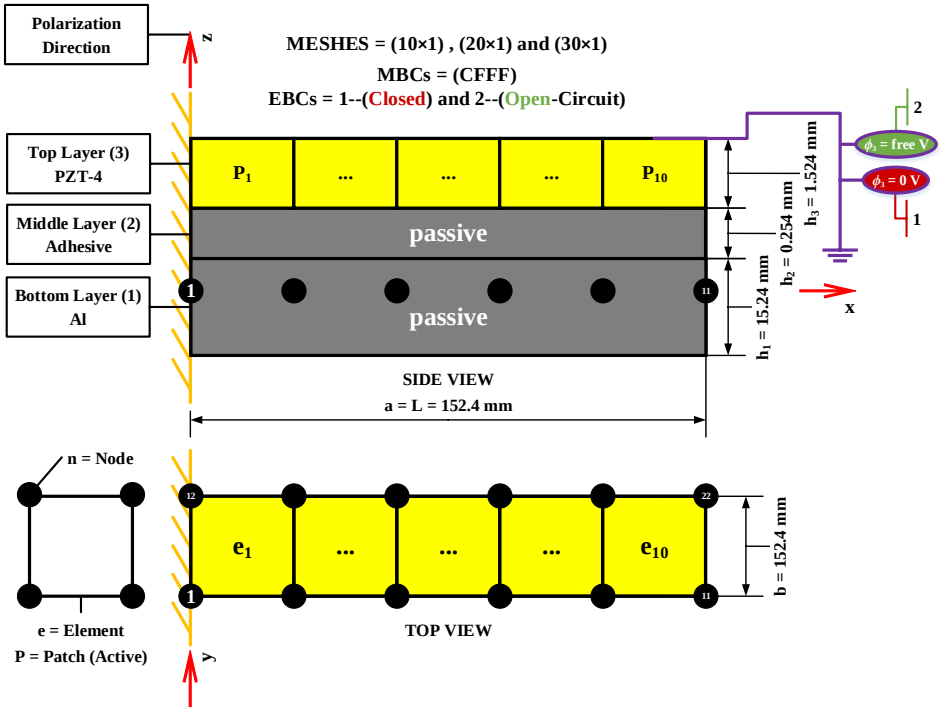

Figure F.8: Validation case study scheme of cantilever beam (dyn.) (Saravanos and Heyliger, 1995).

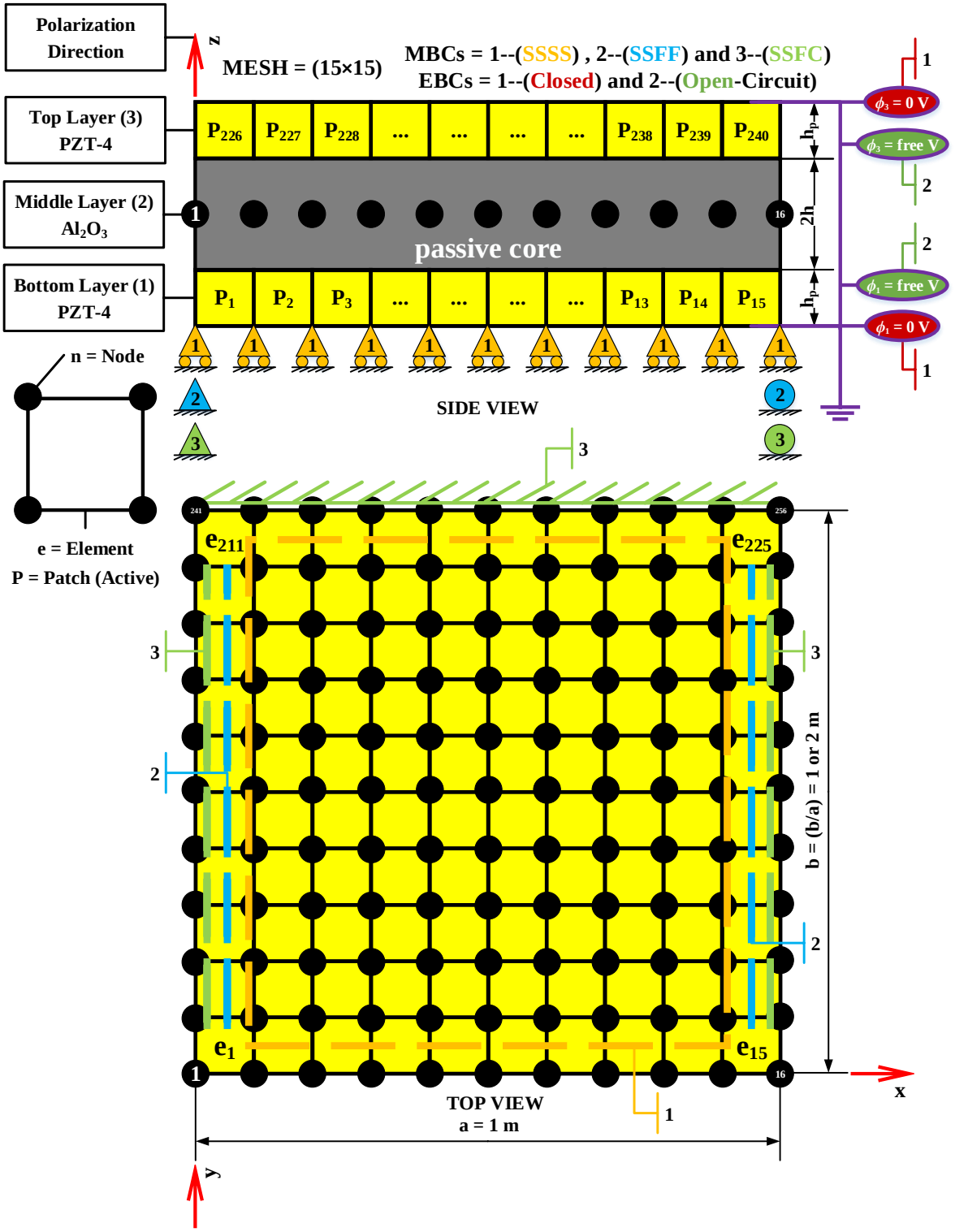

Figure F.9: Validation case study scheme of hybrid rectang. plate (dynamics) (Farsangi et al., 2013).

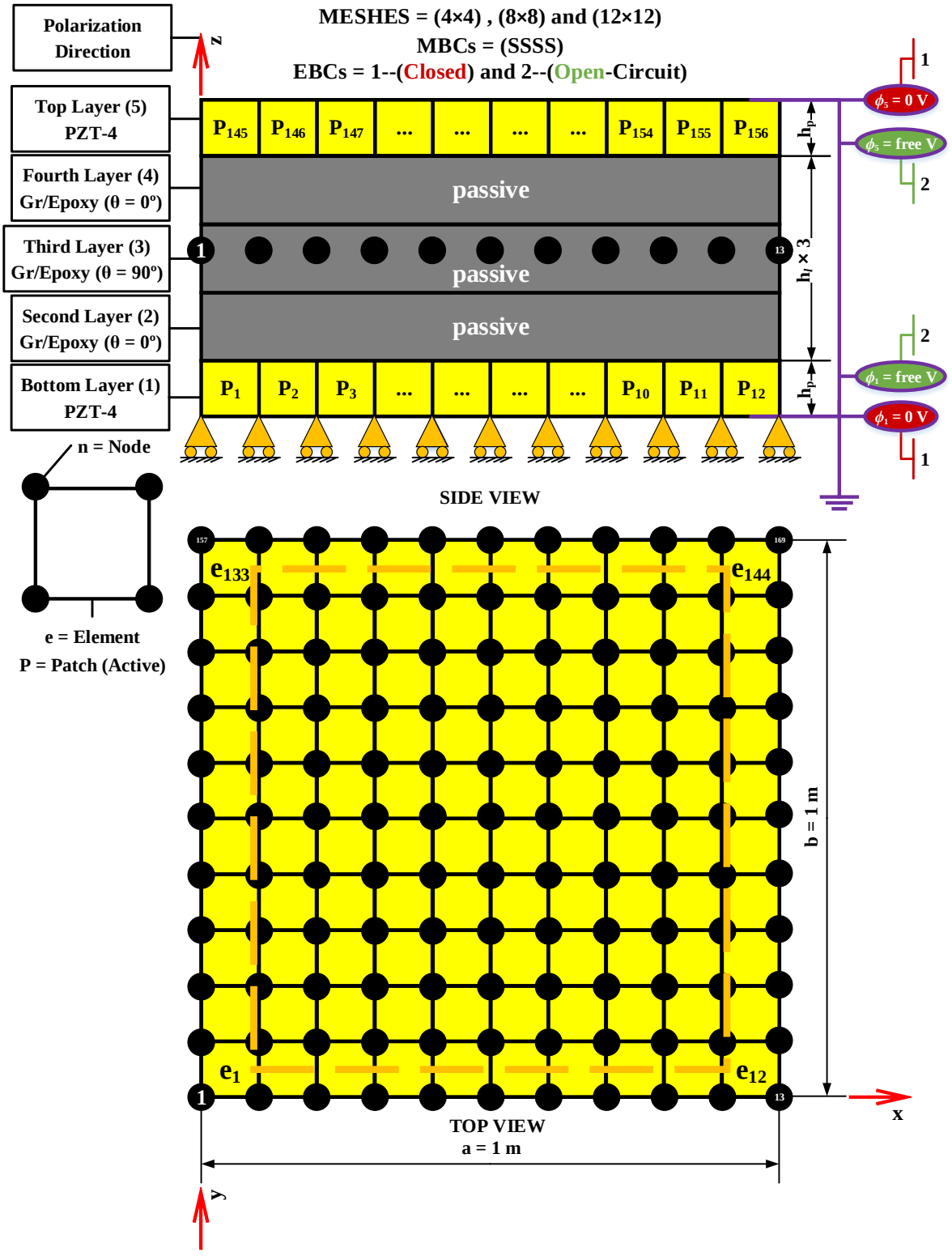

Figure F.10: Validation case study scheme of a 5-ply laminated plate (dyn.) (Saravanos et al., 1997).

Table F.8: Comparison of closed-circuit natural frequencies' deviations, for several approaches, obtained in the validation case study of bimorph plate, $L/h = 10$, (SSFF), with Wang (2004).

		Wang (2004)				
			deviation [%]			
mode no.	**approach**	**frequency** [Hz]	3D FEM	Wang $nsub = 2$	Wang $nsub = 1$	2D Analytical
1	target 3D FEM	6055	–	–	–	–
	target Wang $nsub = 2$	6242	–	–	–	–
	target Wang $nsub = 1$	6190	–	–	–	–
	target 2D Analytical	–	–	–	–	–
	present (10×5)	5930	2.06	4.99	4.20	–
	present (20×10)	5876	2.95	5.86	5.07	–
	present (30×15)	5866	3.12	6.02	5.23	–
2	target 3D FEM	14605	–	–	–	–
	target Wang $nsub = 2$	13827	–	–	–	–
	target Wang $nsub = 1$	13804	–	–	–	–
	target 2D Analytical	15769	–	–	–	–
	present (10×5)	14503	0.70	4.89	5.06	8.03
	present (20×10)	14463	0.97	4.60	4.77	8.28
	present (30×15)	14453	1.04	4.53	4.70	8.35
3	target 3D FEM	23276	–	–	–	–
	target Wang $nsub = 2$	23754	–	–	–	–
	target Wang $nsub = 1$	23561	–	–	–	–
	target 2D Analytical	–	–	–	–	–
	present (10×5)	23490	0.92	1.11	0.30	–
	present (20×10)	22687	2.53	4.49	3.71	–
	present (30×15)	22542	3.15	5.10	4.32	–
4	target 3D FEM	25220	–	–	–	–
	target Wang $nsub = 2$	26612	–	–	–	–
	target Wang $nsub = 1$	26612	–	–	–	–
	target 2D Analytical	–	–	–	–	–
	present (10×5)	33751	33.83	26.83	26.83	–
	present (20×10)	33039	31.00	24.15	24.15	–
	present (30×15)	32885	30.39	23.57	23.57	–
5	target 3D FEM	33990	–	–	–	–
	target Wang $nsub = 2$	33020	–	–	–	–
	target Wang $nsub = 1$	32902	–	–	–	–
	target 2D Analytical	–	–	–	–	–
	present (10×5)	34096	0.31	3.26	3.63	–
	present (20×10)	33535	1.34	1.56	1.92	–
	present (30×15)	33428	1.65	1.24	1.60	–
6	target 3D FEM	48941	–	–	–	–
	target Wang $nsub = 2$	49554	–	–	–	–
	target Wang $nsub = 1$	49197	–	–	–	–
	target 2D Analytical	59677	–	–	–	–
	present (10×5)	51684	5.61	4.30	5.06	13.39
	present (20×10)	48112	1.69	2.91	2.21	19.38
	present (30×15)	47485	2.97	4.17	3.48	20.43

Table F.9: Comparison of open-circuit natural frequencies' deviations, for several approaches, obtained in the validation case study of bimorph plate, $L/h = 10$, (SSFF), with Wang (2004).

		Wang (2004)				
			deviation [%]			
mode no.	**approach**	**frequency** [Hz]	3D FEM	Wang $nsub = 2$	Wang $nsub = 1$	2D Analytical
1	target 3D FEM	6141	–	–	–	–
	target Wang $nsub = 2$	6420	–	–	–	–
	target Wang $nsub = 1$	6379	–	–	–	–
	target 2D Analytical	–	–	–	–	–
	present (10×5)	6196	0.90	3.49	2.87	–
	present (20×10)	6139	0.03	4.37	3.76	–
	present (30×15)	6129	0.20	4.53	3.92	–
2	target 3D FEM	14634	–	–	–	–
	target Wang $nsub = 2$	13904	–	–	–	–
	target Wang $nsub = 1$	13886	–	–	–	–
	target 2D Analytical	16681	–	–	–	–
	present (10×5)	14598	0.25	4.99	5.13	12.49
	present (20×10)	14564	0.48	4.75	4.88	12.69
	present (30×15)	14555	0.54	4.68	4.82	12.74
3	target 3D FEM	23575	–	–	–	–
	target Wang $nsub = 2$	24425	–	–	–	–
	target Wang $nsub = 1$	24272	–	–	–	–
	target 2D Analytical	–	–	–	–	–
	present (10×5)	24522	4.02	0.40	1.03	–
	present (20×10)	23685	0.47	3.03	2.42	–
	present (30×15)	23534	0.17	3.65	3.04	–
4	target 3D FEM	25407	–	–	–	–
	target Wang $nsub = 2$	26967	–	–	–	–
	target Wang $nsub = 1$	26967	–	–	–	–
	target 2D Analytical	–	–	–	–	–
	present (10×5)	34253	34.82	27.02	27.02	–
	present (20×10)	33572	32.14	24.49	24.49	–
	present (30×15)	33422	31.55	23.94	23.94	–
5	target 3D FEM	34114	–	–	–	–
	target Wang $nsub = 2$	33424	–	–	–	–
	target Wang $nsub = 1$	33332	–	–	–	–
	target 2D Analytical	–	–	–	–	–
	present (10×5)	34647	1.56	3.66	3.95	–
	present (20×10)	34101	0.04	2.03	2.31	–
	present (30×15)	33998	0.34	1.72	2.00	–
6	target 3D FEM	49381	–	–	–	–
	target Wang $nsub = 2$	50792	–	–	–	–
	target Wang $nsub = 1$	50509	–	–	–	–
	target 2D Analytical	62375	–	–	–	–
	present (10×5)	53713	8.77	5.75	6.34	13.89
	present (20×10)	50043	1.34	1.47	0.92	19.77
	present (30×15)	49397	0.03	2.75	2.20	20.81

Table F.10: Comparison of natural frequencies' deviations, for several geometry variables, MBCs, EBCs, mesh (15×15), $a = 1\,\mathrm{m}$, obtained in the validation case study of hybrid rectangular plate, with Farsangi et al. (2013). a is the length and b the width of the plate, $2h$ the core thickness and h_p the thickness of each piezoelectric layer.

					Farsangi et al. (2013)								
					target [Hz]			**present** [Hz]			**deviation** [%]		
MBCs	b/a	$2h/a$	$h_p/(2h)$	**EBCs**	1st	2nd	3rd	1st	2nd	3rd	1st	2nd	3rd
(SSSS)	1	0.05	0.1	closed	422.966	1038.436	1633.073	416.805	1043.926	1632.761	1.46	0.53	0.02
				open	429.818	1054.813	1658.196	423.819	1060.754	1658.672	1.40	0.56	0.03
			0.2	closed	405.858	992.919	1556.567	399.443	997.233	1554.241	1.58	0.43	0.15
				open	418.993	1024.066	1604.047	412.907	1029.302	1603.346	1.45	0.51	0.04
		0.1	0.1	closed	816.534	1918.659	2910.463	805.409	1928.825	2910.731	1.36	0.53	0.01
				open	829.094	1945.644	2948.553	818.311	1956.674	2950.240	1.30	0.57	0.06
			0.2	closed	778.274	1810.841	2727.761	766.821	1818.722	2724.642	1.47	0.44	0.11
				open	802.005	1860.773	2797.491	791.282	1870.625	2797.640	1.34	0.53	0.01
	2	0.05	0.1	closed	265.592	422.966	682.077	263.629	419.837	693.730	0.74	0.74	1.71
				open	269.925	429.818	693.003	268.028	426.873	705.126	0.70	0.69	1.75
			0.2	closed	255.093	405.859	653.493	252.977	402.338	663.845	0.83	0.87	1.58
				open	263.416	418.994	674.366	261.436	415.846	685.649	0.75	0.75	1.67
		0.1	0.1	closed	519.218	816.537	1291.421	515.581	810.907	1312.160	0.70	0.69	1.61
				open	527.409	829.098	1310.531	523.911	823.837	1332.084	0.66	0.63	1.64
			0.2	closed	496.460	778.283	1225.300	492.566	771.983	1243.279	0.78	0.81	1.47
				open	512.042	802.024	1261.086	508.441	796.492	1280.716	0.70	0.69	1.56
(SSFF)	1	0.05	0.1	closed	206.189	337.986	763.342	207.075	327.039	747.498	0.43	3.24	2.08
				open	208.514	339.685	771.475	209.374	328.719	755.794	0.41	3.23	2.03
			0.2	closed	198.324	325.041	730.608	199.138	313.980	714.442	0.41	3.40	2.21
				open	202.751	328.241	746.136	203.513	317.151	730.317	0.38	3.38	2.12
		0.1	0.1	closed	404.375	649.789	1421.432	406.187	629.623	1395.124	0.45	3.10	1.85
				open	408.708	652.670	1435.764	410.478	632.507	1409.844	0.43	3.09	1.81
			0.2	closed	387.512	620.529	1341.602	389.177	600.342	1315.161	0.43	3.25	1.97
				open	395.673	625.835	1368.417	397.262	605.677	1342.826	0.40	3.22	1.87
	2	0.05	0.1	closed	209.027	248.830	374.330	209.966	245.709	365.732	0.45	1.25	2.30
				open	211.803	251.256	378.263	212.717	248.092	369.661	0.43	1.26	2.27
			0.2	closed	200.962	239.324	359.581	201.820	236.107	350.778	0.43	1.34	2.45
				open	206.264	243.933	367.098	207.071	240.633	358.303	0.39	1.35	2.40
		0.1	0.1	closed	410.083	485.305	721.037	411.957	479.439	705.053	0.46	1.21	2.22
				open	415.302	489.721	728.174	417.130	483.787	712.228	0.44	1.21	2.19
			0.2	closed	392.803	464.619	687.823	394.511	458.608	671.601	0.43	1.29	2.36
				open	402.675	472.893	701.266	404.294	466.761	685.166	0.40	1.30	2.30
(SSFC)	1	0.05	0.1	closed	268.928	690.400	874.395	265.009	681.644	886.650	1.46	1.27	1.40
				open	271.272	699.012	884.795	267.303	690.442	897.115	1.46	1.23	1.39
			0.2	closed	258.617	660.946	837.299	254.613	651.785	848.573	1.55	1.39	1.35
				open	263.059	677.343	856.916	258.963	668.576	868.307	1.56	1.29	1.33
		0.1	0.1	closed	521.069	1279.972	1626.329	514.077	1265.461	1648.362	1.34	1.13	1.35
				open	525.238	1294.296	1643.159	518.181	1280.201	1665.278	1.34	1.09	1.35
			0.2	closed	498.408	1210.157	1538.612	491.339	1195.171	1558.416	1.42	1.24	1.29
				open	506.178	1236.695	1569.413	499.002	1222.666	1589.416	1.42	1.13	1.27
	2	0.05	0.1	closed	223.354	335.483	545.498	223.019	330.447	544.195	0.15	1.50	0.24
				open	226.144	339.790	553.021	225.772	334.781	551.891	0.16	1.47	0.20
			0.2	closed	214.743	322.211	522.984	214.322	316.978	521.038	0.20	1.62	0.37
				open	220.065	330.453	537.360	219.569	325.286	535.771	0.23	1.56	0.30
		0.1	0.1	closed	437.198	647.963	1033.508	436.658	638.715	1030.967	0.12	1.43	0.25
				open	442.398	655.808	1046.700	441.792	646.645	1044.505	0.14	1.40	0.21
			0.2	closed	418.649	618.485	981.599	417.953	608.960	977.849	0.17	1.54	0.38
				open	428.458	633.282	1006.306	427.634	623.967	1003.316	0.19	1.47	0.30

F.3.3 Optimization

Schemes and results associated with Section 4.1.4.3.

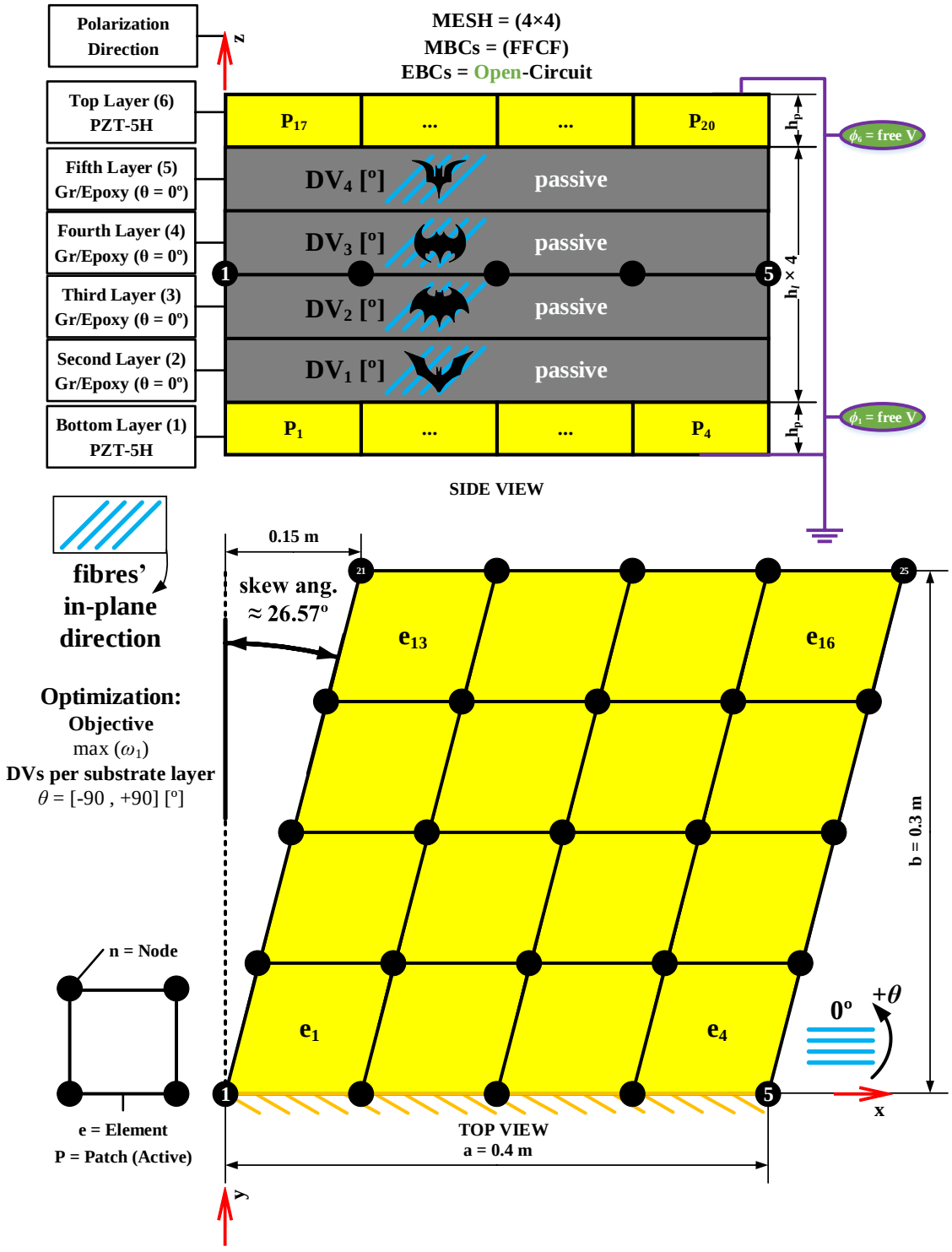

Figure F.11: Validation case study scheme of skew plate (optimization) (Correia et al., 2016).

Table F.11: Optimization results for 79 CSs, about the validation case study (Correia et al., 2001).

cs_no.	OF Best	DV1 (θ_1)	DV2 (θ_2)	DV3 (θ_3)	DV4 (θ_4)	PI	$Ngen$	n	f_{min}	$fmax$	r^0	A^0	$Fper_i$	$Fper_f$	Micro	α	γ	ϵ
79	314.045	70.3	71.2	70.4	70.5	52.02	150	20	0	1	0.5	1	0.08	0.01	TRUE	0.95	0.99	0.001
77	314.027	71.0	69.6	72.4	70.1	52.02	150	20	0	1	0.5	1	0.1	0.2	TRUE	0.95	0.99	0.001
78	313.960	70.6	72.1	75.5	70.0	51.98	150	20	0	1	0.5	1	0.05	0.01	TRUE	0.95	0.99	0.001
76	313.907	69.6	75.6	75.1	70.1	51.96	150	20	0	0.01	0.5	0.5	2	0.01	TRUE	0.98	0.97	0.001
77	313.883	70.7	75.0	73.9	71.5	51.95	50	10	0	1	0.5	1	0.05	0.01	TRUE	0.95	0.99	0.001
78	313.852	69.1	72.1	64.7	70.5	51.93	50	10	0	1	0.5	1	0.08	0.01	TRUE	0.95	0.99	0.001
79	313.491	69.6	74.8	59.8	72.0	51.76	50	10	0	1	0.5	1	0.1	0.2	FALSE	0.95	0.99	0.001
13	313.330	71.9	72.1	85.1	68.0	51.68	50	10	0	0.01	0.5	0.5	2	0.01	FALSE	0.98	0.97	0.001
14	312.973	69.5	59.9	55.8	72.1	51.51	50	10	0	1	0.5	1	2	0.01	FALSE	0.95	0.99	0.001
16	312.908	67.9	84.9	75.3	67.9	51.47	50	10	0	0.01	0.5	0.5	0.9	2	FALSE	0.98	0.97	0.001
17	312.849	71.2	76.8	90.0	68.7	51.45	50	10	0	1	0.5	1	0.1	0.2	TRUE	0.95	0.99	0.001
18	312.724	71.7	54.2	76.2	69.4	51.39	50	10	0	1	0.5	1	0.05	0.1	TRUE	0.95	0.99	0.001
19	312.552	66.0	73.5	76.8	70.5	51.30	50	10	0	1	0.5	1	0.2	0.5	FALSE	0.95	0.99	0.001
20	312.382	69.2	70.7	90.0	68.2	51.22	50	10	0	1	0.5	1	0.01	0.3	TRUE	0.95	0.99	0.001
21	312.297	74.4	55.0	79.2	65.3	51.18	50	10	0	1	0.5	1	0.01	0.05	TRUE	0.95	0.99	0.001
22	311.895	74.5	45.8	63.4	71.4	50.98	50	10	0	1	0.5	1	0.01	0.8	TRUE	0.95	0.99	0.001
23	311.876	72.0	-90.0	78.1	69.2	50.97	50	10	0	1	0.5	1	1	2	FALSE	0.95	0.99	0.001
21	311.793	70.0	-88.8	-90.0	67.2	50.93	50	10	0	0.01	0.5	0.5	0.2	0.5	FALSE	0.98	0.97	0.001
22	311.347	74.3	85.1	89.5	72.9	50.72	50	10	0	1	0.5	1	0	1.7	TRUE	0.95	0.99	0.001
23	310.943	69.3	90.0	48.5	74.2	50.52	50	10	0	1	0.5	1	0.05	0.1	FALSE	0.95	0.99	0.001
24	310.497	75.6	88.9	90.0	69.6	50.31	50	10	0	1	0.5	1	0.5	0.2	TRUE	0.95	0.99	0.001
25	310.315	73.8	44.6	90.0	69.7	50.22	50	10	0	1	0.5	1	0	1.5	FALSE	0.95	0.99	0.001
26	309.955	76.1	90.0	90.0	73.3	50.04	50	10	0	1	0.5	1	0.6	0.8	TRUE	0.95	0.99	0.001
27	308.995	73.6	34.0	45.8	75.2	49.58	50	10	0	1	0.5	1	0	1.5	TRUE	0.95	0.99	0.001
28	308.434	61.0	90.0	90.0	71.3	49.31	50	10	0	1	0.5	1	2	0	TRUE	0.95	0.99	0.001
29	308.391	70.0	66.2	28.7	67.8	49.29	50	10	0	1	0.5	1	0.01	1	TRUE	0.95	0.99	0.001
30	308.224	70.4	90.0	27.6	73.8	49.21	50	10	0	1	0.5	1	0.01	0.3	FALSE	0.95	0.99	0.001
31	308.174	76.3	-84.6	90.0	66.6	49.18	50	10	0	1	0.5	1	1.5	0	FALSE	0.95	0.99	0.001
6	308.073	70.8	63.5	14.3	71.4	49.13	50	10	0	0.01	0.5	0.5	0.5	0.2	FALSE	0.98	0.97	0.001
7	307.680	72.1	-40.7	84.9	69.3	48.94	50	10	0	1	0.5	1	0	2	FALSE	0.95	0.99	0.001
8	307.661	79.2	-90.0	90.0	70.5	48.93	50	10	0	1	0.5	1	0.01	0.2	FALSE	0.95	0.99	0.001
9	307.580	70.2	3.5	68.3	69.6	48.90	50	10	0	1	0.5	1	0.01	0.2	TRUE	0.95	0.99	0.001
10	307.521	72.5	64.7	76.1	80.3	48.87	50	10	0	1	0.5	1	2	1	TRUE	0.95	0.99	0.001
11	307.329	80.2	37.0	63.6	76.7	48.77	50	10	0	1	0.5	1	0.2	0.5	TRUE	0.95	0.99	0.001
12	306.931	71.1	26.5	60.6	63.8	48.58	50	10	0	1	0.5	1	0.6	0.8	FALSE	0.95	0.99	0.001
13	306.816	68.5	90.0	0.0	70.6	48.53	50	10	0	1	0.5	1	1.5	0	TRUE	0.95	0.99	0.001
14	306.461	64.4	-90.0	8.4	71.9	48.35	50	10	0	1	0.5	1	0.01	1	FALSE	0.95	0.99	0.001
15	306.147	76.4	31.0	-64.3	71.0	48.20	50	10	0	1	0.5	1	0.01	0.05	FALSE	0.95	0.99	0.001
16	303.865	71.3	-90.0	-90.0	56.0	47.10	50	10	0	1	0.5	1	2	0	FALSE	0.95	0.99	0.001
17	303.600	75.2	32.8	77.2	81.3	46.97	50	10	0	1	0.5	1	10	3	TRUE	0.95	0.99	0.001
18	303.280	75.7	22.1	62.0	61.8	46.81	50	10	0	1	0.5	1	2	0.01	TRUE	0.95	0.99	0.001
19	302.977	72.4	19.9	15.5	77.9	46.67	50	10	0	1	0.5	1	10	20	TRUE	0.95	0.99	0.001
20	302.918	-90.0	57.5	-88.0	70.5	46.64	50	10	0	1	0.5	1	0.08	0.01	FALSE	0.95	0.99	0.001
10	302.026	69.4	-72.6	52.2	-90.0	46.21	50	10	0	0.01	0.5	0.5	0.6	0.8	FALSE	0.98	0.97	0.001
11	301.988	64.3	54.8	36.3	60.4	46.19	50	10	0	1	0.5	1	0.9	2	TRUE	0.95	0.99	0.001
12	301.828	62.8	68.7	1.0	62.3	46.11	50	10	0	1	0.5	1	1	2	TRUE	0.95	0.99	0.001
11	301.522	75.6	62.4	55.8	-90.0	45.96	50	10	0	0.01	0.5	0.5	1.5	0	FALSE	0.98	0.97	0.001
25	300.658	78.1	-90.0	65.7	90.0	45.54	50	10	0	0.01	0.5	0.5	0	1.7	FALSE	0.98	0.97	0.001
26	300.426	86.2	24.2	79.3	72.5	45.43	50	10	0	1	0.5	1	0.01	0	TRUE	0.95	0.99	0.001
15	300.333	73.5	-90.0	40.0	-90.0	45.39	50	10	0	0.01	0.5	0.5	1	2	FALSE	0.98	0.97	0.001
16	299.565	76.5	28.5	69.7	55.5	45.01	50	10	0	1	0.5	1	0.5	5	TRUE	0.95	0.99	0.001
23	299.164	66.6	-16.4	-60.2	59.4	44.82	50	10	0	0.01	0.5	0.5	0.01	0.3	FALSE	0.98	0.97	0.001
8	299.035	70.8	90.0	33.1	-90.0	44.76	50	10	0	0.01	0.5	0.5	0	2	FALSE	0.98	0.97	0.001
9	298.786	78.4	48.5	39.8	90.0	44.64	50	10	0	1	0.5	1	0.5	0.2	FALSE	0.95	0.99	0.001
17	298.052	71.6	20.7	48.6	-90.0	44.28	50	10	0	0.01	0.5	0.5	0.1	0.2	FALSE	0.98	0.97	0.001
5	297.943	-90.0	62.5	90.0	60.7	44.23	50	10	0	0.01	0.5	0.5	0	1.5	FALSE	0.98	0.97	0.001
18	296.015	-90.0	-90.0	-79.0	74.9	43.30	50	10	0	0.01	0.5	0.5	2	0	FALSE	0.98	0.97	0.001
14	295.863	-90.0	-90.0	-78.0	72.7	43.22	50	10	0	0.01	0.5	0.5	2	1	FALSE	0.98	0.97	0.001
15	295.515	71.4	-69.8	-90.0	-90.0	43.05	50	10	0	1	0.5	1	2	1	FALSE	0.95	0.99	0.001
24	295.438	77.6	-90.0	-90.0	90.0	43.02	50	10	0	0.01	0.5	0.5	0.5	5	FALSE	0.98	0.97	0.001
25	295.420	75.7	-90.0	-90.0	90.0	43.01	50	10	0	1	0.5	1	0	1.7	FALSE	0.95	0.99	0.001
20	295.400	75.4	90.0	90.0	90.0	43.00	50	10	0	0.01	0.5	0.5	10	20	FALSE	0.98	0.97	0.001
21	295.397	-90.0	-90.0	-90.0	75.4	43.00	50	10	0	1	0.5	1	0.5	5	FALSE	0.95	0.99	0.001
22	295.119	71.7	90.0	19.5	90.0	42.86	50	10	0	1	0.5	1	0	2	TRUE	0.95	0.99	0.001
22	294.676	81.3	-90.0	-90.0	-90.0	42.65	50	10	0	0.01	0.5	0.5	10	3	FALSE	0.98	0.97	0.001
23	294.508	71.6	90.0	90.0	-90.0	42.57	50	10	0	1	0.5	1	0.9	2	FALSE	0.95	0.99	0.001
24	294.293	82.4	-90.0	-90.0	-90.0	42.46	50	10	0	1	0.5	1	10	3	FALSE	0.95	0.99	0.001
3	293.128	82.0	-22.5	-74.8	56.0	41.90	50	10	0	0.01	0.5	0.5	0.08	0.01	FALSE	0.98	0.97	0.001
4	292.465	-90.0	-86.8	90.0	84.8	41.58	50	10	0	1	0.5	1	0.01	0.8	FALSE	0.95	0.99	0.001
5	289.380	90.0	90.0	90.0	-90.0	40.08	50	10	0	1	0.5	1	10	20	FALSE	0.95	0.99	0.001
19	287.758	63.1	85.6	-5.0	51.9	39.30	50	10	0	0.01	0.5	0.5	0.01	0.05	FALSE	0.98	0.97	0.001
20	286.845	-90.0	24.9	-89.2	-90.0	38.86	50	10	0	1	0.5	1	0.01	0	FALSE	0.95	0.99	0.001
4	271.659	-58.5	59.2	38.5	72.6	31.51	50	10	0	0.01	0.5	0.5	0.01	1	FALSE	0.98	0.97	0.001
9	271.546	70.6	64.4	-38.7	40.7	31.45	50	10	0	0.01	0.5	0.5	0.01	0.2	FALSE	0.98	0.97	0.001
10	267.411	-90.0	52.5	68.6	-56.3	29.45	50	10	0	1	0.5	1	0.05	0.01	FALSE	0.95	0.99	0.001
12	260.165	72.8	10.3	73.1	-8.8	25.94	50	10	0	0.01	0.5	0.5	0.01	0.8	FALSE	0.98	0.97	0.001
7	258.917	77.1	-82.2	-90.0	-35.8	25.34	50	10	0	0.01	0.5	0.5	0.05	0.1	FALSE	0.98	0.97	0.001
1	254.946	77.4	52.5	-85.3	-19.4	23.42	50	10	0	0.01	0.5	0.5	0.01	0	FALSE	0.98	0.97	0.001
2	231.910	-52.2	-33.1	-50.8	-63.7	12.26	50	10	0	0.01	0.5	0.5	0.05	0.01	FALSE	0.98	0.97	0.001

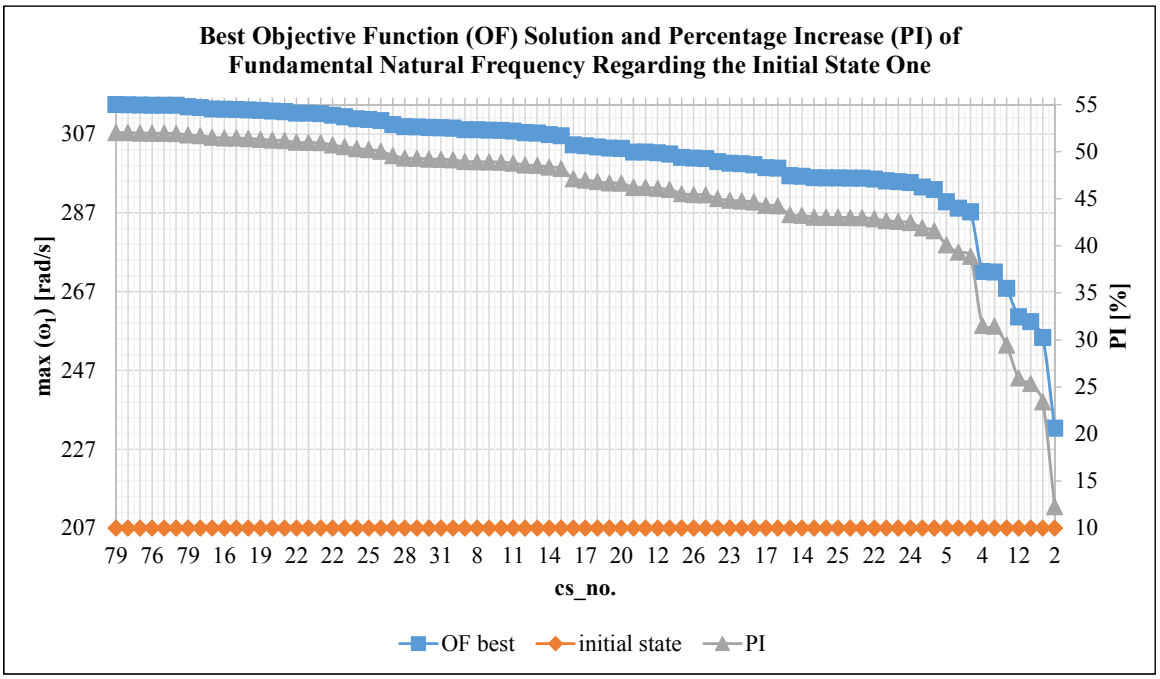

Figure F.12: Optimization results from 79 case studies of maximization of plates' natural frequency, considering different BA inputs; optimization validation (Correia et al., 2001). DVs are each ply angle θ [°]. Please click on the buttons above this caption to toggle between plotted results.

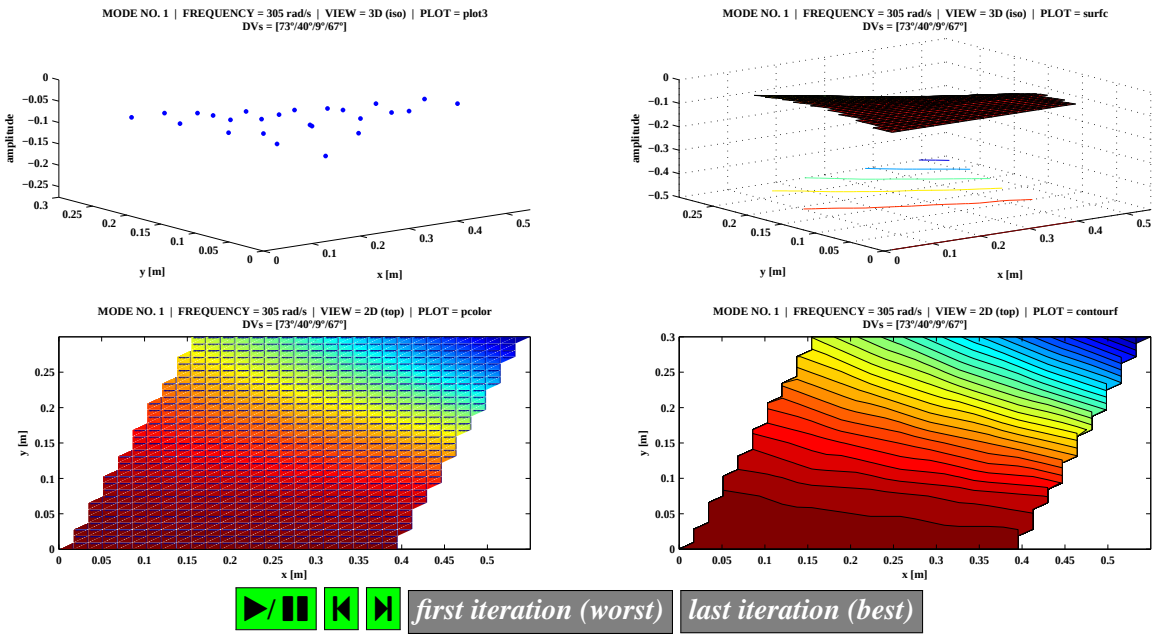

Figure F.13: 3D and 2D amplitude plots of the fundamental free vibrational mode along all successive best iterations found in the overall best case study, out of all 79, associated with Table F.11 (cs_no. 79). Please click on the buttons above this caption to run the animation and toggle between plotted results.

Appendix G

Parametric Studies: Schemes & Results

This appendix gathers schemes and results about several parametric case studies, in order to optimize the thesis' size.

G.1 Finite element convergence

Results associated with Section 4.2.1.

Table G.1: Convergence results of DOF $\max|w|$ [m], for all elements.

cs_no. (mesh)	$\max\|w\|$ [m]									
	AMAPDL	**4BlinLag**	**9BquadLag**	**16BcubLag**	**4BlinKrig**	**9BlinKrig**	**9BquadKrig**	**16BlinKrig**	**16BquadKrig**	**16BcubKrig**
1 (2×2)	1.79E-01	1.79E-01	2.36E-01	2.28E-01	3.46E-06	3.91E-05	2.10E-04	1.57E-03	1.05E-03	2.61E-02
2 (4×4)	2.23E-01	2.23E-01	2.29E-01	2.29E-01	1.70E-05	7.64E-05	3.01E-03	2.63E-03	1.13E-02	2.17E-01
3 (6×6)	2.26E-01	2.26E-01	2.29E-01	2.29E-01	3.94E-05	1.46E-04	1.42E-02	5.18E-03	4.59E-02	2.28E-01
4 (8×8)	2.27E-01	2.27E-01	2.29E-01	2.29E-01	7.07E-05	2.44E-04	3.93E-02	8.63E-03	1.01E-01	2.32E-01
5 (10×10)	2.28E-01	2.28E-01	2.29E-01	2.29E-01	1.11E-04	3.70E-04	7.67E-02	1.27E-02	1.54E-01	2.33E-01
6 (12×12)	2.28E-01	2.28E-01			1.60E-04					
7 (14×14)	2.28E-01	2.28E-01			2.18E-04					
8 (16×16)	2.28E-01	2.28E-01			2.85E-04					
9 (18×18)	2.28E-01	2.28E-01			3.61E-04					
10 (20×20)	2.28E-01	2.28E-01	–	–	4.46E-04	–	–	–	–	–
11 (22×22)	2.28E-01	2.28E-01			5.40E-04					
12 (24×24)	2.28E-01	2.28E-01			6.42E-04					
13 (26×26)	2.28E-01	2.28E-01			7.54E-04					
14 (28×28)	2.28E-01	2.28E-01			8.74E-04					
15 (30×30)	2.28E-01	2.28E-01			1.00E-03					

Table G.2: Convergence results of DOF $\max|\theta_x|$ [rad], for all elements.

cs_no. (mesh)	$\max\|\theta_x\|$ [rad]									
	AMAPDL	**4BlinLag**	**9BquadLag**	**16BcubLag**	**4BlinKrig**	**9BlinKrig**	**9BquadKrig**	**16BlinKrig**	**16BquadKrig**	**16BcubKrig**
1 (2×2)	7.15E-01	7.15E-01	7.74E-01	7.57E-01	1.02E-05	1.13E-04	7.84E-04	4.80E-03	3.36E-03	1.02E-01
2 (4×4)	7.53E-01	7.53E-01	7.59E-01	7.58E-01	5.45E-05	2.57E-04	1.02E-02	1.12E-02	3.85E-02	7.44E-01
3 (6×6)	7.56E-01	7.56E-01	7.58E-01	7.58E-01	1.28E-04	4.95E-04	4.71E-02	1.99E-02	1.54E-01	7.66E-01
4 (8×8)	7.57E-01	7.57E-01	7.58E-01	7.58E-01	2.30E-04	8.30E-04	1.29E-01	3.14E-02	3.35E-01	7.72E-01
5 (10×10)	7.57E-01	7.57E-01	7.58E-01	7.58E-01	3.62E-04	1.26E-03	2.52E-01	4.47E-02	5.11E-01	7.73E-01
6 (12×12)	7.58E-01	7.58E-01			5.23E-04					
7 (14×14)	7.58E-01	7.58E-01			7.13E-04					
8 (16×16)	7.58E-01	7.58E-01			9.32E-04					
9 (18×18)	7.58E-01	7.58E-01			1.18E-03					
10 (20×20)	7.58E-01	7.58E-01	–	–	1.46E-03	–	–	–	–	–
11 (22×22)	7.58E-01	7.58E-01			1.76E-03					
12 (24×24)	7.58E-01	7.58E-01			2.10E-03					
13 (26×26)	7.58E-01	7.58E-01			2.46E-03					
14 (28×28)	7.58E-01	7.58E-01			2.85E-03					
15 (30×30)	7.58E-01	7.58E-01			3.28E-03					

Table G.3: Convergence results of strain $\max|\epsilon_{xx}|$, for all elements.

cs_no. (mesh)	$\max\|\epsilon_{xx}\|$									
	AMAPDL	**4BlinLag**	**9BquadLag**	**16BcubLag**	**4BlinKrig**	**9BlinKrig**	**9BquadKrig**	**16BlinKrig**	**16BquadKrig**	**16BcubKrig**
1 (2×2)	3.58E-04	3.58E-04	9.86E-04	1.01E-03	5.12E-09	1.16E-07	5.19E-07	1.20E-05	1.85E-06	1.20E-04
2 (4×4)	8.81E-04	8.81E-04	1.02E-03	1.03E-03	6.46E-08	3.42E-07	1.23E-05	2.74E-05	3.77E-05	1.05E-03
3 (6×6)	9.68E-04	9.68E-04	1.03E-03	1.03E-03	1.68E-07	6.47E-07	6.26E-05	5.08E-05	1.83E-04	1.05E-03
4 (8×8)	9.98E-04	9.98E-04	1.03E-03	1.03E-03	3.13E-07	1.07E-06	1.78E-04	8.05E-05	4.26E-04	1.06E-03
5 (10×10)	1.01E-03	1.01E-03	1.03E-03	1.04E-03	5.00E-07	1.62E-06	3.50E-04	1.15E-04	6.71E-04	1.06E-03
6 (12×12)	1.02E-03	1.02E-03			7.28E-07					
7 (14×14)	1.02E-03	1.02E-03			9.98E-07					
8 (16×16)	1.03E-03	1.03E-03			1.31E-06					
9 (18×18)	1.03E-03	1.03E-03			1.66E-06					
10 (20×20)	1.03E-03	1.03E-03	–	–	2.05E-06	–	–	–	–	–
11 (22×22)	1.03E-03	1.03E-03			2.49E-06					
12 (24×24)	1.03E-03	1.03E-03			2.96E-06					
13 (26×26)	1.03E-03	1.03E-03			3.48E-06					
14 (28×28)	1.03E-03	1.03E-03			4.04E-06					
15 (30×30)	1.03E-03	1.03E-03			4.63E-06					

Table G.4: Convergence results of strain $\max|\gamma_{xy}|$, for all elements.

cs_no. (mesh)	$\max\|\gamma_{xy}\|$									
	AMAPDL	**4BlinLag**	**9BquadLag**	**16BcubLag**	**4BlinKrig**	**9BlinKrig**	**9BquadKrig**	**16BlinKrig**	**16BquadKrig**	**16BcubKrig**
1 (2×2)	7.15E-04	7.15E-04	2.05E-03	2.42E-03	1.02E-08	2.81E-07	8.44E-07	1.85E-05	6.26E-06	1.09E-04
2 (4×4)	1.81E-03	1.81E-03	2.43E-03	2.55E-03	1.32E-07	8.65E-07	2.42E-05	6.46E-05	1.03E-04	1.80E-03
3 (6×6)	2.15E-03	2.15E-03	2.52E-03	2.58E-03	3.65E-07	1.76E-06	1.32E-04	1.49E-04	4.58E-04	2.23E-03
4 (8×8)	2.31E-03	2.31E-03	2.55E-03	2.59E-03	7.01E-07	2.99E-06	3.86E-04	2.62E-04	1.04E-03	2.42E-03
5 (10×10)	2.40E-03	2.40E-03	2.57E-03	2.60E-03	1.14E-06	4.55E-06	7.78E-04	3.91E-04	1.64E-03	2.51E-03
6 (12×12)	2.45E-03	2.45E-03			1.68E-06					
7 (14×14)	2.49E-03	2.49E-03			2.32E-06					
8 (16×16)	2.51E-03	2.51E-03			3.05E-06					
9 (18×18)	2.53E-03	2.53E-03			3.89E-06					
10 (20×20)	2.54E-03	2.54E-03	–	–	4.83E-06	–	–	–	–	–
11 (22×22)	2.55E-03	2.55E-03			5.86E-06					
12 (24×24)	2.56E-03	2.56E-03			6.99E-06					
13 (26×26)	2.57E-03	2.57E-03			8.22E-06					
14 (28×28)	2.57E-03	2.57E-03			9.55E-06					
15 (30×30)	2.58E-03	2.58E-03			1.10E-05					

Table G.5: Convergence results of strain $\max|\gamma_{xz}|$, for all elements.

cs_no. (mesh)	$\max\|\gamma_{xz}\|$									
	AMAPDL	**4BlinLag**	**9BquadLag**	**16BcubLag**	**4BlinKrig**	**9BlinKrig**	**9BquadKrig**	**16BlinKrig**	**16BquadKrig**	**16BcubKrig**
1 (2×2)	3.60E-06	1.87E-06	3.55E-06	4.20E-06	9.04E-07	5.50E-06	4.12E-06	3.01E-05	1.25E-05	2.61E-05
2 (4×4)	4.56E-06	3.44E-06	4.27E-06	4.64E-06	2.08E-06	1.07E-05	2.60E-06	6.33E-05	5.26E-05	2.07E-05
3 (6×6)	4.55E-06	3.93E-06	4.53E-06	4.78E-06	2.60E-06	1.12E-05	1.67E-05	8.29E-05	1.01E-04	3.30E-06
4 (8×8)	4.57E-06	4.20E-06	4.67E-06	4.85E-06	2.88E-06	1.11E-05	3.86E-05	8.98E-05	1.31E-04	4.17E-06
5 (10×10)	4.61E-06	4.36E-06	4.75E-06	4.90E-06	3.05E-06	1.10E-05	5.56E-05	9.00E-05	1.34E-04	4.58E-06
6 (12×12)	4.65E-06	4.47E-06			3.17E-06					
7 (14×14)	4.69E-06	4.55E-06			3.25E-06					
8 (16×16)	4.72E-06	4.61E-06			3.32E-06					
9 (18×18)	4.75E-06	4.66E-06			3.37E-06					
10 (20×20)	4.77E-06	4.70E-06	–	–	3.41E-06	–	–	–	–	–
11 (22×22)	4.79E-06	4.73E-06			3.44E-06					
12 (24×24)	4.81E-06	4.76E-06			3.47E-06					
13 (26×26)	4.82E-06	4.78E-06			3.49E-06					
14 (28×28)	4.84E-06	4.80E-06			3.51E-06					
15 (30×30)	4.85E-06	4.82E-06			3.53E-06					

Table G.6: Convergence results of stress $\max|\sigma_{xx}|$ [Pa], for all elements.

cs_no. (mesh)	$\max\|\sigma_{xx}\|$ [Pa]									
	AMAPDL	**4BlinLag**	**9BquadLag**	**16BcubLag**	**4BlinKrig**	**9BlinKrig**	**9BquadKrig**	**16BlinKrig**	**16BquadKrig**	**16BcubKrig**
1 (2×2)	9.53E+07	9.53E+07	2.63E+08	2.70E+08	1.36E+03	3.09E+04	1.38E+05	3.19E+06	4.93E+05	3.19E+07
2 (4×4)	2.35E+08	2.35E+08	2.71E+08	2.75E+08	1.72E+04	9.13E+04	3.28E+06	7.31E+06	1.01E+07	2.79E+08
3 (6×6)	2.58E+08	2.58E+08	2.74E+08	2.76E+08	4.48E+04	1.73E+05	1.67E+07	1.35E+07	4.87E+07	2.81E+08
4 (8×8)	2.66E+08	2.66E+08	2.75E+08	2.76E+08	8.35E+04	2.86E+05	4.74E+07	2.15E+07	1.14E+08	2.84E+08
5 (10×10)	2.70E+08	2.70E+08	2.75E+08	2.76E+08	1.33E+05	4.33E+05	9.33E+07	3.07E+07	1.79E+08	2.84E+08
6 (12×12)	2.72E+08	2.72E+08			1.94E+05					
7 (14×14)	2.73E+08	2.73E+08			2.66E+05					
8 (16×16)	2.74E+08	2.74E+08			3.49E+05					
9 (18×18)	2.74E+08	2.74E+08			4.43E+05					
10 (20×20)	2.75E+08	2.75E+08	–	–	5.48E+05	–	–	–	–	–
11 (22×22)	2.75E+08	2.75E+08			6.64E+05					
12 (24×24)	2.75E+08	2.75E+08			7.90E+05					
13 (26×26)	2.75E+08	2.75E+08			9.28E+05					
14 (28×28)	2.75E+08	2.75E+08			1.08E+06					
15 (30×30)	2.76E+08	2.76E+08			1.24E+06					

Table G.7: Convergence results of stress $\max|\tau_{xy}|$ [Pa], for all elements.

cs_no. (mesh)	$\max\|\tau_{xy}\|$ [Pa]									
	AMAPDL	**4BlinLag**	**9BquadLag**	**16BcubLag**	**4BlinKrig**	**9BlinKrig**	**9BquadKrig**	**16BlinKrig**	**16BquadKrig**	**16BcubKrig**
1 (2×2)	5.72E+07	5.72E+07	1.64E+08	1.94E+08	8.19E+02	2.25E+04	6.75E+04	1.48E+06	5.01E+05	8.75E+06
2 (4×4)	1.45E+08	1.45E+08	1.94E+08	2.04E+08	1.06E+04	6.92E+04	1.94E+06	5.17E+06	8.22E+06	1.44E+08
3 (6×6)	1.72E+08	1.72E+08	2.01E+08	2.07E+08	2.92E+04	1.41E+05	1.05E+07	1.19E+07	3.67E+07	1.78E+08
4 (8×8)	1.85E+08	1.85E+08	2.04E+08	2.07E+08	5.61E+04	2.39E+05	3.09E+07	2.10E+07	8.35E+07	1.94E+08
5 (10×10)	1.92E+08	1.92E+08	2.06E+08	2.08E+08	9.11E+04	3.64E+05	6.22E+07	3.13E+07	1.31E+08	2.01E+08
6 (12×12)	1.96E+08	1.96E+08			1.34E+05					
7 (14×14)	1.99E+08	1.99E+08			1.85E+05					
8 (16×16)	2.01E+08	2.01E+08			2.44E+05					
9 (18×18)	2.02E+08	2.02E+08			3.11E+05					
10 (20×20)	2.03E+08	2.03E+08	–	–	3.86E+05	–	–	–	–	–
11 (22×22)	2.04E+08	2.04E+08			4.69E+05					
12 (24×24)	2.05E+08	2.05E+08			5.59E+05					
13 (26×26)	2.05E+08	2.05E+08			6.58E+05					
14 (28×28)	2.06E+08	2.06E+08			7.64E+05					
15 (30×30)	2.06E+08	2.06E+08			8.78E+05					

Table G.8: Convergence results of stress $\max|\tau_{xz}|$ [Pa], for all elements.

cs_no. (mesh)	$\max\|\tau_{xz}\|$ [Pa]									
	AMAPDL	**4BlinLag**	**9BquadLag**	**16BcubLag**	**4BlinKrig**	**9BlinKrig**	**9BquadKrig**	**16BlinKrig**	**16BquadKrig**	**16BcubKrig**
1 (2×2)	9.38E+04	1.25E+05	2.36E+05	2.80E+05	6.03E+04	3.66E+05	2.75E+05	2.01E+06	8.31E+05	1.74E+06
2 (4×4)	2.19E+05	2.29E+05	2.84E+05	3.09E+05	1.39E+05	7.12E+05	1.73E+05	4.22E+06	3.51E+06	1.38E+06
3 (6×6)	2.59E+05	2.62E+05	3.02E+05	3.19E+05	1.73E+05	7.47E+05	1.11E+06	5.52E+06	6.71E+06	2.20E+05
4 (8×8)	2.77E+05	2.80E+05	3.11E+05	3.24E+05	1.92E+05	7.43E+05	2.57E+06	5.99E+06	8.72E+06	2.78E+05
5 (10×10)	2.89E+05	2.91E+05	3.16E+05	3.26E+05	2.03E+05	7.36E+05	3.70E+06	6.00E+06	8.97E+06	3.05E+05
6 (12×12)	2.97E+05	2.98E+05			2.11E+05					
7 (14×14)	3.03E+05	3.03E+05			2.17E+05					
8 (16×16)	3.07E+05	3.08E+05			2.21E+05					
9 (18×18)	3.10E+05	3.11E+05			2.24E+05					
10 (20×20)	3.13E+05	3.13E+05	–	–	2.27E+05	–	–	–	–	–
11 (22×22)	3.15E+05	3.16E+05			2.29E+05					
12 (24×24)	3.17E+05	3.17E+05			2.31E+05					
13 (26×26)	3.19E+05	3.19E+05			2.33E+05					
14 (28×28)	3.20E+05	3.20E+05			2.34E+05					
15 (30×30)	3.21E+05	3.21E+05			2.35E+05					

Table G.9: Convergence results of stress $\max|\sigma_{VM}|$ [Pa], for all elements.

cs_no. (mesh)	$\max\|\sigma_{VM}\|$ [Pa]									
	AMAPDL	**4BlinLag**	**9BquadLag**	**16BcubLag**	**4BlinKrig**	**9BlinKrig**	**9BquadKrig**	**16BlinKrig**	**16BquadKrig**	**16BcubKrig**
1 (2×2)	1.38E+08	1.38E+08	2.88E+08	3.36E+08	1.48E+05	8.99E+05	6.97E+05	6.39E+06	2.27E+06	3.56E+07
2 (4×4)	2.55E+08	2.55E+08	3.37E+08	3.54E+08	2.41E+05	1.25E+06	3.45E+06	1.13E+07	1.50E+07	2.82E+08
3 (6×6)	3.00E+08	3.00E+08	3.49E+08	3.58E+08	3.01E+05	1.30E+06	1.83E+07	2.17E+07	6.39E+07	3.11E+08
4 (8×8)	3.21E+08	3.21E+08	3.54E+08	3.59E+08	3.33E+05	1.29E+06	5.35E+07	3.68E+07	1.45E+08	3.36E+08
5 (10×10)	3.33E+08	3.33E+08	3.57E+08	3.60E+08	3.54E+05	1.30E+06	1.08E+08	5.44E+07	2.27E+08	3.48E+08
6 (12×12)	3.40E+08	3.40E+08			3.68E+05					
7 (14×14)	3.45E+08	3.45E+08			3.79E+05					
8 (16×16)	3.48E+08	3.48E+08			4.29E+05					
9 (18×18)	3.50E+08	3.50E+08			5.43E+05					
10 (20×20)	3.52E+08	3.52E+08	–	–	6.71E+05	–	–	–	–	–
11 (22×22)	3.54E+08	3.54E+08			8.14E+05					
12 (24×24)	3.55E+08	3.55E+08			9.70E+05					
13 (26×26)	3.56E+08	3.56E+08			1.14E+06					
14 (28×28)	3.56E+08	3.56E+08			1.32E+06					
15 (30×30)	3.57E+08	3.57E+08			1.52E+06					

Table G.10: Convergence results of natural frequency ω_1 [Hz], for all elements.

cs_no. (mesh)	ω_1 [Hz]									
	AMAPDL	**4BlinLag**	**9BquadLag**	**16BcubLag**	**4BlinKrig**	**9BlinKrig**	**9BquadKrig**	**16BlinKrig**	**16BquadKrig**	**16BcubKrig**
1 (2×2)	12.63	12.63	9.46	9.37	2780.20	735.76	315.93	75.84	138.94	27.50
2 (4×4)	10.05	10.05	9.37	9.37	1147.99	514.73	82.32	84.41	42.40	9.66
3 (6×6)	9.66	9.66	9.37	9.37	733.01	370.41	37.84	61.07	21.00	9.40
4 (8×8)	9.53	9.53	9.37	9.37	541.36	285.77	22.71	47.66	14.17	9.30
5 (10×10)	9.47	9.47	9.37	9.37	430.02	231.73	16.24	39.46	11.44	9.28
6 (12×12)	9.44	9.44			356.98					
7 (14×14)	9.42	9.42			305.30					
8 (16×16)	9.41	9.41			266.77					
9 (18×18)	9.40	9.40			236.91					
10 (20×20)	9.39	9.39	–	–	213.10	–	–	–	–	–
11 (22×22)	9.39	9.39			193.66					
12 (24×24)	9.38	9.38			177.48					
13 (26×26)	9.38	9.38			163.82					
14 (28×28)	9.38	9.38			152.12					
15 (30×30)	9.38	9.38			141.98					

Table G.11: Convergence results of natural frequency ω_2 [Hz], for all elements.

cs_no. (mesh)	ω_2 [Hz]									
	AMAPDL	**4BlinLag**	**9BquadLag**	**16BcubLag**	**4BlinKrig**	**9BlinKrig**	**9BquadKrig**	**16BlinKrig**	**16BquadKrig**	**16BcubKrig**
1 (2×2)	2305.61	3486.91	25.18	23.67	3491.28	1847.64	1058.59	96.73	318.44	122.81
2 (4×4)	30.96	30.96	23.62	23.42	3244.93	1137.43	274.38	165.89	135.15	27.02
3 (6×6)	26.30	26.30	23.46	23.42	2122.46	822.12	120.90	131.56	64.47	23.98
4 (8×8)	24.96	24.96	23.43	23.42	1525.92	640.48	70.31	107.51	41.34	23.54
5 (10×10)	24.39	24.39	23.42	23.42	1196.58	522.76	48.38	91.55	32.07	23.43
6 (12×12)	24.08	24.08			986.33					
7 (14×14)	23.90	23.90			839.90					
8 (16×16)	23.79	23.79			731.82					
9 (18×18)	23.71	23.71			648.66					
10 (20×20)	23.65	23.65	–	–	582.64	–	–	–	–	–
11 (22×22)	23.61	23.61			528.93					
12 (24×24)	23.58	23.58			484.36					
13 (26×26)	23.55	23.55			446.78					
14 (28×28)	23.54	23.54			414.65					
15 (30×30)	23.52	23.52			386.87					

Table G.12: Convergence results of natural frequency ω_3 [Hz], for all elements.

cs_no. (mesh)	ω_3 [Hz]									
	AMAPDL	**4BlinLag**	**9BquadLag**	**16BcubLag**	**4BlinKrig**	**9BlinKrig**	**9BquadKrig**	**16BlinKrig**	**16BquadKrig**	**16BcubKrig**
1 (2×2)	2561.59	3486.91	25.18	23.67	3491.28	1847.64	1058.59	96.73	447.86	122.81
2 (4×4)	30.96	30.96	23.62	23.42	3244.93	1137.43	274.38	165.89	135.16	27.02
3 (6×6)	26.30	26.30	23.46	23.42	2122.46	822.12	120.90	131.56	64.47	23.98
4 (8×8)	24.96	24.96	23.43	23.42	1525.92	640.48	70.31	107.51	41.34	23.54
5 (10×10)	24.39	24.39	23.42	23.42	1196.58	522.76	48.38	91.55	32.07	23.43
6 (12×12)	24.08	24.08			986.33					
7 (14×14)	23.90	23.90			839.90					
8 (16×16)	23.79	23.79			731.82					
9 (18×18)	23.71	23.71			648.66					
10 (20×20)	23.65	23.65	–	–	582.64	–	–	–	–	–
11 (22×22)	23.61	23.61			528.93					
12 (24×24)	23.58	23.58			484.36					
13 (26×26)	23.55	23.55			446.78					
14 (28×28)	23.54	23.54			414.65					
15 (30×30)	23.52	23.52			386.87					

Table G.13: Convergence results of natural frequency ω_4 [Hz], for all elements.

cs_no. (mesh)	ω_4 [Hz]									
	AMAPDL	**4BlinLag**	**9BquadLag**	**16BcubLag**	**4BlinKrig**	**9BlinKrig**	**9BquadKrig**	**16BlinKrig**	**16BquadKrig**	**16BcubKrig**
1 (2×2)	2900.85	5420.62	39.81	38.00	5931.45	2051.70	1461.62	114.86	447.86	434.48
2 (4×4)	50.50	50.50	37.85	37.47	3554.26	1471.97	632.67	209.39	280.05	64.01
3 (6×6)	42.53	42.53	37.55	37.47	3198.89	1244.77	272.74	208.90	142.03	39.75
4 (8×8)	40.20	40.20	37.49	37.47	2296.22	1030.04	153.47	176.57	88.23	37.94
5 (10×10)	39.18	39.18	37.48	37.47	1786.74	865.46	103.49	151.32	65.85	37.60
6 (12×12)	38.64	38.64			1466.38					
7 (14×14)	38.32	38.32			1245.36					
8 (16×16)	38.12	38.12			1083.22					
9 (18×18)	37.98	37.98			958.99					
10 (20×20)	37.88	37.88	–	–	860.66	–	–	–	–	–
11 (22×22)	37.81	37.81			780.83					
12 (24×24)	37.75	37.75			714.71					
13 (26×26)	37.71	37.71			659.02					
14 (28×28)	37.68	37.68			611.47					
15 (30×30)	37.65	37.65			570.38					

Table G.14: Convergence results of natural frequency ω_5 [Hz], for all elements.

cs_no. (mesh)	ω_5 [Hz]									
	AMAPDL	**4BlinLag**	**9BquadLag**	**16BcubLag**	**4BlinKrig**	**9BlinKrig**	**9BquadKrig**	**16BlinKrig**	**16BquadKrig**	**16BcubKrig**
1 (2×2)	5015.82	7731.72	85.72	50.32	7983.67	3214.47	3169.10	473.72	814.42	446.97
2 (4×4)	107.17	107.17	49.02	46.92	3554.26	2268.93	667.12	215.61	316.39	64.02
3 (6×6)	63.63	63.63	47.30	46.84	3198.89	1573.57	272.74	212.87	142.03	49.90
4 (8×8)	55.18	55.18	46.99	46.83	3182.84	1197.72	153.47	186.49	88.23	47.71
5 (10×10)	51.89	51.89	46.90	46.83	2637.43	969.93	103.49	165.53	67.10	47.10
6 (12×12)	50.25	50.25			2147.74					
7 (14×14)	49.30	49.30			1815.30					
8 (16×16)	48.70	48.70			1574.01					
9 (18×18)	48.30	48.30			1390.46					
10 (20×20)	48.01	48.01	–	–	1245.91	–	–	–	–	–
11 (22×22)	47.81	47.81			1129.02					
12 (24×24)	47.65	47.65			1032.46					
13 (26×26)	47.52	47.52			951.31					
14 (28×28)	47.43	47.43			882.14					
15 (30×30)	47.35	47.35			822.45					

Table G.15: Convergence results of computation time [s], for all elements.

cs_no. (mesh)	**computation time** [s]									
	AMAPDL	**4BlinLag**	**9BquadLag**	**16BcubLag**	**4BlinKrig**	**9BlinKrig**	**9BquadKrig**	**16BlinKrig**	**16BquadKrig**	**16BcubKrig**
1 (2×2)	≈1	0.60	2.30	2.25	0.70	3.89	4.02	37.62	39.03	42.02
2 (4×4)	≈1	0.39	1.36	5.94	0.60	4.09	4.25	41.37	42.97	47.03
3 (6×6)	≈1	0.99	5.23	54.95	0.79	9.23	8.67	92.08	90.72	93.20
4 (8×8)	≈1	1.87	26.08	327.98	1.26	28.56	28.05	376.46	374.03	391.09
5 (10×10)	≈1	3.56	104.02	1277.24	2.34	107.49	106.34	1404.30	1388.92	1462.49
6 (12×12)	≈1	7.41			5.64					
7 (14×14)	≈1	15.18			13.78					
8 (16×16)	≈1	30.31			28.32					
9 (18×18)	≈1	59.01			57.72					
10 (20×20)	≈1	112.17	–	–	113.12	–	–	–	–	–
11 (22×22)	≈1	208.35			209.18					
12 (24×24)	≈1	353.72			351.55					
13 (26×26)	≈1	573.36			596.48					
14 (28×28)	≈1	894.02			933.57					
15 (30×30)	≈1	1345.73			1403.61					

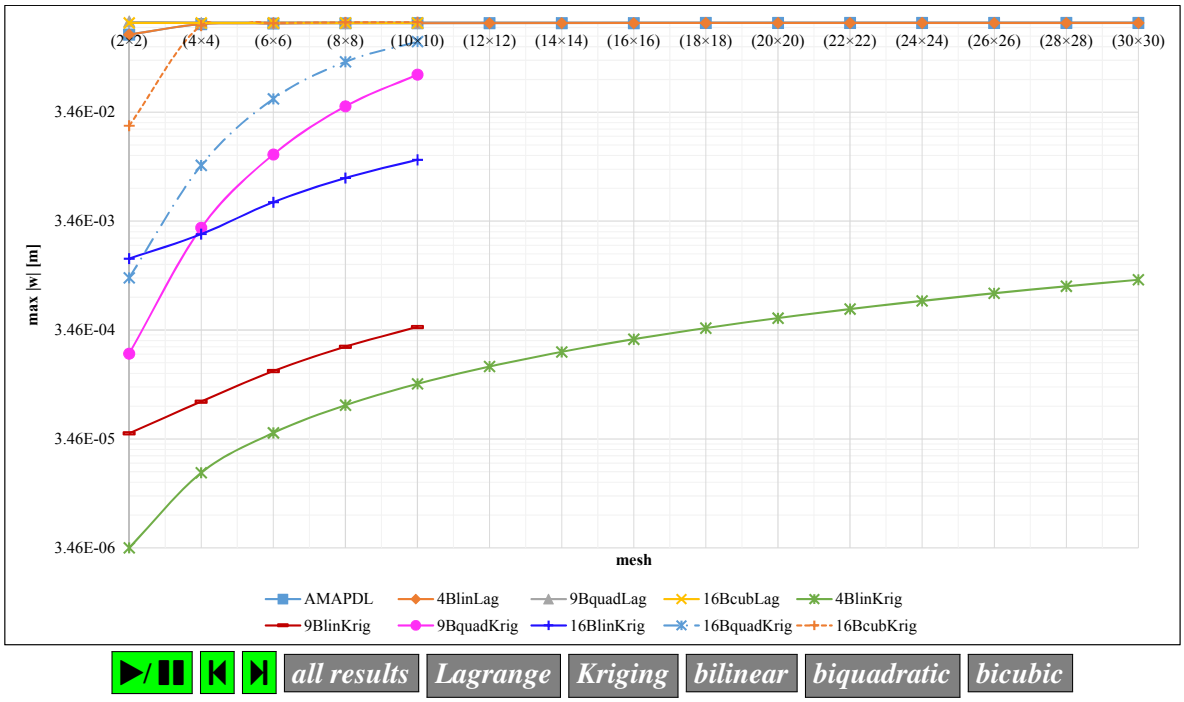

Figure G.1: Convergence results plot of DOF $\max|w|$ [m], for all elements. Please click on the buttons above this caption to run the animation and toggle between plotted results.

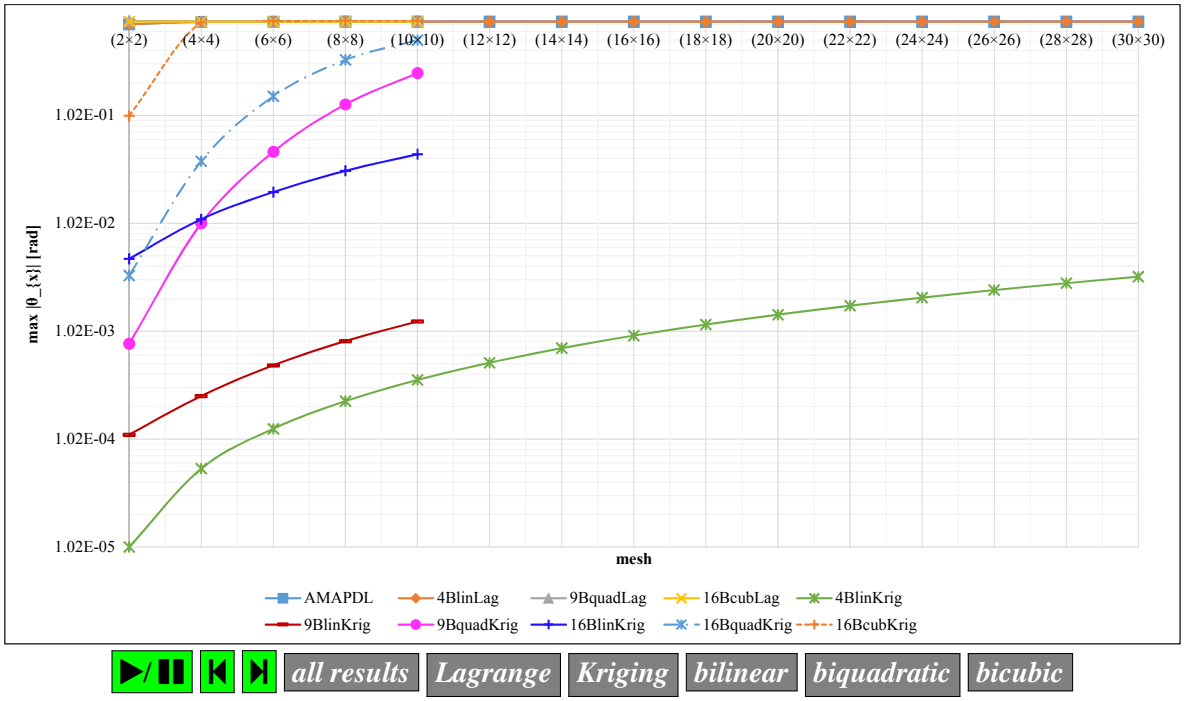

Figure G.2: Convergence results plot of DOF $\max|\theta_x|$ [rad], for all elements. Please click on the buttons above this caption to run the animation and toggle between plotted results.

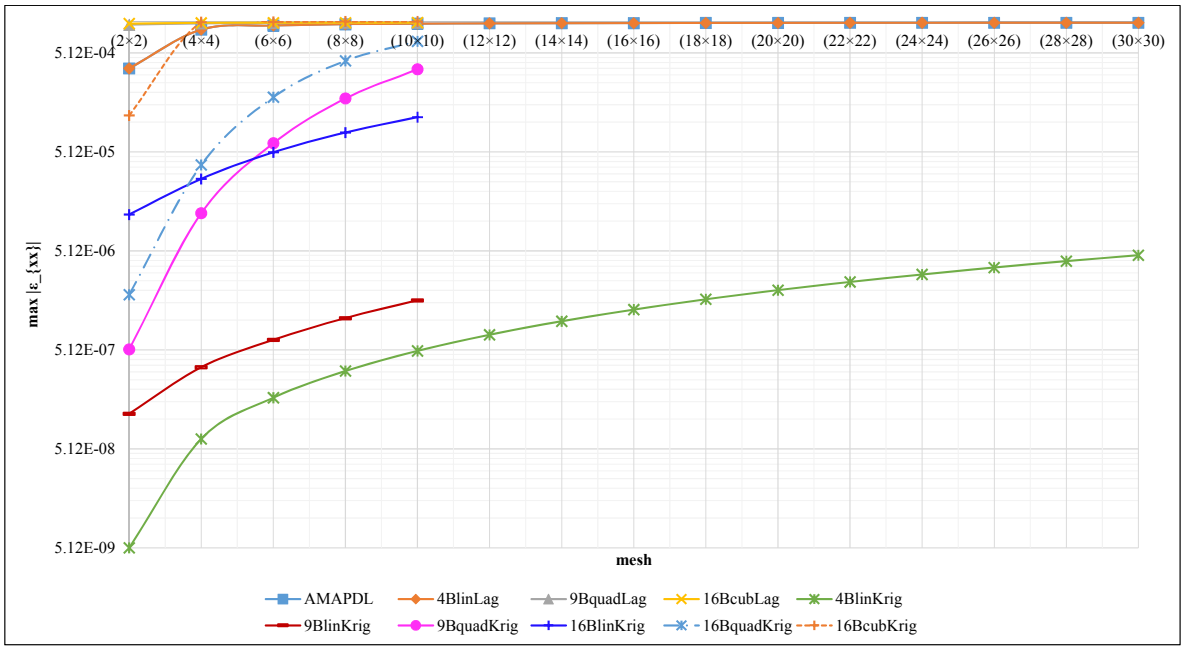



Figure G.3: Convergence results plot of strain $\max|\epsilon_{xx}|$, for all elements. Please click on the buttons above this caption to run the animation and toggle between plotted results.

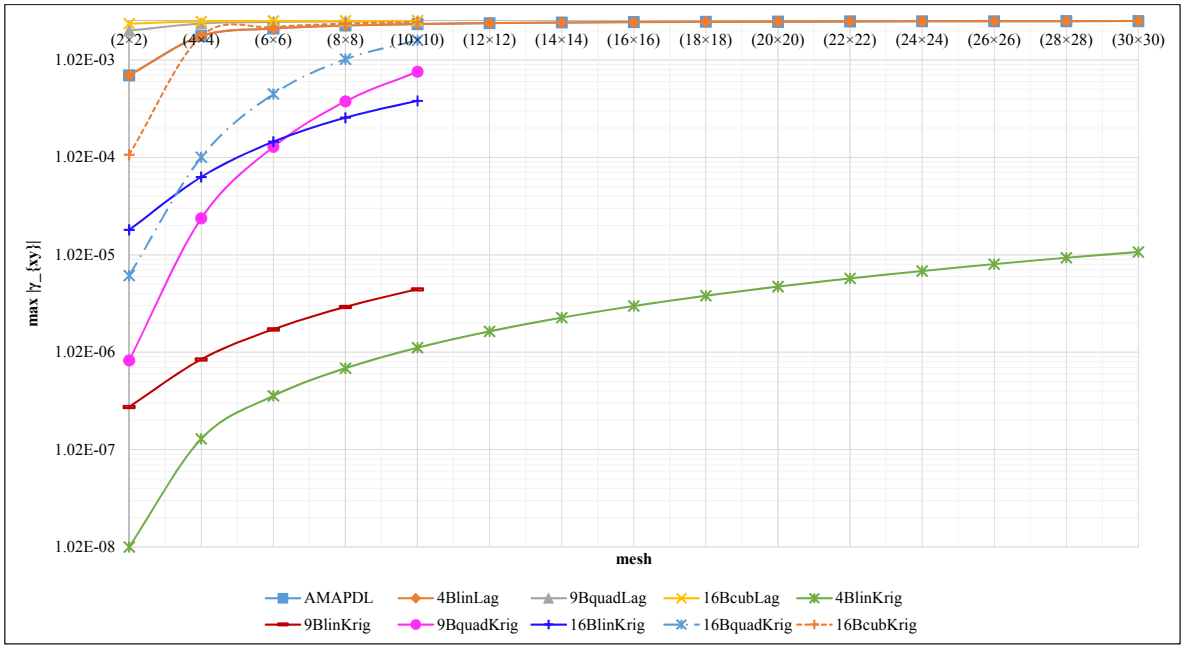



Figure G.4: Convergence results plot of strain $\max|\gamma_{xy}|$, for all elements. Please click on the buttons above this caption to run the animation and toggle between plotted results.

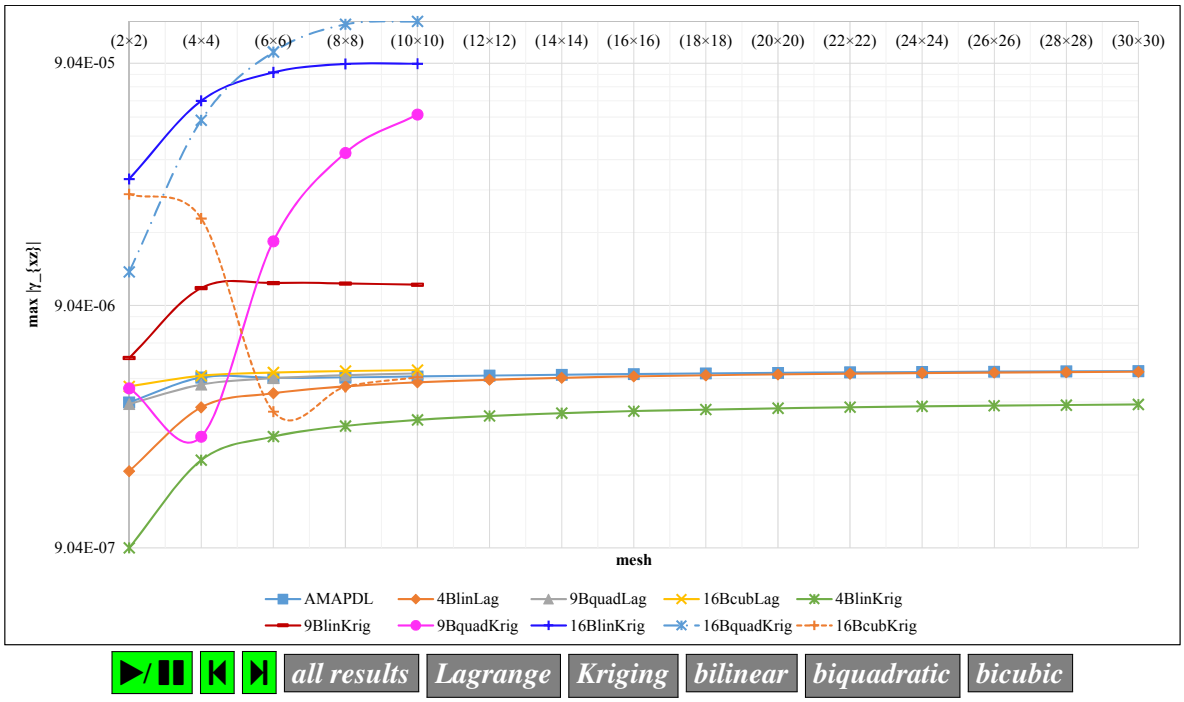

Figure G.5: Convergence results plot of strain $\max|\gamma_{xz}|$, for all elements. Please click on the buttons above this caption to run the animation and toggle between plotted results.

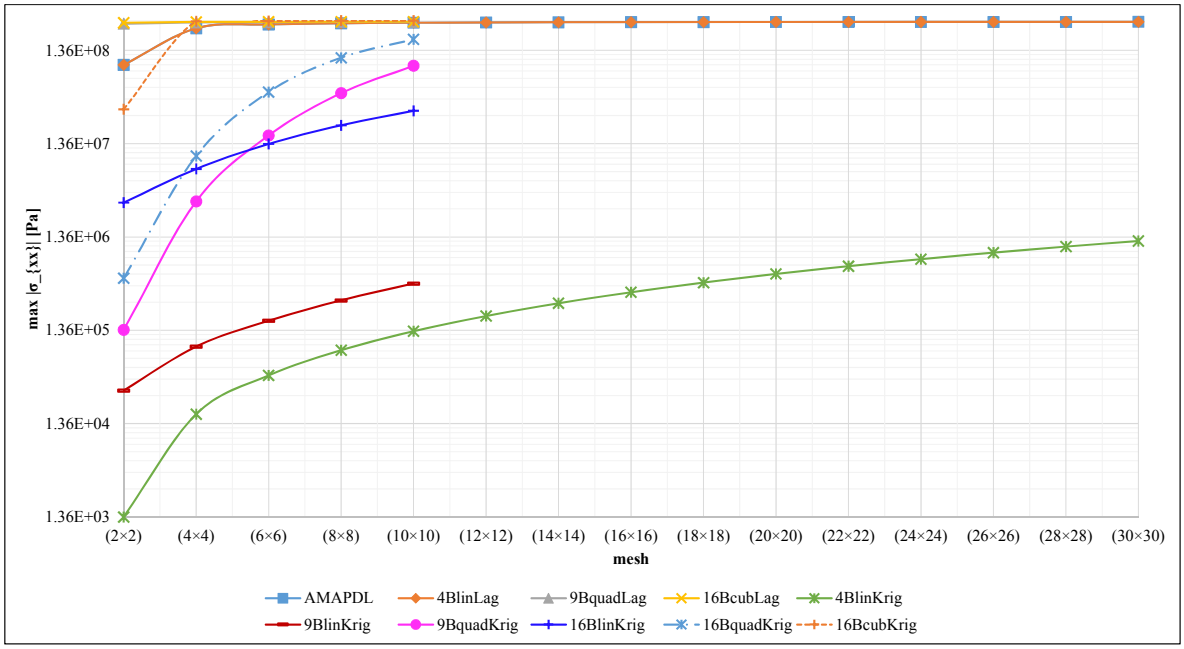

Figure G.6: Convergence results plot of stress $\max|\sigma_{xx}|$ [Pa], for all elements. Please click on the buttons above this caption to run the animation and toggle between plotted results.

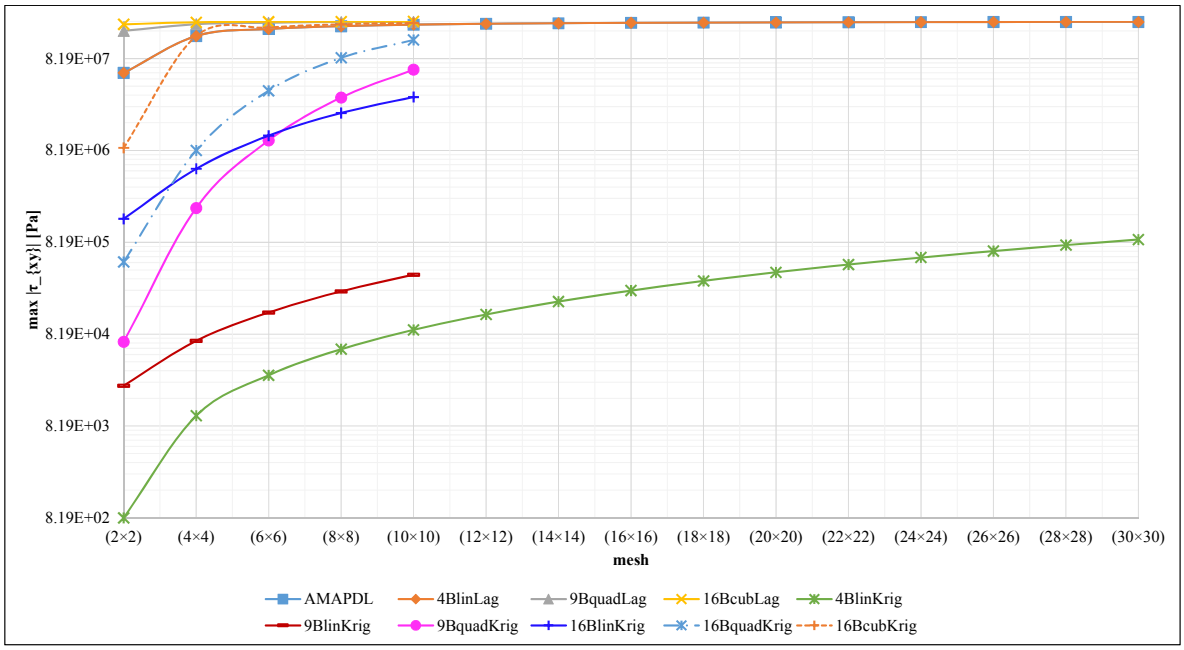

all results | Lagrange | Kriging | bilinear | biquadratic | bicubic

Figure G.7: Convergence results plot of stress $\max|\tau_{xy}|$ [Pa], for all elements. Please click on the buttons above this caption to run the animation and toggle between plotted results.

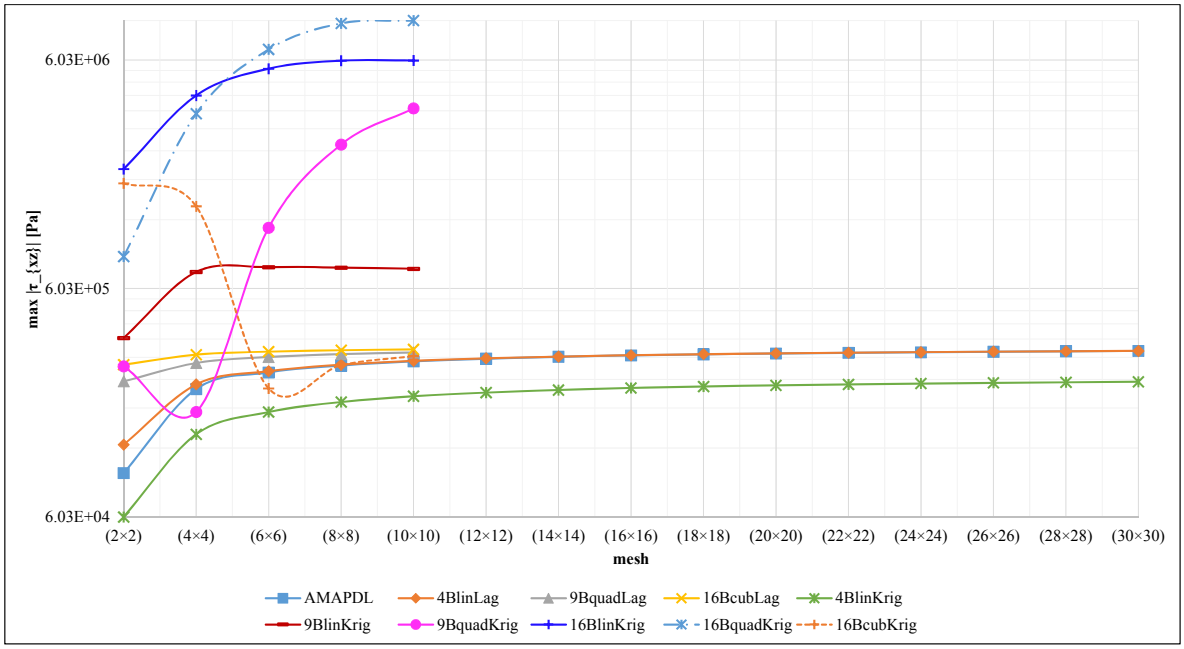

all results | Lagrange | Kriging | bilinear | biquadratic | bicubic

Figure G.8: Convergence results plot of stress $\max|\tau_{xz}|$ [Pa], for all elements. Please click on the buttons above this caption to run the animation and toggle between plotted results.

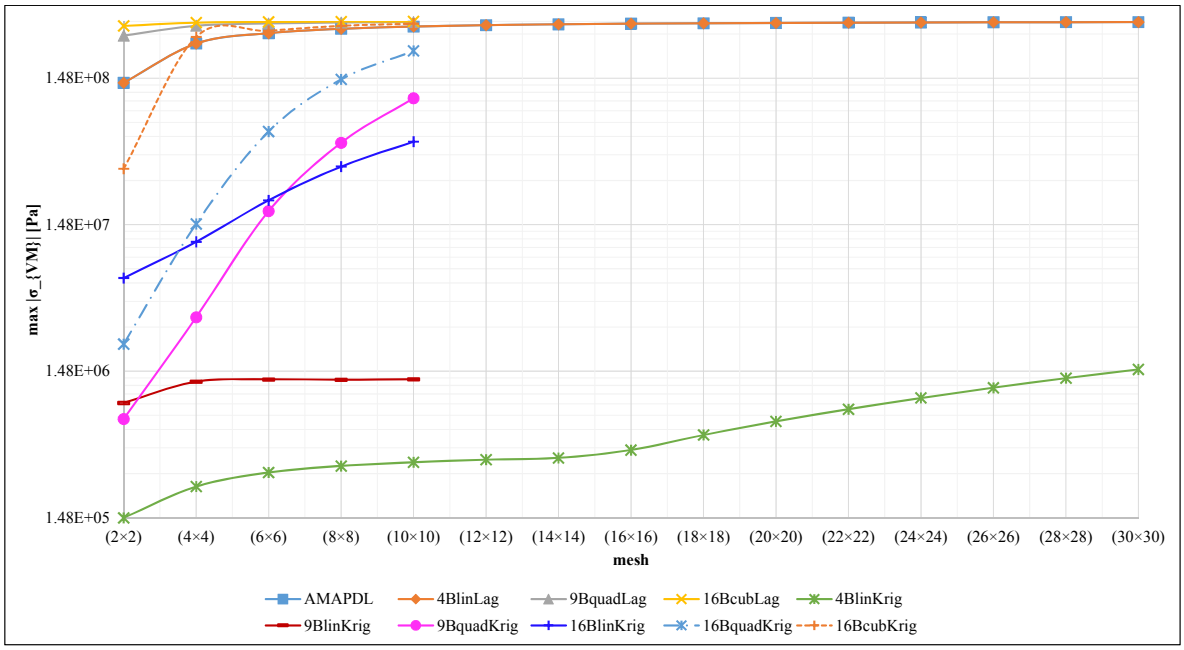

all results Lagrange Kriging bilinear biquadratic bicubic

Figure G.9: Convergence results plot of stress $\max|\sigma_{VM}|$ [Pa], for all elements. Please click on the buttons above this caption to run the animation and toggle between plotted results.

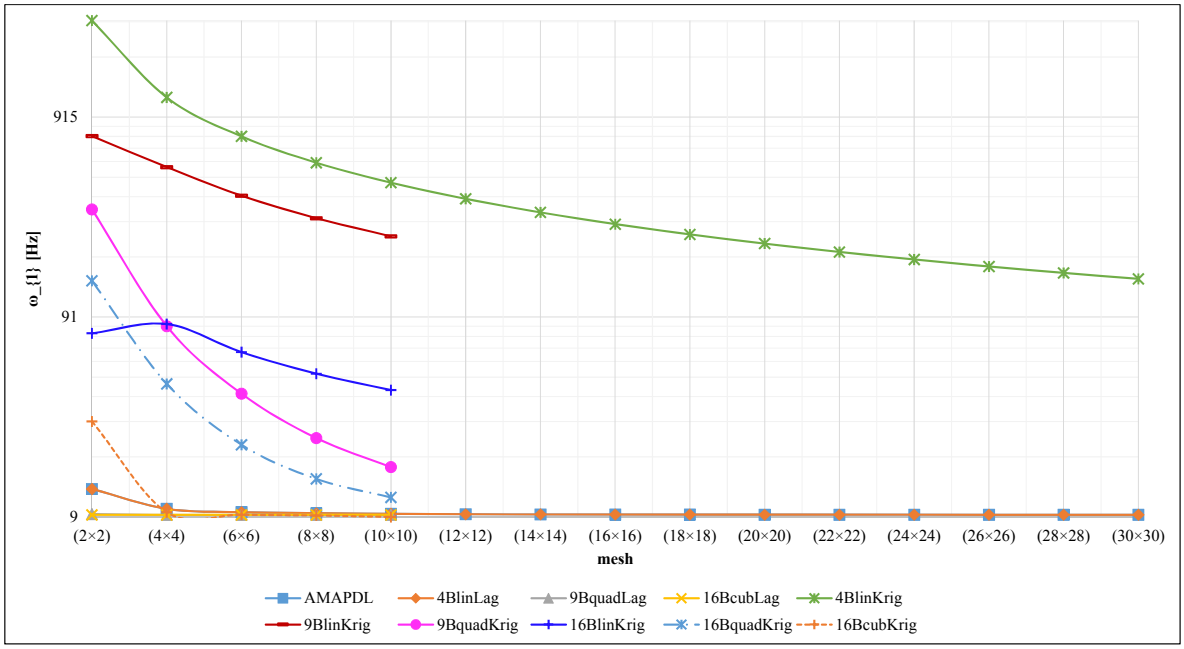

all results Lagrange Kriging bilinear biquadratic bicubic

Figure G.10: Convergence results plot of natural frequency ω_1 [Hz], for all elements. Please click on the buttons above this caption to run the animation and toggle between plotted results.

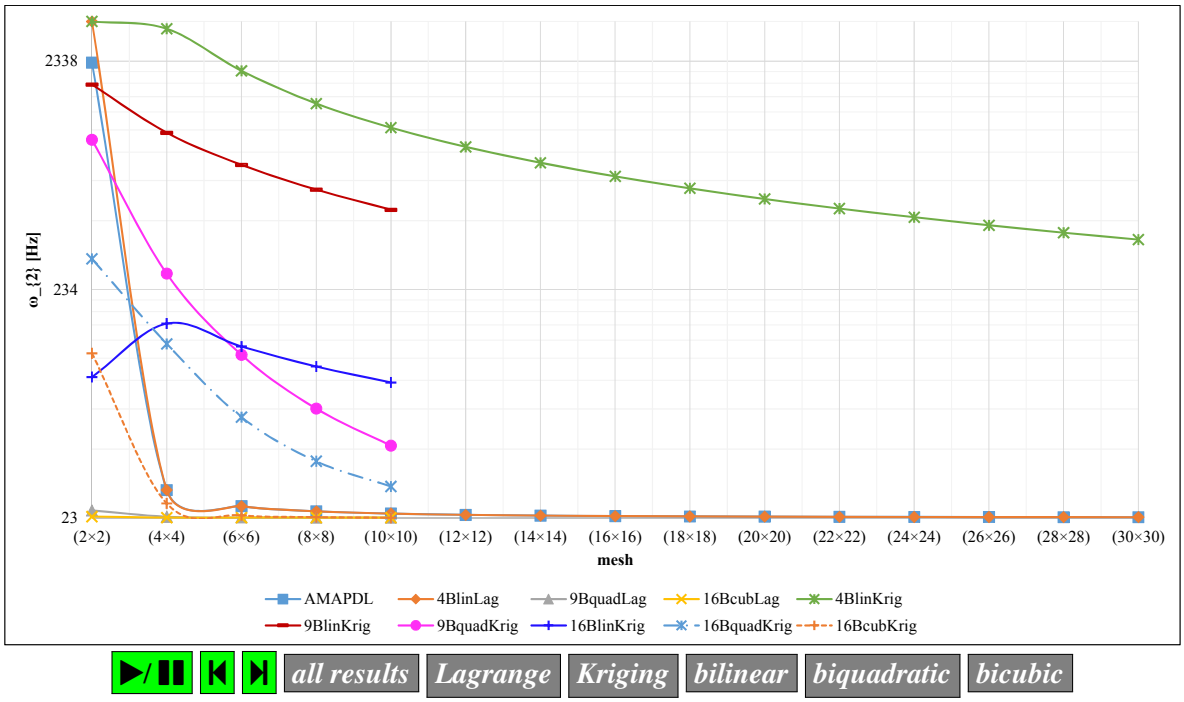

all results | Lagrange | Kriging | bilinear | biquadratic | bicubic

Figure G.11: Convergence results plot of natural frequency ω_2 [Hz], for all elements. Please click on the buttons above this caption to run the animation and toggle between plotted results.

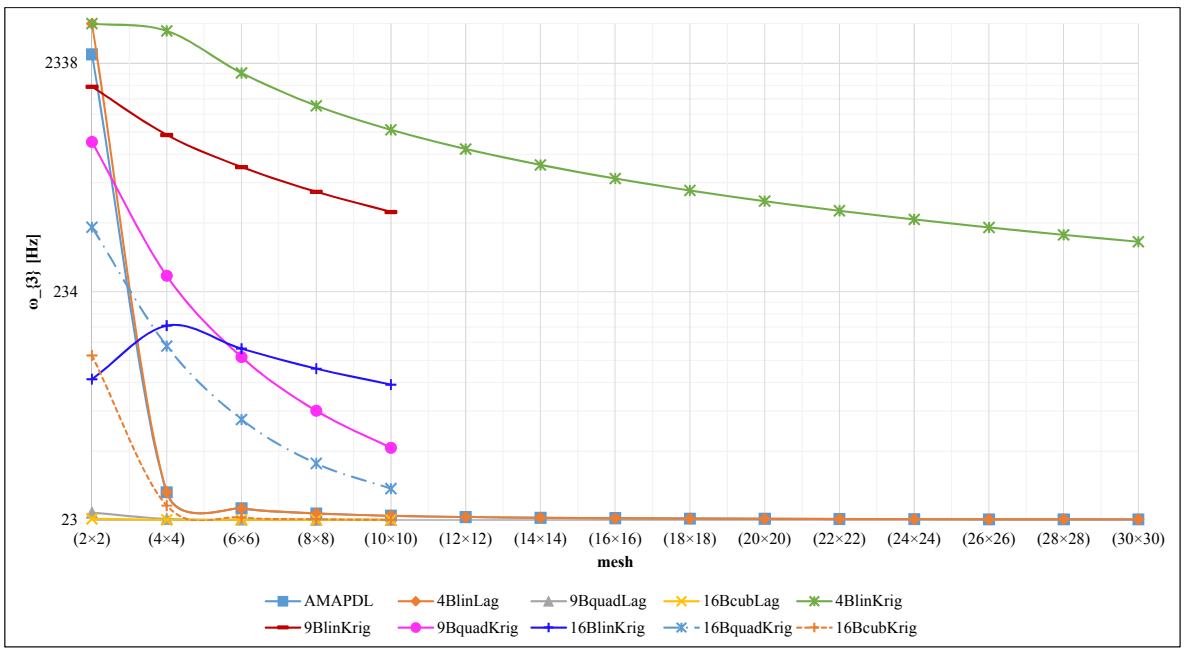

all results | Lagrange | Kriging | bilinear | biquadratic | bicubic

Figure G.12: Convergence results plot of natural frequency ω_3 [Hz], for all elements. Please click on the buttons above this caption to run the animation and toggle between plotted results.

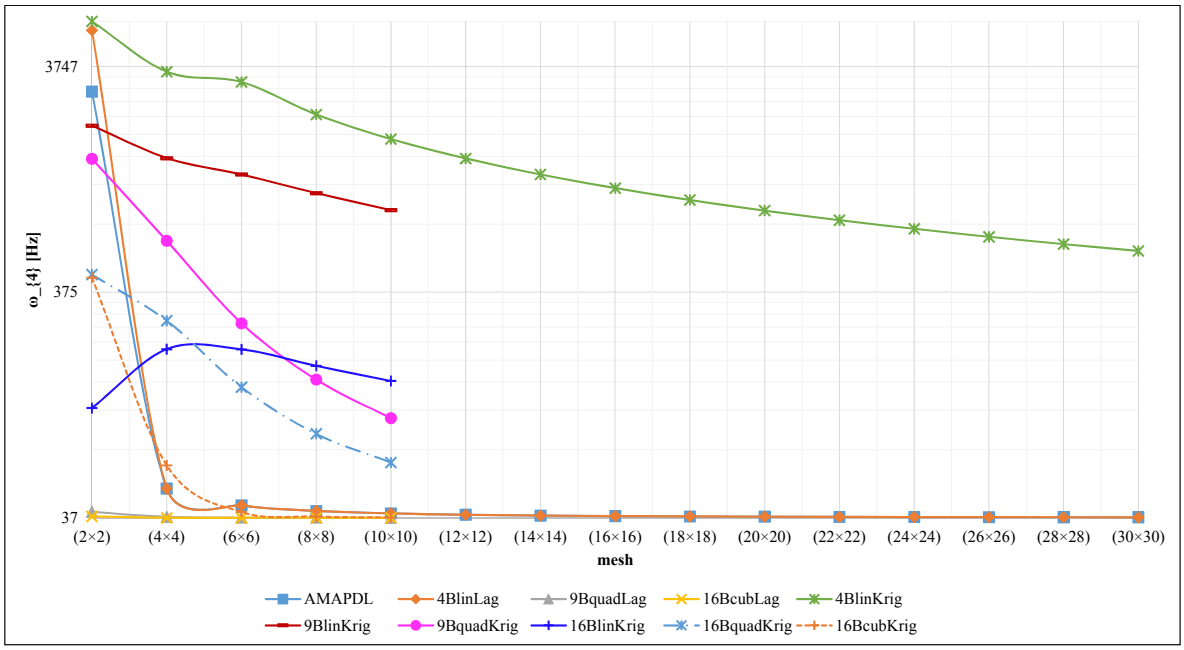

Figure G.13: Convergence results plot of natural frequency ω_4 [Hz], for all elements. Please click on the buttons above this caption to run the animation and toggle between plotted results.

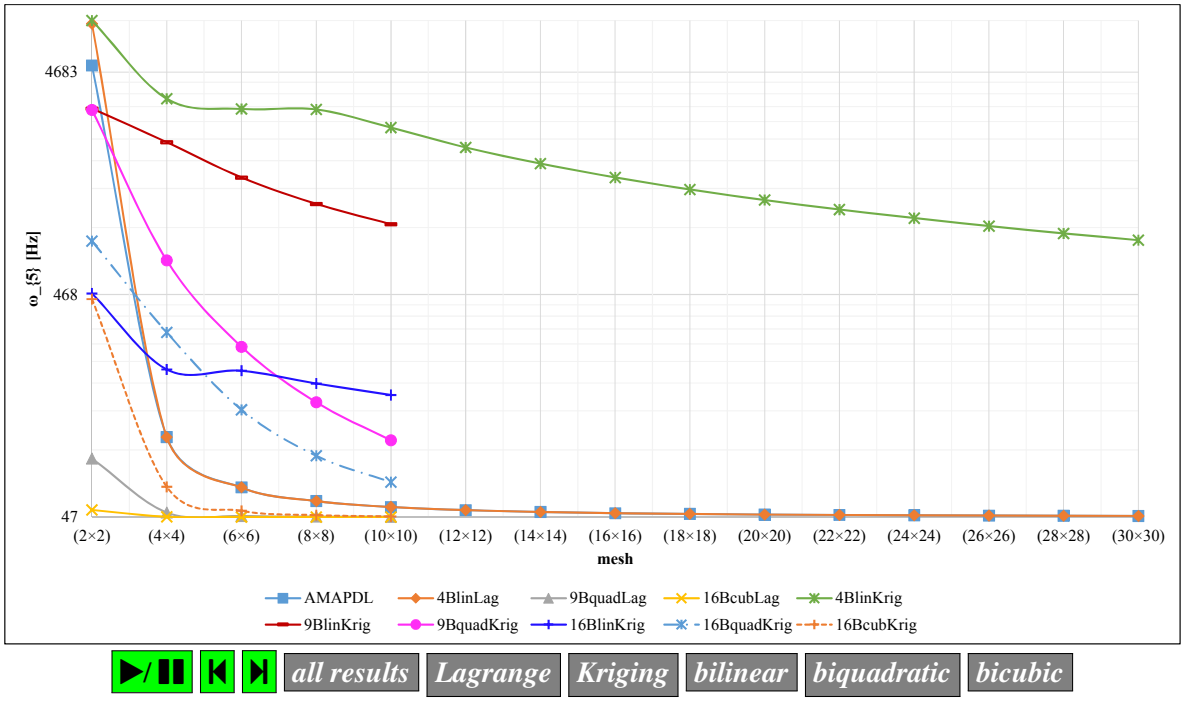

Figure G.14: Convergence results plot of natural frequency ω_5 [Hz], for all elements. Please click on the buttons above this caption to run the animation and toggle between plotted results.

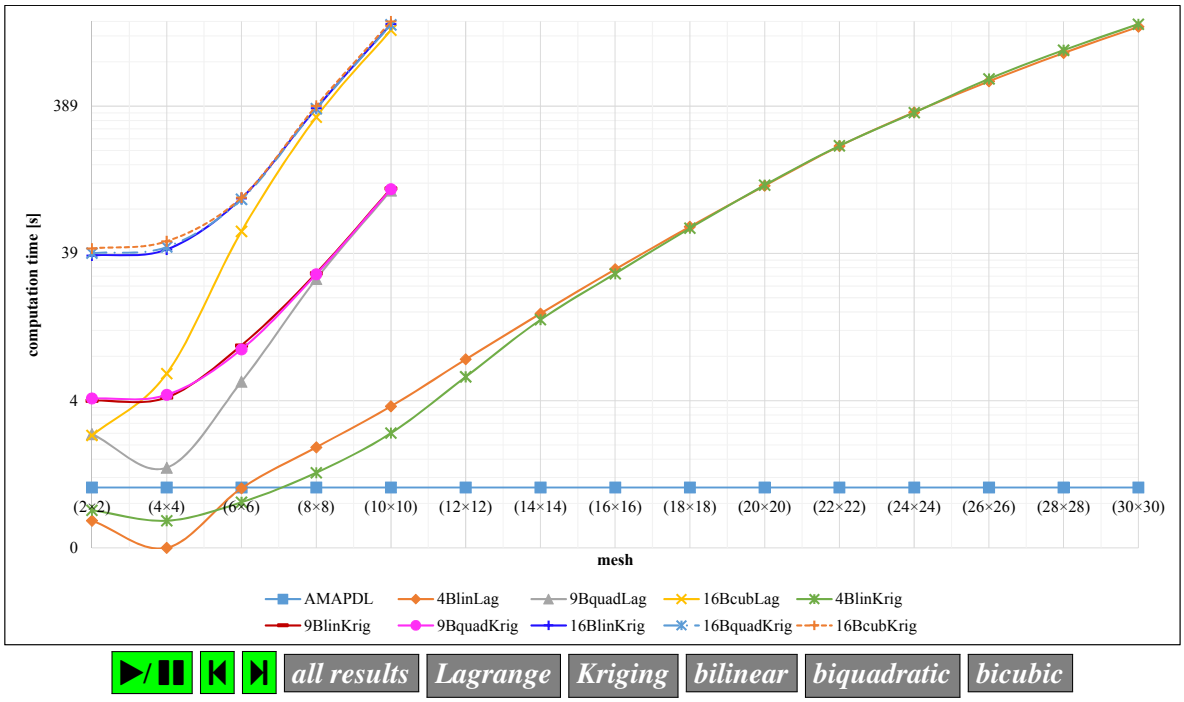

Figure G.15: Convergence results plot of computation time [s], for all elements. Please click on the buttons above this caption to run the animation and toggle between plotted results.

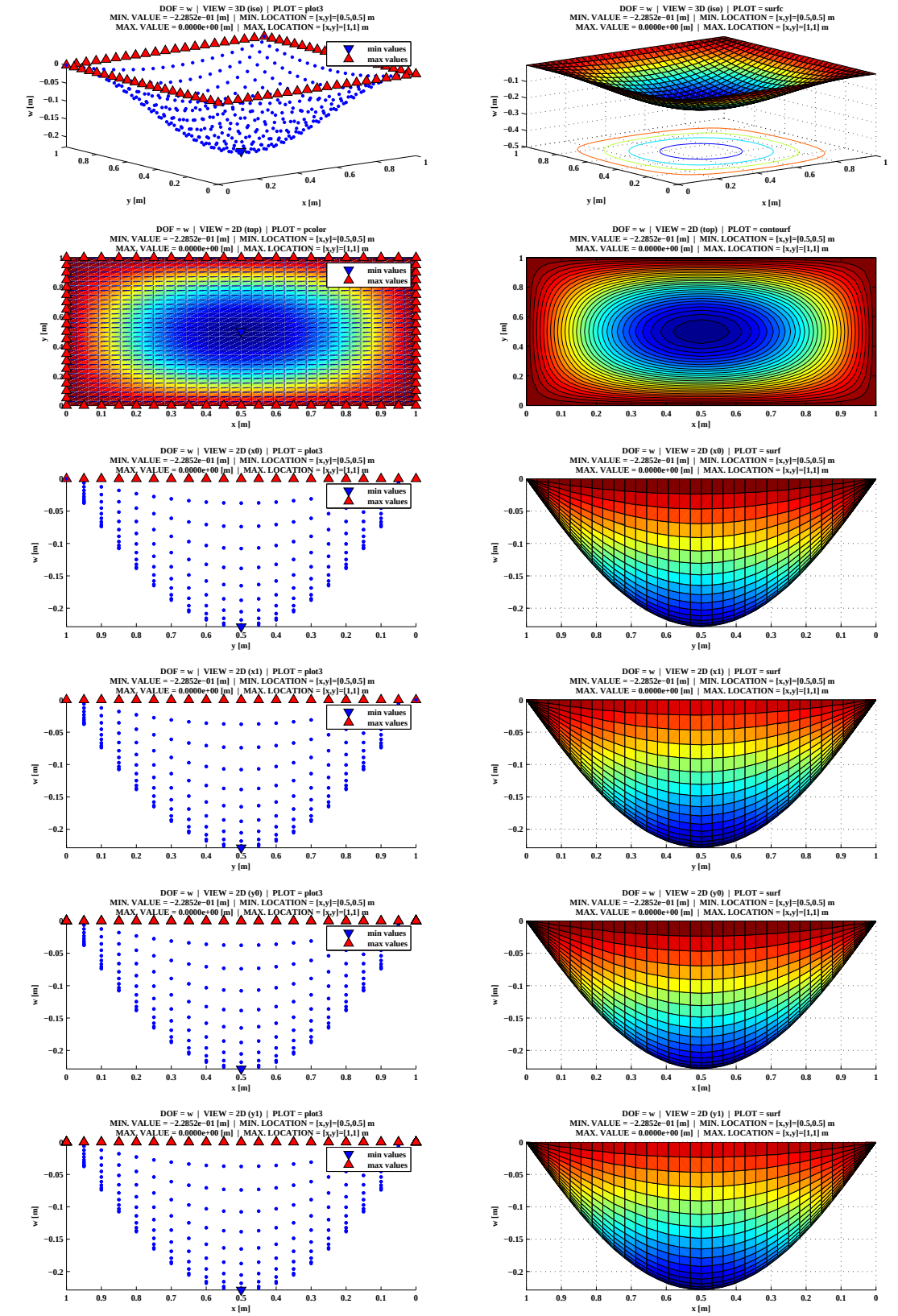

Figure G.16: Statics and dynamics (free vibrations) results obtained from the convergence model using the present FEM platform. 9BquadLag elements with a (10×10) mesh. Please click on the buttons above this caption to run the animation and toggle between plotted results.

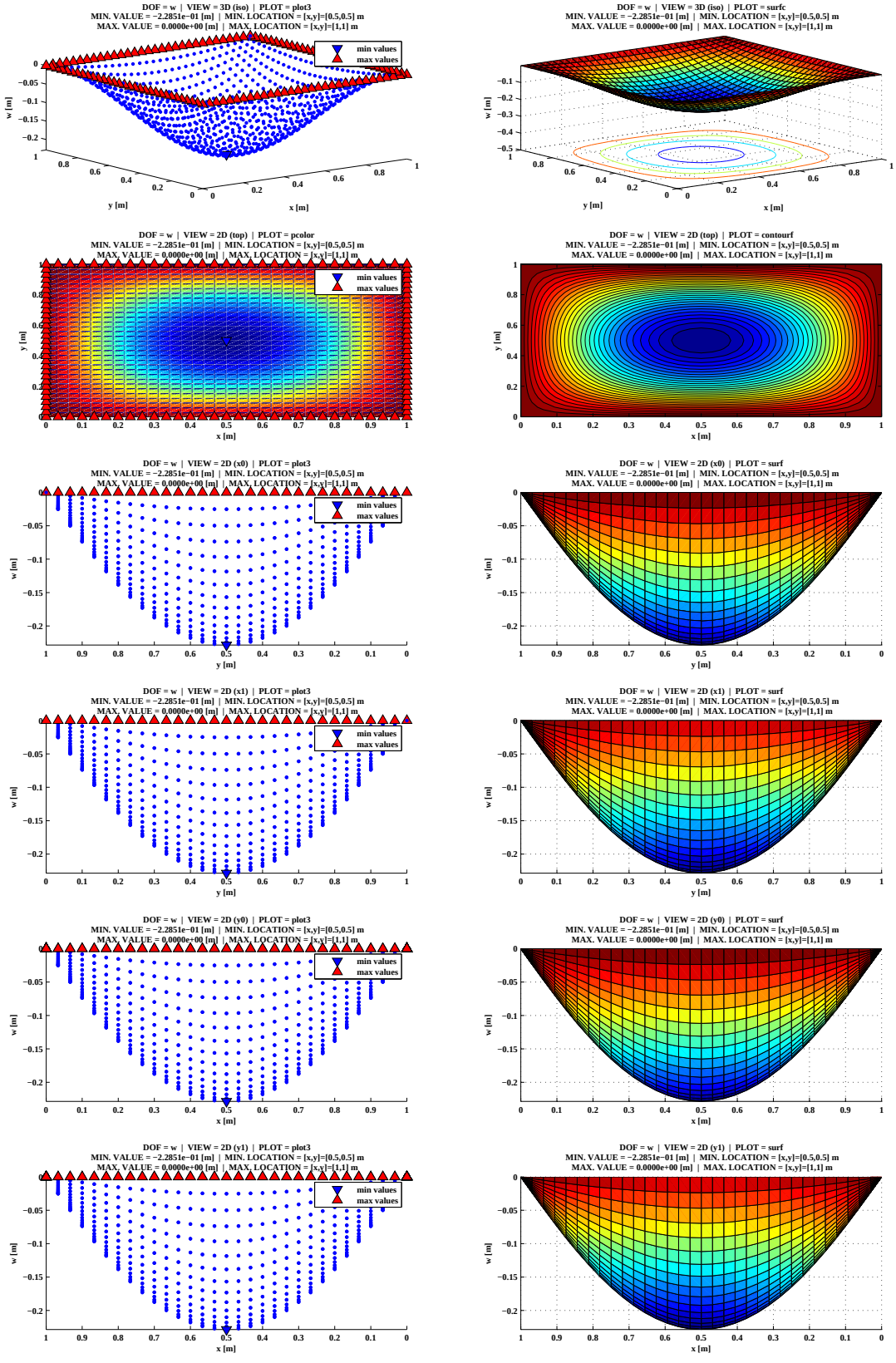

w θ_x θ_y u v ϵ_{xx} ϵ_{yy} γ_{xy} γ_{xz} γ_{yz} σ_{xx} σ_{yy} τ_{xy} τ_{xz} τ_{yz} σ_{VM}

ω_1 ω_2 ω_3 ω_4 ω_5

Figure G.17: Statics and dynamics (free vibrations) results obtained from the convergence model using the present FEM platform. 16BcubLag elements with a (10×10) mesh. Please click on the buttons above this caption to run the animation and toggle between plotted results.

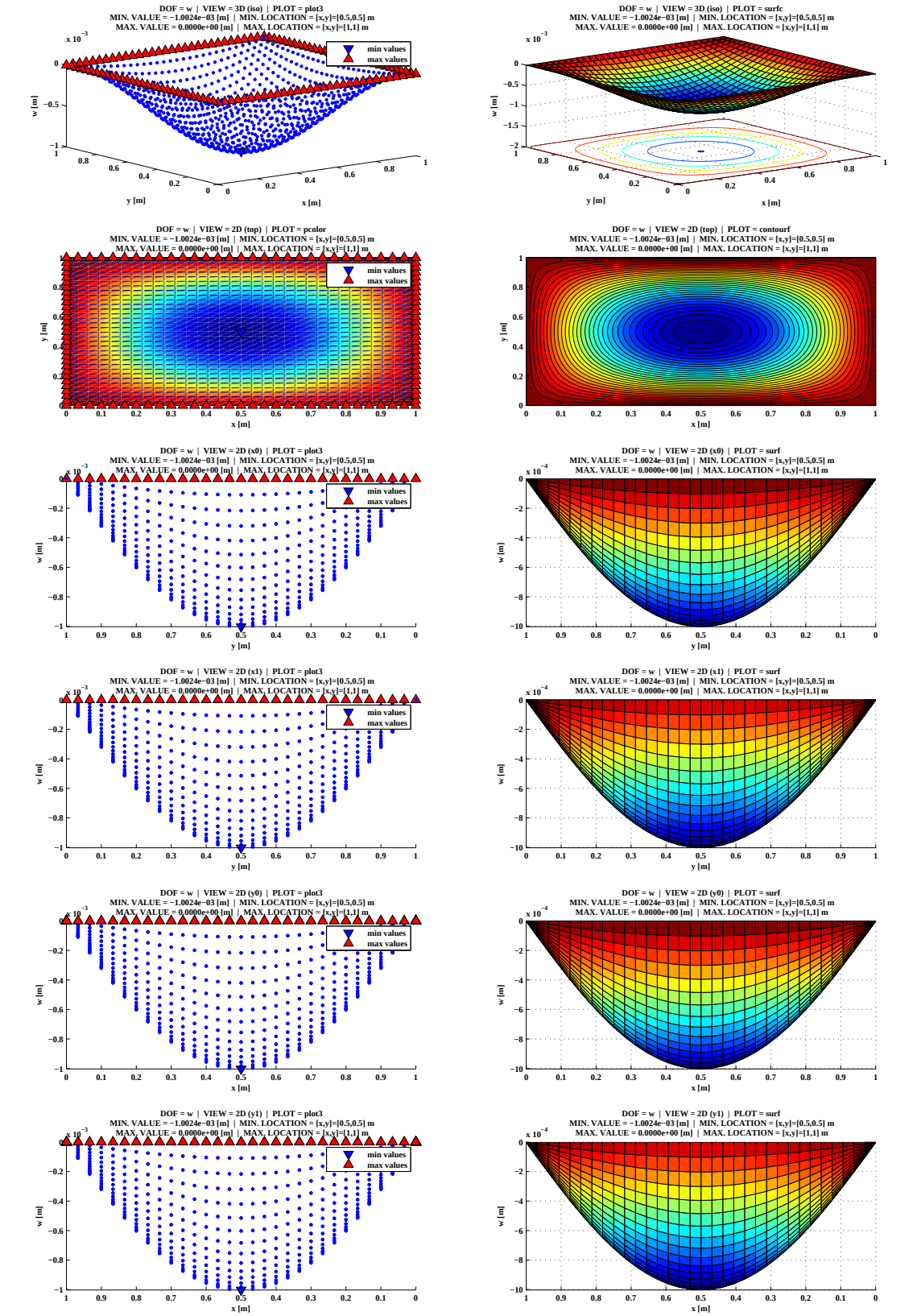

w θ_x θ_y u v ϵ_{xx} ϵ_{yy} γ_{xy} γ_{xz} γ_{yz} σ_{xx} σ_{yy} τ_{xy} τ_{xz} τ_{yz} σ_{VM}

ω_1 ω_2 ω_3 ω_4 ω_5

Figure G.18: Statics and dynamics (free vibrations) results obtained from the convergence model using the present FEM platform. 4BlinKrig elements with a (30×30) mesh. Please click on the buttons above this caption to run the animation and toggle between plotted results.

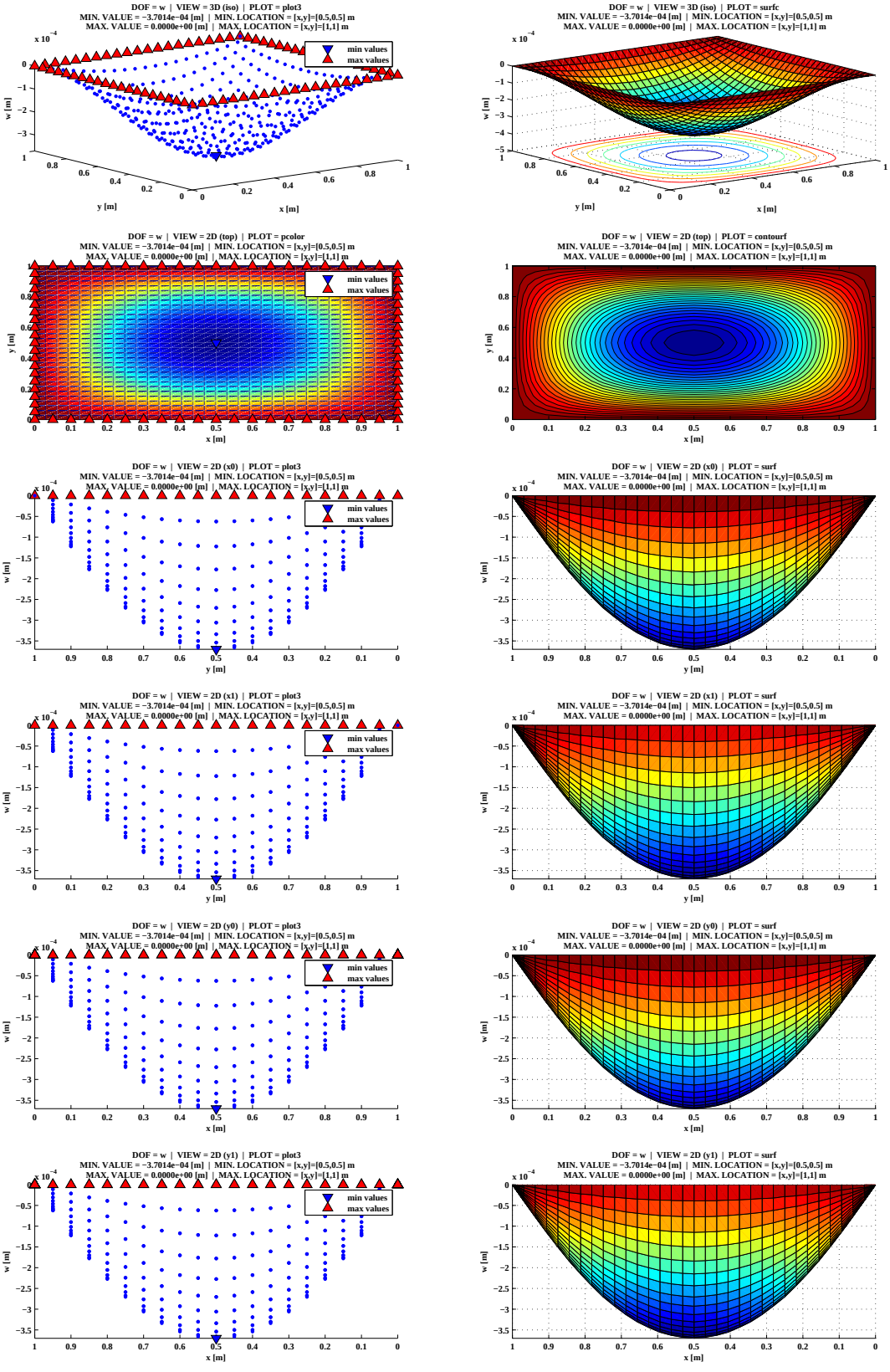

w θ_x θ_y u v ϵ_{xx} ϵ_{yy} γ_{xy} γ_{xz} γ_{yz} σ_{xx} σ_{yy} τ_{xy} τ_{xz} τ_{yz} σ_{VM}

ω_1 ω_2 ω_3 ω_4 ω_5

Figure G.19: Statics and dynamics (free vibrations) results obtained from the convergence model using the present FEM platform. 9BlinKrig elements with a (10×10) mesh. Please click on the buttons above this caption to run the animation and toggle between plotted results.

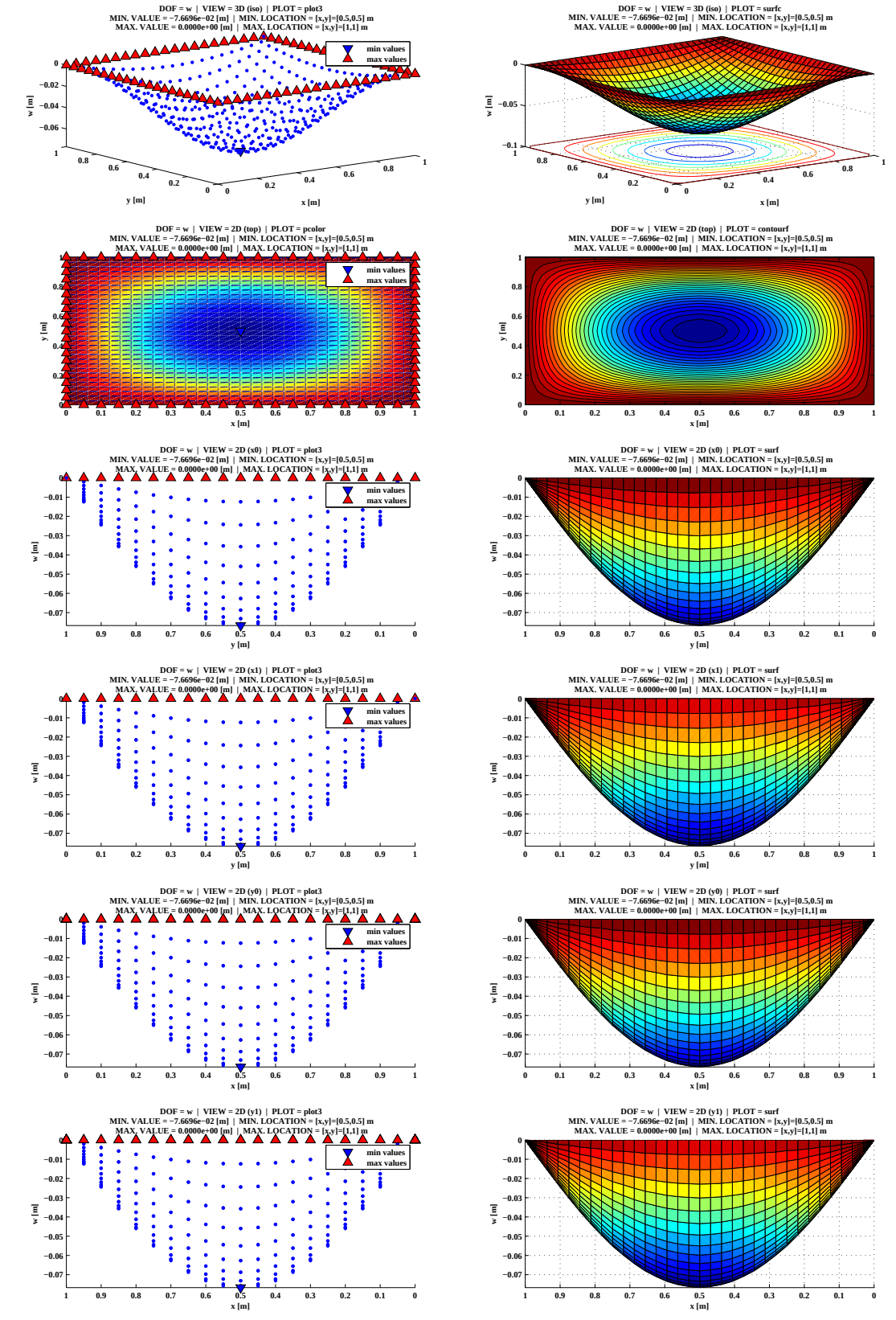

w θ_x θ_y u v ϵ_{xx} ϵ_{yy} γ_{xy} γ_{xz} γ_{yz} σ_{xx} σ_{yy} τ_{xy} τ_{xz} τ_{yz} σ_{VM}

ω_1 ω_2 ω_3 ω_4 ω_5

Figure G.20: Statics and dynamics (free vibrations) results obtained from the convergence model using the present FEM platform. 9BquadKrig elements with a (10×10) mesh. Please click on the buttons above this caption to run the animation and toggle between plotted results.

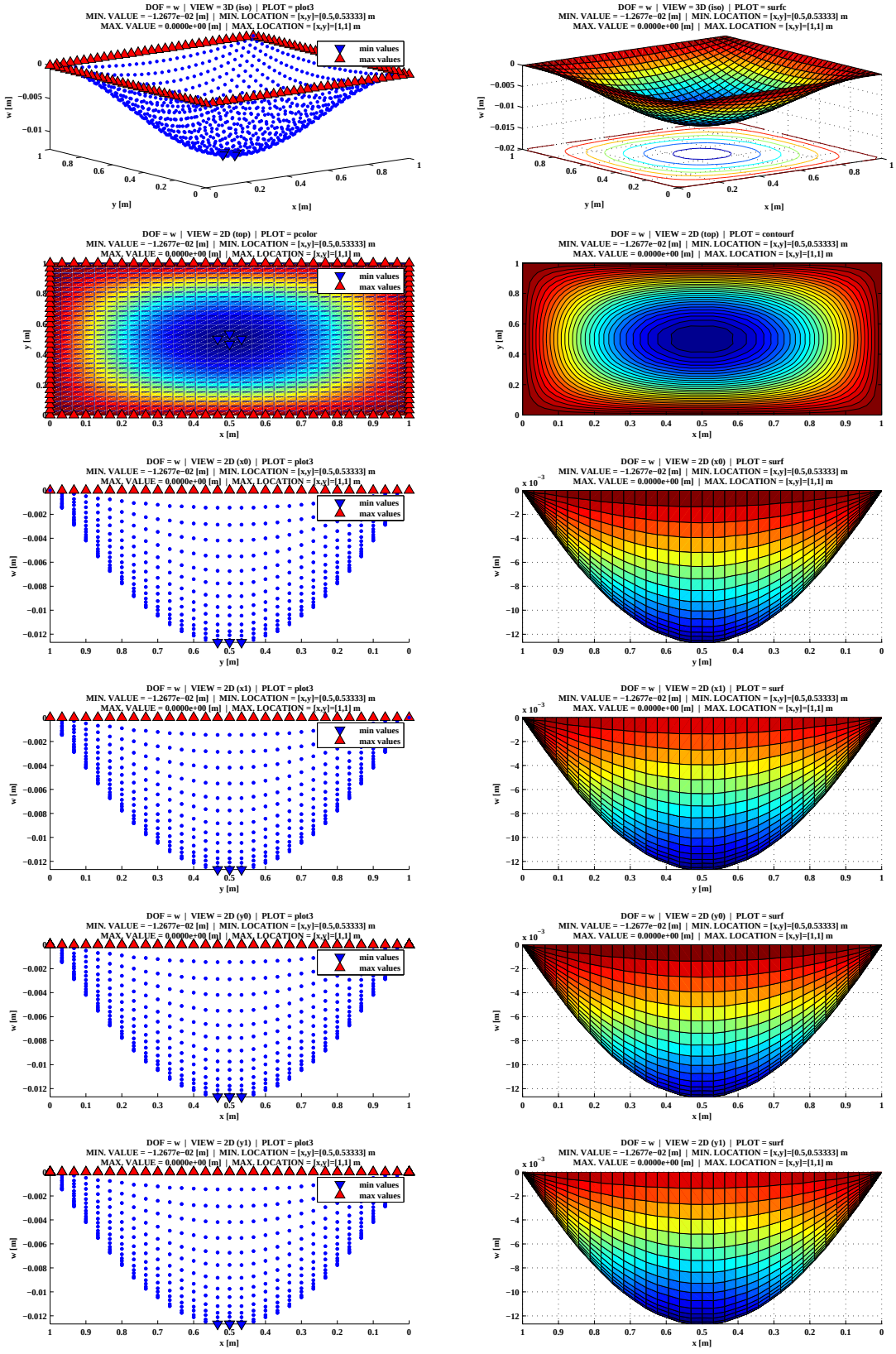

w θ_x θ_y u v ϵ_{xx} ϵ_{yy} γ_{xy} γ_{xz} γ_{yz} σ_{xx} σ_{yy} τ_{xy} τ_{xz} τ_{yz} σ_{VM}

ω_1 ω_2 ω_3 ω_4 ω_5

Figure G.21: Statics and dynamics (free vibrations) results obtained from the convergence model using the present FEM platform. 16BlinKrig elements with a (10×10) mesh. Please click on the buttons above this caption to run the animation and toggle between plotted results.

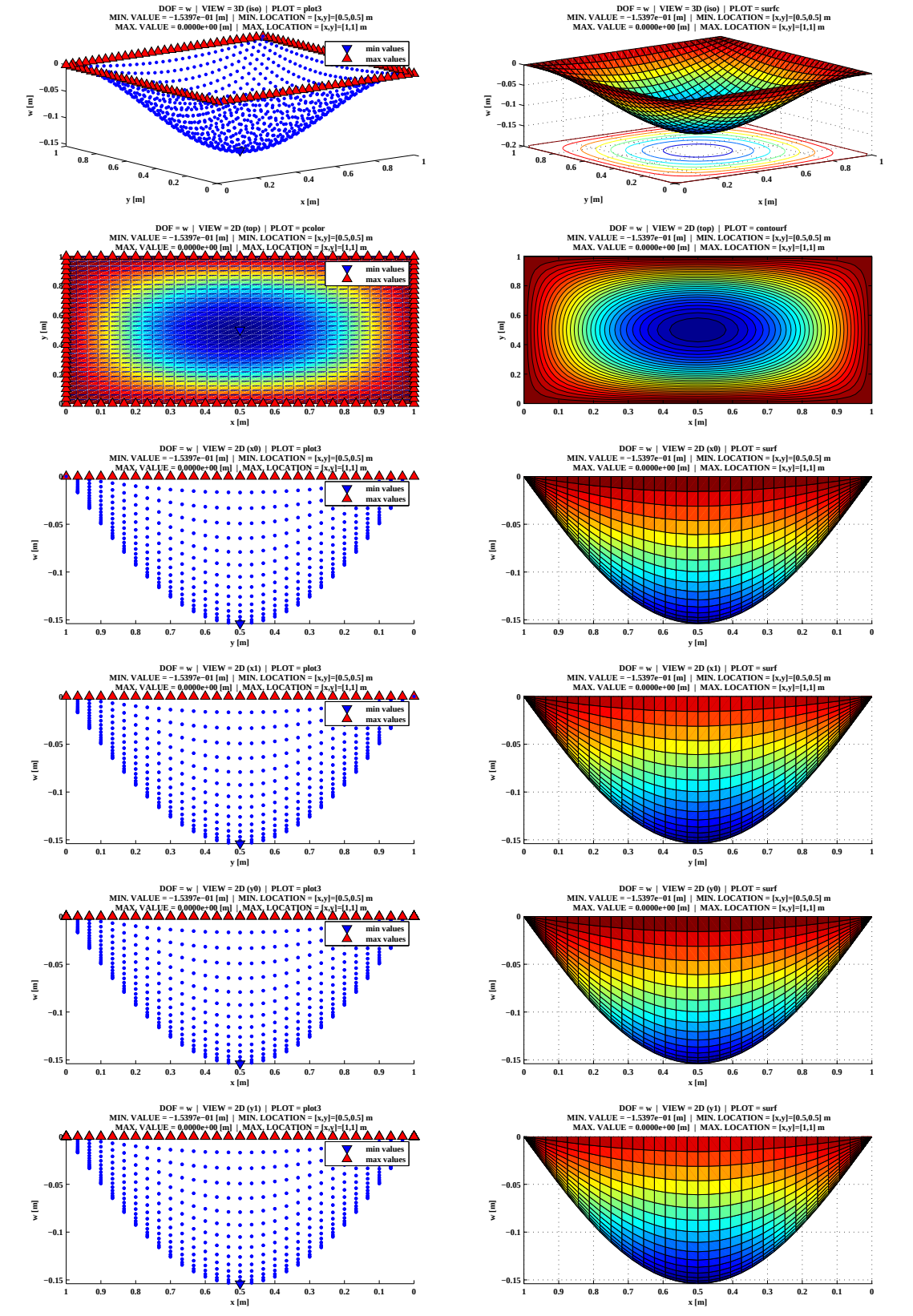

w θ_x θ_y u v ϵ_{xx} ϵ_{yy} γ_{xy} γ_{xz} γ_{yz} σ_{xx} σ_{yy} τ_{xy} τ_{xz} τ_{yz} σ_{VM}

ω_1 ω_2 ω_3 ω_4 ω_5

Figure G.22: Statics and dynamics (free vibrations) results obtained from the convergence model using the present FEM platform. 16BquadKrig elements with a (10×10) mesh. Please click on the buttons above this caption to run the animation and toggle between plotted results.

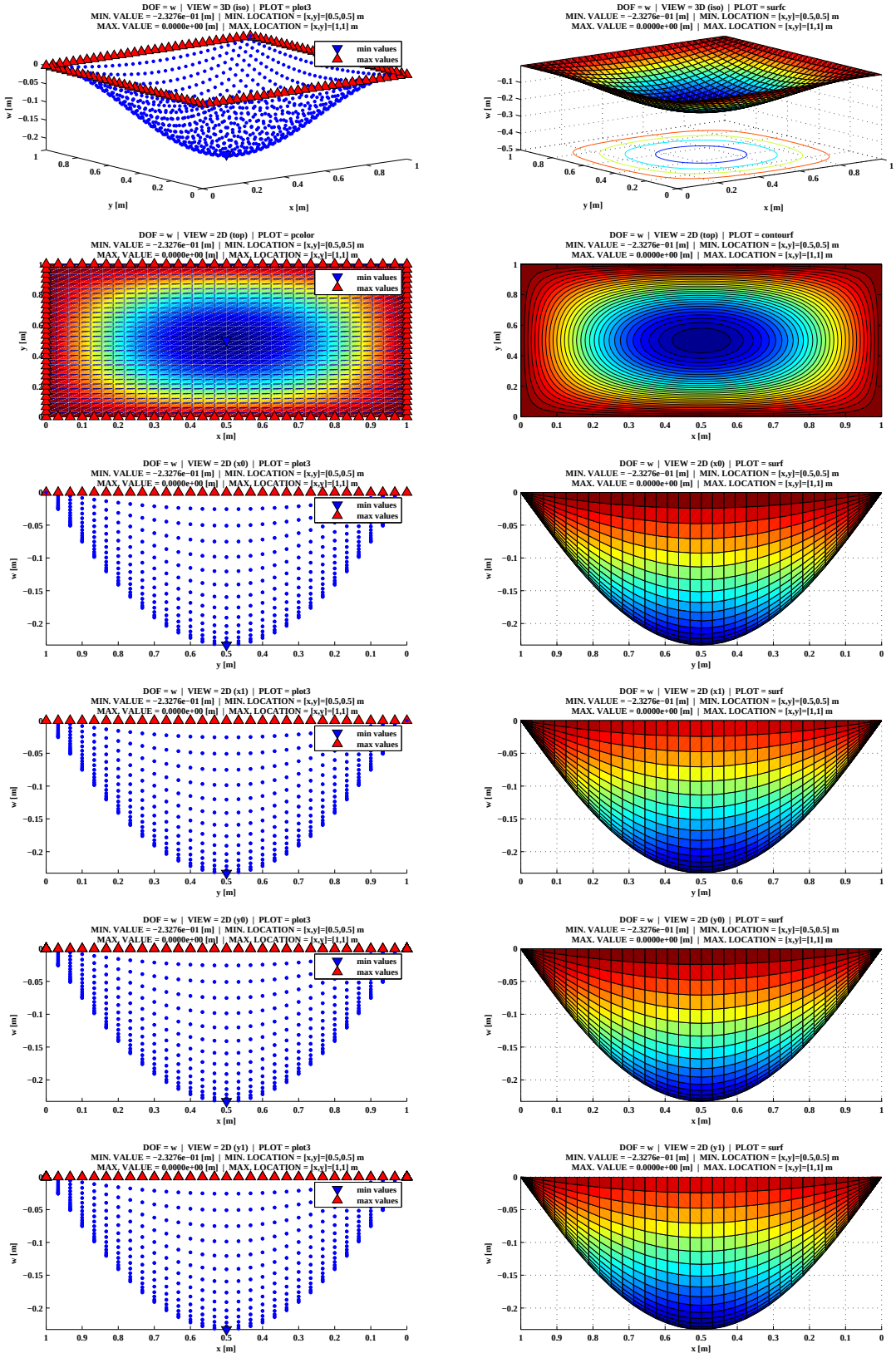

w θ_x θ_y u v ϵ_{xx} ϵ_{yy} γ_{xy} γ_{xz} γ_{yz} σ_{xx} σ_{yy} τ_{xy} τ_{xz} τ_{yz} σ_{VM}

ω_1 ω_2 ω_3 ω_4 ω_5

Figure G.23: Statics and dynamics (free vibrations) results obtained from the convergence model using the present FEM platform. 16BcubKrig elements with a (10×10) mesh. Please click on the buttons above this caption to run the animation and toggle between plotted results.

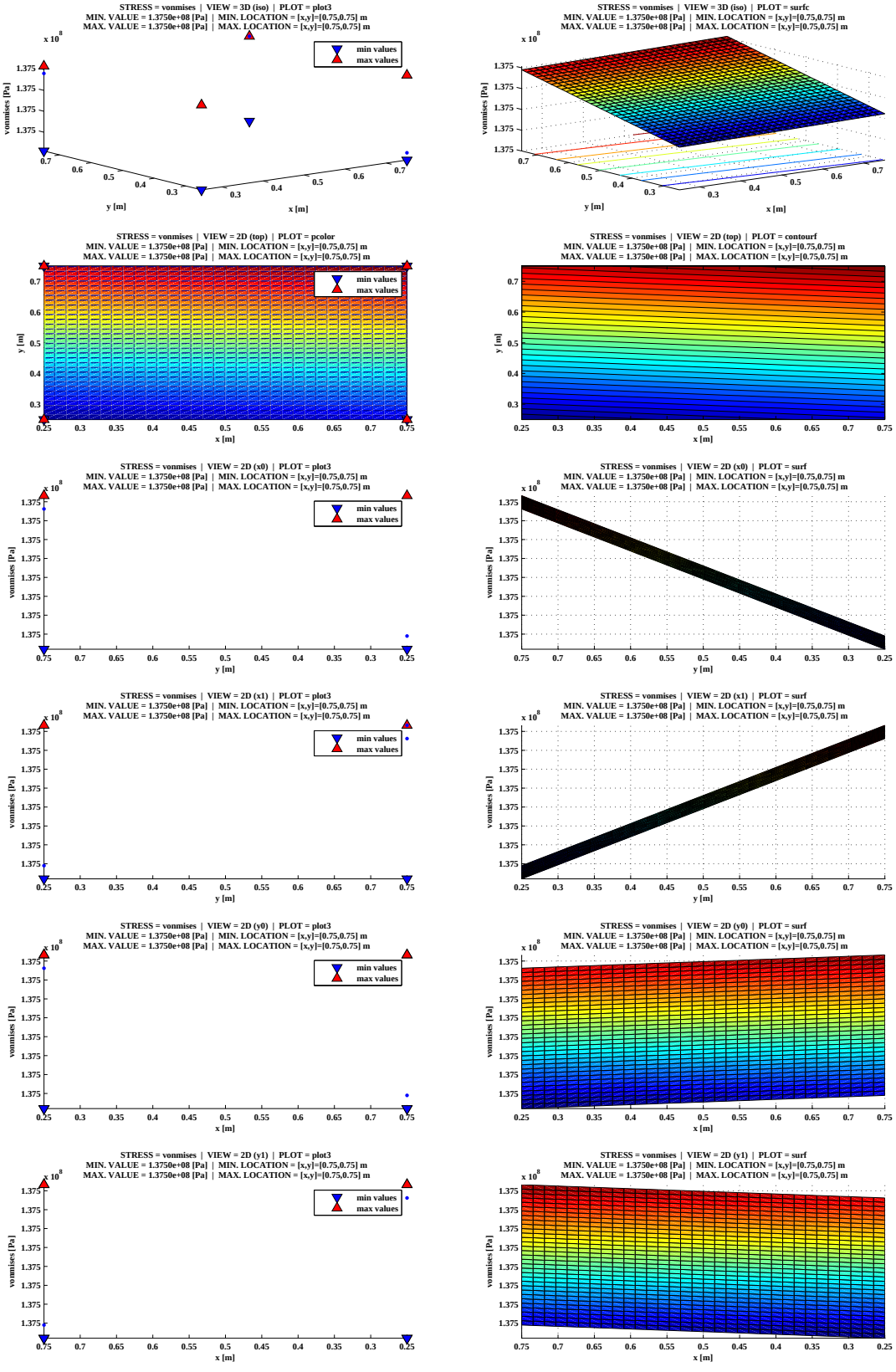

2 4 6 8 10 12 14 16 18 20 22 24 26 28 30

Figure G.24: Von Mises stress results obtained from the convergence model using the present FEM platform, only for visualization. 4BlinLag elements; meshes from (2×2) by (2×2) to (30×30). Please click on the buttons above this caption to run the animation and toggle between plotted results.

G.2 Function. graded, multiscale & hybrid comp. structs.

G.2.1 Statics

Results associated with Section 4.2.2.1.

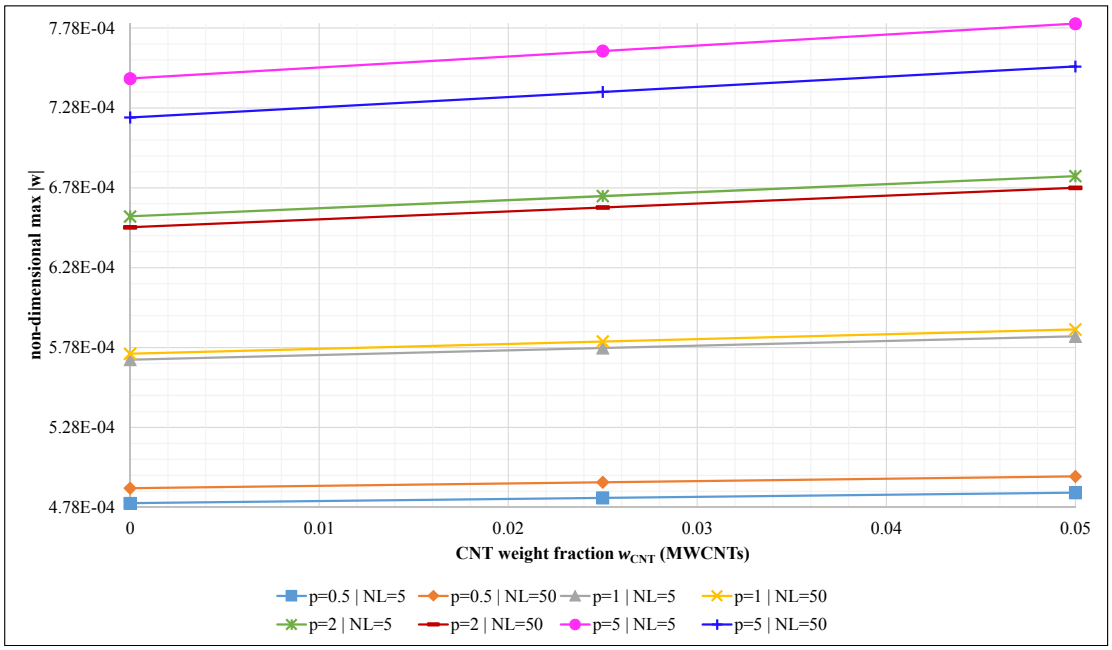

Figure G.25: Non-dimensional max. deflection $\overline{w}$ versus CNT weight fractions w_{CNT} (MWCNTs).

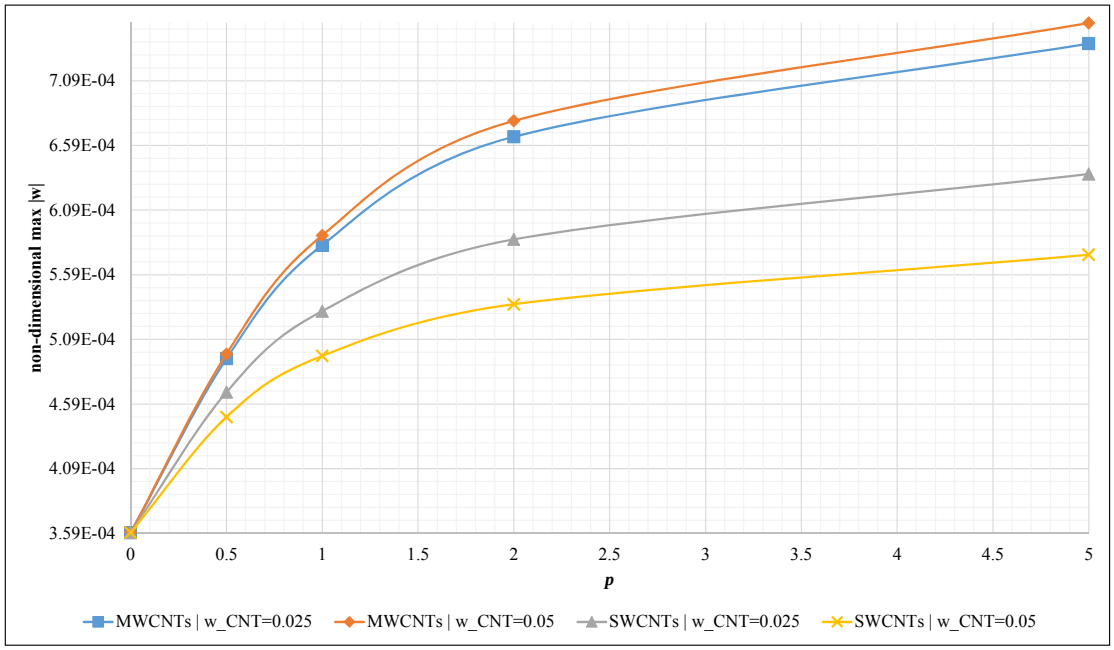

Figure G.26: Non-dimensional max. deflection $\overline{w}$ versus exponents p.

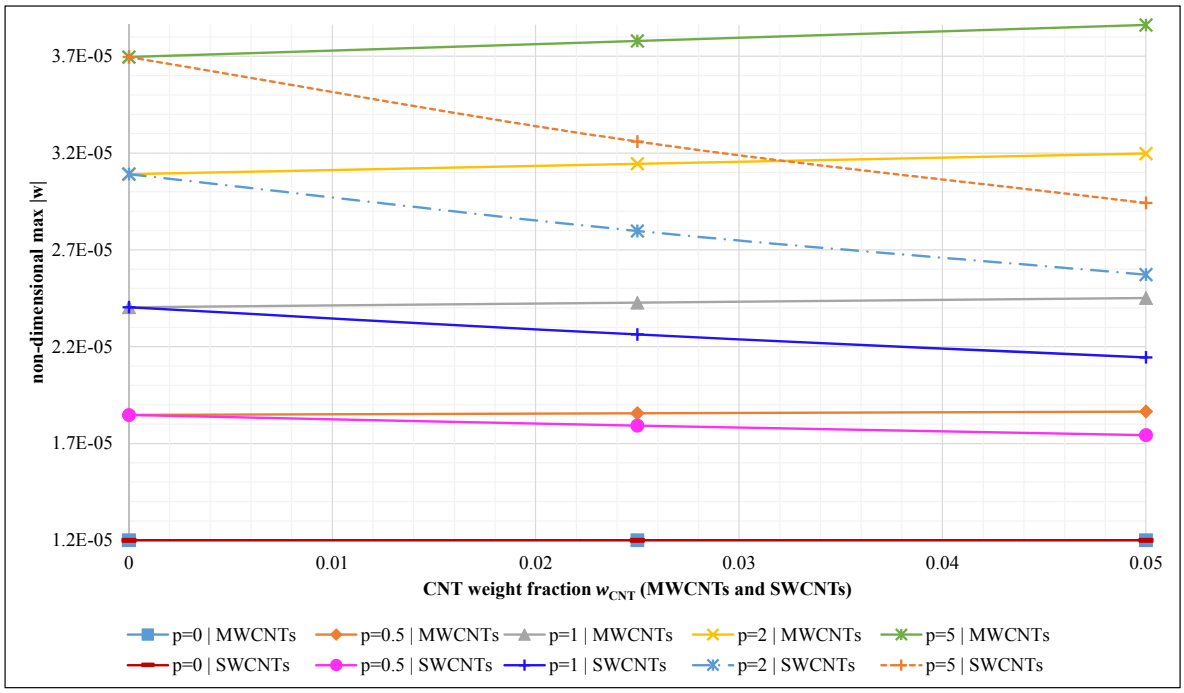

Figure G.27: Non-dimensional max. deflection $\overline{w}$ versus CNT weight fractions w_{CNT}.

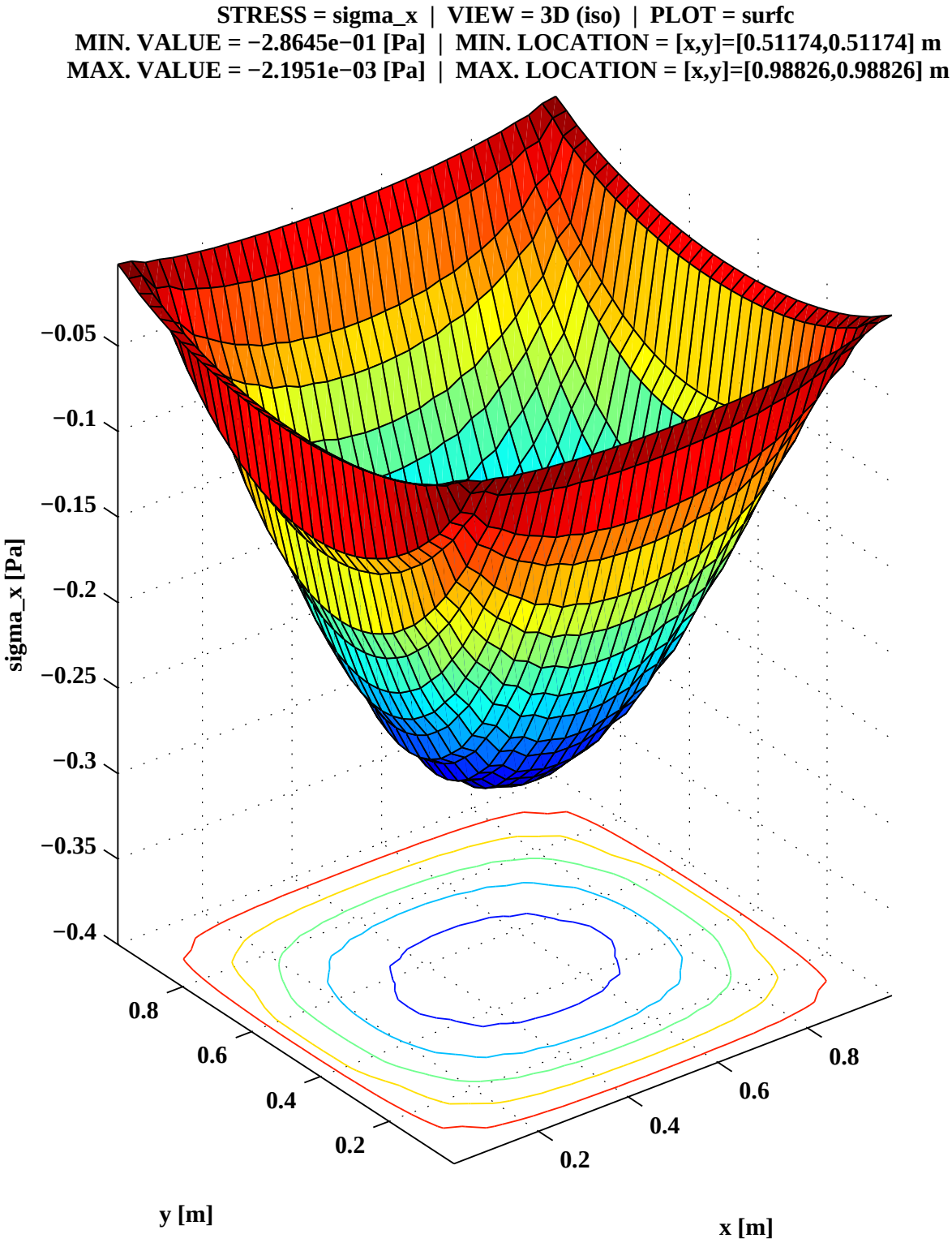

Figure G.28: In-plane non-dimensional normal stress $\overline{\sigma}_{xx}$ $(w_{CNT} = 0)$ (3D).

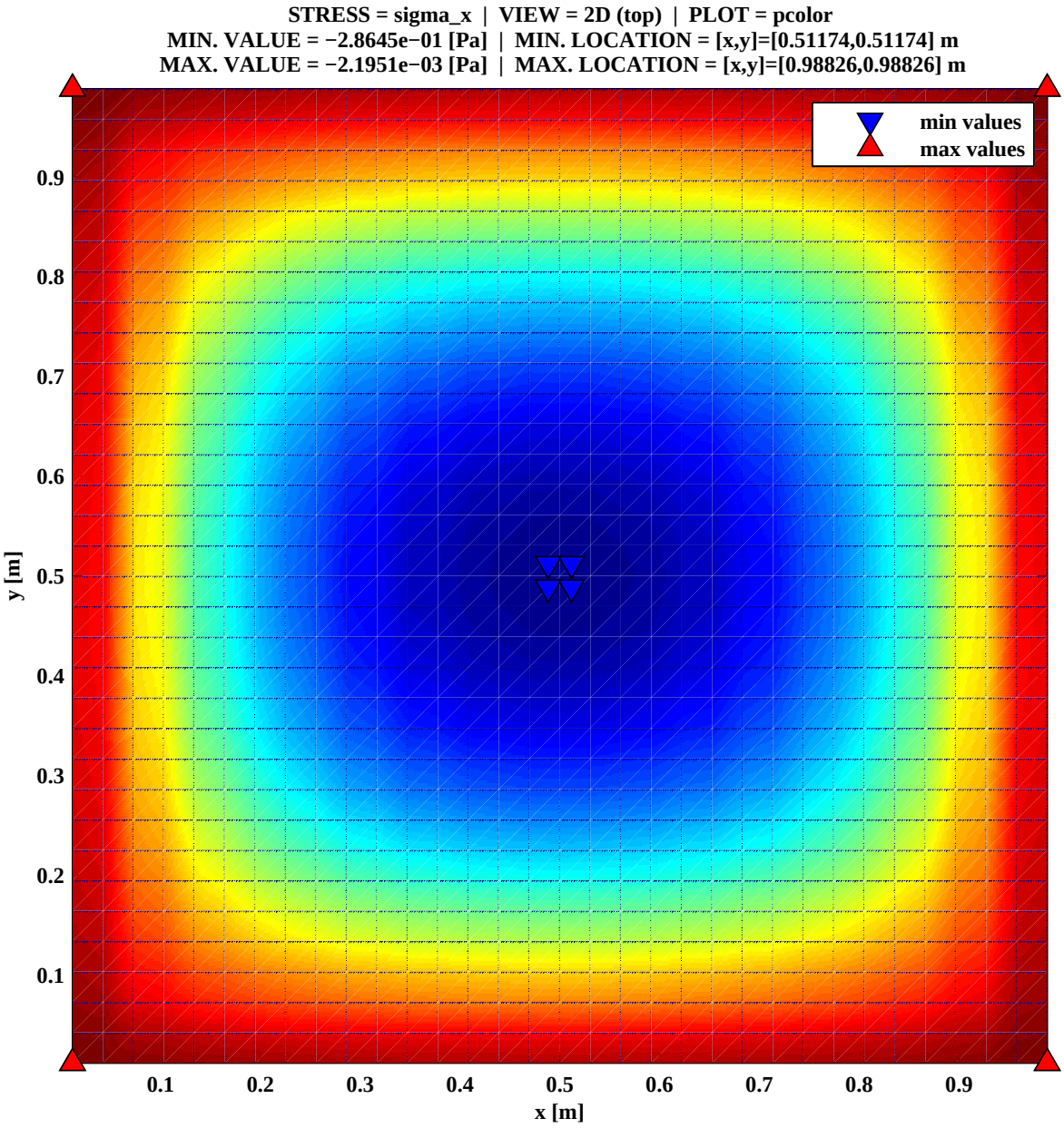

Figure G.29: In-plane non-dimensional normal stress $\overline{\sigma}_{xx}$ $(w_{CNT} = 0)$ (2D).

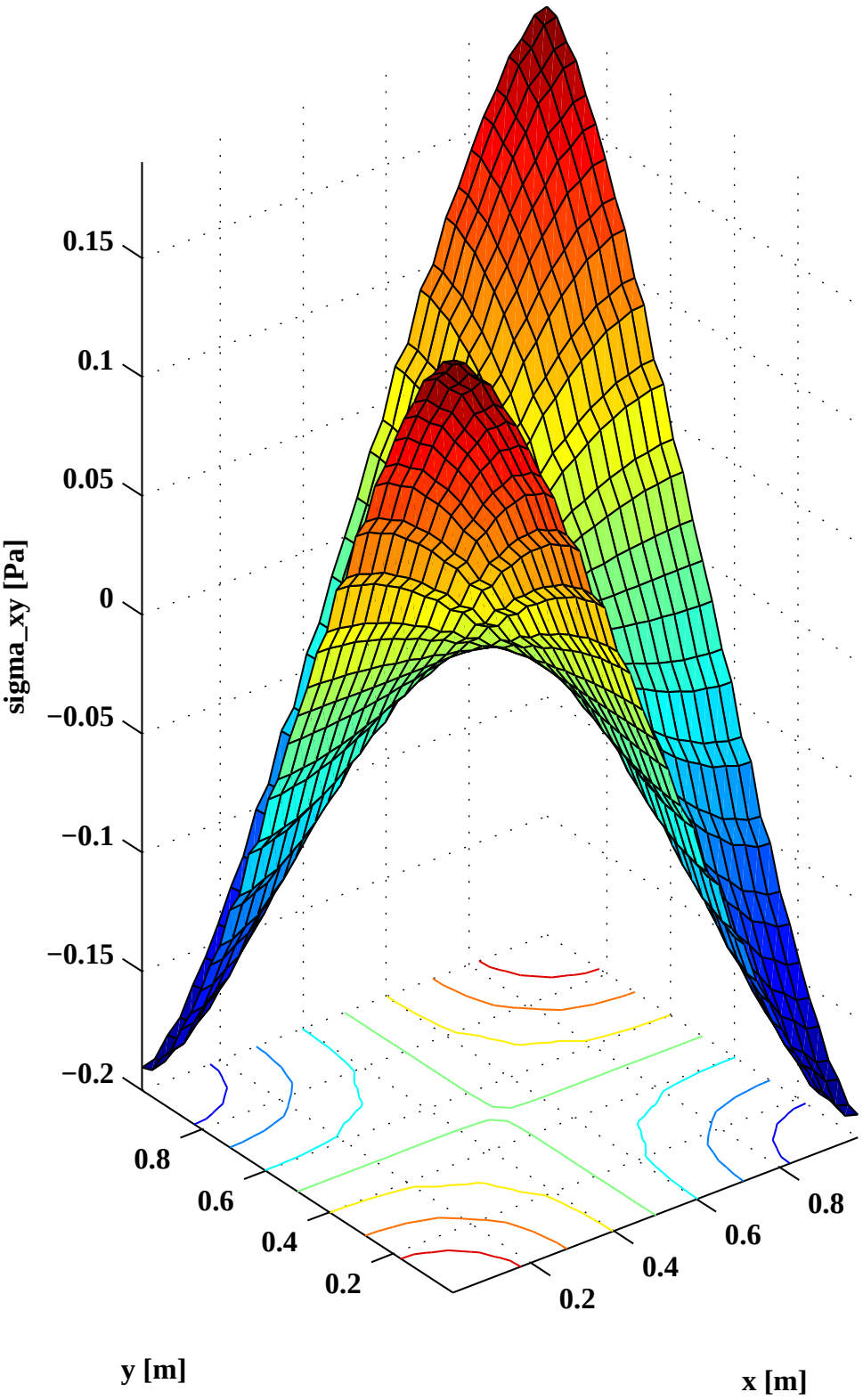

Figure G.30: In-plane shear stress $\overline{\tau}_{xy}$ $(w_{CNT} = 0)$ (3D).

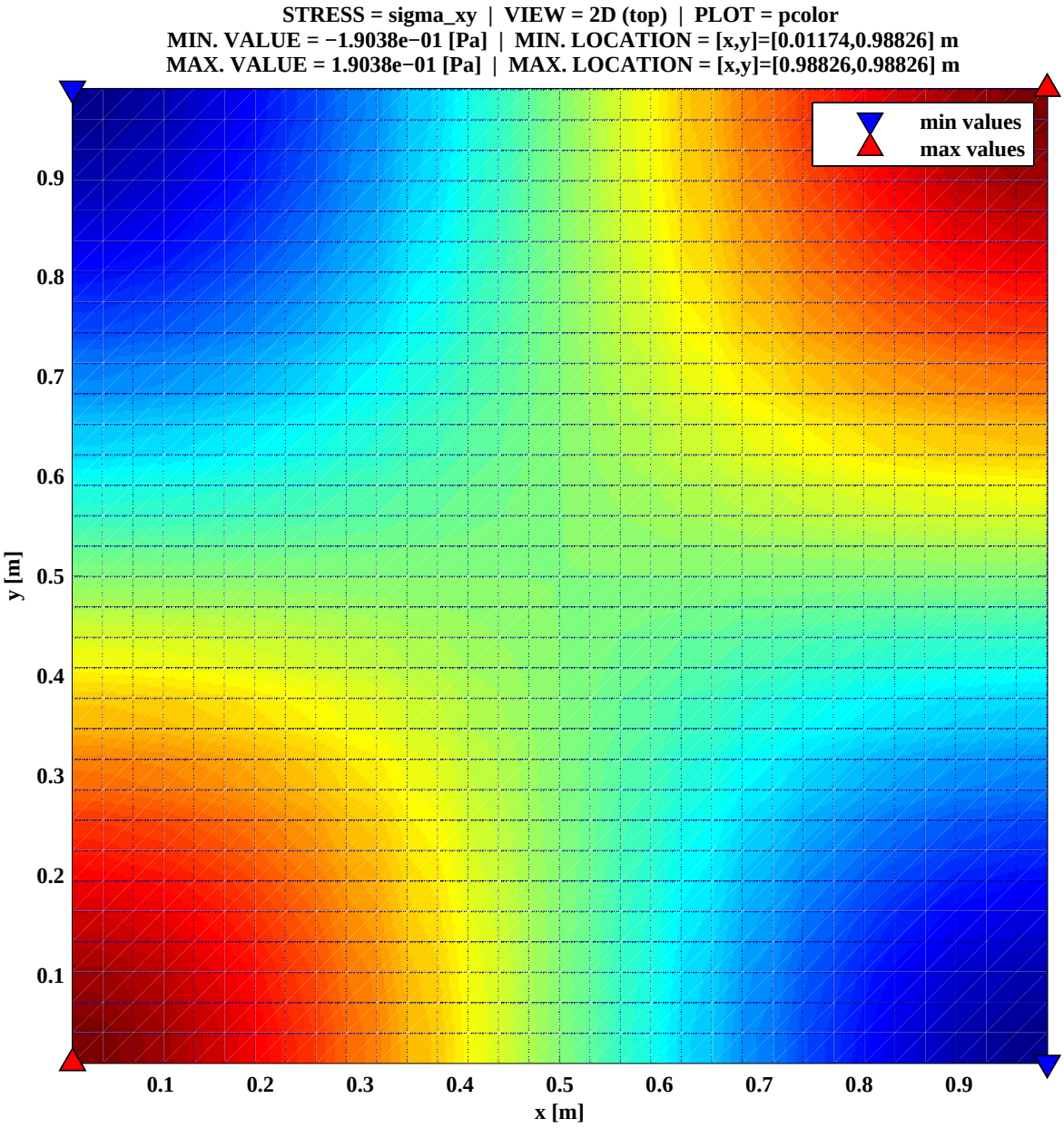

Figure G.31: In-plane shear stress $\overline{\tau}_{xy}$ $(w_{CNT} = 0)$ (2D).

STRESS = sigma_xz | VIEW = 3D (iso) | PLOT = surfc
MIN. VALUE = −3.1081e−02 [Pa] | MIN. LOCATION = [x,y]=[0.95618,0.54382] m
MAX. VALUE = 3.1081e−02 [Pa] | MAX. LOCATION = [x,y]=[0.01174,0.54382] m

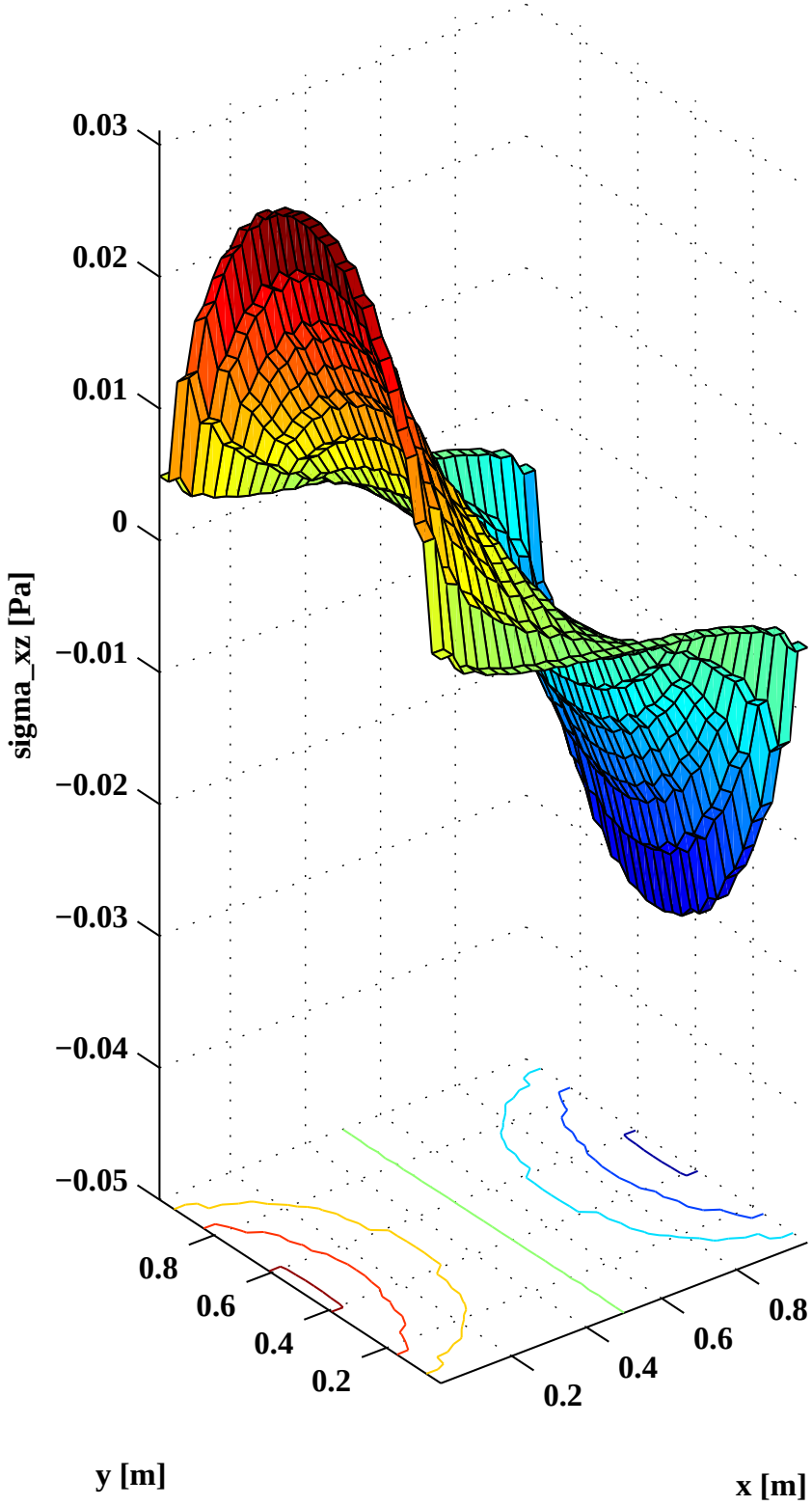

Figure G.32: Interlaminar shear stress $\overline{\tau}_{xz}$ $(w_{CNT} = 0)$ (3D).

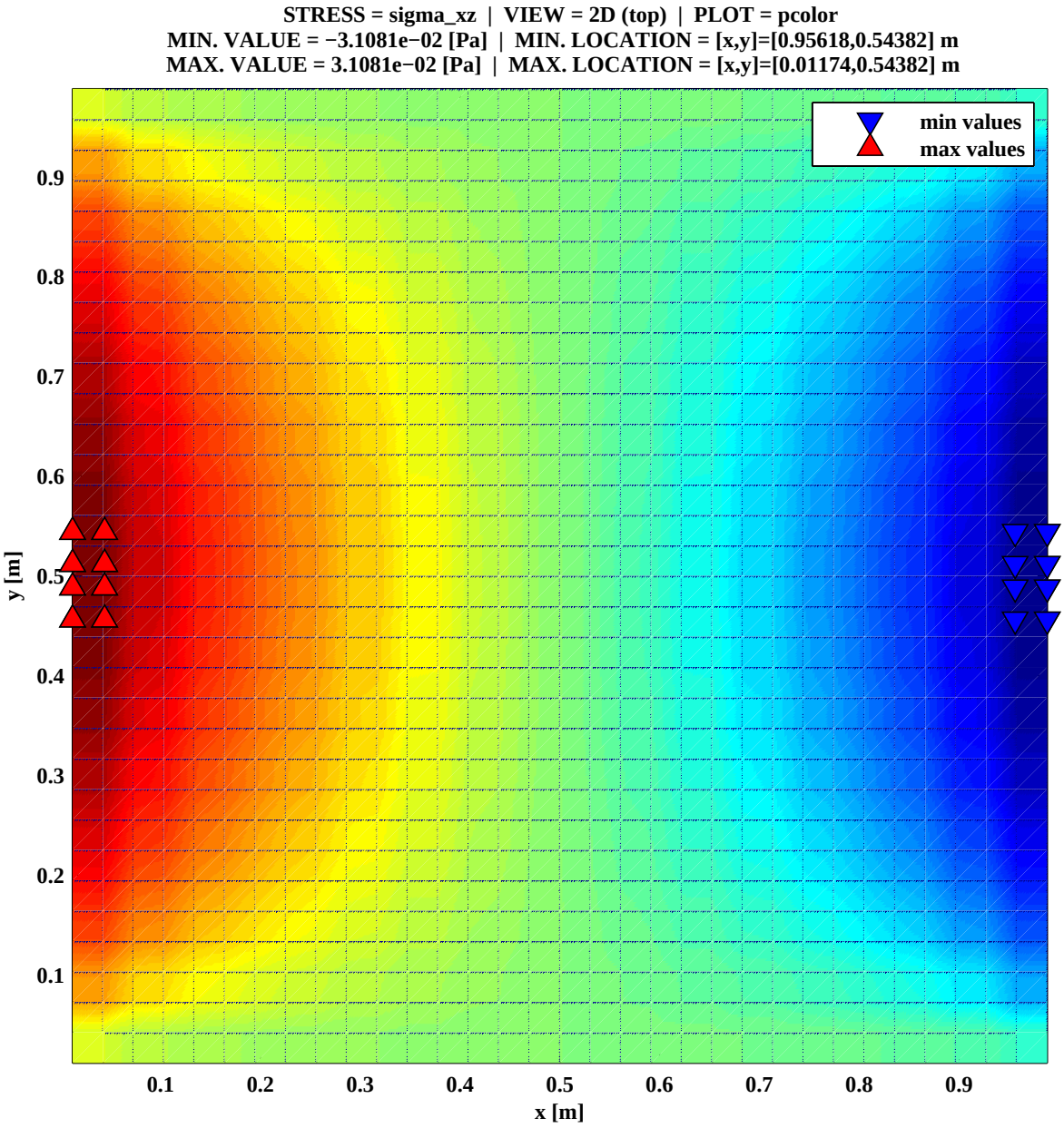

Figure G.33: Interlaminar shear stress $\overline{\tau}_{xz}$ $(w_{CNT} = 0)$ (2D).

STRESS = sigma_xz | VIEW = 3D (iso) | PLOT = surfc
MIN. VALUE = −3.1081e−02 [Pa] | MIN. LOCATION = [x,y]=[0.95618,0.54382] m
MAX. VALUE = 3.1081e−02 [Pa] | MAX. LOCATION = [x,y]=[0.01174,0.54382] m

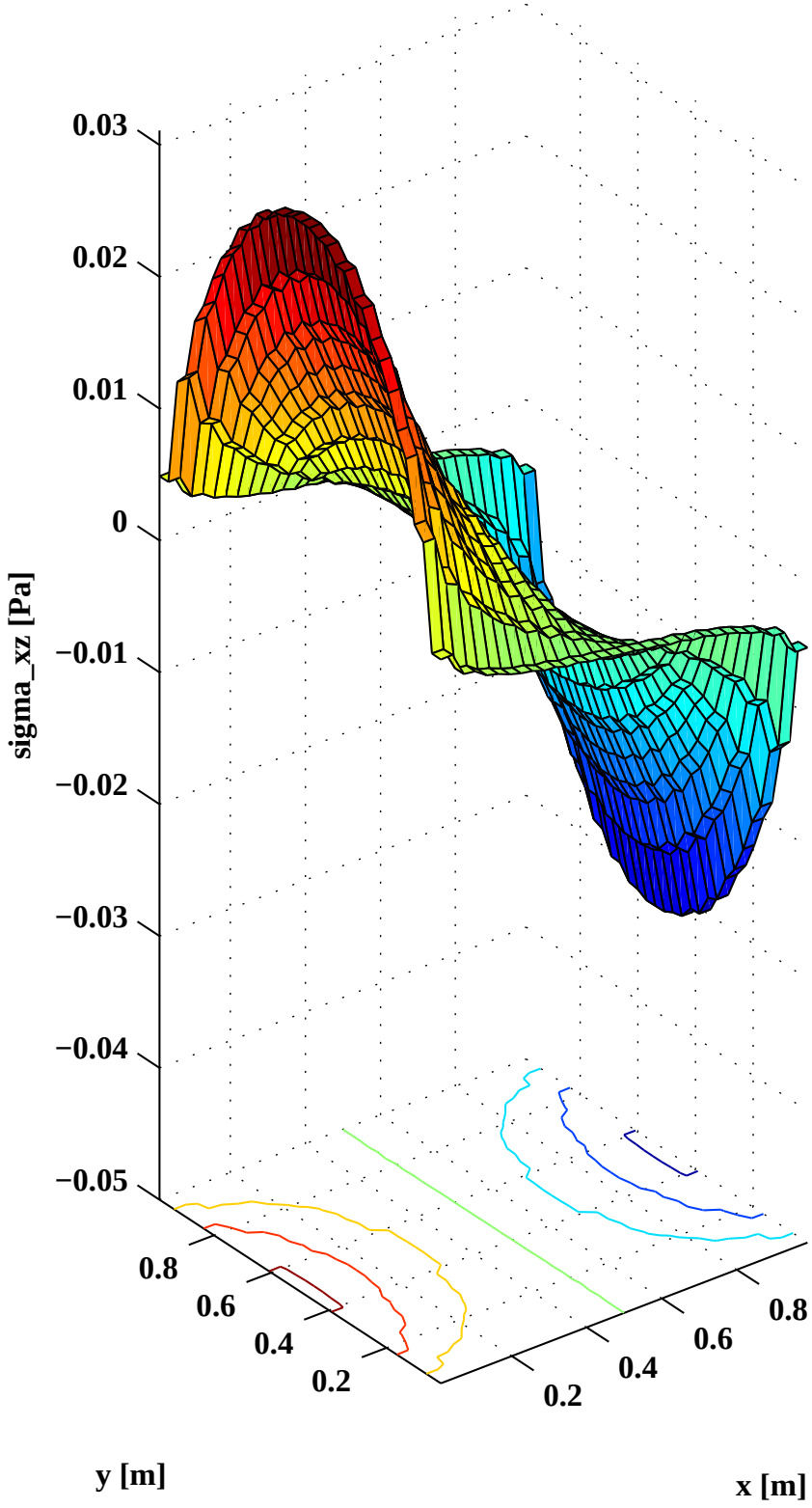

Figure G.34: Interlaminar shear stress $\overline{\tau}_{xz}$ $(w_{CNT} = 0, a/h = 10)$ (3D).

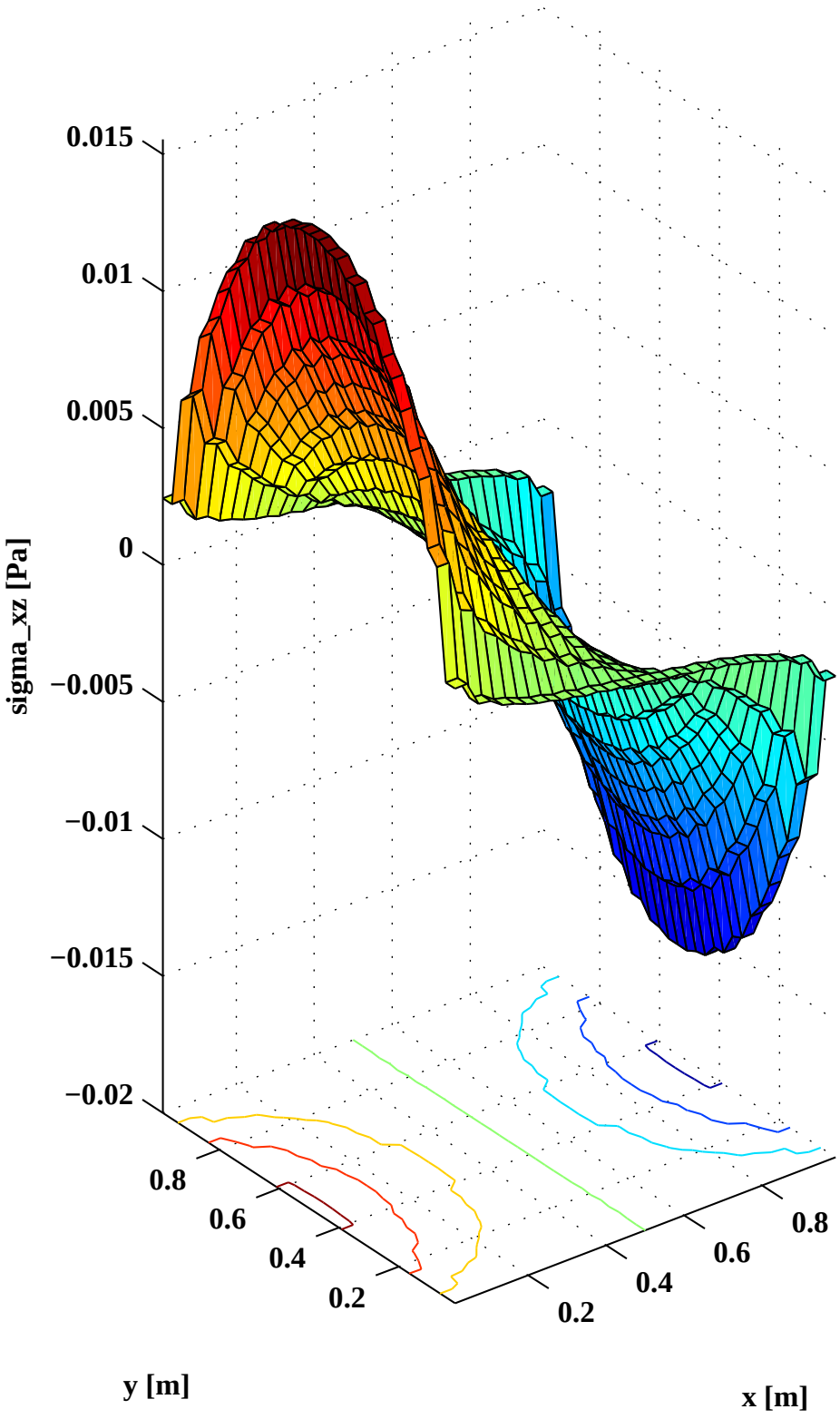

Figure G.35: Interlaminar shear stress $\overline{\tau}_{xz}$ $(w_{CNT} = 0, a/h = 20)$ (3D).

G.2.2 Dynamics (free vibrations)

Results associated with Section 4.2.2.2.

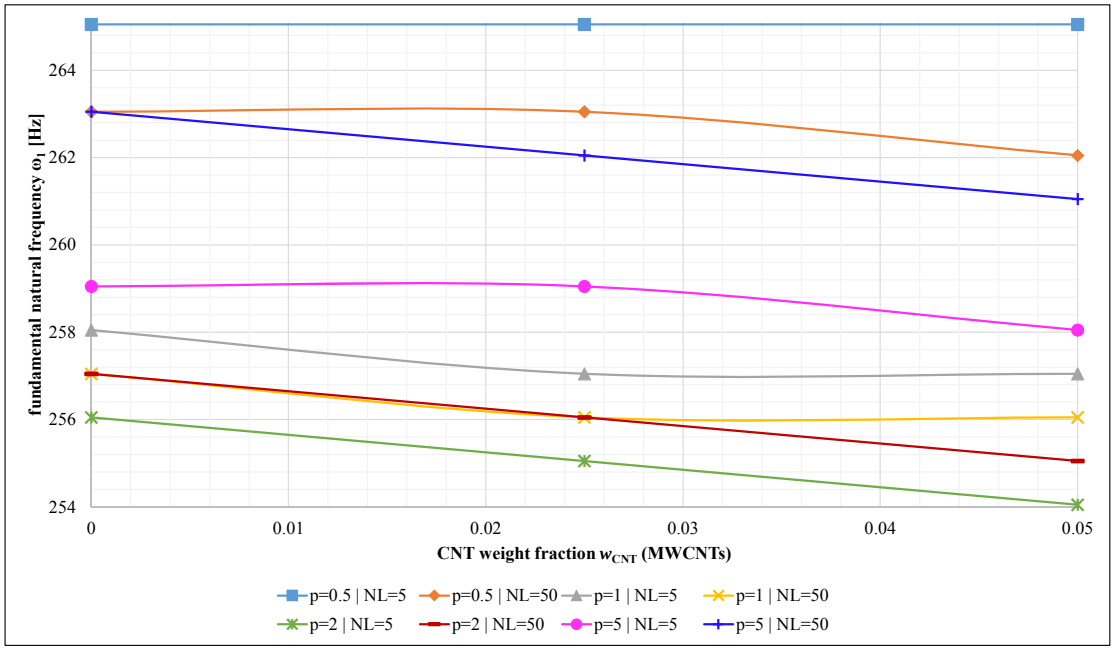

Figure G.36: Fundamental natural frequency ω_1 versus CNT weight fractions w_{CNT} (MWCNTs).

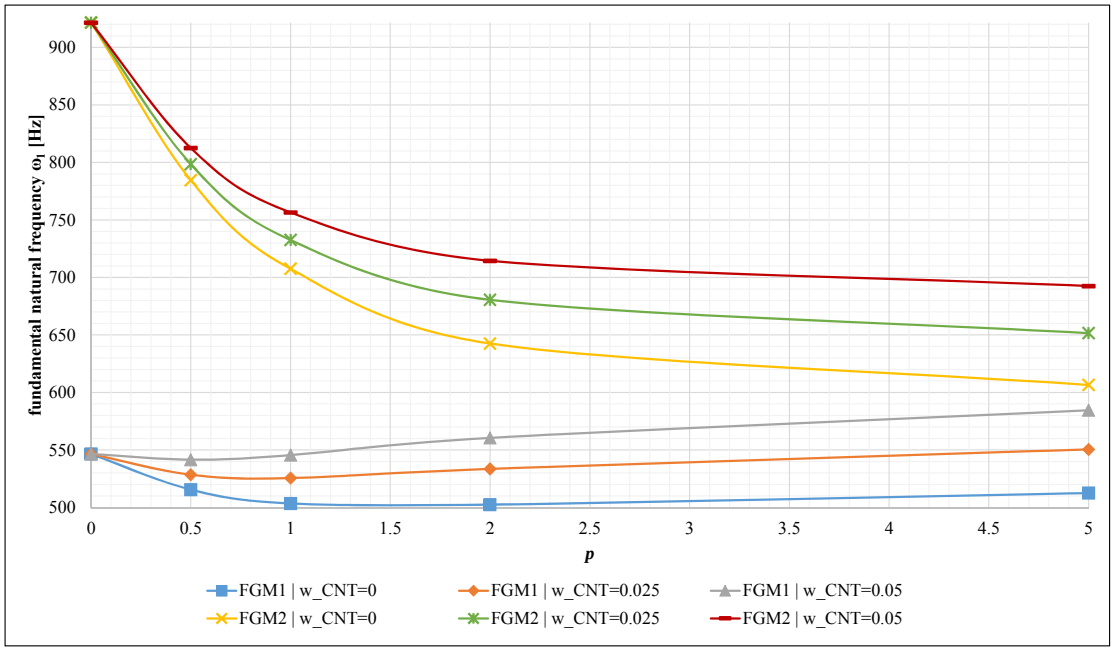

Figure G.37: Fundamental natural frequency ω_1 versus exponents p (SWCNTs).

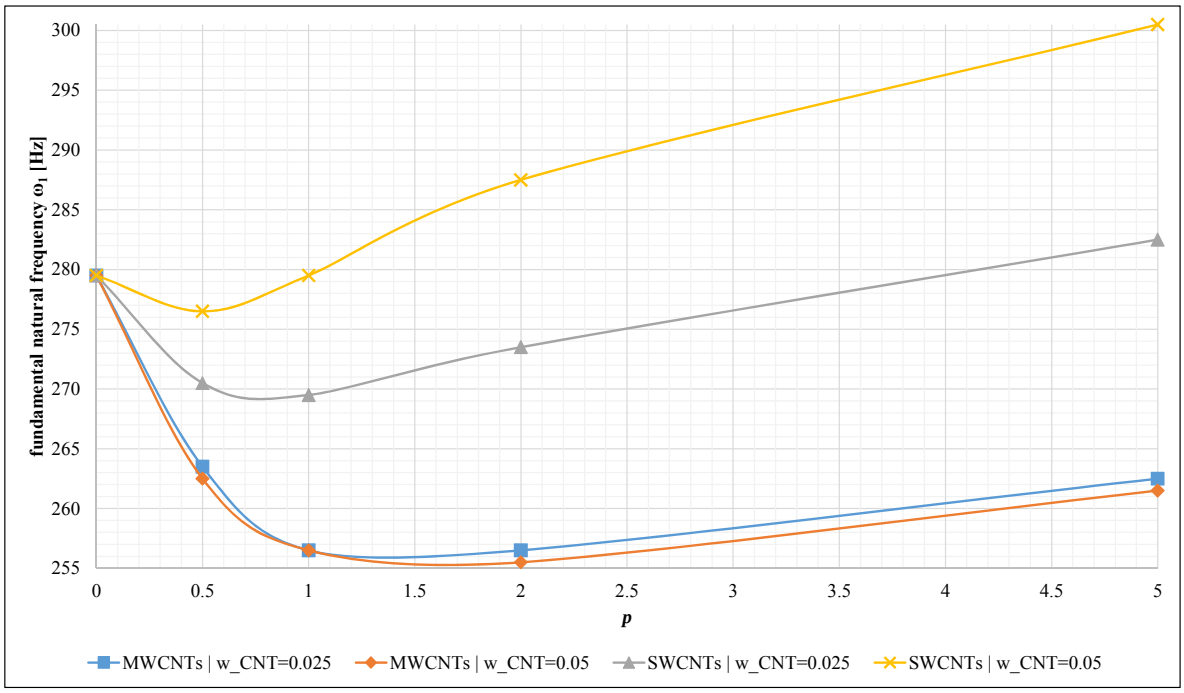

Figure G.38: Fundamental natural frequency ω_1 versus exponents p (FGM1).

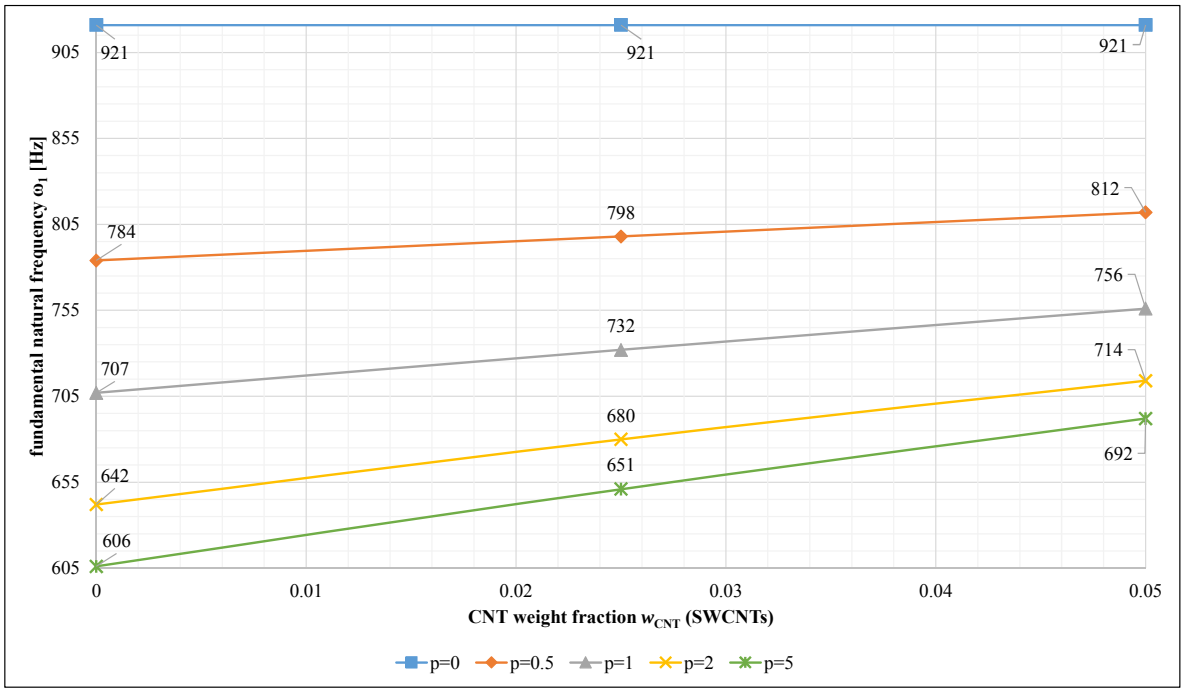

Figure G.39: Fundamental nat. freq. ω_1 versus CNT weight fractions w_{CNT} (FGM2 with SWCNTs).

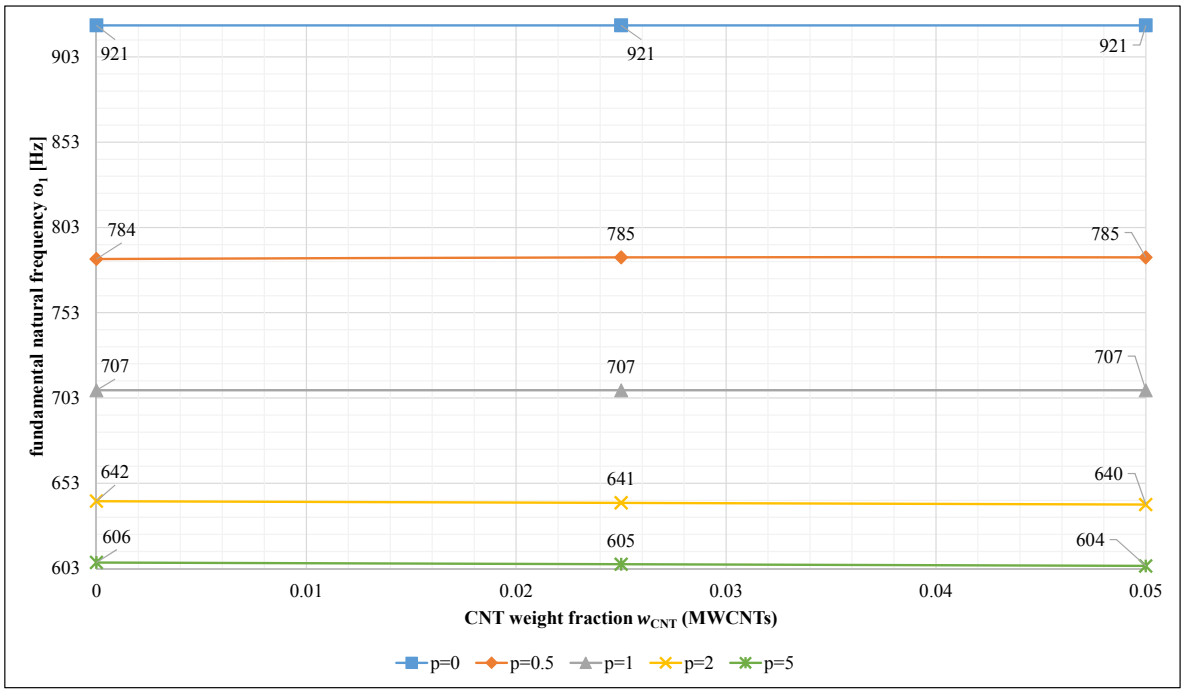

Figure G.40: Fundamental nat. freq. ω_1 versus CNT weight fractions w_{CNT} (FGM2 with MWCNTs).

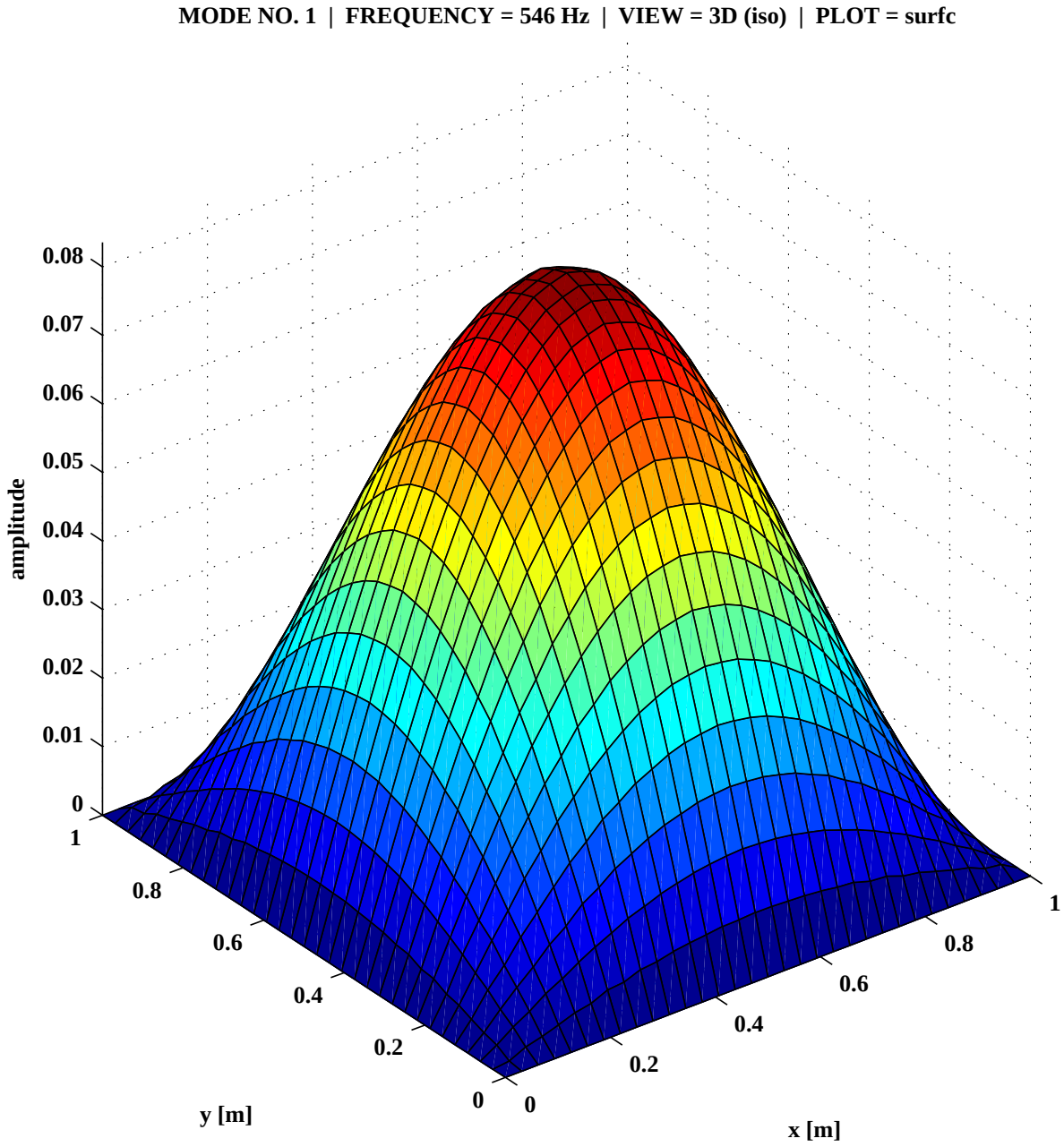

Figure G.41: Fundamental free vibrational mode considering $p = 0$ (3D).

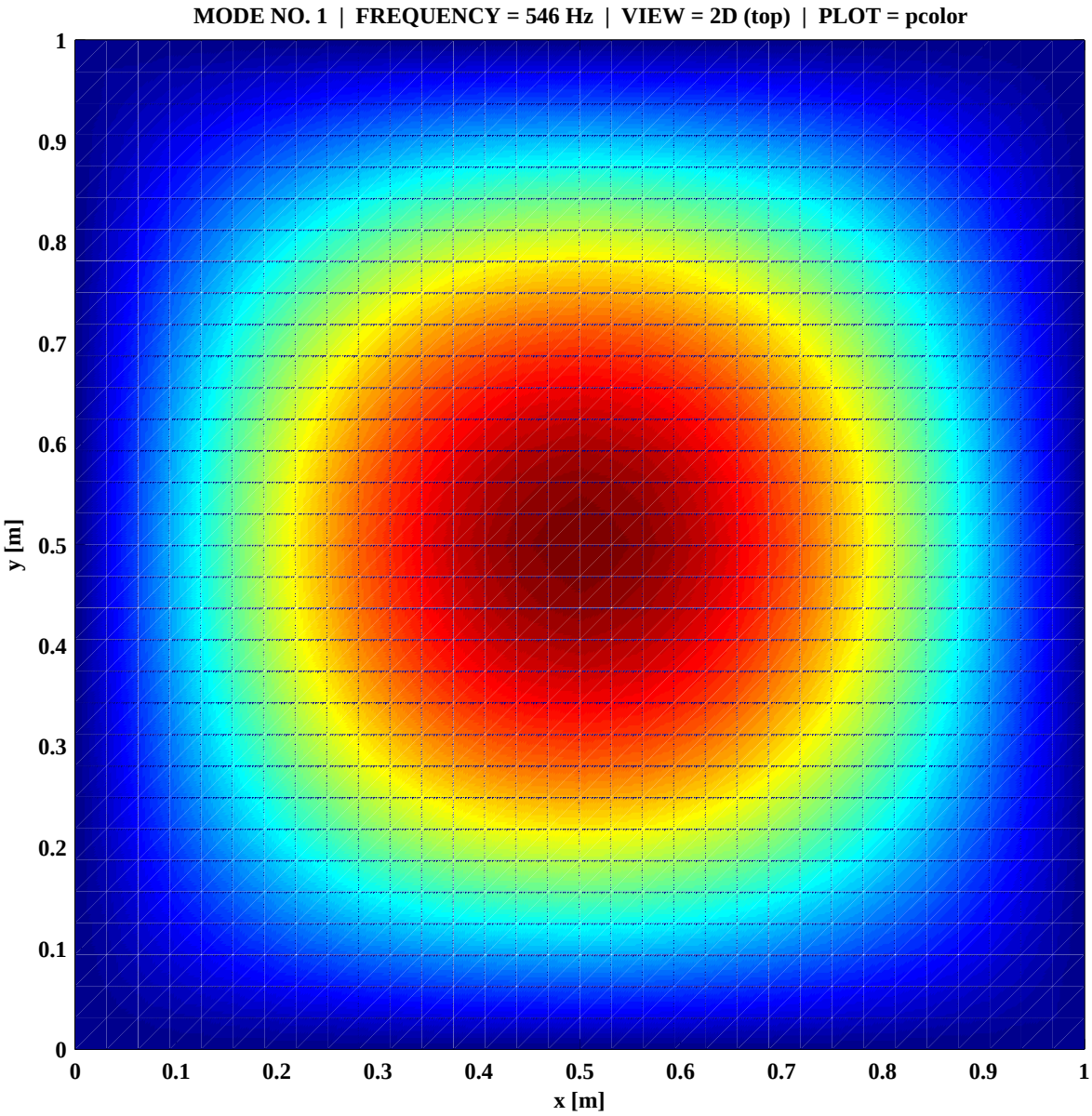

Figure G.42: Fundamental free vibrational mode considering $p = 0$ (2D).

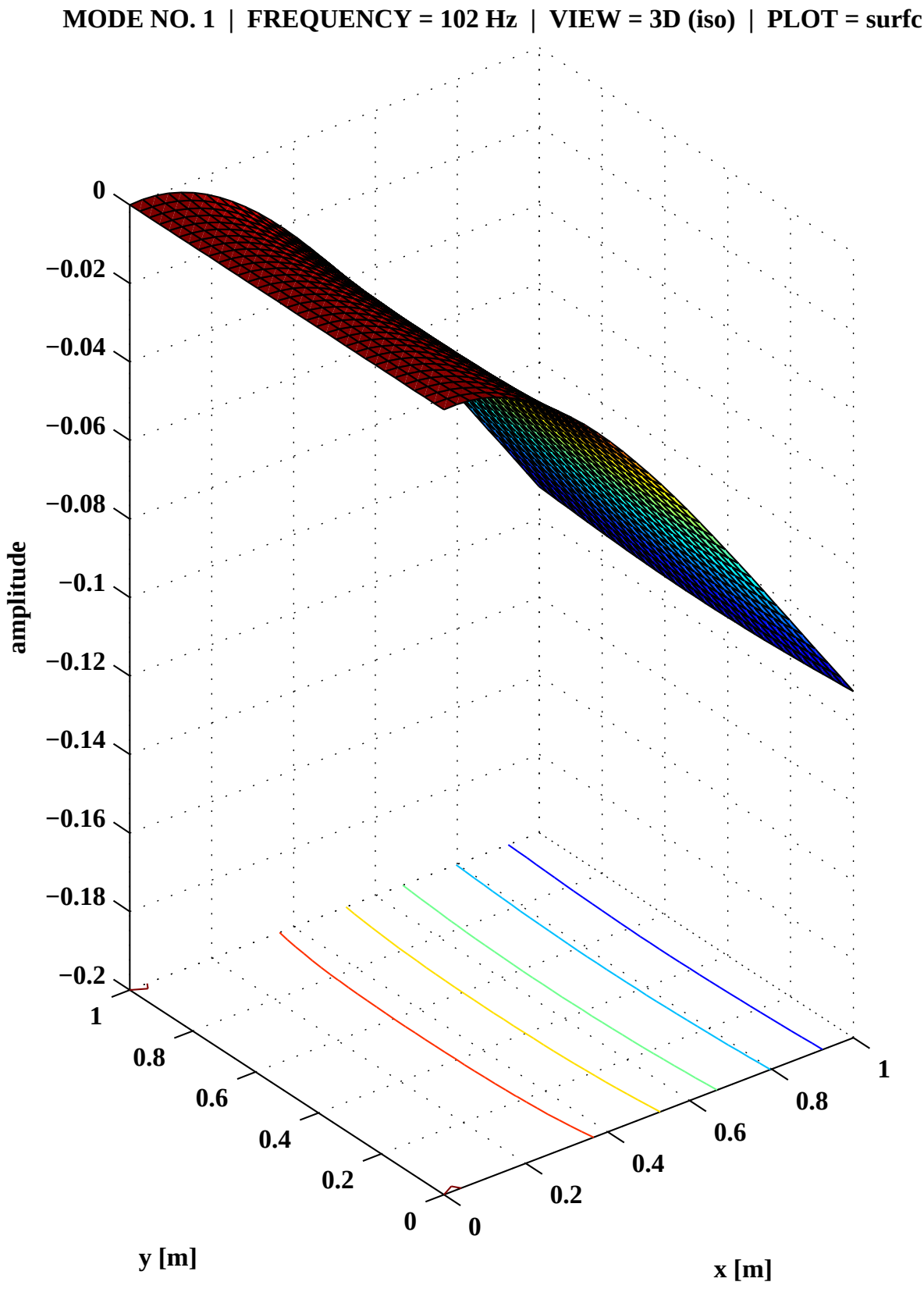

Figure G.43: Fundamental free vibrational mode considering (CFFF) MBCs (3D).

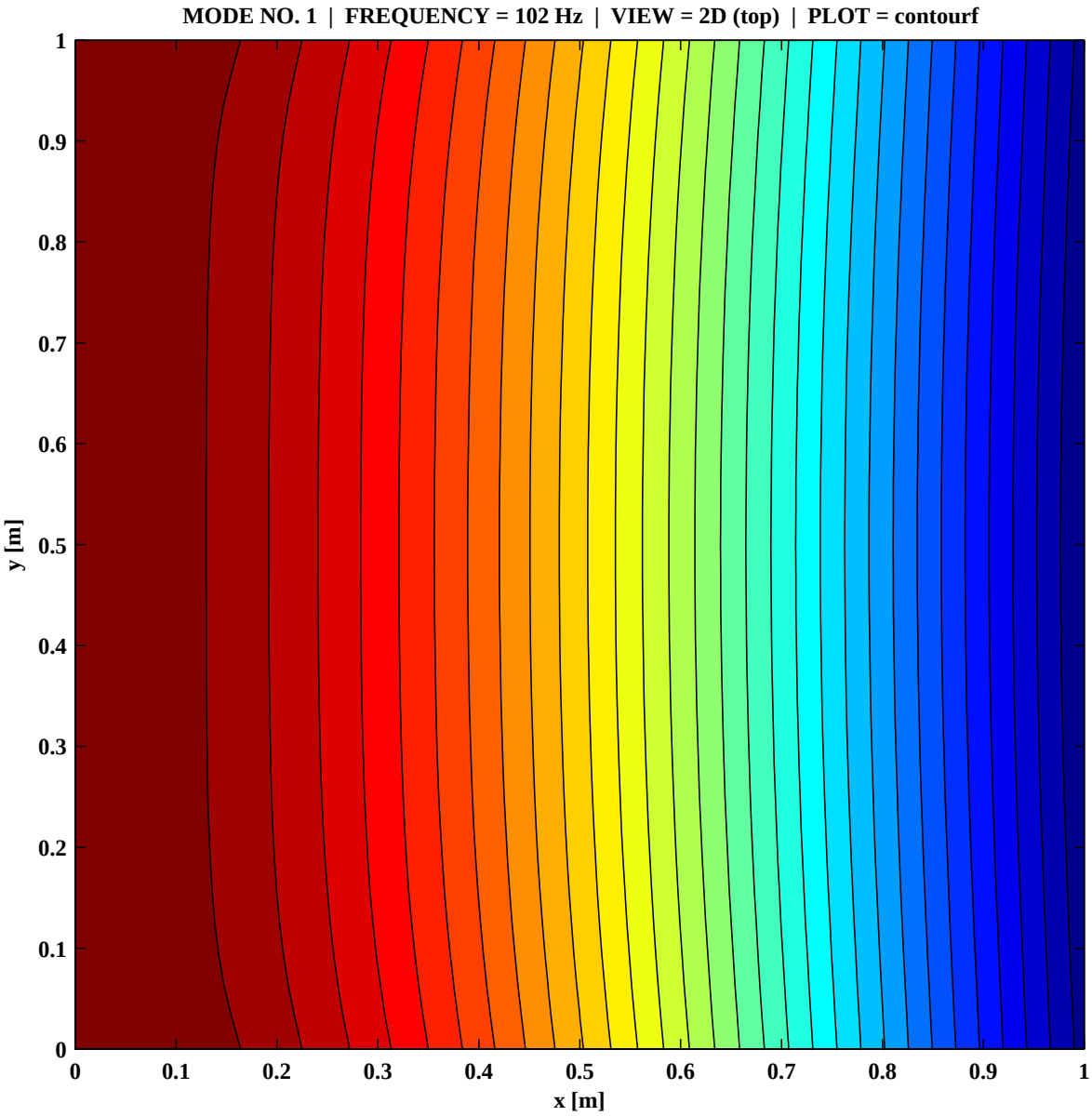

Figure G.44: Fundamental free vibrational mode considering (CFFF) MBCs (2D).

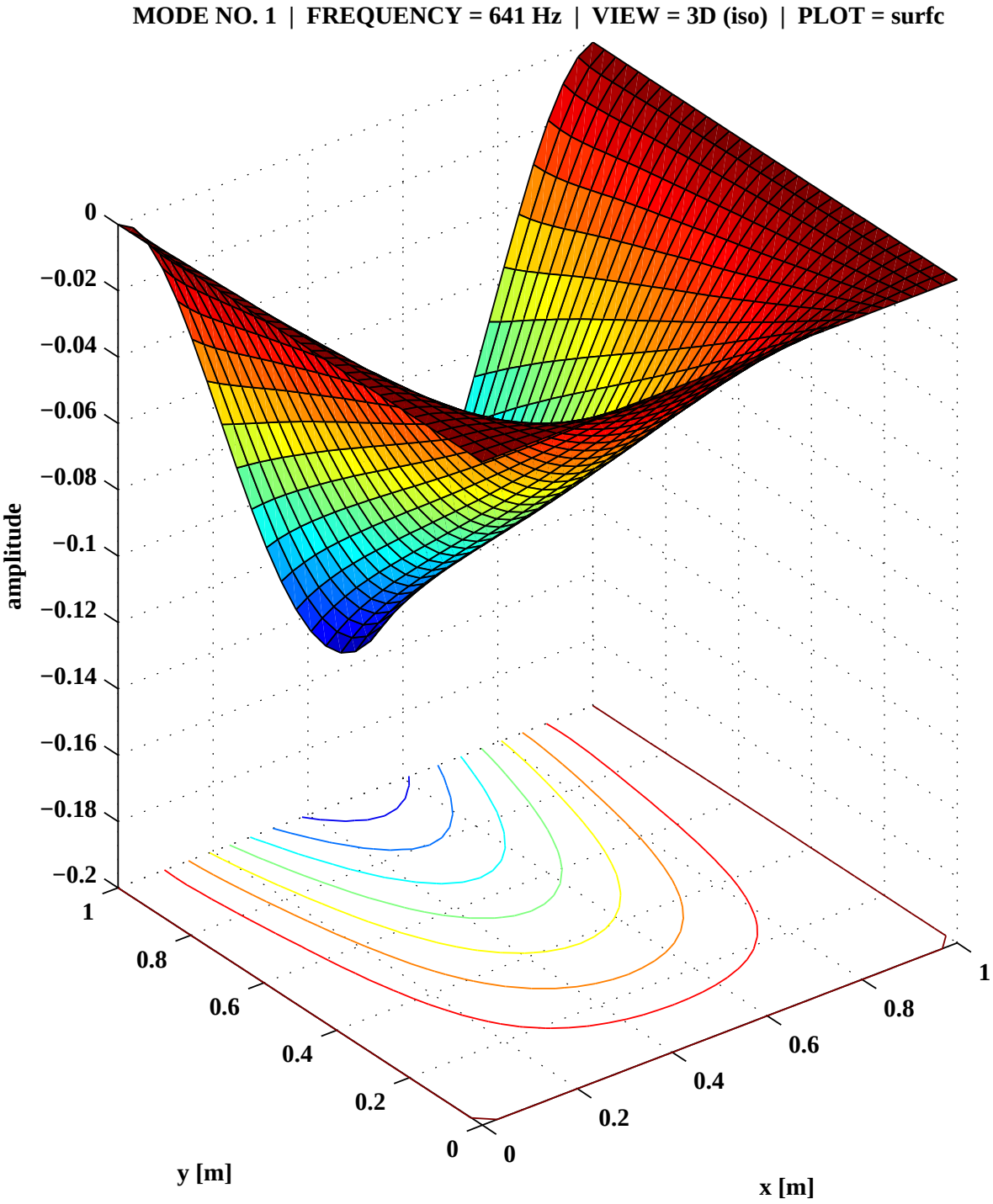

Figure G.45: Fundamental free vibrational mode considering (CCSF) MBCs (3D).

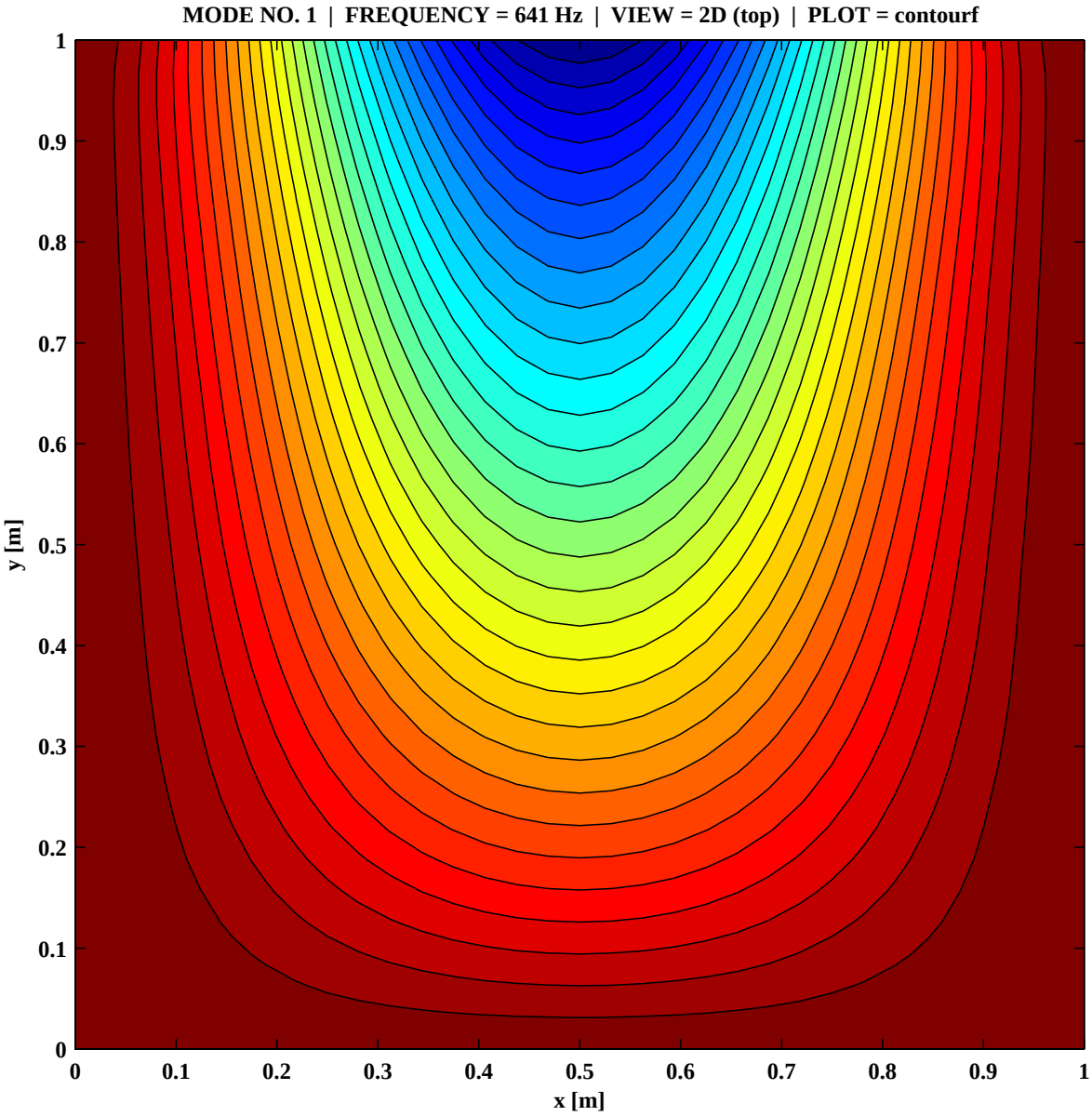

Figure G.46: Fundamental free vibrational mode considering (CCSF) MBCs (2D).

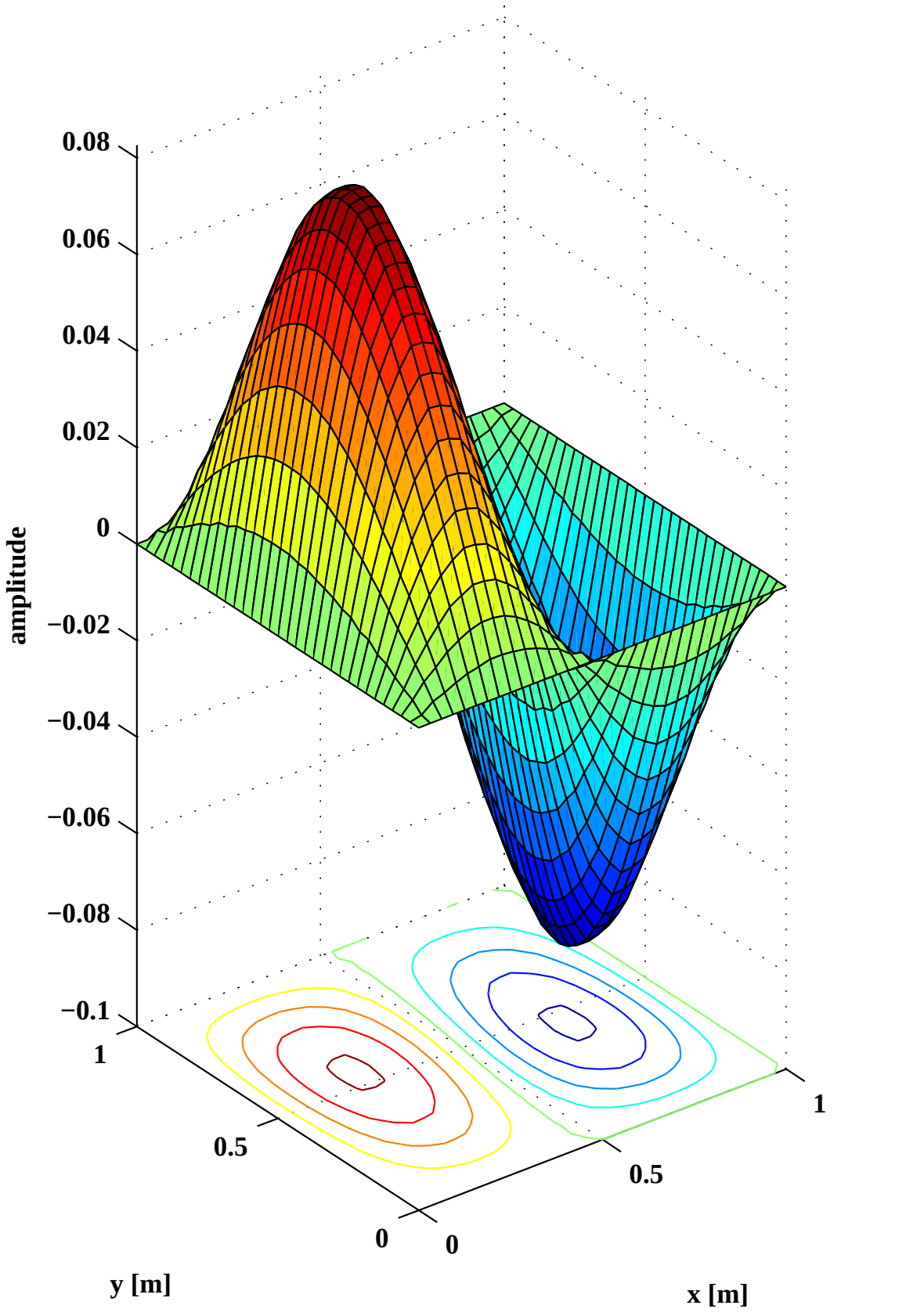

Figure G.47: Second free vibrational mode considering (SSSS) MBCs, FGM1 and $p = 0$ (3D).

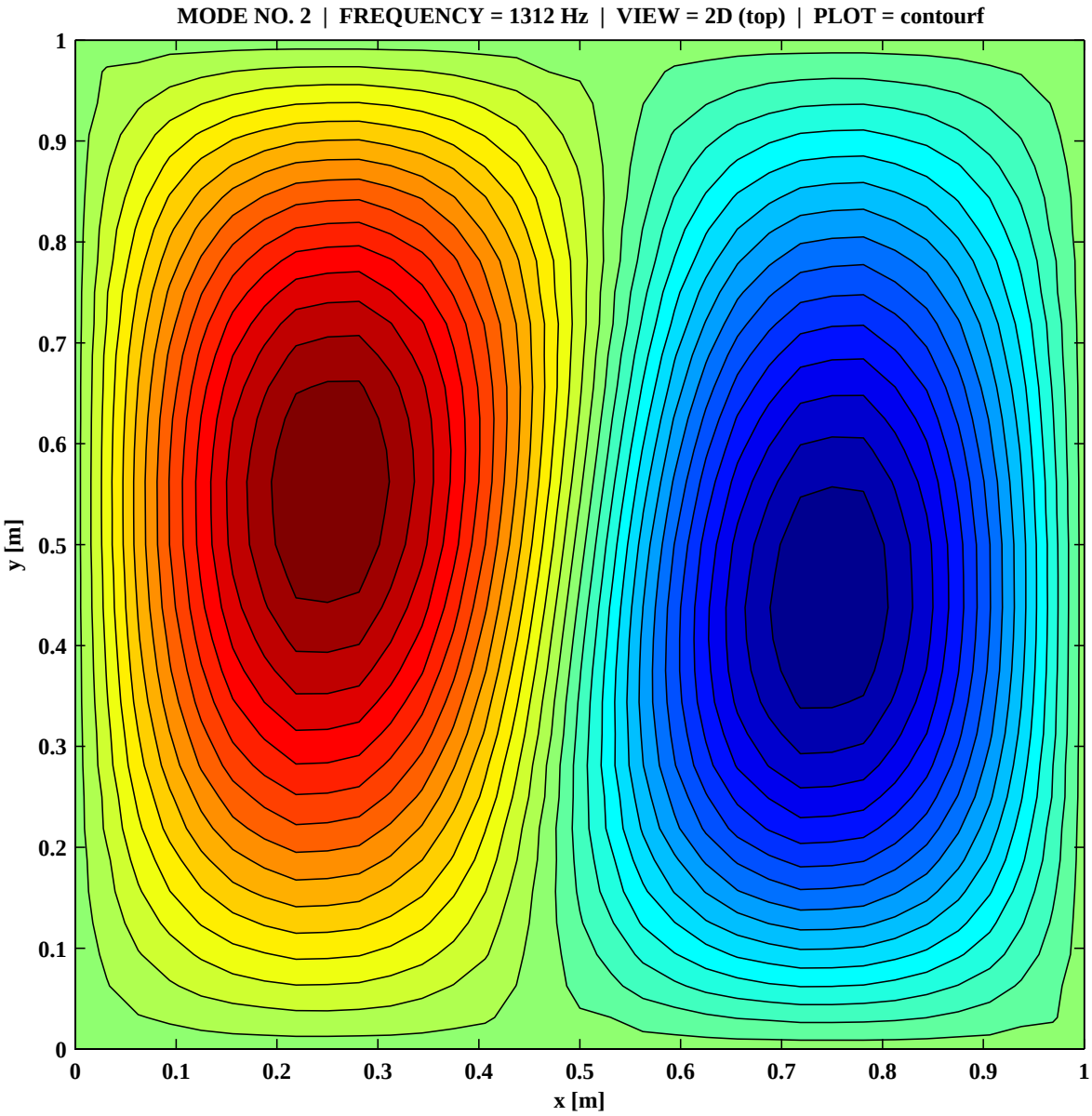

Figure G.48: Second free vibrational mode considering (SSSS) MBCs, FGM1 and $p = 0$ (2D).

G.3 Multilayered smart structures

G.3.1 Statics

Schemes and results associated with Section 4.2.3.1.

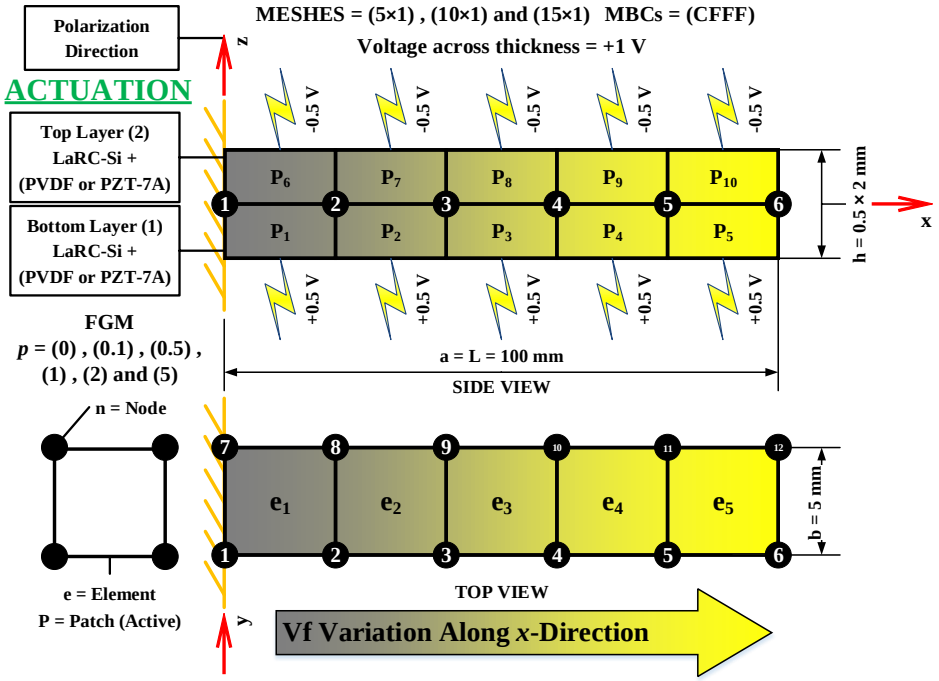

Figure G.49: Parametric CS scheme of longitudinal FGM bimorph beam (statics actuation (CFFF)).

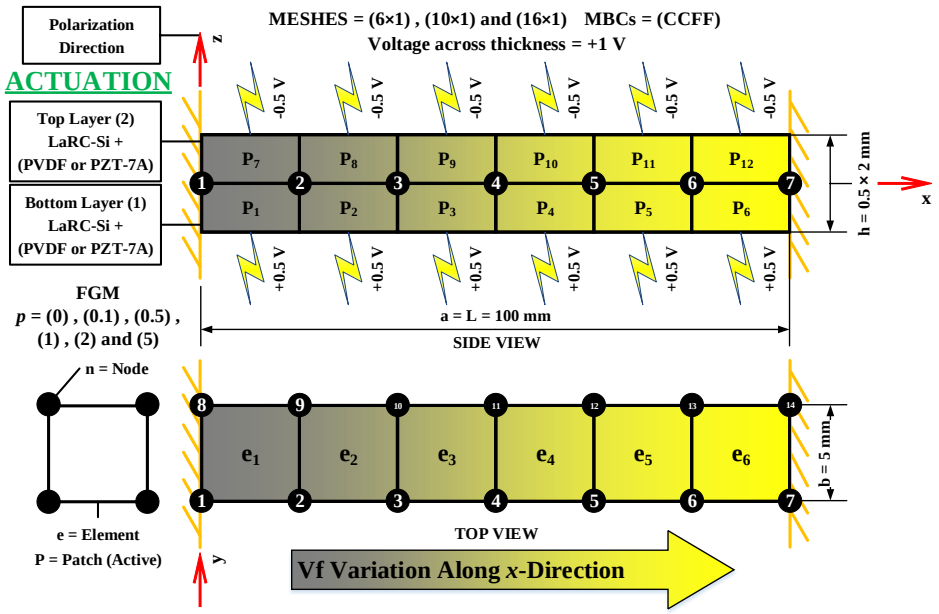

Figure G.50: Parametric CS scheme of longitudinal FGM bimorph beam (statics actuation (CCFF)).

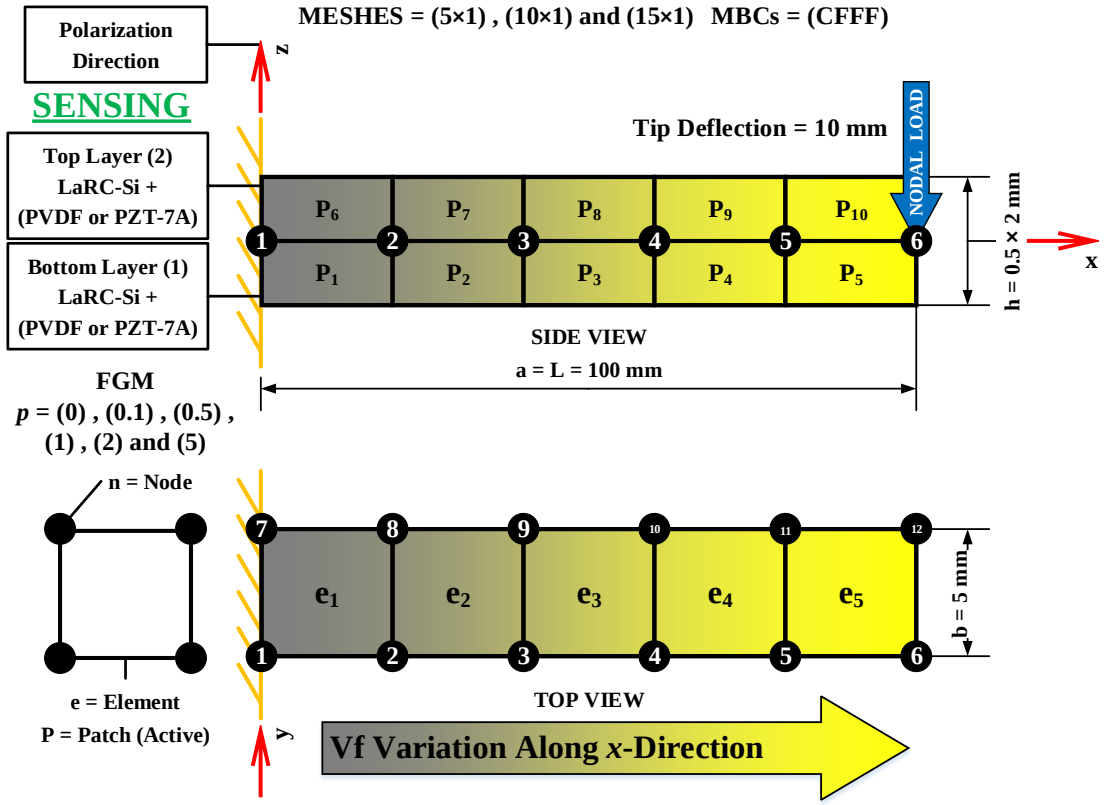

Figure G.51: Parametric CS scheme of longitudinal FGM bimorph beam (statics sensing (CFFF)).

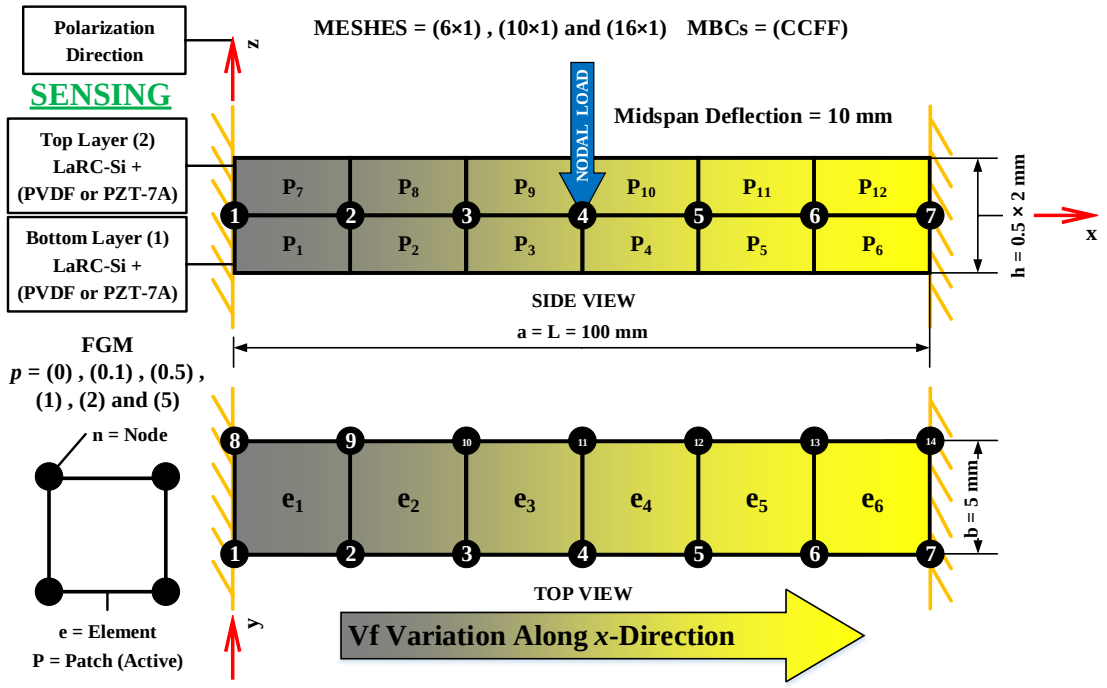

Figure G.52: Parametric CS scheme of longitudinal FGM bimorph beam (statics sensing (CCFF)).

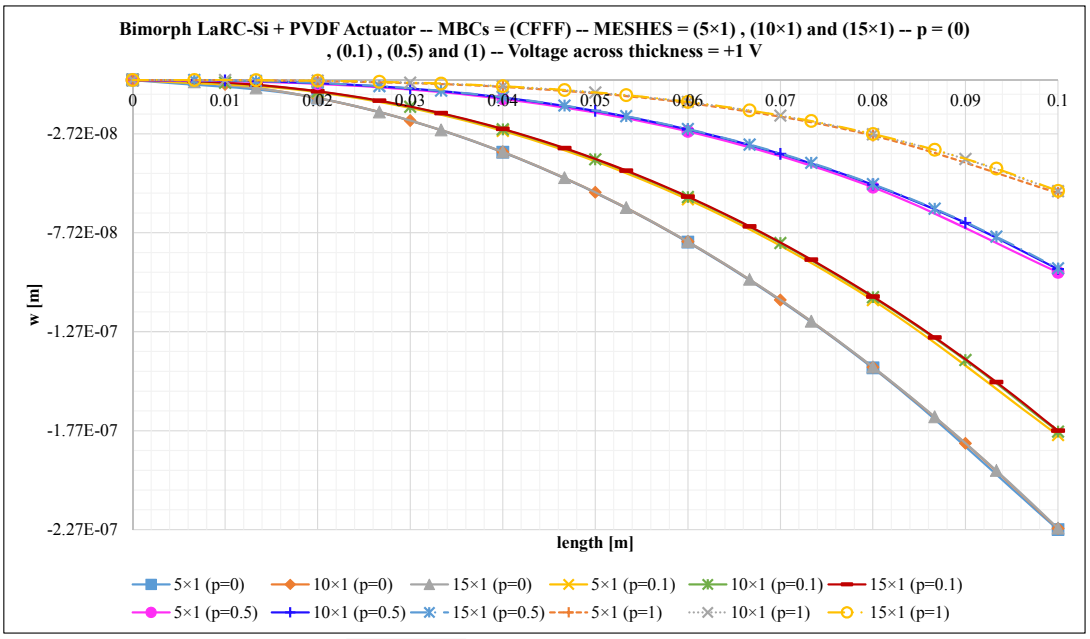

all results | (15×1) | $p = 0$ | $p = 0.1$ | $p = 0.5$ | $p = 1$

Figure G.53: Deflection results from the parametric case study of longitudinal FGM bimorph beam (statics actuation (CFFF)), mixing up LaRC-Si and PVDF, considering several meshes and p-exponents (0, 0.1, 0.5 and 1). Please click on the buttons above this caption to toggle between plotted results.

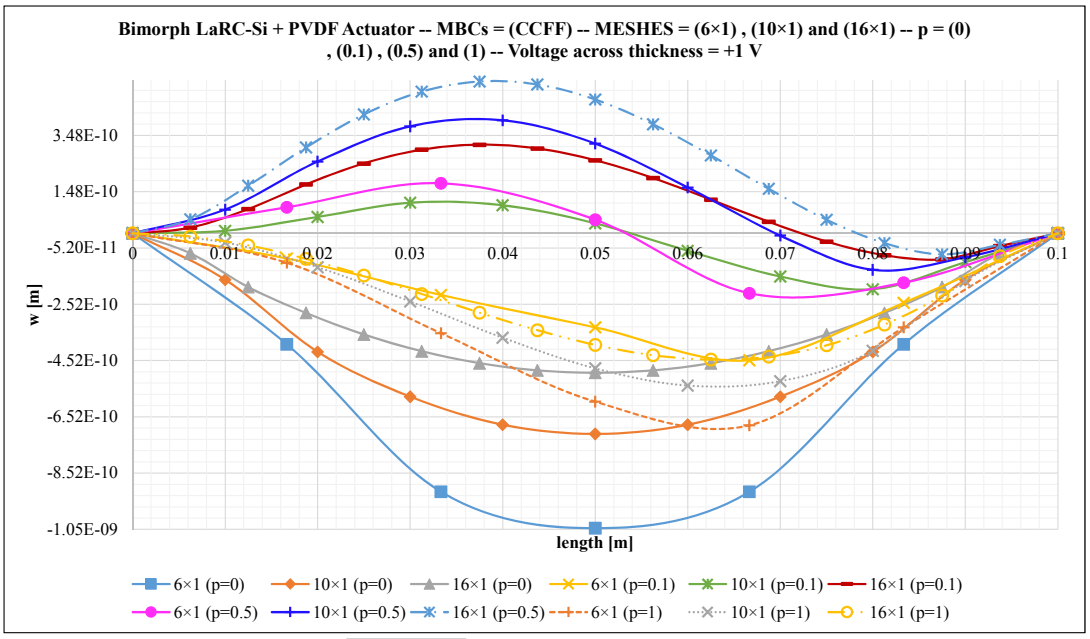

all results | (16×1) | $p = 0$ | $p = 0.1$ | $p = 0.5$ | $p = 1$

Figure G.54: Deflection results from the parametric case study of longitudinal FGM bimorph beam (statics actuation (CCFF)), mixing up LaRC-Si and PVDF, considering several meshes and p-exponents (0, 0.1, 0.5 and 1). Please click on the buttons above this caption to toggle between plotted results.

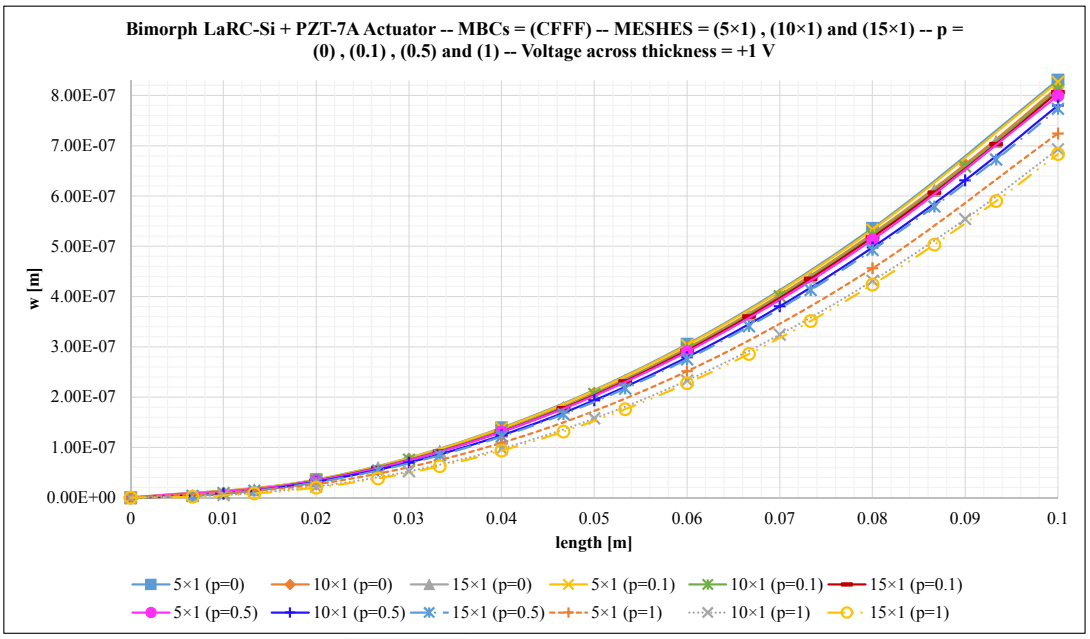

all results | (15×1) | $p = 0$ | $p = 0.1$ | $p = 0.5$ | $p = 1$

Figure G.55: Deflection results from the parametric case study of longitudinal FGM bimorph beam (statics actuation (CFFF)), mixing up LaRC-Si and PZT-7A, with several meshes and p-exponents (0, 0.1, 0.5 and 1). Please click on the buttons above this caption to toggle between plotted results.

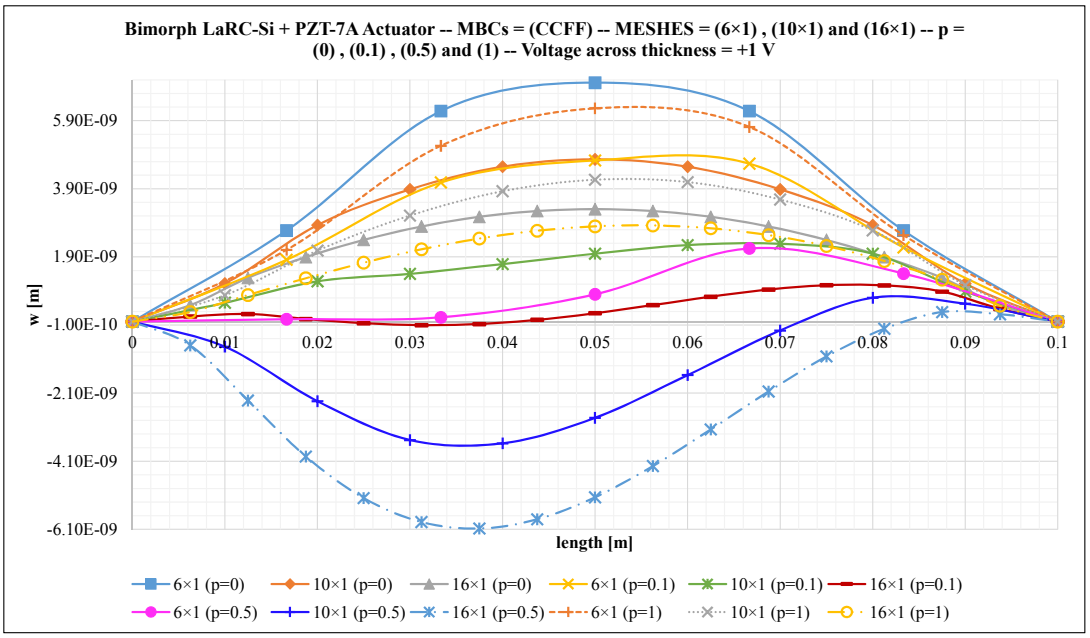

all results | (16×1) | $p = 0$ | $p = 0.1$ | $p = 0.5$ | $p = 1$

Figure G.56: Deflection results from the parametric case study of longitudinal FGM bimorph beam (statics actuation (CCFF)), mixing up LaRC-Si and PZT-7A, with several meshes and p-exponents (0, 0.1, 0.5 and 1). Please click on the buttons above this caption to toggle between plotted results.

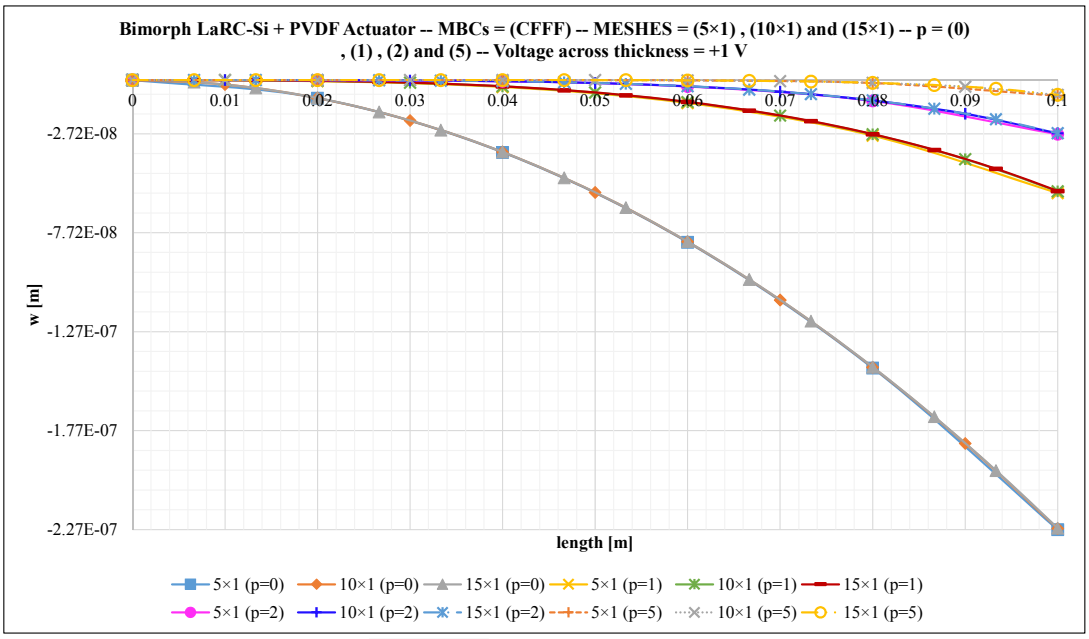

all results | (15×1) | $p = 0$ | $p = 1$ | $p = 2$ | $p = 5$

Figure G.57: Deflection results from the parametric case study of longitudinal FGM bimorph beam (statics actuation (CFFF)), mixing up LaRC-Si and PVDF, considering several meshes and p-exponents (0, 1, 2 and 5). Please click on the buttons above this caption to toggle between plotted results.

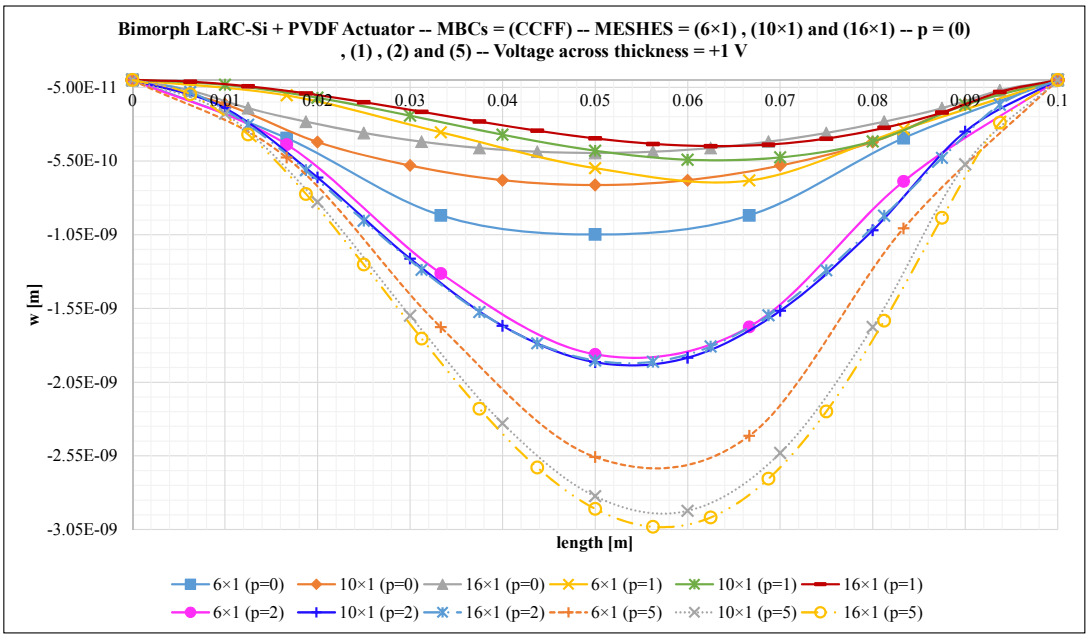

all results | (16×1) | $p = 0$ | $p = 1$ | $p = 2$ | $p = 5$

Figure G.58: Deflection results from the parametric case study of longitudinal FGM bimorph beam (statics actuation (CCFF)), mixing up LaRC-Si and PVDF, considering several meshes and p-exponents (0, 1, 2 and 5). Please click on the buttons above this caption to toggle between plotted results.

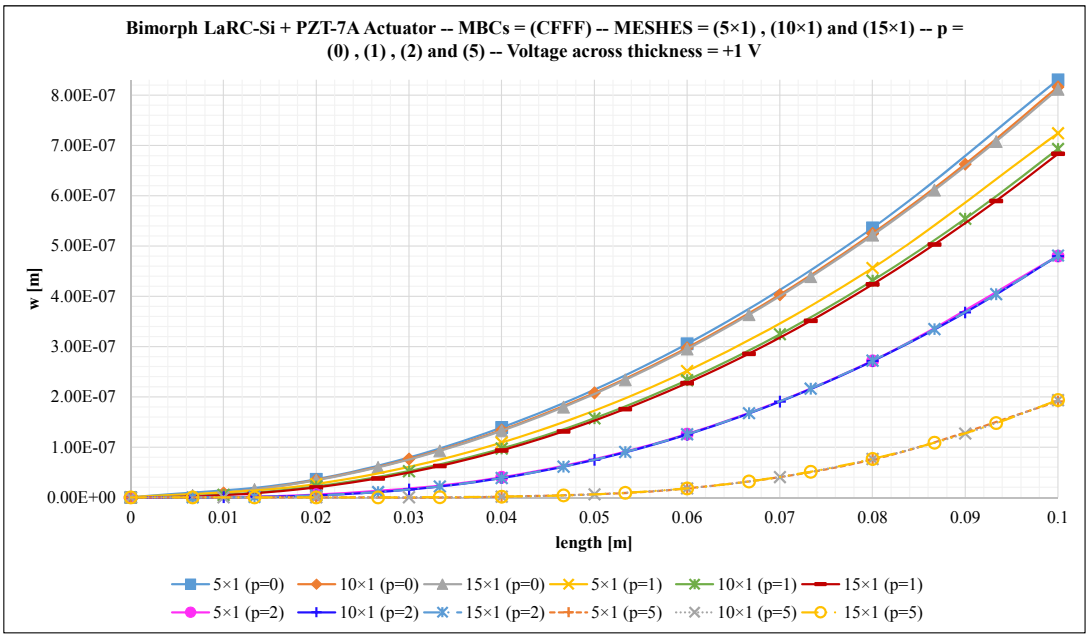

all results | (15×1) | $p = 0$ | $p = 1$ | $p = 2$ | $p = 5$

Figure G.59: Deflection results from the parametric case study of longitudinal FGM bimorph beam (statics actuation (CFFF)), mixing up LaRC-Si and PZT-7A, with several meshes and p-exponents (0, 1, 2 and 5). Please click on the buttons above this caption to toggle between plotted results.

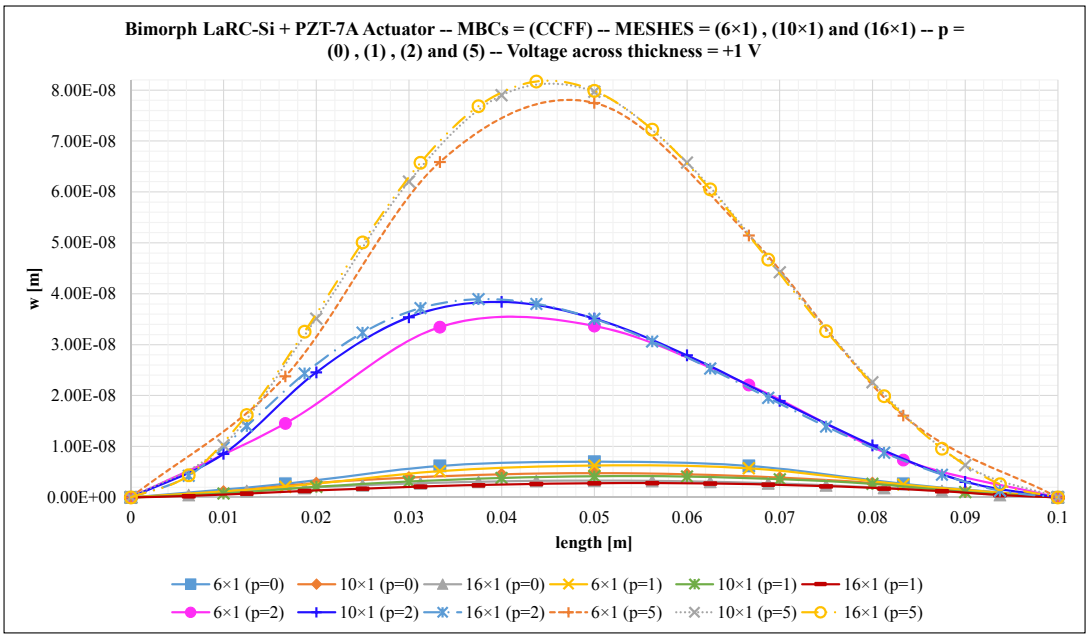

all results | (16×1) | $p = 0$ | $p = 1$ | $p = 2$ | $p = 5$

Figure G.60: Deflection results from the parametric case study of longitudinal FGM bimorph beam (statics actuation (CCFF)), mixing up LaRC-Si and PZT-7A, with several meshes and p-exponents (0, 1, 2 and 5). Please click on the buttons above this caption to toggle between plotted results.

Figure G.61: Deflection results from the parametric CS of longitudinal FGM bimorph beam (statics actuation (CFFF)), mixing up LaRC-Si and PVDF, with several p-exponents (0, 0.1, 0.5, 1, 2 and 5).

Figure G.62: Deflection results from the parametric CS of longitudinal FGM bimorph beam (statics actuation (CCFF)), mixing up LaRC-Si and PVDF, with several p-exponents (0, 0.1, 0.5, 1, 2 and 5).

Figure G.63: Deflection results from the parametric CS of longitudinal FGM bimorph beam (statics actuation (CFFF)), mixing up LaRC-Si and PZT-7A, with several p-exponents (0, 0.1, 0.5, 1, 2 and 5).

Figure G.64: Deflection results from the parametric CS of longitudinal FGM bimorph beam (statics actuation (CCFF)), mixing up LaRC-Si and PZT-7A, with several p-exponents (0, 0.1, 0.5, 1, 2 and 5).

Table G.16: Deflections [m] associated with plotted results in Figure G.61.

x [m]	p					
	0	0.1	0.5	1	2	5
0.0000	0.00E+00	0.00E+00	0.00E+00	0.00E+00	0.00E+00	0.00E+00
0.0067	-1.02E-09	-5.86E-10	-1.19E-10	-2.04E-11	-6.58E-13	-2.62E-17
0.0133	-4.07E-09	-2.43E-09	-5.72E-10	-1.24E-10	-8.04E-12	-6.01E-15
0.0200	-9.12E-09	-5.69E-09	-1.53E-09	-3.98E-10	-3.85E-11	-9.52E-14
0.0267	-1.62E-08	-1.04E-08	-3.13E-09	-9.33E-10	-1.20E-10	-6.80E-13
0.0333	-2.53E-08	-1.68E-08	-5.49E-09	-1.83E-09	-2.91E-10	-3.15E-12
0.0400	-3.63E-08	-2.47E-08	-8.73E-09	-3.18E-09	-6.04E-10	-1.11E-11
0.0467	-4.94E-08	-3.44E-08	-1.30E-08	-5.09E-09	-1.12E-09	-3.24E-11
0.0533	-6.45E-08	-4.58E-08	-1.83E-08	-7.68E-09	-1.93E-09	-8.22E-11
0.0600	-8.16E-08	-5.89E-08	-2.48E-08	-1.11E-08	-3.12E-09	-1.87E-10
0.0667	-1.01E-07	-7.39E-08	-3.26E-08	-1.54E-08	-4.82E-09	-3.92E-10
0.0733	-1.22E-07	-9.07E-08	-4.19E-08	-2.08E-08	-7.16E-09	-7.70E-10
0.0800	-1.45E-07	-1.09E-07	-5.27E-08	-2.73E-08	-1.03E-08	-1.43E-09
0.0867	-1.70E-07	-1.30E-07	-6.50E-08	-3.53E-08	-1.45E-08	-2.55E-09
0.0933	-1.97E-07	-1.53E-07	-7.92E-08	-4.48E-08	-1.99E-08	-4.41E-09
0.1000	-2.27E-07	-1.77E-07	-9.52E-08	-5.61E-08	-2.69E-08	-7.46E-09

Table G.17: Deflections [m] associated with plotted results in Figure G.62.

x [m]	p					
	0	0.1	0.5	1	2	5
0.0000	0.00E+00	0.00E+00	0.00E+00	0.00E+00	0.00E+00	0.00E+00
0.0063	-7.12E-11	2.03E-11	4.97E-11	-1.13E-11	-8.21E-11	-9.71E-11
0.0125	-1.91E-10	8.60E-11	1.69E-10	-4.28E-11	-3.04E-10	-3.70E-10
0.0188	-2.83E-10	1.74E-10	3.05E-10	-9.07E-11	-6.12E-10	-7.73E-10
0.0250	-3.60E-10	2.48E-10	4.22E-10	-1.50E-10	-9.55E-10	-1.25E-09
0.0313	-4.19E-10	2.97E-10	5.04E-10	-2.16E-10	-1.29E-09	-1.75E-09
0.0375	-4.61E-10	3.15E-10	5.40E-10	-2.82E-10	-1.57E-09	-2.23E-09
0.0438	-4.87E-10	3.01E-10	5.29E-10	-3.44E-10	-1.79E-09	-2.63E-09
0.0500	-4.95E-10	2.60E-10	4.75E-10	-3.97E-10	-1.90E-09	-2.91E-09
0.0563	-4.87E-10	1.97E-10	3.87E-10	-4.33E-10	-1.91E-09	-3.03E-09
0.0625	-4.61E-10	1.20E-10	2.77E-10	-4.49E-10	-1.81E-09	-2.97E-09
0.0688	-4.19E-10	4.10E-11	1.58E-10	-4.39E-10	-1.60E-09	-2.70E-09
0.0750	-3.60E-10	-2.94E-11	4.82E-11	-3.98E-10	-1.29E-09	-2.25E-09
0.0813	-2.83E-10	-7.77E-11	-3.47E-11	-3.25E-10	-9.22E-10	-1.63E-09
0.0875	-1.91E-10	-9.24E-11	-7.47E-11	-2.21E-10	-5.29E-10	-9.35E-10
0.0938	-7.12E-11	-4.51E-11	-4.11E-11	-8.12E-11	-1.67E-10	-2.89E-10
0.1000	0.00E+00	0.00E+00	0.00E+00	0.00E+00	0.00E+00	0.00E+00

Table G.18: Deflections [m] associated with plotted results in Figure G.63.

x [m]	p					
	0	0.1	0.5	1	2	5
0.0000	0.00E+00	0.00E+00	0.00E+00	0.00E+00	0.00E+00	0.00E+00
0.0067	4.02E-09	3.96E-09	3.44E-09	1.82E-09	6.15E-11	6.45E-15
0.0133	1.55E-08	1.53E-08	1.36E-08	8.09E-09	8.93E-10	5.91E-13
0.0200	3.41E-08	3.37E-08	3.03E-08	2.00E-08	3.93E-09	1.16E-11
0.0267	5.97E-08	5.91E-08	5.38E-08	3.80E-08	1.06E-08	8.87E-11
0.0333	9.25E-08	9.16E-08	8.42E-08	6.25E-08	2.19E-08	4.19E-10
0.0400	1.32E-07	1.31E-07	1.22E-07	9.35E-08	3.86E-08	1.45E-09
0.0467	1.79E-07	1.78E-07	1.66E-07	1.31E-07	6.13E-08	3.97E-09
0.0533	2.34E-07	2.32E-07	2.17E-07	1.76E-07	9.01E-08	9.08E-09
0.0600	2.95E-07	2.93E-07	2.75E-07	2.27E-07	1.25E-07	1.80E-08
0.0667	3.63E-07	3.61E-07	3.41E-07	2.86E-07	1.67E-07	3.17E-08
0.0733	4.39E-07	4.36E-07	4.13E-07	3.51E-07	2.16E-07	5.10E-08
0.0800	5.21E-07	5.18E-07	4.93E-07	4.24E-07	2.72E-07	7.66E-08
0.0867	6.11E-07	6.07E-07	5.79E-07	5.03E-07	3.35E-07	1.09E-07
0.0933	7.08E-07	7.04E-07	6.73E-07	5.90E-07	4.04E-07	1.48E-07
0.1000	8.12E-07	8.07E-07	7.73E-07	6.83E-07	4.81E-07	1.94E-07

Table G.19: Deflections [m] associated with plotted results in Figure G.64.

x [m]	p					
	0	0.1	0.5	1	2	5
0.0000	0.00E+00	0.00E+00	0.00E+00	0.00E+00	0.00E+00	0.00E+00
0.0063	4.82E-10	1.49E-10	-6.98E-10	2.80E-10	4.27E-09	4.37E-09
0.0125	1.29E-09	2.24E-10	-2.32E-09	7.82E-10	1.41E-08	1.62E-08
0.0188	1.89E-09	7.75E-11	-3.96E-09	1.27E-09	2.44E-08	3.26E-08
0.0250	2.40E-09	-4.61E-11	-5.18E-09	1.73E-09	3.24E-08	5.01E-08
0.0313	2.80E-09	-1.04E-10	-5.89E-09	2.12E-09	3.72E-08	6.57E-08
0.0375	3.08E-09	-7.09E-11	-6.08E-09	2.44E-09	3.89E-08	7.68E-08
0.0438	3.25E-09	5.15E-11	-5.80E-09	2.67E-09	3.80E-08	8.17E-08
0.0500	3.30E-09	2.46E-10	-5.16E-09	2.80E-09	3.51E-08	7.99E-08
0.0563	3.25E-09	4.84E-10	-4.24E-09	2.82E-09	3.06E-08	7.22E-08
0.0625	3.08E-09	7.30E-10	-3.17E-09	2.74E-09	2.53E-08	6.05E-08
0.0688	2.80E-09	9.41E-10	-2.05E-09	2.54E-09	1.96E-08	4.67E-08
0.0750	2.40E-09	1.07E-09	-1.02E-09	2.22E-09	1.39E-08	3.27E-08
0.0813	1.89E-09	1.06E-09	-2.11E-10	1.78E-09	8.77E-09	1.99E-08
0.0875	1.29E-09	8.85E-10	2.81E-10	1.23E-09	4.48E-09	9.59E-09
0.0938	4.82E-10	3.76E-10	2.17E-10	4.66E-10	1.30E-09	2.60E-09
0.1000	0.00E+00	0.00E+00	0.00E+00	0.00E+00	0.00E+00	0.00E+00

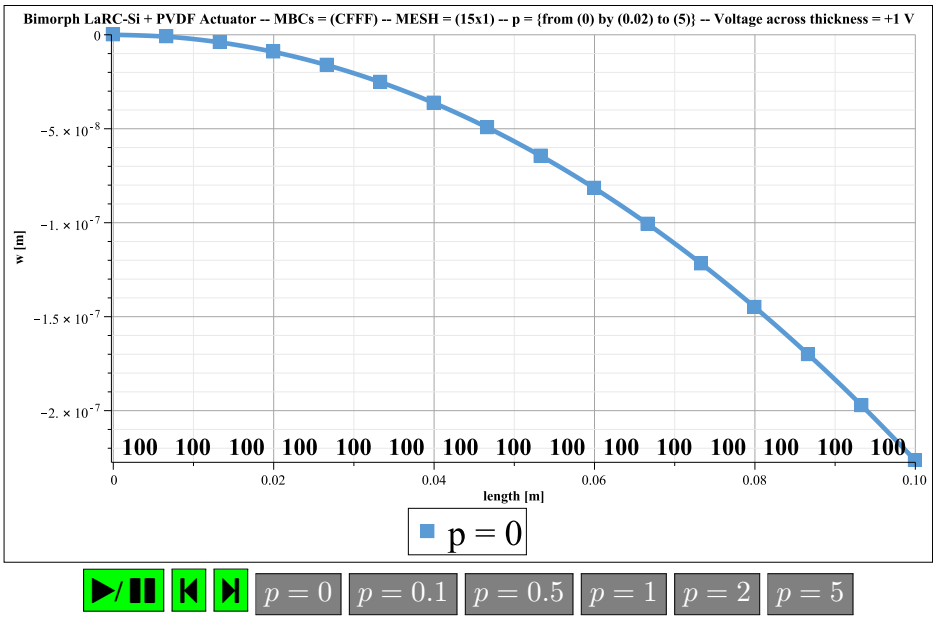

Figure G.65: Deflection results from the parametric case study of longitudinal FGM bimorph beam (statics actuation (CFFF)), mixing up LaRC-Si and PVDF, considering 251 p-exponents (from 0 by 0.02 to 5). Note that the bold numbers above the x-axis correspond to the percentage $[\%]$ of piezoelectric material, $V_{f,r}^{ex}$, mixed up in each element along the beam's length, at each frame. Please click on the buttons above this caption to run the animation and toggle between plotted results.

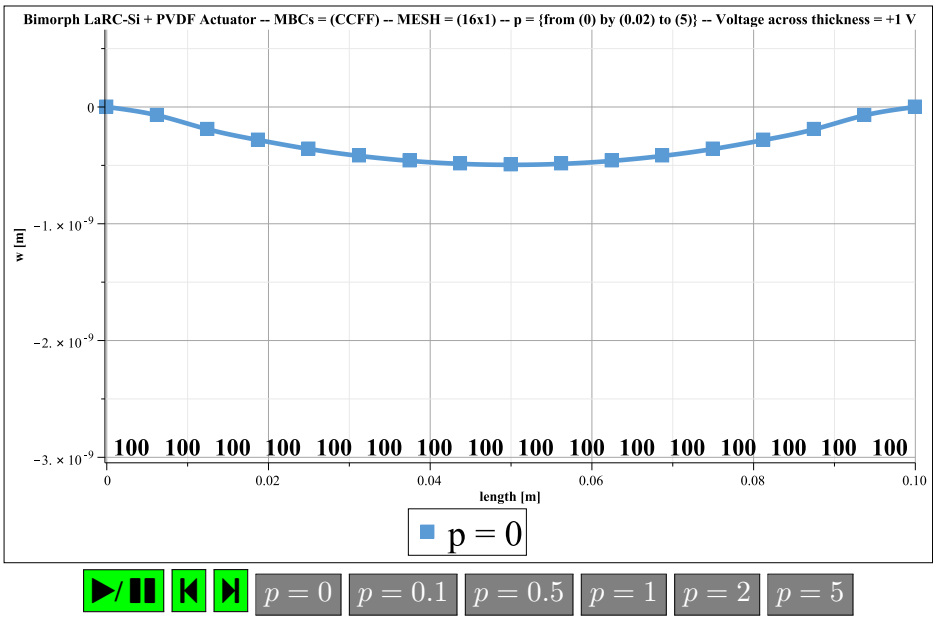

Figure G.66: Deflection results from the parametric case study of longitudinal FGM bimorph beam (statics actuation (CCFF)), mixing up LaRC-Si and PVDF, considering 251 p-exponents (from 0 by 0.02 to 5). Note that the bold numbers above the x-axis correspond to the percentage $[\%]$ of piezoelectric material, $V_{f,r}^{ex}$, mixed up in each element along the beam's length, at each frame. Please click on the buttons above this caption to run the animation and toggle between plotted results.

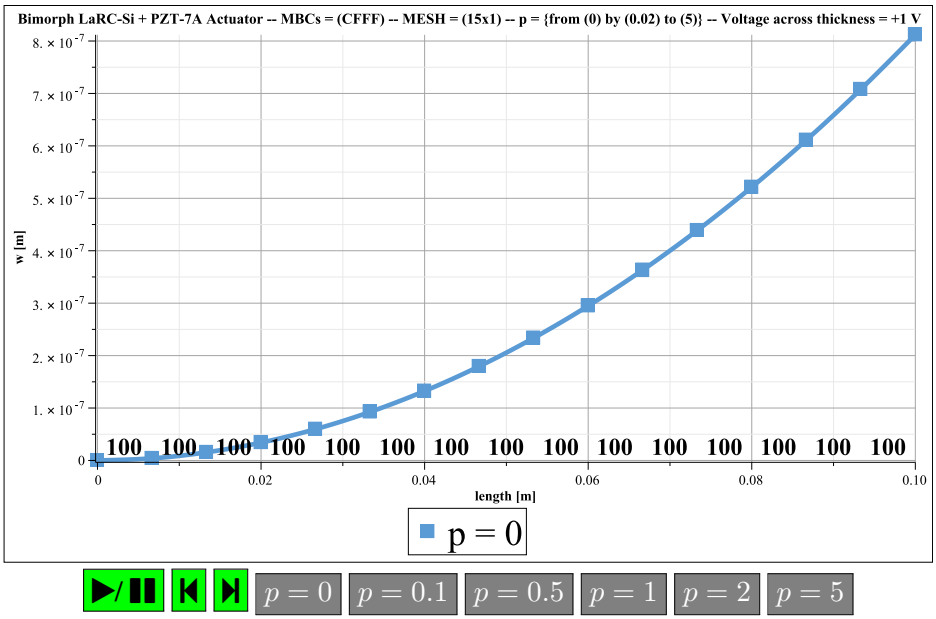

Figure G.67: Deflection results from the parametric case study of longitudinal FGM bimorph beam (statics actuation (CFFF)), mixing up LaRC-Si and PZT-7A, considering 251 p-exponents (from 0 by 0.02 to 5). Note that the bold numbers above the x-axis correspond to the percentage $[\%]$ of piezoelectric material, $V_{f,r}^{ex}$, mixed up in each element along the beam's length, at each frame. Please click on the buttons above this caption to run the animation and toggle between plotted results.

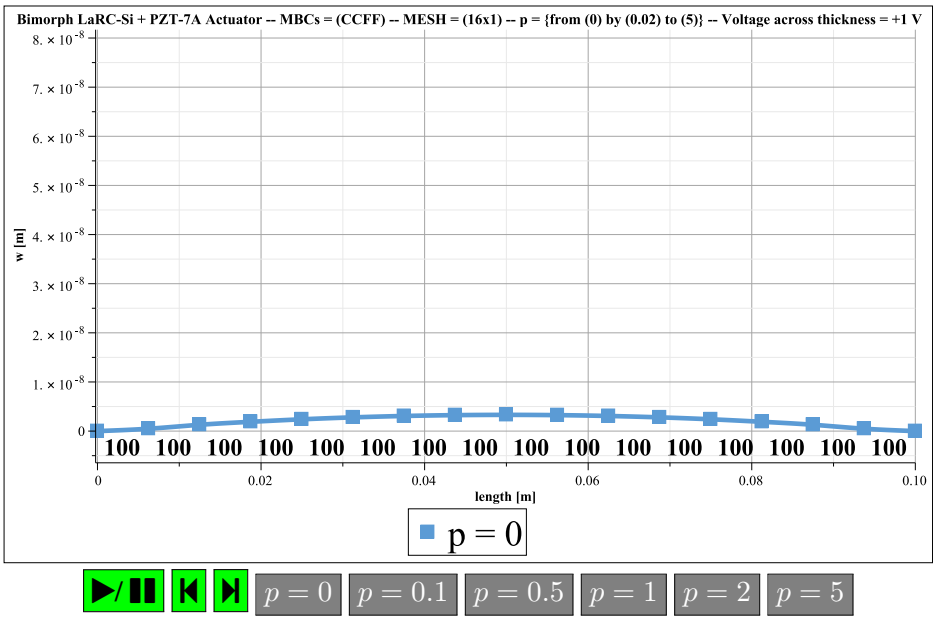

Figure G.68: Deflection results from the parametric case study of longitudinal FGM bimorph beam (statics actuation (CCFF)), mixing up LaRC-Si and PZT-7A, considering 251 p-exponents (from 0 by 0.02 to 5). Note that the bold numbers above the x-axis correspond to the percentage $[\%]$ of piezoelectric material, $V_{f,r}^{ex}$, mixed up in each element along the beam's length, at each frame. Please click on the buttons above this caption to run the animation and toggle between plotted results.

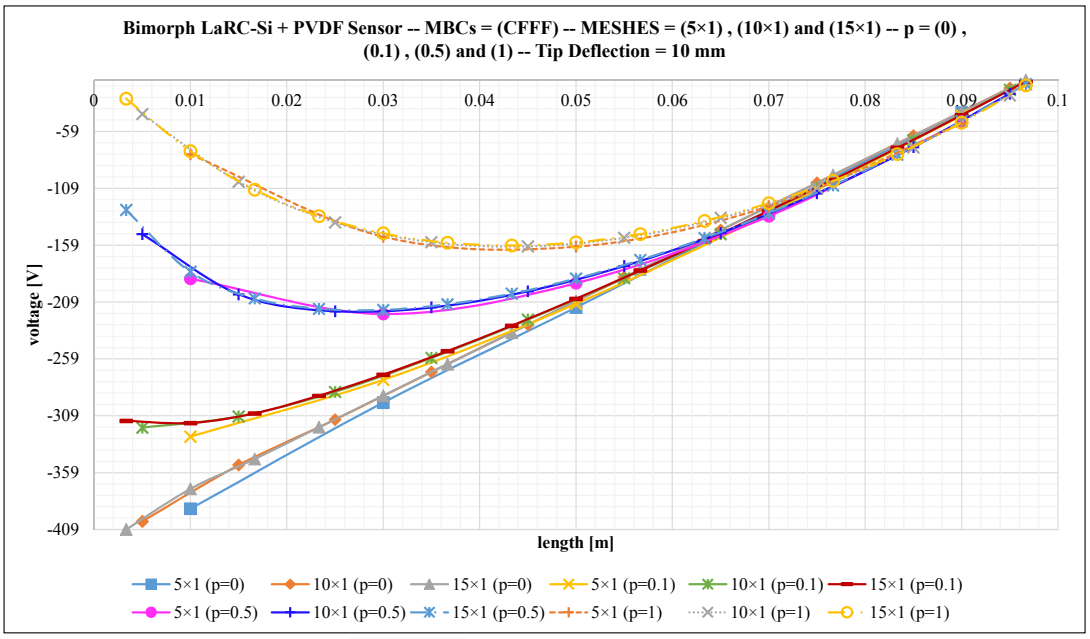

all results | (15×1) | $p = 0$ | $p = 0.1$ | $p = 0.5$ | $p = 1$

Figure G.69: Voltage results from the parametric case study of longitudinal FGM bimorph beam (statics sensing (CFFF)), mixing up LaRC-Si and PVDF, considering several meshes and p-exponents (0, 0.1, 0.5 and 1). Please click on the buttons above this caption to toggle between plotted results.

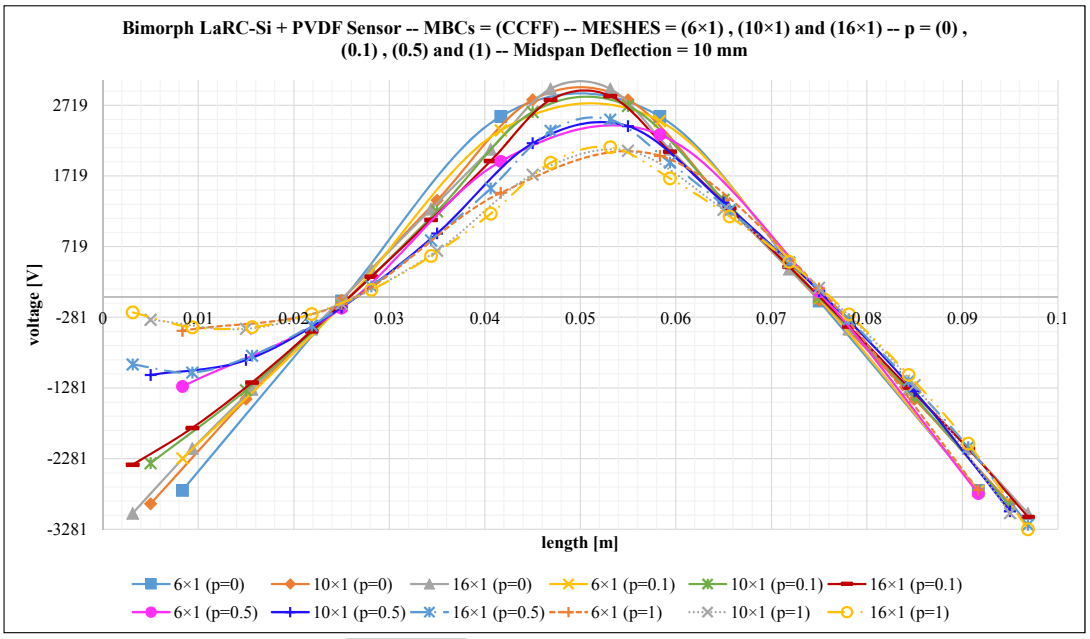

all results | (16×1) | $p = 0$ | $p = 0.1$ | $p = 0.5$ | $p = 1$

Figure G.70: Voltage results from the parametric case study of longitudinal FGM bimorph beam (statics sensing (CCFF)), mixing up LaRC-Si and PVDF, considering several meshes and p-exponents (0, 0.1, 0.5 and 1). Please click on the buttons above this caption to toggle between plotted results.

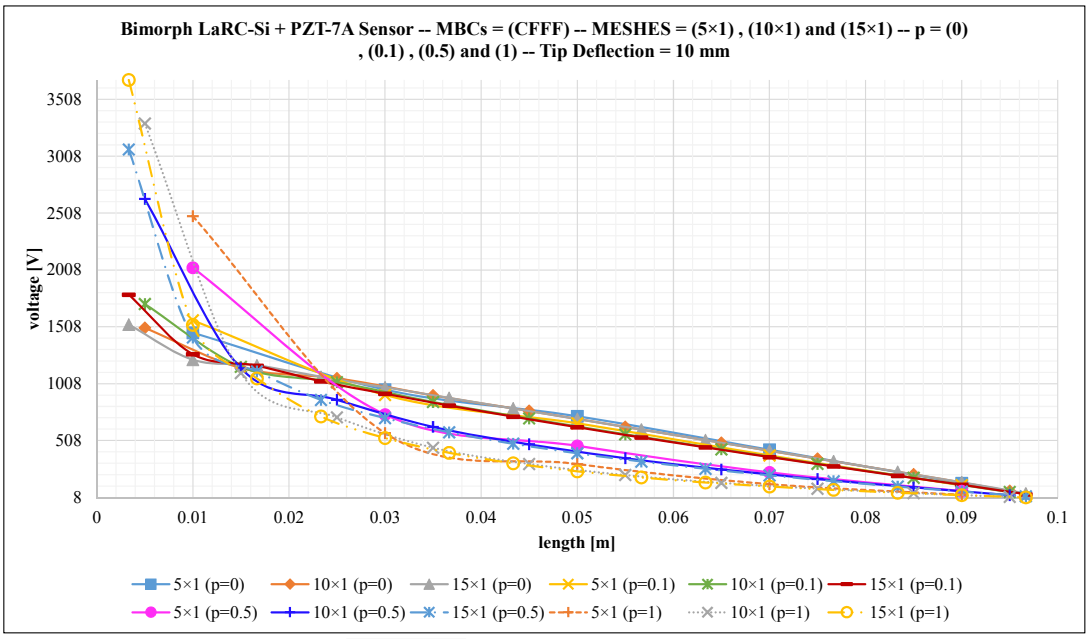

all results | (15×1) | $p = 0$ | $p = 0.1$ | $p = 0.5$ | $p = 1$

Figure G.71: Voltage results from the parametric case study of longitudinal FGM bimorph beam (statics sensing (CFFF)), mixing up LaRC-Si and PZT-7A, considering several meshes and p-exponents (0, 0.1, 0.5 and 1). Please click on the buttons above this caption to toggle between plotted results.

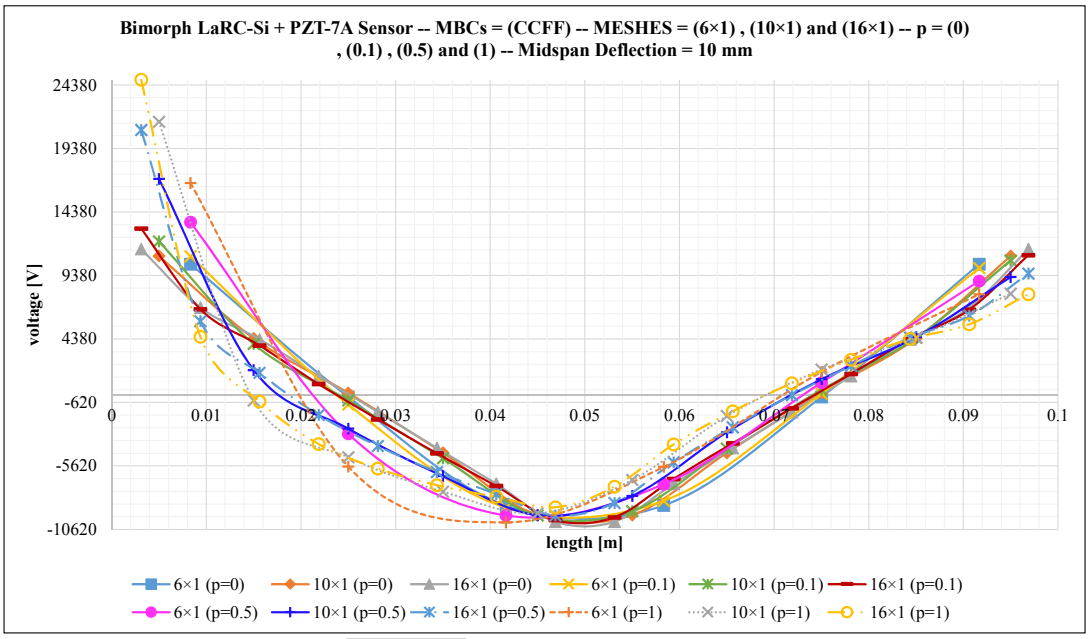

all results | (16×1) | $p = 0$ | $p = 0.1$ | $p = 0.5$ | $p = 1$

Figure G.72: Voltage results from the parametric case study of longitudinal FGM bimorph beam (statics sensing (CCFF)), mixing up LaRC-Si and PZT-7A, considering several meshes and p-exponents (0, 0.1, 0.5 and 1). Please click on the buttons above this caption to toggle between plotted results.

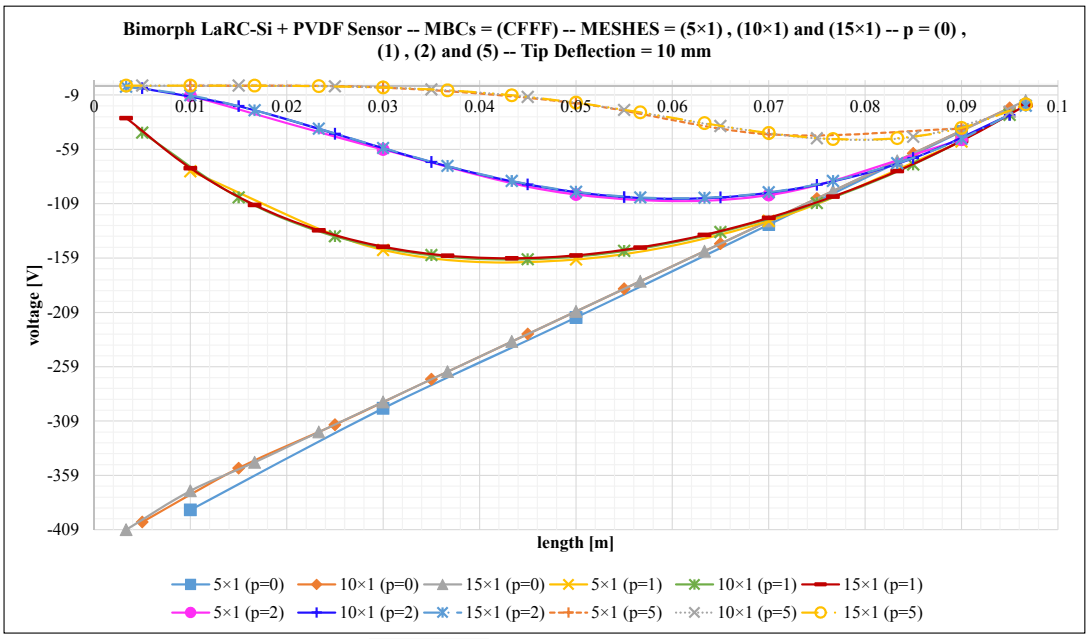

all results | (15×1) | $p = 0$ | $p = 1$ | $p = 2$ | $p = 5$

Figure G.73: Voltage results from the parametric case study of longitudinal FGM bimorph beam (statics sensing (CFFF)), mixing up LaRC-Si and PVDF, considering several meshes and p-exponents (0, 1, 2 and 5). Please click on the buttons above this caption to toggle between plotted results.

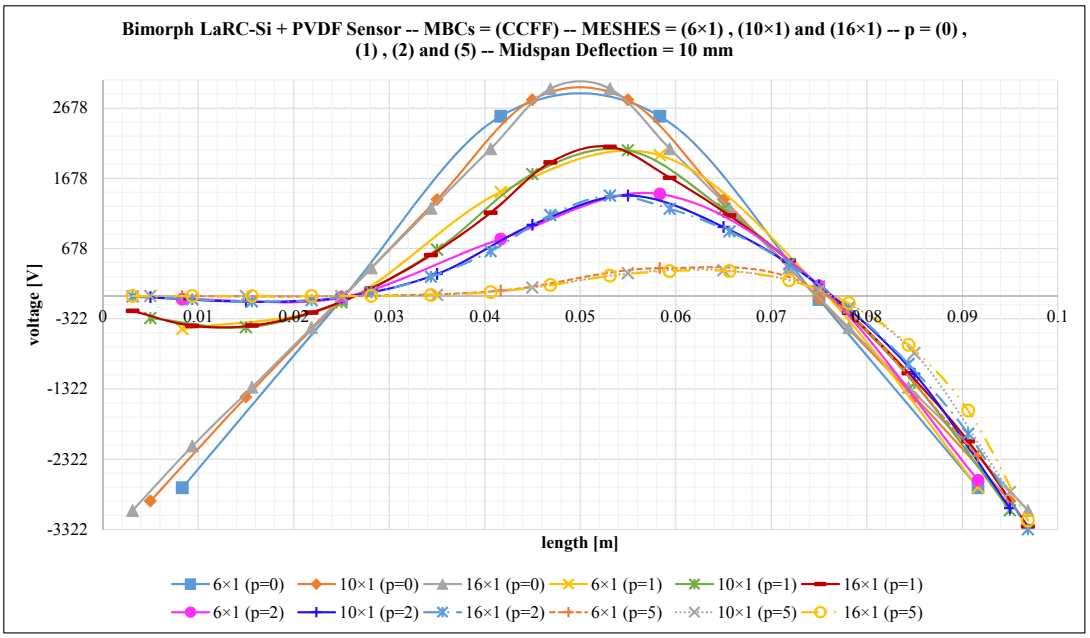

all results | (16×1) | $p = 0$ | $p = 1$ | $p = 2$ | $p = 5$

Figure G.74: Voltage results from the parametric case study of longitudinal FGM bimorph beam (statics sensing (CCFF)), mixing up LaRC-Si and PVDF, considering several meshes and p-exponents (0, 1, 2 and 5). Please click on the buttons above this caption to toggle between plotted results.

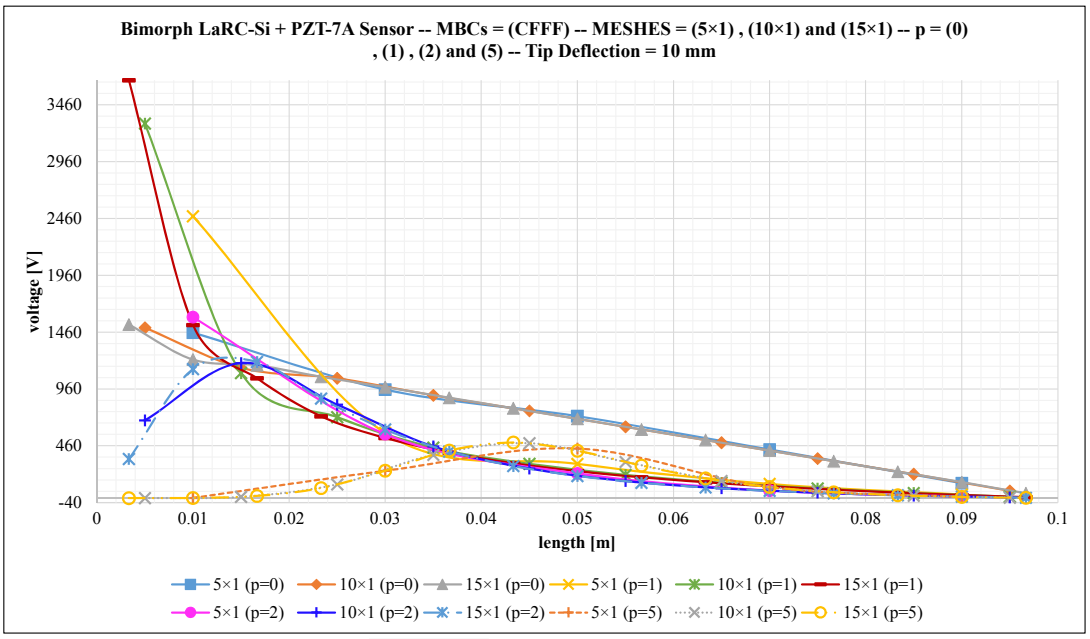

all results | (15×1) | $p = 0$ | $p = 1$ | $p = 2$ | $p = 5$

Figure G.75: Voltage results from the parametric case study of longitudinal FGM bimorph beam (statics sensing (CFFF)), mixing up LaRC-Si and PZT-7A, considering several meshes and p-exponents (0, 1, 2 and 5). Please click on the buttons above this caption to toggle between plotted results.

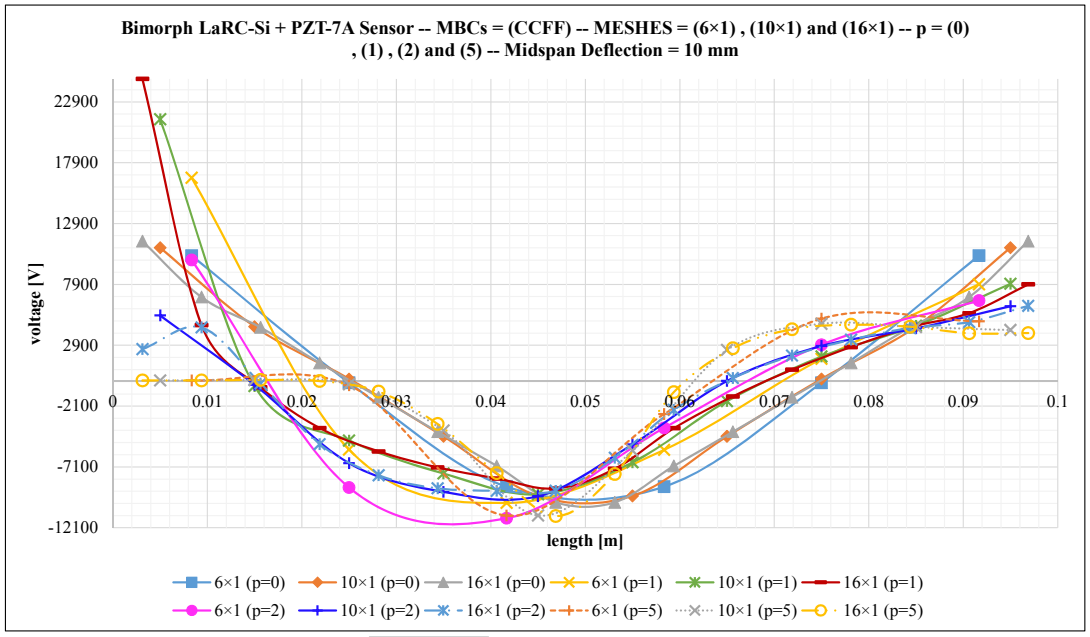

all results | (16×1) | $p = 0$ | $p = 1$ | $p = 2$ | $p = 5$

Figure G.76: Voltage results from the parametric case study of longitudinal FGM bimorph beam (statics sensing (CCFF)), mixing up LaRC-Si and PZT-7A, considering several meshes and p-exponents (0, 1, 2 and 5). Please click on the buttons above this caption to toggle between plotted results.

Figure G.77: Voltage results from the parametric CS of longitudinal FGM bimorph beam (statics sensing (CFFF)), mixing up LaRC-Si and PVDF, with several p-exponents (0, 0.1, 0.5, 1, 2 and 5).

Figure G.78: Voltage results from the parametric CS of longitudinal FGM bimorph beam (statics sensing (CCFF)), mixing up LaRC-Si and PVDF, with several p-exponents (0, 0.1, 0.5, 1, 2 and 5).

Figure G.79: Voltage results from the parametric CS of longitudinal FGM bimorph beam (statics sensing (CFFF)), mixing up LaRC-Si and PZT-7A, with several p-exponents (0, 0.1, 0.5, 1, 2 and 5).

Figure G.80: Voltage results from the parametric CS of longitudinal FGM bimorph beam (statics sensing (CCFF)), mixing up LaRC-Si and PZT-7A, with several p-exponents (0, 0.1, 0.5, 1, 2 and 5).

Table G.20: Voltages [V] associated with plotted results in Figure G.77.

x [m]	p					
	0	0.1	0.5	1	2	5
0.0033	-409	-313	-128	-30	-1	0
0.0100	-373	-315	-182	-76	-9	0
0.0167	-347	-307	-206	-110	-23	0
0.0233	-319	-291	-215	-133	-40	-1
0.0300	-291	-273	-216	-148	-57	-2
0.0367	-263	-252	-211	-157	-74	-4
0.0433	-236	-229	-201	-159	-88	-9
0.0500	-208	-206	-188	-156	-98	-16
0.0567	-180	-181	-172	-149	-103	-25
0.0633	-152	-155	-153	-137	-103	-35
0.0700	-125	-129	-131	-122	-98	-44
0.0767	-97	-101	-106	-102	-88	-49
0.0833	-69	-73	-79	-79	-72	-48
0.0900	-42	-44	-50	-51	-49	-39
0.0967	-14	-15	-17	-18	-19	-17

Table G.21: Voltages [V] associated with plotted results in Figure G.78.

x [m]	p					
	0	0.1	0.5	1	2	5
0.0031	-3053	-2366	-948	-211	-7	0
0.0094	-2137	-1846	-1063	-423	-46	0
0.0156	-1300	-1202	-823	-420	-78	0
0.0219	-449	-476	-395	-232	-59	-1
0.0281	400	295	157	109	49	2
0.0344	1250	1100	808	586	275	14
0.0406	2098	1933	1544	1186	638	55
0.0469	2952	2796	2359	1905	1154	157
0.0531	2952	2851	2517	2126	1429	289
0.0594	2098	2064	1908	1686	1243	356
0.0656	1250	1260	1235	1147	922	355
0.0719	400	435	496	506	454	225
0.0781	-449	-409	-308	-239	-169	-101
0.0844	-1300	-1273	-1182	-1096	-968	-694
0.0906	-2137	-2141	-2117	-2067	-1961	-1632
0.0969	-3053	-3105	-3217	-3280	-3322	-3195

Table G.22: Voltages [V] associated with plotted results in Figure G.79.

x [m]	p					
	0	0.1	0.5	1	2	5
0.0033	1527	1791	3067	3677	343	0
0.0100	1218	1267	1414	1524	1134	2
0.0167	1169	1165	1115	1054	1198	19
0.0233	1067	1029	865	719	876	89
0.0300	976	919	705	530	603	241
0.0367	883	815	580	400	411	419
0.0433	790	718	480	307	282	489
0.0500	697	625	395	237	195	416
0.0567	604	535	323	183	136	286
0.0633	511	448	259	139	94	173
0.0700	418	363	202	104	64	97
0.0767	325	280	150	74	42	52
0.0833	232	198	103	49	25	25
0.0900	140	119	60	27	13	11
0.0967	42	36	18	8	3	2

Table G.23: Voltages [V] associated with plotted results in Figure G.80.

x [m]	p					
	0	0.1	0.5	1	2	5
0.0031	11456	13071	20837	24792	2579	0
0.0094	6851	6715	5774	4561	4357	7
0.0156	4359	3865	1709	-556	-253	44
0.0219	1453	829	-1607	-3899	-5231	-37
0.0281	-1370	-1944	-4050	-5821	-7796	-911
0.0344	-4216	-4633	-6099	-7139	-8855	-3574
0.0406	-7024	-7204	-7832	-8049	-9062	-7607
0.0469	-10010	-9885	-9523	-8878	-9065	-11142
0.0531	-10010	-9661	-8544	-7252	-6343	-7685
0.0594	-7024	-6635	-5331	-3923	-2413	-957
0.0656	-4216	-3843	-2578	-1311	198	2648
0.0719	-1370	-1070	-43	892	2053	4214
0.0781	1453	1634	2270	2741	3353	4582
0.0844	4359	4377	4483	4383	4322	4416
0.0906	6851	6687	6211	5532	4804	3884
0.0969	11456	10981	9533	7901	6136	3900

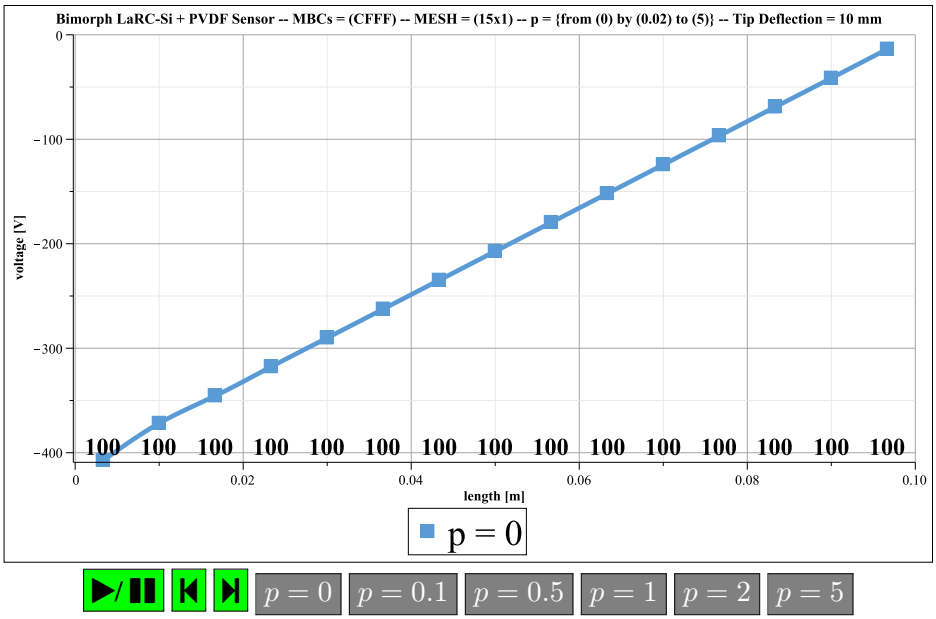

Figure G.81: Voltage results from the parametric case study of longitudinal FGM bimorph beam (statics sensing (CFFF)), mixing up LaRC-Si and PVDF, considering 251 p-exponents (from 0 by 0.02 to 5). Note that the bold numbers above the x-axis correspond to the percentage $[\%]$ of piezoelectric material, $V_{f,r}^{ex}$, mixed up in each element along the beam's length, at each frame. Please click on the buttons above this caption to run the animation and toggle between plotted results.

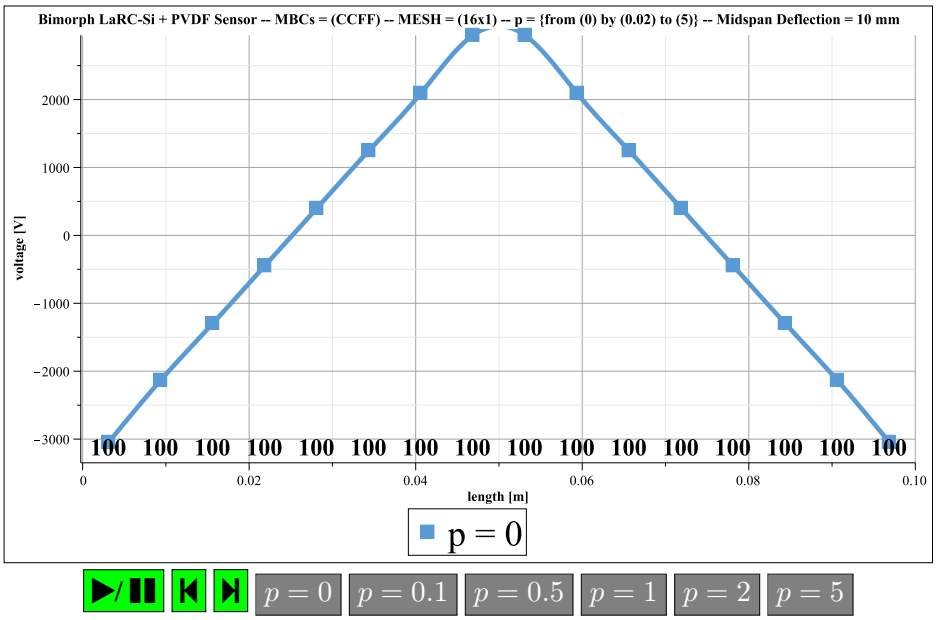

Figure G.82: Voltage results from the parametric case study of longitudinal FGM bimorph beam (statics sensing (CCFF)), mixing up LaRC-Si and PVDF, considering 251 p-exponents (from 0 by 0.02 to 5). Note that the bold numbers above the x-axis correspond to the percentage $[\%]$ of piezoelectric material, $V_{f,r}^{ex}$, mixed up in each element along the beam's length, at each frame. Please click on the buttons above this caption to run the animation and toggle between plotted results.

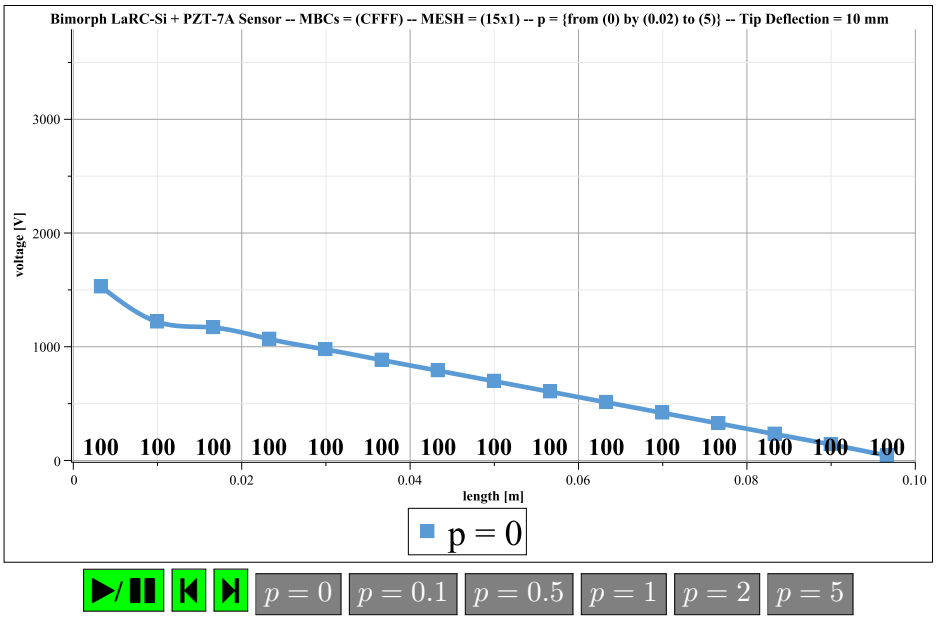

Figure G.83: Voltage results from the parametric case study of longitudinal FGM bimorph beam (statics sensing (CFFF)), mixing up LaRC-Si and PZT-7A, considering 251 p-exponents (from 0 by 0.02 to 5). Note that the bold numbers above the x-axis correspond to the percentage $[\%]$ of piezoelectric material, $V_{f,r}^{ex}$, mixed up in each element along the beam's length, at each frame. Please click on the buttons above this caption to run the animation and toggle between plotted results.

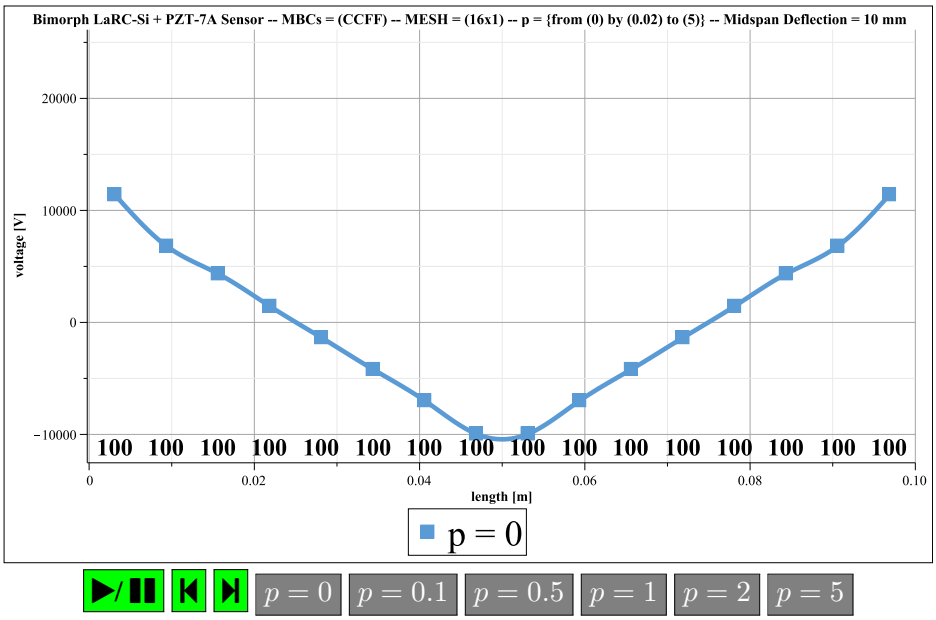

Figure G.84: Voltage results from the parametric case study of longitudinal FGM bimorph beam (statics sensing (CCFF)), mixing up LaRC-Si and PZT-7A, considering 251 p-exponents (from 0 by 0.02 to 5). Note that the bold numbers above the x-axis correspond to the percentage $[\%]$ of piezoelectric material, $V_{f,r}^{ex}$, mixed up in each element along the beam's length, at each frame. Please click on the buttons above this caption to run the animation and toggle between plotted results.

G.3.2 Dynamics (free vibrations)

Schemes and results associated with Section 4.2.3.2.

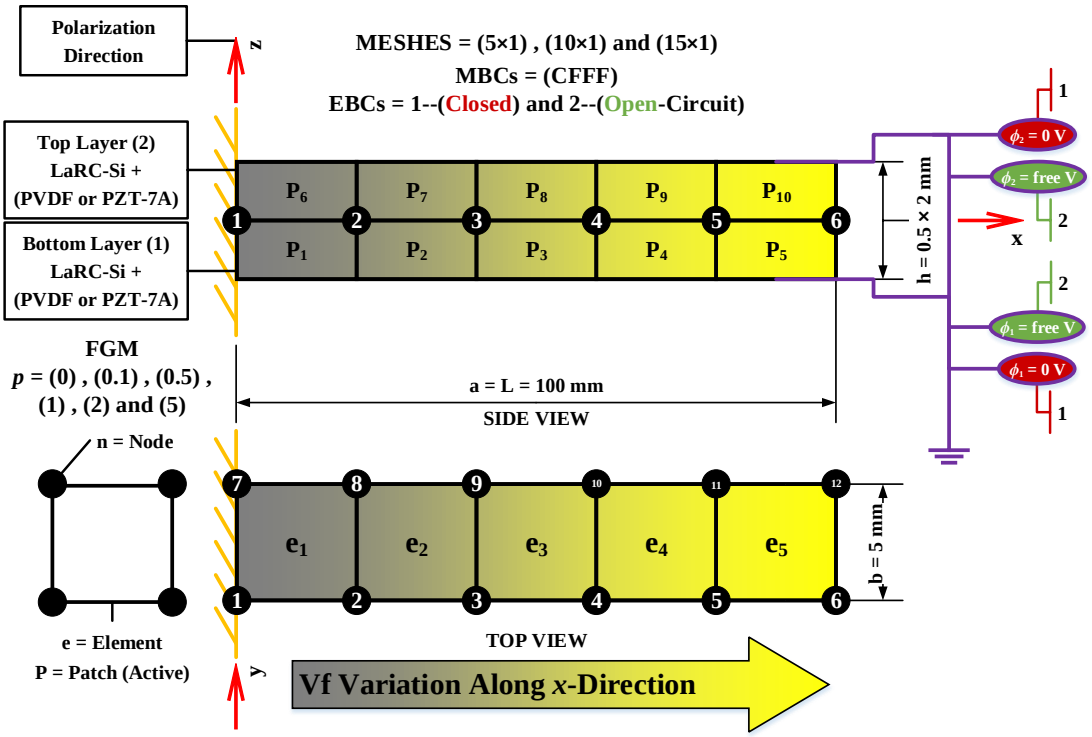

Figure G.85: Parametric case study scheme of longitudinal FGM bimorph beam (dynamics (CFFF)).

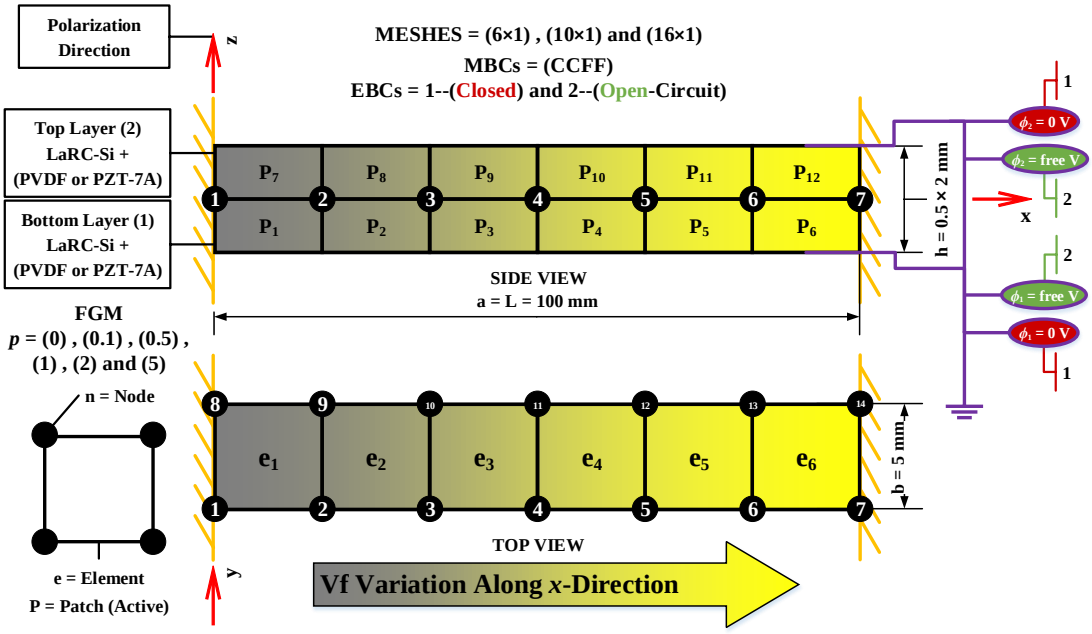

Figure G.86: Parametric case study scheme of longitudinal FGM bimorph beam (dynamics (CCFF)).

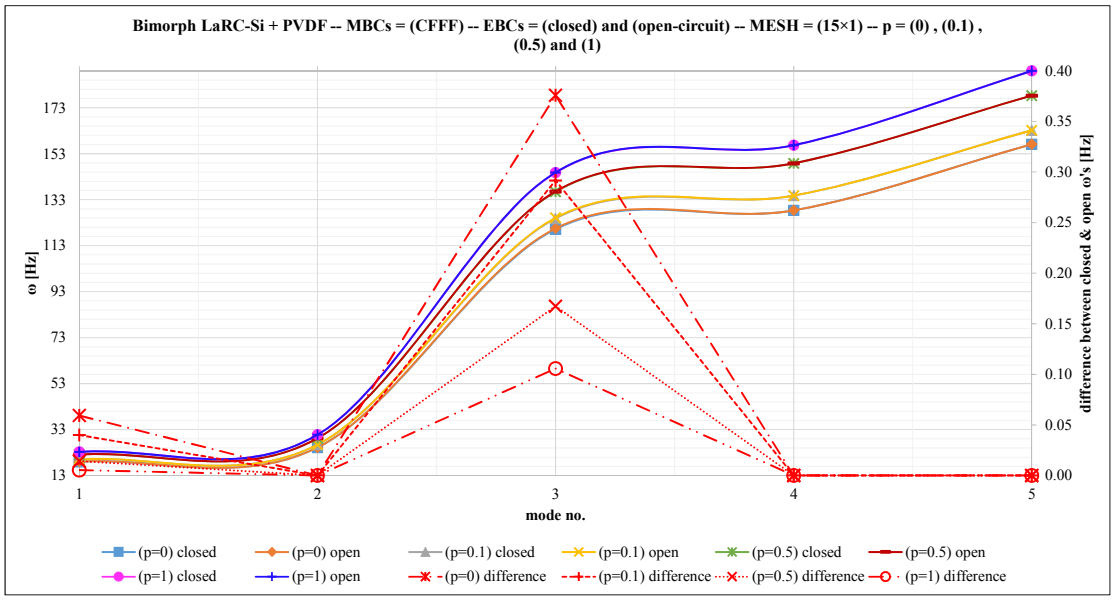

all results *hide differences* *only closed-circuit* *only open-circuit*

Figure G.87: Natural frequencies results of the first five free vibrational modes from the parametric case study of longitudinal FGM bimorph beam (dynamics (CFFF)), mixing up LaRC-Si and PVDF, considering several EBCs and p-exponents (0, 0.1, 0.5 and 1). Please click on the buttons above this caption to toggle between plotted results.

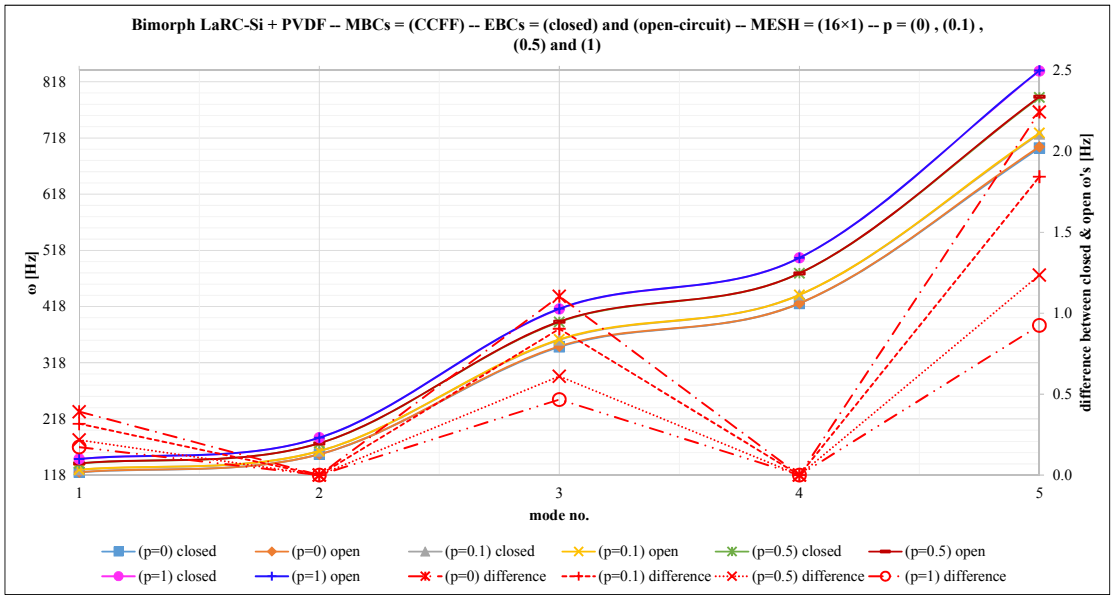

all results *hide differences* *only closed-circuit* *only open-circuit*

Figure G.88: Natural frequencies results of the first five free vibrational modes from the parametric case study of longitudinal FGM bimorph beam (dynamics (CCFF)), mixing up LaRC-Si and PVDF, considering several EBCs and p-exponents (0, 0.1, 0.5 and 1). Please click on the buttons above this caption to toggle between plotted results.

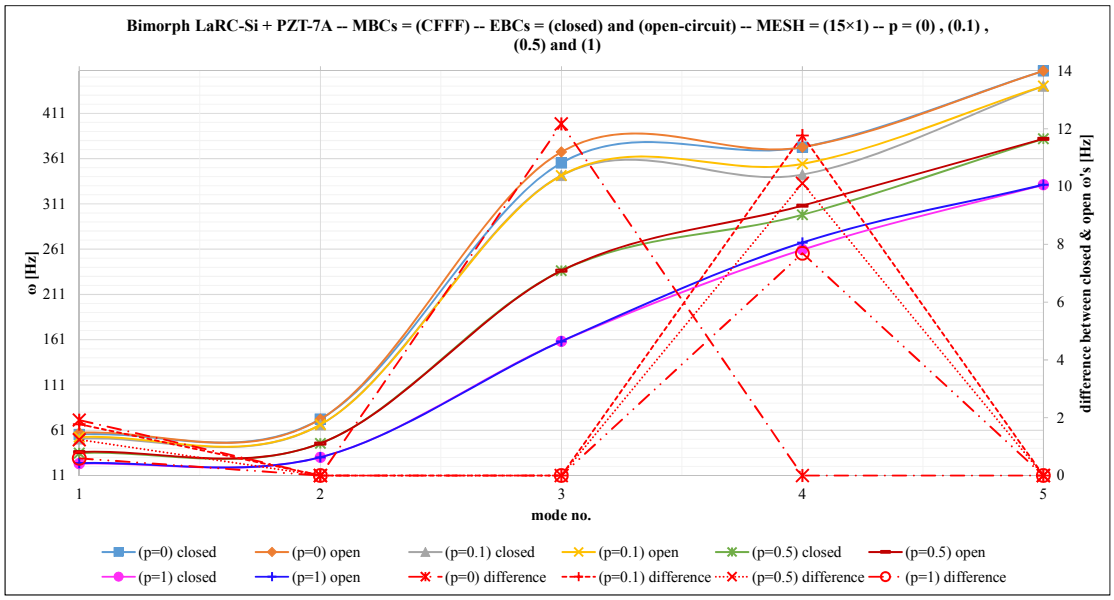

all results *hide differences* *only closed-circuit* *only open-circuit*

Figure G.89: Natural frequencies results of the first five free vibrational modes from the parametric case study of longitudinal FGM bimorph beam (dynamics (CFFF)), mixing up LaRC-Si and PZT-7A, considering several EBCs and p-exponents (0, 0.1, 0.5 and 1). Please click on the buttons above this caption to toggle between plotted results.

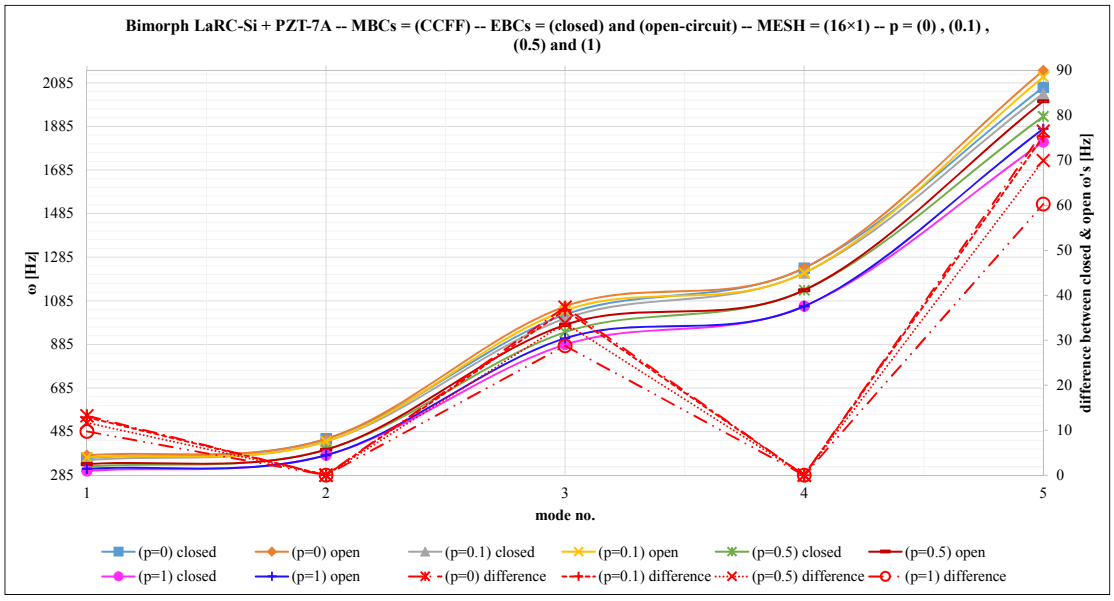

all results *hide differences* *only closed-circuit* *only open-circuit*

Figure G.90: Natural frequencies results of the first five free vibrational modes from the parametric case study of longitudinal FGM bimorph beam (dynamics (CCFF)), mixing up LaRC-Si and PZT-7A, considering several EBCs and p-exponents (0, 0.1, 0.5 and 1). Please click on the buttons above this caption to toggle between plotted results.

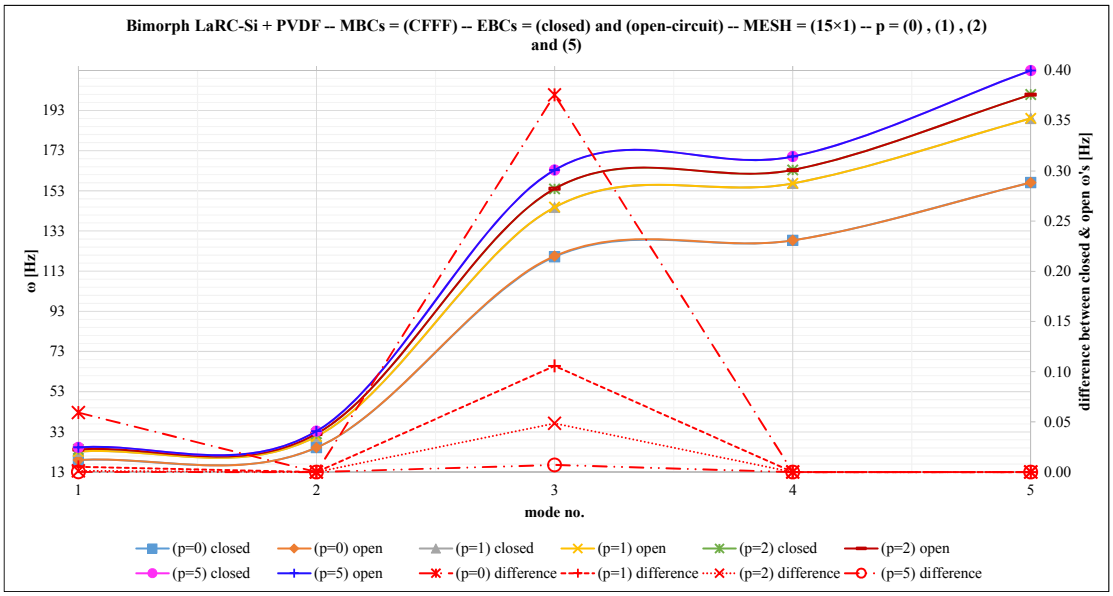

all results *hide differences* *only closed-circuit* *only open-circuit*

Figure G.91: Natural frequencies results of the first five free vibrational modes from the parametric case study of longitudinal FGM bimorph beam (dynamics (CFFF)), mixing up LaRC-Si and PVDF, considering several EBCs and p-exponents (0, 1, 2 and 5). Please click on the buttons above this caption to toggle between plotted results.

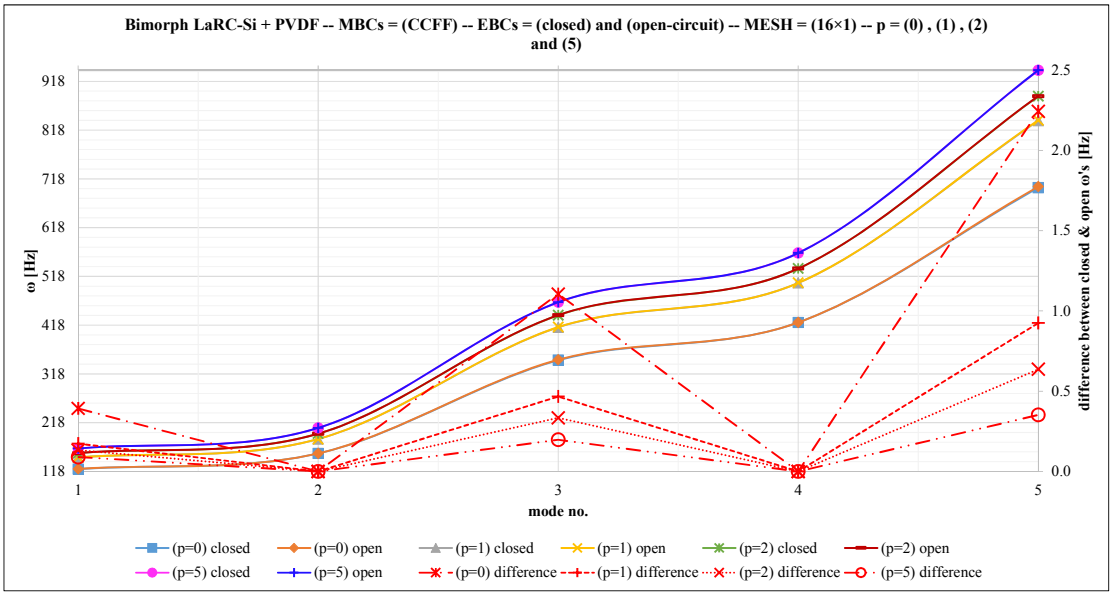

all results *hide differences* *only closed-circuit* *only open-circuit*

Figure G.92: Natural frequencies results of the first five free vibrational modes from the parametric case study of longitudinal FGM bimorph beam (dynamics (CCFF)), mixing up LaRC-Si and PVDF, considering several EBCs and p-exponents (0, 1, 2 and 5). Please click on the buttons above this caption to toggle between plotted results.

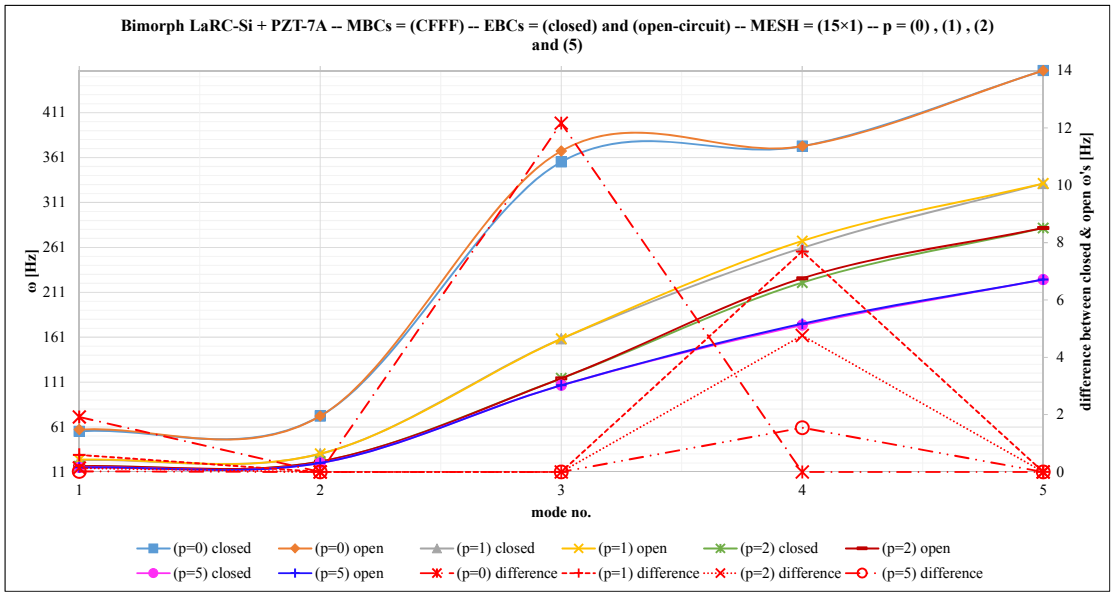

all results | *hide differences* | *only closed-circuit* | *only open-circuit*

Figure G.93: Natural frequencies results of the first five free vibrational modes from the parametric case study of longitudinal FGM bimorph beam (dynamics (CFFF)), mixing up LaRC-Si and PZT-7A, considering several EBCs and p-exponents (0, 1, 2 and 5). Please click on the buttons above this caption to toggle between plotted results.

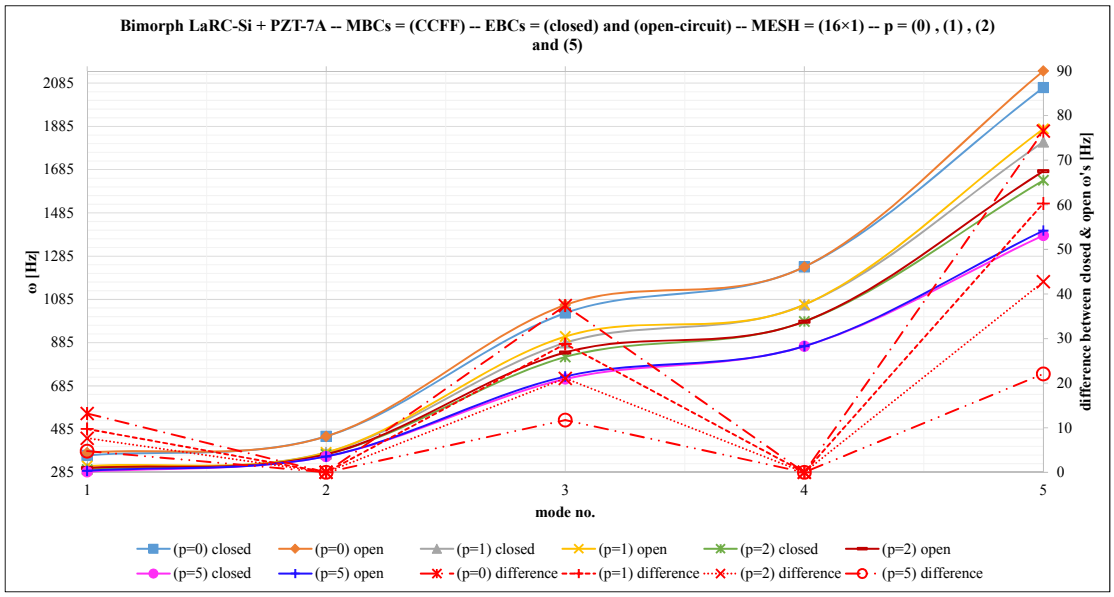

all results | *hide differences* | *only closed-circuit* | *only open-circuit*

Figure G.94: Natural frequencies results of the first five free vibrational modes from the parametric case study of longitudinal FGM bimorph beam (dynamics (CCFF)), mixing up LaRC-Si and PZT-7A, considering several EBCs and p-exponents (0, 1, 2 and 5). Please click on the buttons above this caption to toggle between plotted results.

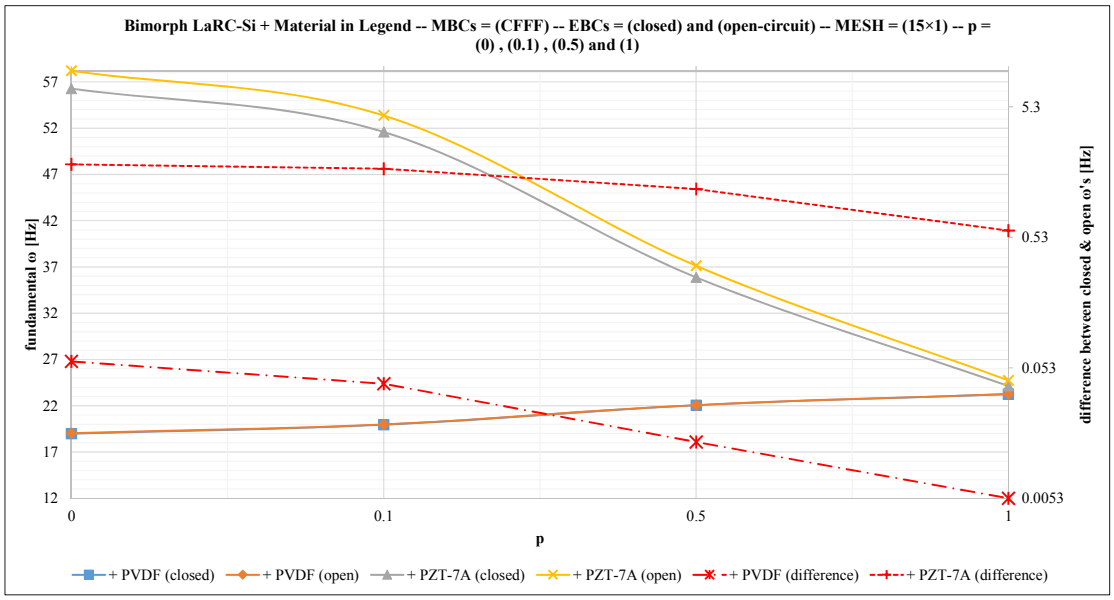

all results *hide differences* *only closed-circuit* *only open-circuit*

Figure G.95: Fundamental natural frequencies results from the parametric case study of longitudinal FGM bimorph beam (dynamics (CFFF)), considering several EBCs and p-exponents (0, 0.1, 0.5 and 1), to compare both LaRC-Si + (PVDF or PZT-7A) mixtures. Please click on the buttons above this caption to toggle between plotted results.

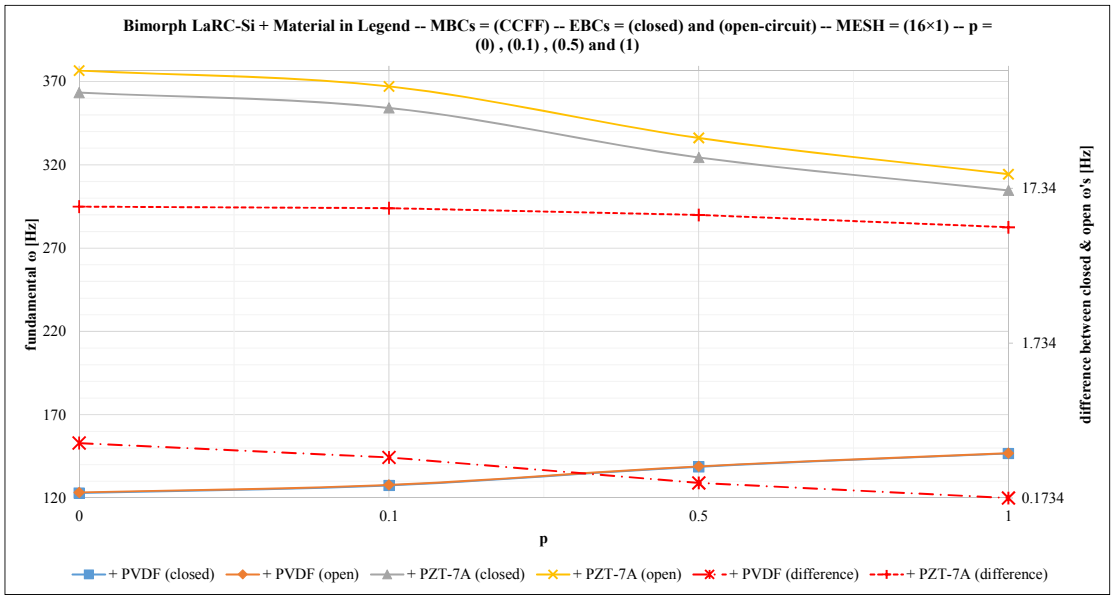

all results *hide differences* *only closed-circuit* *only open-circuit*

Figure G.96: Fundamental natural frequencies results from the parametric case study of longitudinal FGM bimorph beam (dynamics (CCFF)), considering several EBCs and p-exponents (0, 0.1, 0.5 and 1), to compare both LaRC-Si + (PVDF or PZT-7A) mixtures. Please click on the buttons above this caption to toggle between plotted results.

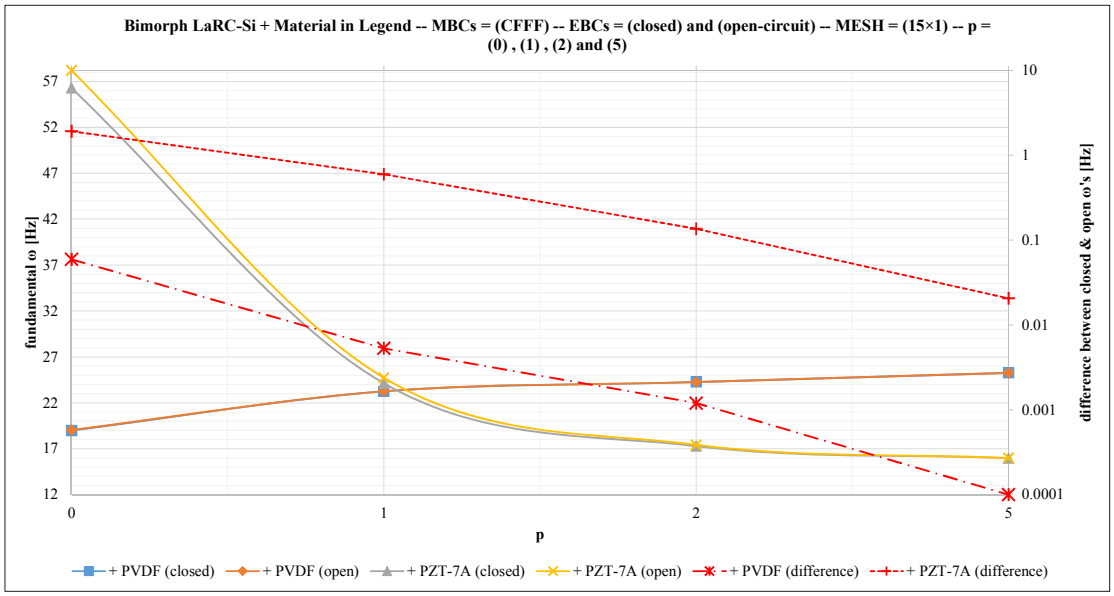

all results *hide differences* *only closed-circuit* *only open-circuit*

Figure G.97: Fundamental natural frequencies results from the parametric case study of longitudinal FGM bimorph beam (dynamics (CFFF)), considering several EBCs and p-exponents (0, 1, 2 and 5), to compare both LaRC-Si + (PVDF or PZT-7A) mixtures. Please click on the buttons above this caption to toggle between plotted results.

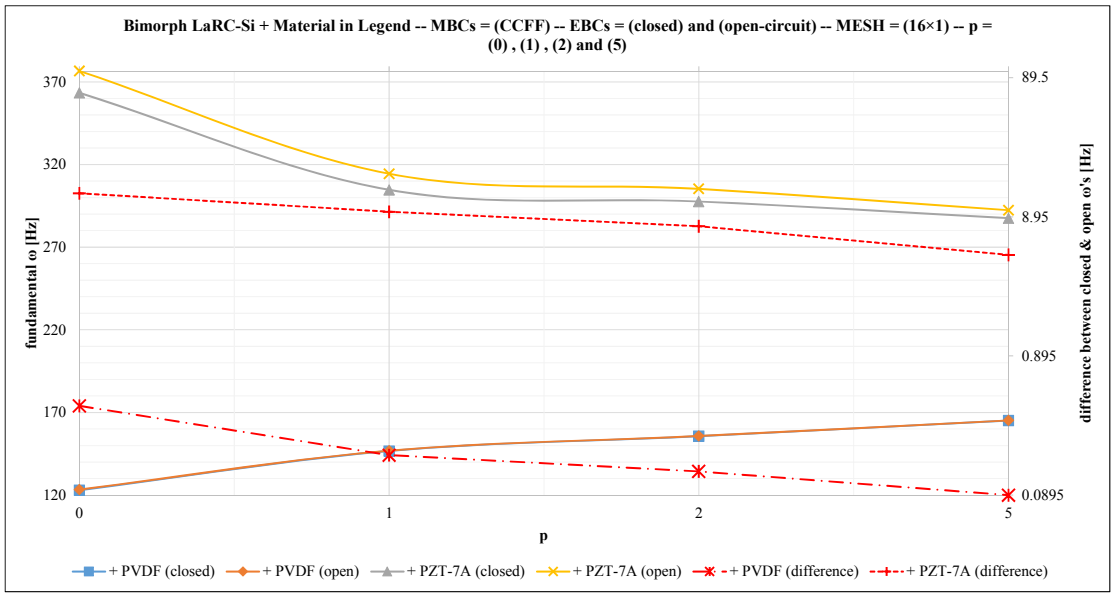

all results *hide differences* *only closed-circuit* *only open-circuit*

Figure G.98: Fundamental natural frequencies results from the parametric case study of longitudinal FGM bimorph beam (dynamics (CCFF)), considering several EBCs and p-exponents (0, 1, 2 and 5), to compare both LaRC-Si + (PVDF or PZT-7A) mixtures. Please click on the buttons above this caption to toggle between plotted results.

Table G.24: Natural frequencies [Hz] associated with plotted results in Figures G.87 and G.91.

	mesh					
EBCs	(5×1)	(10×1)	(15×1)	(5×1)	(10×1)	(15×1)
mode no.	p					
closed	0	0	0	0.1	0.1	0.1
1	19.3059	19.0533	18.9783	20.2058	20.0036	19.9448
2	48.9737	30.1846	25.1819	51.2597	31.6714	26.4389
3	133.2015	122.2439	120.1463	137.7362	126.8583	124.8133
4	249.6050	153.8411	128.3438	261.2552	161.4180	134.7495
5	317.1773	189.5226	157.1213	328.4415	196.6906	163.1792
open	0	0	0	0.1	0.1	0.1
1	19.3686	19.1135	19.0376	20.2489	20.0442	19.9848
2	48.9737	30.1846	25.1819	51.2597	31.6714	26.4389
3	133.6382	122.6305	120.5221	138.0824	127.1592	125.1050
4	249.6050	153.8411	128.3438	261.2552	161.4180	134.7495
5	317.1773	189.5226	157.1213	328.4415	196.6906	163.1792
closed	0.5	0.5	0.5	1	1	1
1	22.3168	22.1201	22.0601	23.5817	23.3268	23.2505
2	56.7596	35.0194	29.1959	60.0264	36.9190	30.7434
3	150.0598	138.6091	136.4355	159.3971	147.1161	144.7554
4	289.2858	178.4814	148.8008	305.9370	188.1638	156.6889
5	359.4420	215.0777	178.2769	382.4860	228.2927	189.0294
open	0.5	0.5	0.5	1	1	1
1	22.3324	22.1346	22.0744	23.5874	23.3322	23.2558
2	56.7596	35.0194	29.1959	60.0264	36.9190	30.7434
3	150.2596	138.7812	136.6028	159.5236	147.2247	144.8611
4	289.2858	178.4814	148.8008	305.9370	188.1638	156.6889
5	359.4420	215.0777	178.2769	382.4860	228.2927	189.0294
closed	2	2	2	5	5	5
1	24.6802	24.3521	24.2594	25.7951	25.3723	25.2602
2	62.8223	38.5275	32.0570	65.6462	40.1358	33.3716
3	169.8799	156.5616	153.9968	181.0772	166.2227	163.3703
4	320.1899	196.3643	163.3855	334.5847	204.5626	170.0871
5	407.6506	242.8358	200.9113	433.5256	257.5397	212.8747
open	2	2	2	5	5	5
1	24.6815	24.3533	24.2606	25.7952	25.3724	25.2603
2	62.8223	38.5275	32.0570	65.6462	40.1358	33.3716
3	169.9414	156.6118	154.0453	181.0889	166.2303	163.3774
4	320.1899	196.3643	163.3855	334.5847	204.5626	170.0871
5	407.6506	242.8358	200.9113	433.5256	257.5397	212.8747

Table G.25: Natural frequencies [Hz] associated with plotted results in Figures G.88 and G.92.

	mesh					
EBCs	(6×1)	(10×1)	(16×1)	(6×1)	(10×1)	(16×1)
mode no.			p			
closed	0	0	0	0.1	0.1	0.1
1	135.8285	126.2948	122.9583	140.5130	130.8694	127.5338
2	272.9312	191.1685	155.0910	282.3200	198.0206	160.7692
3	446.3993	368.4962	346.0993	461.3344	381.4565	358.6050
4	786.3161	530.0825	423.5552	813.1515	548.6563	438.6764
5	1182.7334	788.3070	700.1056	1221.5649	815.6875	725.0996
open	0	0	0	0.1	0.1	0.1
1	136.2906	126.7066	123.3504	140.8908	131.2035	127.8509
2	272.9312	191.1685	155.0910	282.3200	198.0206	160.7692
3	447.9569	369.7057	347.2045	462.6228	382.4486	359.5087
4	786.3161	530.0825	423.5552	813.1515	548.6563	438.6764
5	1187.0229	790.9264	702.3487	1225.1416	817.8478	726.9431
closed	0.5	0.5	0.5	1	1	1
1	152.9449	142.4212	138.7683	162.1755	150.7251	146.7265
2	307.4513	215.4088	174.7047	325.8572	227.8089	184.5347
3	502.7398	415.5738	390.5912	534.0212	440.5025	413.6324
4	886.4787	597.4654	477.1970	939.9893	632.5906	504.6821
5	1332.1493	889.1957	790.2245	1416.6429	943.1137	837.2957
open	0.5	0.5	0.5	1	1	1
1	153.1967	142.6483	138.9854	162.3683	150.9048	146.8999
2	307.4513	215.4088	174.7047	325.8572	227.8089	184.5347
3	503.5764	416.2374	391.2018	534.6183	441.0029	414.0992
4	886.4787	597.4654	477.1970	939.9893	632.5906	504.6821
5	1334.4045	890.6237	791.4606	1418.1437	944.1603	838.2203
closed	2	2	2	5	5	5
1	172.4848	159.9981	155.6257	183.5333	169.9084	165.0962
2	346.2989	241.6122	195.5171	368.7259	256.5064	207.2549
3	567.7194	467.3275	438.4603	603.6088	496.1426	465.0948
4	996.6514	670.0647	534.1389	1059.0913	710.9452	566.0109
5	1506.7455	1000.3106	887.3145	1600.0884	1061.2477	940.6684
open	2	2	2	5	5	5
1	172.6219	160.1332	155.7583	183.6072	169.9941	165.1857
2	346.2989	241.6122	195.5171	368.7259	256.5064	207.2549
3	568.0968	467.6761	438.7941	603.7628	496.3312	465.2924
4	996.6514	670.0647	534.1389	1059.0913	710.9452	566.0109
5	1507.5755	1001.0043	887.9508	1600.3328	1061.5864	941.0205

Table G.26: Natural frequencies [Hz] associated with plotted results in Figures G.89 and G.93.

	mesh					
EBCs	(5×1)	(10×1)	(15×1)	(5×1)	(10×1)	(15×1)
mode no.	p					
closed	0	0	0	0.1	0.1	0.1
1	56.9264	56.4216	56.2797	52.8138	51.8823	51.5965
2	146.3432	88.8394	73.3070	135.6351	81.6210	67.1622
3	392.1324	361.8252	356.1922	382.4427	349.7572	342.3117
4	745.8687	452.7855	373.6213	691.3057	416.0053	343.3455
5	948.7416	558.3526	457.8432	923.6142	539.3552	441.1103
open	0	0	0	0.1	0.1	0.1
1	59.1127	58.4062	58.1991	54.8740	53.7288	53.3721
2	146.3432	88.8394	73.3070	135.6351	81.6210	67.1622
3	407.6425	374.6233	368.3603	397.5766	362.1649	342.3117
4	745.8687	452.7855	373.6213	691.3057	416.0053	355.1097
5	948.7416	558.3526	457.8432	923.6142	539.3552	441.1103
closed	0.5	0.5	0.5	1	1	1
1	38.9574	36.6690	35.8805	27.3287	24.8524	24.1395
2	99.4886	57.4082	46.5384	69.1284	38.6671	31.2401
3	347.3480	292.6197	237.2157	310.7651	197.1035	159.2458
4	507.1051	307.7359	298.8888	352.3727	269.2554	260.5120
5	829.8981	472.5656	382.8777	727.4297	410.2375	332.1338
open	0.5	0.5	0.5	1	1	1
1	40.5520	38.0049	37.1223	28.3717	25.5686	24.7357
2	99.4886	57.4082	46.5384	69.1284	38.6671	31.2401
3	360.9156	292.6197	237.2157	322.2046	197.1035	159.2458
4	507.1051	318.5507	309.0014	352.3727	277.7765	268.2044
5	829.8981	472.5656	382.8777	727.4297	410.2375	332.1338
closed	2	2	2	5	5	5
1	18.2602	17.4588	17.2835	16.7932	16.1183	15.9758
2	45.7109	27.3284	22.6191	42.7751	25.4995	21.0966
3	233.0134	139.3084	115.3028	199.2607	129.9824	107.5394
4	258.2475	227.0577	221.8651	218.0429	178.3069	174.5641
5	588.7308	343.6811	282.5821	466.0151	273.4798	225.2144
open	2	2	2	5	5	5
1	18.4436	17.5948	17.4192	16.8153	16.1392	15.9964
2	45.7109	27.3284	22.6191	42.7751	25.4995	21.0966
3	233.0134	139.3084	115.3028	201.3128	129.9824	107.5394
4	265.3553	232.0287	226.6248	218.0429	179.9156	176.1071
5	588.7308	343.6811	282.5821	466.0151	273.4798	225.2144

Table G.27: Natural frequencies [Hz] associated with plotted results in Figures G.90 and G.94.

	mesh					
EBCs	(6×1)	(10×1)	(16×1)	(6×1)	(10×1)	(16×1)
mode no.			***p***			
closed	0	0	0	0.1	0.1	0.1
1	397.4696	372.0072	363.3993	390.3984	363.6037	354.1777
2	814.3732	563.5381	451.4627	799.3632	550.6108	439.8967
3	1300.0293	1083.6428	1022.0897	1287.7341	1067.5718	1004.0639
4	2351.4831	1565.8437	1235.4047	2324.2956	1541.6114	1213.2125
5	3414.1648	2311.2033	2064.7087	3401.2936	2286.5765	2036.6260
open	0	0	0	0.1	0.1	0.1
1	414.9762	386.4855	376.6133	407.6030	377.7875	367.0891
2	814.3732	563.5381	451.4627	799.3632	550.6108	439.8967
3	1361.7047	1126.7225	1059.4837	1348.6011	1109.9733	1040.8040
4	2351.4831	1565.8437	1235.4047	2324.2956	1541.6114	1213.2125
5	3596.4687	2406.7780	2141.2389	3581.8401	2380.8578	2112.0122
closed	0.5	0.5	0.5	1	1	1
1	367.1566	336.4942	324.4588	347.3565	316.3907	304.6718
2	748.2397	508.2597	402.3142	700.7946	475.4369	376.7481
3	1238.2530	1010.0090	941.2004	1175.1482	951.1338	884.3124
4	2208.6580	1451.6299	1134.1286	2054.6103	1354.9541	1060.2258
5	3318.0673	2187.5989	1930.8373	3157.7035	2061.2836	1813.5184
open	0.5	0.5	0.5	1	1	1
1	383.1087	349.4751	336.1270	361.5191	327.5401	314.4007
2	748.2397	508.2597	402.3142	700.7946	475.4369	376.7481
3	1295.3439	1049.3910	975.0220	1226.4486	985.5666	913.1066
4	2208.6580	1451.6299	1134.1286	2054.6103	1354.9541	1060.2258
5	3488.9907	2275.7847	2000.8432	3312.7066	2139.2091	1873.8180
closed	2	2	2	5	5	5
1	327.7626	305.1115	297.6485	310.5625	293.6676	287.6153
2	655.0103	457.1737	368.4053	627.3266	443.1912	358.6304
3	1056.7174	870.2538	818.4716	893.4946	758.0542	716.9215
4	1833.8358	1237.0708	982.3259	1589.9808	1088.0677	868.1601
5	2780.7427	1840.1531	1635.5620	2195.6114	1543.5143	1380.8831
open	2	2	2	5	5	5
1	338.1711	313.3887	305.3018	316.5562	298.7869	292.3836
2	655.0103	457.1737	368.4053	627.3266	443.1912	358.6304
3	1095.0437	894.6041	839.5426	913.0353	771.5590	728.6535
4	1833.8358	1237.0708	982.3259	1589.9808	1088.0677	868.1601
5	2901.5443	1894.8247	1678.3111	2246.8920	1571.6050	1402.9636

Table G.28: Differences between closed and open-circuit natural frequencies [Hz] from Table G.24.

	mesh					
	(5×1)	(10×1)	(15×1)	(5×1)	(10×1)	(15×1)
	p					
mode no.	0	0	0	0.1	0.1	0.1
1	0.0627	0.0602	0.0593	0.0431	0.0406	0.0400
2	0.0000	0.0000	0.0000	0.0000	0.0000	0.0000
3	0.4367	0.3866	0.3758	0.3462	0.3009	0.2917
4	0.0000	0.0000	0.0000	0.0000	0.0000	0.0000
5	0.0000	0.0000	0.0000	0.0000	0.0000	0.0000
–	0.5	0.5	0.5	1	1	1
1	0.0156	0.0145	0.0143	0.0057	0.0054	0.0053
2	0.0000	0.0000	0.0000	0.0000	0.0000	0.0000
3	0.1998	0.1721	0.1673	0.1265	0.1086	0.1057
4	0.0000	0.0000	0.0000	0.0000	0.0000	0.0000
5	0.0000	0.0000	0.0000	0.0000	0.0000	0.0000
–	2	2	2	5	5	5
1	0.0013	0.0012	0.0012	0.0001	0.0001	0.0001
2	0.0000	0.0000	0.0000	0.0000	0.0000	0.0000
3	0.0615	0.0502	0.0485	0.0117	0.0076	0.0071
4	0.0000	0.0000	0.0000	0.0000	0.0000	0.0000
5	0.0000	0.0000	0.0000	0.0000	0.0000	0.0000

Table G.29: Differences between closed and open-circuit natural frequencies [Hz] from Table G.25.

	mesh					
	(6×1)	(10×1)	(16×1)	(6×1)	(10×1)	(16×1)
	p					
mode no.	0	0	0	0.1	0.1	0.1
1	0.4621	0.4118	0.3921	0.3778	0.3341	0.3171
2	0.0000	0.0000	0.0000	0.0000	0.0000	0.0000
3	1.5576	1.2095	1.1052	1.2884	0.9921	0.9037
4	0.0000	0.0000	0.0000	0.0000	0.0000	0.0000
5	4.2895	2.6194	2.2431	3.5767	2.1603	1.8435
–	0.5	0.5	0.5	1	1	1
1	0.2518	0.2271	0.2171	0.1928	0.1797	0.1734
2	0.0000	0.0000	0.0000	0.0000	0.0000	0.0000
3	0.8366	0.6636	0.6106	0.5971	0.5004	0.4668
4	0.0000	0.0000	0.0000	0.0000	0.0000	0.0000
5	2.2552	1.4280	1.2361	1.5008	1.0466	0.9246
–	2	2	2	5	5	5
1	0.1371	0.1351	0.1326	0.0739	0.0857	0.0895
2	0.0000	0.0000	0.0000	0.0000	0.0000	0.0000
3	0.3774	0.3486	0.3338	0.1540	0.1886	0.1976
4	0.0000	0.0000	0.0000	0.0000	0.0000	0.0000
5	0.8300	0.6937	0.6363	0.2444	0.3387	0.3521

Table G.30: Differences between closed and open-circuit natural frequencies [Hz] from Table G.26.

	mesh					
	(5 × 1)	(10 × 1)	(15 × 1)	(5 × 1)	(10 × 1)	(15 × 1)
	p					
mode no.	0	0	0	0.1	0.1	0.1
1	2.1863	1.9846	1.9194	2.0602	1.8465	1.7756
2	0.0000	0.0000	0.0000	0.0000	0.0000	0.0000
3	15.5101	12.7981	12.1681	15.1339	12.4077	0.0000
4	0.0000	0.0000	0.0000	0.0000	0.0000	11.7642
5	0.0000	0.0000	0.0000	0.0000	0.0000	0.0000
–	0.5	0.5	0.5	1	1	1
1	1.5946	1.3359	1.2418	1.0430	0.7162	0.5962
2	0.0000	0.0000	0.0000	0.0000	0.0000	0.0000
3	13.5676	0.0000	0.0000	11.4395	0.0000	0.0000
4	0.0000	10.8148	10.1126	0.0000	8.5211	7.6924
5	0.0000	0.0000	0.0000	0.0000	0.0000	0.0000
–	2	2	2	5	5	5
1	0.1834	0.1360	0.1357	0.0221	0.0209	0.0206
2	0.0000	0.0000	0.0000	0.0000	0.0000	0.0000
3	0.0000	0.0000	0.0000	2.0521	0.0000	0.0000
4	7.1078	4.9710	4.7597	0.0000	1.6087	1.5430
5	0.0000	0.0000	0.0000	0.0000	0.0000	0.0000

Table G.31: Differences between closed and open-circuit natural frequencies [Hz] from Table G.27.

	mesh					
	(6 × 1)	(10 × 1)	(16 × 1)	(6 × 1)	(10 × 1)	(16 × 1)
	p					
mode no.	0	0	0	0.1	0.1	0.1
1	17.5066	14.4783	13.2140	17.2046	14.1838	12.9114
2	0.0000	0.0000	0.0000	0.0000	0.0000	0.0000
3	61.6754	43.0797	37.3940	60.8670	42.4015	36.7401
4	0.0000	0.0000	0.0000	0.0000	0.0000	0.0000
5	182.3039	95.5747	76.5302	180.5465	94.2813	75.3862
–	0.5	0.5	0.5	1	1	1
1	15.9521	12.9809	11.6682	14.1626	11.1494	9.7289
2	0.0000	0.0000	0.0000	0.0000	0.0000	0.0000
3	57.0909	39.3820	33.8216	51.3004	34.4328	28.7942
4	0.0000	0.0000	0.0000	0.0000	0.0000	0.0000
5	170.9234	88.1858	70.0059	155.0031	77.9255	60.2996
–	2	2	2	5	5	5
1	10.4085	8.2772	7.6533	5.9937	5.1193	4.7683
2	0.0000	0.0000	0.0000	0.0000	0.0000	0.0000
3	38.3263	24.3503	21.0710	19.5407	13.5048	11.7320
4	0.0000	0.0000	0.0000	0.0000	0.0000	0.0000
5	120.8016	54.6716	42.7491	51.2806	28.0907	22.0805

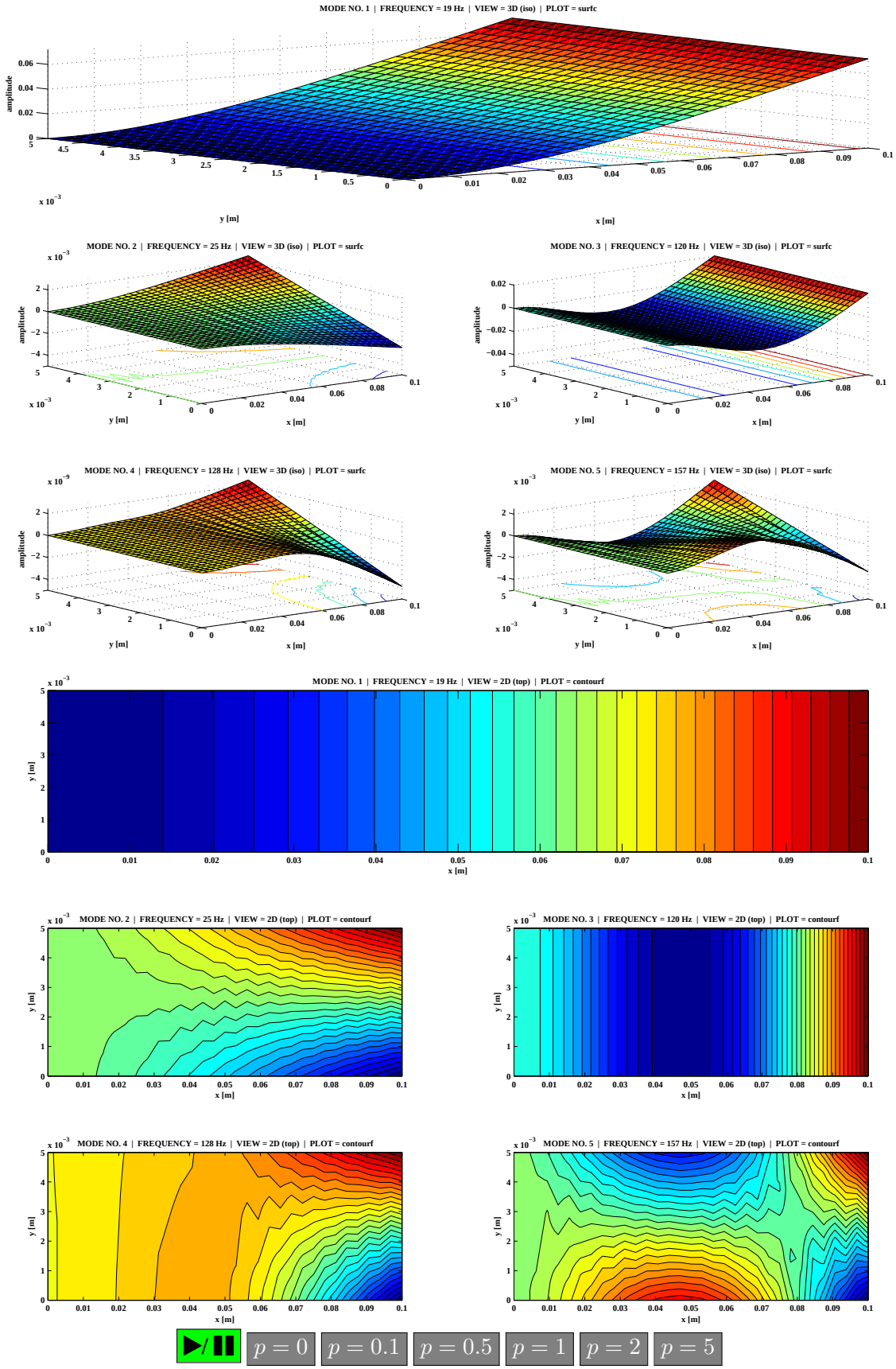

Figure G.99: The first five free vibrational modes (3D and 2D views) from the parametric case study of longitudinal FGM bimorph beam (dynamics (CFFF)), mixing up LaRC-Si and PVDF, considering closed-circuit and several p-exponents (0, 0.1, 0.5, 1, 2 and 5). Please click on the buttons above this caption to run the animation and toggle between plotted results.

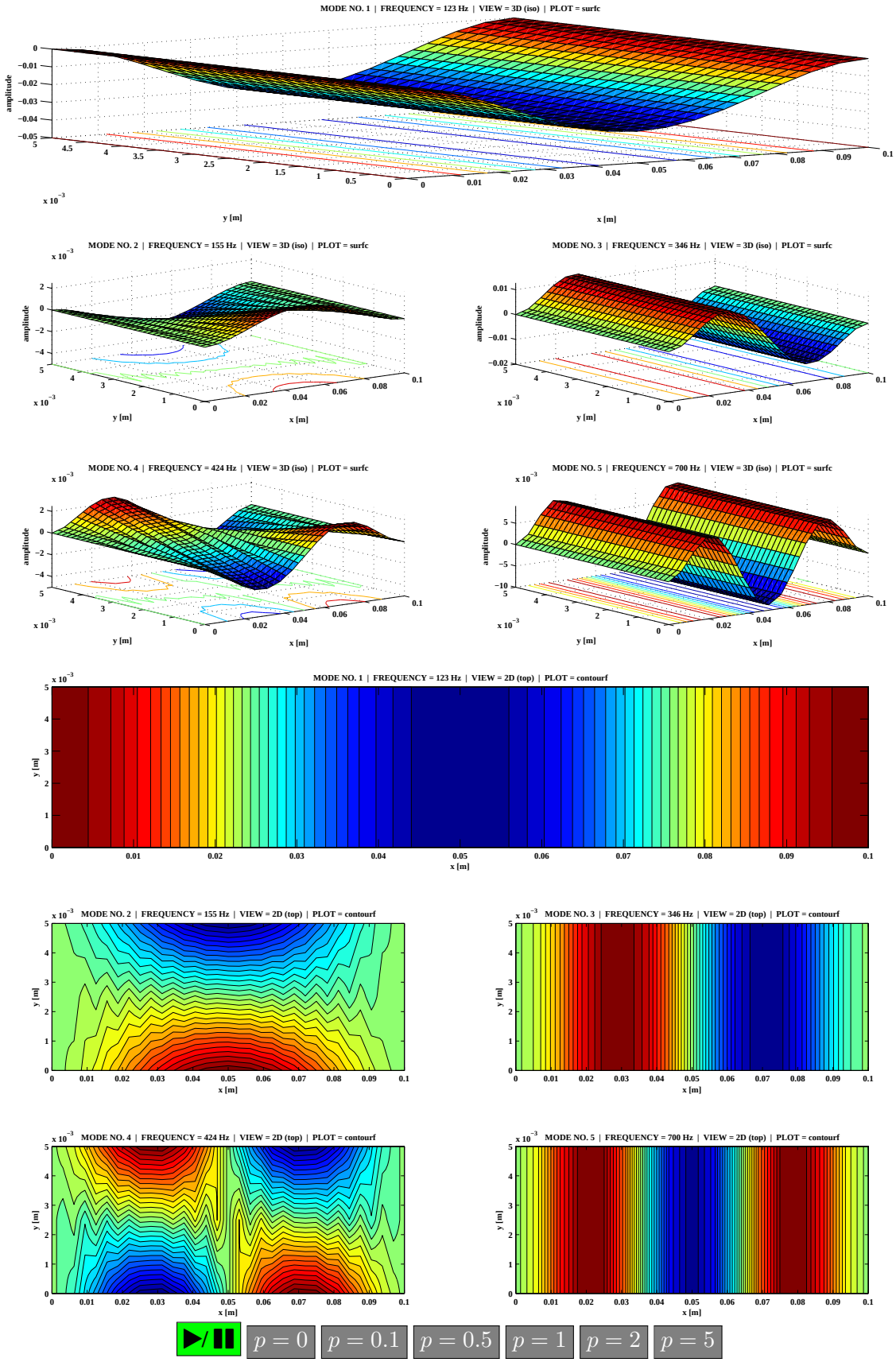

Figure G.100: The first five free vibrational modes (3D and 2D views) from the parametric case study of longitudinal FGM bimorph beam (dynamics (CCFF)), mixing up LaRC-Si and PVDF, considering closed-circuit and several p-exponents (0, 0.1, 0.5, 1, 2 and 5). Please click on the buttons above this caption to run the animation and toggle between plotted results.

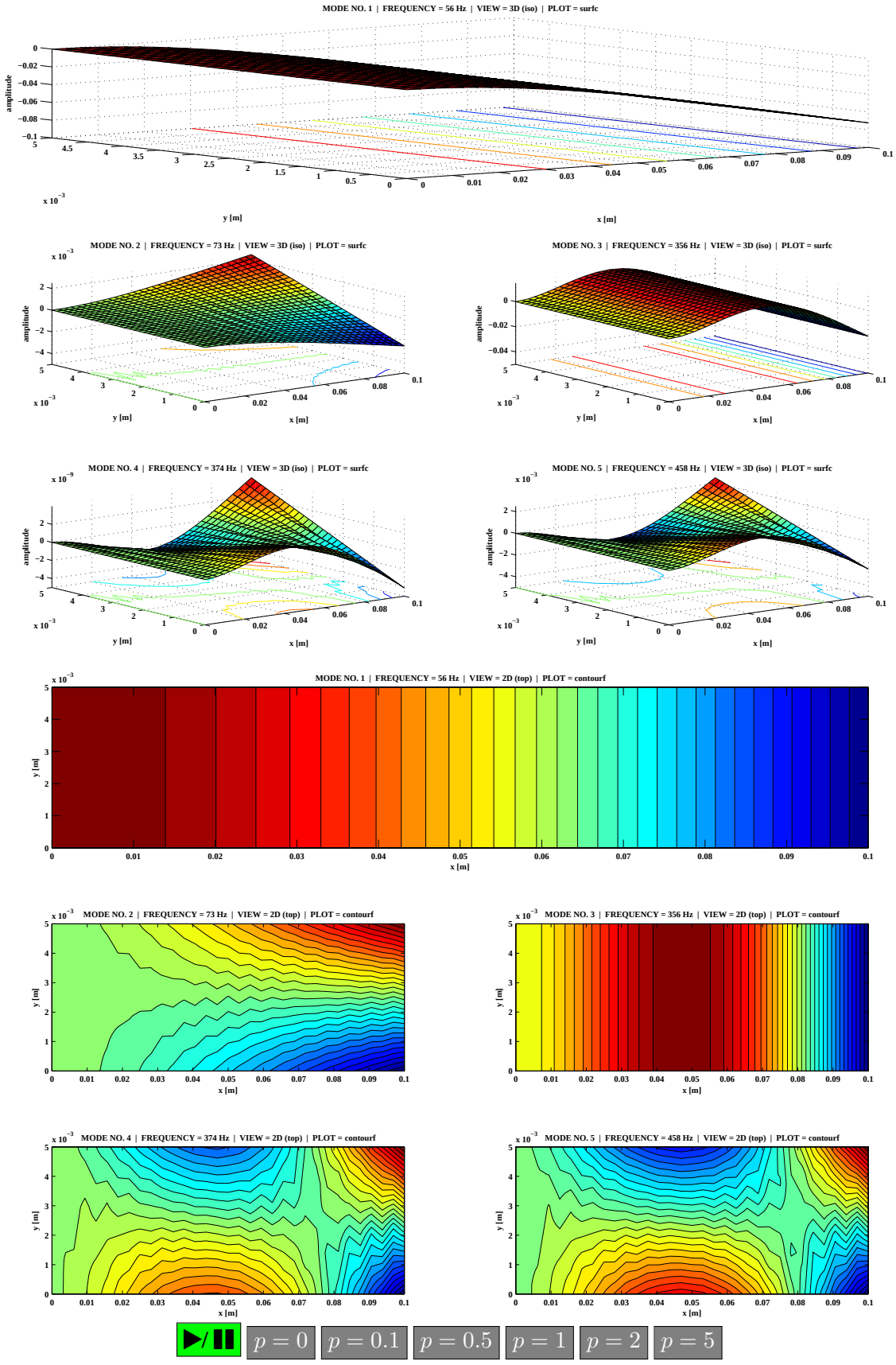

Figure G.101: The first five free vibrational modes (3D and 2D views) from the parametric case study of longitudinal FGM bimorph beam (dynamics (CFFF)), mixing up LaRC-Si and PZT-7A, considering closed-circuit and several p-exponents (0, 0.1, 0.5, 1, 2 and 5). Please click on the buttons above this caption to run the animation and toggle between plotted results.

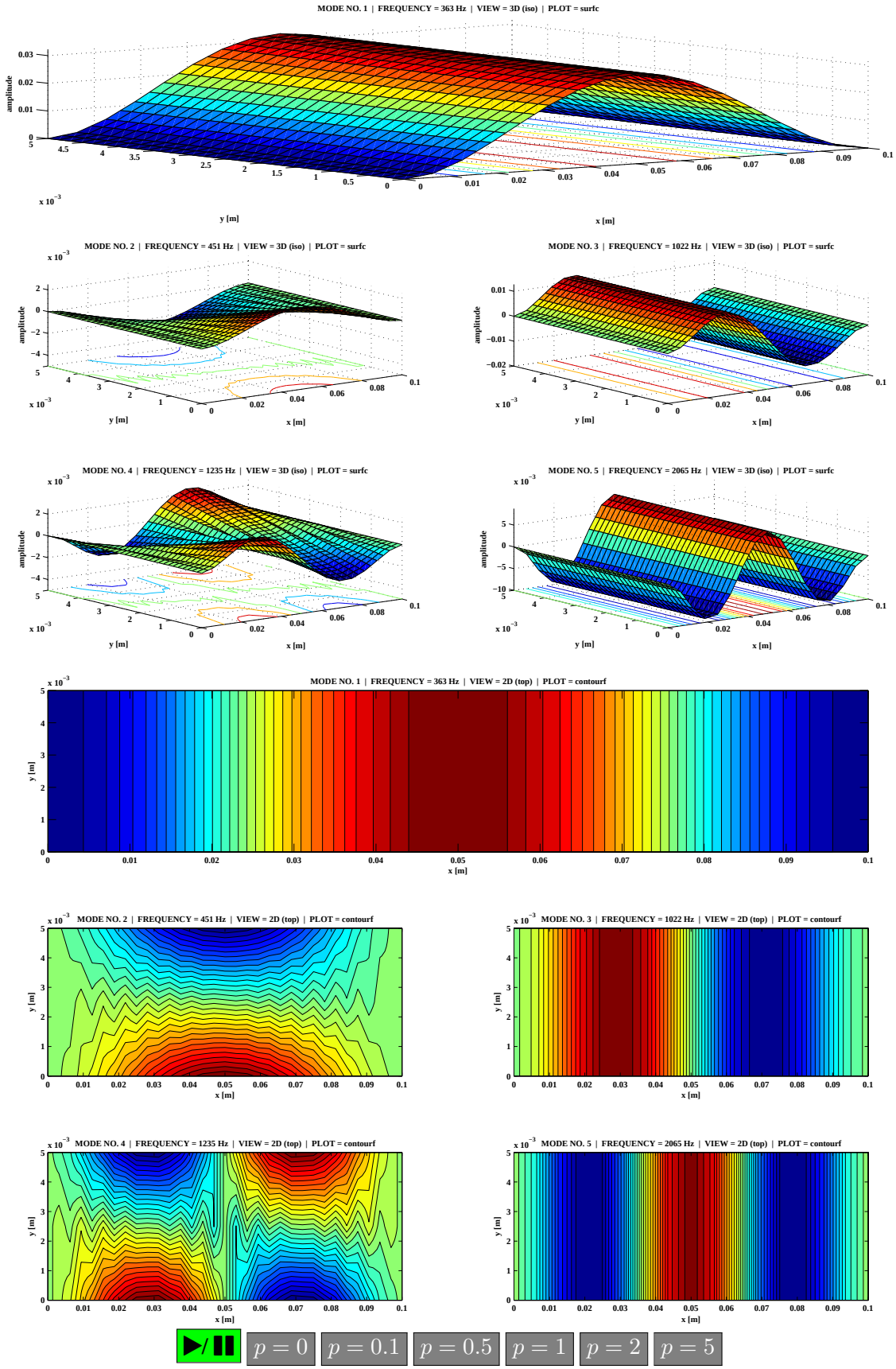

Figure G.102: The first five free vibrational modes (3D and 2D views) from the parametric case study of longitudinal FGM bimorph beam (dynamics (CCFF)), mixing up LaRC-Si and PZT-7A, considering closed-circuit and several p-exponents (0, 0.1, 0.5, 1, 2 and 5). Please click on the buttons above this caption to run the animation and toggle between plotted results.

Appendix H

Optimization Studies: Schemes & Results

This appendix gathers schemes and results about several optimization case studies, in order to optimize the thesis' size.

H.1 Multilayered smart structures

H.1.1 Minimization of beams' deflections

Schemes and results associated with Section 4.3.1.1.

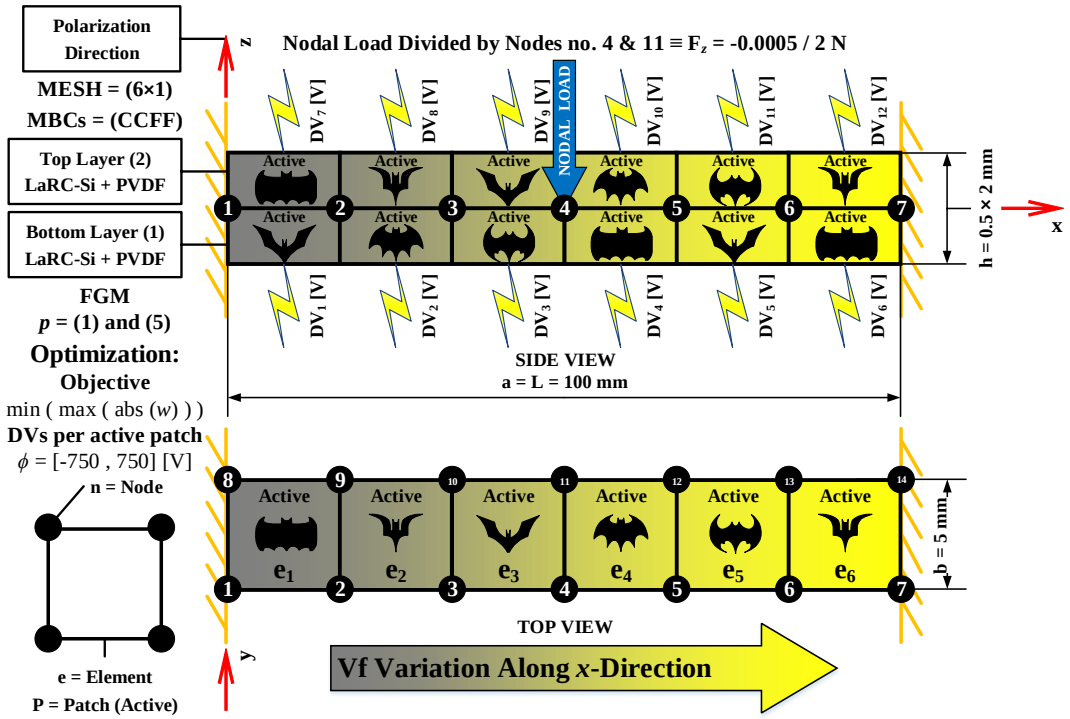

Figure H.1: Optimization case study scheme for minimization of beams' deflections.

Table H.1: HBA parameters used to compute all case studies presented in Figure H.2.

Class	BA Parameter	Value
Problem Definition	Optimization Objective	MINIMIZATION
	d	12
	N_{gen}	50
	n	50
Echolocation	f_{min}	0
	f_{max}	0.01
	r^0	0.5
	A^0	0.5
Solution Modification	Hybrid (BA+DE)	TRUE
	Adaptive	TRUE
	$Fper_i$	see Table H.2
	$Fper_f$	see Table H.2
	Micro	FALSE
Constants	α	0.98
	γ	0.97
	ϵ	0.001

Table H.2: Random combinations of DE perturbation factors $Fper_i$ and $Fper_f$, sorted from the minimum (best) to the maximum (worst) deflection obtained from the CSs presented in Figure H.2.

cs_no.	w $(\times 10^{-7}$ [m])	$\boldsymbol{Fper_i}$	$\boldsymbol{Fper_f}$
11 (best)	1.03	1.5	0
18	1.40	2	0
10	2.16	0.6	0.8
25	2.67	0	1.7
12	2.67	0.01	0.8
13	3.38	2	0.01
8	4.41	0	2
14	4.54	2	1
16	4.73	0.9	2
6	5.00	0.5	0.2
21	5.12	0.2	0.5
5	5.73	0	1.5
15	5.94	1	2
4	6.21	0.01	1
22	6.60	10	3
20	9.30	10	20
24	11.47	0.5	5
19	12.00	0.01	0.05
9	13.80	0.01	0.2
17	16.45	0.1	0.2
23	19.24	0.01	0.3
1	19.78	0.01	0
7	24.47	0.05	0.1
2	29.20	0.05	0.01
3 (worst)	32.01	0.08	0.01

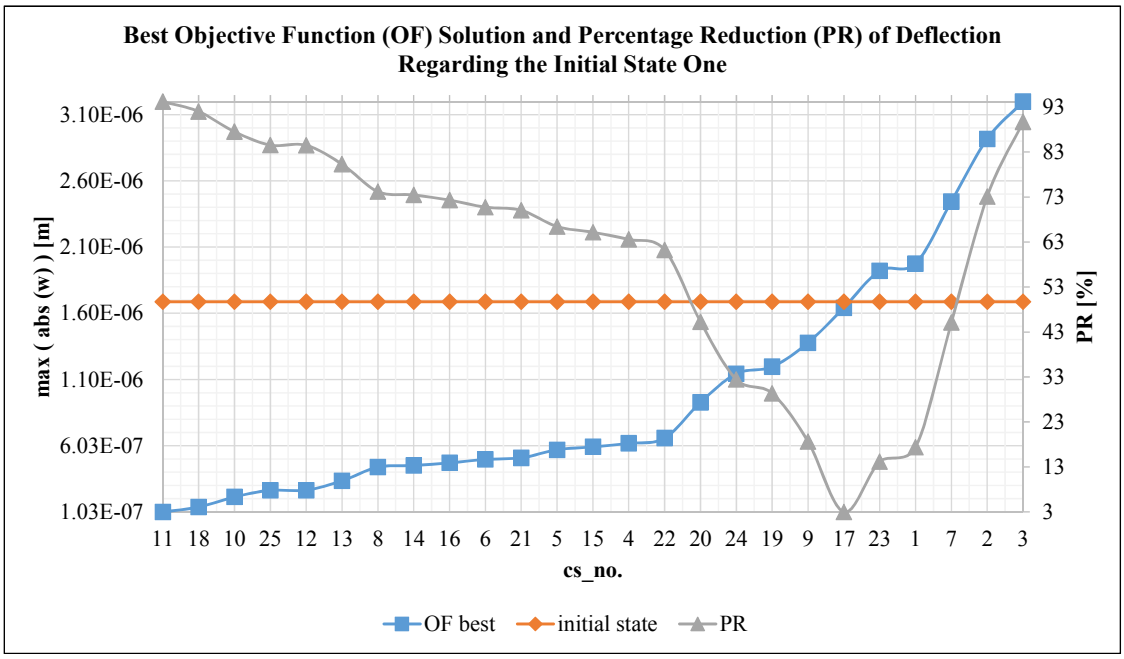

OF best and PR | $DV_{1..6}$ | $DV_{7..12}$ | $Fper_i$ *and* $Fper_f$

Figure H.2: Optimization results from 25 case studies ($N_{gen} = 50$ gens and $n = 50$ bats each) of min. of beams' deflections, mixing up LaRC-Si and PVDF, considering $p = 1$ and different random combinations of DE perturbation factors $Fper_i$ and $Fper_f$. DVs are the electric potentials ϕ [V] applied to each patch. Please click on the buttons above this caption to toggle between plotted results.

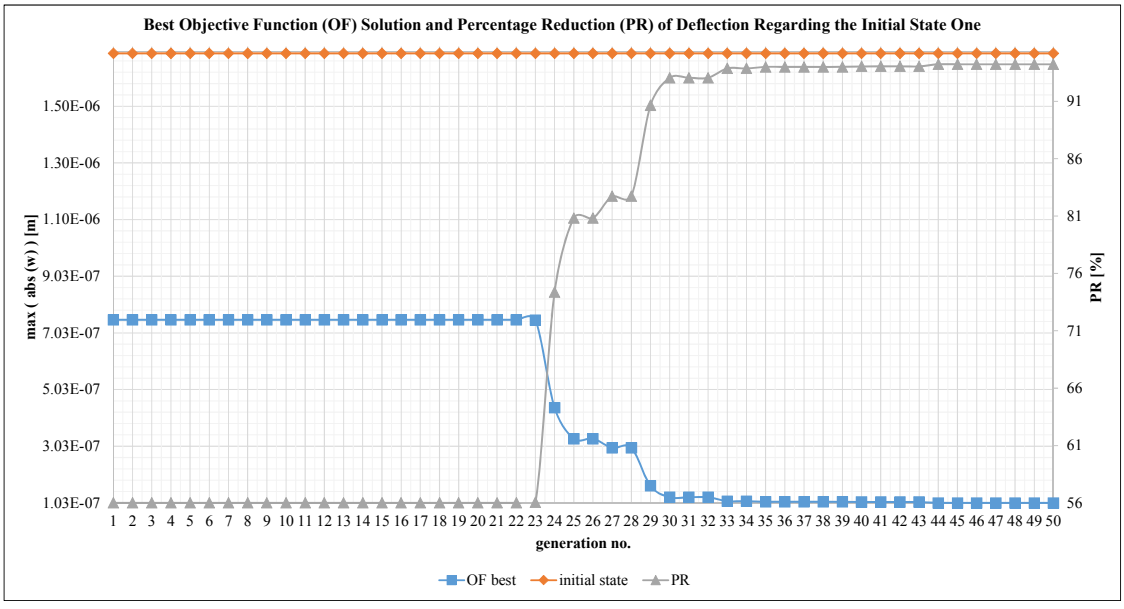

OF best and PR | $DV_{1..12}$

Figure H.3: Optimization results, for all generations, from the best case study found in Figure H.2. Please click on the buttons above this caption to toggle between plotted results.

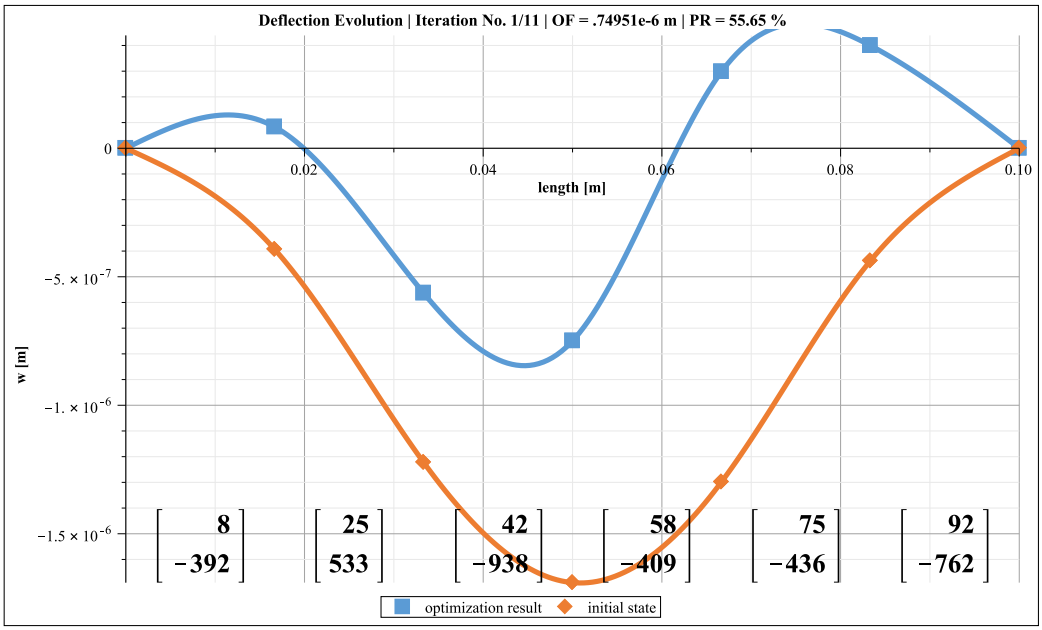

Figure H.4: Deflection plots of all successive best iterations found in the case study associated with Figure H.3. Note that the bold numbers above the x-axis (first row) correspond to the percentage $[\%]$ of piezoelectric material, $V_{f,r}^{ex}$, mixed up in each element along the beam's length, at each frame. Note that the bold numbers above the x-axis (second row) correspond to the voltage $[\mathrm{V}]$ in each element along the beam's length, at each frame. Please click on the buttons above this caption to run the animation and toggle between plotted results.

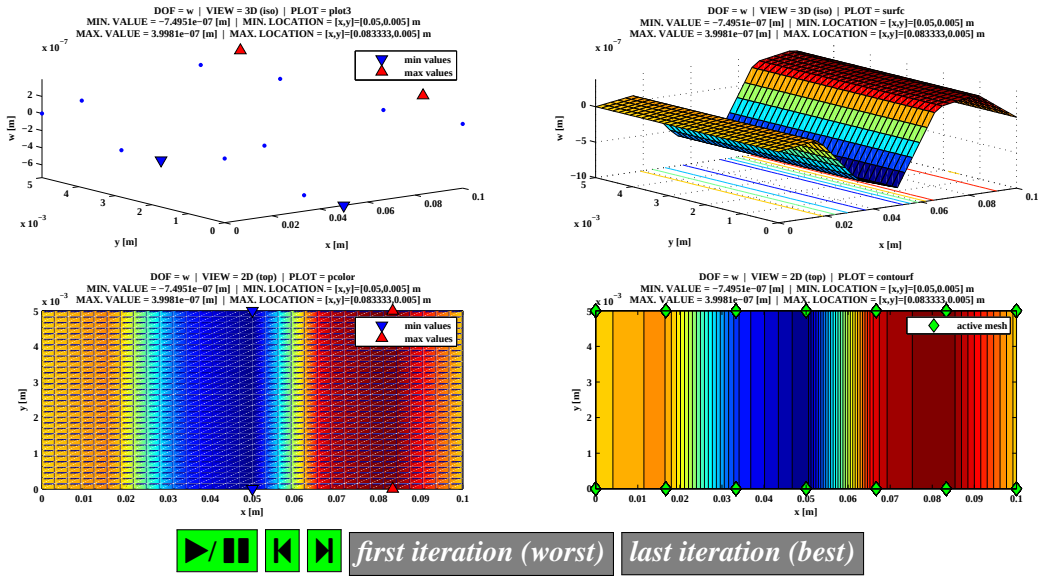

Figure H.5: 3D and 2D deflection plots of all successive best iterations found in the case study associated with Figure H.3. Please click on the buttons above this caption to run the animation and toggle between plotted results.

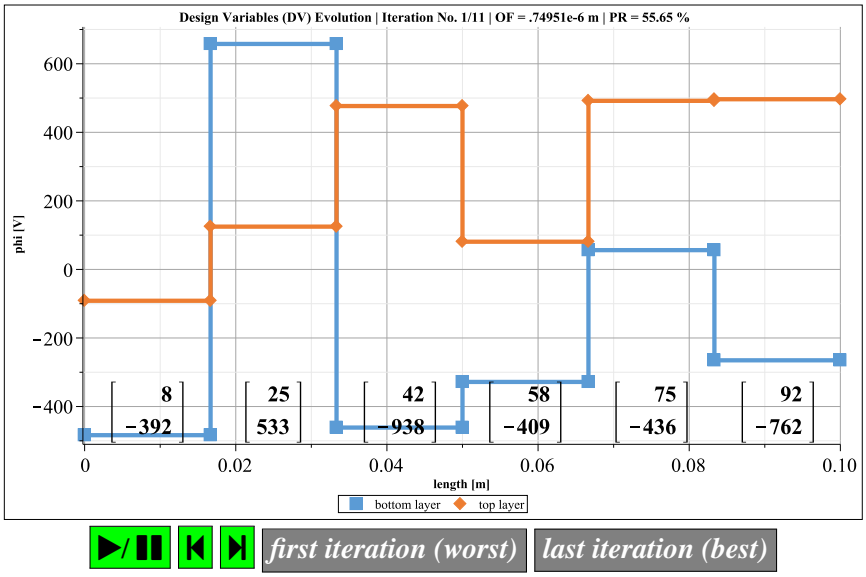

Figure H.6: Electric potentials plots of all successive best iterations found in the case study associated with Figure H.3. Note that the bold numbers above the x-axis (first row) correspond to the percentage $[\%]$ of piezoelectric material, $V_{f,r}^{ex}$, mixed up in each element along the beam's length, at each frame. Note that the bold numbers above the x-axis (second row) correspond to the voltage $[\mathrm{V}]$ in each element along the beam's length, at each frame. Please click on the buttons above this caption to run the animation and toggle between plotted results.

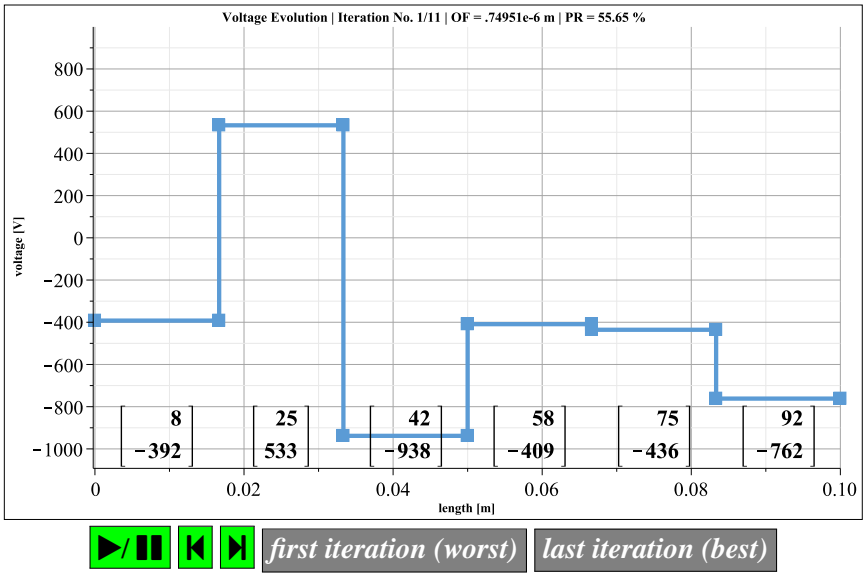

Figure H.7: Voltage plots of all successive best iterations found in the case study associated with Figure H.3. Note that the bold numbers above the x-axis (first row) correspond to the percentage $[\%]$ of piezoelectric material, $V_{f,r}^{ex}$, mixed up in each element along the beam's length, at each frame. Note that the bold numbers above the x-axis (second row) correspond to the voltage $[\mathrm{V}]$ in each element along the beam's length, at each frame. Please click on the buttons above this caption to run the animation and toggle between plotted results.

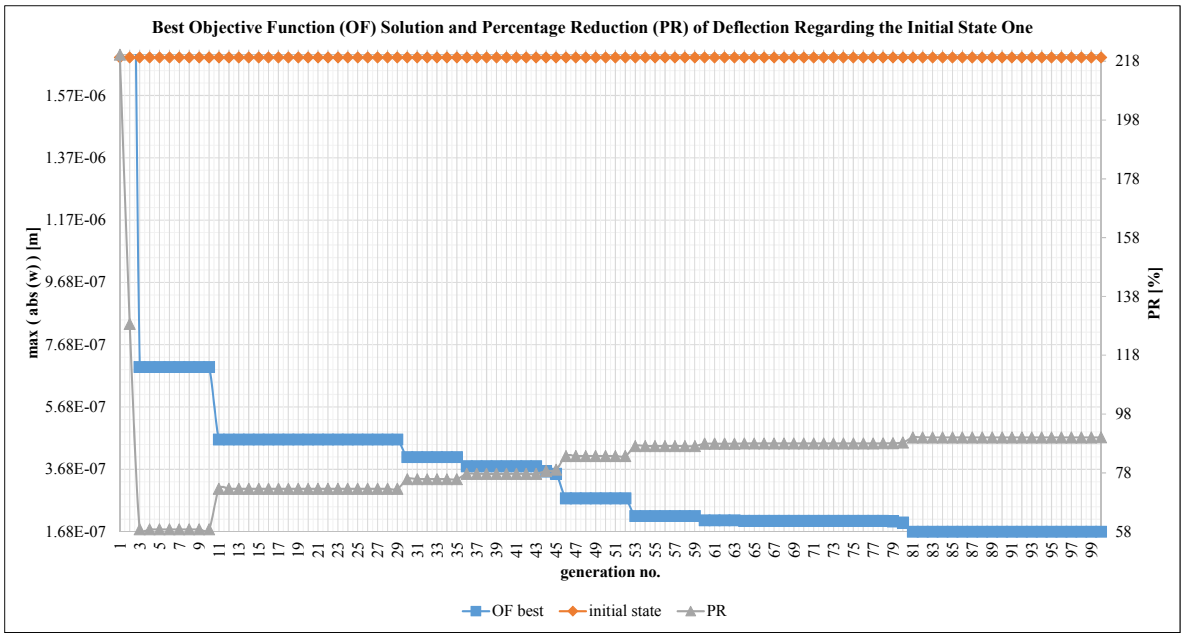

OF best and PR $DV_{1..12}$

Figure H.8: Optimization results, for all generations, for the best case study found in Figure H.2, i.e. $Fper_i = 1.5$ and $Fper_f = 0$, but computed with $N_{gen} = 100$. Please click on the buttons above this caption to toggle between plotted results.

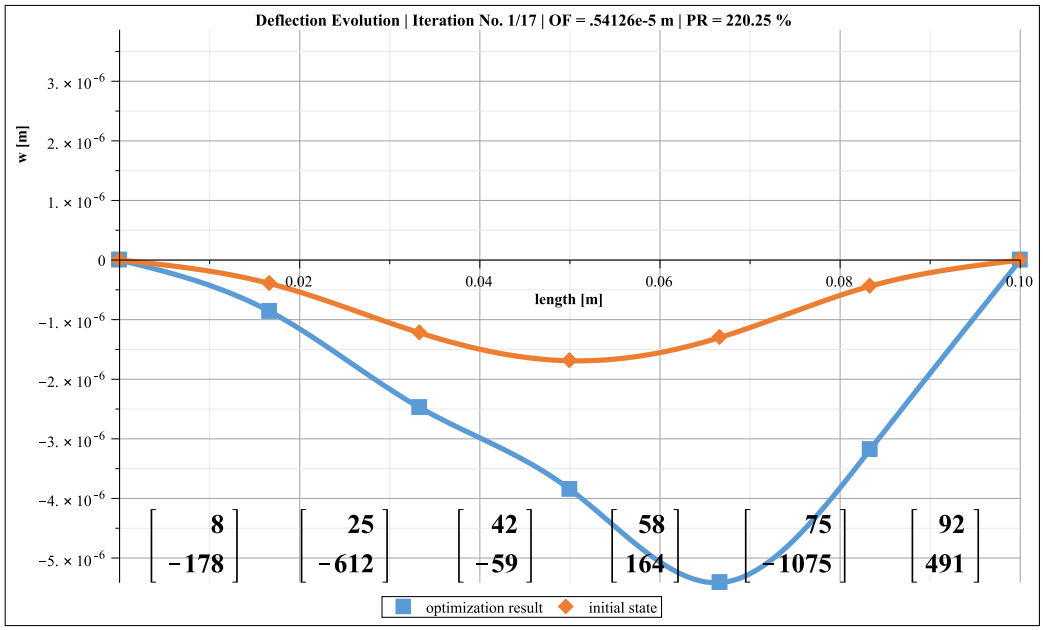

Figure H.9: Deflection plots of all successive best iterations found in the case study associated with Figure H.8. Note that the bold numbers above the x-axis (first row) correspond to the percentage $[\%]$ of piezoelectric material, $V_{f,r}^{ex}$, mixed up in each element along the beam's length, at each frame. Note that the bold numbers above the x-axis (second row) correspond to the voltage $[\mathrm{V}]$ in each element along the beam's length, at each frame. Please click on the buttons above this caption to run the animation and toggle between plotted results.

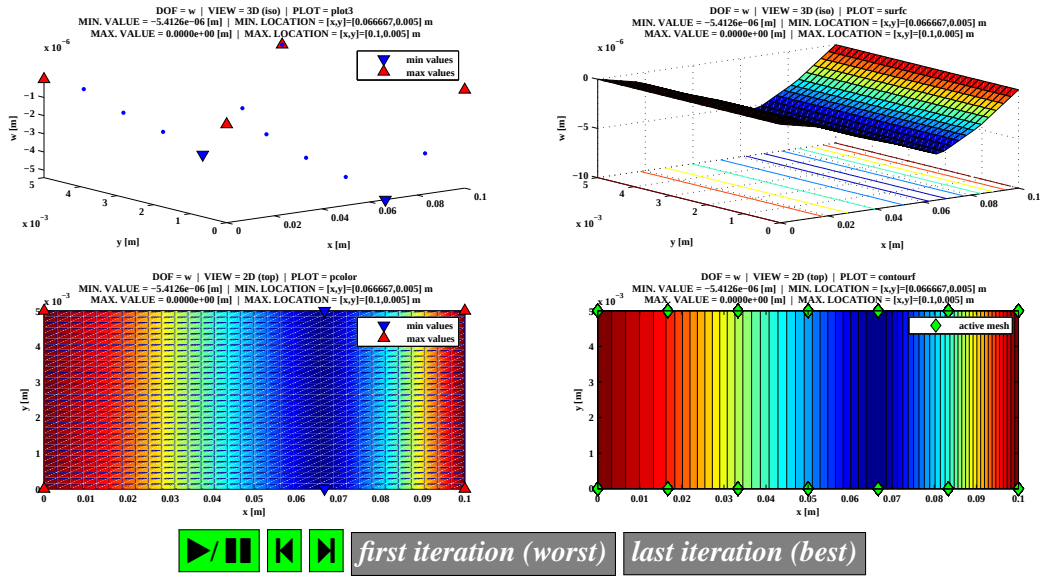

Figure H.10: 3D and 2D deflection plots of all successive best iterations found in the case study associated with Figure H.8. Please click on the buttons above this caption to run the animation and toggle between plotted results.

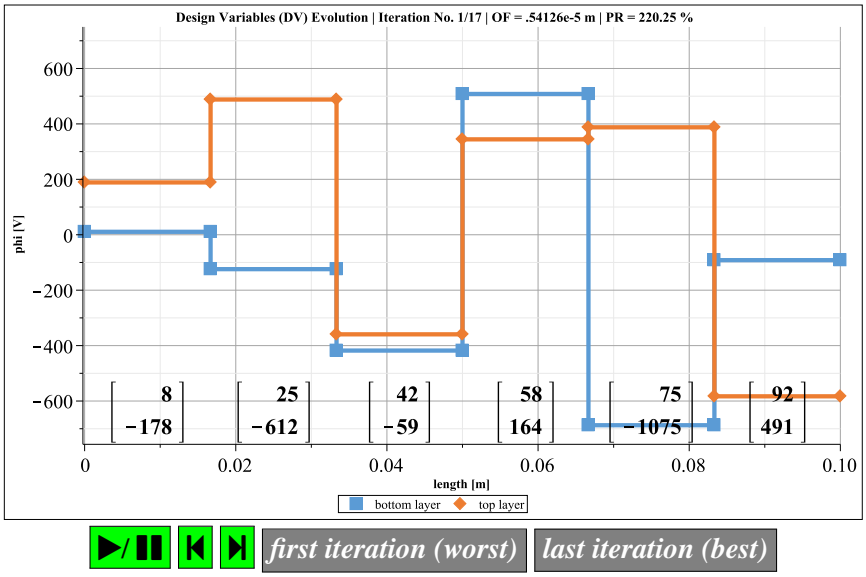

Figure H.11: Electric potentials plots of all successive best iterations found in the case study associated with Figure H.8. Note that the bold numbers above the x-axis (first row) correspond to the percentage $[\%]$ of piezoelectric material, $V_{f,r}^{ex}$, mixed up in each element along the beam's length, at each frame. Note that the bold numbers above the x-axis (second row) correspond to the voltage $[\mathrm{V}]$ in each element along the beam's length, at each frame. Please click on the buttons above this caption to run the animation and toggle between plotted results.

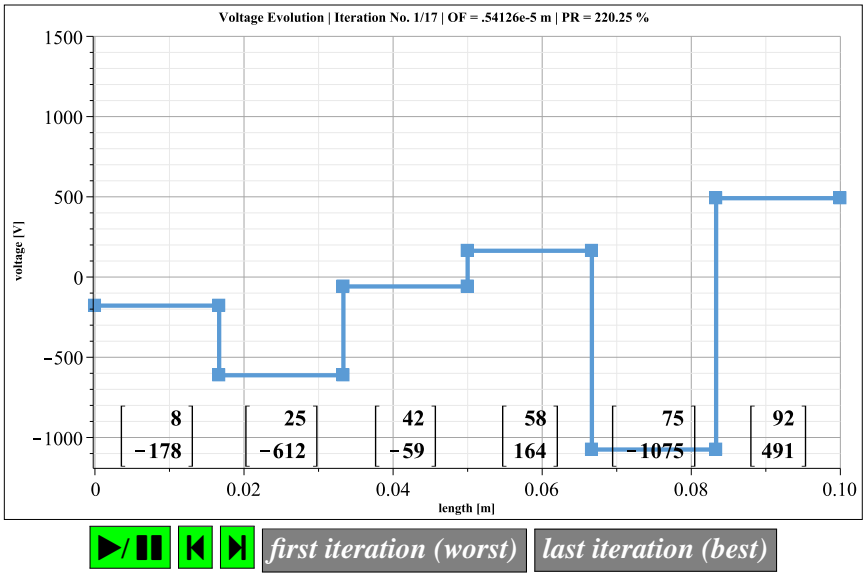

Figure H.12: Voltage plots of all successive best iterations found in the case study associated with Figure H.8. Note that the bold numbers above the x-axis (first row) correspond to the percentage $[\%]$ of piezoelectric material, $V_{f,r}^{ex}$, mixed up in each element along the beam's length, at each frame. Note that the bold numbers above the x-axis (second row) correspond to the voltage $[\mathrm{V}]$ in each element along the beam's length, at each frame. Please click on the buttons above this caption to run the animation and toggle between plotted results.

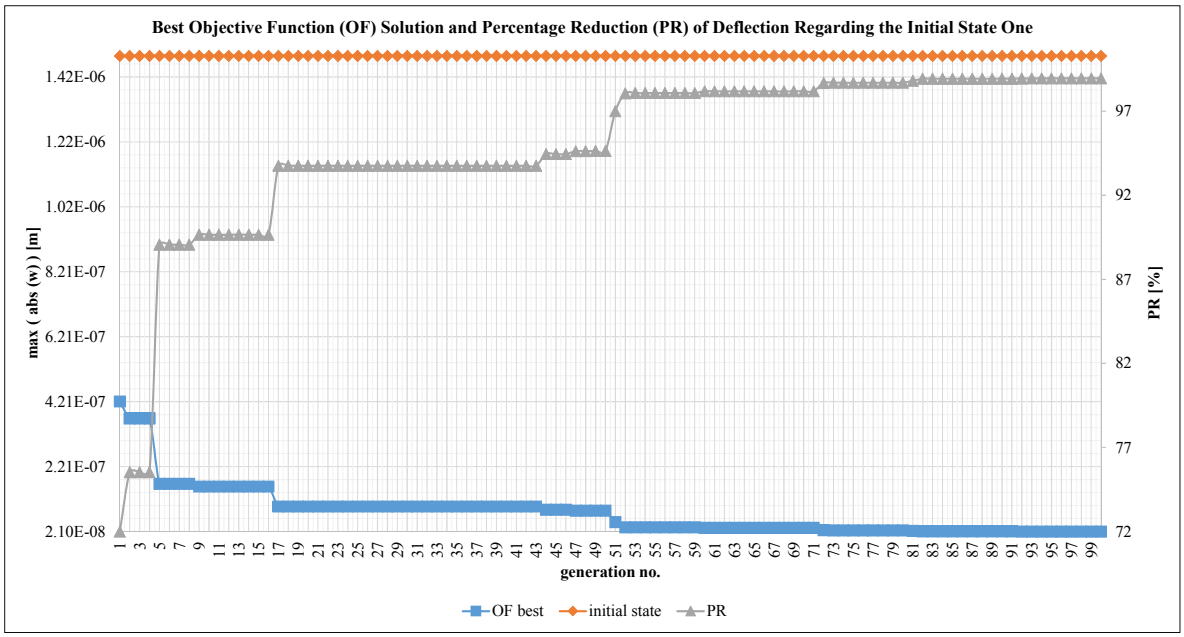

OF best and PR $DV_{1..12}$

Figure H.13: Optimization results, for all generations, for the same case study in Figure H.8, i.e. $Fper_i = 1.5$ and $Fper_f = 0$, $N_{gen} = 100$, but computed with $p = 5$ instead of $p = 1$. Please click on the buttons above this caption to toggle between plotted results.

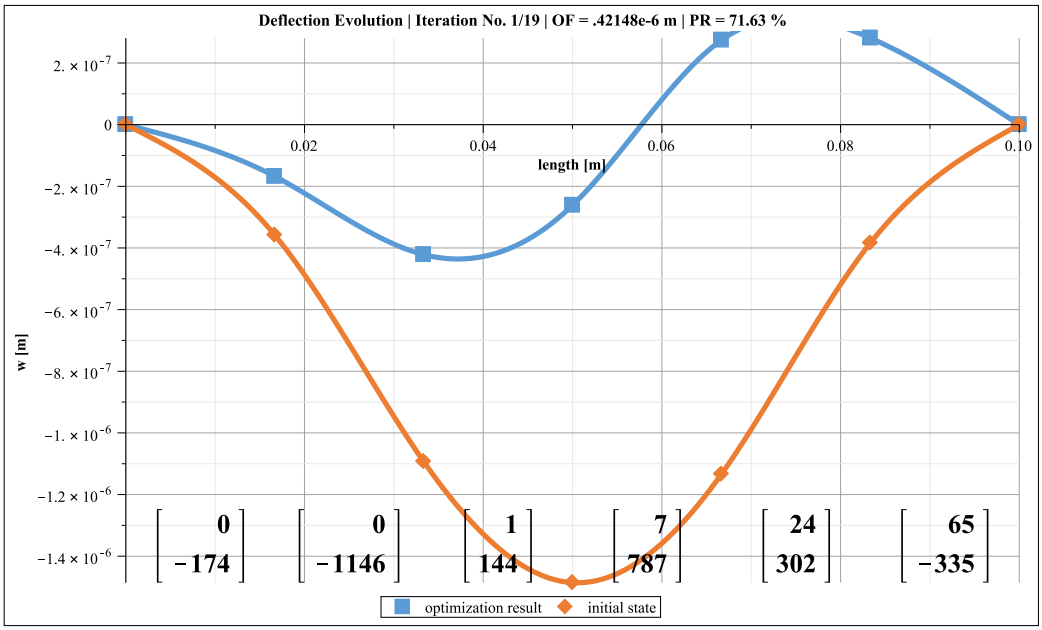

Figure H.14: Deflection plots of all successive best iterations found in the case study associated with Figure H.13. Note that the bold numbers above the x-axis (first row) correspond to the percentage $[\%]$ of piezoelectric material, $V_{f,r}^{ex}$, mixed up in each element along the beam's length, at each frame. Note that the bold numbers above the x-axis (second row) correspond to the voltage $[\mathrm{V}]$ in each element along the beam's length, at each frame. Please click on the buttons above this caption to run the animation and toggle between plotted results.

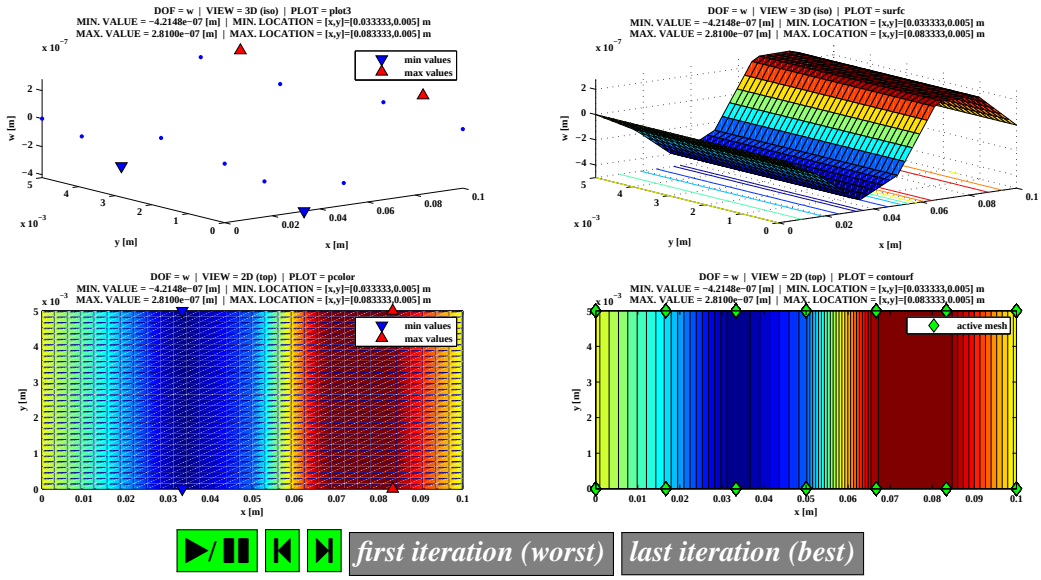

Figure H.15: 3D and 2D deflection plots of all successive best iterations found in the case study associated with Figure H.13. Please click on the buttons above this caption to run the animation and toggle between plotted results.

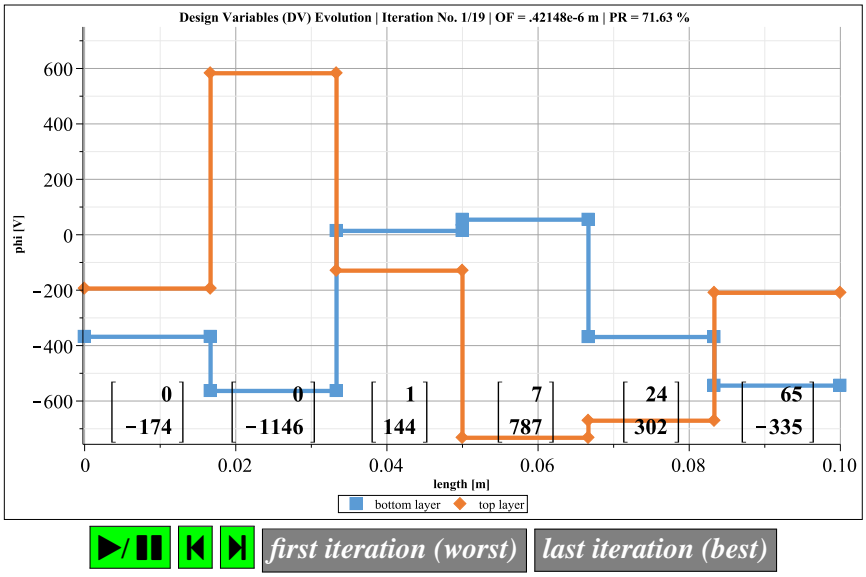

Figure H.16: Electric potentials plots of all successive best iterations found in the case study associated with Figure H.13. Note that the bold numbers above the x-axis (first row) correspond to the percentage $[\%]$ of piezoelectric material, $V_{f,r}^{ex}$, mixed up in each element along the beam's length, at each frame. Note that the bold numbers above the x-axis (second row) correspond to the voltage $[\mathrm{V}]$ in each element along the beam's length, at each frame. Please click on the buttons above this caption to run the animation and toggle between plotted results.

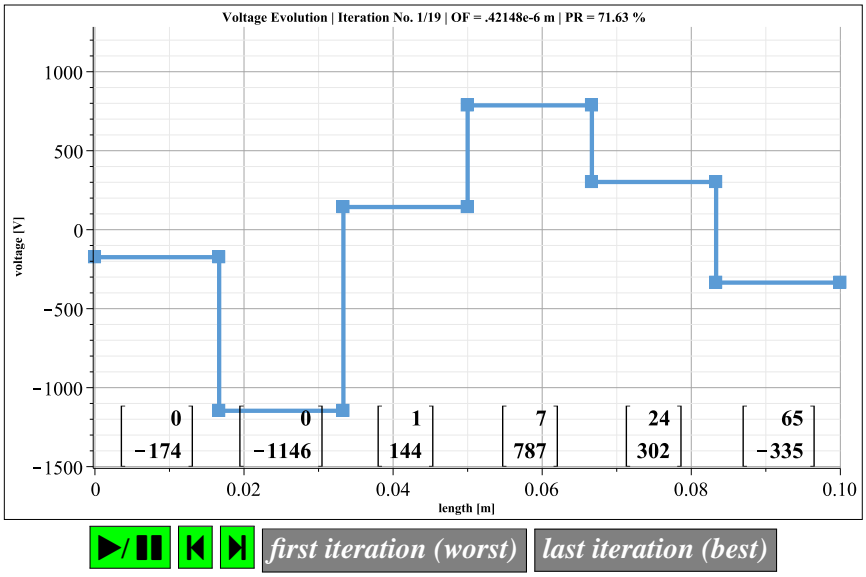

Figure H.17: Voltage plots of all successive best iterations found in the case study associated with Figure H.13. Note that the bold numbers above the x-axis (first row) correspond to the percentage $[\%]$ of piezoelectric material, $V_{f,r}^{ex}$, mixed up in each element along the beam's length, at each frame. Note that the bold numbers above the x-axis (second row) correspond to the voltage $[\mathrm{V}]$ in each element along the beam's length, at each frame. Please click on the buttons above this caption to run the animation and toggle between plotted results.

H.1.2 Minimization of plates' deflections

Schemes and results associated with Section 4.3.1.2.

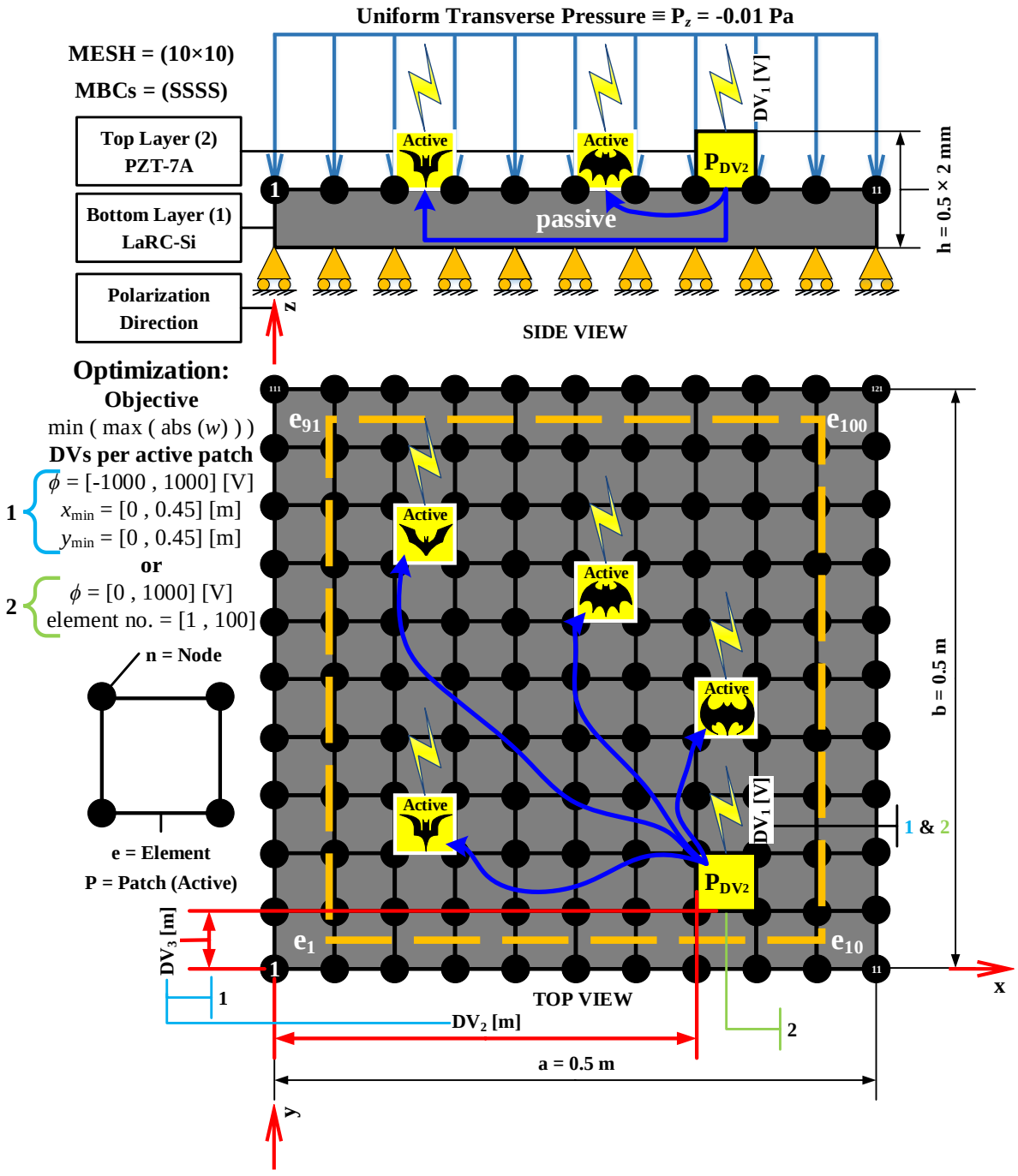

Figure H.18: Optimization case study scheme for minimization of plates' deflections.

Table H.3: MHBA parameters used to compute all case studies presented in Figures H.46 and H.47.

Class	BA Parameter	Value
Problem Definition	Optimization Objective	MINIMIZATION
	d	from 2 to 12 (depending on no. patches)
	N_{gen}	50
	n	10
Echolocation	f_{min}	0
	f_{max}	2
	r^0	0.01
	A^0	2
Solution Modification	Hybrid (BA+DE)	TRUE
	Adaptive	TRUE
	$Fper_i$	see Table H.4
	$Fper_f$	see Table H.4
	Micro	TRUE (All Gens, Step 5 Gens & Step 10 Gens)
Constants	α	0.95
	γ	0.97
	ϵ	0.001

Table H.4: Random combinations of DE perturbation factors $Fper_i$ and $Fper_f$, sorted from the minimum (best) to the maximum (worst) deflection obtained from the CSs presented in Figure H.19.

cs_no.	w ($\times 10^{-5}$ [m])	$Fper_i$	$Fper_f$	cs_no.	w ($\times 10^{-5}$ [m])	$Fper_i$	$Fper_f$
1 (best)	1.99	0.01	0	**... 32**	3.44	25	30
3	2.00	0.05	0.01	29	3.57	7	4
17	2.02	0.08	0.01	31	3.63	60	10
10	2.05	0.01	1	44	3.64	80	95
40	2.10	0	1.5	24	3.81	1000	0
46	2.10	0.5	0.2	20	3.91	5	15
26	2.14	0.05	0.1	36	4.02	70	4
21	2.29	0	2	4	4.07	50	10
45	2.32	0.01	0.2	49	4.07	0.8	20
50	2.37	0.6	0.8	37	4.11	0.005	0.01
41	2.49	1.5	0	11	4.14	0.01	5
34	2.64	0.01	0.8	33	4.30	70	10
12	2.64	2	0.01	13	4.44	5	0.5
2	2.67	2	1	8	4.50	50	0
5	2.67	1	2	6	4.50	70	10
47	2.69	0.9	2	23	4.80	15	20
38	2.73	0.1	0.2	30	4.88	20	80
22	2.77	2	0	14	4.90	10	20
9	2.78	0.01	0.05	28	4.98	3	2
19	2.90	10	20	25	5.24	0	1000
18	2.97	0.2	0.5	15	5.45	100	50
35	3.01	10	3	16	5.47	50	100
39	3.28	0.01	0.3	43	5.62	40	50
7	3.31	0.5	5	48	6.52	7	15
42 ...	3.34	0	1.7	**27 (worst)**	6.56	100	200

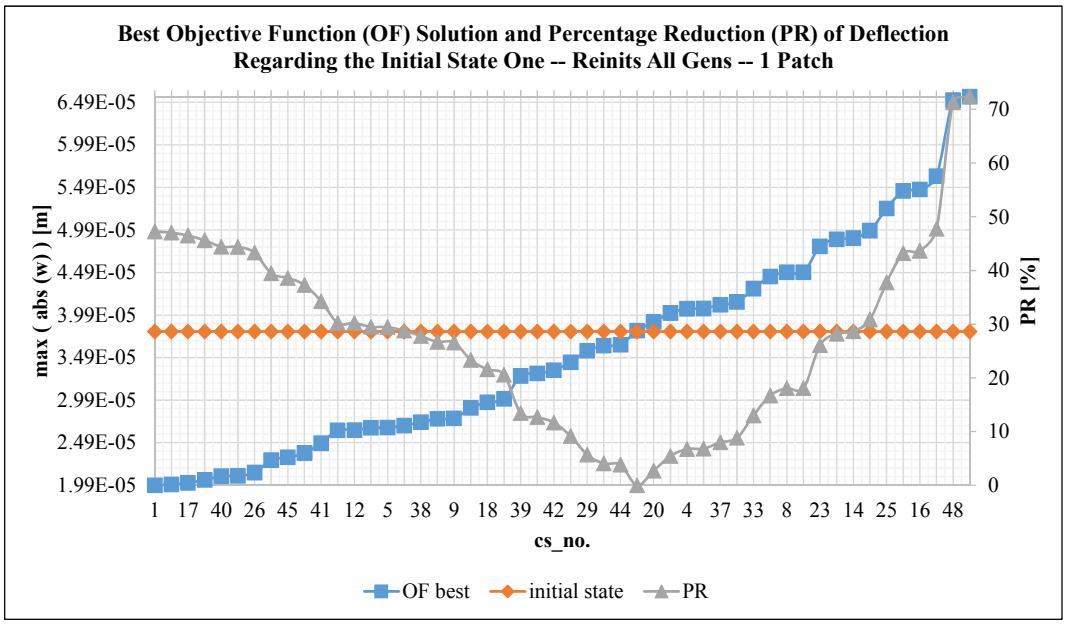

OF best and PR | DV_1 | $DV_{2..3}$ | $Fper_i$ *and* $Fper_f$

Figure H.19: Optimization results from 50 case studies ($N_{gen} = 50$ gens and $n = 10$ bats each) of min. of plates' deflections, bottom passive layer (LaRC-Si) with 1 patch on top (PZT-7A), considering different random combinations of DE perturbation factors $Fper_i$ and $Fper_f$. DVs are the electric potential ϕ [V] applied to the patch and its location, i.e. minimum coordinates x_{min} [m] and y_{min} [m]. Population's locations reinitialized randomly before each generation. Please click on the buttons above this caption to toggle between plotted results.

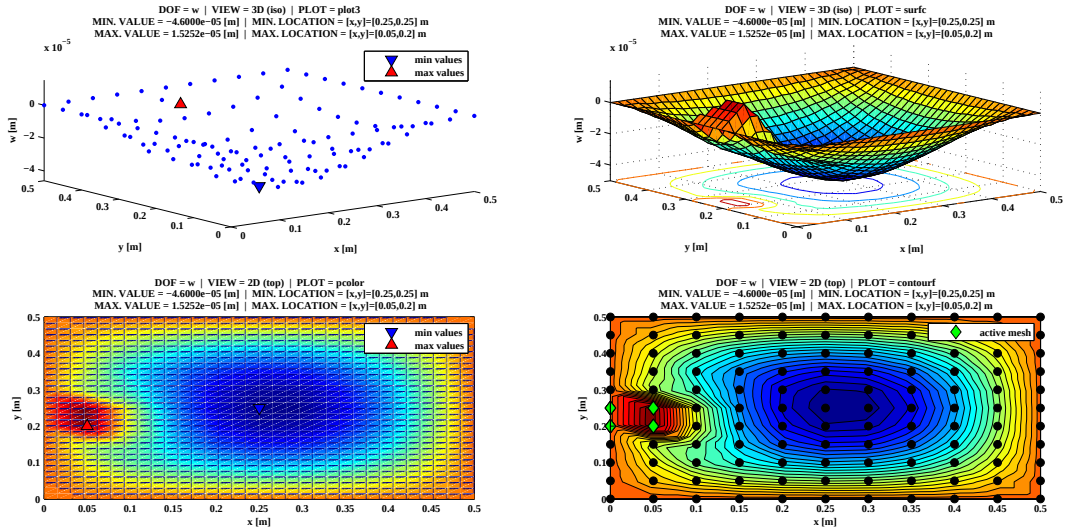

▶/❚❚ | ⏮ | ⏭ | *first iteration (worst)* | *last iteration (best)*

Figure H.20: 3D and 2D deflection plots of all successive best iterations found in the overall best case study, out of all 50, associated with Figure H.19. Please click on the buttons above this caption to run the animation and toggle between plotted results.

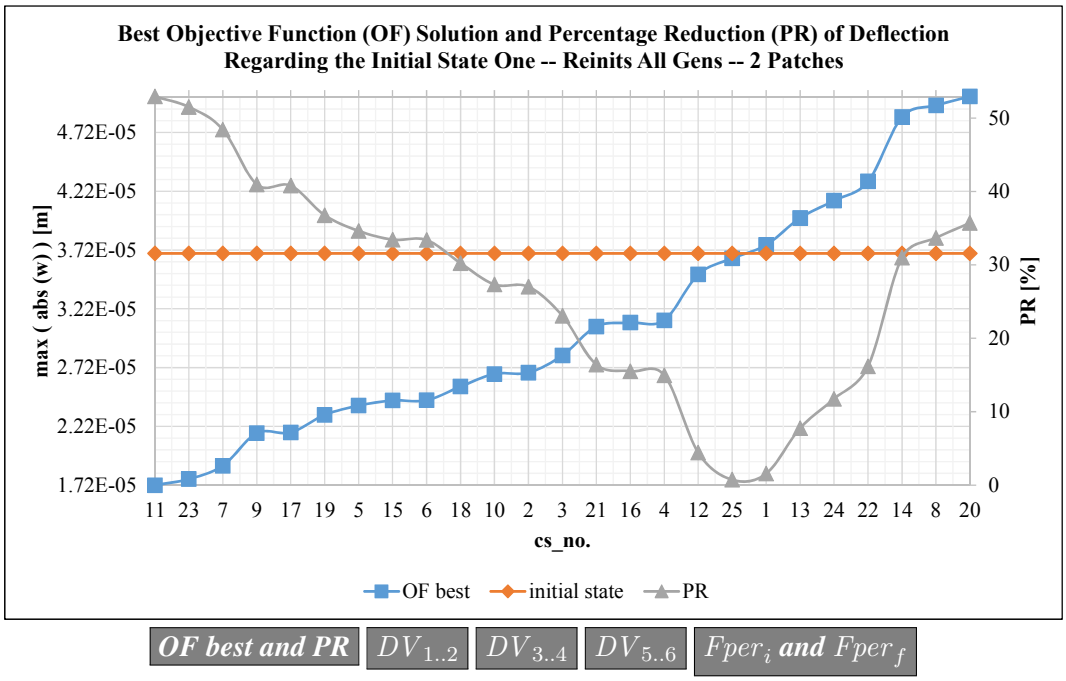

Figure H.21: Optimization results from 25 case studies ($N_{gen} = 50$ gens and $n = 10$ bats each) of min. of plates' deflections, bottom passive layer (LaRC-Si) with 2 independent patches on top (PZT-7A), considering the combinations of DE perturbation factors $Fper_i$ and $Fper_f$ matching the 25 best CSs in Table H.4. DVs are the electric potentials ϕ [V] applied to each patch and their locations, i.e. minimum coordinates x_{min} [m] and y_{min} [m]. Population's locations reinitialized randomly before each gen. Please click on the buttons above this caption to toggle between plotted results.

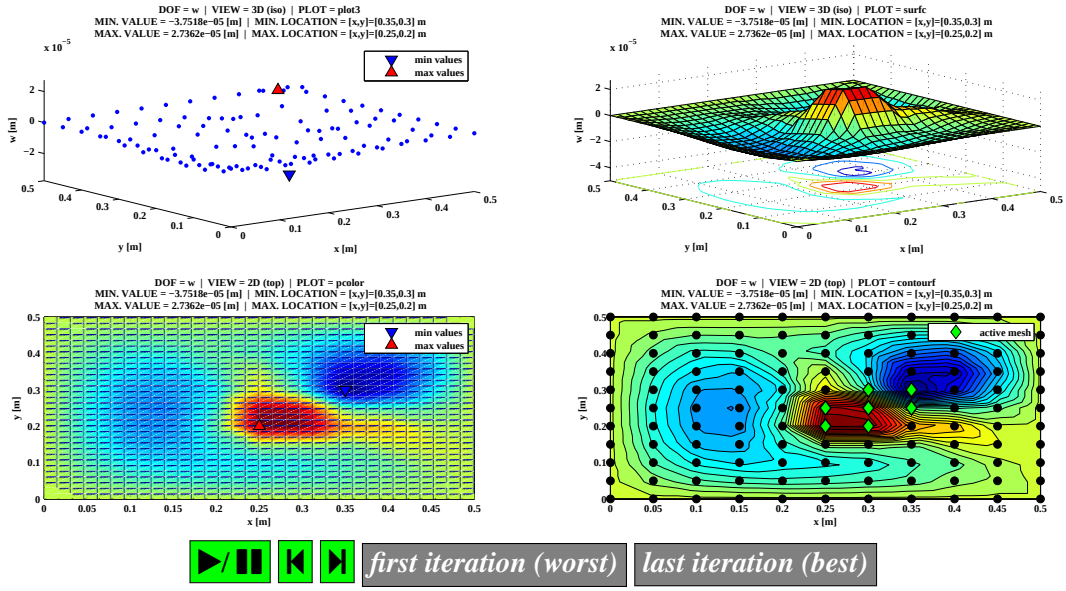

Figure H.22: 3D and 2D deflection plots of all successive best iterations found in the overall best case study, out of all 25, associated with Figure H.21. Please click on the buttons above this caption to run the animation and toggle between plotted results.

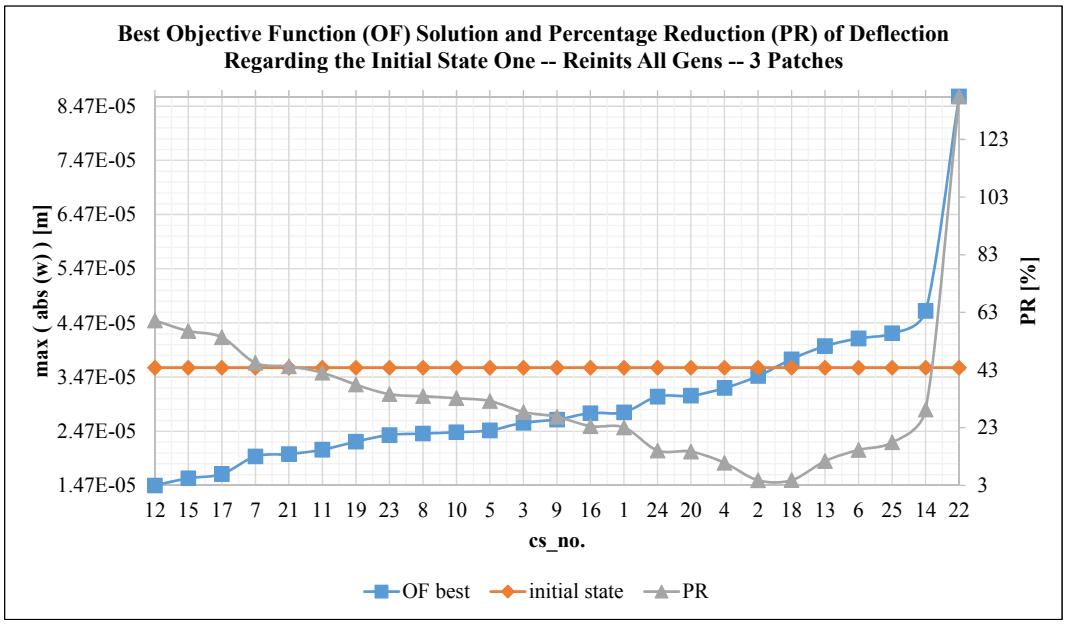

OF best and PR | $DV_{1..3}$ | $DV_{4..6}$ | $DV_{7..9}$ | $Fper_i$ *and* $Fper_f$

Figure H.23: Optimization results from 25 case studies ($N_{gen} = 50$ gens and $n = 10$ bats each) of min. of plates' deflections, bottom passive layer (LaRC-Si) with 3 independent patches on top (PZT-7A), considering the combinations of DE perturbation factors $Fper_i$ and $Fper_f$ matching the 25 best CSs in Table H.4. DVs are the electric potentials ϕ [V] applied to each patch and their locations, i.e. minimum coordinates x_{min} [m] and y_{min} [m]. Population's locations reinitialized randomly before each gen. Please click on the buttons above this caption to toggle between plotted results.

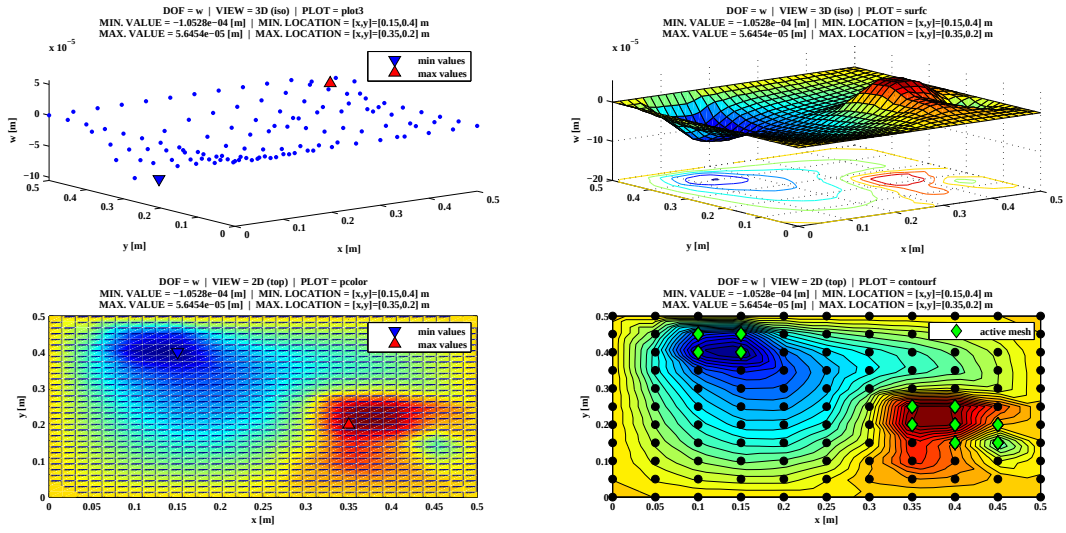

▶/❚❚ | ⏮ | ⏭ | *first iteration (worst)* | *last iteration (best)*

Figure H.24: 3D and 2D deflection plots of all successive best iterations found in the overall best case study, out of all 25, associated with Figure H.23. Please click on the buttons above this caption to run the animation and toggle between plotted results.

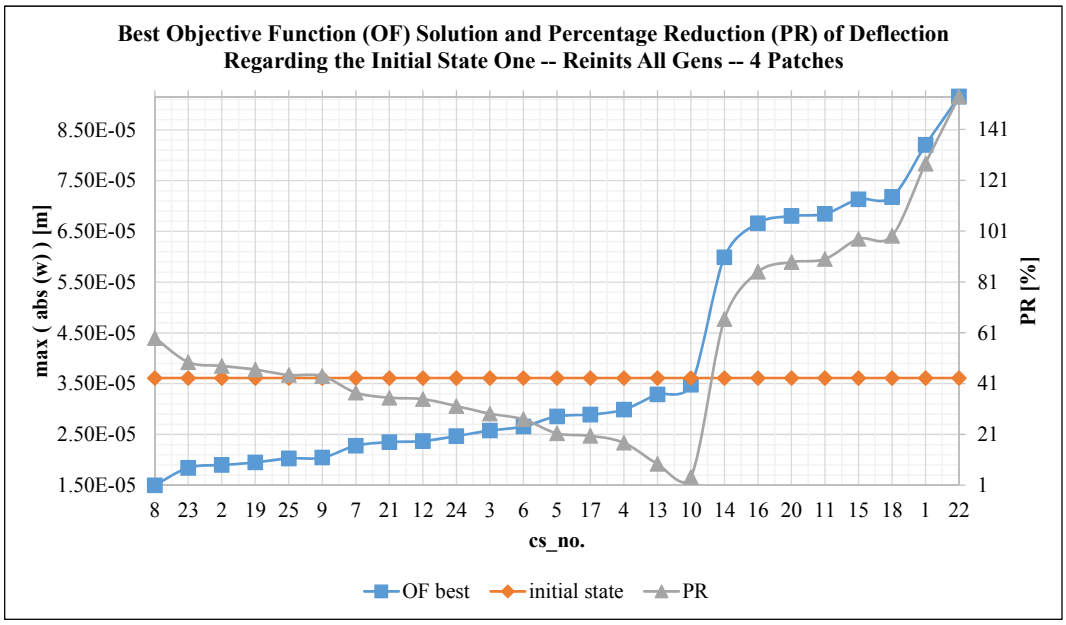

Figure H.25: Optimization results from 25 case studies ($N_{gen} = 50$ gens and $n = 10$ bats each) of min. of plates' deflections, bottom passive layer (LaRC-Si) with 4 independent patches on top (PZT-7A), considering the combinations of DE perturbation factors $Fper_i$ and $Fper_f$ matching the 25 best CSs in Table H.4. DVs are the electric potentials ϕ [V] applied to each patch and their locations, i.e. minimum coordinates x_{min} [m] and y_{min} [m]. Population's locations reinitialized randomly before each gen. Please click on the buttons above this caption to toggle between plotted results.

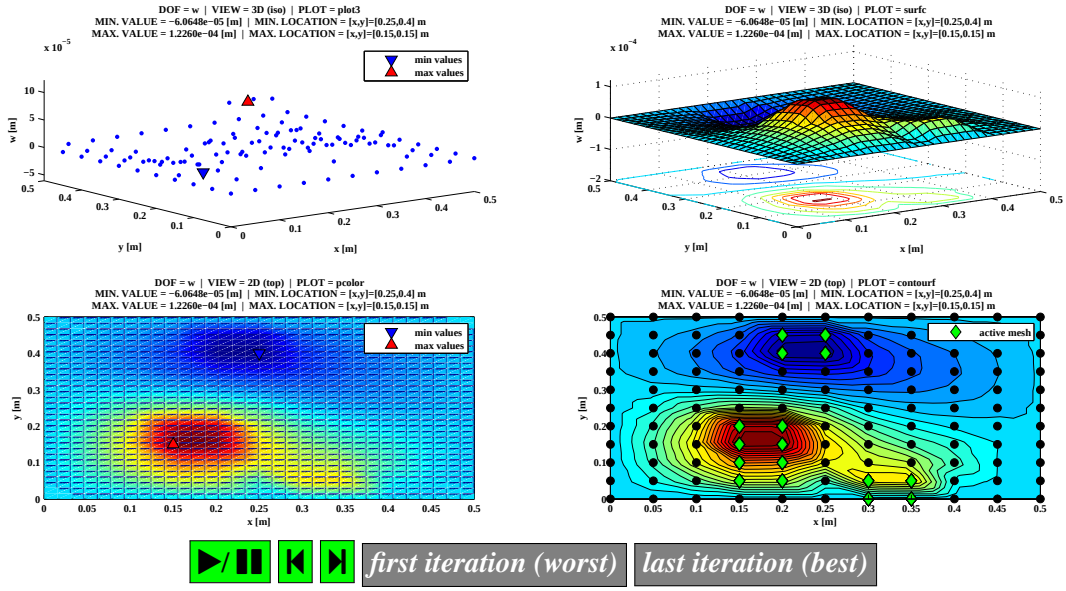

Figure H.26: 3D and 2D deflection plots of all successive best iterations found in the overall best case study, out of all 25, associated with Figure H.25. Please click on the buttons above this caption to run the animation and toggle between plotted results.

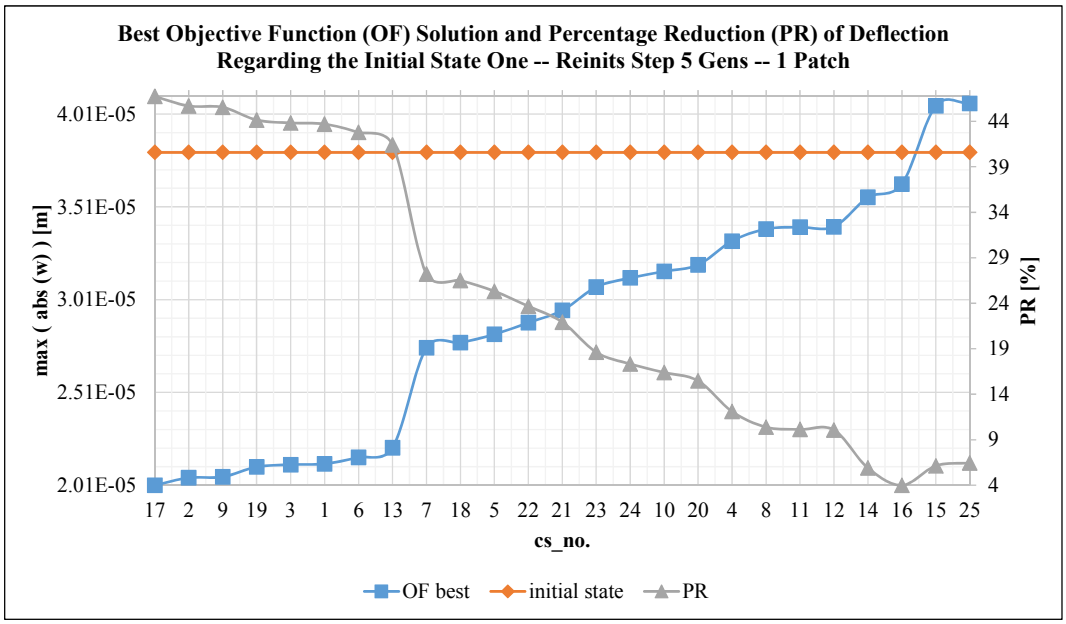

OF best and PR | DV_1 | DV_2 | $Fper_i$ *and* $Fper_f$

Figure H.27: Optimization results from 25 case studies ($N_{gen} = 50$ gens and $n = 10$ bats each) of min. of plates' deflections, bottom passive layer (LaRC-Si) with 1 patch on top (PZT-7A), considering the combinations of DE perturbation factors $Fper_i$ and $Fper_f$ matching the 25 best case studies in Table H.4. DVs are the electric potential ϕ [V] applied to the patch and its location indirectly, i.e. the element no. (discrete integer) selection from the (10×10) mesh. Reinits Step 5 Gens. Please click on the buttons above this caption to toggle between plotted results.

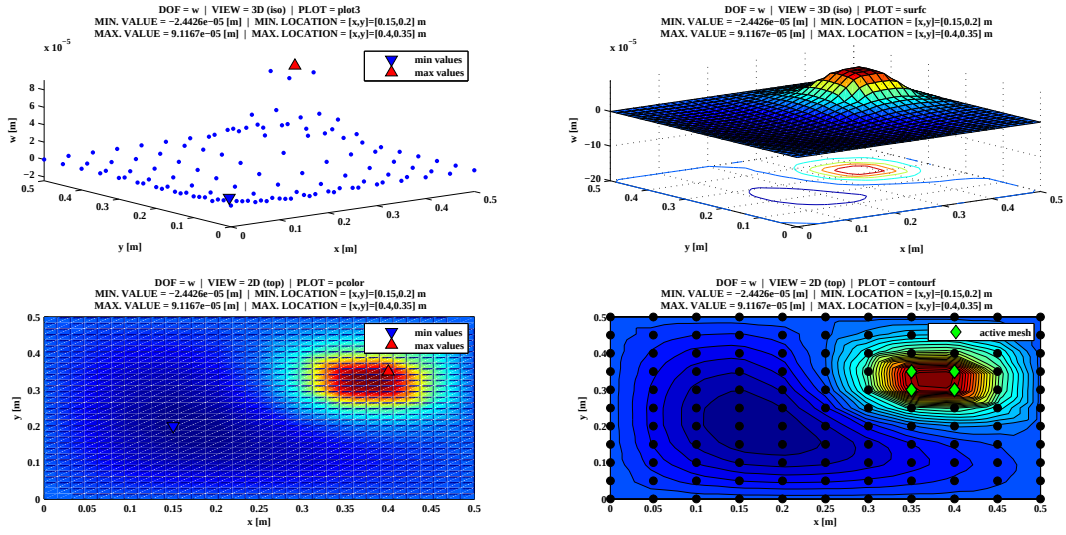

first iteration (worst) | *last iteration (best)*

Figure H.28: 3D and 2D deflection plots of all successive best iterations found in the overall best case study, out of all 25, associated with Figure H.27. Please click on the buttons above this caption to run the animation and toggle between plotted results.

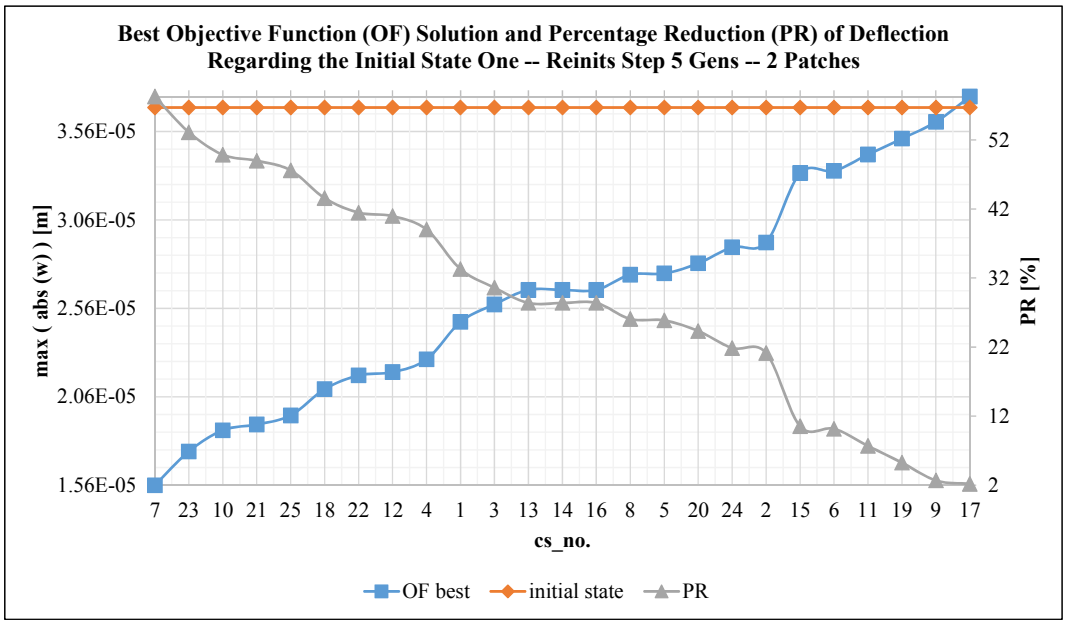

Figure H.29: Optimization results from 25 case studies ($N_{gen} = 50$ gens and $n = 10$ bats each) of min. of plates' deflections, bottom passive layer (LaRC-Si) with 2 independent patches on top (PZT-7A), considering the combinations of DE perturbation factors $Fper_i$ and $Fper_f$ matching the 25 best case studies in Table H.4. DVs are the electric potentials ϕ [V] applied to each patch and their locations indirectly, i.e. the element no. (discrete integers) selection from the (10×10) mesh. Reinits Step 5 Gens. Please click on the buttons above this caption to toggle between plotted results.

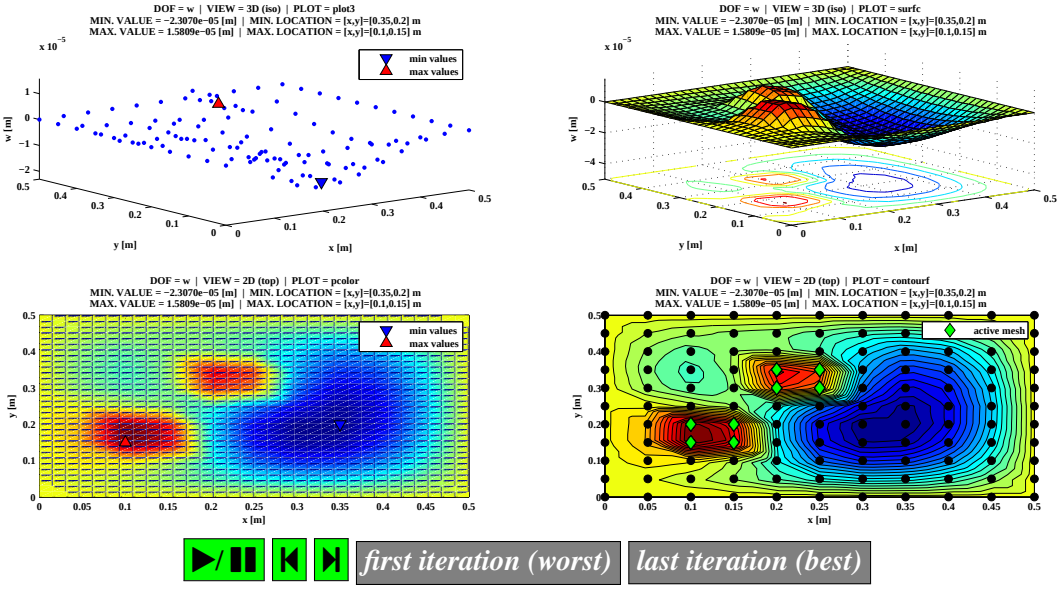

Figure H.30: 3D and 2D deflection plots of all successive best iterations found in the overall best case study, out of all 25, associated with Figure H.29. Please click on the buttons above this caption to run the animation and toggle between plotted results.

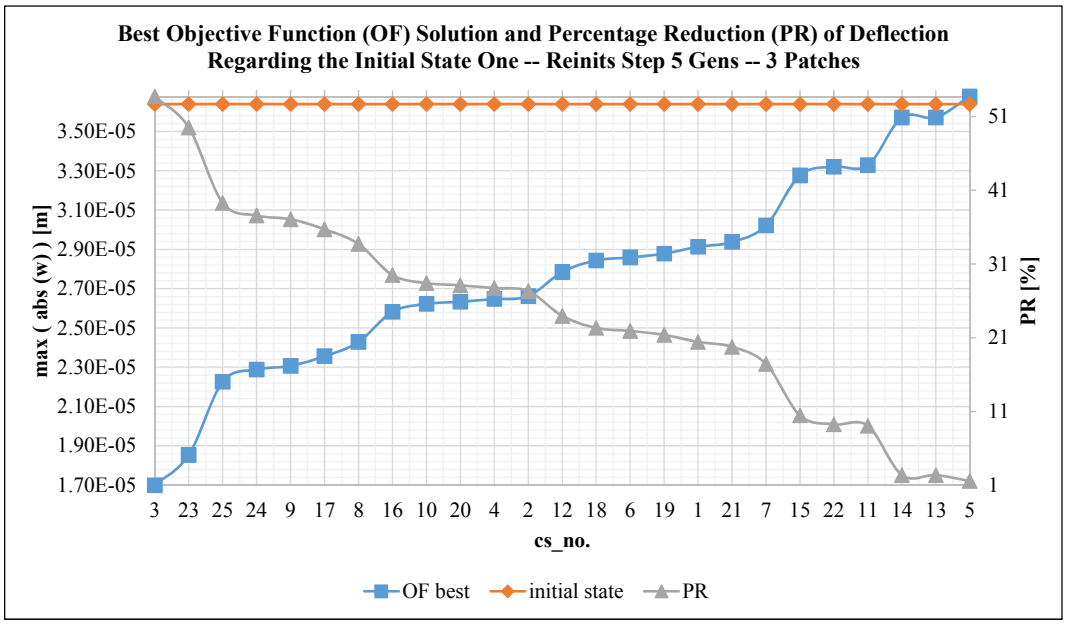

OF best and PR | $DV_{1..3}$ | $DV_{4..6}$ | $Fper_i$ *and* $Fper_f$

Figure H.31: Optimization results from 25 case studies ($N_{gen} = 50$ gens and $n = 10$ bats each) of min. of plates' deflections, bottom passive layer (LaRC-Si) with 3 independent patches on top (PZT-7A), considering the combinations of DE perturbation factors $Fper_i$ and $Fper_f$ matching the 25 best case studies in Table H.4. DVs are the electric potentials ϕ [V] applied to each patch and their locations indirectly, i.e. the element no. (discrete integers) selection from the (10×10) mesh. Reinits Step 5 Gens. Please click on the buttons above this caption to toggle between plotted results.

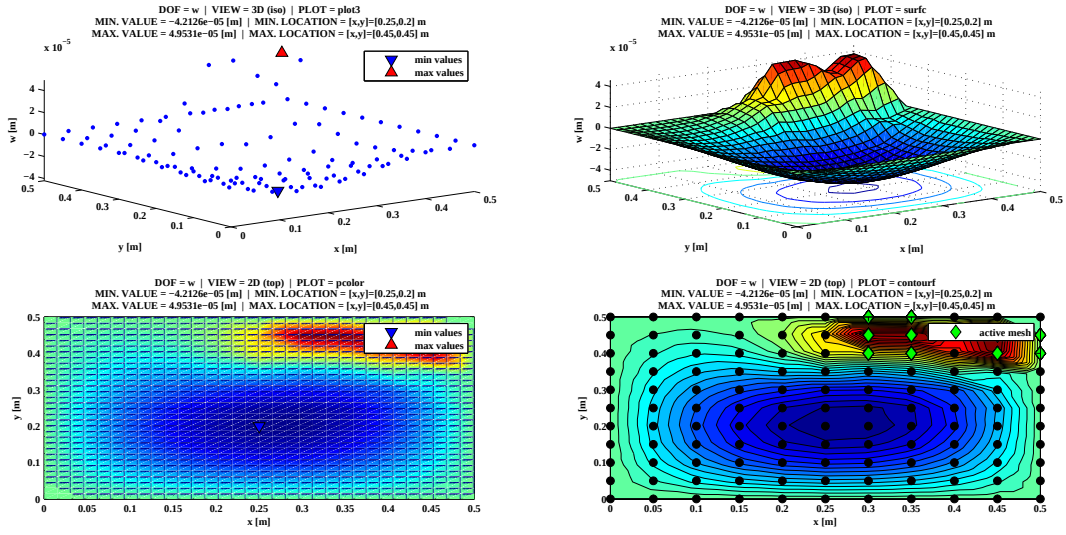

▶/❚❚ | ⏮ | ⏭ | *first iteration (worst)* | *last iteration (best)*

Figure H.32: 3D and 2D deflection plots of all successive best iterations found in the overall best case study, out of all 25, associated with Figure H.31. Please click on the buttons above this caption to run the animation and toggle between plotted results.

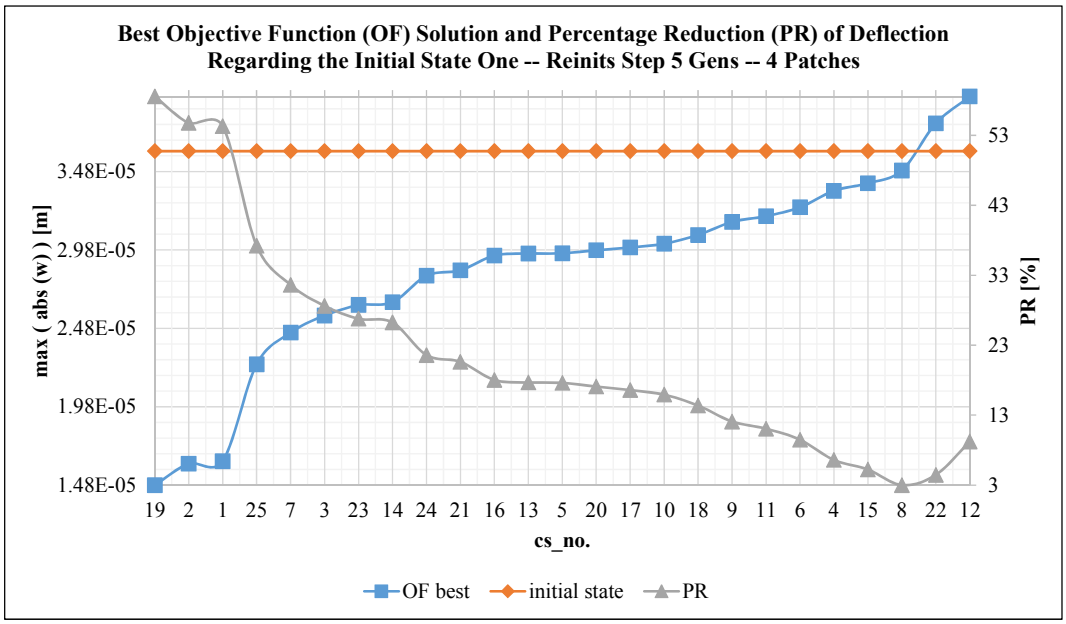

Figure H.33: Optimization results from 25 case studies ($N_{gen} = 50$ gens and $n = 10$ bats each) of min. of plates' deflections, bottom passive layer (LaRC-Si) with 4 independent patches on top (PZT-7A), considering the combinations of DE perturbation factors $Fper_i$ and $Fper_f$ matching the 25 best case studies in Table H.4. DVs are the electric potentials ϕ [V] applied to each patch and their locations indirectly, i.e. the element no. (discrete integers) selection from the (10×10) mesh. Reinits Step 5 Gens. Please click on the buttons above this caption to toggle between plotted results.

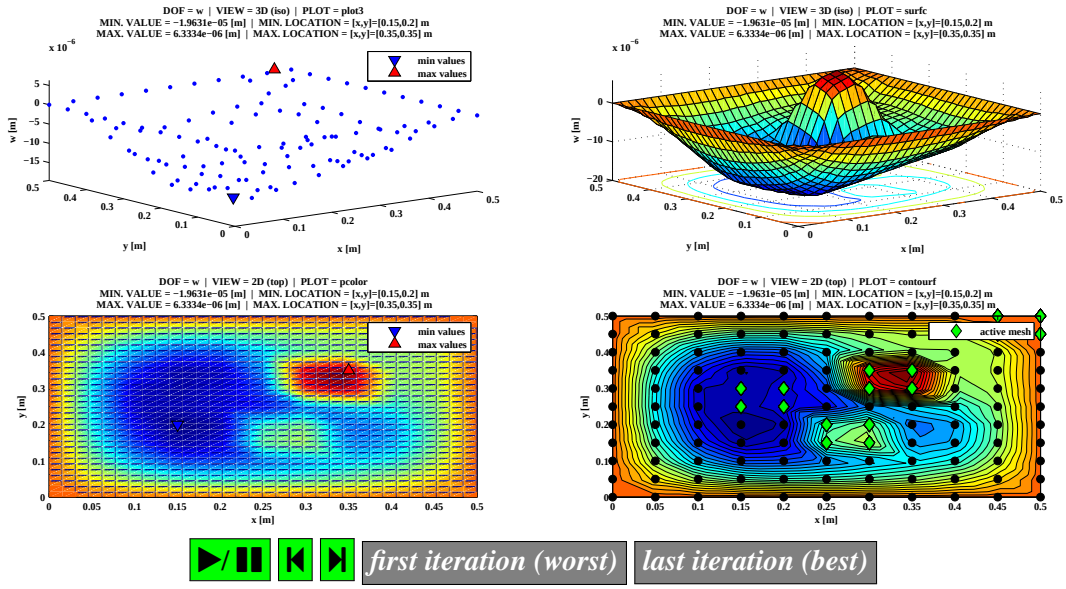

Figure H.34: 3D and 2D deflection plots of all successive best iterations found in the overall best case study, out of all 25, associated with Figure H.33. Please click on the buttons above this caption to run the animation and toggle between plotted results.

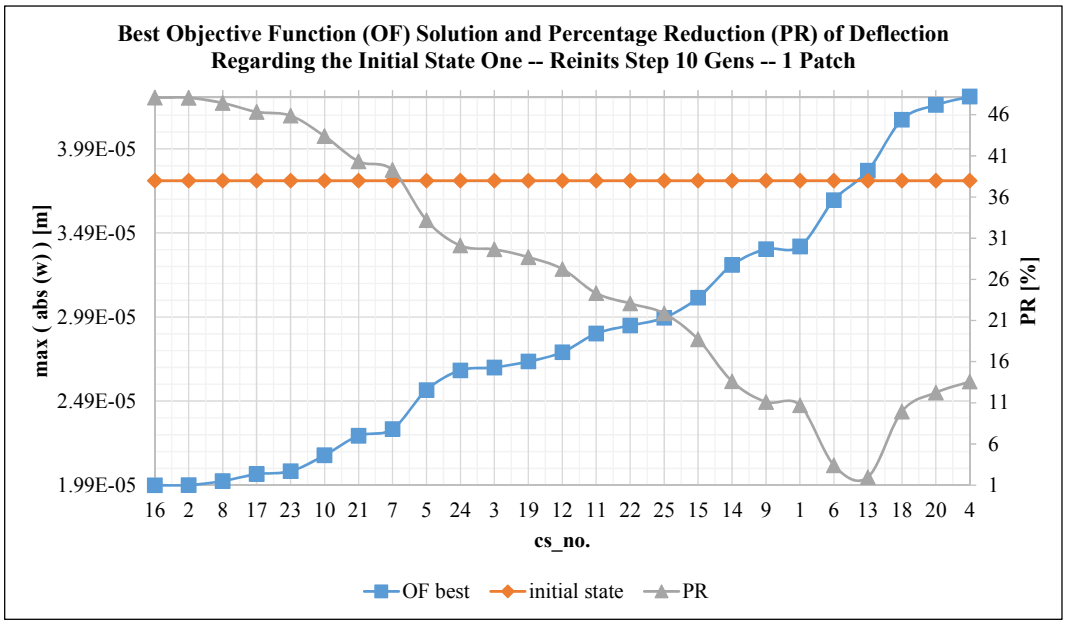

OF best and PR | DV_1 | DV_2 | $Fper_i$ *and* $Fper_f$

Figure H.35: Optimization results from 25 case studies ($N_{gen} = 50$ gens and $n = 10$ bats each) of min. of plates' deflections, bottom passive layer (LaRC-Si) with 1 patch on top (PZT-7A), considering the combinations of DE perturbation factors $Fper_i$ and $Fper_f$ matching the 25 best case studies in Table H.4. DVs are the electric potential ϕ [V] applied to the patch and its location indirectly, i.e. the element no. (discrete integer) selection from the (10×10) mesh. Reinits Step 10 Gens. Please click on the buttons above this caption to toggle between plotted results.

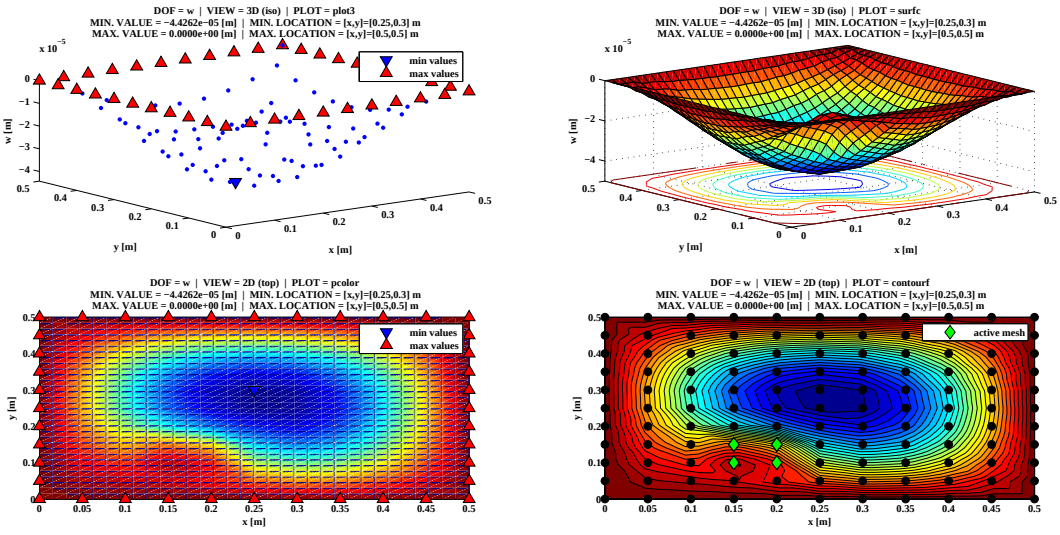

▶/❚❚ | ⏮ | ⏭ | *first iteration (worst)* | *last iteration (best)*

Figure H.36: 3D and 2D deflection plots of all successive best iterations found in the overall best case study, out of all 25, associated with Figure H.35. Please click on the buttons above this caption to run the animation and toggle between plotted results.

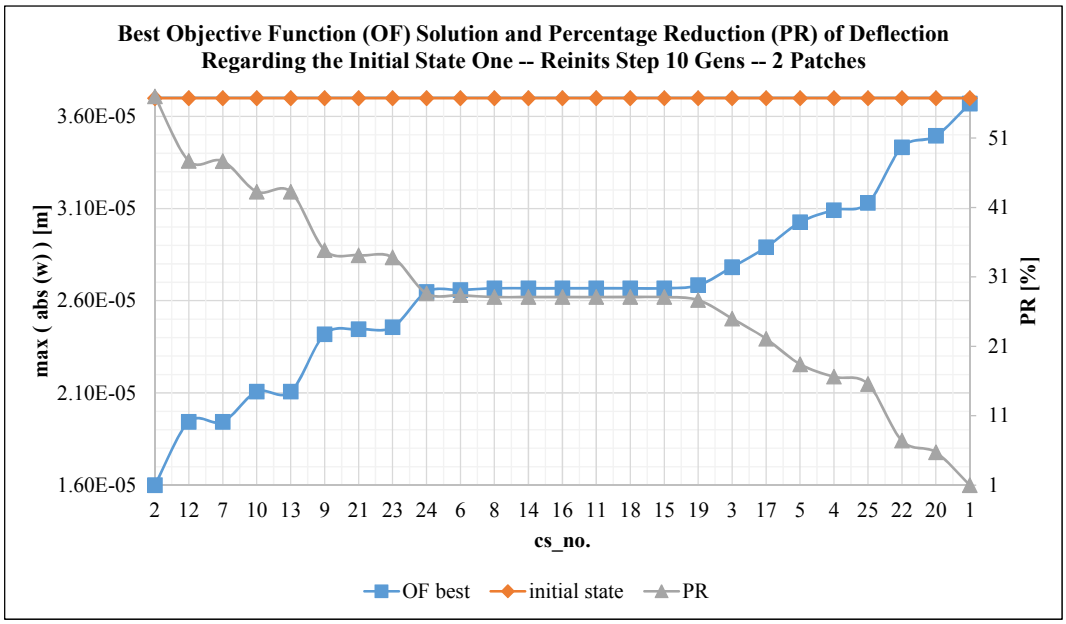

OF best and PR | $DV_{1..2}$ | $DV_{3..4}$ | $Fper_i$ *and* $Fper_f$

Figure H.37: Optimization results from 25 case studies ($N_{gen} = 50$ gens and $n = 10$ bats each) of min. of plates' deflections, bottom passive layer (LaRC-Si) with 2 independent patches on top (PZT-7A), considering the combinations of DE perturbation factors $Fper_i$ and $Fper_f$ matching the 25 best case studies in Table H.4. DVs are the electric potentials ϕ [V] applied to each patch and their locations indirectly, i.e. the element no. (discrete integers) selection from the (10×10) mesh. Reinits Step 10 Gens. Please click on the buttons above this caption to toggle between plotted results.

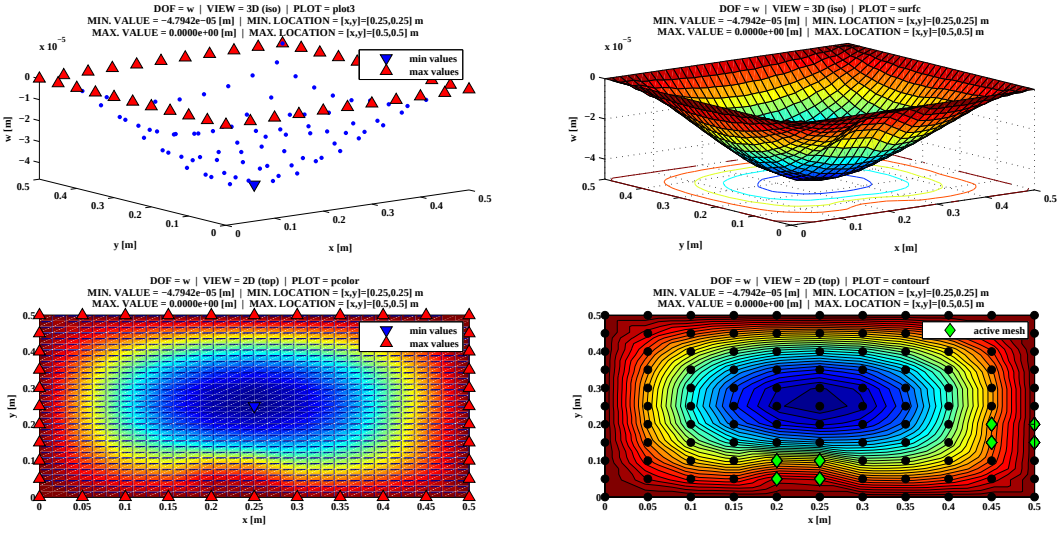

▶/❚❚ | ⏮ | ⏭ | *first iteration (worst)* | *last iteration (best)*

Figure H.38: 3D and 2D deflection plots of all successive best iterations found in the overall best case study, out of all 25, associated with Figure H.37. Please click on the buttons above this caption to run the animation and toggle between plotted results.

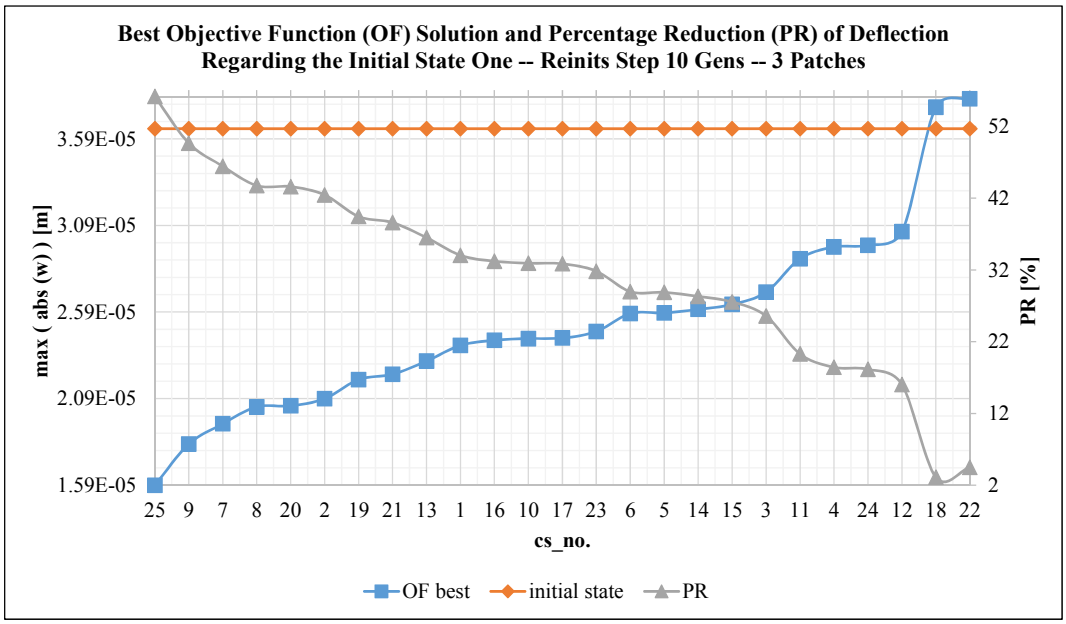

OF best and PR | $DV_{1..3}$ | $DV_{4..6}$ | $Fper_i$ *and* $Fper_f$

Figure H.39: Optimization results from 25 case studies ($N_{gen} = 50$ gens and $n = 10$ bats each) of min. of plates' deflections, bottom passive layer (LaRC-Si) with 3 independent patches on top (PZT-7A), considering the combinations of DE perturbation factors $Fper_i$ and $Fper_f$ matching the 25 best case studies in Table H.4. DVs are the electric potentials ϕ [V] applied to each patch and their locations indirectly, i.e. the element no. (discrete integers) selection from the (10×10) mesh. Reinits Step 10 Gens. Please click on the buttons above this caption to toggle between plotted results.

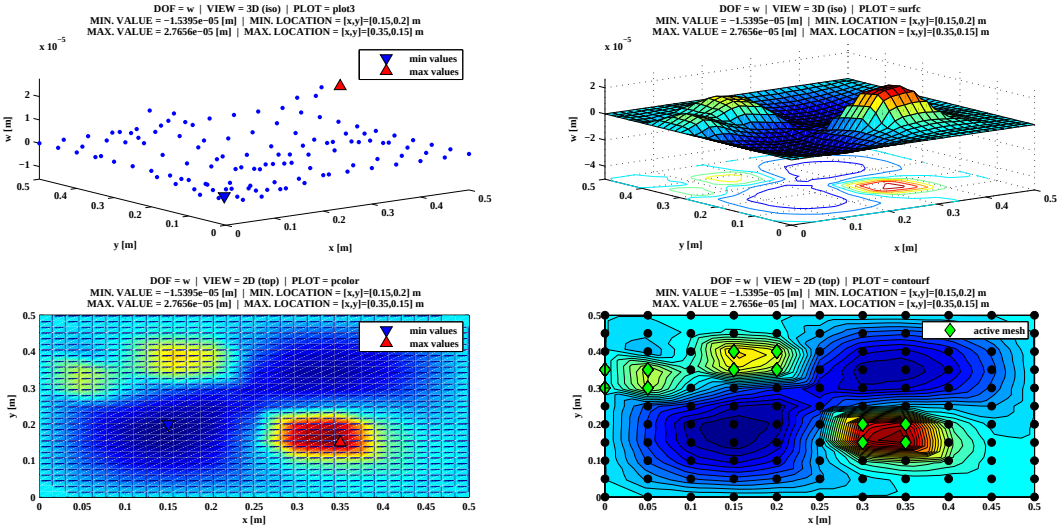

▶/❚❚ | ⏮ | ⏭ | *first iteration (worst)* | *last iteration (best)*

Figure H.40: 3D and 2D deflection plots of all successive best iterations found in the overall best case study, out of all 25, associated with Figure H.39. Please click on the buttons above this caption to run the animation and toggle between plotted results.

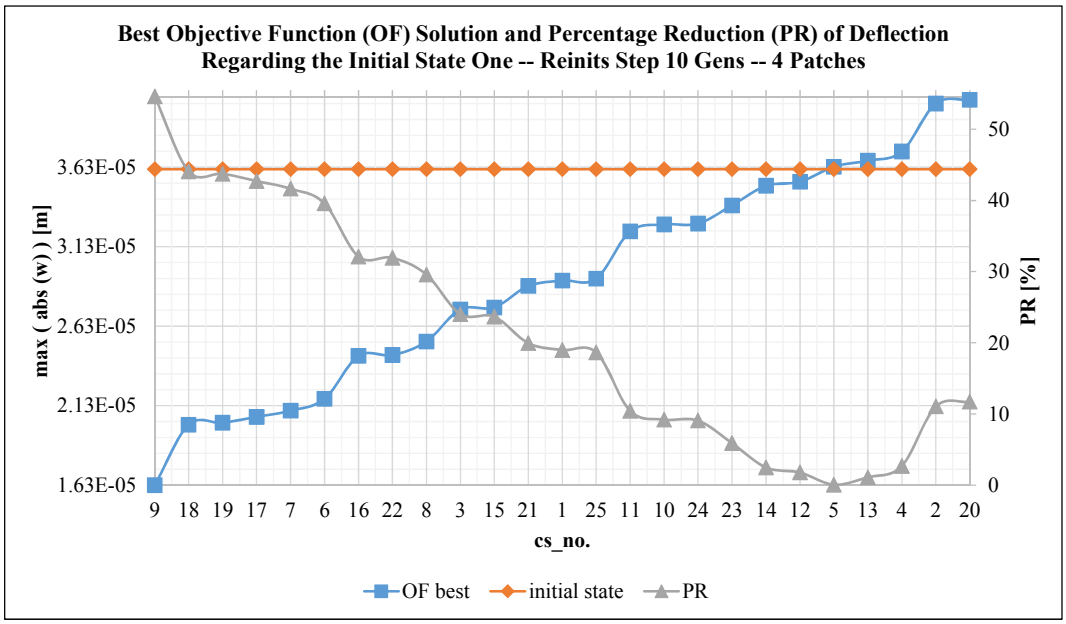

OF best and PR | $DV_{1..4}$ | $DV_{5..8}$ | $Fper_i$ *and* $Fper_f$

Figure H.41: Optimization results from 25 case studies ($N_{gen} = 50$ gens and $n = 10$ bats each) of min. of plates' deflections, bottom passive layer (LaRC-Si) with 4 independent patches on top (PZT-7A), considering the combinations of DE perturbation factors $Fper_i$ and $Fper_f$ matching the 25 best case studies in Table H.4. DVs are the electric potentials ϕ [V] applied to each patch and their locations indirectly, i.e. the element no. (discrete integers) selection from the (10×10) mesh. Reinits Step 10 Gens. Please click on the buttons above this caption to toggle between plotted results.

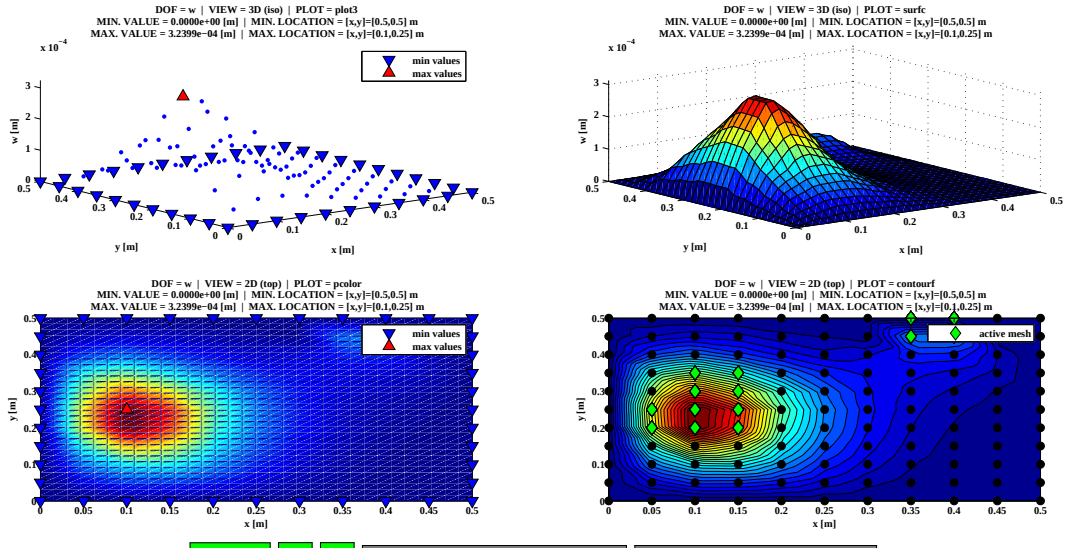

first iteration (worst) | *last iteration (best)*

Figure H.42: 3D and 2D deflection plots of all successive best iterations found in the overall best case study, out of all 25, associated with Figure H.41. Please click on the buttons above this caption to run the animation and toggle between plotted results.

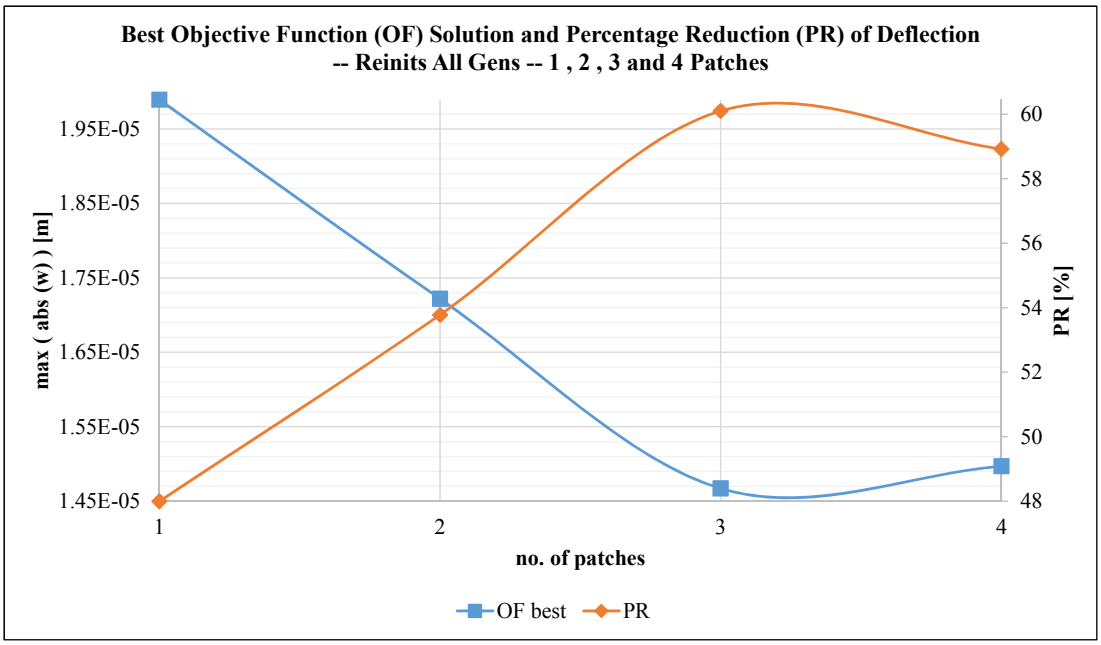

OF best and PR *OF best* *PR*

Figure H.43: Summary of the optimization results (OF best and PR) from the case studies associated with Figures H.19, H.21, H.23 and H.25. Population's locations reinitialized randomly before each generation. Please click on the buttons above this caption to toggle between plotted results.

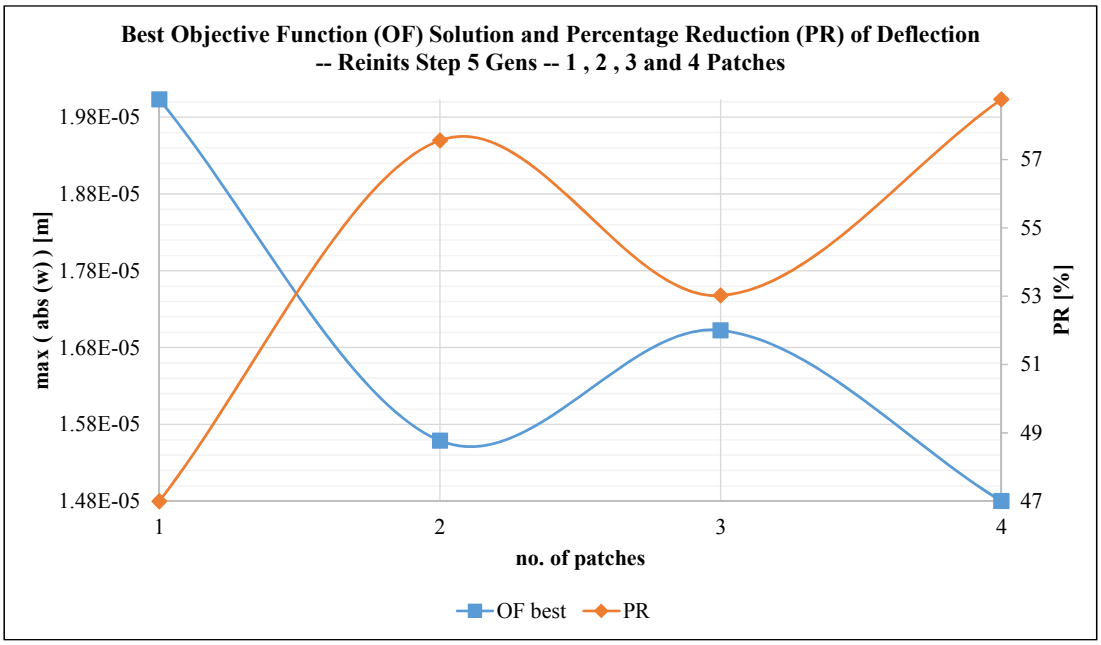

OF best and PR *OF best* *PR*

Figure H.44: Summary of the optimization results (OF best and PR) from the case studies associated with Figures H.27, H.29, H.31 and H.33. Reinits Step 5 Gens. Please click on the buttons above this caption to toggle between plotted results.

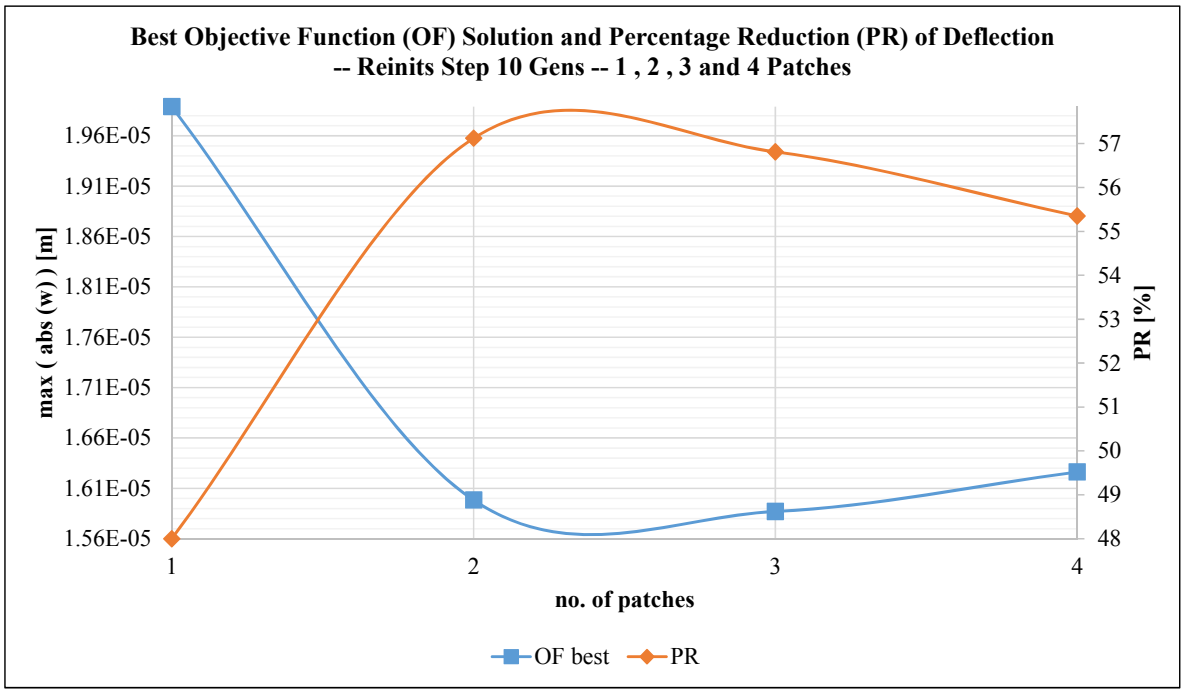

OF best and PR *OF best* *PR*

Figure H.45: Summary of the optimization results (OF best and PR) from the case studies associated with Figures H.35, H.37, H.39 and H.41. Reinits Step 10 Gens. Please click on the buttons above this caption to toggle between plotted results.

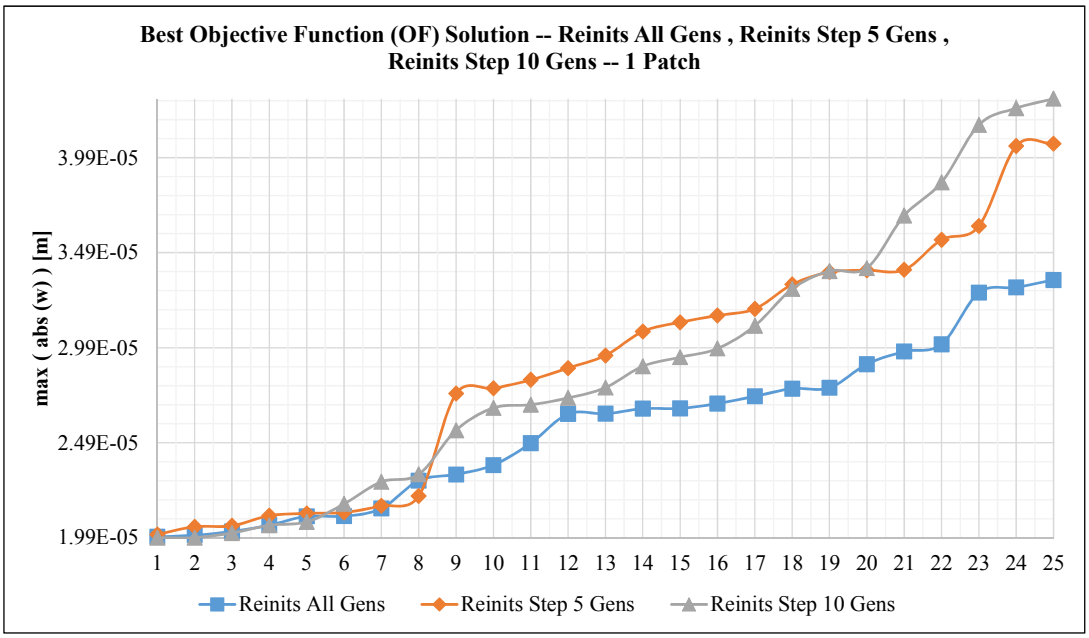

1 patch *2 patches* *3 patches* *4 patches*

Figure H.46: Summary of the optimization results (OF best) from all case studies (Figures H.43 to H.45), comparing the three types of population's locations reinitializations, for 1, 2, 3 and 4 patches, individually. Please click on the buttons above this caption to toggle between plotted results.

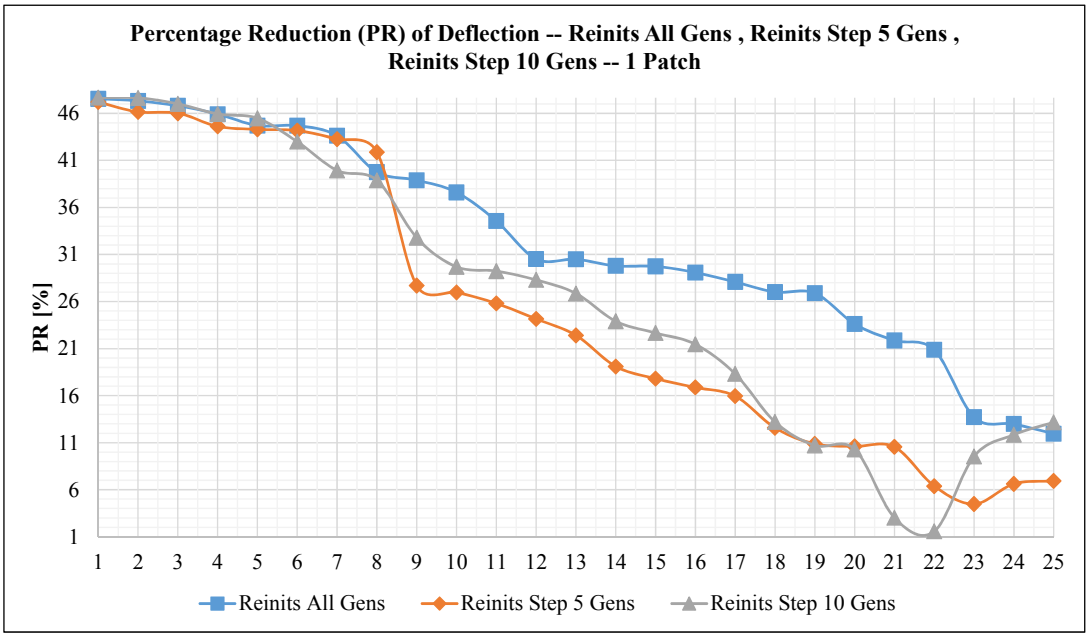

1 patch *2 patches* *3 patches* *4 patches*

Figure H.47: Summary of the optimization results (PR) from all case studies (Figures H.43 to H.45), comparing the three types of population's locations reinitializations, for 1, 2, 3 and 4 patches, individually. Please click on the buttons above this caption to toggle between plotted results.

Table H.5: Deflections ($\times 10^{-5}$ [m]) / PR [%] associated with plotted results in Figures H.46 and H.47.

no. patches	1			2			3			4		
type reinit	All	Step 5	Step 10	All	Step 5	Step 10	All Gens	Step 5	Step 10	All	Step 5	Step 10
1	1.99 / 48	2.01 / 47	1.99 / 48	1.72 / 53	1.56 / 58	1.60 / 57	1.47 / 60	1.70 / 53	1.59 / 56	1.50 / 58	1.48 / 59	1.63 / 55
2	2.00 / 47	2.05 / 46	1.99 / 48	1.78 / 52	1.75 / 53	1.94 / 48	1.60 / 56	1.86 / 49	1.82 / 50	1.84 / 49	1.62 / 55	2.01 / 44
3	2.02 / 47	2.05 / 46	2.01 / 47	1.89 / 49	1.87 / 49	1.94 / 47	1.68 / 54	2.23 / 39	1.94 / 47	1.90 / 47	1.63 / 55	2.02 / 44
4	2.05 / 46	2.10 / 45	2.05 / 46	2.17 / 41	1.90 / 48	2.10 / 43	2.00 / 45	2.29 / 37	2.04 / 44	1.95 / 46	2.25 / 38	2.05 / 43
5	2.10 / 45	2.12 / 44	2.07 / 45	2.17 / 41	1.96 / 47	2.10 / 43	2.05 / 44	2.31 / 37	2.04 / 44	2.03 / 44	2.45 / 32	2.09 / 42
average of above PRs	46.46	45.66	46.75	47.33	51.06	47.58	51.67	42.94	48.23	48.95	47.72	45.76
average of above 3		46.29			48.66			47.61			47.48	
STDEV.P of above PRs	1.04	1.07	0.89	5.15	3.81	5.01	6.24	6.86	4.67	5.05	10.76	4.70
average of above 3		1.00			4.66			5.92			6.84	
6	2.10 / 45	2.12 / 44	2.17 / 43	2.32 / 37	2.10 / 43	2.42 / 35	2.13 / 42	2.36 / 35	2.09 / 43	2.04 / 43	2.56 / 29	2.17 / 40
7	2.14 / 44	2.16 / 43	2.28 / 40	2.40 / 35	2.18 / 41	2.44 / 34	2.28 / 37	2.43 / 33	2.20 / 40	2.28 / 37	2.63 / 27	2.44 / 33
8	2.29 / 40	2.21 / 42	2.32 / 39	2.45 / 34	2.20 / 40	2.45 / 34	2.40 / 34	2.59 / 29	2.23 / 39	2.35 / 35	2.65 / 27	2.44 / 32
9	2.32 / 39	2.75 / 28	2.55 / 33	2.45 / 34	2.27 / 39	2.65 / 28	2.43 / 33	2.63 / 28	2.30 / 37	2.37 / 34	2.82 / 22	2.53 / 30
10	2.37 / 38	2.77 / 27	2.67 / 30	2.56 / 31	2.48 / 33	2.66 / 28	2.45 / 33	2.64 / 28	2.39 / 34	2.47 / 32	2.85 / 21	2.73 / 24
11	2.49 / 35	2.82 / 26	2.69 / 29	2.67 / 28	2.58 / 30	2.66 / 28	2.49 / 32	2.65 / 27	2.42 / 34	2.58 / 29	2.95 / 18	2.74 / 24
12	2.64 / 31	2.88 / 24	2.72 / 28	2.68 / 27	2.66 / 28	2.66 / 28	2.63 / 28	2.67 / 27	2.43 / 33	2.66 / 26	2.96 / 18	2.88 / 20
13	2.64 / 30	2.95 / 22	2.78 / 27	2.83 / 23	2.66 / 28	2.66 / 28	2.69 / 26	2.79 / 23	2.44 / 33	2.86 / 21	2.96 / 18	2.91 / 19
14	2.67 / 30	3.07 / 19	2.89 / 24	3.07 / 17	2.66 / 28	2.66 / 28	2.80 / 23	2.85 / 22	2.47 / 32	2.89 / 20	2.98 / 18	2.92 / 19
15	2.67 / 30	3.12 / 18	2.94 / 23	3.11 / 16	2.75 / 26	2.66 / 28	2.82 / 23	2.86 / 21	2.58 / 29	2.99 / 17	3.00 / 17	3.22 / 11
16	2.69 / 29	3.16 / 17	2.98 / 21	3.13 / 15	2.76 / 25	2.66 / 28	3.11 / 15	2.88 / 21	2.58 / 29	3.29 / 9	3.02 / 16	3.27 / 10
17	2.73 / 28	3.19 / 16	3.10 / 18	3.52 / 5	2.82 / 24	2.68 / 27	3.13 / 14	2.92 / 20	2.60 / 29	3.48 / 4	3.08 / 15	3.27 / 9
18	2.77 / 27	3.32 / 13	3.30 / 13	3.65 / 1	2.91 / 21	2.78 / 25	3.27 / 10	2.94 / 19	2.63 / 28	5.99 / 66	3.16 / 13	3.39 / 6
19	2.78 / 27	3.39 / 11	3.39 / 11	3.77 / 2	2.93 / 21	2.89 / 22	3.49 / 4	3.03 / 17	2.70 / 26	6.66 / 84	3.20 / 11	3.51 / 3
20	2.90 / 24	3.40 / 11	3.41 / 10	4.00 / 8	3.33 / 10	3.02 / 18	3.80 / 4	3.28 / 10	2.89 / 21	6.80 / 88	3.25 / 10	3.53 / 2
21	2.97 / 22	3.40 / 11	3.68 / 3	4.15 / 12	3.34 / 10	3.09 / 16	4.04 / 11	3.33 / 9	2.96 / 19	6.85 / 90	3.36 / 7	3.63 / 0
22	3.01 / 21	3.56 / 6	3.86 / 2	4.31 / 17	3.43 / 7	3.13 / 15	4.18 / 15	3.33 / 9	2.97 / 18	7.13 / 97	3.41 / 6	3.67 / 2
23	3.28 / 14	3.63 / 4	4.16 / 10	4.86 / 31	3.52 / 5	3.43 / 7	4.28 / 17	3.58 / 2	3.05 / 16	7.18 / 99	3.49 / 3	3.72 / 3
24	3.31 / 13	4.05 / 7	4.25 / 12	4.95 / 34	3.62 / 2	3.49 / 6	4.69 / 29	3.58 / 2	3.77 / 3	8.20 / 127	3.79 / 5	4.03 / 11
25	3.34 / 12	4.06 / 7	4.30 / 13	5.03 / 36	3.76 / 2	3.67 / 1	8.65 / 137	3.68 / 1	3.82 / 5	9.16 / 153	3.96 / 10	4.05 / 12

H.1.3 Approximation of beams' deflections to 2 control points

Schemes and results associated with Section 4.3.1.3.

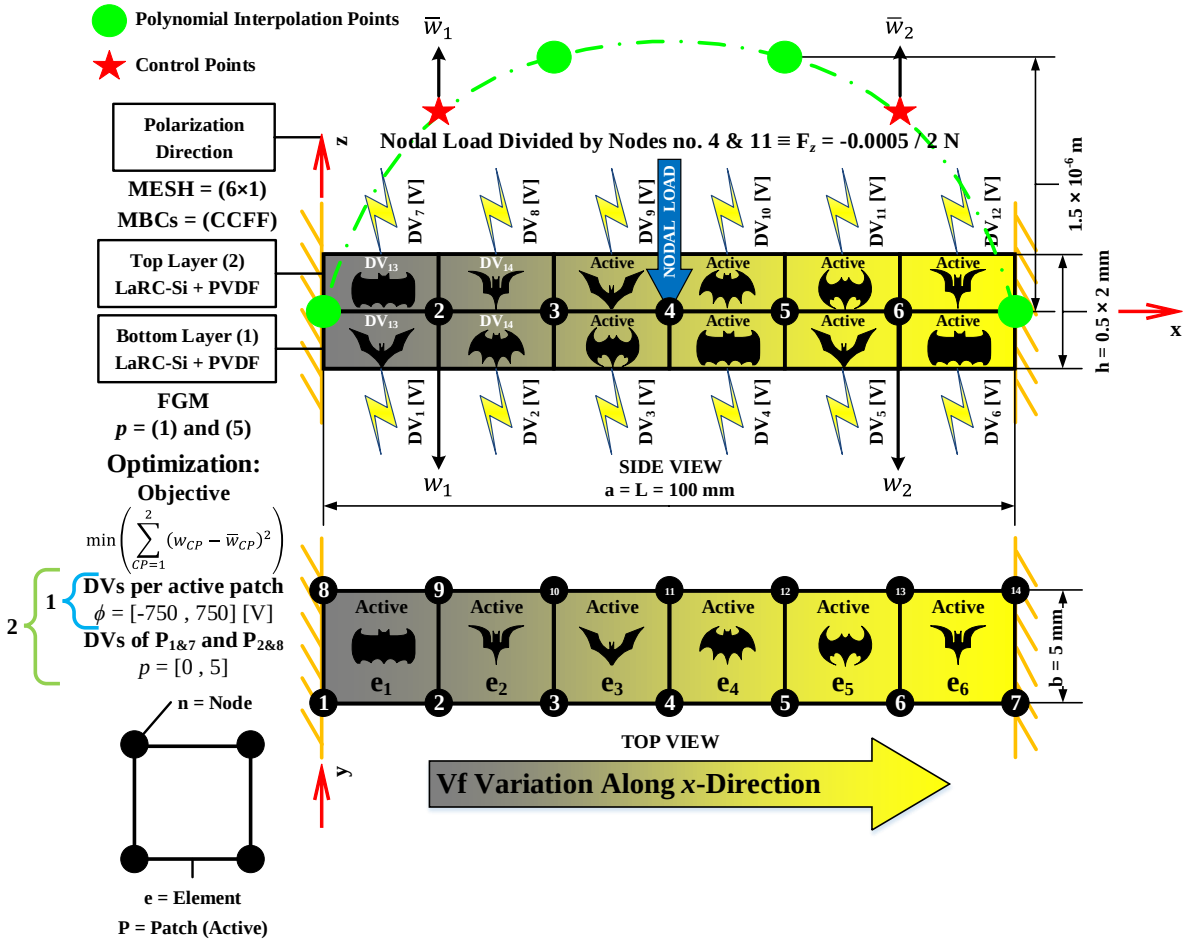

Figure H.48: Optimization case study scheme for approx. of beams' deflections to 2 control points.

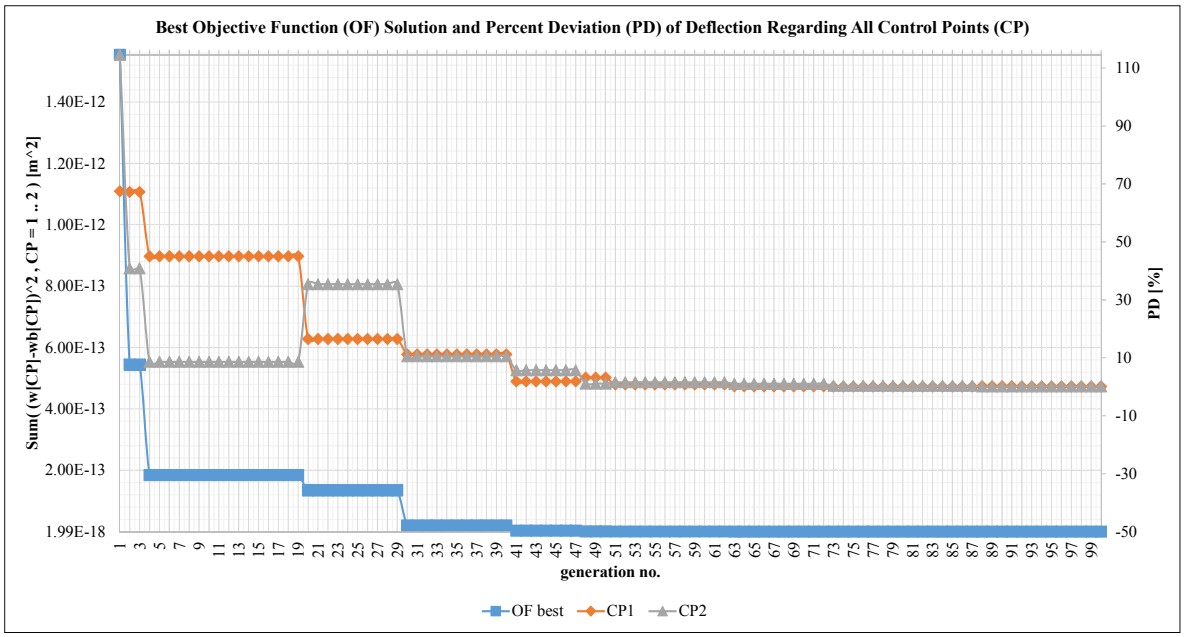

OF best and PD $DV_{1..12}$

Figure H.49: Optimization results, for all generations, from the case study of approximation of beams' deflections to 2 control points, mixing up LaRC-Si and PVDF, considering $p = 1$ and the same BA parameters from Figure H.8. DVs are the electric potentials ϕ [V] applied to each patch. Please click on the buttons above this caption to toggle between plotted results.

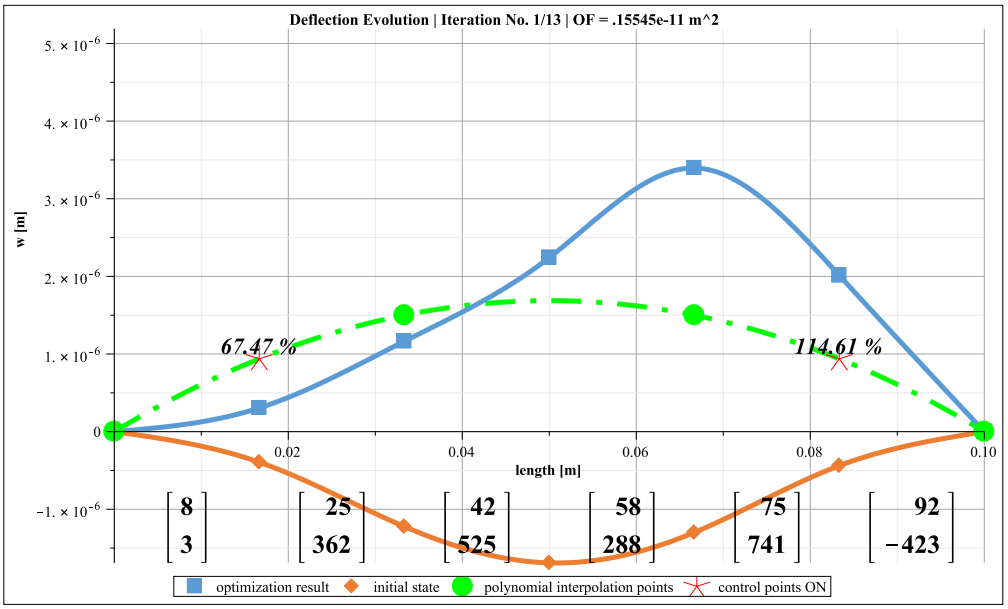

Figure H.50: Deflection plots of all successive best iterations found in the case study associated with Figure H.49. Note that the bold numbers above the x-axis (first row) correspond to the percentage $[\%]$ of piezoelectric material, $V_{f,r}^{ex}$, mixed up in each element along the beam's length, at each frame. Note that the bold numbers above the x-axis (second row) correspond to the voltage $[\mathrm{V}]$ in each element along the beam's length, at each frame. Note that the bold percentages above each control point correspond to the deviation $[\%]$ between w_{CP} and $\overline{w}_{CP}$, at each frame. Please click on the buttons above this caption to run the animation and toggle between plotted results.

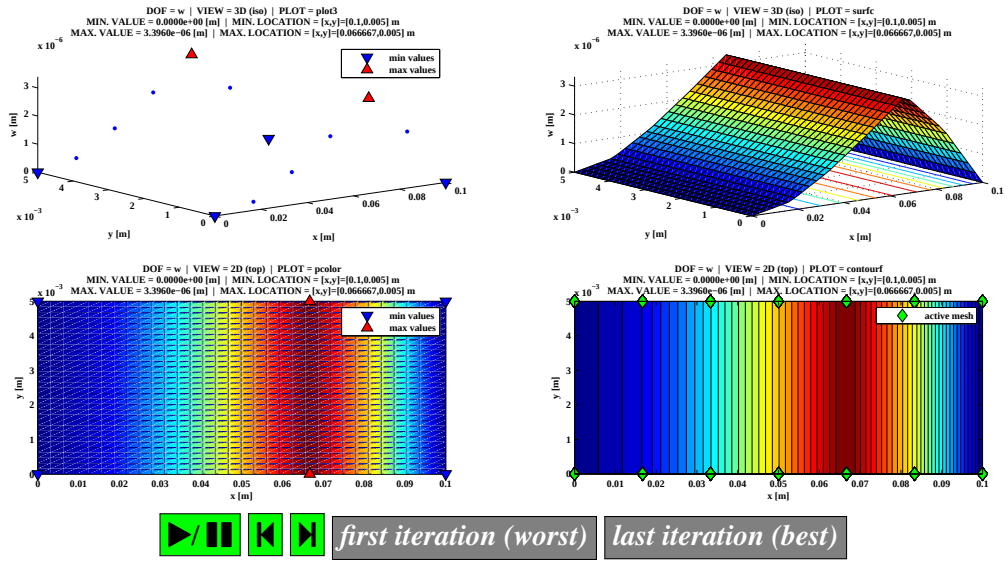

Figure H.51: 3D and 2D deflection plots of all successive best iterations found in the case study associated with Figure H.49. Please click on the buttons above this caption to run the animation and toggle between plotted results.

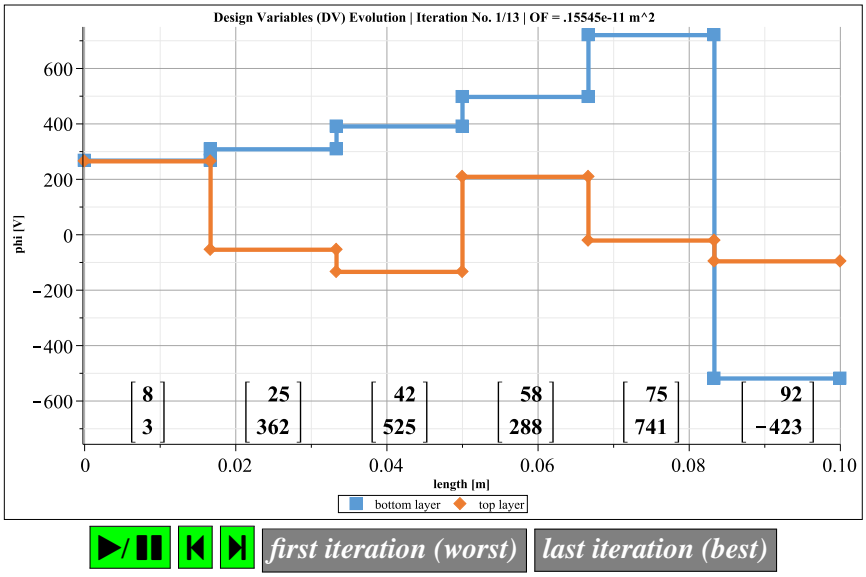

Figure H.52: Electric potentials plots of all successive best iterations found in the case study associated with Figure H.49. Note that the bold numbers above the x-axis (first row) correspond to the percentage $[\%]$ of piezoelectric material, $V_{f,r}^{ex}$, mixed up in each element along the beam's length, at each frame. Note that the bold numbers above the x-axis (second row) correspond to the voltage $[\mathrm{V}]$ in each element along the beam's length, at each frame. Please click on the buttons above this caption to run the animation and toggle between plotted results.

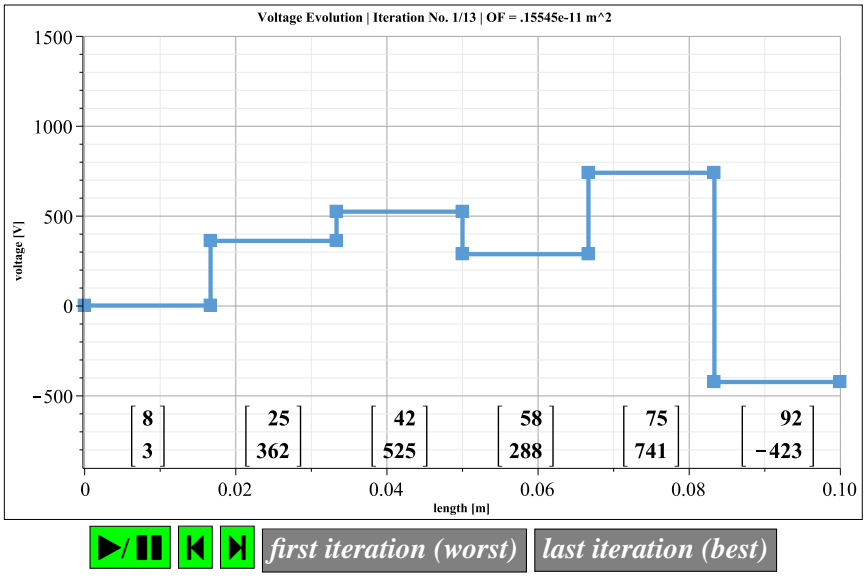

Figure H.53: Voltage plots of all successive best iterations found in the case study associated with Figure H.49. Note that the bold numbers above the x-axis (first row) correspond to the percentage $[\%]$ of piezoelectric material, $V_{f,r}^{ex}$, mixed up in each element along the beam's length, at each frame. Note that the bold numbers above the x-axis (second row) correspond to the voltage $[\mathrm{V}]$ in each element along the beam's length, at each frame. Please click on the buttons above this caption to run the animation and toggle between plotted results.

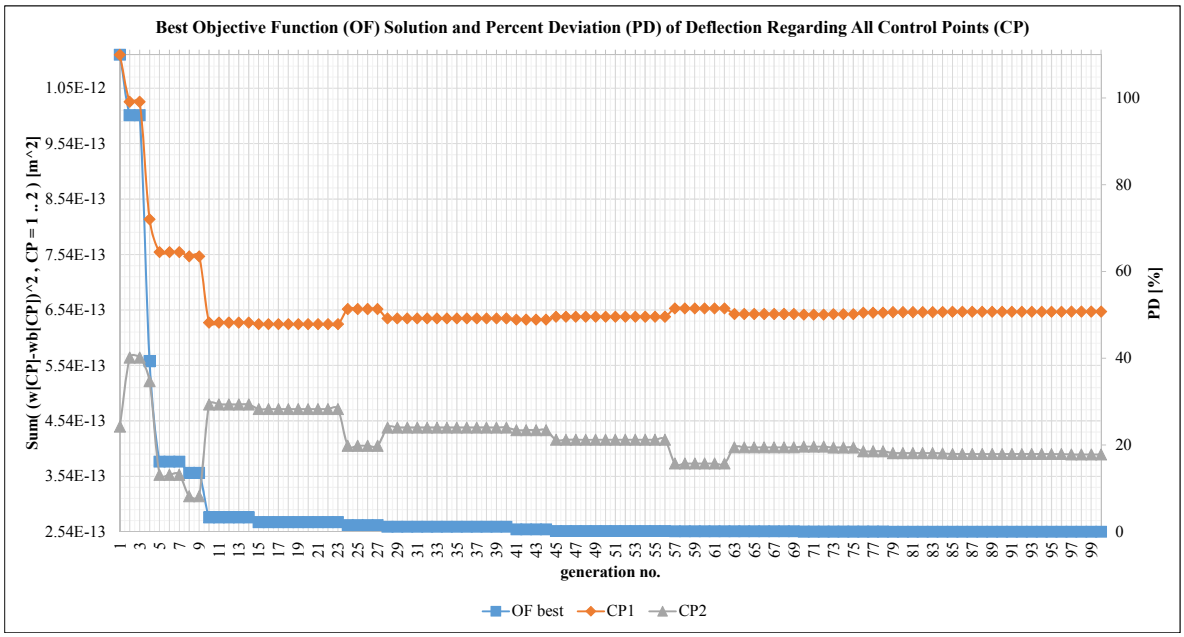

OF best and PD $DV_{1..12}$

Figure H.54: Optimization results, for all generations, from the case study of approximation of beams' deflections to 2 control points, mixing up LaRC-Si and PVDF, considering $p = 5$ and the same BA parameters from Figure H.8. DVs are the electric potentials ϕ [V] applied to each patch. Please click on the buttons above this caption to toggle between plotted results.

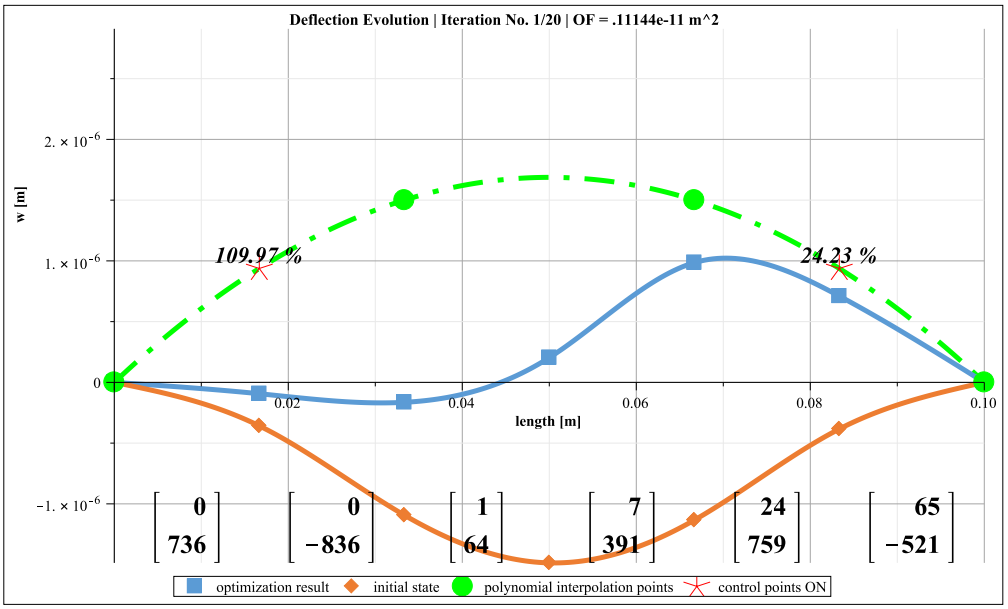

Figure H.55: Deflection plots of all successive best iterations found in the case study associated with Figure H.54. Note that the bold numbers above the x-axis (first row) correspond to the percentage $[\%]$ of piezoelectric material, $V_{f,r}^{ex}$, mixed up in each element along the beam's length, at each frame. Note that the bold numbers above the x-axis (second row) correspond to the voltage $[\mathrm{V}]$ in each element along the beam's length, at each frame. Note that the bold percentages above each control point correspond to the deviation $[\%]$ between w_{CP} and $\overline{w}_{CP}$, at each frame. Please click on the buttons above this caption to run the animation and toggle between plotted results.

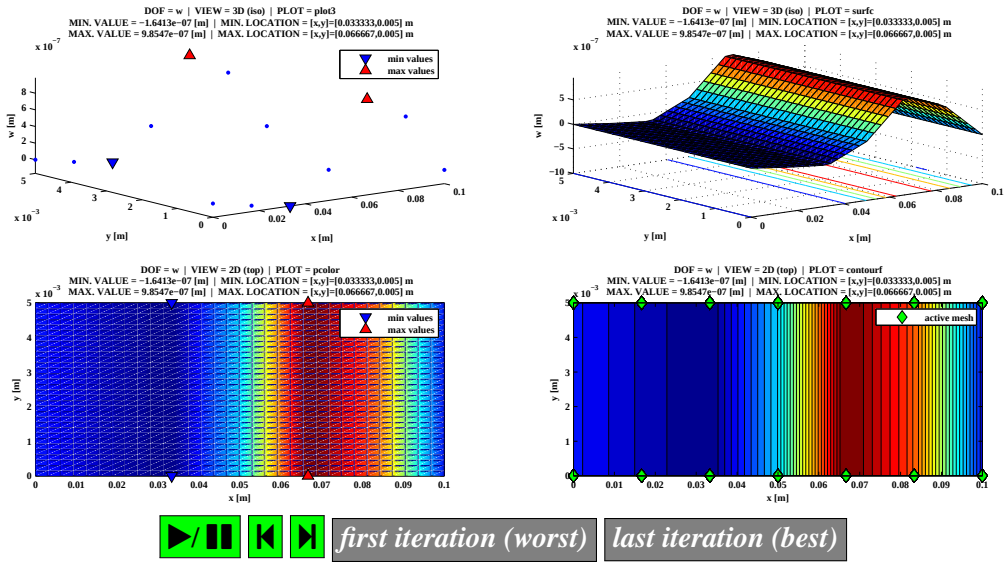

Figure H.56: 3D and 2D deflection plots of all successive best iterations found in the case study associated with Figure H.54. Please click on the buttons above this caption to run the animation and toggle between plotted results.

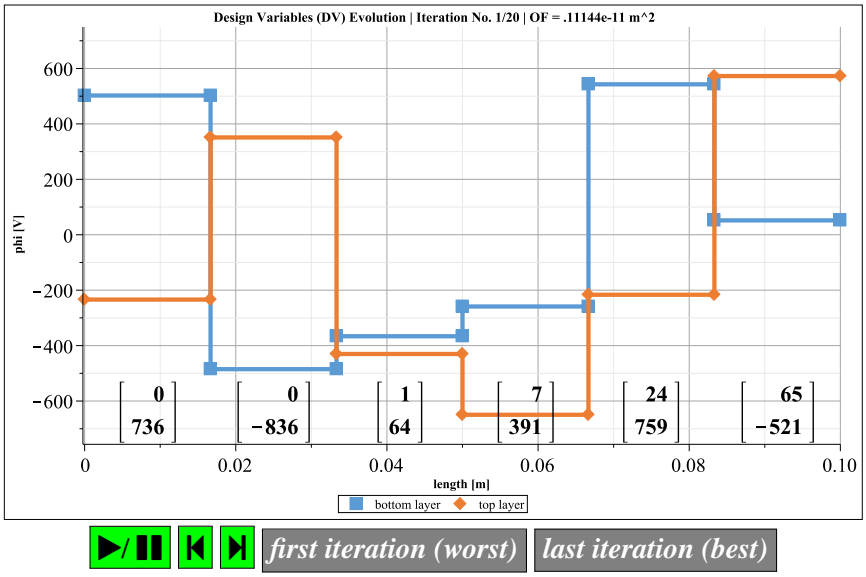

Figure H.57: Electric potentials plots of all successive best iterations found in the case study associated with Figure H.54. Note that the bold numbers above the x-axis (first row) correspond to the percentage $[\%]$ of piezoelectric material, $V_{f,r}^{ex}$, mixed up in each element along the beam's length, at each frame. Note that the bold numbers above the x-axis (second row) correspond to the voltage $[\mathrm{V}]$ in each element along the beam's length, at each frame. Please click on the buttons above this caption to run the animation and toggle between plotted results.

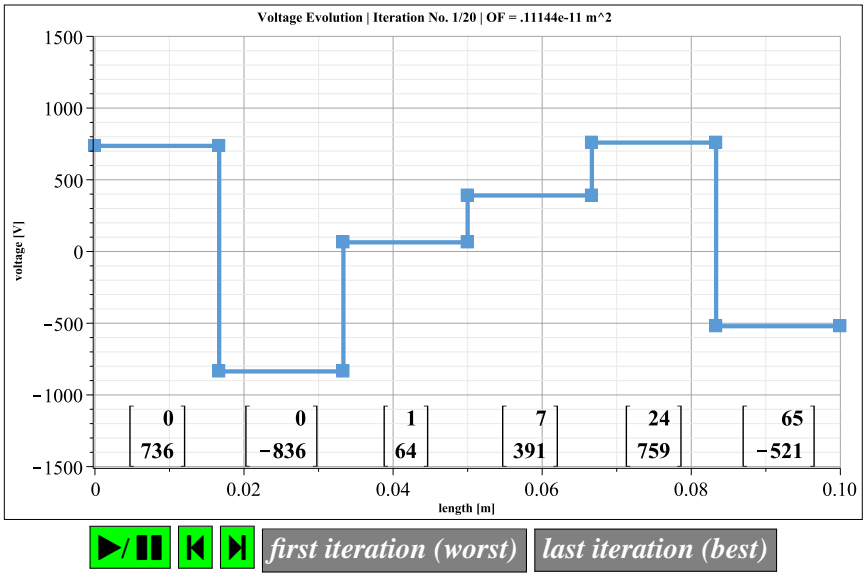

Figure H.58: Voltage plots of all successive best iterations found in the case study associated with Figure H.54. Note that the bold numbers above the x-axis (first row) correspond to the percentage $[\%]$ of piezoelectric material, $V_{f,r}^{ex}$, mixed up in each element along the beam's length, at each frame. Note that the bold numbers above the x-axis (second row) correspond to the voltage $[\mathrm{V}]$ in each element along the beam's length, at each frame. Please click on the buttons above this caption to run the animation and toggle between plotted results.

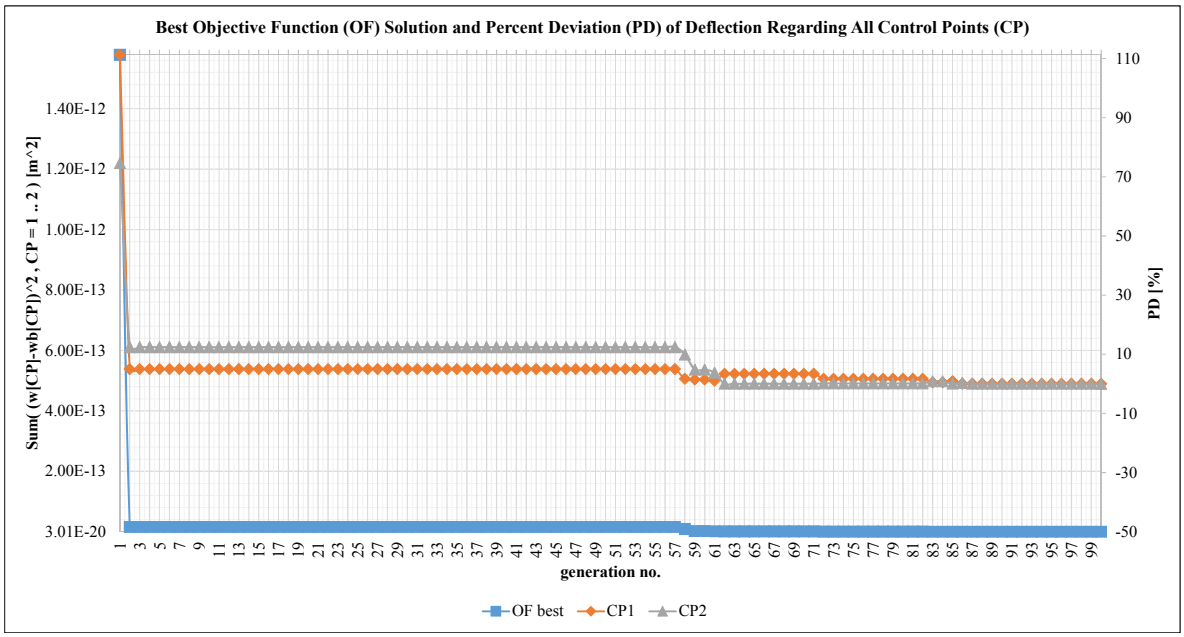

OF best and PD $DV_{1..12}$ $DV_{13..14}$

Figure H.59: Optimization results, for all generations, from the case study of approximation of beams' deflections to 2 control points, mixing up LaRC-Si and PVDF, considering $p = 5$ and the same BA parameters from Figure H.8. DVs are the electric potentials ϕ [V] applied to each patch, one different p-exponent for both patches no.1 and 7, one different p-exponent for both patches no.2 and 8. Please click on the buttons above this caption to toggle between plotted results.

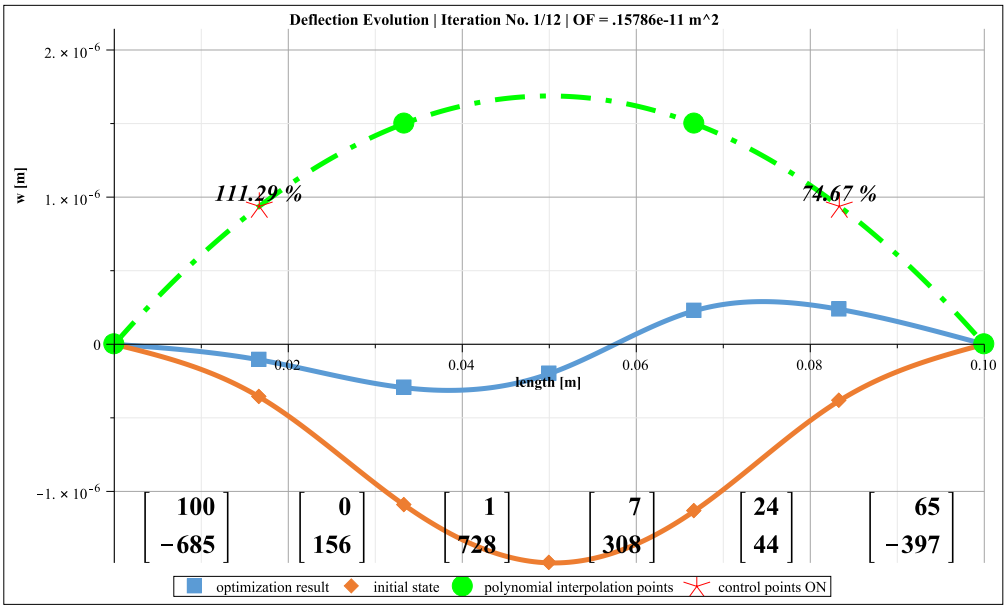

Figure H.60: Deflection plots of all successive best iterations found in the case study associated with Figure H.59. Note that the bold numbers above the x-axis (first row) correspond to the percentage $[\%]$ of piezoelectric material, $V_{f,r}^{ex}$, mixed up in each element along the beam's length, at each frame. Note that the bold numbers above the x-axis (second row) correspond to the voltage $[\mathrm{V}]$ in each element along the beam's length, at each frame. Note that the bold percentages above each control point correspond to the deviation $[\%]$ between w_{CP} and $\overline{w}_{CP}$, at each frame. Please click on the buttons above this caption to run the animation and toggle between plotted results.

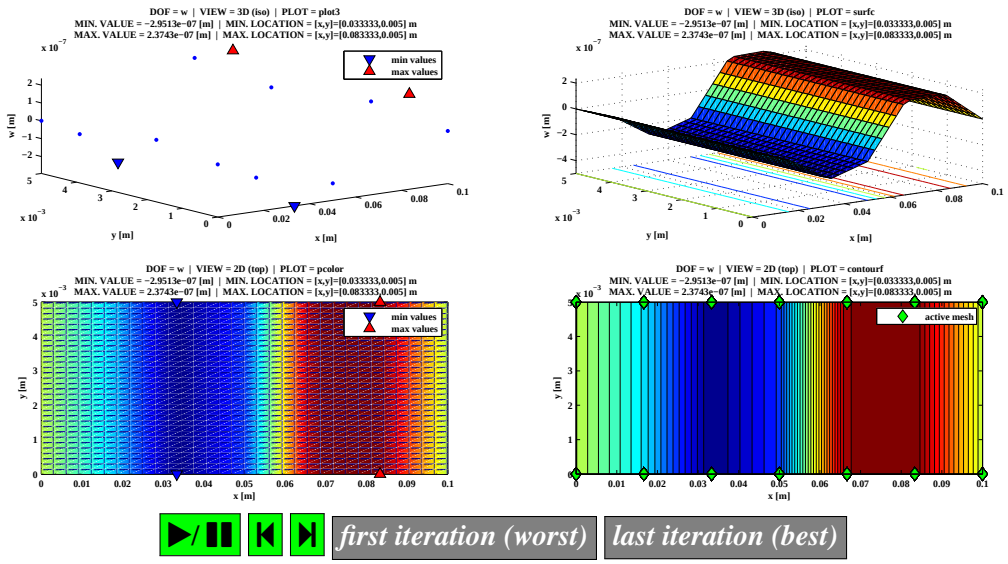

Figure H.61: 3D and 2D deflection plots of all successive best iterations found in the case study associated with Figure H.59. Please click on the buttons above this caption to run the animation and toggle between plotted results.

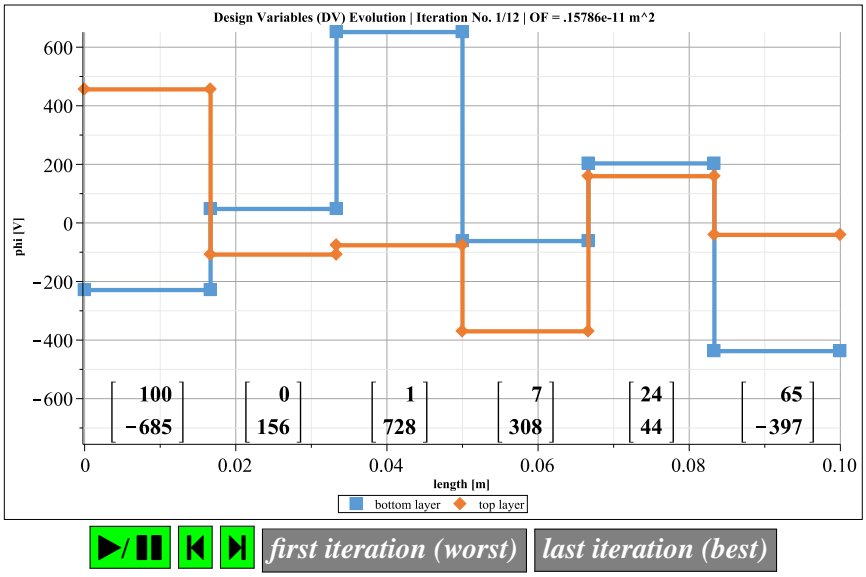

Figure H.62: Electric potentials plots of all successive best iterations found in the case study associated with Figure H.59. Note that the bold numbers above the x-axis (first row) correspond to the percentage $[\%]$ of piezoelectric material, $V_{f,r}^{ex}$, mixed up in each element along the beam's length, at each frame. Note that the bold numbers above the x-axis (second row) correspond to the voltage $[\mathrm{V}]$ in each element along the beam's length, at each frame. Please click on the buttons above this caption to run the animation and toggle between plotted results.

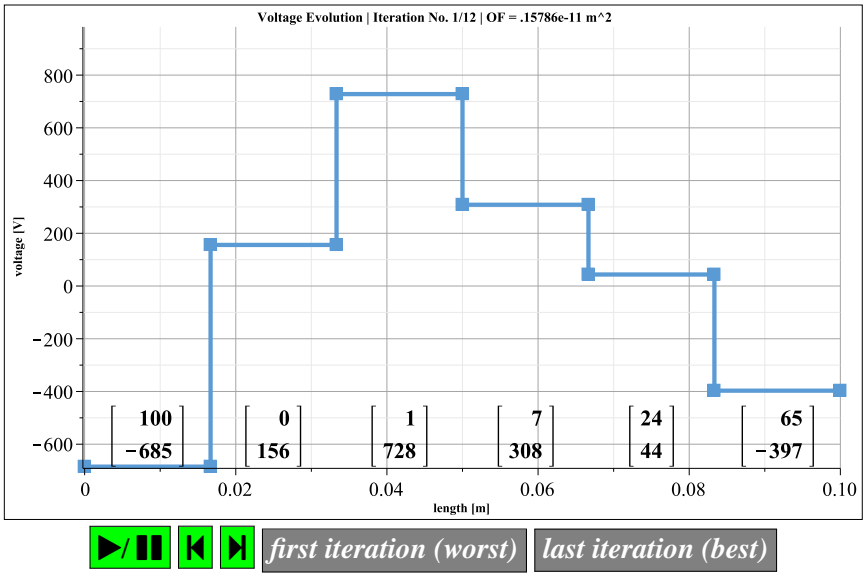

Figure H.63: Voltage plots of all successive best iterations found in the case study associated with Figure H.59. Note that the bold numbers above the x-axis (first row) correspond to the percentage $[\%]$ of piezoelectric material, $V_{f,r}^{ex}$, mixed up in each element along the beam's length, at each frame. Note that the bold numbers above the x-axis (second row) correspond to the voltage $[\mathrm{V}]$ in each element along the beam's length, at each frame. Please click on the buttons above this caption to run the animation and toggle between plotted results.

H.1.4 Approximation of beams' deflections to 3 control points

Schemes and results associated with Section 4.3.1.4.

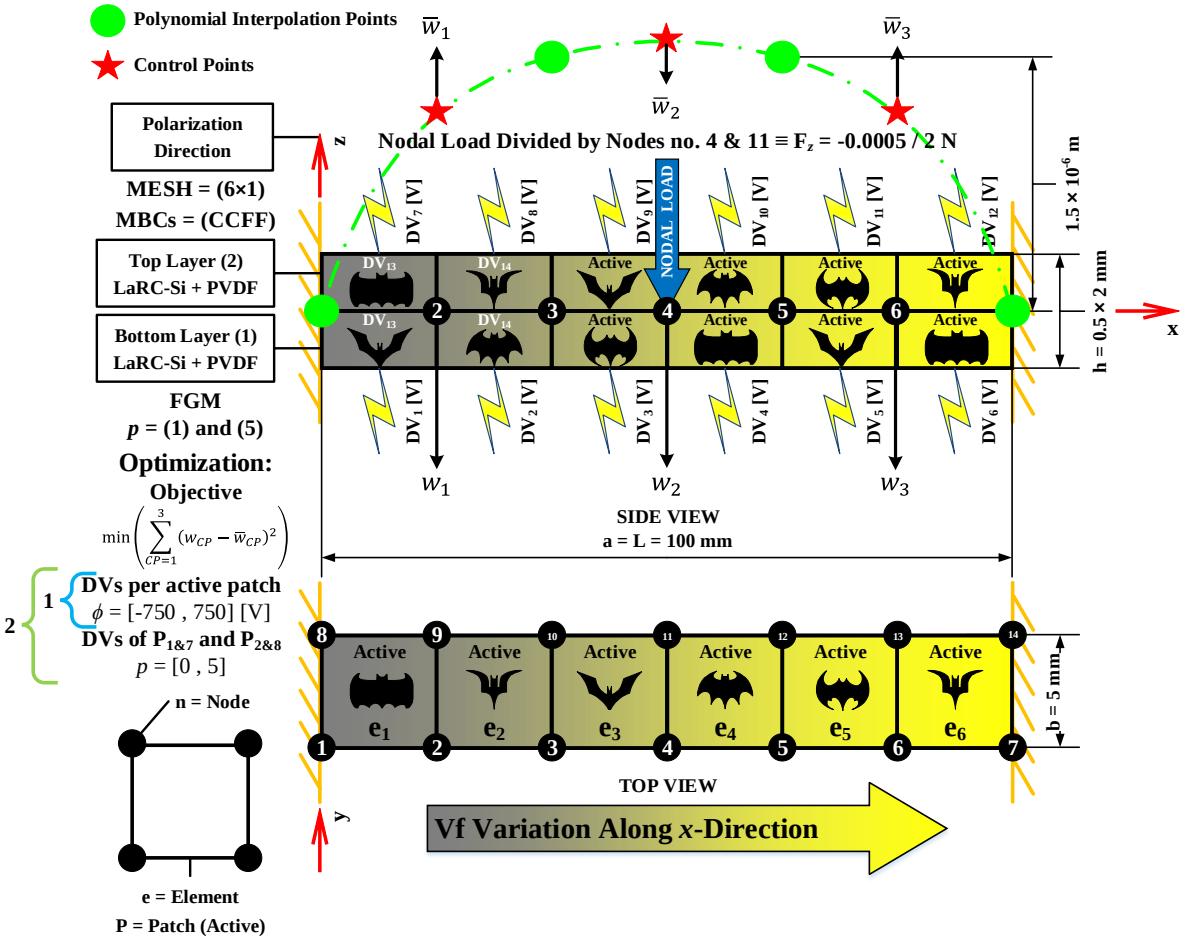

Figure H.64: Optimization case study scheme for approx. of beams' deflections to 3 control points.

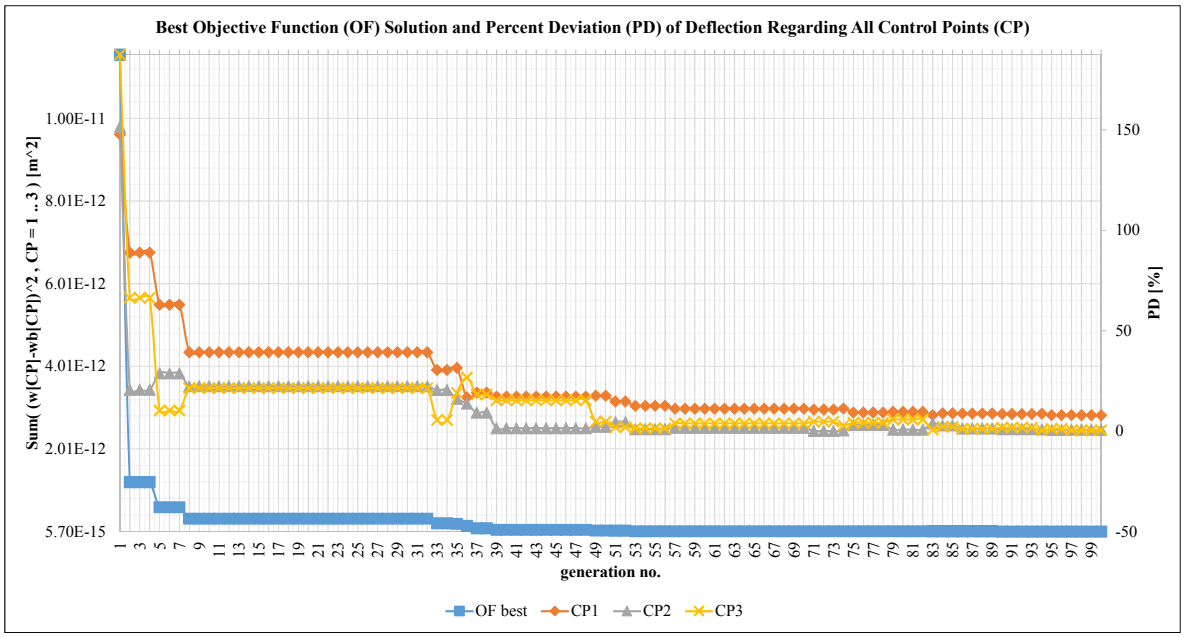

OF best and PD $DV_{1..12}$

Figure H.65: Optimization results, for all generations, from the case study of approximation of beams' deflections to 3 control points, mixing up LaRC-Si and PVDF, considering $p = 1$ and the same BA parameters from Figure H.8. DVs are the electric potentials ϕ [V] applied to each patch. Please click on the buttons above this caption to toggle between plotted results.

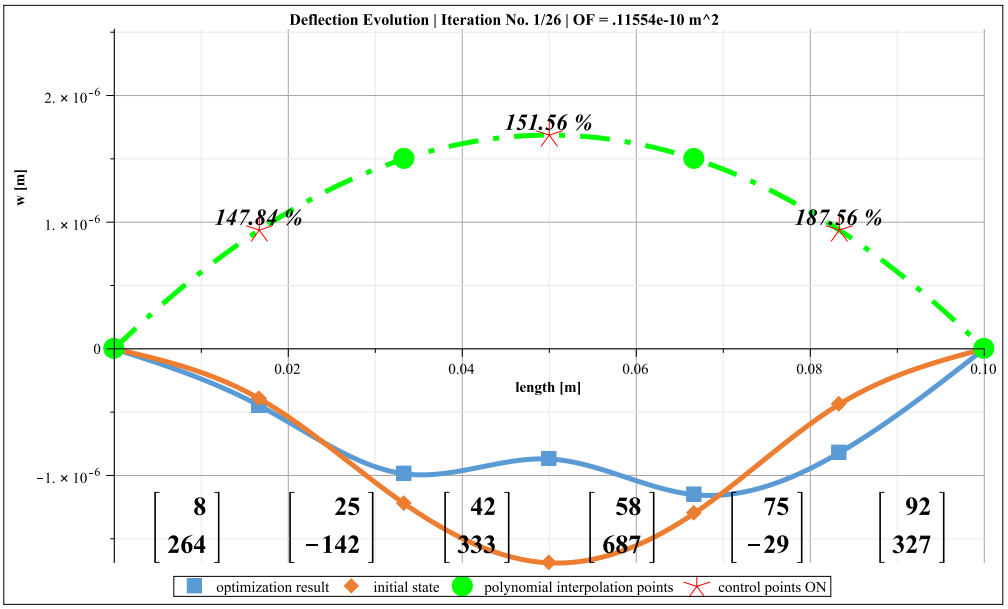

Figure H.66: Deflection plots of all successive best iterations found in the case study associated with Figure H.65. Note that the bold numbers above the x-axis (first row) correspond to the percentage $[\%]$ of piezoelectric material, $V_{f,r}^{ex}$, mixed up in each element along the beam's length, at each frame. Note that the bold numbers above the x-axis (second row) correspond to the voltage $[\mathrm{V}]$ in each element along the beam's length, at each frame. Note that the bold percentages above each control point correspond to the deviation $[\%]$ between w_{CP} and $\overline{w}_{CP}$, at each frame. Please click on the buttons above this caption to run the animation and toggle between plotted results.

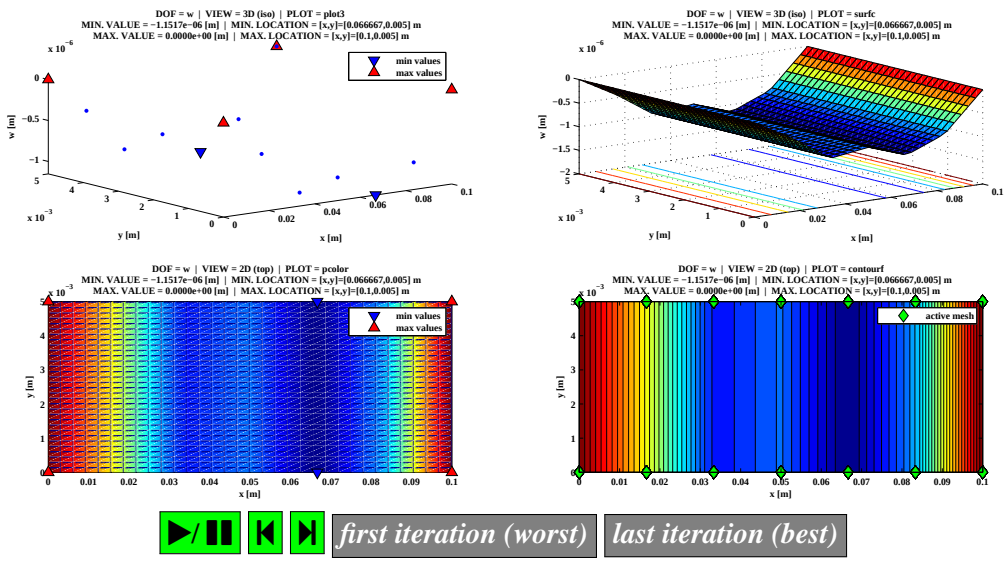

Figure H.67: 3D and 2D deflection plots of all successive best iterations found in the case study associated with Figure H.65. Please click on the buttons above this caption to run the animation and toggle between plotted results.

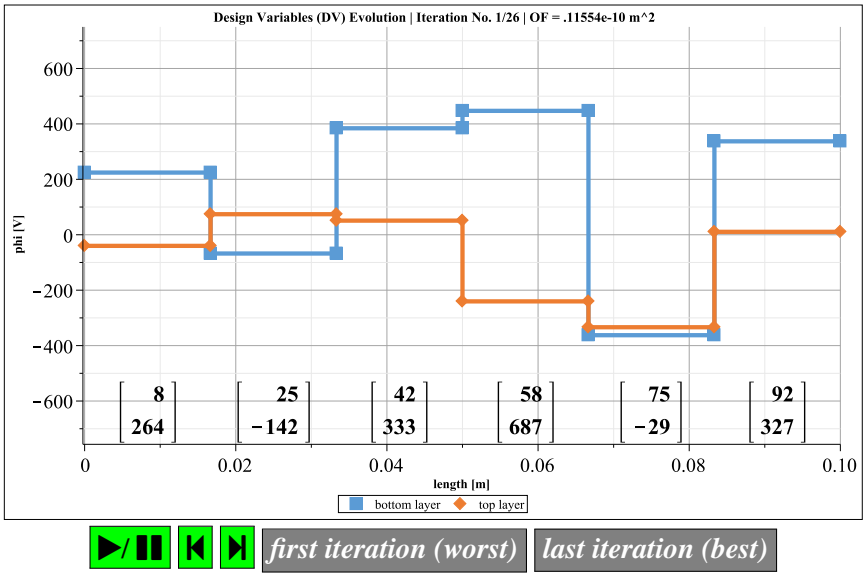

Figure H.68: Electric potentials plots of all successive best iterations found in the case study associated with Figure H.65. Note that the bold numbers above the x-axis (first row) correspond to the percentage $[\%]$ of piezoelectric material, $V_{f,r}^{ex}$, mixed up in each element along the beam's length, at each frame. Note that the bold numbers above the x-axis (second row) correspond to the voltage $[\mathrm{V}]$ in each element along the beam's length, at each frame. Please click on the buttons above this caption to run the animation and toggle between plotted results.

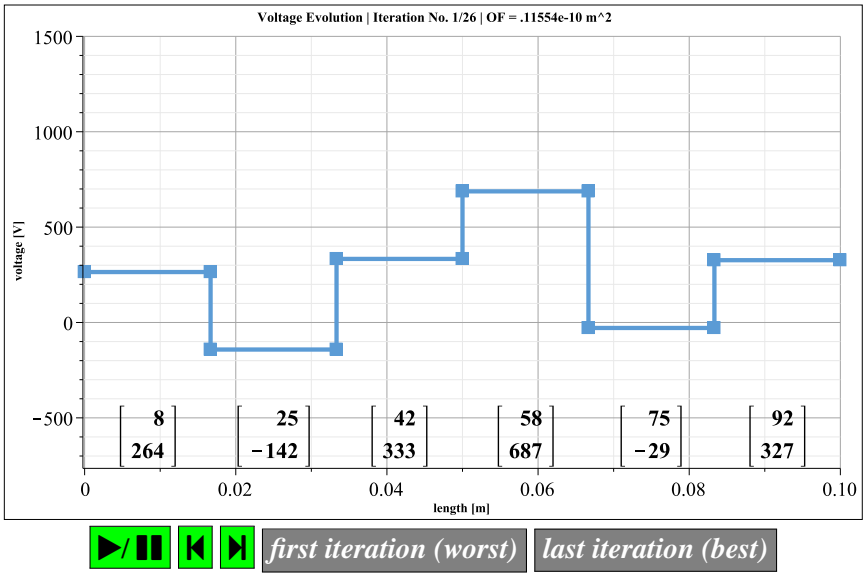

Figure H.69: Voltage plots of all successive best iterations found in the case study associated with Figure H.65. Note that the bold numbers above the x-axis (first row) correspond to the percentage $[\%]$ of piezoelectric material, $V_{f,r}^{ex}$, mixed up in each element along the beam's length, at each frame. Note that the bold numbers above the x-axis (second row) correspond to the voltage $[\mathrm{V}]$ in each element along the beam's length, at each frame. Please click on the buttons above this caption to run the animation and toggle between plotted results.

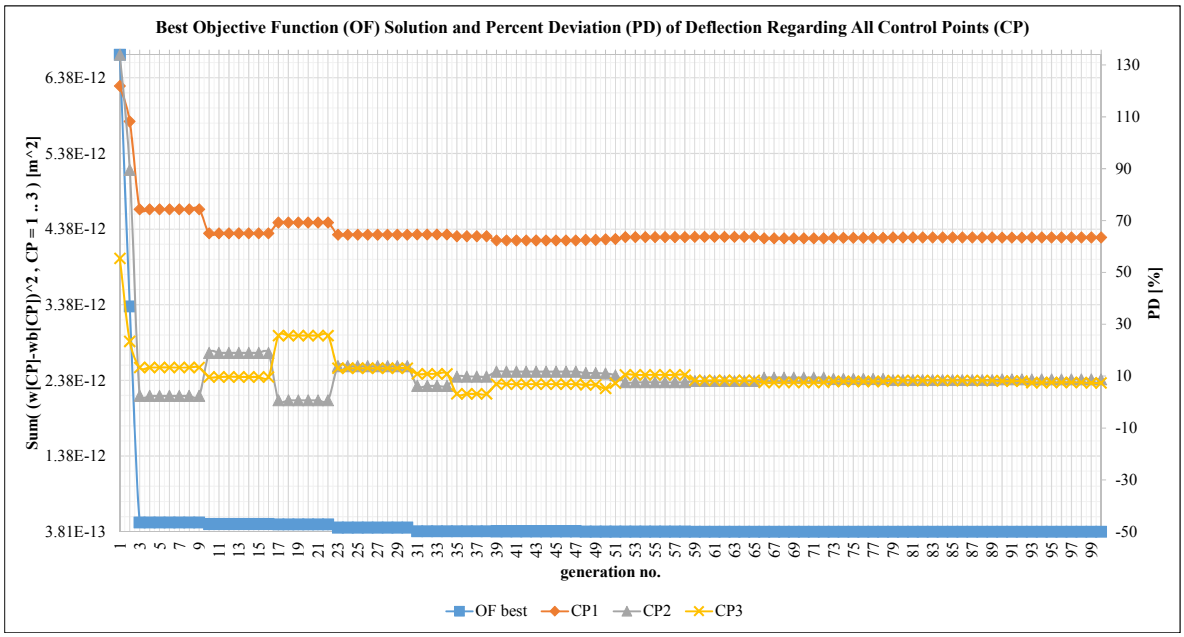

OF best and PD $DV_{1..12}$

Figure H.70: Optimization results, for all generations, from the case study of approximation of beams' deflections to 3 control points, mixing up LaRC-Si and PVDF, considering $p = 5$ and the same BA parameters from Figure H.8. DVs are the electric potentials ϕ [V] applied to each patch. Please click on the buttons above this caption to toggle between plotted results.

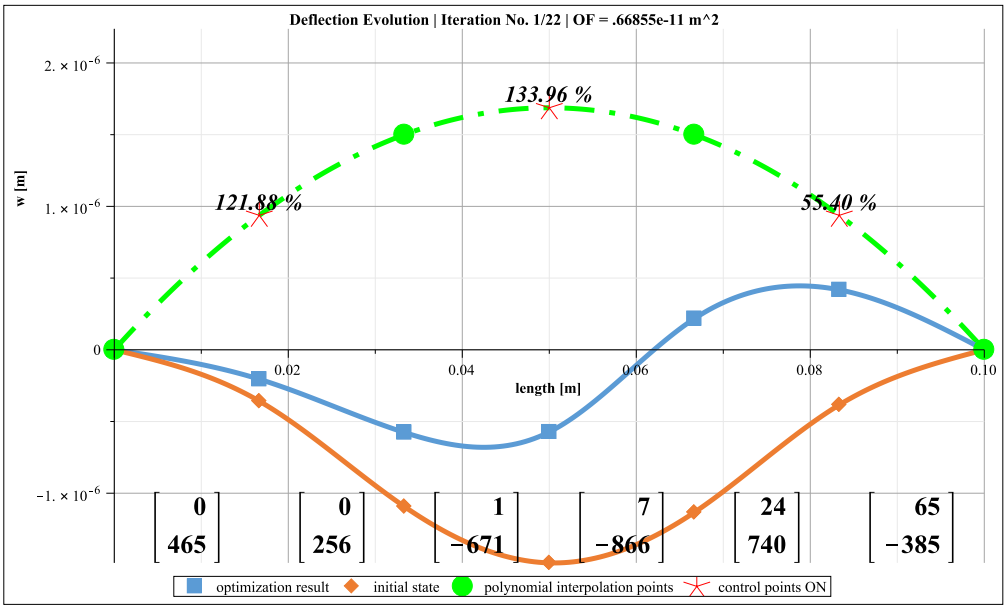

Figure H.71: Deflection plots of all successive best iterations found in the case study associated with Figure H.70. Note that the bold numbers above the x-axis (first row) correspond to the percentage $[\%]$ of piezoelectric material, $V_{f,r}^{ex}$, mixed up in each element along the beam's length, at each frame. Note that the bold numbers above the x-axis (second row) correspond to the voltage $[\mathrm{V}]$ in each element along the beam's length, at each frame. Note that the bold percentages above each control point correspond to the deviation $[\%]$ between w_{CP} and $\overline{w}_{CP}$, at each frame. Please click on the buttons above this caption to run the animation and toggle between plotted results.

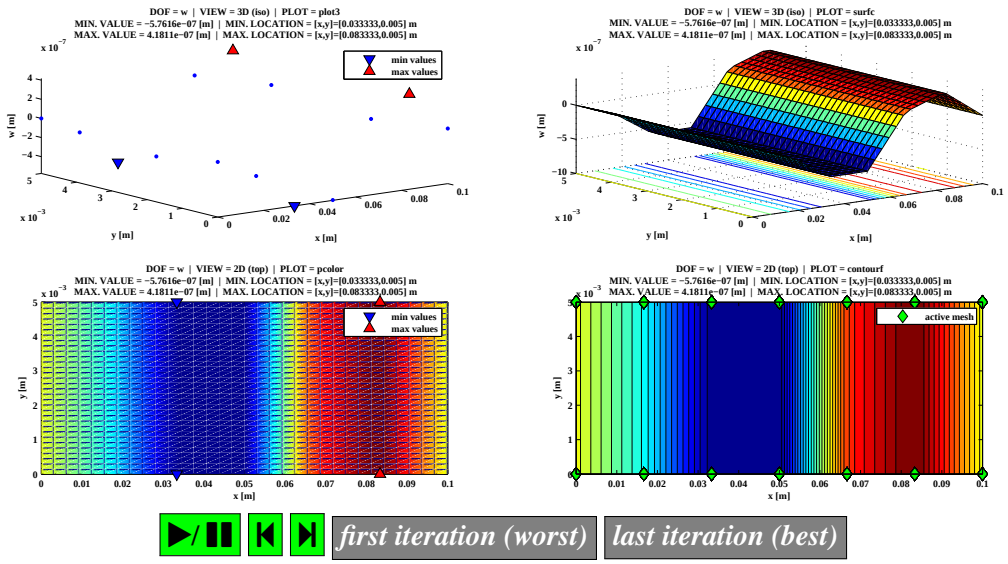

Figure H.72: 3D and 2D deflection plots of all successive best iterations found in the case study associated with Figure H.70. Please click on the buttons above this caption to run the animation and toggle between plotted results.

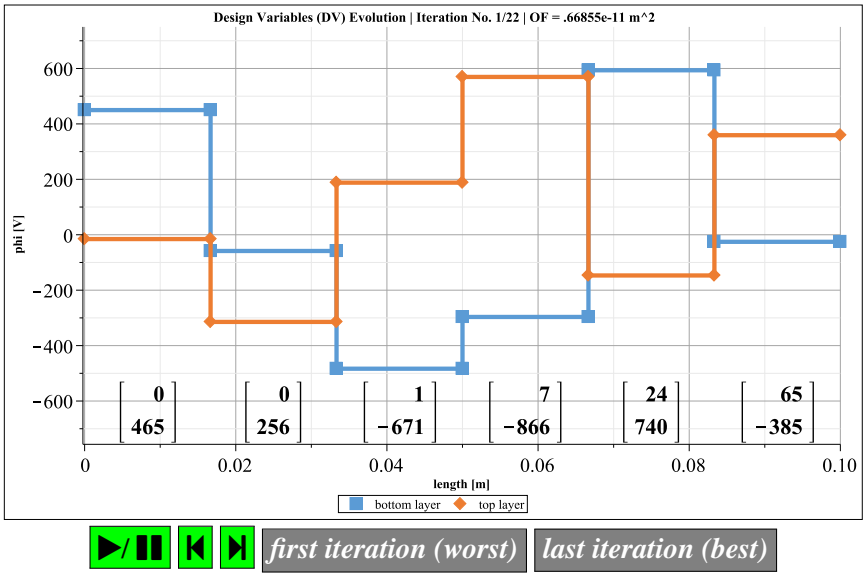

Figure H.73: Electric potentials plots of all successive best iterations found in the case study associated with Figure H.70. Note that the bold numbers above the x-axis (first row) correspond to the percentage $[\%]$ of piezoelectric material, $V_{f,r}^{ex}$, mixed up in each element along the beam's length, at each frame. Note that the bold numbers above the x-axis (second row) correspond to the voltage $[\mathrm{V}]$ in each element along the beam's length, at each frame. Please click on the buttons above this caption to run the animation and toggle between plotted results.

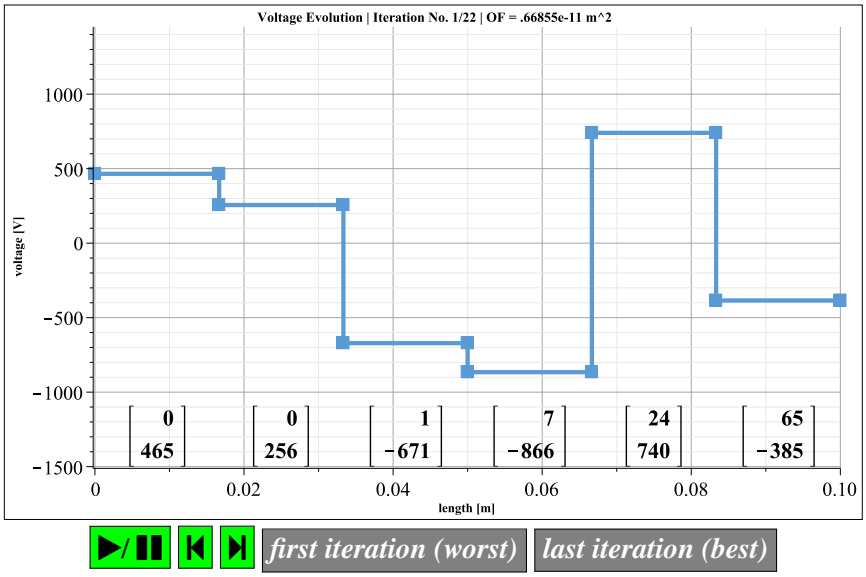

Figure H.74: Voltage plots of all successive best iterations found in the case study associated with Figure H.70. Note that the bold numbers above the x-axis (first row) correspond to the percentage $[\%]$ of piezoelectric material, $V_{f,r}^{ex}$, mixed up in each element along the beam's length, at each frame. Note that the bold numbers above the x-axis (second row) correspond to the voltage $[\mathrm{V}]$ in each element along the beam's length, at each frame. Please click on the buttons above this caption to run the animation and toggle between plotted results.

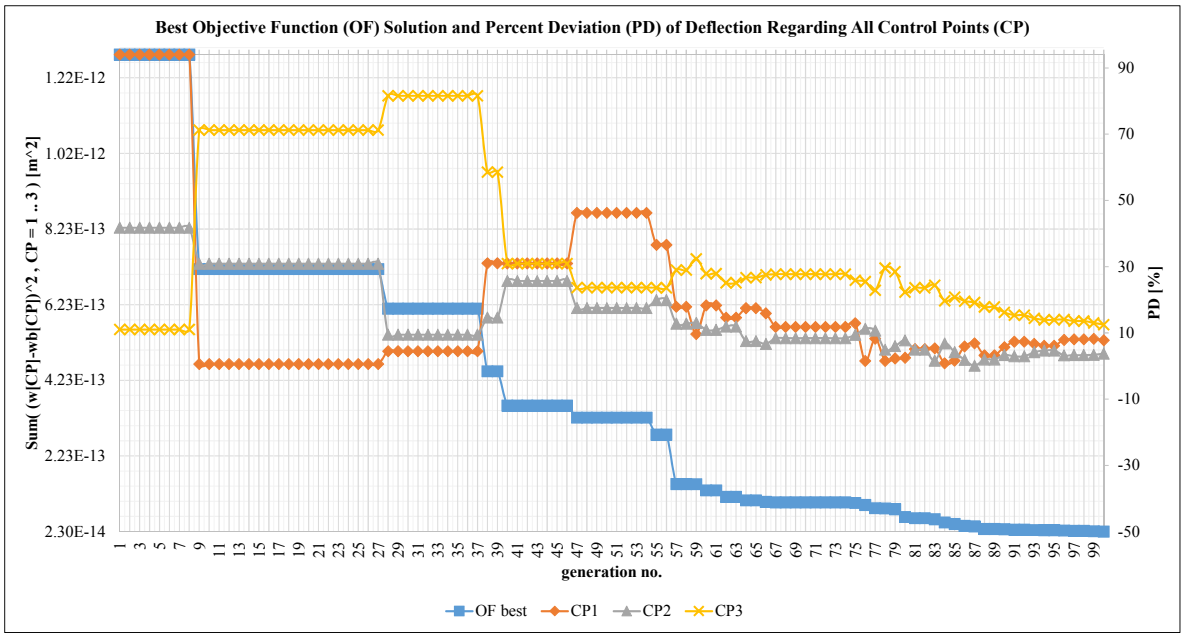

OF best and PD $DV_{1..12}$ $DV_{13..14}$

Figure H.75: Optimization results, for all generations, from the case study of approximation of beams' deflections to 3 control points, mixing up LaRC-Si and PVDF, considering $p = 5$ and the same BA parameters from Figure H.8. DVs are the electric potentials ϕ [V] applied to each patch, one different p-exponent for both patches no.1 and 7, one different p-exponent for both patches no.2 and 8. Please click on the buttons above this caption to toggle between plotted results.

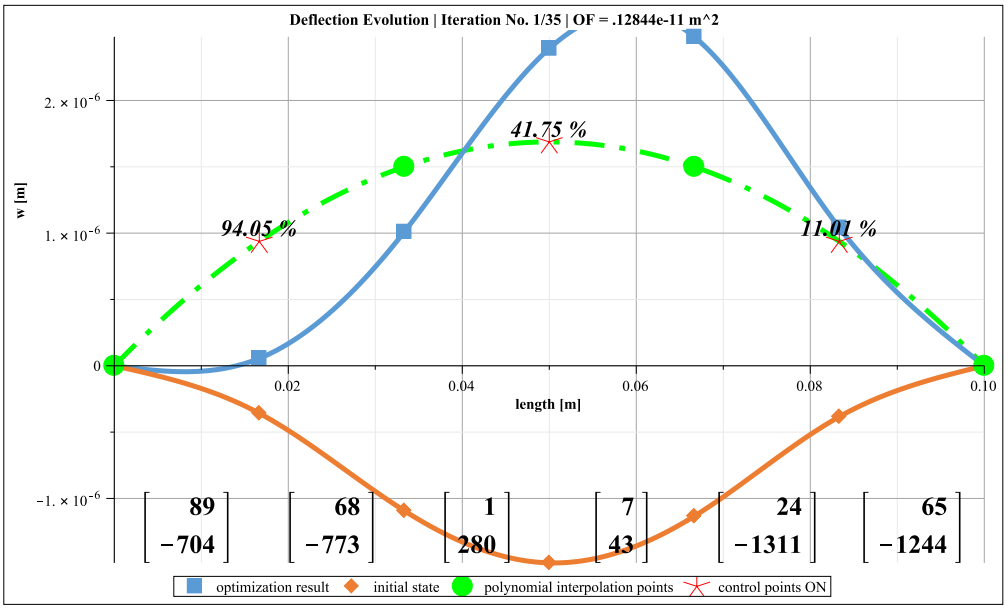

Figure H.76: Deflection plots of all successive best iterations found in the case study associated with Figure H.75. Note that the bold numbers above the x-axis (first row) correspond to the percentage $[\%]$ of piezoelectric material, $V_{f,r}^{ex}$, mixed up in each element along the beam's length, at each frame. Note that the bold numbers above the x-axis (second row) correspond to the voltage $[\mathrm{V}]$ in each element along the beam's length, at each frame. Note that the bold percentages above each control point correspond to the deviation $[\%]$ between w_{CP} and $\overline{w}_{CP}$, at each frame. Please click on the buttons above this caption to run the animation and toggle between plotted results.

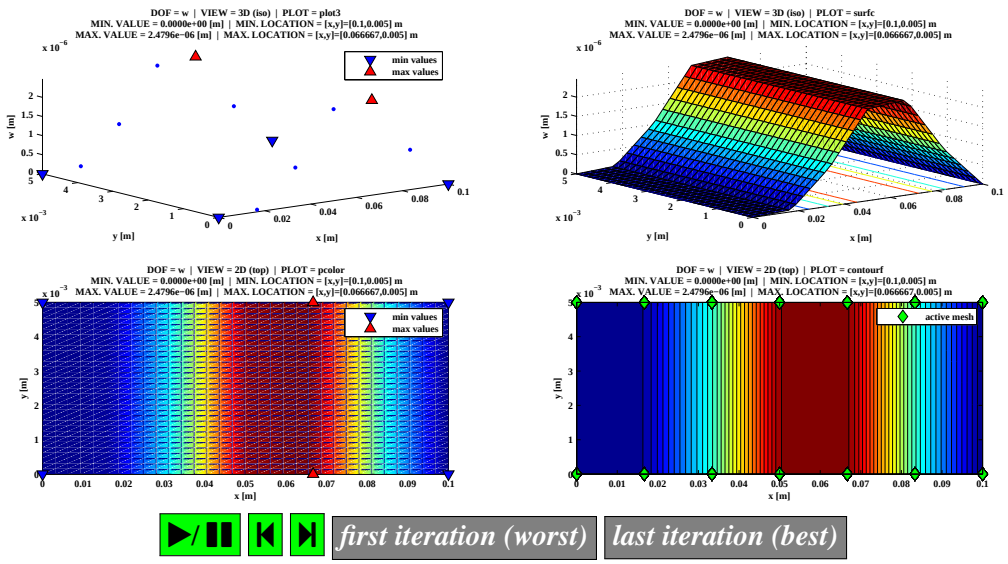

Figure H.77: 3D and 2D deflection plots of all successive best iterations found in the case study associated with Figure H.75. Please click on the buttons above this caption to run the animation and toggle between plotted results.

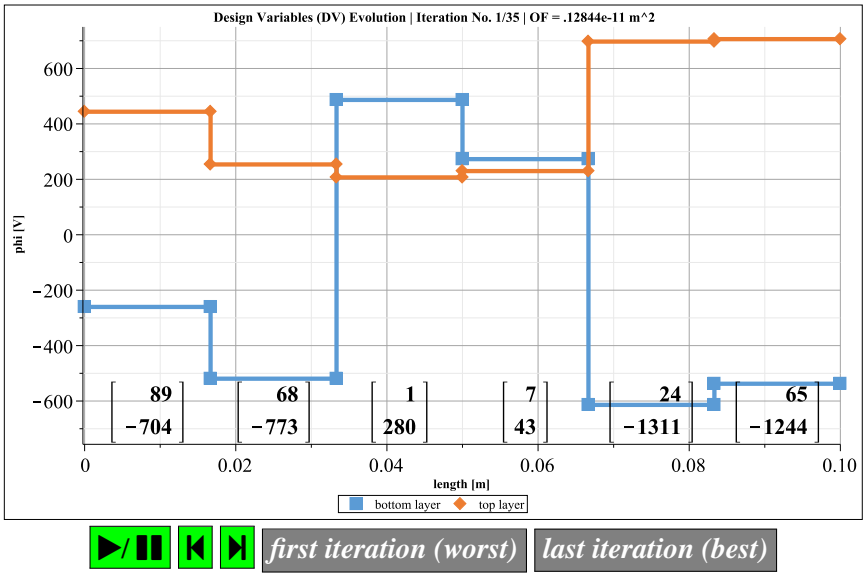

Figure H.78: Electric potentials plots of all successive best iterations found in the case study associated with Figure H.75. Note that the bold numbers above the x-axis (first row) correspond to the percentage $[\%]$ of piezoelectric material, $V_{f,r}^{ex}$, mixed up in each element along the beam's length, at each frame. Note that the bold numbers above the x-axis (second row) correspond to the voltage $[\mathrm{V}]$ in each element along the beam's length, at each frame. Please click on the buttons above this caption to run the animation and toggle between plotted results.

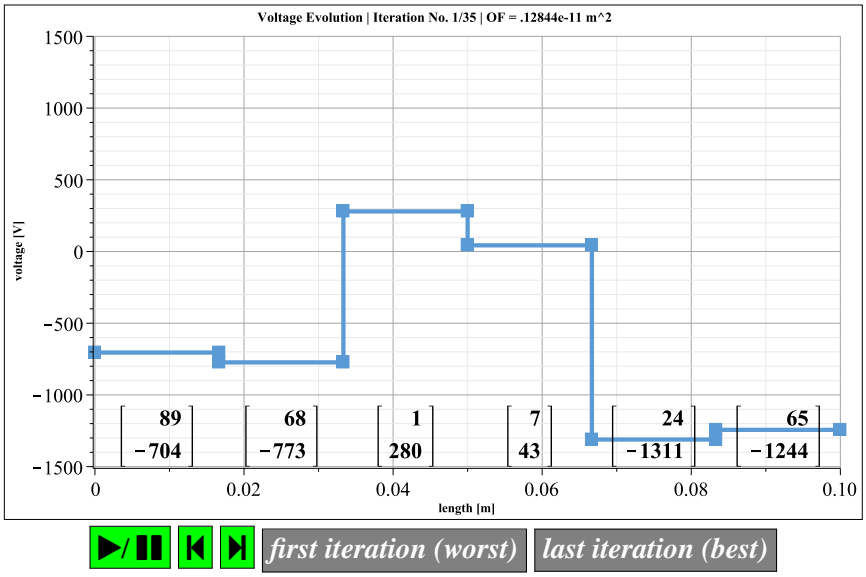

Figure H.79: Voltage plots of all successive best iterations found in the case study associated with Figure H.75. Note that the bold numbers above the x-axis (first row) correspond to the percentage $[\%]$ of piezoelectric material, $V_{f,r}^{ex}$, mixed up in each element along the beam's length, at each frame. Note that the bold numbers above the x-axis (second row) correspond to the voltage $[\mathrm{V}]$ in each element along the beam's length, at each frame. Please click on the buttons above this caption to run the animation and toggle between plotted results.

H.1.5 Maximization of fundamental natural frequencies (non-skew. beams)

Schemes and results associated with Section 4.3.1.5.

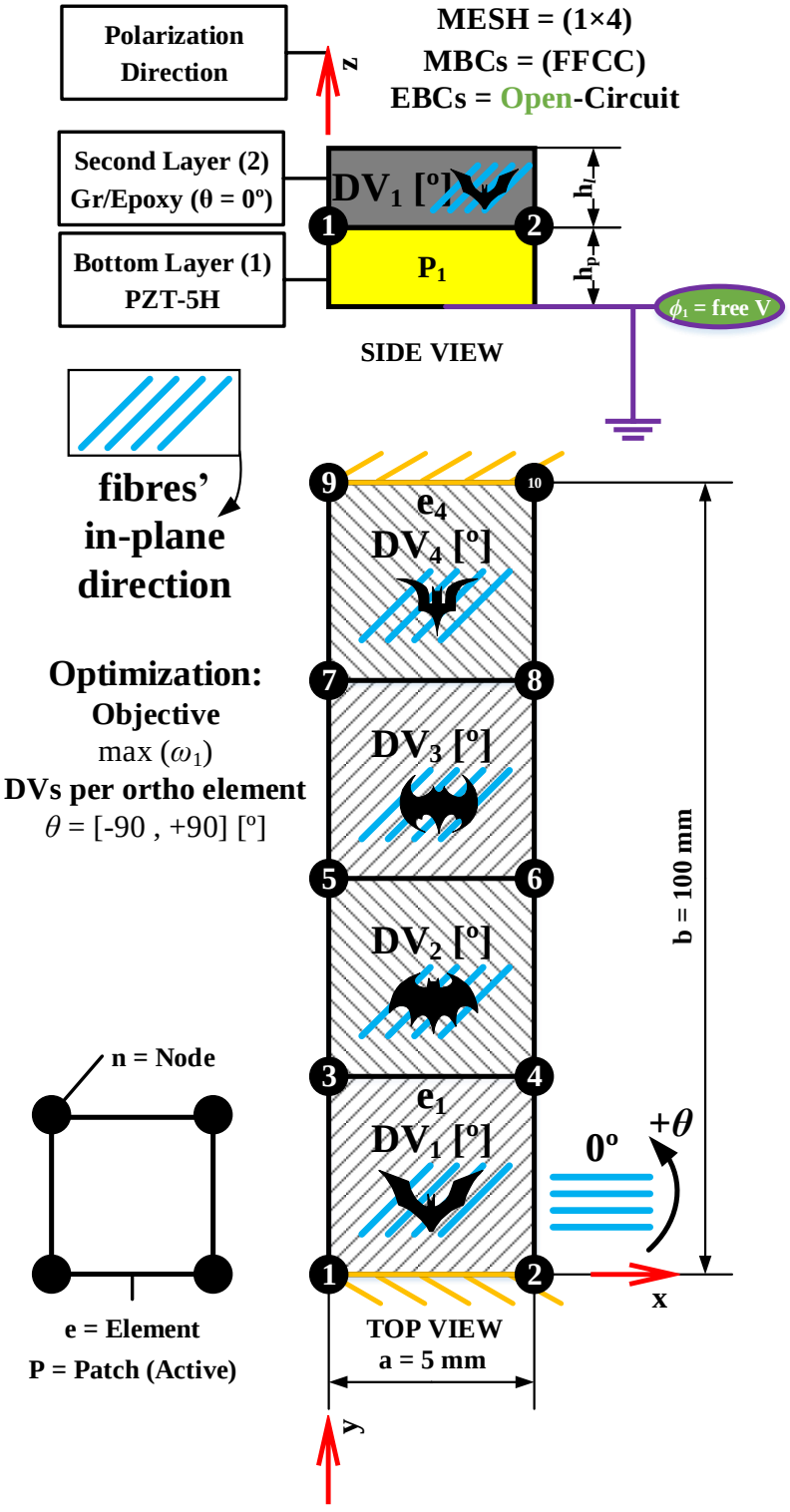

Figure H.80: Optimization case study scheme for max. ω_1 of non-skewed beams.

Table H.6: MHBA parameters used to compute the case study presented in Figure H.80.

Class	BA Parameter	Value
Problem Definition	Optimization Objective	MAXIMIZATION
	d	4
	N_{gen}	150
	n	20
Echolocation	f_{min}	0
	f_{max}	1
	r^0	0.5
	A^0	1
Solution Modification	Hybrid (BA+DE)	TRUE
	Adaptive	TRUE
	$Fper_i$	0.08
	$Fper_f$	0.01
	Micro	TRUE (Step 10 Gens, only)
Constants	α	0.95
	γ	0.99
	ϵ	0.001

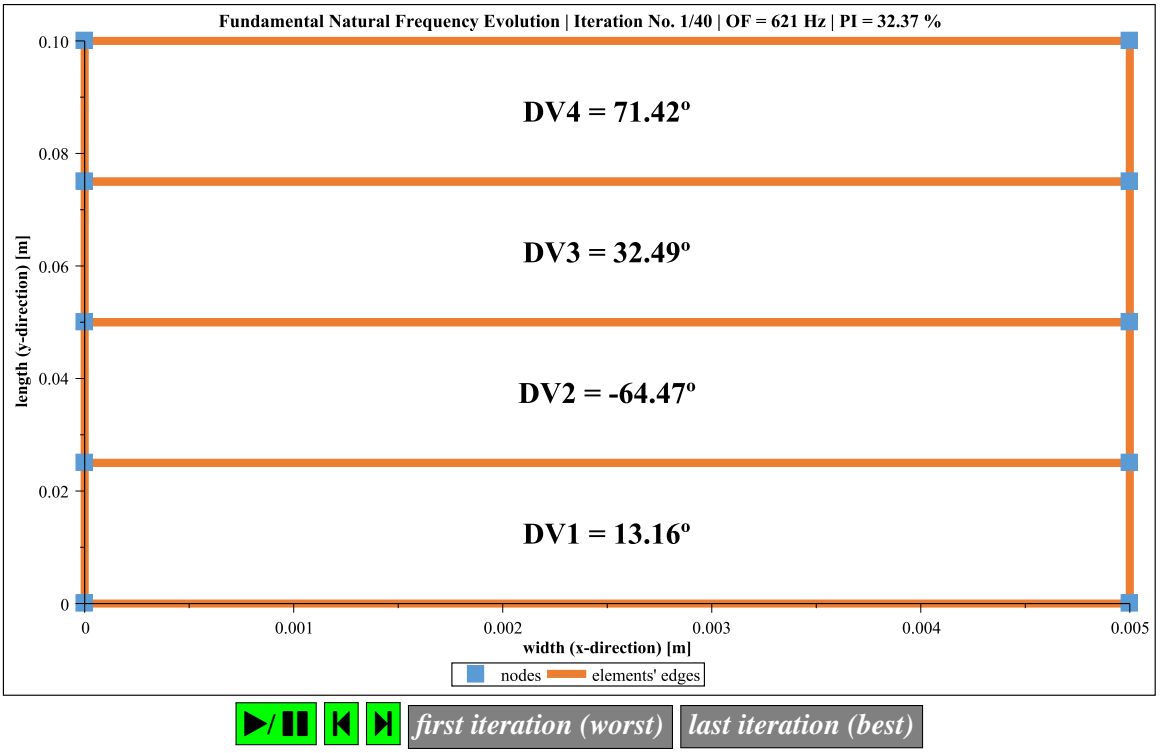

Figure H.81: Parametric 2D plots of all successive best iterations found in the case study associated with Figure H.80, concerning DVs' fibre orientations in [°], as well as OF best ω_1 and PI, at each frame. Please click on the buttons above this caption to run the animation and toggle between plotted results.

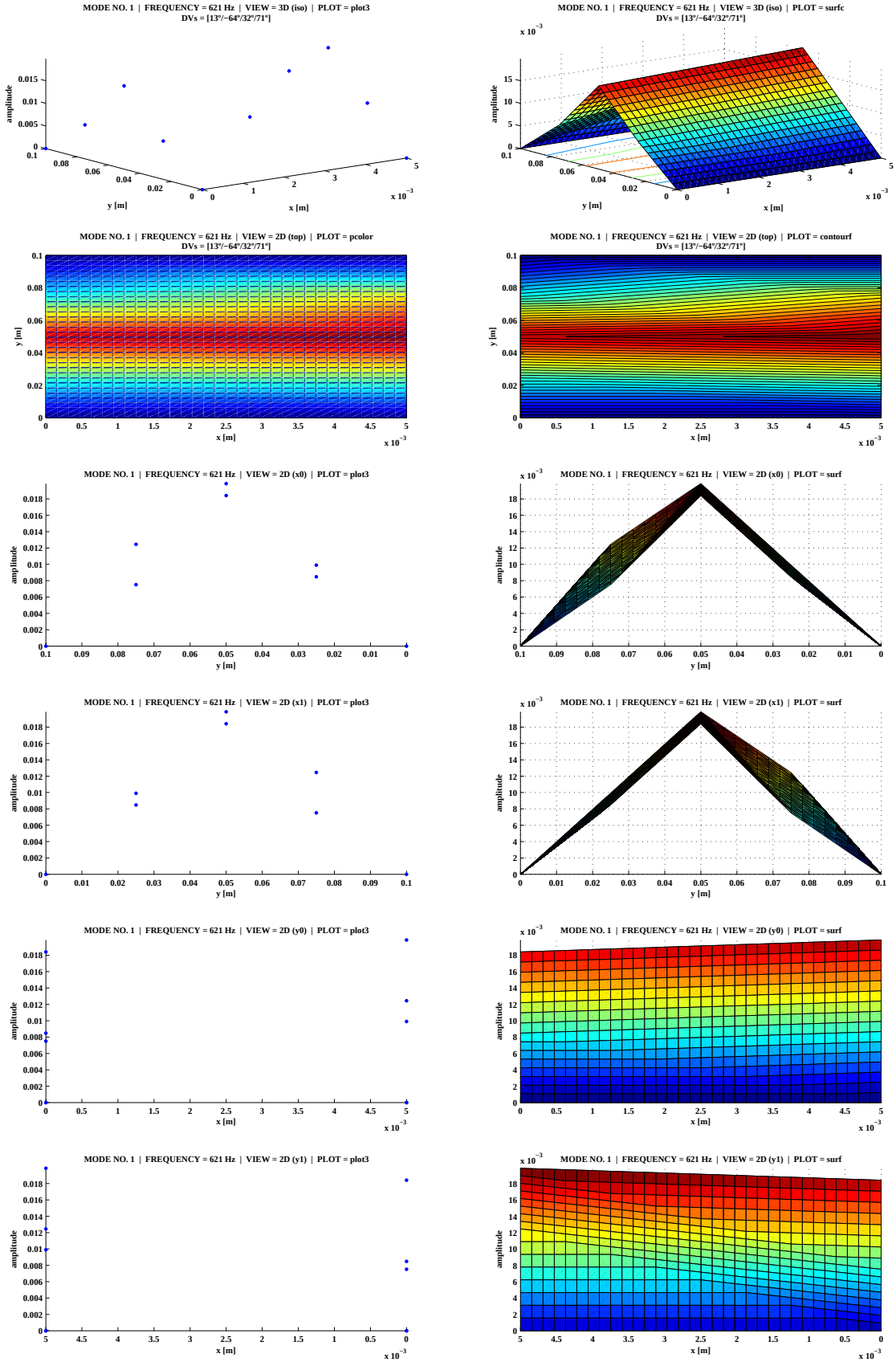

Figure H.82: 3D and 2D fundamental free vibrational mode amplitude's distributions of all successive best iterations found in the case study associated with Figure H.80. Please click on the buttons above this caption to run the animation and toggle between plotted results.

H.1.6 Maximization of fundamental natural frequencies (skewed beams)

Schemes and results associated with Section 4.3.1.6.

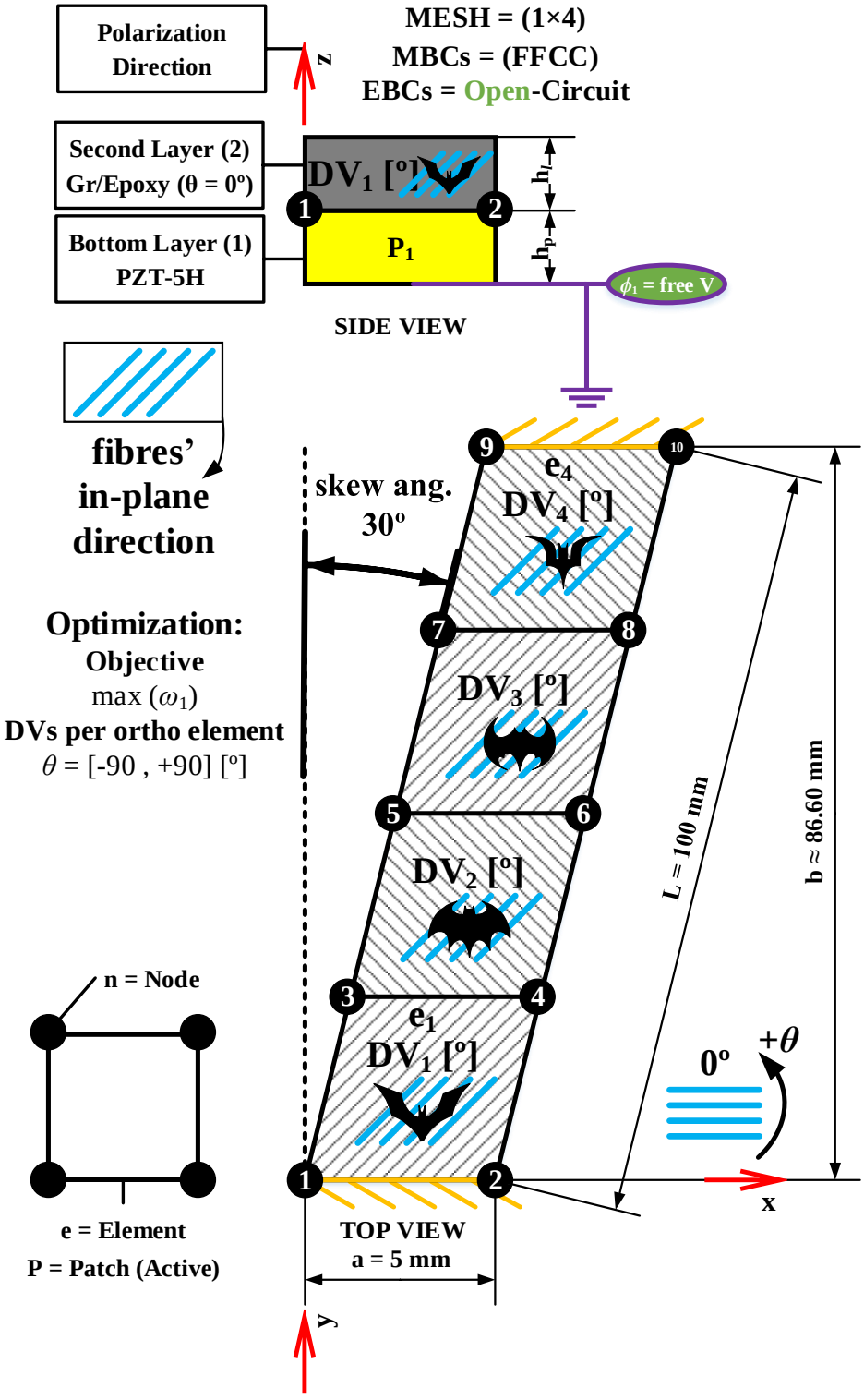

Figure H.83: Optimization case study scheme for max. ω_1 of skewed beams.

Table H.7: Optimization results for 8 CSs, about the optimization case study in Figure H.83.

cs_no.	OF Best	DV1 (θ_1)	DV2 (θ_2)	DV3 (θ_3)	DV4 (θ_4)	PI	N_{gen}	n	f_{min}	f_{max}	r^0	A^0	$Fper_i$	$Fper_f$	Micro	α	γ	ϵ
7	1017.288	60.0	60.2	59.9	60.0	116.27	150	20	0	1	0.5	1	0.05	0.01	TRUE	0.95	0.99	0.001
3	1017.230	59.7	59.5	59.8	59.6	116.26	150	20	0	1	0.5	1	0.05	0.01	TRUE	0.95	0.99	0.001
5	1017.218	59.6	59.7	59.7	59.4	116.26	150	20	0	0.01	0.5	0.5	2	0.01	TRUE	0.98	0.97	0.001
8	1008.811	60.0	58.8	54.3	59.1	114.47	150	20	0	1	0.5	1	0.08	0.01	TRUE	0.95	0.99	0.001
2	944.358	24.6	61.2	58.4	60.8	100.77	150	20	0	1	0.5	1	0.1	0.2	TRUE	0.95	0.99	0.001
6	940.603	65.9	58.4	62.1	-90.0	99.97	150	20	0	1	0.5	1	0.1	0.2	TRUE	0.95	0.99	0.001
4	928.349	60.6	-90.0	58.6	59.4	97.36	150	20	0	1	0.5	1	0.08	0.01	TRUE	0.95	0.99	0.001
1	928.145	60.4	-90.0	57.0	59.6	97.32	150	20	0	0.01	0.5	0.5	2	0.01	TRUE	0.98	0.97	0.001

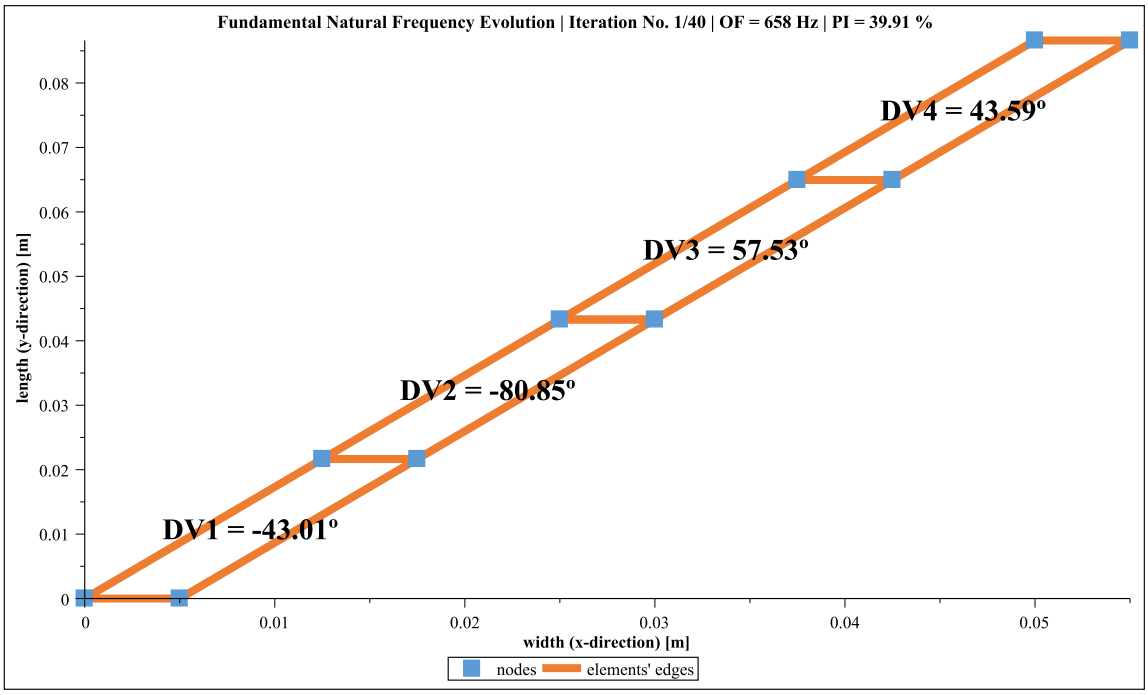

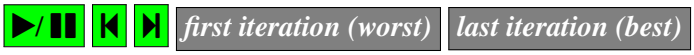

Figure H.84: Parametric 2D plots of all successive best iterations found in the case study associated with Figure H.83, concerning DVs' fibre orientations in $[^{\circ}]$, as well as OF best ω_1 and PI, at each frame. Please click on the buttons above this caption to run the animation and toggle between plotted results.

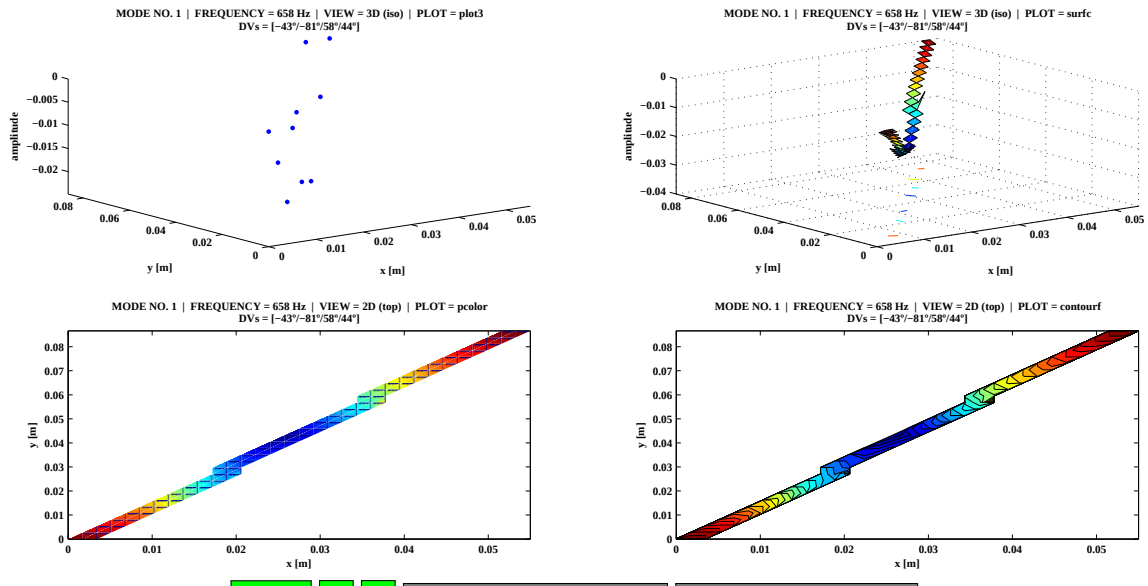

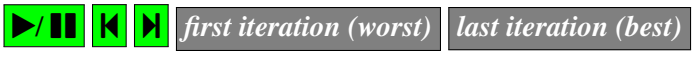

Figure H.85: 3D and 2D fundamental free vibrational mode amplitude's distributions of all successive best iterations found in the case study associated with Figure H.83. Please click on the buttons above this caption to run the animation and toggle between plotted results.

H.1.7 Maximization of fundamental natural frequencies (skewed plates)

Schemes and results associated with Section 4.3.1.7.

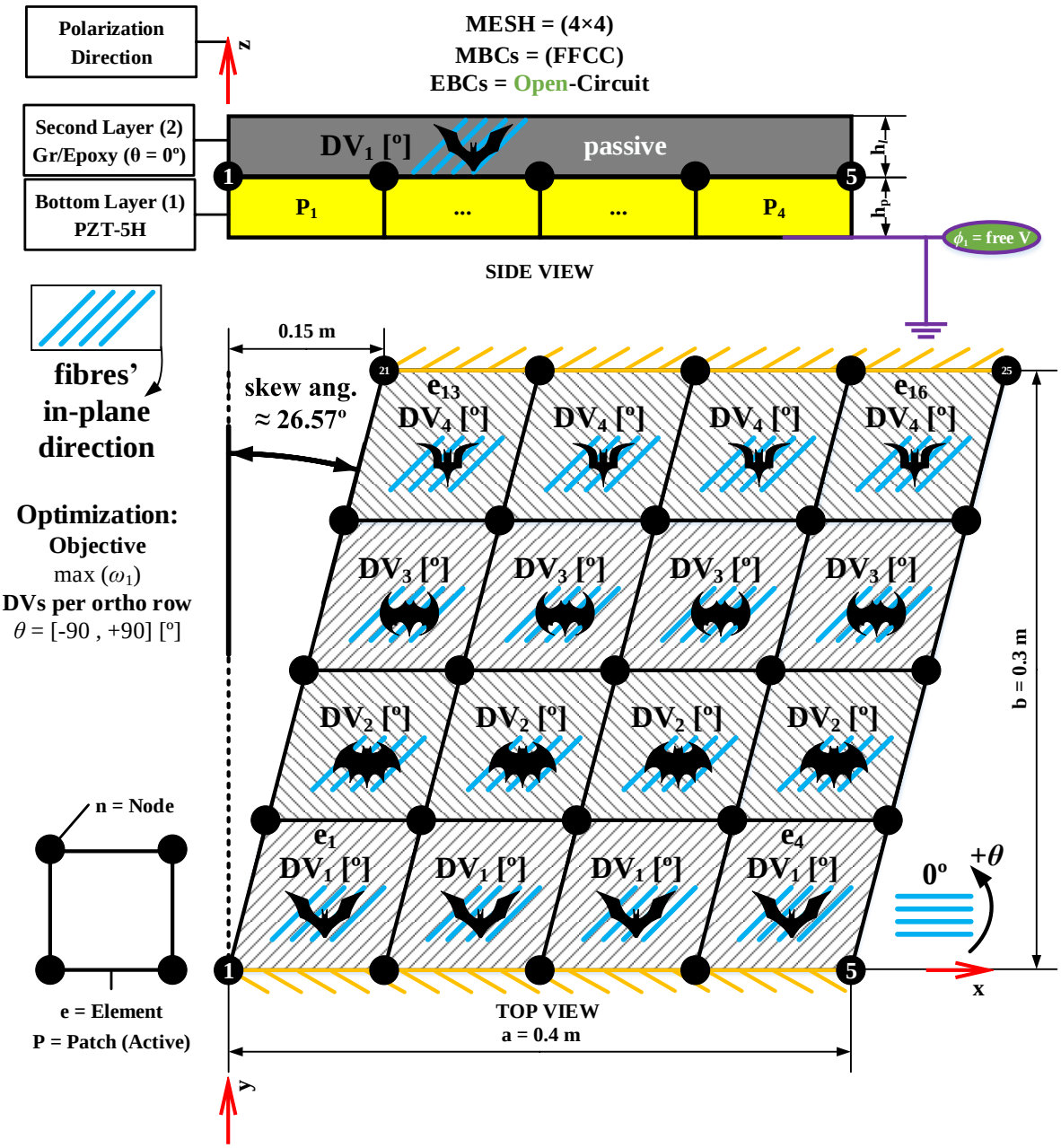

Figure H.86: Optimization case study scheme for max. ω_1 of skewed plates.

Table H.8: Optimization results for 8 CSs, about the optimization case study in Figure H.86.

cs_no.	OF Best	DV1 (θ_1)	DV2 (θ_2)	DV3 (θ_3)	DV4 (θ_4)	PI	N_{gen}	n	f_{min}	f_{max}	r^0	A^0	$Fper_i$	$Fper_f$	Micro	α	γ	ϵ
8	114.334	-87.8	80.9	78.2	90.0	121.97	150	20	0	1	0.5	1	0.08	0.01	TRUE	0.95	0.99	0.001
4	114.310	-89.8	79.0	78.6	90.0	121.92	150	20	0	1	0.5	1	0.08	0.01	TRUE	0.95	0.99	0.001
5	114.278	90.0	79.8	79.6	90.0	121.86	150	20	0	0.01	0.5	0.5	2	0.01	TRUE	0.98	0.97	0.001
1	114.264	90.0	80.2	80.6	-89.4	121.83	150	20	0	0.01	0.5	0.5	2	0.01	TRUE	0.98	0.97	0.001
3	114.251	89.8	79.7	80.3	90.0	121.81	150	20	0	1	0.5	1	0.05	0.01	TRUE	0.95	0.99	0.001
6	114.242	89.9	79.1	79.9	-90.0	121.79	150	20	0	1	0.5	1	0.1	0.2	TRUE	0.95	0.99	0.001
2	114.183	-90.0	80.1	78.7	-90.0	121.67	150	20	0	1	0.5	1	0.1	0.2	TRUE	0.95	0.99	0.001
7	112.548	90.0	-90.0	-90.0	-89.8	118.50	150	20	0	1	0.5	1	0.05	0.01	TRUE	0.95	0.99	0.001

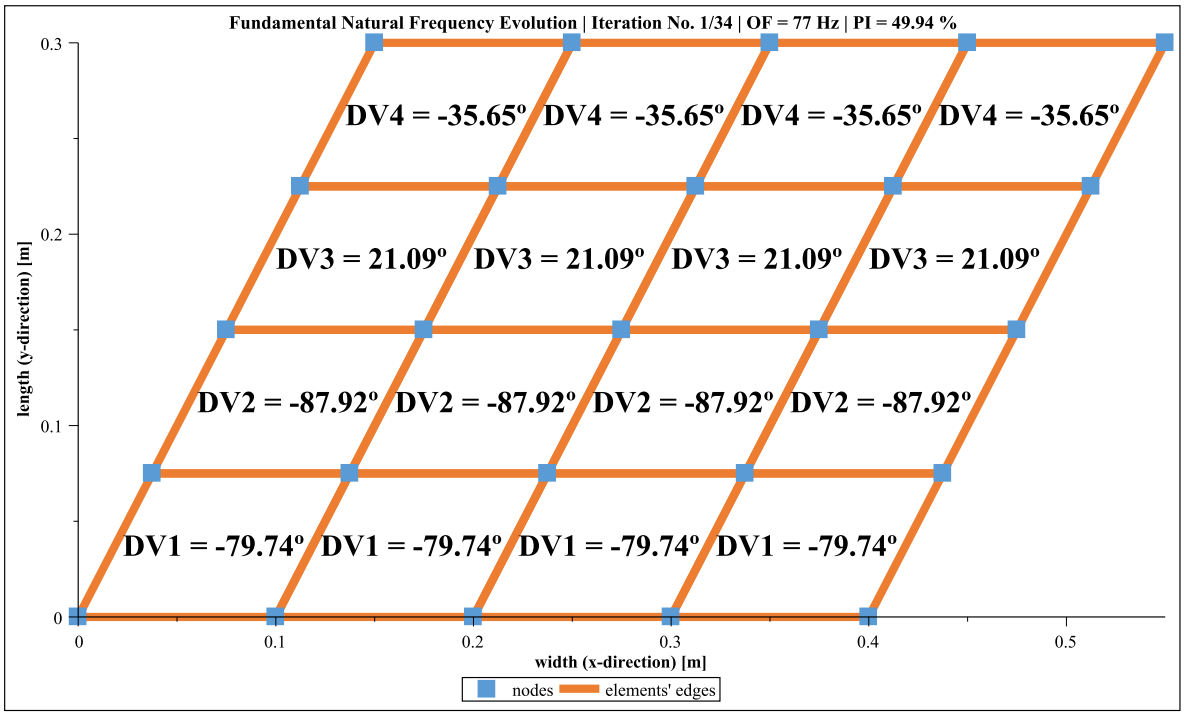

Figure H.87: Parametric 2D plots of all successive best iterations found in the case study associated with Figure H.86, concerning DVs' fibre orientations in [°], as well as OF best ω_1 and PI, at each frame. Please click on the buttons above this caption to run the animation and toggle between plotted results.

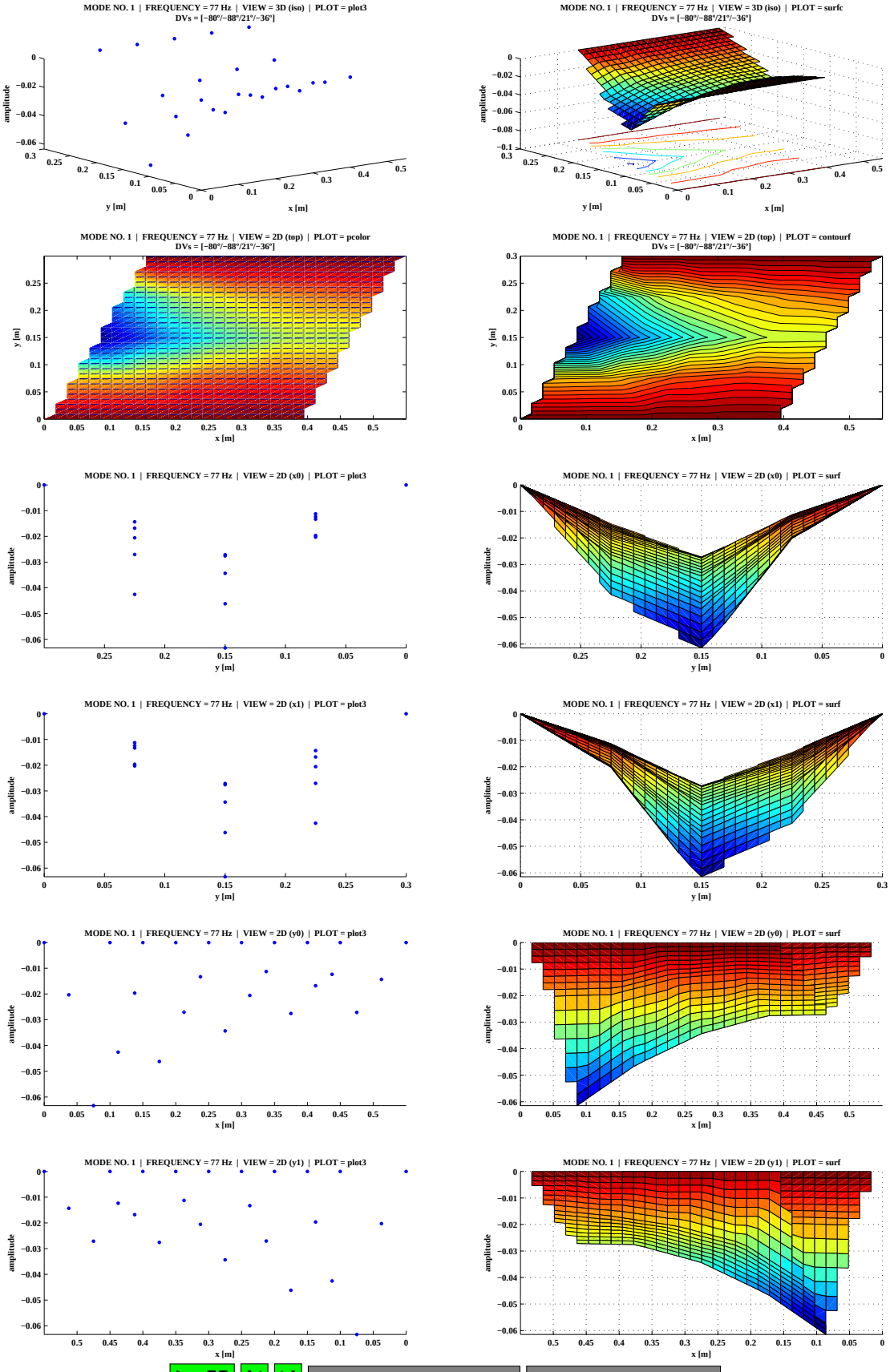

Figure H.88: 3D and 2D fundamental free vibrational mode amplitude's distributions of all successive best iterations found in the case study associated with Figure H.86. Please click on the buttons above this caption to run the animation and toggle between plotted results.

Appendix I

Future Work

This appendix includes several information associated with future work, concerning the present thesis.

I.1 Maplet® GUI platform

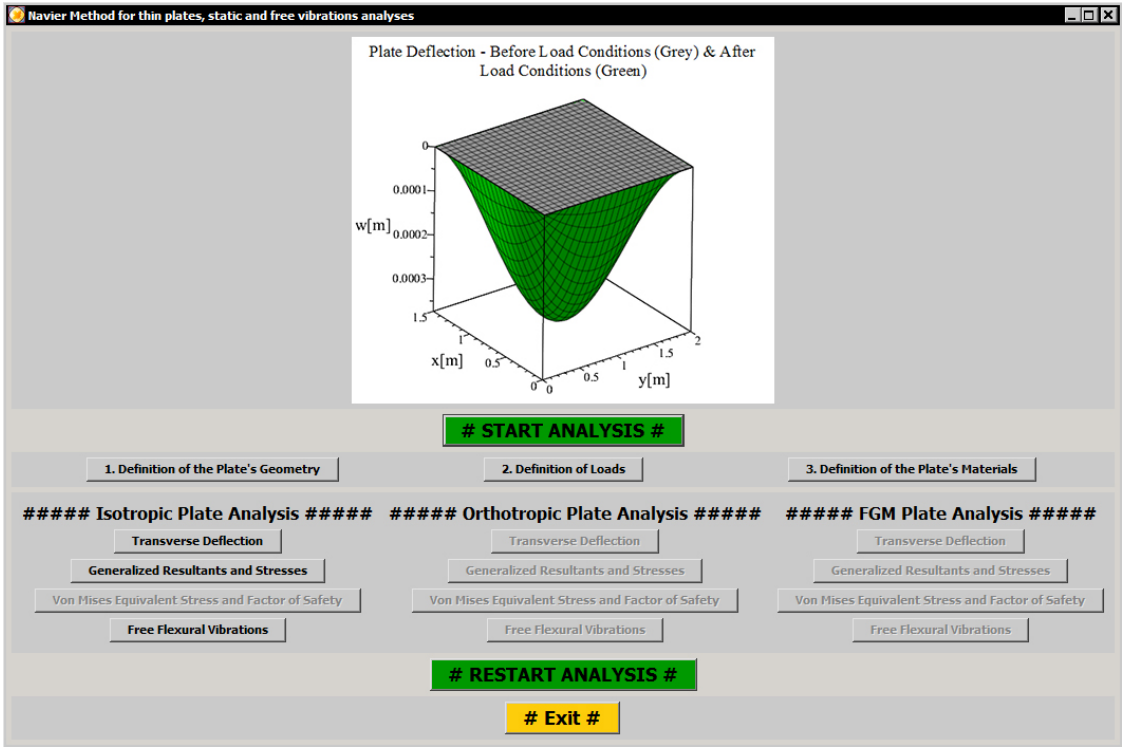

Figure I.1: Main simulator panel.

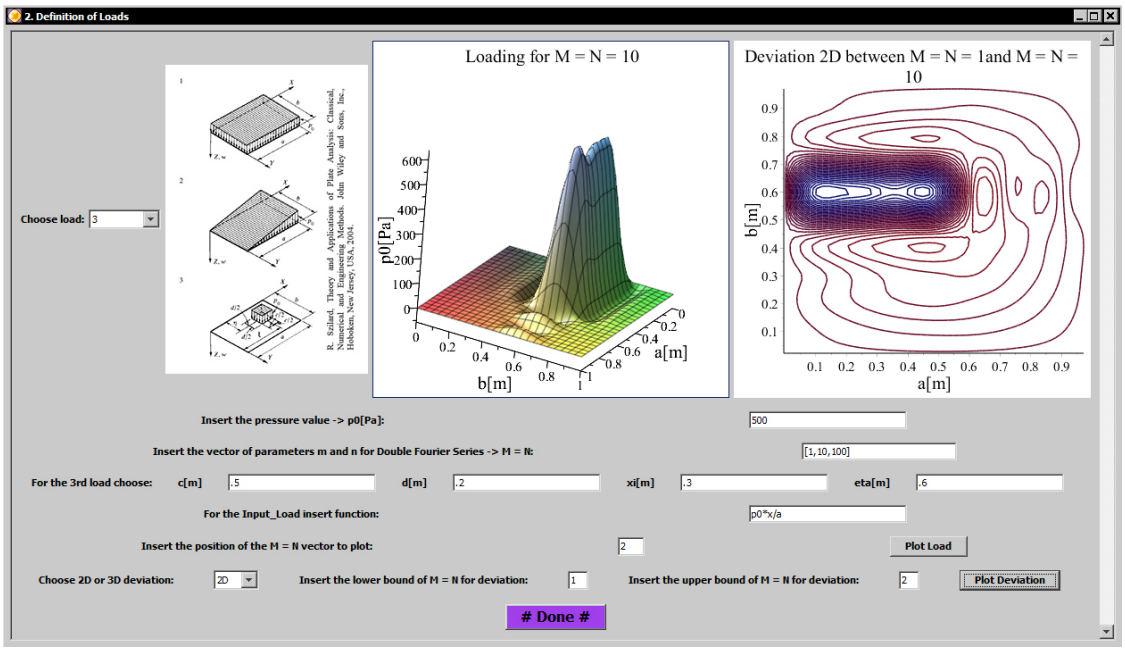

Figure I.2: Definition of the load imposed to the plate.

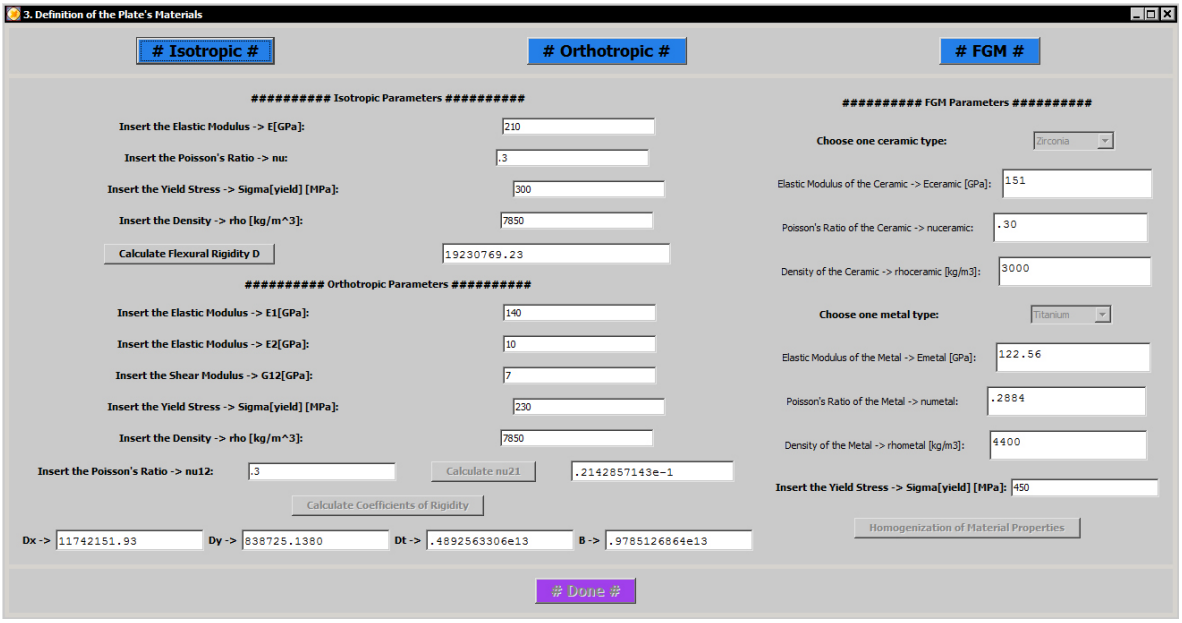

Figure I.3: Characterization of the different type materials' properties.

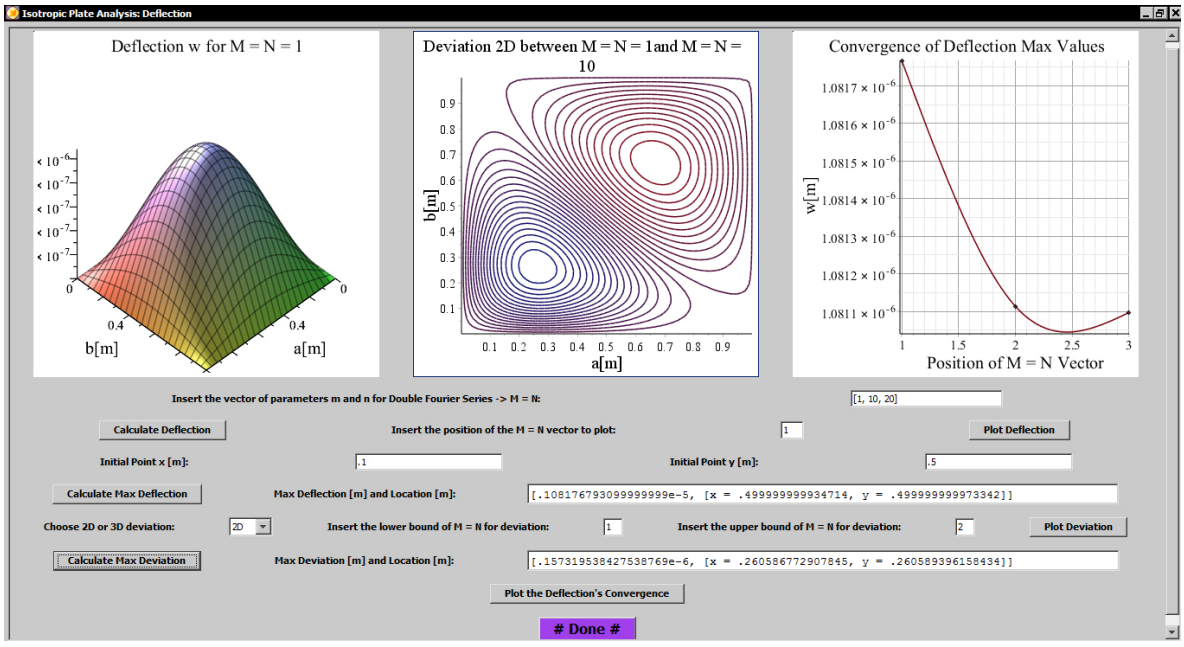

Figure I.4: Characterization of the plate's transverse deflection.

I.2 Experimental set-up: smart testing workbench

I.2.1 Equipment and materials

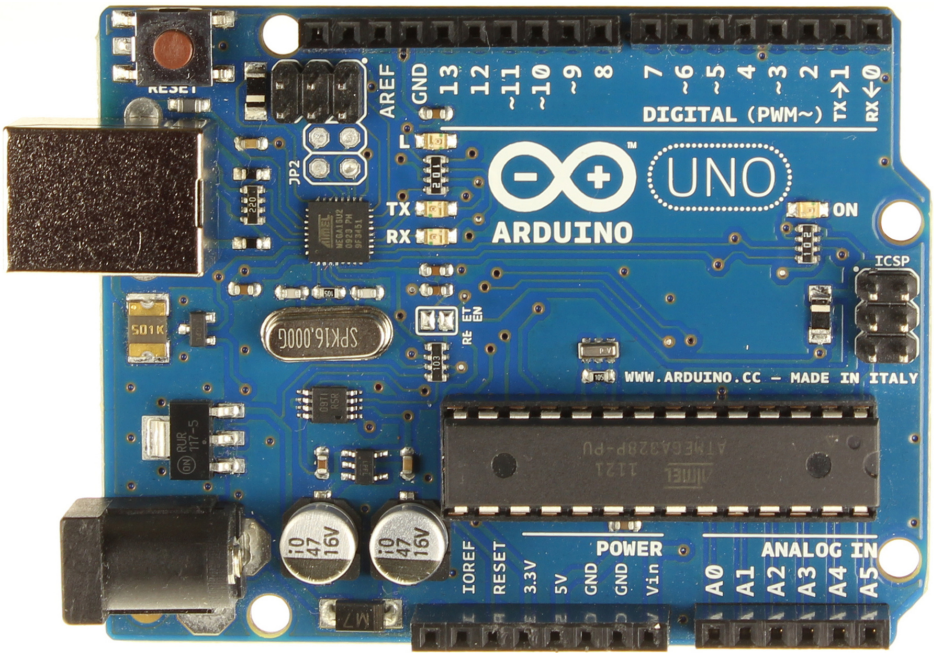

Figure I.5: Micro-controller Arduino® UNO. From Arduino® (2016).

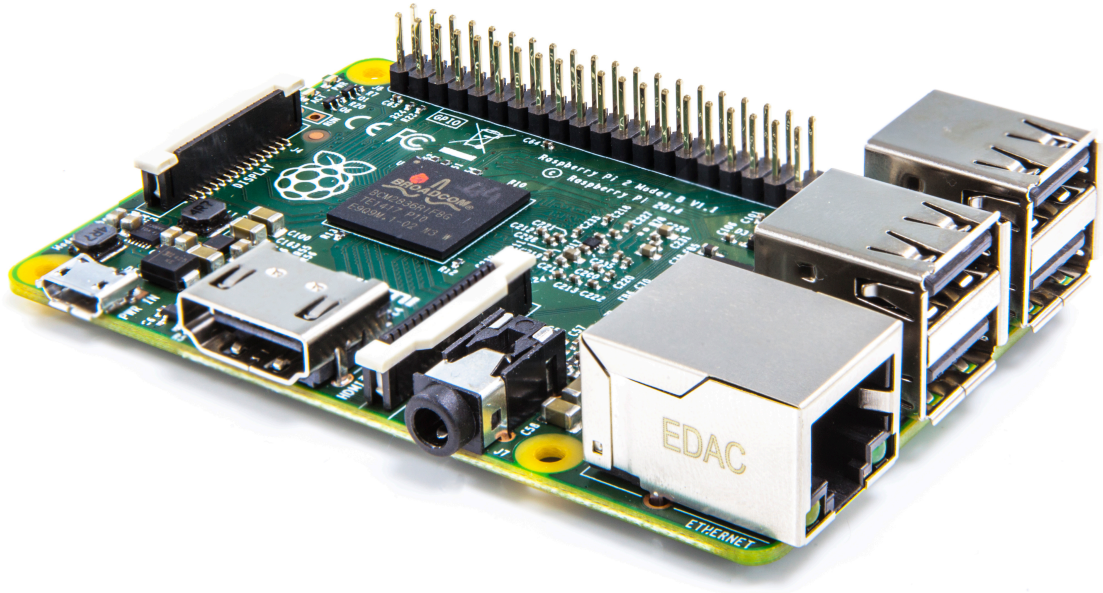

Figure I.6: Micro-computer Raspberry Pi® 2 Model B V1.1. From Raspberry Pi® (2016).

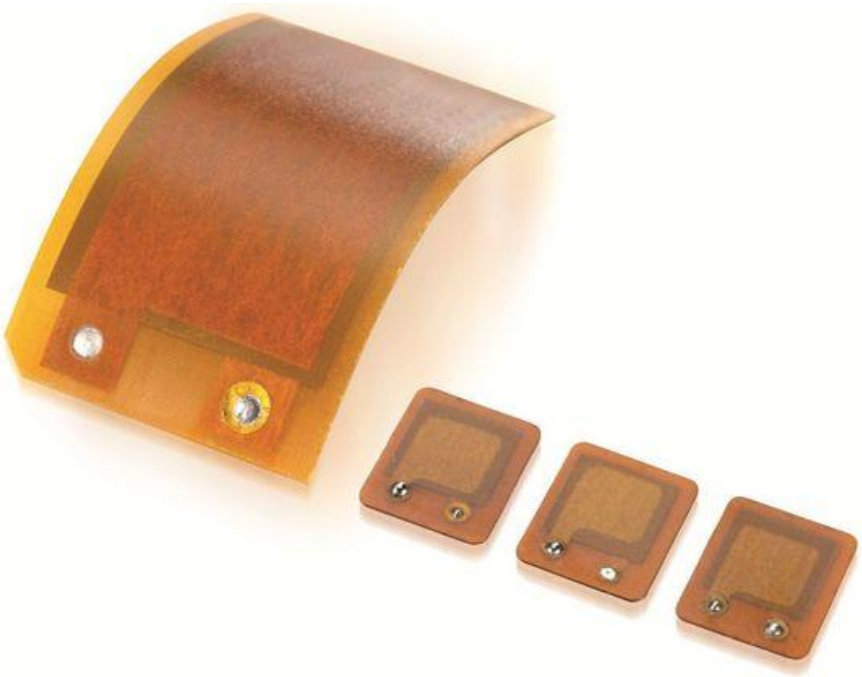

Figure I.7: Piezoelectric patches, DuraAct Patch Transducers. From PI-Ceramic® (2016a).

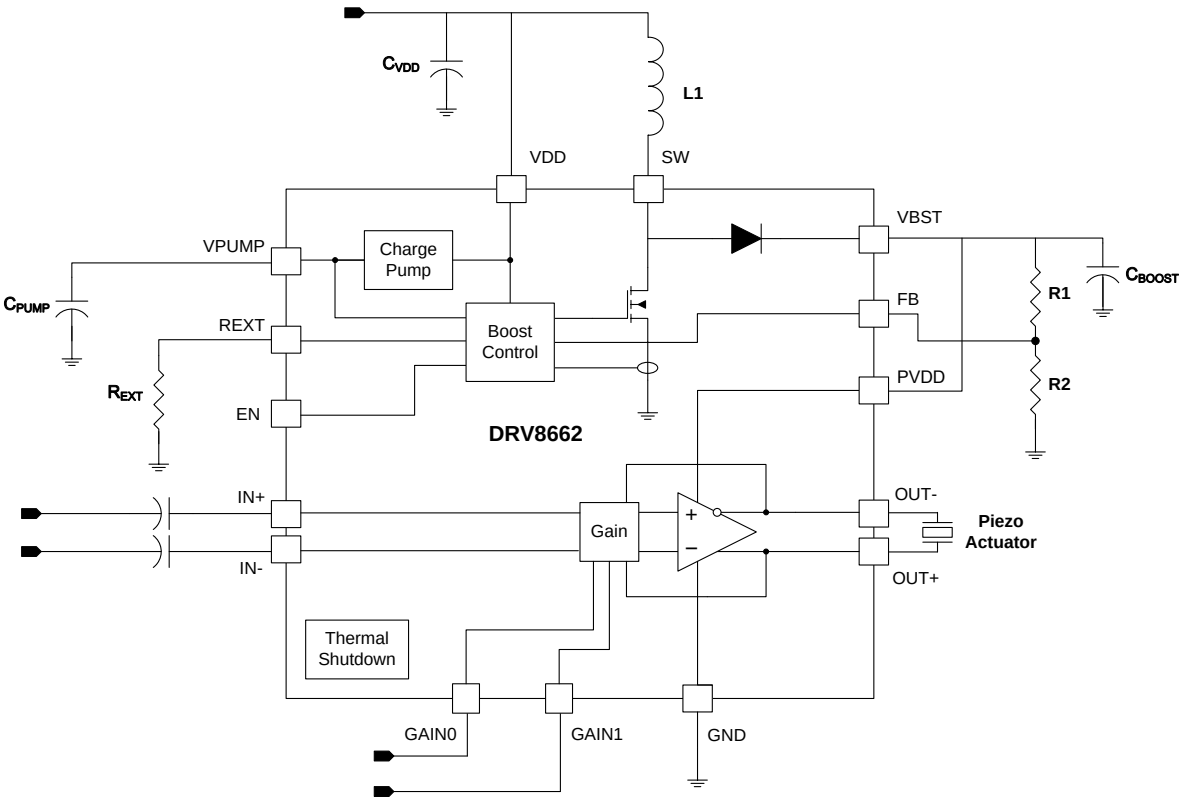

Figure I.8: DRV8662 Piezo Haptic Driver with Integrated Boost Converter (functional block diagram). From Texas Instruments® (2016).

I.2.2 Companies' emails

I.2.2.1 Example of email sent to companies

Good afternoon,

I am a Mechanical Engineering Master's Degree student from Portugal and I study in Instituto Superior de Engenharia de Lisboa (ISEL).

Currently I am writing my Dissertation, which is about the Mechanical Behaviour of Adaptive Structures.

My main goal is to program an optimization algorithm based on Finite Element Method routines, modelling piezoelectric actuators on structures.

Following that, I would like to build a relatively small workbench (e.g. $500 \times 300\,\mathrm{mm}$*) to test one or two different set-ups of instrumented structures controlled by an Arduino (active actuators and sensors) and be able to compare the experimental outputs with my algorithm's results.*

Since this is the first time I want to work with piezo actuators, I am sending this email to get some feedback about this subject (hopefully as soon as possible), in order to find an adequate budget to buy piezo actuators and sensors.

So, the main question is: if, for example, I decide to study a simple aluminium plate of small dimensions, exciting it with a sinusoidal load and try to attenuate its vibrations, which piezo actuator would you recommend? In addition, would I need a piezo amplifier or is it possible to actuate the component with a different source? How much would cost me one piezo actuator (like a bending plate) plus its essential peripherals to do something like this in a small scale?

Finally, assuming that I want to use the same piezo actuator on different structures' surfaces, is it easily movable after glued the first time? Is there an easier solution besides the glued one (using fasteners, bolts or something similar)?

I really want to thank you for your time and ask if you can answer to this email until the end of this week.

Best regards, Diogo Costa.

I.2.2.2 Example of email received from companies no.1

Dear Diogo Costa,

Thank you for your email and your interest in our products. For your experiments I recommend to use one of our P1 type MFCs. To get a little more background regarding these flexible piezoelectric actuators I've attached our MFC brochure to this email. As you can see there the MFCs are available in different sizes so that you can chose a good one with respect to your experiments. The voltage range for the P1 type MFC is from $-500\,\mathrm{V}$ *to* $+1500\,\mathrm{V}$ *so that you will need a high voltage amplifier for that. We offer different types of amplifiers on our website. The MFC – as every other piezo element as well – is a capacitive load for an amplifier so that with increasing frequency the current consumption raises as well. Our small AMD2012 modules are only able to deliver a small current (low power) so that you are limited depending on the MFC size to max* $10\,\mathrm{Hz}$*. For higher frequencies you need to take either the HVA1500/50 or the PA05039 amplifier model*

http://www.smart-material.com/PiezoElectronics-product-main.html?defaulttab=1

We recommend to bond the MFC permanently onto a structure using one of the recommended Epoxy glues (please check our FAQs) as the shear strength of the glue layer is essential for a good performance. Using a non-permanent solution like self-adhesive tapes will generate shear losses and if

you peel the MFC of after the test you will definitely crack and destroy the piezoceramic fibres inside the MFC. Prices for all products you will also find on our website under "Price & Order" http://www.smart-material.com/OrderingPricelist/SQLOrderDE.php
Hope this helps!
Best Regards, Jan.

I.2.2.3 Example of email received from companies no.2

Dear Diogo,
Thank you very much for your email.

It is not quite clear for me the requirements of the piezo actuators you are looking for, so I will give you an overview of the piezos we offer.

Here are all the piezo actuators we offer: http://www.thorlabs.com/navigation.cfm?guide_id=82. For your application, I guess you will need rather the piezo chips than modular actuators, since you will attach the pizeo to a small mass and excite it.

We offer a series of piezo chips, mainly varying from the drive voltage and maximum displacement. The simple piezoelectric chips offer a displacement from $0.7\,\mu\mathrm{m} - 3.6\,\mu\mathrm{m}$*: http://www.thorlabs.com/newgrouppage9.cfm?objectgroup_id=7563.*

Thorlabs also offers two varieties of stacked piezo actuators. The co-fired piezoelectric stacks (http://www.thorlabs.com/newgrouppage9.cfm?objectgroup_id=61) offer maximum displacements from $4.6\,\mu\mathrm{m}$ *to* $17.4\,\mu\mathrm{m}$*, by stacking multiple piezo chips together. And we offer one with a built-in strain gauge for positional feedback, PZS001, the feedback from the strain gauge is used by the controller to provide linear operation of the piezo-electric actuator. Our discrete piezoelectric stacks can supply maximum displacements from* $9.2\,\mu\mathrm{m}$ *to* $57.5\,\mu\mathrm{m}$*. For more information about the design and function of piezoelectric chips, please see our piezoelectric tutorial, http://www.thorlabs.com/NewGroupPage9.cfm?ObjectGroup_ID=5030.*

Unfortunately we don't have a driver to drive these piezos at their resonant frequency. The driving voltage is usually from $75\,\mathrm{V} - 150\,\mathrm{V}$ *for a maximum displacement. You can use an amplifier if your voltage source is small.*

The piezo chips or stacks can be glued to the other material, this will be easiest. However, I am not sure if removing it will damage the piezo accidently, e.g. by force, so to make sure, I will suggest you use two separate piezos.
I hope the information will help you start. Please feel free to ask if there is anything remains unclear.
Best regards, Huihong.

I.2.2.4 Example of email received from companies no.3

Dear Diogo,

Attached you can find a quotation (see Figure I.9)*. Instead of offering you 5 units I offered you 6, the reason in simple. For orders below 300 € you have to pay the delivery cost (30 €) if you order one more ceramic you are a bit over 300 € and you do not have to pay this delivery cost.*

I think It is more cost effective in this way. If you prefer the 5 patches let me know and I redo the quotation.

As you saw the price for 5 units or more is cheaper than for one. This happens with all our ceramics.
For further information do not hesitate to contact me
Best regards Laura.

I.2.2.5 Piezoelectric patches' quotation

miCos Iberia S.L., Pl. de la Vila, 15, 1 A,·E-08800 Vilanova i la Geltrú· Phone: +34-93-816 03 80

miCos Iberia S.L.
Pl. de la Vila 15, 1A
E-08800 Vilanova i la Geltrú
Tel: +34 93 816 03 80
Fax: +34 93 816 03 79
info@pimicos.es
www.pimicos.es

Fundação da Faculdade de Ciências
Instituto Superior de Engenharia de Lisboa

Diogo Miguel Silva Costa
Rua Conselheiro Emídio Navarro, 1
1959-007 Lisboa
Portugal
Teléfono:
Fax:
CIF: PT 503183504

Quotation 201503112

Quotation Date 17/12/2015
Customer 02702
CIF Micos Iberia S.L B64338783

Position	Product Name	Quantity	Unit Price	Discount	Extended Price
	P-876.SP1 DuraAct(TM) Patch Transducer, 16 x 13 x 0,5 mm				
1	**P-876.SP1**	6	51,00 €	0%	306,00 €

Subtotal	**306,00 €**
Total 0%	**0,00 €**
Total amount	**306,00 €**

Delivery time:	approx 4 - 5 weeks after receipt of order
Conditions of payment:	Transportation included. For orders below € 300 applies a surcharge of 30 €
Method of payment:	To pay within 30 days after receipt of the goods
Bank:	Caixa Penedès; C/Llibertat, 134;08800 Vilanova i la Geltrú
Account number:	CCC: 2081 0049 87 3300015360
Validity of quotation:	60 days

If you have any further questions, please contact us. Thank you for your interest; we look forward to hearing from you soon.

With best regards,

Sra. Laura Luna
phone: +34-93 816 03 80
info@pimicos.es

Figure I.9: PI-Ceramic® piezoelectric patches' quotation.